

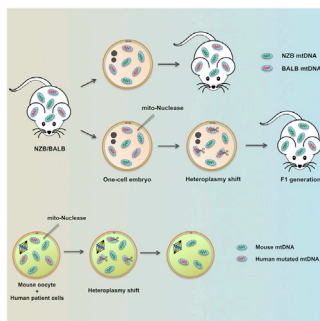


Cell

Volume 161
Number 3

April 23, 2015

www.cell.com



Genome Editing of Germline Mitochondria

PAGE 459

Currently, there is no treatment for inherited disorders caused by mutations in mtDNA. Using mitochondria-targeted nucleases, Reddy et al. eliminate germline mtDNA mutations to prevent their transgenerational transmission. This strategy represents a potential therapeutic avenue for treating human mitochondrial disease.

T Cells Keep Their Distance

PAGE 486

T cells are typically thought to kill cells from within an infected tissue. However, Guidotti et al. find that in viral hepatitis, cytotoxic T cells control the infection without migrating into the liver parenchyma. Rather, they arrest within the small blood vessels that permeate the liver

and probe proximal hepatocytes for the presence of antigens, secreting cytokines and killing infected cells. Liver fibrosis limits this process, explaining why immune surveillance is compromised during chronic hepatitis.

Tackling Replication Head On

PAGE 513

Eukaryotic DNA replication gets underway when two copies of the replicative helicase are loaded at an origin to initiate bidirectional replication. Using single-molecule assays, Ticaud et al. show that distinct mechanisms load the two helicases and that interactions between the first and second helicases ensure a head-to-head architecture, setting the origin up for bidirectional DNA synthesis.

NET Capture of Human Transcription

PAGE 526 and PAGE 541

Nojima et al. and Mayer et al. develop independent methods rooted in native elongating transcript sequencing in human cells to capture high-resolution snapshots of the dynamic events during transcription. The two studies provide insights into poII regulation and movement and the coordination between transcription and pre-mRNA splicing. Together, the two studies offer detailed insights into the multiple layers of transcriptional regulation.

Cracking Compacted Chromatin

PAGE 555

Pioneer transcription factors access compacted chromatin and initiate cell-fate changes. Soufi et al. now discover that this characteristic activity, important for initiating reprogramming, relates to a TF's ability to target partial motifs displayed on the nucleosome surface. For other TFs, tagging along with a pioneer factor enhances their partial motif recognition and allows nucleosome binding.

Gradient on a Curve

PAGE 569

Intestinal villi form through mechanically induced buckling of the epithelial surface. Shyer et al. show that this change in tissue architecture concentrates the morphogen sonic hedgehog under the villus tip, thereby restricting stem cells to the villus base.

Lipids Mediate Chatter across the Membrane

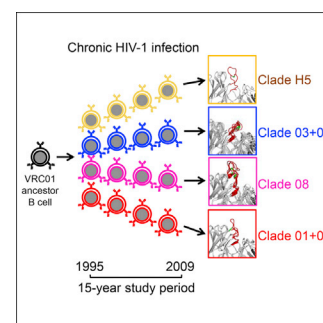
PAGE 581

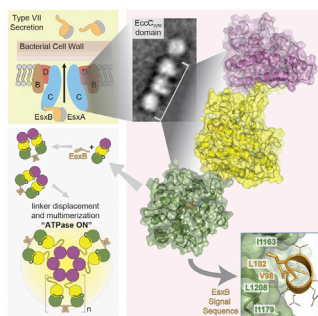
Raghupathy et al. discover that transbilayer interactions mediated by long acyl chain-containing lipids are pivotal in generating actin-dependent nanoclusters of outer membrane lipid anchored proteins. Inner-leaflet phosphatidylserine serves as the link between the outer-leaflet lipid and the actin cytoskeleton. These interactions could form the basis for generation of functional lipid domains at the plasma membrane.

“Boyhood” for Neutralizing Antibodies

PAGE 470

Broadly neutralizing antibodies control HIV infection but are hard to elicit. To understand how they develop, Wu et al. followed the antibody response in a patient during 15 years of HIV-1 infection. They find that the potent VRC01 broadly neutralizing antibody lineage evolves from a single B cell. Antibody maturation occurs at a gradually decreasing evolutionary rate over many years, matching the rate of evolution of the virus, in order to achieve extraordinary antibody diversity necessary for viral neutralization.





Engineering Your Own Escape

PAGE 501

Type VII protein secretion is critical for virulence of several medically important pathogens. Rosenberg et al. reveal that for translocation to occur, the virulence protein EsxB first has to help assemble and activate the structure that secretes it.

The Benefit of the Burn

PAGE 595

Lactate is a well-known product of anaerobic metabolism, and now Lee et al. demonstrate that it can signal a hypoxic response that is independent of the well-characterized HIF pathway. Lactate binds to and stabilizes the NDRG3 protein enabling it to activate signaling that promotes cell growth and angiogenesis. Thus, lactate can serve a protective role under hypoxic stress.

Edema Explained

PAGE 610

Neuronal swelling is the major cause of death in traumatic and ischemic brain injuries. Rungta et al. reveal that this process is initiated when aberrant entry of sodium ions and depolarization activates the voltage-gated chloride channel, SLC26A11. The increase of cytoplasmic sodium and chloride causes an osmotic imbalance that leads to water entry and cytotoxic edema, a mechanism that could be targeted to prevent and treat brain edema.

Coincidence Detection in Maternal Inheritance

PAGE 634

Stronger effects of maternal genomes than paternal ones on offspring have been attributed to maternal RNA and imprinting. However, in the case of mutations causing congenital eye disease, the skewed inheritance pattern, as shown by Chou et al., results from altered binding interactions that become combinatorially disruptive for Vitamin A delivery when it occurs both within the fetus and from maternal tissues supplying the placenta. The findings define a new type of physiological maternal inheritance.

Ripple Effect of Human Mutations

PAGE 647

To determine the effects of disease-associated mutations on protein activities in the context of biological networks, Sahni et al. perform a systematic characterization of protein-chaperone, protein-protein, and protein-DNA interactions of missense alleles implicated in human genetic disorders. The analysis reveals surprisingly widespread and specific perturbations of macromolecular interactions with disease alleles. Distinct disease mutations in the same gene that give rise to different interaction profiles often result in distinct disease phenotypes.

Any Sequence, Every Protein

PAGE 661

Approaches for assessing what transcription factors bind to a given DNA sequence are currently limited, rendering it difficult to elucidate gene regulatory architecture and to understand the impacts of mutations in non-coding regions. Bass et al. move to fill this gap by applying yeast one-hybrid assays to human TFs and enhancers and disease-associated mutations in non-coding regions. The study uncovers principles of TF-enhancer interaction in disease and development, and provides a readily expandable resource of candidate interaction patterns.

A TOP Method to Get Proteins into Cells

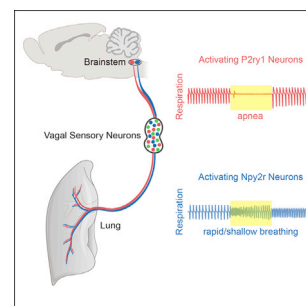
PAGE 674

While methods for introducing nucleic acids into target cells are well-developed, it's more of a challenge for proteins, particularly when transducing primary cells. A new method (iTOP) developed by D'Astolfo et al. addresses this challenge, drawing on salt-mediated macropinocytosis in conjunction with a small molecule. This technique may be especially helpful for the manipulation of cells that are otherwise difficult to transfect or for gene-editing in primary cells.

Finding the Nerve to Breathe

PAGE 622

The vagus nerve is a complex heterogeneous assembly of neurons controlling many aspects of physiology. Chang et al. begin to get a molecular genetic handle on these neurons by identifying two classes of molecularly distinct sensory cells with differing lung-to-brain connectivity patterns. Optogenetic activation of one class acutely silences breathing, trapping animals in a state of exhalation, while activating the other causes rapid and shallow breathing.



HIV Antibodies Return to Clinical Trials

Almost 35 years after the first cases of immunodeficiency associated with HIV were reported, the HIV infection has spread worldwide, reaching nearly 40 million people. Antiretroviral therapy has evolved at a fast pace, and combined drug therapy is now part of the standard care of HIV-infected individuals, successfully preserving their health and lifespan in most cases. The endless capacity of the virus to subvert the host immune response and to persist in a latent state nonetheless has been frustrating and challenges the expectation that a definitive cure and an effective vaccine would be easily achievable.

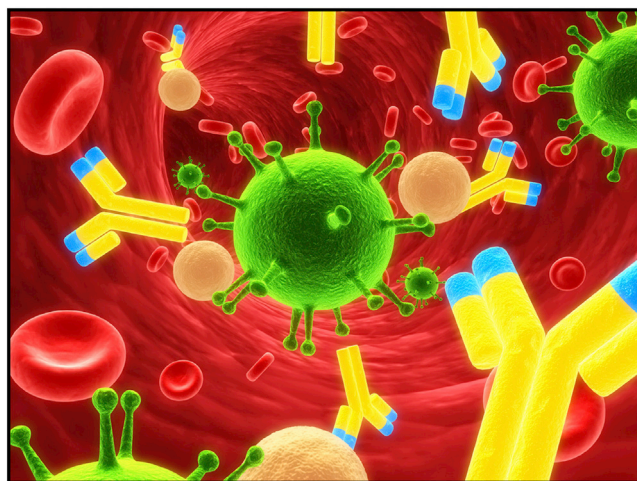
Immunotherapy using combinations of monoclonal antibodies that are injected in infected subjects to neutralize the virus and stimulate immune-mediated killing of infected cells was a particularly promising concept. However, it failed to demonstrate any efficacy in initial pre-clinical and clinical studies in part due the ability of the virus to rapidly mutate and escape the antibodies. [Caskey et al. \(2015\)](#) now return to this original concept and report the initial results of a first-in-humans dose escalation phase 1 clinical trial using the 3BNC117 anti-HIV antibody in infected and uninfected people. The antibody infusion is safe and well-tolerated, and a single injection is able to reduce the viral load of infected subjects by 0.8–2.5 log₁₀ for up to 1 month. What is different about the 3BNC117 antibody that gives it an advantage over the virus?

In recent years, it has become clear that a small fraction of people living with HIV-1 develop a flavor of antibodies with a very particular feature: they are very potent at neutralizing different variants of the HIV ([West et al., 2014](#)). These molecules, termed broadly neutralizing antibodies (bNAbs), usually target regions of the viral envelope that are conserved in viral isolates from different origins,

and therefore, they are able to bind and neutralize a large fraction of variants of the virus. The evolution in the methods to isolate and clone antibodies allowed researchers to identify several bNAbs and study their characteristics and the sites that they bind to in the virus. In contrast to the first generation of monoclonal antibodies that were ineffective as HIV-1 immunotherapy, 3BNC117 is a very potent broadly neutralizing antibody, capable of neutralizing 195 out of 237 different HIV-1 strains ([Scheid et al., 2011](#)). Its target is the CD4-binding site on the viral protein gp120, the portion of the molecule that interacts with the CD4 receptor in the host cells. This interaction is crucial for the initial stages of the viral infection, and therefore, it is a conserved site among different strains of the virus and it is one of the few sites in the protein that are not decorated with the glycan shield that protects it against antibody recognition.

Broadly neutralizing antibodies are the almost perfect tool against not just HIV-1 but also other highly mutagenic viruses such as influenza, and stimulating individuals to produce them with vaccines is a current goal. The problem is that they are very difficult to elicit under natural conditions. The study of their properties shows that they accumulate a large number of somatic mutations, deletions, and insertions that are infrequent in conventional antibodies ([West et al., 2014](#)). Likely, they take many years to arise during natural infection, and the reasons why a few people develop them—but the majority of the infected humans does not—are unknown. Identifying bNAbs that are naturally generated is an important strategy to overcome this barrier, as they could be used to treat or promote passive protection against the infection. In fact, the combination of different potent broadly neutralizing antibodies suppresses HIV-1 viral load in humanized mice. Additionally, therapy with single bNAbs can suppress viremia in non-human primates infected with a simian immunodeficiency virus that is closely related to the human virus ([West et al., 2014](#)).

The antibodies are only able to suppress HIV infection for a limited period in experimental models and in the new clinical trial. In humanized mice and non-human primates, the viremia remains suppressed as long as the concentration of the antibody in the blood remains within therapeutic range. In the new clinical trial, 3BNC117-resistant viruses emerged in a fraction of the patients 28 days after the infusion ([Caskey et al., 2015](#)). Still, the fact that some individuals did respond to immunotherapy, even if transiently, renews the hopes that this strategy is worthy of pursuing. As with antiretroviral drugs, combination of different reagents may prove to be more efficacious than single-antibody therapy in humans. In addition, engineering bNAbs to improve their effector functions—for instance, antibody-dependent cellular cytotoxicity ([Bournazos et al., 2014](#))—or to increase the affinity for their targets could also contribute to their clinical efficacy. Finally, antibodies are expensive to produce, so it is unlikely that they will become the first line of treatment for patients with HIV in



Several potent anti-HIV broadly neutralizing antibodies have been identified to date and have the potential to be used in strategies to treat and prevent HIV spread in combination with other types of drugs. Image from iStockphoto/Eraxion.

monotherapy. However, in combination with drugs that can activate latent viruses, interfering and potentially clearing the latent HIV-1 reservoir (Halper-Stromberg et al., 2014), they may be critical to development of the long-sought cure for HIV infection.

REFERENCES

- Bournazos, S., Klein, F., Pietzsch, J., Seaman, M.S., Nussenzweig, M.C., and Ravetch, J.V. (2014). *Cell* 158, 1243–1253.
- Caskey, M., Klein, F., Lorenzi, J.C.C., Seaman, M.S., West, A.P., Buckley, N., Kremer, G., Nogueira, L., Brauschweig, M., Scheid, J.F., et al. (2015). *Nature*. Published online April 8, 2015. <http://dx.doi.org/10.1038/nature14411>.
- Halper-Stromberg, A., Lu, C.L., Klein, F., Horwitz, J.A., Bournazos, S., Nogueira, L., Eisenreich, T.R., Liu, C., Gazumyan, A., Schaefer, U., et al. (2014). *Cell* 158, 989–999.
- Scheid, J.F., Mouquet, H., Ueberheide, B., Diskin, R., Klein, F., Oliveira, T.Y., Pietzsch, J., Fenyo, D., Abadir, A., Velinzon, K., et al. (2011). *Science* 333, 1633–1637.
- West Jr., A.P., Scharf, L., Scheid, J.F., Klein, F., Bjorkman, P.J., and Nussenzweig, M.C. (2014). *Cell* 156, 633–648.

João Monteiro

Natural Evolution of Broadly Neutralizing Antibodies

Galit Alter¹ and Dan H. Barouch^{1,2,*}

¹Ragon Institute of MGH, MIT, and Harvard, Cambridge, MA 02138, USA

²Center for Virology and Vaccine Research, Beth Israel Deaconess Medical Center, Boston, MA 02215, USA

*Correspondence: dbarouch@bidmc.harvard.edu

<http://dx.doi.org/10.1016/j.cell.2015.04.007>

Wu et al. couple next-generation sequencing with structural analysis to illuminate the key processes that enable the natural evolution and selection of broadly neutralizing antibodies to HIV-1, providing a potential roadmap for the development of HIV-1 vaccine strategies to accelerate the induction of protective antibodies.

The generation of broadly reactive neutralizing antibodies is the holy grail of HIV-1 vaccine research, but no HIV-1 vaccine candidate has realized this goal to date. A substantial fraction of HIV-1-infected individuals is able to induce broadly neutralizing antibody responses over time (Mikell et al., 2011; Gray et al., 2011). Interestingly, high viral loads and chronic antigen exposure typically appear to contribute to the generation of broadly neutralizing antibodies (Piantadosi et al., 2009; Liao et al., 2013), although some broadly neutralizing antibodies have also been cloned from subjects with spontaneous control of viral replication. These antibodies typically have high levels of somatic mutations (Burton et al., 2012; West et al., 2014). Although the prospect of designing a vaccine that can induce this degree of somatic hypermutation is daunting, understanding the natural evolutionary path of the development of these antibodies may provide important clues for the generation of vaccine immunogens and strategies that ultimately aim to recapitulate this pathway.

In a tour-de-force study in this issue of *Cell*, Wu et al. (2015) used next-generation sequencing coupled with detailed structural determinations to reconstruct the evolutionary process that led to the development of a series of potent and broad neutralizing antibodies directed against the CD4 binding site in a single donor from 1995 to 2009. Evolutionary analyses highlight the remarkable diversity of the VRC01 lineage, with at least six heavy-chain lineages and five light-chain lineages. Interestingly, these clonal families fell into three major clades, with up to

25% intra-clade sequence divergence and up to 50% inter-family divergence. Each clade exhibited marked increases in somatic hypermutation over this period of time, suggestive of progressive evolution over 15 years. Remarkably, all clonal families were represented at the earliest time points, suggesting early selection that continued to expand in parallel in a progressive manner over the study period. Strikingly, new families reflecting the selection of novel germline B cell populations by the evolving virus did not emerge. These data collectively point to the early selection and progressive development of a finite set of naive B cell families.

Despite dramatic sequence diversity among the clades, all representative antibodies from each family recognized an almost identical footprint on the viral envelope, sharing up to 95% conservation in the paratope surface. However, each family evolved a different structural solution to reach the unusual deeply recessed shape of this site of vulnerability on the HIV-1 envelope, illustrating that there are several immunologic solutions to the same structural antigenic problem. These results argue that the immune system harbors a remarkable capacity to explore a wide landscape of solutions to neutralize difficult epitopes. The early selection of several germline B cells followed by continuous evolution over a substantial period of time may therefore be critical for the generation of broadly neutralizing antibody responses.

It is well known that HIV-1 mutates at a remarkable frequency, ~1.5 substitutions per 100 nucleotides per year. Interestingly, this mutation rate was surpassed

by the evolution of the VRC01 lineage, which incorporated ~2 substitutions per 100 nucleotides per year. Thus, the humoral immune response evolved more rapidly than the virus in this individual, suggesting a mechanism by which antibody lineages can achieve extraordinary diversity in the setting of chronic HIV-1 infection (Figure 1). The mutation rates in the evolution of other broadly neutralizing antibodies showed even higher mutation rates of 9 to 11 substitutions per 100 nucleotides per year for the V1V2-specific antibody CAP256 and the CD4 binding site-specific antibody CH103. It is unclear whether these accelerated rates of mutation are attributable to higher viral loads in the CAP256 and CH103 donors, easier to neutralize features of the antibody paratopes, peculiarities in the host background of the donors, or simply the fact that these antibodies evolved within the first year of infection under distinct inflammatory conditions. However, for all three antibodies, kinetic analyses of evolutionary rates suggested a trend toward more rapid evolution of the antibody response in early infection that slowed during later states of infection. These data suggest the importance of developing vaccine strategies that drive rapid and persistent B cell selection at these levels. Defining the key triggers that drive accelerated somatic hypermutation, which would allow B cells to explore immunologic solutions more quickly and rigorously, may therefore improve the ability of vaccines to elicit broadly neutralizing antibodies to HIV-1.

The concept that carefully selected Env immunogens may be able to guide B cell

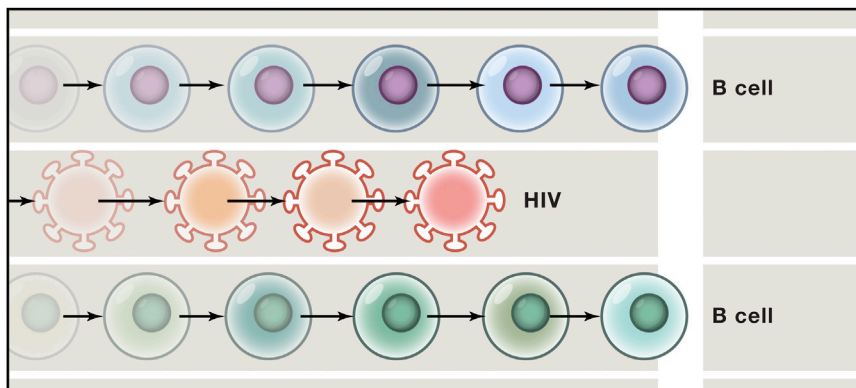


Figure 1. Relative Kinetics of the Evolution of HIV-1 and the VRC01 Antibody Lineage

The antibody lineage evolved more rapidly than the virus did in this individual, suggesting a mechanism by which B cells can achieve extraordinary diversity in the setting of chronic HIV-1 infection.

development down a particular pathway by sequential vaccination strategies has gained support. The evolutionary complexity highlighted in this study, however, suggests that the design or selection of discrete immunogens able to recapitulate antigen-driven B cell selection pathways will be challenging. Strategies that aim to deliver persistent immunogens, such as with the use of replicating vectors, are therefore being explored. Whether viral evolution is also required to drive broadly neutralizing antibody responses remains to be determined. Although a burst in viral diversity has been linked to the rapid evolution of neutralizing responses in certain cases

(Liao et al., 2013), some broadly neutralizing antibodies have been isolated from subjects that exhibit spontaneous control of viral replication and therefore reduced viral diversity.

Several unanswered questions remain. One key question is whether similar degrees of evolutionary complexity are required for the development of broadly neutralizing antibodies against other key targets, such as the V2 or V3 glycan-dependent epitopes, the membrane-proximal external region, and the gp120-gp41 binding interface. Another important question is whether triggers that drive accelerated somatic hypermutation can be defined and utilized to allow vaccine-

elicited B cells to explore immunologic solutions more rapidly. Overall, the present studies chart the development of CD4 binding site antibodies in a remarkable level of detail, providing insights into the plasticity of the immune response and the path to the generation of broadly neutralizing antibodies.

REFERENCES

- Burton, D.R., Ahmed, R., Barouch, D.H., Butera, S.T., Crotty, S., Godzik, A., Kaufmann, D.E., McElrath, M.J., Nussenzweig, M.C., Pulendran, B., et al. (2012). *Cell Host Microbe* 12, 396–407.
- Gray, E.S., Madiga, M.C., Hermanus, T., Moore, P.L., Wibmer, C.K., Tumba, N.L., Werner, L., Mlisana, K., Sibeko, S., Williamson, C., et al.; CAPRISA002 Study Team (2011). *J. Virol.* 85, 4828–4840.
- Liao, H.X., Lynch, R., Zhou, T., Gao, F., Alam, S.M., Boyd, S.D., Fire, A.Z., Roskin, K.M., Schramm, C.A., Zhang, Z., et al.; NISC Comparative Sequencing Program (2013). *Nature* 496, 469–476.
- Mikell, I., Sather, D.N., Kalams, S.A., Altfield, M., Alter, G., and Stamatatos, L. (2011). *PLoS Pathog.* 7, e1001251. <http://dx.doi.org/10.1371/journal.ppat.1001251>.
- Piantadosi, A., Panteleeff, D., Blish, C.A., Baeten, J.M., Jaoko, W., McClelland, R.S., and Overbaugh, J. (2009). *J. Virol.* 83, 10269–10274.
- West, A.P., Jr., Scharf, L., Scheid, J.F., Klein, F., Bjorkman, P.J., and Nussenzweig, M.C. (2014). *Cell* 156, 633–648.
- Wu, X., Zhang, Z., Schramm, C.A., Joyce, M.G., Do Kwon, Y., Zhou, T., Sheng, Z., Zhang, B., O'Dell, S., McKee, K., et al. (2015). *Cell* 161, this issue, 470–485.

Single-Molecule Visualization of MCM2-7 DNA Loading: Seeing Is Believing

Gheorghe Chistol¹ and Johannes C. Walter^{1,2,*}

¹Department of Biological Chemistry and Molecular Pharmacology, Harvard Medical School, Boston, MA 02115, USA

²Howard Hughes Medical Institute

*Correspondence: johannes_walter@hms.harvard.edu

<http://dx.doi.org/10.1016/j.cell.2015.04.006>

The first event in the initiation of eukaryotic DNA replication is the recruitment of the MCM2-7 ATPase, the core of the replicative DNA helicase, to origins. Ticaú et al. use single-molecule imaging to reveal how ORC, Cdc6, and Cdt1 cooperate to load MCM2-7 onto DNA, enabling bidirectional replication.

Eukaryotic cells copy their vast genomes by initiating DNA replication from thousands of origins of replication. To insure that replication initiates at every origin precisely once per cell cycle, cells divide the process of initiation into two stages. In G1 phase, two copies of the MCM2-7 ATPase are loaded onto origin DNA to form a “pre-replication complex” (pre-RC) (Figure 1). This process requires three “licensing” factors: a hexameric AAA+ ATPase called ORC (origin recognition complex), another AAA+ ATPase called Cdc6, and Cdt1. When it is first loaded, MCM2-7 encircles double-stranded DNA and is inactive as a DNA helicase. In S phase, the two MCM2-7 complexes associate with the helicase co-factors, Cdc45 and GINS, forming two active CMG helicases that encircle single-stranded DNA, unwind the origin, and nucleate the assembly of two replisomes that travel away from the origin, copying DNA as they go. Importantly, once cells enter S phase, multiple mechanisms prevent de novo MCM2-7 loading onto origins. As a result, each origin fires only once per cell cycle. In this issue, Ticaú et al. (2015) use single-molecule imaging to reveal how yeast MCM2-7 double hexamers are loaded at replication origins (Figure 1).

Recent studies showed that ORC, Cdc6, Cdt1, and MCM2-7 are necessary and sufficient for pre-RC assembly (Remus et al., 2009); revealed various MCM2-7 loading intermediates (Fernández-Cid et al., 2013; Sun et al., 2013; Sun et al., 2014); and determined how MCM2-7 subunits interact via their

N termini within the so-called double hexamer (Costa et al., 2014; Sun et al., 2014). However, the most fundamental question—how an origin containing a single ORC-binding site supports the head-to-head loading of two MCM2-7 molecules—remains unanswered: Are the two MCM2-7 hexamers loaded simultaneously or one at a time? Are the two MCMs loaded via the same or different mechanisms? Does one DNA-bound ORC complex load both MCM2-7 hexamers, or is there participation by a second ORC bound at a cryptic site? Of the helicase-loading intermediates captured in recent structural studies, which complexes are on pathway? Other questions refer to the exact roles of Cdc6 and Cdt1 and the order in which they arrive and depart from the origin during licensing.

To answer these questions, Ticaú et al. established a single-molecule loading assay with recombinant yeast proteins. A fluorescently labeled DNA containing the yeast origin of replication was immobilized on a coverslip and imaged via total internal reflection fluorescence microscopy. One or two fluorescently labeled licensing factors (for example, MCM2-7 and Cdc6, or MCM2-7 and Cdt1) and ATP were added to the flow cell, and protein binding and unbinding on DNA was monitored in real time by co-localizing the fluorescent signals from the nucleic acid and the protein of interest. This assay determined the arrival and departure times of proteins relative to each other and identified short-lived intermediates not detected in ensemble or structural approaches. Photobleaching experiments

established the stoichiometry of bound factors.

Monitoring the binding of fluorescently labeled MCM2-7 hexamers to DNA revealed that MCM2-7 is recruited one hexamer at a time, providing definitive support for previous models (Fernández-Cid et al., 2013; Sun et al., 2013, 2014). The authors then examined the relative timing of Cdc6 and Cdt1 recruitment to replication origins. MCM2-7 and Cdt1 form a hetero-heptameric complex in solution (Kawasaki et al., 2006) while DNA-bound ORC forms a complex with Cdc6 (Sun et al., 2012). The single-molecule approach showed that Cdc6 binds to ORC before MCM2-7•Cdt1 arrives at an origin, indicating that Cdc6 primes the origin recognition complex to recruit the first MCM2-7 hexamer (Figure 1). Moreover, after MCM2-7•Cdt1 binding, Cdc6 is always released before Cdt1. Interestingly, Cdc6/Cdt1 departure times are significantly longer after loading of the second MCM2-7 ring compared to the first MCM2-7 ring, suggesting that the two hexamers are recruited differently. In addition, the kinetics of Cdc6/Cdt1 departure suggests that several processes occur between the arrival of MCM2-7 and the release of Cdc6/Cdt1. The number and identity of these steps is unclear and should be investigated in future studies.

Finally, Ticaú et al. examined ORC dynamics during pre-RC assembly. By simultaneously monitoring fluorescently labeled ORC and MCM2-7, they discovered that a single ORC complex remains bound to the origin during the arrival of

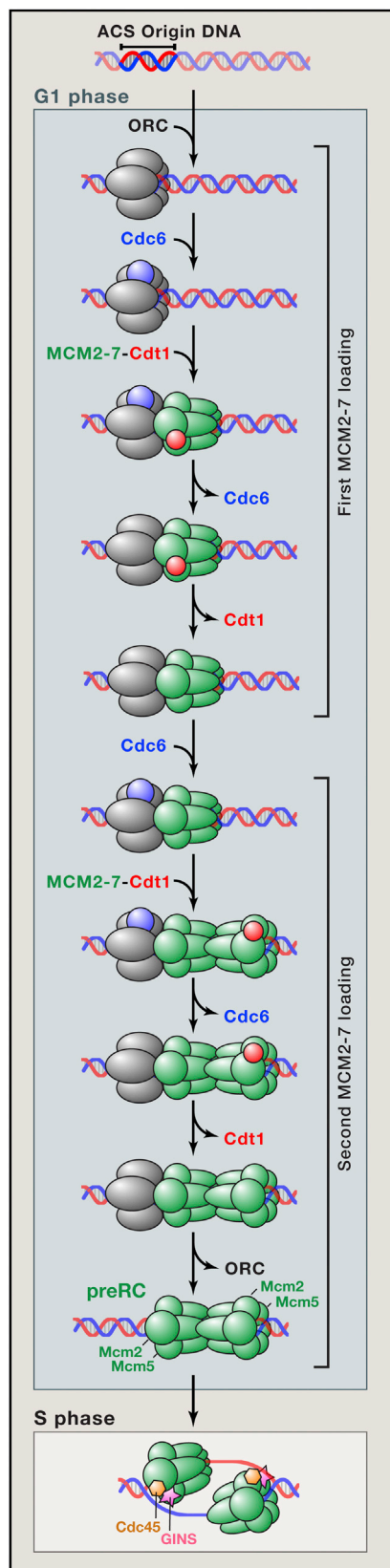


Figure 1. Loading Stages of the Eukaryotic Replicative Helicase

During G1, the eukaryotic replicative helicase is loaded as a preRC complex at the replication origin (ACS in yeast). Each preRC consists of two MCM2–7 hexamers encircling dsDNA. Establishing the necessary head-to-head association of the hexamers involves cooperation between the origin recognition complex (ORC) and licensing factors Cdc6 and Cdt1. At the beginning of the S phase, the preRC is activated and associates with Cdc45 and GINS to form two CMG complexes that travel on ssDNA away from the origin. Ticaú et al. dissected the stages of preRC loading.

both MCM2–7 hexamers, ruling out any models that require two ORCs to form a preRC (Figure 1). Importantly, ORC interacts with the C-terminal domains of MCM2–7 during loading (Sun et al., 2013), yet in the final pre-RC, the two MCM2–7 rings interact via their N termini. Therefore, ORC cannot recruit the first and second MCM2–7 hexamers by the same mechanism, in agreement with the longer departure time of Cdc6/Cdt1 after the second MCM2–7 arrival. As MCM2–7 complexes do not interact in solution, the first loaded MCM2–7 complex must adopt a conformation that is competent for interaction with the second MCM2–7 through their N termini. Notably, Cdc6 binding (presumably to ORC) precedes loading of the second MCM2–7 complex, suggesting that it is required for this event. It will be interesting to understand how Cdc6 performs this function, given its distal location relative to the second MCM2–7 loading event (Figure 1). Ticaú et al. also revealed that ORC dissociates from the origin soon after loading of the second MCM2–7, disfavoring mechanisms in which one DNA-bound ORC assembles several pre-RCs.

The work by Ticaú et al. is complemented by a study in *Molecular Cell* (Duzdevich et al., 2015), which explores other facets of pre-RC assembly, as well as downstream events of origin activation. This work shows that Cdc6 reduces the affinity of soluble ORC for DNA, effectively insuring that ORC normally binds DNA before Cdc6. Inducing pre-RC activation with yeast S-phase extract reveals that activation of the two MCM2–7 complexes in the pre-RC is temporally and thus probably mechanistically coupled. The study

also confirms models featuring actively replicating forks containing a single copy of the MCM2–7 ATPase. Finally, experiments by Duzdevich and colleagues support the findings of Ticaú et al. that one and the same ORC complex directs the loading of both MCM2–7 hexamers comprising the preRC.

The work by Ticaú et al. illustrates the power of simultaneously labeling pairs of proteins and watching them assemble into a multi-protein complex. The work provides the most definitive roadmap to date of the complex process underlying pre-RC assembly and identifies which intermediates should be pursued in structural studies. Now that origin unwinding and replisome assembly have also been reconstituted with purified components (Yeeles et al., 2015), we can expect the full power of single-molecule analysis to be applied to understanding the dynamics of these processes.

REFERENCES

- Costa, A., Renault, L., Swuec, P., Petojevic, T., Pesavento, J.J., Ilves, I., MacLellan-Gibson, K., Fleck, R.A., Botchan, M.R., and Berger, J.M. (2014). *Elife* 3, e03273.
- Duzdevich, D., Warner, M.D., Ticaú, S., Ivica, N.A., Bell, S.P., and Greene, E.C. (2015). *Mol. Cell* 58. Published online April 23, 2015. <http://dx.doi.org/10.1016/j.molcel.2015.03.017>.
- Fernández-Cid, A., Riera, A., Tognetti, S., Herrera, M.C., Samel, S., Evrin, C., Winkler, C., Gardenal, E., Uhle, S., and Speck, C. (2013). *Mol. Cell* 50, 577–588.
- Kawasaki, Y., Kim, H.D., Kojima, A., Seki, T., and Sugino, A. (2006). *Genes Cells* 11, 745–756.
- Remus, D., Beuron, F., Tolun, G., Griffith, J.D., Morris, E.P., and Diffley, J.F.X. (2009). 139, 719–730.
- Sun, J., Kawakami, H., Zech, J., Speck, C., Stillman, B., and Li, H. (2012). *Structure* 20, 534–544.
- Sun, J., Evrin, C., Samel, S.A., Fernández-Cid, A., Riera, A., Kawakami, H., Stillman, B., Speck, C., and Li, H. (2013). *Nat. Struct. Mol. Biol.* 20, 944–951.
- Sun, J., Fernandez-Cid, A., Riera, A., Tognetti, S., Yuan, Z., Stillman, B., Speck, C., and Li, H. (2014). *Genes Dev.* 28, 2291–2303.
- Ticaú, S., Friedman, L.J., Ivica, N.A., Gelles, J., and Bell, S.P. (2015). *Cell* 161, this issue, 513–525.
- Yeeles, J.T.P., Deegan, T.D., Janska, A., Early, A., and Diffley, J.F. (2015). *Nature* 519, 431–435.

Gradients Are Shaping Up

Tobias Bollenbach¹ and Carl-Philipp Heisenberg^{1,*}

¹Institute of Science and Technology Austria, Am Campus 1, 3400 Klosterneuburg, Austria

*Correspondence: heisenberg@ist.ac.at

<http://dx.doi.org/10.1016/j.cell.2015.04.009>

In animal embryos, morphogen gradients determine tissue patterning and morphogenesis. Shyer et al. provide evidence that, during vertebrate gut formation, tissue folding generates graded activity of signals required for subsequent steps of gut growth and differentiation, thereby revealing an intriguing link between tissue morphogenesis and morphogen gradient formation.

The graded distribution of morphogens plays a fundamental role in many developmental and disease-related processes. Such morphogen gradients control cell differentiation in a concentration-dependent manner and thus provide positional information about the distance from the morphogen source (Wolpert, 1969; Figure 1A). In the neural tube, for example, the graded distribution of the signaling molecule Sonic hedgehog (Shh) triggers the specification of different neuronal subtypes along the dorsal-ventral axis (Dessaud et al., 2007). The molecular and cellular mechanisms leading to the formation of morphogen gradients have been analyzed in detail, and several models have emerged explaining gradient formation on the basis of signal production, spreading, and degradation (Kicheva et al., 2012). However, gradient formation has nearly exclusively been analyzed in effectively planar two-dimensional cell layers, where the signals spread within the plane of the tissue. Interestingly, recent work suggests that signaling within the zebrafish lateral line primordium can be spatially constrained by the formation of microluminal structures (Durdu et al., 2014), pointing at the importance of incorporating three-dimensional tissue morphogenesis in generating graded signaling activities. In this issue of *Cell*, Shyer et al. (2015) present evidence that three-dimensional rearrangements of tissues can generate gradients of signaling molecules in the surrounding tissues. These results provide important insight into the coupling of tissue morphogenesis and gradient formation with consequences for cell fate specification and tissue patterning.

The lumen of the gut in chick undergoes a series of morphogenetic processes

transforming the initially smooth lumen lining into a surface densely decorated with individual villi, required for effective absorption of nutrients within the gut (Coulombre and Coulombre, 1958). This transformation is thought to be triggered by growth of the lumen surface coupled to compressive forces from surrounding tissues restricting the expansion of the proliferating tissue and thus causing the lumen surface to buckle. The transformation of buckles into villi critically depends not only on general growth under spatial confinement but also on a drop in proliferation at the tip of the folds and redistribution of stem cells to the base of the forming villi. The study by Shyer et al. (2015) addresses the mechanism underlying this redistribution of stem cells, which are initially uniformly distributed in the early gut.

Confirming previous work (Karlsson et al., 2000), the authors show that, in the distal mesenchyme of the nascent villi, a “villus cluster” forms. The cells of this cluster express several signaling factors inhibiting stem cell specification and proliferation in the overlying distal epithelium of the forming villi. This raises the question as to the molecular and cellular mechanisms by which the villus cluster is formed at the villi tip. The Shh signaling pathway has previously been implicated in the formation of the villus cluster. Thus, the authors hypothesized that local Shh signaling at the villi tip might induce the villus cluster. However, as the authors had previously shown that *shh* mRNA is uniformly distributed throughout the gut endoderm, other mechanisms than restricting *shh* expression to tip cells of the forming villi had to be tested.

In a set of elegant experiments, inspired by predictions from theoretical modeling,

the authors show that the formation of villi would generate local maxima of Shh signaling activity at the villi tips responsible for the induction of the villus cluster below. To this end, the authors assumed that Shh is secreted equally by all endodermal cells, diffuses within the underlying mesenchyme, and is degraded. Crucially, the morphological changes of the forming villus are captured by changing boundary conditions, which lead to a steady-state concentration profile with maximum concentration at the tip of the villus; this maximum concentration increases as the villus grows more acute (Figure 1B). If the induction of the villus cluster requires high Shh concentrations, this scenario would explain its localization to the tip. To test this scenario directly, the authors undertook explant experiments in which they either prevent buckling by flipping the epithelium inside out or induce premature folding by placing slabs of embryonic gut on fine grids forcing the surface to bend. These experiments clearly show that preventing gut buckling abolishes the localized induction of villus clusters, whereas forcing premature buckling induces premature villus clusters. The key role of Shh in this process was further supported by experiments showing that Shh protein displays a graded distribution with maxima at the villi tips and that modulating Shh signaling activity affects villus cluster formation. Collectively, these data provide strong support for an instructive function of surface buckling in establishing local maxima of Shh signaling activity responsible for villus cluster formation.

Several questions arise from this work. Foremost, we still know very little about how the Shh gradient forms: is Shh production/secretion homogenous? Does

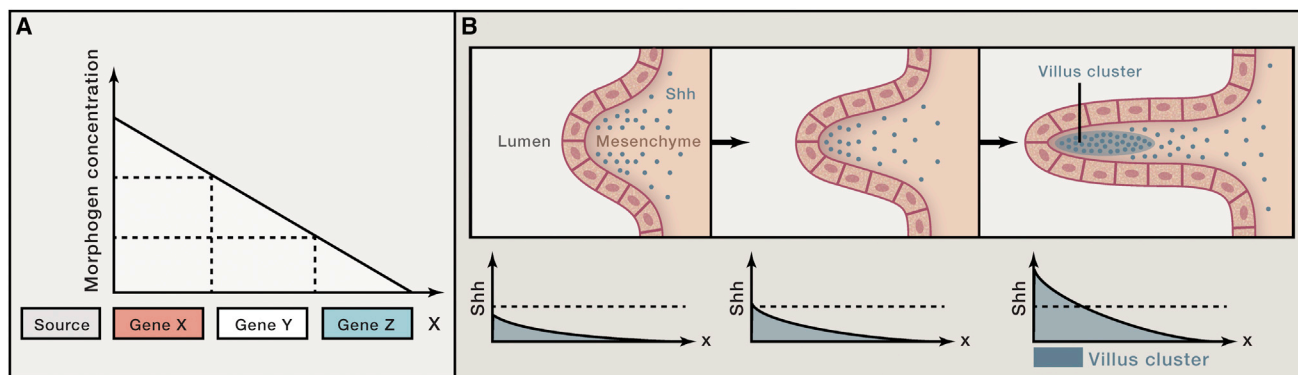


Figure 1. Forming a Morphogen Gradient by Tissue Folding

(A) Schematic of morphogen gradient model: morphogens are secreted by source cells and form a graded concentration profile in the target tissue, where cells express different target genes (X, Y, and Z) and ultimately adopt different cell fates dependent on the morphogen concentration.

(B) Tissue folding leads to villi formation in the gut. Shh molecules are shown in blue. As the villi grow more acute, the maximal Shh concentration at the tip increases; the Shh concentration ultimately exceeds a high threshold (dotted lines) above which the formation of the villus cluster in the underlying mesenchyme is induced.

Shh simply diffuse in the extracellular space? How does it get degraded? Although the model predicts the generation of local maxima of Shh signaling activity upon gut folding, there are several signaling-related processes beyond the geometrical change of the tissue that might be affected by the folding process itself. For instance, signal secretion from the gut epithelium to the villus cluster might be modified by changes in the apical-to-basal proportion of gut epithelial cells due to cell shape changes during the buckling process. Moreover, Shh signal propagation and degradation within the villus cluster mesenchyme might be modulated by cellular rearrangements within the cluster as a result of cluster shape changes during villi formation. Finally, reciprocal BMP signaling activity induced within the villus cluster by Shh signaling from the gut epithelium and required for restricting the proliferative activity within the forming villi might itself be altered by cluster shape changes during the folding process. Experimentally

determining potential changes in such processes during villi formation and incorporating them as parameters into a theoretical model of villi formation as a function of Shh and BMP signaling will likely generate intriguing predictions about the behavior of this system, which, in turn, can be tested experimentally.

Another issue, related to the points discussed above, is the precise spatiotemporal relationship between Shh and BMP signaling activity and tissue morphogenesis. As observed for other feedback mechanisms (Brandman and Meyer, 2008), the time delays between Shh/BMP signaling and the different morphogenetic processes leading to villi formation (tissue folding and cell proliferation) will be critical for the outcome of the process. It will be interesting to determine how quickly cells within the mesenchyme upon reception of Shh signals from the villi tip can upregulate BMP expression and how quickly BMP receiving cells within the gut epithelium can switch off the proliferative activity. Again, experimentally

addressing such delays and incorporating them as parameters in theoretical model will likely produce informative predictions about the process itself.

REFERENCES

- Brandman, O., and Meyer, T. (2008). *Science* 322, 390–395.
- Coulombre, A.J., and Coulombre, J.L. (1958). *J. Embryol. Exp. Morphol.* 6, 403–411.
- Dessaud, E., Yang, L.L., Hill, K., Cox, B., Ulloa, F., Ribeiro, A., Mynett, A., Novitch, B.G., and Briscoe, J. (2007). *Nature* 450, 717–720.
- Durdu, S., Iskar, M., Revenu, C., Schieber, N., Kunze, A., Bork, P., Schwab, Y., and Gilmour, D. (2014). *Nature* 515, 120–124.
- Karlsson, L., Lindahl, P., Heath, J.K., and Betsholtz, C. (2000). *Development* 127, 3457–3466.
- Kicheva, A., Bollenbach, T., Wartlick, O., Jülicher, F., and González-Gaitan, M. (2012). *Curr. Opin. Genet. Dev.* 22, 527–532.
- Shyer, A.E., Huycke, T.R., Lee, C., Mahadevan, L., and Tabin, C.J. (2015). *Cell* 161, this issue, 569–580.
- Wolpert, L. (1969). *J. Theor. Biol.* 25, 1–47.

Membrane Nanoclusters—Tails of the Unexpected

Erdinc Sezgin,¹ Simon J. Davis,¹ and Christian Eggeling^{1,*}

¹MRC Human Immunology Unit, Weatherall Institute of Molecular Medicine, University of Oxford, OX39DS Oxford, UK

*Correspondence: christian.eggeling@rdm.ox.ac.uk

<http://dx.doi.org/10.1016/j.cell.2015.04.008>

The existence, nature, and role of highly ordered membrane domains, often referred to as lipid rafts, have been highly debated by cell biologists for many years. In this issue, Raghupathy et al. describe molecular mechanisms leading to the formation of ordered lipid-protein clusters.

The lipid raft concept as a membrane organizing principle that modulates cellular functionality has been controversial ever since it was first proposed (Simons and Ikonen, 1997). The question was, do lipid rafts really exist, and if so, what is their exact composition, size, and lifetime? It has become the general notion that lipid rafts are at most transient molecular assemblies that might bring together different molecules on small spatial scales, leading to brief local increases in molecular order and compartmentalization that could influence cellular events, including signaling (Lingwood and Simons, 2010). But what about other sources of membrane microheterogeneity?

In a technical tour de force presented in this issue of *Cell*, Raghupathy et al. (2015) use experiments and simulations to systematically analyze the molecular mechanisms underlying the formation of membrane assemblies comprising glycosylphosphatidylinositol (GPI)-anchored proteins (GPI-APs). Synthetic fluorescent GPI-AP analogs, which the authors incorporate into the outer plasma-membrane leaflet of Chinese hamster ovary cells, exhibit nanoclustering on <100 nm scales, as indicated by a decrease in fluorescence anisotropy due to Förster resonance energy transfer effects (Goswami et al., 2008). Surprisingly, nanocluster formation is remarkably dependent on the length of the acyl chain forming the GPI anchor: clustering is only observed for GPI-APs with long saturated acyl chains containing ≥ 18 carbon atoms, suggesting an interdigitation-based mechanism. Nanoclustering diminishes upon cholesterol depletion in actin-depleted cell blebs and for mutant cell lines deficient in the inner-leaflet lipid phosphatidylserine (PS). In the PS-depleted cells, only the addition of PS with at least one long saturated chain

restored nanoclustering. Intriguingly, the effect is also enhanced upon expression of proteins specifically linking PS to the actin cytoskeleton—that is, protein domains capable of binding PS and able to mediate the interaction of the lipids with cytoplasmic actin filaments. Atomistic molecular-dynamic simulations confirm the observations with respect to the cholesterol-assisted inner-leaflet coupling of immobilized PS and GPI-APs, both of which again require long saturated acyl chains. The simulations also reveal an apparently high degree of molecular order in the nanoclusters. Finally, like the GPI-APs, a long acyl chain containing fluorescent phosphoethanolamine lipid analog exhibits PS- and cholesterol-dependent nanoclustering in the outer leaflet.

The experiments of Raghupathy et al. (2015) show that nanoclusters form by transbilayer coupling only in the presence of long unsaturated acyl chains, cholesterol, and immobilization of one of the partners (Figure 1). In the proposed model, it is this immobilization, usually

by cortical actin, that determines where and when the clusters will be stabilized. Thus, it is actin dynamics that control domain formation at the outer leaflet of the cell membrane. Taken individually, caveats could perhaps be identified for some of the experimental approaches used by Raghupathy et al. (2015). For example, it is not known if cell blebs, where nanoclustering is not observed, are truly actin free. However, the sum of the experimental and theoretical studies amounts to a convincing argument for a new mechanism of nanocluster formation. Interestingly, the experiments and simulations suggest that transbilayer coupling can work both ways. That is, when the GPI-APs are clustered and immobilized extracellularly, PS lipids form correlated patches intracellularly. Such effects might provide a mechanism for relaying signals from the extra- to the intracellular space of the cell.

Although the actin-dependent organization of GPI-APs into clusters was established some time ago (Goswami et al.,

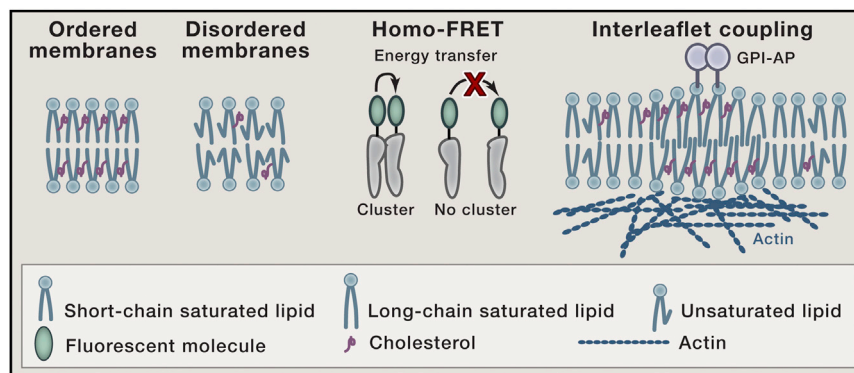


Figure 1. Ordered Membrane Domain Formation

Raghupathy et al. (2015) provide evidence for inter-leaflet coupling as a mechanism of membrane nanoclustering of lipid-anchored molecules such as GPI-APs but only in the presence of long unsaturated acyl chain anchored molecules on both sides, cholesterol, and more importantly, immobilization of one of the partners—for example, by the cortical actin cytoskeleton.

2008), with the underlying mechanism now teased apart (Raghupathy et al., 2015), the question remains of how these instances of nanoclusters fit into the more general “lipid raft” concept. Specifically, what is the relation of these clusters to the many different types of molecular assemblies at the membrane that have all been defined as lipid rafts, including GPI-AP clusters? The generality of traditional raft models based on detergent-resistant membrane patches (Simons and Ikonen, 1997) or phase-separated model membranes of ternary lipid mixtures has been undermined by multiple experiments (e.g., Honigsmann et al., 2014a). Yet, the principle of phase separation as a structural and functional principle cannot be fully set aside. For example, giant plasma membrane vesicles derived from living cells, which contain the cellular membrane proteins and lipids but lack cytoskeleton and are incapable of energy-dependent processes, have the potential to phase separate as well, with proteins and lipids showing a distinct preference for one of the phases, albeit at unphysiological temperatures (Sezgin et al., 2012). It seems likely that the sources of cell membrane heterogeneity are themselves heterogeneous and that not all of the structures form via the same mechanism. For instance, although specific lipids, cholesterol, and/or the cortical cytoskeleton regulate some protein assemblies and membrane-assisted signaling events, others appear to be completely independent of these factors. Moreover, molecules observed to behave similarly in one exper-

imental context appear to have different characteristics when observed using other approaches and conditions (e.g., different cells or expression levels).

To avoid confusion, it seems very important to defer from generalizing from single experimental or theoretical observations and specifically to avoid the temptation to refer to all types of membrane assemblies as lipid rafts. As the authors themselves stress, the new work addresses only the formation of clusters of long-acyl-chain-containing lipid-anchored proteins, which may not as yet exemplify a general organizing principle. However, it is possible that processes similar to those depicted by Raghupathy et al. (2015) have an important role in the formation of other membrane assemblies. For instance, in several cases, the cortical cytoskeleton (Honigsmann et al., 2014b; Kusumi et al., 2010) and inter-leaflet coupling (Spillane et al., 2014) have, among other factors such as membrane curvature (Larsen et al., 2015), been shown to drive the organization of membrane molecules. It will be of great interest to determine the extent to which the pinning of inner-leaflet lipids to cortical actin in combination with inter-leaflet coupling involving specific lipids and cholesterol drives the transient assembly of other types of membrane molecules, if at all. An important related question concerns whether the lifetimes of the observed structures are sufficient to influence membrane protein function. At the very least, the new work sets the technical standard for these types of inquiries.

ACKNOWLEDGMENTS

The authors thank Christoffer Lagerholm (WIMM, Oxford) for comments on the manuscript. E.S. is supported by EMBO Long Term and Marie Skłodowska-Curie Postdoctoral Fellowships, and C.E. and S.J.D. are supported by the MRC, Wellcome Trust, BBSRC, ESRC, and Wolfson Foundation.

REFERENCES

- Goswami, D., Gowrishankar, K., Bilgrami, S., Ghosh, S., Raghupathy, R., Chadda, R., Vishwakarma, R., Rao, M., and Mayor, S. (2008). *Cell* 135, 1085–1097.
- Honigsmann, A., Mueller, V., Ta, H., Schoenle, A., Sezgin, E., Hell, S.W., and Eggeling, C. (2014a). *Nat. Commun.* 5, 5412.
- Honigsmann, A., Sadeghi, S., Keller, J., Hell, S.W., Eggeling, C., and Vink, R. (2014b). *eLife* 3, e01671.
- Kusumi, A., Shirai, Y.M., Koyama-Honda, I., Suzuki, K.G.N., and Fujiwara, T.K. (2010). *FEBS Lett.* 584, 1814–1823.
- Larsen, J.B., Jensen, M.B., Bhatia, V.K., Pedersen, S.L., Bjørnholm, T., Iversen, L., Uline, M., Szleifer, I., Jensen, K.J., Hatzakis, N.S., et al. (2015). *Nat. Chem. Biol.* 11, 192–194.
- Lingwood, D., and Simons, K. (2010). *Science* 327, 46–50.
- Raghupathy, R., Anilkumar, A.A., Polley, A., Singh, P.P., Yadav, M., Johnson, C., Suryawanshi, S., Saikam, V., Sawant, S.D., Panda, A., et al. (2015). *Cell* 161, this issue, 581–594.
- Sezgin, E., Kaiser, H.-J., Baumgart, T., Schwillie, P., Simons, K., and Levental, I. (2012). *Nat. Protoc.* 7, 1042–1051.
- Simons, K., and Ikonen, E. (1997). *Nature* 387, 569–572.
- Spillane, K.M., Ortega-Arroyo, J., de Wit, G., Eggeling, C., Ewers, H., Wallace, M.I., and Kukura, P. (2014). *Nano Lett.* 14, 5390–5397.

A Genetic Clog in the Vitamin A Transport Machinery

Ming Zhong¹ and Hui Sun^{1,*}

¹Howard Hughes Medical Institute, Department of Physiology and Jules Stein Eye Institute, David Geffen School of Medicine, University of California, Los Angeles, CA 90095, U.S.A

*Correspondence: hsun@mednet.ucla.edu
<http://dx.doi.org/10.1016/j.cell.2015.04.020>

Chou et al. discover a new mode of maternal inheritance by analyzing human mutations in plasma retinol binding protein (RBP). Mechanistically, these mutations simultaneously lower RBP's affinity for vitamin A and greatly increase its affinity for its cell-surface receptor, thus dominantly blocking the transmembrane transport of vitamin A.

Vitamin A has been the light sensor for vision, or its equivalent, from life's beginnings. The diversification of its function to regulating cell growth and differentiation, which occurred about 500 million years ago, coincided with the emergence of a long-range and specific vitamin A transport system consisting of a blood carrier protein called plasma retinol binding protein (RBP) and its cell-surface receptor (STRA6), which mediates vitamin A uptake (Kawaguchi et al., 2007). Many organs depend on vitamin A action; however, the eye is still the organ most sensitive to vitamin A deficiency, the loss of RBP, or the loss of STRA6 (Zhong et al., 2012). Studies of human mutations leading to congenital eye malformation allowed Tom Glaser and colleagues, in this issue of *Cell*, to uncover a new mode of maternal inheritance and its intricate mechanism involving RBP, STRA6, and vitamin A (Chou et al., 2015).

Glaser's team identified human RBP mutations that cause eye malformation such as anophthalmia, microphthalmia, and coloboma, but the phenotypes are preferentially transmitted if the mutations are inherited from the mother. Through a series of elegant biochemical analyses, they discovered that these mutant RBPs block vitamin A transport by STRA6 in a precise and dominant manner. To understand this mechanism, it is useful to understand the major players involved in specific vitamin A transport. Under physiological conditions, vitamin A/RBP complex (termed holo-RBP) associates with transthyretin (TTR) to increase its molecular weight and thus prevent removal by kidney filtration. Holo-RBP dissociates from the

complex to bind to its cell-surface receptor STRA6 due to its higher affinity for STRA6 than for TTR (Kawaguchi et al., 2011). STRA6 then catalyzes vitamin A release from holo-RBP and its transport into the cell where it is stored (Kawaguchi et al., 2011). After losing its cargo, RBP (apo-RBP) has greatly decreased affinity for TTR and is lost through kidney filtration, which prevents its accumulation in the blood (Figure 1). RBP mutations identified in this study confer several properties that are important for their pathogenicity and the way they affect this process. First, while these mutant RBPs are as well secreted as the wild-type protein, they bind vitamin A weakly and tend to lose their cargo in a receptor-independent manner. Second, like wild-type holo-RBP, the mutant ones can still bind to TTR; however, they have an affinity for STRA6 that is 30- to 40-fold higher than that of wild-type RBP (Figure 1). These properties lead to the sequestration of STRA6 by the mutant RBP, decreasing its ability to transport vitamin A into the cell. Indeed, although the blood of mutation carriers may contain about 66% wild-type RBP and only 33% mutant RBP, the blocking effect is sufficient to cause the malformation phenotypes.

A longstanding puzzle in the field was the discrepancy between the way human mutations in RBP and STRA6 affect eye development. While mutations in STRA6 cause anophthalmia and other developmental defects (Pasutto et al., 2007), all previously identified RBP mutations did not. As this study shows, a key to this puzzle is the placenta's role in vitamin A delivery. Previously identified mutations in RBP were recessive and thus unlikely

to inactivate both maternal and fetal RBP because only the fetus could be homozygous for the mutation. In contrast, dominant RBP mutations, like those discovered in this study, can simultaneously inactivate the mother's and fetal RBP. Similarly, human mutations in RBP and its receptor do not necessarily generate the same phenotypes for the same reason. A human embryo without STRA6 can be directly impacted by the loss of placental absorption of vitamin A from maternal RBP. In contrast, a human embryo without RBP still has STRA6 and functional maternal RBP to ensure vitamin A delivery to the embryo through the placenta. Thus, the dominant human RBP mutations mimic STRA6 mutations in their ability to inactivate both maternal and fetal RBP-mediated transport and therefore can cause anophthalmia. The fact that the dominant RBP mutation can only exert its effect on maternal delivery of vitamin A to the fetus if it is maternal explains this new mode of maternal inheritance.

A related question highlighted by this study is the contrast between humans and mice in phenotypic variability even for null mutations in this pathway. For example, human pathologies caused by STRA6 mutations are highly variable, ranging from the "milder" phenotype of anophthalmia to more systemic developmental defects (Pasutto et al., 2007). However, under standard laboratory conditions, STRA6 knockout mice, like RBP knockout mice, have vision-specific phenotypes that lead to blindness due to lack of vitamin A (Amengual et al., 2014; Ruiz et al., 2012). As pointed out here, a key to this puzzle is an RBP-independent pathway mediated by vitamin A esters

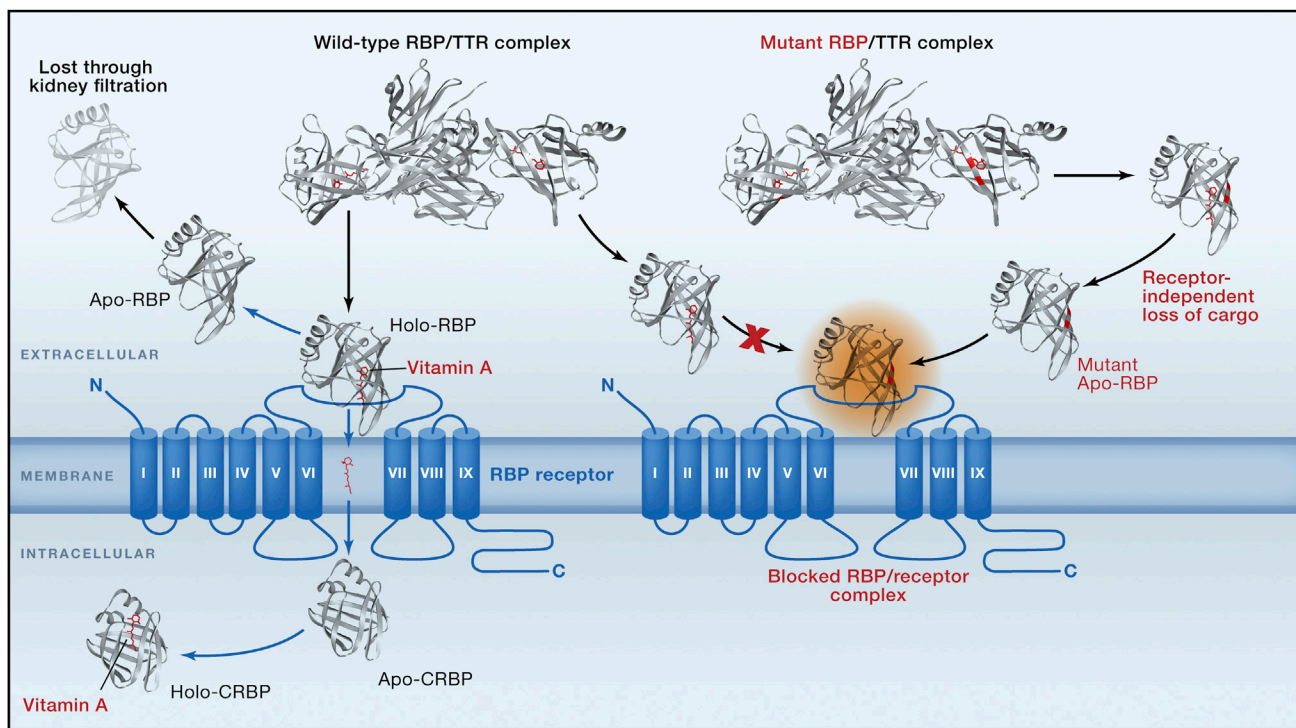


Figure 1. Schematic Diagrams of RBP/Receptor Interaction

Schematic diagrams comparing RBP/receptor interaction under physiological conditions and the pathological conditions revealed by Chou et al. (2015). Under physiological conditions (left diagram), holo-RBP dissociates from the RBP/TTR complex to bind to the RBP receptor STRA6 due to its higher affinity for STRA6 than for TTR. STRA6 catalyzes retinol release from holo-RBP and retinol transport into the cell to be stored by binding to CRBP, or by conversion to retinyl esters by LRAT (not shown). After losing its cargo retinol, RBP (apo-RBP) can no longer bind to TTR and is lost through kidney filtration. As depicted in the right diagram, human RBP mutant A55T or A57T (marked in red in RBP structures) tends to lose vitamin A in a receptor-independent manner, but has much higher affinity for STRA6 than wild-type RBP (the mutant RBP/receptor complex is marked by a red circle). These RBP mutants compete with wild-type RBP in binding to STRA6 to impede the transmembrane transport of vitamin A.

(retinyl esters) borrowing the lipoprotein delivery pathway. This pathway can partly compensate for the lack of RBP if sufficient and constant vitamin A is available (Quadro et al., 2005). Retinyl ester bound to lipoprotein depends on immediate vitamin A intake from food because its source is the small intestine. Unlike the RBP system, the retinyl ester pathway is not homeostatically regulated, cannot mobilize the vast amount of vitamin A stored in the liver, and is directly influenced by fluctuating vitamin A intake (Green and Green, 1994). Therefore, pathological phenotype becomes highly variable and ranges from eye-specific pathology to embryonic lethality when only this pathway is depended on for vitamin A delivery in mice (Quadro et al., 2005) or in humans (Pasutto et al., 2007). Another facet of this RBP-independent pathway is that it is associated with toxicity due to its lack of ho-

meostatic control and specificity (Smith and Goodman, 1976). An increase of 10% in retinyl ester in the blood is regarded as a sign of vitamin A overload in humans.

This study also illustrates how RBP and its receptor have been finely tuned for each other in evolution. Tighter binding is not necessarily better and can even be pathogenic. Each RBP protein transports only one vitamin A molecule and STRA6 only takes up one vitamin A molecule at a time from RBP. Therefore, the STRA6/RBP interaction must be sufficiently strong and specific to achieve vitamin A uptake, but not too strong or prolonged to prevent RBP from delivering the next vitamin A molecule. The unexpected existence of super-binding RBP mutants in humans revealed a new mode of inheritance depending on the genetic buildup of both mother and fetus.

ACKNOWLEDGMENTS

H.S. is supported by NIH grant R01 EY018144. H.S. is an Early Career Scientist of the Howard Hughes Medical Institute.

REFERENCES

- Amengual, J., Zhang, N., Kemerer, M., Maeda, T., Palczewski, K., and Von Lintig, J. (2014). *Hum. Mol. Genet.* 23, 5402–5417.
- Chou, C.M., Nelson, C., Tarle, S.A., Pribila, J.T., Bardakjian, T., Woods, S., Schneider, A., and Glaser, T. (2015). *Cell* 161, this issue, 634–646.
- Green, M.H., and Green, J.B. (1994). Dynamics and Control of Plasma Retinol. In *Vitamin A in Health and Disease*, R. Blomhoff, ed. (Marcel Dekker, Inc.).
- Kawaguchi, R., Yu, J., Honda, J., Hu, J., Whitelegge, J., Ping, P., Wiita, P., Bok, D., and Sun, H. (2007). *Science* 315, 820–825.
- Kawaguchi, R., Yu, J., Ter-Stepanian, M., Zhong, M., Cheng, G., Yuan, Q., Jin, M., Travis, G.H.,

- Ong, D., and Sun, H. (2011). *ACS Chem. Biol.* 6, 1041–1051.
- Pasutto, F., Sticht, H., Hammersen, G., Gillesen-Kaesbach, G., Fitzpatrick, D.R., Nürnberg, G., Brasch, F., Schirmer-Zimmermann, H., Tolmie, J.L., Chitayat, D., et al. (2007). *Am. J. Hum. Genet.* 80, 550–560.
- Quadro, L., Hamberger, L., Gottesman, M.E., Wang, F., Colantuoni, V., Blaner, W.S., and Mendelsohn, C.L. (2005). *Endocrinology* 146, 4479–4490.
- Ruiz, A., Mark, M., Jacobs, H., Klopfenstein, M., Hu, J., Lloyd, M., Habib, S., Tosha, C., Radu, R.A., Ghyselinck, N.B., et al. (2012). *Invest. Ophthalmol. Vis. Sci.* 53, 3027–3039.
- Smith, F.R., and Goodman, D.S. (1976). *N. Engl. J. Med.* 294, 805–808.
- Zhong, M., Kawaguchi, R., Kassai, M., and Sun, H. (2012). *Nutrients* 4, 2069–2096.

A Primer to Single-Particle Cryo-Electron Microscopy

Yifan Cheng,¹ Nikolaus Grigorieff,² Pawel A. Penczek,³ and Thomas Walz^{4,*}

¹Department of Biochemistry and Biophysics, University of California, San Francisco, CA 94158, USA

²Janelia Research Campus, 19700 Helix Drive, Ashburn, VA 20147, USA

³Department of Biochemistry and Molecular Biology, The University of Texas–Houston Medical School, 6431 Fannin Street, MSB 6.220, Houston, TX 77030, USA

⁴Department of Cell Biology and Howard Hughes Medical Institute, Harvard Medical School, 240 Longwood Avenue, Boston, MA 02115, USA

*Correspondence: twalz@hms.harvard.edu

<http://dx.doi.org/10.1016/j.cell.2015.03.050>

Cryo-electron microscopy (cryo-EM) of single-particle specimens is used to determine the structure of proteins and macromolecular complexes without the need for crystals. Recent advances in detector technology and software algorithms now allow images of unprecedented quality to be recorded and structures to be determined at near-atomic resolution. However, compared with X-ray crystallography, cryo-EM is a young technique with distinct challenges. This primer explains the different steps and considerations involved in structure determination by single-particle cryo-EM to provide an overview for scientists wishing to understand more about this technique and the interpretation of data obtained with it, as well as a starting guide for new practitioners.

Introduction

Cryo-electron microscopy (cryo-EM) has the ability to provide 3D structural information of biological molecules and assemblies by imaging non-crystalline specimens (single particles). Although the development of the cryo-EM technique began in the 1970s, in the last decade the achievement of near-atomic resolution (<4 Å) has attracted wide attention to the approach.

The remarkable progress in single-particle cryo-EM in the last 2 years has primarily been enabled by the development of direct electron detector device (DDD) cameras (Faruqi and McMullan, 2011; Li et al., 2013a; Milazzo et al., 2011). DDD cameras have a superior detective quantum efficiency (DQE), a measure of the combined effects of the signal and noise performance of an imaging system (McMullan et al., 2009), and the underlying complementary metal-oxide semiconductor (CMOS) technology makes it possible to collect dose-fractionated image stacks, referred to as movies, that allow computational correction of specimen movements (Bai et al., 2013; Campbell et al., 2012; Li et al., 2013a). Together, these features produce images of unprecedented quality, which, in turn, improves the results of digital image processing. In parallel, the continually increasing computer power allows the use of increasingly sophisticated image processing algorithms, resulting in greatly improved and more reliable 3D density maps (see also Cheng, 2015, this issue).

Much effort has been invested in simplifying and automating the collection of EM images and the use of image processing software (reviewed in Lyumkis et al., 2010). The problematic issue with single-particle EM, however, is that there is still no objective quality criterion that is simple and easy to use, such as the R-free value in X-ray crystallography, that would allow one to assess whether the determined density map is accurate or not. Even the resolution of a density map remains subject to controversies. The remaining unresolved issues may not always

be fully appreciated by new practitioners and, if overlooked, can lead to questionable results. A recent example is the 6-Å-resolution structure of the HIV-1 envelope glycoprotein (Mao et al., 2013), which prompted a number of commentaries questioning the validity of the structure (Henderson, 2013; Subramaniam, 2013; van Heel, 2013). This primer seeks to inform about the practical nuts and bolts behind determining a structure by single-particle cryo-EM and to guide new practitioners through the workflow (Figure 1) and important caveats and considerations. Also, as these authors' opinions may not always be shared by everybody in the field, the reader is encouraged to consult other texts on single-particle EM, such as Bai et al. (2015), Frank (2006), Lau and Rubinstein (2013), Milne et al. (2013), and Orlova and Saibil (2011).

Protein Purification for Single-Particle Cryo-EM

Single-particle EM depends on the computational averaging of thousands of images of identical particles. If particles exhibit variable conformation or composition (heterogeneity), more homogeneous subsets can be generated using classification procedures (more below). However, whenever possible, structural heterogeneity should be minimized through biochemical means to simplify structure determination. Biochemical analyses by SDS-PAGE and gel-filtration chromatography are not sufficient to assess whether a sample is suitable for EM analysis, as apparently intact complexes can be a mixture of compositionally different sub-complexes, and even compositionally homogeneous complexes can potentially adopt many different conformations. The most informative way to judge the quality of a protein sample is to visualize it by negative-stain EM. In addition to providing high contrast, the negative staining procedure also tends to induce proteins to adsorb to the carbon film in one or only few preferred orientations, making it easier to assess

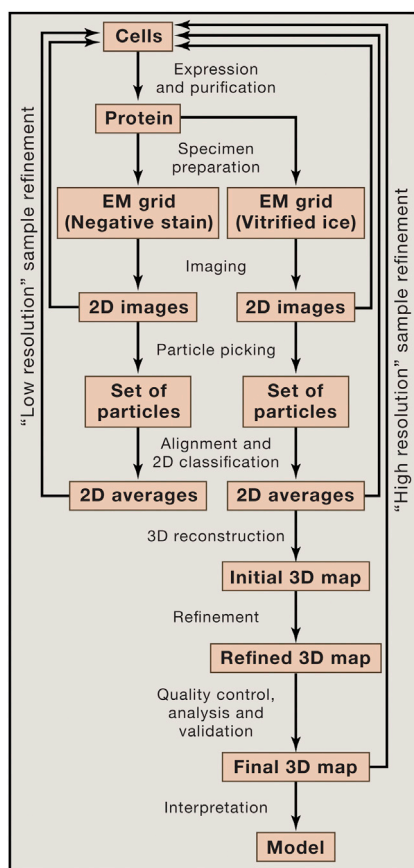


Figure 1. The Steps Involved in Structure Determination by Single-Particle Cryo-EM

A single-particle project should start with a characterization of the specimen in negative stain (left arm of the workflow). Only once the EM images, or potentially 2D class averages, are satisfactory, i.e., the particles are monodisperse and show little aggregation and a manageable degree of heterogeneity (“low-resolution” sample refinement), is the sample ready for analysis by cryo-EM (right arm of the workflow). The images, 2D class averages and 3D maps obtained with vitrified specimens may indicate that the sample requires further improvement to reach near-atomic resolution (“high-resolution” sample refinement).

sample homogeneity (Ohi et al., 2004). The kind of information negative-stain EM provides is described in [Supplemental Information](#).

Structural heterogeneity can be caused by compositional or conformational variability of the target. Compositional heterogeneity, typically the result of sub-stoichiometric components or dissociation of loosely associated subunits, can be addressed in various ways. Ideally, buffer conditions can be found that stabilize the target complex. A promising approach to identify suitable buffer conditions is the Thermofluor-based screening approach (Ericsson et al., 2006). In the case of a sub-stoichiometric subunit, this subunit can be tagged for affinity purification, thus increasing the fraction of complexes containing it in the final preparation. An approach that has proven useful in reducing compositional heterogeneity is mild chemical cross-linking with glutaraldehyde. More control over the cross-linking reaction is obtained with the GraFix technique, in which the sample is

centrifuged into a combined glycerol/glutaraldehyde gradient (Kastner et al., 2008). A variation of this approach is “on column” cross-linking, in which the sample is cross-linked over a size-exclusion column (Shukla et al., 2014). Whichever approach is used, one must keep in mind that cross-linking can introduce artifacts. For example, flexible extensions can become glued together, resulting in a non-physiological structure. Also, if a complex can adopt different conformations, cross-linking can stabilize just one particular state, typically the most compact organization (e.g., Shukla et al., 2014). Hence, native sample always has to be analyzed, too, to understand how cross-linking affects the structure of the target.

Conformational heterogeneity tends to be more difficult to overcome, especially if one or several domains are flexibly tethered to the remainder of a protein. In this case, structural analysis may be restricted to negative-stain EM studies. Alternatively, chemical cross-linking can potentially be used to minimize the conformational heterogeneity, but the physiological relevance of the resulting structures will have to be carefully assessed. Another way to reduce conformational heterogeneity is to lock the target in a defined functional state, which can sometimes be accomplished by adding substrates, inhibitors, ligands, co-factors, or any other molecule affecting the function of the target.

The greatly improved image quality provided by DDD cameras and the availability of ever more sophisticated image-processing software have made structural heterogeneity more manageable. Still, investing time to minimize structural heterogeneity by biochemical tools will always simplify subsequent image processing steps, and it will substantially reduce the risk of obtaining incorrect density maps. Every new project should thus always start with an optimization phase, in which negative-stain EM is used as a tool to optimize protein purification (Figure 1). In rare cases, negative staining will introduce artificial heterogeneity. The only option to exclude this possibility is to look at vitrified specimens by cryo-EM.

Specimen Preparation for Single-Particle Cryo-EM

Before a biological specimen can be imaged, it has to be prepared so it survives the vacuum of the electron microscope, which causes sample dehydration, and the exposure to electrons, which results in radiation damage (the deposition of energy on the specimen by inelastic scattering events that causes breakage of chemical bonds and ultimately structural collapse). The most commonly used preparation techniques, negative staining and vitrification, are briefly discussed in [Supplemental Information](#).

Specimens used for single-particle EM usually consist of purified sample on a carbon film with a support structure. The support structure is most commonly a copper grid, and the carbon film can either be a continuous film, typically used to prepare negatively stained samples, or a holey film, commonly used to prepare vitrified specimens. A problem with EM grids is that thin carbon films are not very stable and are poor conductors at low temperature. This is thought to contribute to the occurrence of beam-induced movement, which can degrade image quality. Therefore, different grid designs have been explored to increase the conductivity of EM grids, such as using doped silicon carbide as the substrate (Cryomesh; Yoshioka et al., 2010),

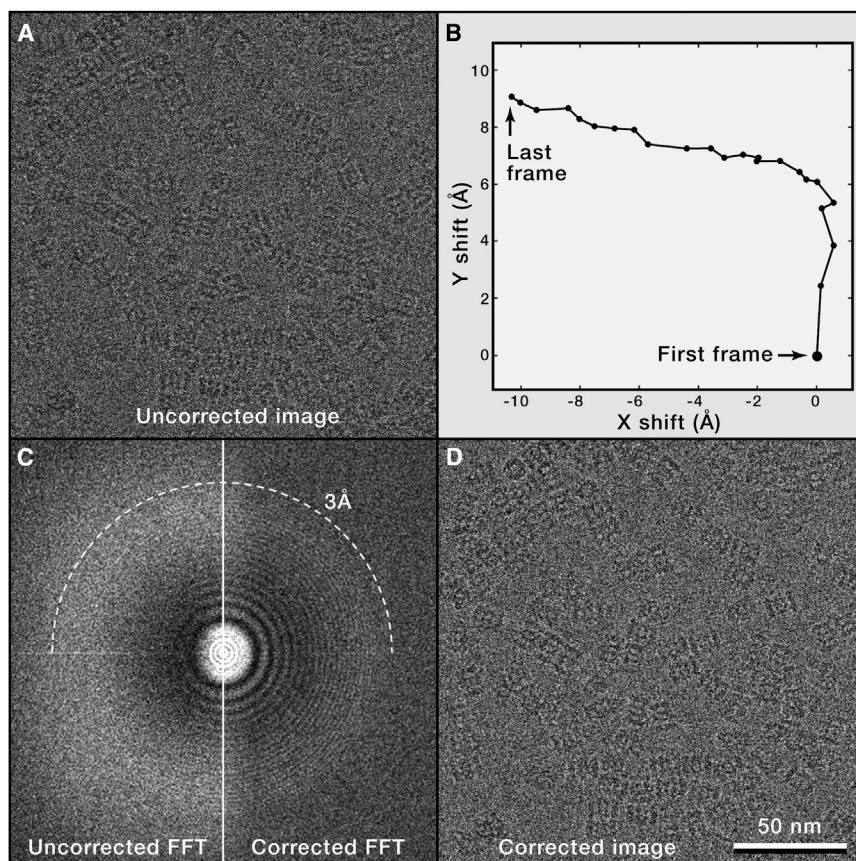


Figure 2. Single-Particle Cryo-EM Images with Motion Correction

Most data recorded with DDD cameras are dose-fractionated image stacks (movies) that can be motion-corrected.

(A) A typical cryo-EM image of vitrified archaeal 20S proteasome particles embedded in a thin layer of vitreous ice. The image is the sum of the raw movie frames without motion correction.

(B) Trace of motion of all movie frames determined using a whole-frame motion-correction algorithm (Li et al., 2013a). Note that the movement between frames is large at the beginning but then slows down.

(C) Left: the power spectrum calculated from the sum of the raw movie frames without motion correction. Right: the power spectrum calculated from the sum of movie frames after motion correction. Motion correction restores Thon rings to close to 3-Å resolution (dashed circle).

(D) Sum of the movie frames that were shifted according to the shifts shown in (B). Note that the images shown in (A) and (D) are indistinguishable by eye, but differ significantly in the quality of the Thon rings seen in their power spectra (C).

and to make them more mechanically stable, such as using gold support (Russo and Passmore, 2014). Before the specimen can be applied, grids have to be rendered hydrophilic, which is typically done with a glow discharger (or, less commonly, with a plasma cleaner).

A perfect vitrified specimen is characterized by an amorphous ice layer of sufficient thickness to accommodate the particles (but ideally not much thicker so that particles are clearly visible), and particles that are well distributed across the field of view and adopt a wide range of orientations. A thin layer of vitrified ice is reasonably transparent and allows particles to be seen clearly (Figures 2 and S1A), while crystalline ice adds a strong texture of dark contrast (bend contours) that usually disguises the embedded particles (Figure S1B).

Semi-automated plungers, such as Vitrobot (FEI) and Cryo-plunge (Gatan), have made it much easier to reproducibly obtain high-quality vitrified specimens. However, care has to be taken to transfer the grids quickly between plunger and cryo-specimen holder and to minimize exposing the liquid nitrogen to air to avoid ice contamination (Figure S1C). An occasional problem is ice that has the appearance of “leopard skin” (Figure S1D). It is unclear what causes this pattern and how it can be avoided, but particles picked from images of such ice areas can still yield reliable 3D maps.

The ice layer should be as thin as possible to achieve high contrast between the molecule and the surrounding ice layer

and to minimize defocus spread due to different heights of the molecules in the ice layer, which can hamper high-resolution structure determination. Importantly, if particles cannot be seen reasonably easily by eye, the sample should not be used for data collection. Parameters that affect ice thickness are described in [Supplemental Information](#).

The ice layer usually tends to be thicker around the edge of a hole and thinner in the center. Large molecules, such as viruses and ribosomes, may thus be excluded from the center of a hole. This effect is stronger with specimens containing detergent, which lowers the surface tension, making it also more challenging to produce thin ice. If thin ice is desired, it helps to use holey carbon grids with smaller holes.

A good vitrified specimen shows a high density of molecules in different orientations. Many particles in a hole reduces the number of images that have to be collected, but ideally the molecules should not touch each other. A problem that is often encountered is that only very few molecules are observed in the holes of the carbon film. A large percentage of molecules is removed during blotting with filter paper, and preparation of vitrified specimens thus requires a much higher sample concentration than preparation of negatively stained specimens. It is not unusual, however, that even with very highly concentrated samples, few particles are seen in the holes. Reasons for this problem can be that the molecules preferentially adsorb to the carbon film, diluting them from the holes, or that they denature as they come into contact with the air/water interface due to the surface tension. An effective solution to deal with the preferential adsorption to the carbon film is to apply the sample twice. The first application will saturate the carbon film with protein, and it is therefore more likely that more particles remain in the holes when the sample is applied a second time. Alternatively, the grid can be

covered by a thin carbon or graphene support film or by a lipid monolayer to which the molecules can adsorb. However, with the exception of graphene, additional support films will reduce image contrast, and all substrates have the potential to induce molecules to adopt preferred orientations. Finally, the grid can be decorated with a self-assembled monolayer to pacify the support film and drive the molecules into the holes (Meyerson et al., 2014). Protein denaturation at the air/water interface can be addressed by using thicker ice (which will, however, reduce image contrast), by using a support film that adsorbs the molecules (but also reduces image contrast), or by chemically fixing the sample before vitrification (which has the potential, however, to affect the structure).

Occasionally particles adopt preferred orientations, presumably due to interactions with the air/water interface. This causes a problem for the reconstruction of a 3D density map, which requires multiple views. One can attempt to overcome this problem by using thicker ice, by adding low amounts of detergent (lowering the surface tension of the air/water interface), or by using a thin support film to which the molecules can adsorb and which will thus keep them away from the air/water interface. One can also try to change the glow-discharge parameters or to modify the protein, e.g., by adding/removing affinity tags. If none of these approaches are successful, it is possible (but technically very challenging) to collect images of tilted specimens, but this usually prevents achieving high resolution.

Image Acquisition for Single-Particle Cryo-EM

Structure determination by single-particle cryo-EM, especially if near-atomic resolution is targeted, requires acquisition of high-quality images, i.e., images with high contrast and with sufficient resolution to answer the biological questions being asked. In addition, particularly for high-resolution projects, high efficiency is beneficial to make them economical, i.e., one should be able to collect a large number of micrographs within a reasonable time-frame. Thus, automation of key steps may be called for. While modern electron microscopes are capable of delivering resolutions better than 2 Å, collection of good-contrast, high-resolution images of vitrified specimens remains challenging. It is therefore critical not only to align the electron microscope with great care but also to choose appropriate imaging conditions. Adjustable settings include, but are not limited to, selection of the condenser aperture and spot size, reduction of imaging aberration by coma-free alignment (all briefly discussed in Supplemental Information), as well as issues related to the optimization of image contrast, such as appropriate defocus settings, selection of objective aperture, and the electron dose used. To learn about contrast enhancement by using phase plates, the reader is referred to Glaeser (2013).

The contrast of vitrified biological specimens is very low, and if images were taken in focus, they would contain little, if any, useful information. Images are therefore taken in bright-field mode of the electron microscope while applying underfocus (Frank, 2006). Given a thin object, images are linear projections of the Coulomb potential of the specimen, the fundamental property necessary for subsequent computational reconstruction of its 3D structure. The images are modulated by the contrast transfer function (CTF), a quasi-periodic sine function in reciprocal

space, the periodicity of which depends, among other parameters, on the defocus setting (Wade, 1992; and Supplemental Information). Furthermore, the amplitudes of the high spatial frequencies (high-resolution detail) in an image are attenuated by an envelope function of the CTF. Its rate of decline depends on the spatial coherence of the electron beam, and it increases with increasing image defocus. Therefore, a higher defocus boosts the low-resolution image contrast but weakens the high-resolution contrast, limiting the frequency range of useful information. Thus, it is best to use the smallest possible defocus that still creates sufficient low-resolution image contrast to clearly see the particles. This means that for large molecules, e.g., viruses, a small underfocus can be used. For small particles (molecular mass less than 200 kDa), however, it is often necessary to underfocus by a few micrometers, which will limit the resolution that can be achieved. Importantly, as the CTF has multiple zero crossings, some information within a single image is lost, which is the reason why images have to be collected at different underfocus settings to sample the entire reciprocal space (Penczek, 2010a; Zhu et al., 1997).

The use of an objective aperture increases amplitude contrast by cutting off electrons scattered at high angles. However, as it also sets a cut-off limit for the resolution, a relatively large objective aperture has to be used for high-resolution single-particle cryo-EM imaging (e.g., 70 μm or 100 μm).

Using a higher electron dose also increases image contrast, but higher electron doses will increase radiation damage. Therefore, for single-exposure images and to achieve high resolution, the electron dose is typically kept below $\sim 20 \text{ e}^-/\text{\AA}^2$. Much higher electron doses can be used when movies are recorded (see below). The dose rate also needs to be considered and depends on the type of detector being used for imaging. For imaging on film or when a charge-coupled device (CCD) camera is used, a high dose rate (high beam intensity) is typically used to keep the exposure short ($\sim 1 \text{ s}$ or less), which minimizes the extent of specimen drift during exposure. Short exposures are also preferred when integrating DDD cameras are used to collect single-exposure images, but longer exposures can be used when they are operated in movie mode, which reduces or eliminates the problem of specimen drift (see below). The situation is different for electron-counting DDD cameras. To ensure that electrons are counted properly, the dose rate must be kept below $\sim 10 \text{ e}^-/\text{pixel}/\text{sec}$ (based on current technology) on the camera (Li et al., 2013b; Ruskin et al., 2013). Higher dose rates adversely affect electron counting, thus lowering the DQE and image contrast.

A factor contributing to the recent improvement of attainable resolution in cryo-EM is the movie mode available on some DDD cameras. Here, the total electron dose is fractionated into a series of image frames that can be aligned to compensate for specimen drift and beam-induced movement, thus reducing image blurring (Figure 2) (Brilot et al., 2012; Campbell et al., 2012; Li et al., 2013a). After alignment, the frames are averaged, and the resulting image is used for subsequent structure determination. Movies are made possible by the fast readout and the “rolling shutter” mode of CMOS detectors that underlie all DDD cameras and some newer scintillator-based cameras. Some software packages also allow for sub-frame alignment

to account for local motions that occur during beam exposure (Rubinstein and Brubaker, 2014; Scheres, 2014). Movies also offer the possibility to optimize the overall Signal-to-Noise Ratio (SNR) in images of specimens affected by radiation damage. Early frames correspond to a low electron dose and therefore contain high-resolution signal from the least damaged specimen. However, early frames are also often still affected by fast specimen movement (Figure 2B), blurring the high-resolution information. While specimen movement typically slows down and affects later frames less, these correspond to a higher accumulated dose and increasingly lack high-resolution information. When movie frames are averaged, a relative weighting can be applied that optimizes the signal in the final average (Campbell et al., 2012; Scheres, 2014). As an intermediate measure to improve high-resolution image contrast, one can exclude the initial two or three frames (which are often still affected by high initial specimen movement), as well as the later frames that correspond to a total dose of $\sim 20 \text{ e}^-/\text{\AA}^2$ and higher from the frame averages. However, this strategy results in the loss of low-resolution contrast. Therefore, it may currently be best to use images containing all the movie frames in the alignment step during image processing and to use images without the initial and final frames to calculate the final 3D map (Li et al., 2013a).

The attainable resolution depends on the pixel size on the specimen level, which, in turn, depends on the effective magnification. The physical pixel sizes of digital cameras vary as well as the exact position of the cameras in the optical path. Therefore, the image pixel size has to be calibrated not only for each magnification but also for every microscope/camera combination (a protocol for how to calibrate the magnification is described in Supplemental Information). The Nyquist theorem specifies that the theoretically attainable resolution is limited to twice the pixel size, but interpolation errors introduced by image processing operations and low DQE values of the detector near the Nyquist frequency limit the practically attainable resolution further (Penczek, 2010b). As a rule of thumb, the practical resolution limit is closer to three times the pixel size.

Image Processing

A significant part of the workload of a single-particle project is taken up by the processing of the recorded images. The main steps are discussed here, including correction of the microscope CTF, selection of particles and preparation of image stacks, generation of an initial structure and its refinement, treatment of structural heterogeneity, assessment of resolution, and interpretation of the final 3D density maps. A number of software packages exist that have been developed over the last four decades and are still being improved. While the development of software is important for the success of single-particle cryo-EM, the recent groundbreaking results are primarily due to the use of direct detectors and the recording of movies. Prior to their common use, none of the currently employed algorithms and software packages was capable of yielding results comparable to what is now possible. After direct detectors and movies were adopted, near-atomic resolution was achieved with several software packages, including SPIDER (Frank et al., 1981), EMAN2 (Tang et al., 2007), FREALIGN (Grigorieff, 2007), RELION

(Scheres, 2012), and SPARX (Hohn et al., 2007). To date, EMAN/EMAN2 has been, and continues to be, the most popular software, owing to its extensive options, flexibility, and user friendliness. However, users new to cryo-EM may find it easier to start with more specialized software, such as RELION, which offers streamlined processing with fewer options and one main algorithmic approach (maximum likelihood). This primer is not meant to serve as a manual for any specific image processing software package, but instead tries to relate basic concepts, which may be implemented in different ways in different software packages.

Estimation of CTF Parameters and Correction for Its Effects

The accurate estimation of CTF parameters is important for both the initial evaluation of micrograph quality and subsequent structure determination. To calculate the CTF, the parameters that have to be known are acceleration voltage, spherical aberration, defocus, astigmatism, and percentage of amplitude contrast. Voltage and spherical aberration are instrument parameters that are usually used without further refinement (although the value for the spherical aberration provided by the manufacturer may not be completely accurate). The defocus is set during data collection, but the setting is only approximate. More accurate values for defocus and astigmatism are obtained by fitting a calculated CTF pattern (e.g., Mindell and Grigorieff, 2003) to the Thon rings (semi-circular intensity oscillations induced by the CTF seen in the power spectrum of the image [Thon, 1966]). The contribution of the amplitude contrast is typically assumed as 5%–10% for cryo-EM images.

Once the CTF parameters have been determined and as long as a set of particle views that differ by defocus settings is available, correction for the CTF effects is possible and straightforward (Penczek, 2010a). It can be done for both amplitudes and phases (full CTF correction) or only for the phases (phase flipping). For more detail on CTF estimation and correction, see Supplemental Information.

Ultimately, the determined 3D structure should be corrected for the reciprocal space envelope functions that suppress high-frequency information, and thus visual resolvability of map details. These envelope functions describe effects of microscope optics, limitations of digital scanners and cameras, and errors in orientation parameters assigned to particle images (Jensen, 2001 and section on power spectrum adjustment in Supplemental Information).

Particle Picking

Once a dataset has been collected, movies have been aligned and averaged (if applicable), and good micrographs have been selected (e.g., based on Thon rings being visible to high resolution in all directions), a project continues with the labor-intensive process of particle picking. The quality of the selected particles is a major factor in the subsequent analysis, as inclusion of too many poor particles may preclude successful structure determination. Moreover, methods aimed at cleaning up the selected particles are not very robust, and many artifacts pass all tests and adversely affect subsequent data processing efforts. Particles can be selected in a manual, semi-automated, and fully

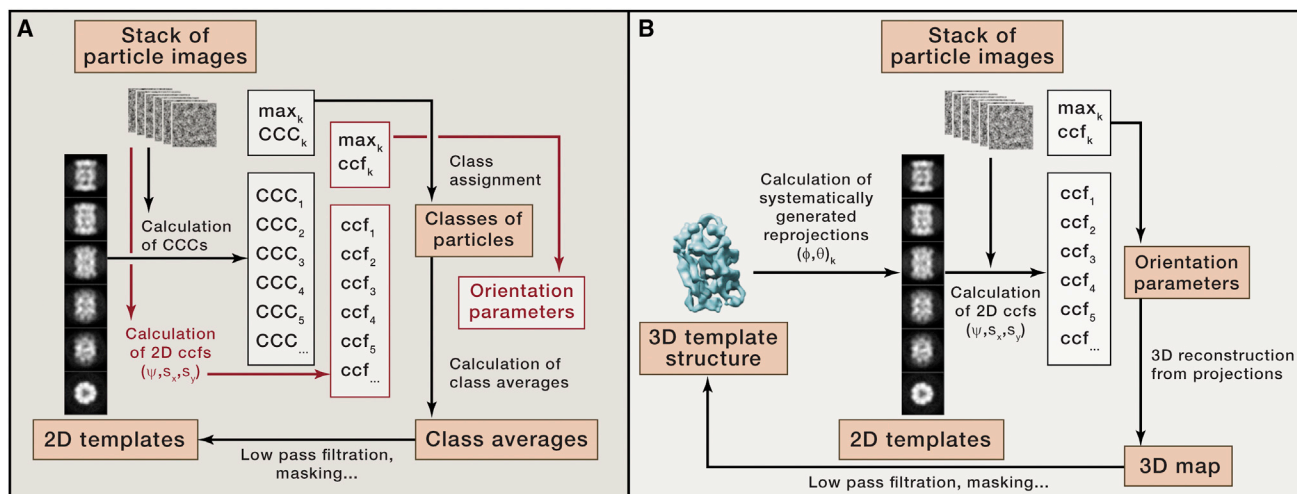


Figure 3. Principle of the K-means Algorithm Used in Single-Particle EM Structure Determination Protocols

(A) In the basic K-means algorithm, the particle images are compared with a set of class averages using a correlation measure that yields the class assignment. Based on the updated class assignments, new class averages are then calculated. Simply by adding 2D alignment of the images to the templates using a correlation function, the algorithm is converted to multi-reference alignment (MRA) (indicated by text in red font).

(B) Principle of the projection matching technique used for 3D single-particle EM structure refinement. The best match of an image to a template yields the Euler angles that were used to generate the template, while a 2D alignment step yields the third, in-plane Euler angle and the two in-plane translations, the total of five orientation parameters required for the 3D reconstruction step.

automated manner. In the early stages of analysis, particularly when little is known about the shape of the protein and the distribution of the projection views, the manual approach is preferable. A trained and careful practitioner can obtain much better results than automated approaches, but the risk is that humans tend to focus on more familiar and better visible particle views, thus omitting less frequently appearing orientations that may be needed for successful structure determination. In semi-automated approaches, the computer performs an initial step of detection of putative particles in a micrograph. All candidates are windowed, and the user removes poor particles from the gallery of possible candidates. Fully automated procedures can be divided into three groups: those that rely on ad hoc steps of denoising and contrast enhancement followed by a search for regions of a given size that emerge above the background level (Adiga et al., 2004); those that extract orientation-independent statistical features from regions of micrographs that may contain particles and proceed with classification (Hall and Patwardhan, 2004; Lata et al., 1995); and those that employ templates, i.e., either class averages of particles selected from micrographs or projections from a known 3D structure of the complex (Chen and Grigorieff, 2007; Huang and Penczek, 2004; Sigworth, 2004). The use of fully automated procedures carries even higher risks of introducing bias, as positively correlating noise features are indistinguishable from weak but valid signal. Therefore, one faces the risk of eventually merely reproducing the template structure. The study of the HIV-1 envelope glycoprotein is a prominent example in which template bias likely played a deciding role (Mao et al., 2013). Good practice is therefore to rely on template-based particle picking only if particles are clearly visible in the micrographs.

With particle coordinates identified in the micrographs, the particles are windowed and assembled into a stack. The initial

locations are not very precise. Therefore, the window size should exceed the approximate particle size by at least 30% (more for small particles). For issues relating to aliasing and density normalization, see [Supplemental Information](#).

2D Clustering and Formation of Class Averages

The first step in single-particle EM structure determination is the analysis of the 2D image dataset, particularly the alignment and grouping of the data into homogenous subsets. There are several reasons for why it is best to begin with 2D analysis: (1) 2D datasets contain image artifacts, invalid particles, or simply empty fields that should be removed; (2) the angular distribution of the particle views is unknown and if the set is dominated by just a few views, 3D analysis is unlikely to succeed; and (3) computational ab initio 3D structure determination requires high-SNR input data, as is present in high-quality class averages.

Various strategies have been proposed to deal with the problem of alignment and clustering of large sets of single-particle EM images (Joyeux and Penczek, 2002; Penczek, 2008), but all are fundamentally rooted in the popular K-means clustering algorithm (Figure 3A). As most steps in single-particle EM analysis use a variant of this algorithm, including 2D multi-reference alignment, 3D multi-reference refinement, even 3D structure refinement (projection matching), the principles and properties of K-means clustering are described in [Supplemental Information](#).

A straightforward implementation of the K-means algorithm in single-particle EM analysis is 2D multi-reference alignment (MRA) (van Heel and Stöckler-Meilicke, 1985), a process in which the dataset is presented with K seed templates, and all images are aligned to and compared with all templates and assigned to the one they most resemble. The process is iterative: a new

set of templates is computed by averaging images based on results from the initial grouping (including transformations given by alignment of the data in the previous step), and the whole procedure is repeated until a stable solution is reached. To accelerate the procedure, one can employ an additional step of principal component analysis (PCA) executed so that the clustering is actually performed using factorial coordinates, not the original images (for in-depth reading, see [Frank, 2006](#)). All major single-particle EM software packages contain a version of MRA, often with various heuristics aimed at improved performance, particularly with respect to the problem of “group collapse”: as MRA combines alignment with clustering, the process is unstable in that the more common particle views produce large, high-SNR class averages, which in turn “attract” less common or more noisy images, eventually leading to the disappearance of less populous groups.

In light of the fundamental shortcomings of MRA (see [Supplemental Information](#)), the iterative stable alignment and clustering (ISAC) method has been developed ([Yang et al., 2012](#)). This method uses a dedicated clustering algorithm to counteract group collapse and employs a multi-level validation strategy of the identified groups, thus yielding uniquely homogeneous classes of images (see [Supplemental Information](#) for more information).

Calculation of Initial Structures

Ab initio 3D structure determination is necessary in cases in which no reasonable templates or guesses for the structure exist. Even though new implementations of 3D structure refinement algorithms are increasingly robust, initial templates, when available, can contain significant errors and an attempt to initialize structure refinement with such templates and raw EM particles is likely to fail. When available, 3D templates can be used, e.g., a low-resolution negative-stain EM 3D reconstruction, an appropriately filtered X-ray model or an EM map of a homolog ([Beckmann et al., 1997](#)). If high point-group symmetry is present, particularly icosahedral symmetry, some refinement algorithms will converge properly with random initialization. However, it is always better to execute all steps indicated in this and the previous sections, because extensive validation methodology built into the 2D analysis and ab initio steps significantly increases confidence in the final outcome.

Ab initio structure determination methods can be broadly divided into those that require additional experiments, typically in the form of tilt pairs, and those that use only data of untilted specimens and rely entirely on computational strategies to deliver the structure.

The earliest and still the most commonly used ab initio tilt-based structure determination method is the random conical tilt (RCT) approach ([Radermacher et al., 1987](#)). Because one of the orientation parameters is set experimentally (tilt angle) and others can be computed in a robust manner (in-plane rotation, tilt angle correction), the method will deliver a reliable initial structure. It is, however, difficult to collect high-tilt data of acceptable quality, especially for vitrified specimens, in which case charging and beam-induced movement can be severe. Most RCT work is thus done using negatively stained specimens, but the artifacts associated with staining ([Cheng et al., 2006](#)) and the missing

cone problem ([Frank, 2006](#)) that further degrades the quality of the 3D map limit the utility of the resulting structures. However, RCT is a virtually foolproof method and its outcome will immensely increase the confidence in the final structure.

Computational ab initio structure determination methods seek to determine five orientation parameters (three Euler angles and two translations) for each projection image such that the resulting 3D structure is “best” in the sense of some mathematical criterion. Due to the low quality of EM data and also due to the time needed for the calculations, virtually all ab initio methods in use assume the input to be a relatively small set (<1,000) of class averages that result from 2D analysis. Since the success of the 3D orientation search strongly depends on the data quality, it is particularly important that the used class averages represent homogeneous particle groups.

The earliest computational ab initio structure determination approach is based on the central section theorem: since Fourier transforms of 2D projections of a 3D object are central sections through the 3D Fourier transform of the object, Fourier transforms of any two projections will intersect along a line, called a “common line.” The common-lines approach was first implemented in IMAGIC as “angular reconstitution,” taking advantage of the existence of a mathematical solution for orienting three projections ([van Heel, 1987](#)). Thus, in angular reconstitution, the user selects triplets of class averages, and multiple triplets are then merged into a common framework, yielding the final 3D structure. The procedure depends critically on user choices and one is thus advised to explore various combinations to gain confidence in the ultimate outcome.

A recently introduced approach to ab initio 3D structure determination, which shows great promise in producing reliable initial models, is based on projection matching using the stochastic hill climbing (SHC) algorithm. The SHC strategy was first implemented in the software package SIMPLE ([Elmlund and Elmlund, 2012](#)), and has been expanded to the “validation of individual parameter reproducibility” (VIPER) approach, which incorporates validation steps into the structure determination process, monitoring the orientation parameters ([Penczek, 2014a](#)). See [Supplemental Information](#) for further information on projection matching, SHC and VIPER.

Structure Refinement and Resolution

After obtaining an initial map, the structure has to be refined to obtain the final map ([Figures 4A–4D](#)). All single-particle EM packages use a more or less elaborate version of the 3D projection matching procedure ([Figure 3B](#) and [Supplemental Information](#)) for structure refinement. It modifies the orientation parameters of single-particle images (projections) to achieve a better match with reprojections computed from the current approximation of the structure ([Penczek, 2008](#)). While all implementations share the same principle of projection matching, the details of the methodology and the degree to which the user can control the process vary widely and are discussed in [Supplemental Information](#).

Progress of the refinement is monitored by a number of indicators, in particular the Fourier shell correlation (FSC) curve ([Figure 4E](#)), which provides information on the level of the SNR as a function of the spatial frequency ([Penczek, 2010c](#)), and

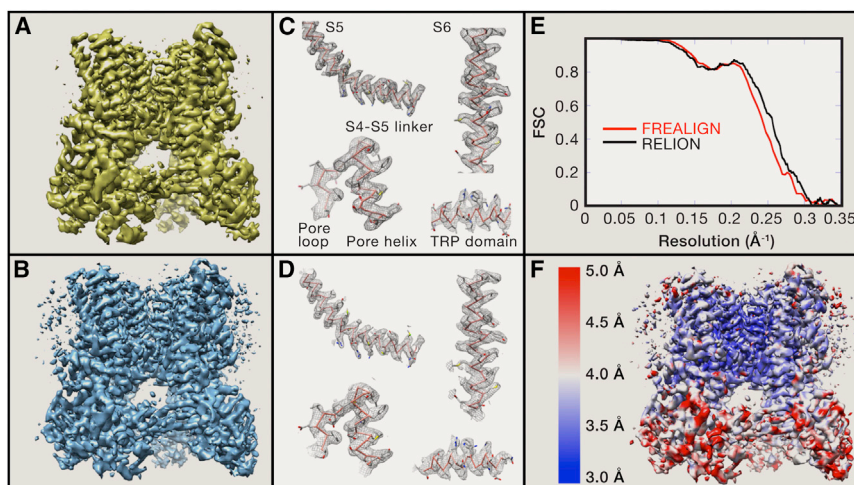


Figure 4. Evaluation and Validation of a 3D EM Structure

Critical evaluation of EM structural results is of utmost importance due to potential model bias and unavoidable noise alignment inherent to the single-particle EM structure determination method. Ultimate confirmation of the map, particularly of the details at the limit of the resolution claimed, is best done by independent structure determination, possibly using different software packages, even if one uses the same dataset. Here, we show the results of two outcomes for the structure determination of the TRPV1 channel.

(A) Originally, the structure was solved using RELION (Scheres, 2012); the refinement was initialized with an RCT model, and the final map represents the best class produced by 3D MRA (Liao et al., 2013).

(B) The structure determination was repeated using the same 2D dataset. 2D MRA was performed using IMAGIC (van Heel et al., 1996), an initial model was generated using EMAN2 (Tang et al., 2007), and refinement and 3D MRA were done in FREALIGN (Grigorieff, 2007; Lyumkis et al., 2013).

For consistency, the rotationally averaged power spectrum of map (B) was set to that of map (A). Interestingly, while the two maps are visually very similar, only ~60% of particles in the best class determined by RELION coincide with those in the best class determined by FREALIGN. This difference likely reflects limitations of *K*-means-based clustering approaches and, possibly, points to the fact that the number of classes used was too low.

(C and D) The side-chain densities in the best parts of the map shown in (A) agree with those of the map shown in (B), validating these details. However, some weaker peripheral density features in the maps shown in (A) and (B) exhibit noticeable differences (see [Supplemental Information](#) and [Figure S2](#)).

(E) Angular uncertainty and blurring affects the FSC curves, and thus the resolution reported: calculation of 3D reconstructions using multiple, probability-weighted copies of each particle image (“soft matching,” see [Supplemental Information](#)) can lead to an apparent improvement in the resolution (RELION, black curve) while hard matching yields more conservative results (FREALIGN, red curve). The difference is, however, too small to affect the interpretation of the maps and also lies within the general uncertainty bounds of the FSC methodology, which also depends on other data-processing steps, as, for example, masking of the map.

(F) The resolution of the map is non-uniform. The local resolution of the map shown in (B) was calculated (Penczek, 2014c) and indicates that densities within the membrane domain, and particularly around the pore, are better resolved than those in the extracellular domains. 3D maps were rendered using UCSF Chimera (Pettersen et al., 2004).

the resolution of the map. The FSC curve is obtained by splitting the dataset into halves, calculating a volume from each half, and computing correlation coefficients within resolution shells extracted from Fourier transforms of the two volumes. Importantly, the definition requires that the noise in the two structures should be independent, a condition difficult to meet in practice and often compromised by refining a single dataset while evaluating the FSC with two structures computed from half-subsets of the entire set. “Resolution” in single-particle EM is then a somewhat arbitrarily chosen cut-off level of the SNR or FSC curve. For example, the resolution can be defined as the spatial frequency at which the FSC curve is 0.5 or as the spatial frequency at which the SNR is 1.0 (corresponding to an FSC of 0.33), the level at which the power of the signal is equal to the power of the noise. Another common choice of threshold is 0.143, the value selected based on relating EM results to those in X-ray crystallography (Rosenthal and Henderson, 2003).

A common problem in structure refinement is so-called “over-fitting” of the data—the emergence of features in an EM map due to the alignment of noise. Over-fitting arises due to the fact that the dataset is refined without reference to external standards (at least before the emergence of secondary-structure features whose generic appearance is known), and, therefore, it is not known what constitutes “signal” and what is “noise” (Stewart and Grigorieff, 2004). As a result, artifacts are created by chance and further enhanced by alignment of the noise components in the data, leading to inflated FSC values and an artificially high resolution. It was realized early on that in order to ensure inde-

pendence of noise in the half-dataset maps used to calculate the FSC, the half-datasets must be refined independently (e.g., Grigorieff, 2000). This avoids exaggerated resolution estimates using the FSC, an approach that has recently been reiterated (Scheres, 2012) and is now often referred to as the “gold standard” refinement procedure (Henderson et al., 2012). It has to be noted, however, that even this procedure has limitations, as (1) it is impossible to have true independence between the half datasets; (2) the approach tends to underestimate the resolution potential of the data; and (3) for all existing refinement algorithms, each of the half-structures suffers independently from the described “over-fitting” problem. There are also a number of image-processing steps that result in a nominal improvement of the resolution without actually improving the image alignment parameters (Figure 4E) or map. An obvious example is masking of the structure, as the shape of the mask and the way its edges are attenuated may have a significant impact on the FSC curve. One can also set density values to a constant when they are lower than a certain level, a step that is akin to solvent flattening in X-ray crystallography. Since none of these operations are codified in the field and since the FSC curve is also dependent on other factors beyond the ones mentioned here, it is the opinion of the authors that there is currently no real “gold standard” procedure for structure refinement and resolution estimation of an EM map. An approach equally useful to the “gold standard” procedure to obtain an adequate resolution estimate is simply to limit the refinement frequency to a resolution lower than the one of the reference map.

In conclusion, the quality of an EM map is described by the entire FSC curve, not just the resolution, and there are EM maps with the same nominal resolution that differ significantly in overall quality (Ludtke and Serysheva, 2013). The reverse is also true, namely that the reported nominal resolution reflects the overall resolution of the entire density map but it does not account for local variation. The EM map with the highest nominal resolution is not necessarily the best one, because values at lower frequencies often matter more for connectivity and interpretability of the map. Hence, the resolution reported for an EM map should be treated as a broad guideline rather than a firm number.

3D Multi-Reference Alignment

Many samples will contain structural heterogeneity. When its presence is detected (for example by calculating a variance map, see below), a possibility is to use 3D multi-reference alignment (3D MRA) to extract more homogeneous subsets. Current implementations are natural extensions of the basic projection-matching procedure and employ principles of the *K*-means algorithm: the user has to provide a number of initial 3D templates and the program aligns each single-particle image to all 3D templates to find the best-matching one. When all images are assigned, new 3D reconstructions are calculated and used as new references. The method proved to be successful in many applications (Brink et al., 2004; Heymann et al., 2003; Loerke et al., 2010; Schüler et al., 2006), particularly when “focusing” on a variable sub-region to make the assignments (Penczek et al., 2006). The shortcomings of 3D MRA are those of the *K*-means algorithm: a strong bias toward initial templates, solutions that depend on the number *K* of requested classes, and a lack of validation of the results. In light of these limitations, the applicability of 3D MRA should be guided by the concurrent examination of the local variability of the map (Penczek 2014c). Indeed, if the procedure succeeded in separating the dataset into homogeneous classes, the distribution of 3D variability within each group should be uniform (in practice it tends to be proportional to the density distribution of the map). Any residual local variability that exceeds what is reasonably expected, particularly at locations where map density is low, signals that 3D MRA should be continued with an increased number of classes and possibly in the “focused” mode. The 3D MRA procedure works best for complexes exhibiting substoichiometric ligand binding in which a fragmented appearance of the ligand would indicate failure of the procedure, and results can be validated by the appearance of secondary structure elements in the 3D class averages.

Structure Validation and Interpretation

As explained above, the indication of a certain resolution by the FSC alone does not demonstrate the validity of the refined structure. Independent refinement of two exclusive subsets of the data increases confidence in the resolution but does not necessarily confirm the validity of a structure. This is particularly true for reconstructions that do not resolve secondary structure features. Because refinement is typically initialized with the same 3D template, even if low-pass filtered, this undermines the independence assumption. Furthermore, the FSC may fail entirely to indicate resolution when there is significant misalignment of the particle images. All current refinement software may display

this behavior of the FSC, including software that performs separate refinement of subsets of the data. It is therefore equally important to also apply other plausibility criteria to the results whenever possible (see below).

In case of a heterogeneous dataset, the refinement itself might be correct, but the structure, being a superposition of various states, will have limited biological relevance. Therefore, additional tests are recommended, particularly those that reveal the localized real-space quality of the map. First, it is possible to compute the local resolution of the map using a wavelet-based (Kucukelbir et al., 2014) or an FSC-equivalent approach (Penczek, 2014b) (Figure 4F). Local real-space variability of the map can be assessed using a simplified variance approach (Penczek, 2014c). More information could be obtained from analysis of correlations within the map, as in 3D PCA, by statistical resampling (Penczek et al., 2011), which is computationally demanding and yields only low-resolution information. A local variability analysis can also serve as a means to establish plausible initial templates for 3D MRA (Spahn and Penczek, 2009).

The overall validation of an EM map depends on the resolution reached. We can distinguish three resolution regimes that may help confirm the resolution indicated by the FSC. A *low-resolution* map (>10 Å) reveals the overall shape of a complex and possibly the relative arrangement of major modules. Here, docking of X-ray segments is unreliable, and flexible fitting should be avoided. An *intermediate-resolution* map (4–10 Å) reveals secondary structure details and the relative arrangement of modules. It enables unique fitting of X-ray segments and can be used to detect conformational changes. A *high-resolution* map (<4 Å) clearly resolves secondary structure elements (e.g., α helices) and some individual residues, allowing polypeptide backbone tracing (Figures 4C and 4D) and precise fitting of X-ray segments. It also provides a detailed description of conformational changes. Keeping in mind that the precise resolution number attached to the map can often not be reliably established, one should focus on arguments that give confidence that the overall appearance of the map is correct. Thus, for low-resolution maps, the best evidence is provided by tilt experiments, particularly by initiating the project by RCT reconstruction. While final details of the map might be debatable, at least the possibility of major mistakes is minimized. A map at intermediate resolution can be confirmed if the appearance of subunits agrees with the appearance of segments determined by X-ray crystallography, if available. A measure of confidence can also be provided by a posteriori tilt experiments (Henderson et al., 2011). In these experiments, often referred to as “tilt test,” a small set of image pairs is collected, one untilted and a second with a small sample tilt, for example 10 degree. The test requires projection matching of the particles from the tilt pairs to the EM map that is to be validated. If the difference between the views determined for the tilt pairs corresponds (within error) to the known tilt angle, the EM map is considered valid. High-resolution maps must display known features of secondary structure elements and density for bulky side chains. These features can be further corroborated with a plausible atomic model that can also be used to obtain an independent resolution estimate by converting it to pseudo-electron density and low-pass filtering it to the claimed resolution of the EM map.

The interpretation of EM maps depends mainly on three factors: the resolution of the map, the established presence of multiple conformational states in the sample, and the availability of X-ray crystallographic segments of some components, of the entire complex or of one of its homologs. High-resolution EM maps can be analyzed in the same manner as X-ray maps by performing de novo backbone tracing. Furthermore, because EM experiments yield both amplitudes and phases, it is possible to arrive at reliable atomic models even in cases in which crystallographic efforts were unsuccessful or comparison with an atomic model is difficult. In addition, the availability of local resolution and variability measures is helpful in avoiding over-interpretation of poorly resolved regions of EM maps. At high resolution, docking of X-ray segments can be done with high precision, thus increasing apparent resolvability of the results and making it possible to detect atomic scale conformational changes with respect to the X-ray results. Similarly, availability of high-resolution structures of multiple functional states of the complex makes single-particle EM a unique tool to study protein dynamics.

Intermediate-resolution EM maps offer insights into the arrangement of subunits and localization of functional sites of macromolecular complexes. Structure interpretation can be augmented by docking of X-ray segments, if available, which also improves the precision of feature localization. The docking can be accomplished, for example, using UCSF Chimera (Pettersen et al., 2004). However, as the resolution of EM maps gets worse, so does the precision of docking. While some progress has been made in this area, reliable computational tools to assess docking uncertainty as a function of map quality are lacking, so some caution is needed to avoid over-interpretation of the results.

The main utility of low-resolution EM maps is in revealing the overall architecture of a complex. Results of docking X-ray segments should be interpreted with utmost caution, because determining the best-fitting position of a given segment does not mean that it is its only possible localization, creating the possibility of major mistakes. At the same time, low-resolution EM maps have the added value that they can often provide a stepping stone toward higher resolution, and thus more informative results.

Concluding Remarks

Structure determination by single-particle cryo-EM is an increasingly popular approach, but like most experimental methodologies, it is important not to approach it with “plug and play” assumptions. We hope that the information provided in this Primer will be helpful in guiding the execution of this technique and the interpretation of data obtained with it.

SUPPLEMENTAL INFORMATION

Supplemental Information includes Supplemental Text and two figures and can be found with this article online at <http://dx.doi.org/10.1016/j.cell.2015.03.050>.

AUTHOR CONTRIBUTIONS

Authors are listed alphabetically and contributed equally to the manuscript. They can be contacted directly: yicheng@ucsf.edu (Y.C.), niko@grigorieff.com

(N.G.), pawel.a.penczek@uth.tmc.edu (P.A.P.), twalz@hms.harvard.edu (T.W.).

ACKNOWLEDGMENTS

The authors thank Rita De Zorzi for providing images of the AMPA receptor and Tim Grant for calculating 2D class averages and an initial reconstruction of the TRPV1 channel using IMAGIC and EMAN2. This work was supported by grants from the NIH (R01 GM098672, R01 GM082893, and P50 GM082250 to Y.C.; R01 GM060635 to P.A.P.). N.G. and T.W. are investigators with the Howard Hughes Medical Institute.

REFERENCES

- Adiga, P.S., Malladi, R., Baxter, W., and Glaeser, R.M. (2004). A binary segmentation approach for boxing ribosome particles in cryo EM micrographs. *J. Struct. Biol.* **145**, 142–151.
- Bai, X.C., Fernandez, I.S., McMullan, G., and Scheres, S.H. (2013). Ribosome structures to near-atomic resolution from thirty thousand cryo-EM particles. *eLife* **2**, e00461.
- Bai, X.C., McMullan, G., and Scheres, S.H. (2015). How cryo-EM is revolutionizing structural biology. *Trends Biochem. Sci.* **40**, 49–57.
- Beckmann, R., Bubeck, D., Grassucci, R., Penczek, P., Verschoor, A., Blobel, G., and Frank, J. (1997). Alignment of conduits for the nascent polypeptide chain in the ribosome-Sec61 complex. *Science* **278**, 2123–2126.
- Brilot, A.F., Chen, J.Z., Cheng, A., Pan, J., Harrison, S.C., Potter, C.S., Carragher, B., Henderson, R., and Grigorieff, N. (2012). Beam-induced motion of vitrified specimen on holey carbon film. *J. Struct. Biol.* **177**, 630–637.
- Brink, J., Ludtke, S.J., Kong, Y., Wakil, S.J., Ma, J., and Chiu, W. (2004). Experimental verification of conformational variation of human fatty acid synthase as predicted by normal mode analysis. *Structure* **12**, 185–191.
- Campbell, M.G., Cheng, A., Brilot, A.F., Moeller, A., Lyumkis, D., Veisler, D., Pan, J., Harrison, S.C., Potter, C.S., Carragher, B., and Grigorieff, N. (2012). Movies of ice-embedded particles enhance resolution in electron cryo-microscopy. *Structure* **20**, 1823–1828.
- Chen, J.Z., and Grigorieff, N. (2007). SIGNATURE: a single-particle selection system for molecular electron microscopy. *J. Struct. Biol.* **157**, 168–173.
- Cheng, Y. (2015). Single-particle cryo-EM at crystallographic resolution. *Cell* **161**, this issue, 450–457.
- Cheng, Y., Wolf, E., Larvie, M., Zak, O., Aisen, P., Grigorieff, N., Harrison, S.C., and Walz, T. (2006). Single particle reconstructions of the transferrin-transferrin receptor complex obtained with different specimen preparation techniques. *J. Mol. Biol.* **355**, 1048–1065.
- Elmlund, D., and Elmlund, H. (2012). SIMPLE: Software for *ab initio* reconstruction of heterogeneous single-particles. *J. Struct. Biol.* **180**, 420–427.
- Ericsson, U.B., Hallberg, B.M., Detitta, G.T., Dekker, N., and Nordlund, P. (2006). Thermofluor-based high-throughput stability optimization of proteins for structural studies. *Anal. Biochem.* **357**, 289–298.
- Faruqi, A.R., and McMullan, G. (2011). Electronic detectors for electron microscopy. *Q. Rev. Biophys.* **44**, 357–390.
- Frank, J. (2006). Three-dimensional electron microscopy of macromolecular assemblies: visualization of biological molecules in their native state (New York: Oxford University Press).
- Frank, J., Shimkin, B., and Dowse, H. (1981). SPIDER—a modular software system for electron image processing. *Ultramicroscopy* **6**, 343–358.
- Glaeser, R.M. (2013). Invited review article: Methods for imaging weak-phase objects in electron microscopy. *Rev. Sci. Instrum.* **84**, 111101.
- Grigorieff, N. (2000). Resolution measurement in structures derived from single particles. *Acta Crystallogr. D Biol. Crystallogr.* **56**, 1270–1277.
- Grigorieff, N. (2007). FREALIGN: high-resolution refinement of single particle structures. *J. Struct. Biol.* **157**, 117–125.

- Hall, R.J., and Patwardhan, A. (2004). A two step approach for semi-automated particle selection from low contrast cryo-electron micrographs. *J. Struct. Biol.* **145**, 19–28.
- Henderson, R. (2013). Avoiding the pitfalls of single particle cryo-electron microscopy: Einstein from noise. *Proc. Natl. Acad. Sci. USA* **110**, 18037–18041.
- Henderson, R., Chen, S., Chen, J.Z., Grigorieff, N., Passmore, L.A., Ciccarelli, L., Rubinstein, J.L., Crowther, R.A., Stewart, P.L., and Rosenthal, P.B. (2011). Tilt-pair analysis of images from a range of different specimens in single-particle electron cryomicroscopy. *J. Mol. Biol.* **413**, 1028–1046.
- Henderson, R., Sali, A., Baker, M.L., Carragher, B., Devkota, B., Downing, K.H., Egelman, E.H., Feng, Z., Frank, J., Grigorieff, N., et al. (2012). Outcome of the first electron microscopy validation task force meeting. *Structure* **20**, 205–214.
- Heymann, J.B., Cheng, N., Newcomb, W.W., Trus, B.L., Brown, J.C., and Steven, A.C. (2003). Dynamics of herpes simplex virus capsid maturation visualized by time-lapse cryo-electron microscopy. *Nat. Struct. Biol.* **10**, 334–341.
- Hohn, M., Tang, G., Goodyear, G., Baldwin, P.R., Huang, Z., Penczek, P.A., Yang, C., Glaeser, R.M., Adams, P.D., and Ludtke, S.J. (2007). SPARX, a new environment for Cryo-EM image processing. *J. Struct. Biol.* **157**, 47–55.
- Huang, Z., and Penczek, P.A. (2004). Application of template matching technique to particle detection in electron micrographs. *J. Struct. Biol.* **145**, 29–40.
- Jensen, G.J. (2001). Alignment error envelopes for single particle analysis. *J. Struct. Biol.* **133**, 143–155.
- Joyeux, L., and Penczek, P.A. (2002). Efficiency of 2D alignment methods. *Ultramicroscopy* **92**, 33–46.
- Kastner, B., Fischer, N., Golas, M.M., Sander, B., Dube, P., Boehringer, D., Hartmuth, K., Deckert, J., Hauer, F., Wolf, E., et al. (2008). GraFix: sample preparation for single-particle electron cryomicroscopy. *Nat. Methods* **5**, 53–55.
- Kucukelbir, A., Sigworth, F.J., and Tagare, H.D. (2014). Quantifying the local resolution of cryo-EM density maps. *Nat. Methods* **11**, 63–65.
- Lata, K.R., Penczek, P., and Frank, J. (1995). Automatic particle picking from electron micrographs. *Ultramicroscopy* **58**, 381–391.
- Lau, W.C., and Rubinstein, J.L. (2013). Single particle electron microscopy. *Methods Mol. Biol.* **955**, 401–426.
- Li, X., Mooney, P., Zheng, S., Booth, C.R., Braunfeld, M.B., Gubbens, S., Agard, D.A., and Cheng, Y. (2013a). Electron counting and beam-induced motion correction enable near-atomic-resolution single-particle cryo-EM. *Nat. Methods* **10**, 584–590.
- Li, X., Zheng, S.Q., Egami, K., Agard, D.A., and Cheng, Y. (2013b). Influence of electron dose rate on electron counting images recorded with the K2 camera. *J. Struct. Biol.* **184**, 251–260.
- Liao, M., Cao, E., Julius, D., and Cheng, Y. (2013). Structure of the TRPV1 ion channel determined by electron cryo-microscopy. *Nature* **504**, 107–112.
- Loerke, J., Giesebrecht, J., and Spahn, C.M. (2010). Multiparticle cryo-EM of ribosomes. *Methods Enzymol.* **483**, 161–177.
- Ludtke, S.J., and Serysheva, I.I. (2013). Single-particle cryo-EM of calcium release channels: structural validation. *Curr. Opin. Struct. Biol.* **23**, 755–762.
- Lyumkis, D., Moeller, A., Cheng, A., Herold, A., Hou, E., Irving, C., Jacovetty, E.L., Lau, P.W., Mulder, A.M., Pulkas, J., et al. (2010). Automation in single-particle electron microscopy connecting the pieces. *Methods Enzymol.* **483**, 291–338.
- Lyumkis, D., Brilot, A.F., Theobald, D.L., and Grigorieff, N. (2013). Likelihood-based classification of cryo-EM images using FREALIGN. *J. Struct. Biol.* **183**, 377–388.
- Mao, Y., Wang, L., Gu, C., Herschhorn, A., Désormeaux, A., Finzi, A., Xiang, S.H., and Sodroski, J.G. (2013). Molecular architecture of the uncleaved HIV-1 envelope glycoprotein trimer. *Proc. Natl. Acad. Sci. USA* **110**, 12438–12443.
- McMullan, G., Chen, S., Henderson, R., and Faruqi, A.R. (2009). Detective quantum efficiency of electron area detectors in electron microscopy. *Ultramicroscopy* **109**, 1126–1143.
- Meyerson, J.R., Rao, P., Kumar, J., Chittori, S., Banerjee, S., Pierson, J., Mayer, M.L., and Subramaniam, S. (2014). Self-assembled monolayers improve protein distribution on holey carbon cryo-EM supports. *Sci. Rep.* **4**, 7084.
- Milazzo, A.C., Cheng, A., Moeller, A., Lyumkis, D., Jacovetty, E., Polukas, J., Ellisman, M.H., Xuong, N.H., Carragher, B., and Potter, C.S. (2011). Initial evaluation of a direct detection device detector for single particle cryo-electron microscopy. *J. Struct. Biol.* **176**, 404–408.
- Milne, J.L., Borgnia, M.J., Bartesaghi, A., Tran, E.E., Earl, L.A., Schauder, D.M., Lengyel, J., Pierson, J., Patwardhan, A., and Subramaniam, S. (2013). Cryo-electron microscopy—a primer for the non-microscopist. *FEBS J.* **280**, 28–45.
- Mindell, J.A., and Grigorieff, N. (2003). Accurate determination of local defocus and specimen tilt in electron microscopy. *J. Struct. Biol.* **142**, 334–347.
- Ohi, M., Li, Y., Cheng, Y., and Walz, T. (2004). Negative staining and image classification – powerful tools in modern electron microscopy. *Biol. Proced. Online* **6**, 23–34.
- Orlova, E.V., and Saibil, H.R. (2011). Structural analysis of macromolecular assemblies by electron microscopy. *Chem. Rev.* **111**, 7710–7748.
- Penczek, P.A. (2008). Single Particle Reconstruction. In *International Tables for Crystallography*, U. Shmueli, ed. (New York: Springer), pp. 375–388.
- Penczek, P.A. (2010a). Image restoration in cryo-electron microscopy. *Methods Enzymol.* **482**, 35–72.
- Penczek, P.A. (2010b). Fundamentals of three-dimensional reconstruction from projections. *Methods Enzymol.* **482**, 1–33.
- Penczek, P.A. (2010c). Resolution measures in molecular electron microscopy. *Methods Enzymol.* **482**, 73–100.
- Penczek, P.A. (2014a). sxvip. In SPARX Wiki (<http://sparx-em.org/sparxwiki/sxvip>).
- Penczek, P.A. (2014b). sxlocres. In SPARX Wiki (<http://sparx-em.org/sparxwiki/sxlocres>).
- Penczek, P.A. (2014c). sx3dvariability. In SPARX Wiki (<http://sparx-em.org/sparxwiki/sx3dvariability>).
- Penczek, P.A., Frank, J., and Spahn, C.M.T. (2006). A method of focused classification, based on the bootstrap 3D variance analysis, and its application to EF-G-dependent translocation. *J. Struct. Biol.* **154**, 184–194.
- Penczek, P.A., Kimmel, M., and Spahn, C.M. (2011). Identifying conformational states of macromolecules by eigen-analysis of resampled cryo-EM images. *Structure* **19**, 1582–1590.
- Petersen, E.F., Goddard, T.D., Huang, C.C., Couch, G.S., Greenblatt, D.M., Meng, E.C., and Ferrin, T.E. (2004). UCSF Chimera—a visualization system for exploratory research and analysis. *J. Comput. Chem.* **25**, 1605–1612.
- Radermacher, M., Wagenknecht, T., Verschoor, A., and Frank, J. (1987). Three-dimensional reconstruction from a single-exposure, random conical tilt series applied to the 50S ribosomal subunit of *Escherichia coli*. *J. Microsc.* **146**, 113–136.
- Rosenthal, P.B., and Henderson, R. (2003). Optimal determination of particle orientation, absolute hand, and contrast loss in single-particle electron cryomicroscopy. *J. Mol. Biol.* **333**, 721–745.
- Rubinstein, J.L., and Brubaker, M.A. (2014). Alignment of cryo-EM movies of individual particles by global optimization of image translations. *arXiv* arXiv:1409.6789, <http://arxiv.org/abs/1409.6789>.
- Ruskin, R.S., Yu, Z., and Grigorieff, N. (2013). Quantitative characterization of electron detectors for transmission electron microscopy. *J. Struct. Biol.* **184**, 385–393.
- Russo, C.J., and Passmore, L.A. (2014). Electron microscopy: Ultrastable gold substrates for electron cryomicroscopy. *Science* **346**, 1377–1380.
- Scheres, S.H.W. (2012). RELION: implementation of a Bayesian approach to cryo-EM structure determination. *J. Struct. Biol.* **180**, 519–530.
- Scheres, S.H.W. (2014). Beam-induced motion correction for sub-megadalton cryo-EM particles. *eLife* **3**, e03665.

- Schüler, M., Connell, S.R., Lescoute, A., Giesebrecht, J., Dabrowski, M., Schroer, B., Mielke, T., Penczek, P.A., Westhof, E., and Spahn, C.M.T. (2006). Structure of the ribosome-bound cricket paralysis virus IRES RNA. *Nat. Struct. Mol. Biol.* **13**, 1092–1096.
- Shukla, A.K., Westfield, G.H., Xiao, K., Reis, R.I., Huang, L.Y., Tripathi-Shukla, P., Qian, J., Li, S., Blanc, A., Oleskie, A.N., et al. (2014). Visualization of arrestin recruitment by a G-protein-coupled receptor. *Nature* **512**, 218–222.
- Sigworth, F.J. (2004). Classical detection theory and the cryo-EM particle selection problem. *J. Struct. Biol.* **145**, 111–122.
- Spahn, C.M., and Penczek, P.A. (2009). Exploring conformational modes of macromolecular assemblies by multiparticle cryo-EM. *Curr. Opin. Struct. Biol.* **19**, 623–631.
- Stewart, A., and Grigorieff, N. (2004). Noise bias in the refinement of structures derived from single particles. *Ultramicroscopy* **102**, 67–84.
- Subramaniam, S. (2013). Structure of trimeric HIV-1 envelope glycoproteins. *Proc. Natl. Acad. Sci. USA* **110**, E4172–E4174.
- Tang, G., Peng, L., Baldwin, P.R., Mann, D.S., Jiang, W., Rees, I., and Ludtke, S.J. (2007). EMAN2: an extensible image processing suite for electron microscopy. *J. Struct. Biol.* **157**, 38–46.
- Thon, F. (1966). Zur Defokussierungsabhängigkeit des Phasenkontrastes bei der elektronenmikroskopischen Abbildung. *Z Naturforschung* **21a**, 476–478.
- van Heel, M. (1987). Angular reconstitution: *a posteriori* assignment of projection directions for 3D reconstruction. *Ultramicroscopy* **21**, 111–123.
- van Heel, M. (2013). Finding trimeric HIV-1 envelope glycoproteins in random noise. *Proc. Natl. Acad. Sci. USA* **110**, E4175–E4177.
- van Heel, M., and Stöffler-Meilicke, M. (1985). Characteristic views of *E. coli* and *B. stearothermophilus* 30S ribosomal subunits in the electron microscope. *EMBO J.* **4**, 2389–2395.
- van Heel, M., Harauz, G., Orlova, E.V., Schmidt, R., and Schatz, M. (1996). A new generation of the IMAGIC image processing system. *J. Struct. Biol.* **116**, 17–24.
- Wade, R.H. (1992). A brief look at imaging and contrast transfer. *Ultramicroscopy* **46**, 145–156.
- Yang, Z., Fang, J., Chittuluru, J., Asturias, F.J., and Penczek, P.A. (2012). Iterative stable alignment and clustering of 2D transmission electron microscope images. *Structure* **20**, 237–247.
- Yoshioka, C., Carragher, B., and Potter, C.S. (2010). Cryomesh: a new substrate for cryo-electron microscopy. *Microsc. Microanal.* **16**, 43–53.
- Zhu, J., Penczek, P.A., Schröder, R., and Frank, J. (1997). Three-dimensional reconstruction with contrast transfer function correction from energy-filtered cryoelectron micrographs: procedure and application to the 70S *Escherichia coli* ribosome. *J. Struct. Biol.* **118**, 197–219.

Single-Particle Cryo-EM at Crystallographic Resolution

Yifan Cheng^{1,*}

¹Department of Biochemistry and Biophysics, University of California San Francisco, 600 16th Street, San Francisco, CA 94158, USA

*Correspondence: ycheng@ucsf.edu

<http://dx.doi.org/10.1016/j.cell.2015.03.049>

Until only a few years ago, single-particle electron cryo-microscopy (cryo-EM) was usually not the first choice for many structural biologists due to its limited resolution in the range of nanometer to subnanometer. Now, this method rivals X-ray crystallography in terms of resolution and can be used to determine atomic structures of macromolecules that are either refractory to crystallization or difficult to crystallize in specific functional states. In this review, I discuss the recent breakthroughs in both hardware and software that transformed cryo-microscopy, enabling understanding of complex biomolecules and their functions at atomic level.

A major goal of structural biology is to provide mechanistic understanding of critical biological processes. The most detailed insights come from atomic structures of macromolecules and complexes involved in these processes in relevant functional states. Beyond basic research, obtaining atomic structures of drug targets is also a standard approach in the pharmaceutical industry in the design and optimization of therapeutic compounds.

Prior to 2013, most atomic structures deposited in the protein data bank (PDB) were determined by X-ray crystallography. This technique starts with crystallization of molecules that are homogeneous in both composition and conformation. Once the 3D crystals are of sufficient size to diffract X-rays, they are used for structure determination. The resolution of crystal structures is largely determined by how well the molecules are ordered (or aligned to each other) in the crystal. After 100 years of development and maturation, X-ray crystallography has become a routine method, delivering a wealth of structural information about important biomolecules and cellular processes (Jones, 2014; Shi, 2014). While X-ray crystallography will continue to play an important role in answering many biological questions, it completely depends on growth of well-ordered 3D crystals. Producing such crystals, however, is a major bottleneck for challenging targets, such as integral membrane proteins of mammalian origin or chromatin in complex with its modifiers. In the last 2 years, single particle electron cryo-microscopy (cryo-EM) has emerged as a technique for determining atomic resolution structures at better than 4-Å resolution, comparable to many solved using crystallographic approaches. It has now determined a number of structures of proteins and complexes that have vexed crystallographers.

The Way Electron Cryo-Microscopy Works

Rather than determining structures from diffraction of 3D crystals, single-particle cryo-EM determines structures by computationally combining images of many individual macromolecules in identical or similar conformations (Frank et al., 1978). In this

approach, samples of purified molecules in solution are applied to an EM grid covered with a thin holey carbon film and blotted by a filter paper to remove most of solution so that a thin liquid layer is formed across the holes in the carbon film. This is followed by plunge-freezing in liquid ethane cooled by liquid nitrogen. This method was originally developed by Dubochet and colleagues (Dubochet et al., 1982), and improved significantly with semi-automated plunge-freezer machine to improve reproducibility. After plunge-freezing, frozen-hydrated molecules are embedded in a thin layer of vitreous ice (Figure 1A) that preserves the native structure to the atomic level (Taylor and Glaeser, 1974), prevents dehydration of biological samples within the vacuum of an electron microscope, and reduces the effects of radiation damage (Stark et al., 1996). Molecules embedded in a thin layer of vitreous ice adopt a range of orientations, which are then imaged using an electron beam (Figure 1B). Each particle image is a 2D projection of a molecule, whose spatial orientation and position are defined by six geometric parameters. These include three Euler angles and two in-plane positional parameters. The sixth parameter is the defocus that defines the z position along the direction of the electron beam and is often assumed to be the same for all particles in a micrograph (or image). After further correction for aberrational errors of the microscope, a 3D structure can be reconstructed by combining images of many molecules that have been aligned to each other. The resolution of the reconstruction is improved iteratively by refining the first five geometric parameters for each particle to high accuracy (Frank, 1996). The final 3D reconstruction is a Coulomb potential density map that can be interpreted in the same way as electron density maps determined by X-ray crystallography (Figures 1C and 1D).

Both X-ray and electron beams cause radiation damage to biological samples. For X-ray diffraction, a larger crystal with coherently packed molecules can tolerate a high total dose and often diffracts to high resolution because more molecules contribute to the diffraction. For single-particle cryo-EM, the total electron dose used to image each molecule is set to a very low

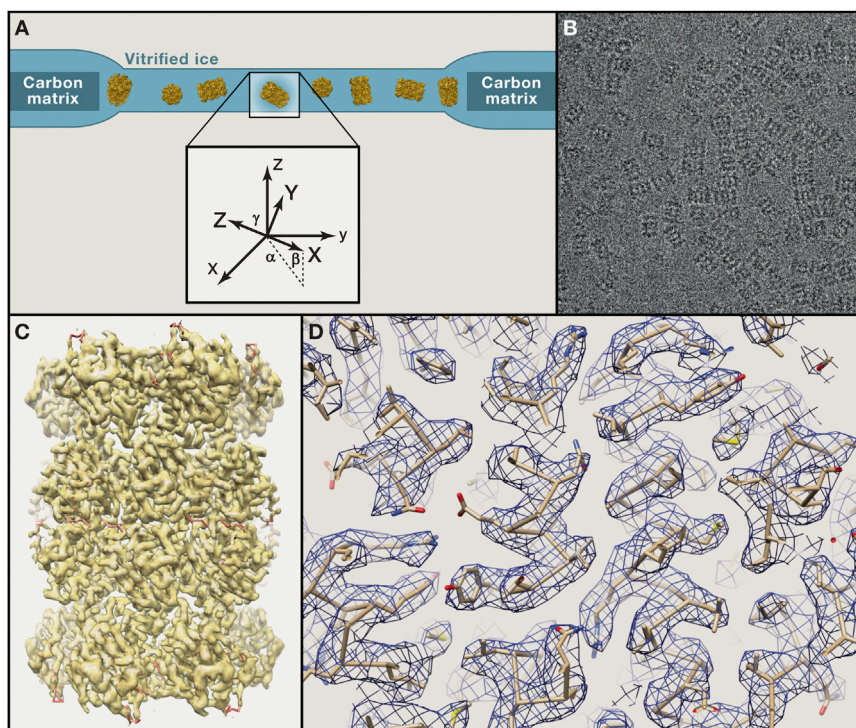


Figure 1. Single-Particle Cryo-EM

(A) Purified biological molecules are embedded in a thin layer of vitreous ice, in which they ideally adopt random orientations. The orientations are specified by the in-plane position parameters, x and y , and three Euler angles α , β , and γ , which are refined iteratively to high accuracies. The defocus values of the images are currently often determined separately.

(B) Typical image of frozen-hydrated archaeal 20S proteasomes.

(C) 3D reconstruction of the 20S proteasome at 3.3-Å resolution.

(D) Side-chain densities of the map shown in (B) are comparable with those seen in maps determined by X-ray crystallography at a similar resolution.

level to preserve structural information at the subnanometer-resolution level. The consequence of such low-dose imaging is that individual images have a very poor signal-to-noise ratio (SNR). Hence, images from many identical or similar molecules must be averaged to enhance the SNR as well as to provide the different views needed to calculate a 3D reconstruction (De Rosier and Klug, 1968). Therefore, the total number of particle images used in a reconstruction has a similar significance to the size of a 3D crystal. Similarly, the accuracy of image alignment in single-particle EM is analogous to how well molecules are packed in a 3D crystal.

Provided that a sufficient number of images containing high-resolution information are classified and aligned accurately, single-particle cryo-EM will produce a 3D reconstruction at atomic resolution. An atomic model can then be built de novo based on fitting the known sequences into the density map from the reconstruction. Furthermore, electron micrographs are real-space images containing both amplitude and phase information. Thus, cryo-EM structure determination does not have a “phase problem” as in X-ray crystallography, but its amplitudes are less accurate than that measured from X-ray diffractions.

Resolution Determinants of Single-Particle Cryo-EM Reconstructions

Considering the scattering power of electrons versus X-rays, and the amount of information present in an image of a single molecule that can be used to determine the precise position and orientation of the molecule, Richard Henderson predicted that single-particle cryo-EM can, in theory, determine atomic-resolution structures of biological molecules as small as 100 kDa in molecular weight (Henderson, 1995). However, there are many

obstacles took many years, but by 2008, it was possible to achieve resolutions that were sufficient to visualize side-chain densities (~ 3.8 Å) (Yu et al., 2008; Zhang et al., 2008), and to determine the first de novo atomic structure (3.3 Å) of a non-enveloped icosahedral virus (Zhang et al., 2010). Because of their large sizes and high symmetry, icosahedral virus particles were among the first for which high-resolution maps were obtained, and now it is quite feasible to determine reconstructions of such samples at resolutions better than 4 Å (Chen et al., 2009; Wolf et al., 2010; Yu et al., 2011). However, it has been much harder to achieve similar resolutions for molecules that are smaller and/or less symmetric.

Nowadays, an electron microscope with 200 kV or 300 kV acceleration voltage and a field emission gun (FEG) electron source can typically deliver images with a resolution of better than 2 Å. Therefore, the achievable resolution of single particle cryo-EM is not limited by the resolution power of a modern microscope itself, but rather by the conditions required to image frozen-hydrated biological samples and the unique properties of such samples. Determining a high-resolution 3D reconstruction requires that 2D projection images contain sufficient information at both high and low resolutions. The amount of high-resolution information present in images determines the possible final resolution of a 3D reconstruction. However, low-resolution information, i.e., image contrast, is also required to visualize particles. Together, they determine how well a homogeneous set of molecules can be computationally selected for averaging, how accurately these images can be aligned, and the total number of images that are required to achieve a certain resolution. For any electron micrographs, both image amplitudes and phases are modulated by the contrast transfer function (CTF) of the

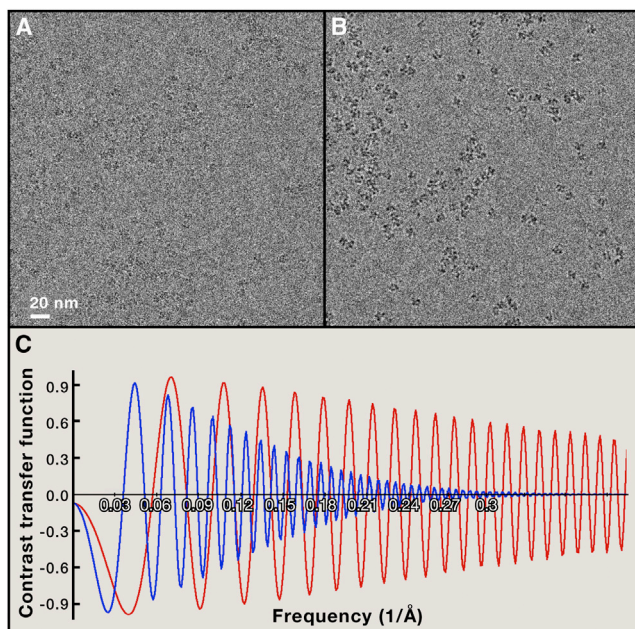


Figure 2. Influence of CTF on Image Contrast and Resolution

(A and B) Image of human transferrin receptor-transferrin complex recorded using a scintillator camera. The microscope was equipped with a FEG and operated at 200 kV. Particles in image recorded with a defocus of 1.2 μm (A) are almost invisible, but shown with strong contrast in the image recorded with a defocus of 3.0 μm (B).

(C) Simulations of CTF at 1.2 μm (red) and 3.0 μm (blue) defoci, with an acceleration voltage of 200 kV and angular spread of 0.07 mrad. Note that 3 μm defocus generates sufficient contrast for particles with a molecular weight of ~ 300 kDa, CTF envelope drops to close to zero at 3- ~ 4 - \AA resolution.

microscope, which is mostly a sine function with an envelope that reduces the amplitude at high resolution, such as shown in Figure 2C. The overall envelope of the CTF function combines effects from many factors, including the spatial and temporal coherence of the electron beam, specimen motion, the modulation transfer function (MTF) of the image recording device, and others. The contribution of the spatial coherence to the envelope is also a function of the defocus. A small defocus maximizes the envelope at high resolution but minimizes the CTF at low resolution. Thus, to obtain the best high-resolution signal, an image must be recorded with a small defocus, which results, however, in a poor image contrast. The converse is also true: to obtain good contrast, an image has to be recorded with a relatively large defocus, which reduces, however, the high-resolution signal (Figure 2). Both low- and high-resolution signals are further reduced by the MTF of the image-recording device.

This is not a serious problem for a radiation-resistant specimen. Using a sufficient electron dose, a modern electron microscope can image, for example, a single layer of graphene at atomic or near-atomic resolution with good contrast (Urban, 2011). The weak low-resolution signal is compensated by a high-electron dose, which generates sufficient image contrast. However, this approach is not possible for biological samples, which are sensitive to radiation damage (Henderson and Glaeser, 1985). To visualize frozen-hydrated biological mole-

cules with sufficient contrast, one has to record images with some defocus (Figures 2A and 2B), which causes a reduction in the high-resolution signal (Figure 2C). Hence, imaging frozen-hydrated biological molecules always requires a fine balance between contrast and resolution. Note that such balance is always influenced by the microscope hardware, such as the spatial coherence of the electron beam, the image recording device, etc., as well as by the size and symmetry of the molecule being studied.

The first breakthrough in boosting the resolution of single-particle cryo-EM maps came from the use of FEGs, which generate an electron beam with much better spatial coherence than a thermo-ionic electron source (Zhou and Chiu, 1993). While FEGs do not change the oscillation of the CTF function, at the same defocus, high-resolution signal is better preserved in images recorded with a microscope equipped with a FEG than with a thermo-ionic electron source. FEGs thus enable structure determinations at subnanometer resolutions for molecules ranging from icosahedral viruses (Böttcher et al., 1997; Conway et al., 1997; Zhou et al., 2000) to molecules as small as ~ 300 kDa with mere 2-fold symmetry (Cheng et al., 2004).

Manufacturers made many efforts to improve microscope performance. State-of-the-art electron microscopes nowadays use constant-power electromagnetic lenses to improve stability, parallel illumination to reduce image phase error induced by beam tilt (Glaeser et al., 2011), very high vacuum to reduce water contamination on frozen-hydrated samples loaded into the microscope column, and better computer control for sophisticated and automated microscope tuning and data acquisition (Suloway et al., 2005), etc. All these features helped to improve the efficiency of as well as the resolution achievable by single-particle cryo-EM, and they eventually enabled the first de novo atomic structure determination of an icosahedral virus (Zhang et al., 2010). Large and highly symmetrical particles, such as icosahedral viruses, have certain advantages in achieving better resolution by single-particle cryo-EM. They can be imaged with very small defocus to preserve the high-resolution signal while still provide sufficient image contrast. However, the same approach does not work for small molecules. Images of small molecules must be recorded using a much larger defocus, thus trading high-resolution signal for image contrast. The need to use a relatively large defocus to generate image contrast was a major obstacle in achieving even subnanometer-resolution maps for proteins smaller than 300 kDa without high symmetry. Overcoming these limitations required new technologies. The simple use of small defocus without any other means to generate sufficient image contrast led to featureless images and controversial results (Henderson, 2013; Mao et al., 2013).

Recent Technological Advances in Single-Particle Cryo-EM

Some recent technological advances led to a major breakthrough in achievable resolution, resulting, in a short period of time, in 3- to ~ 5 - \AA -resolution structures of biological molecules ranging from ribosomal particles to integral membrane proteins (Allegretti et al., 2014; Amunts et al., 2014; Liao et al., 2013; Lu et al., 2014; Vinothkumar et al., 2014). Some of these structures were determined for proteins with known atomic structures,

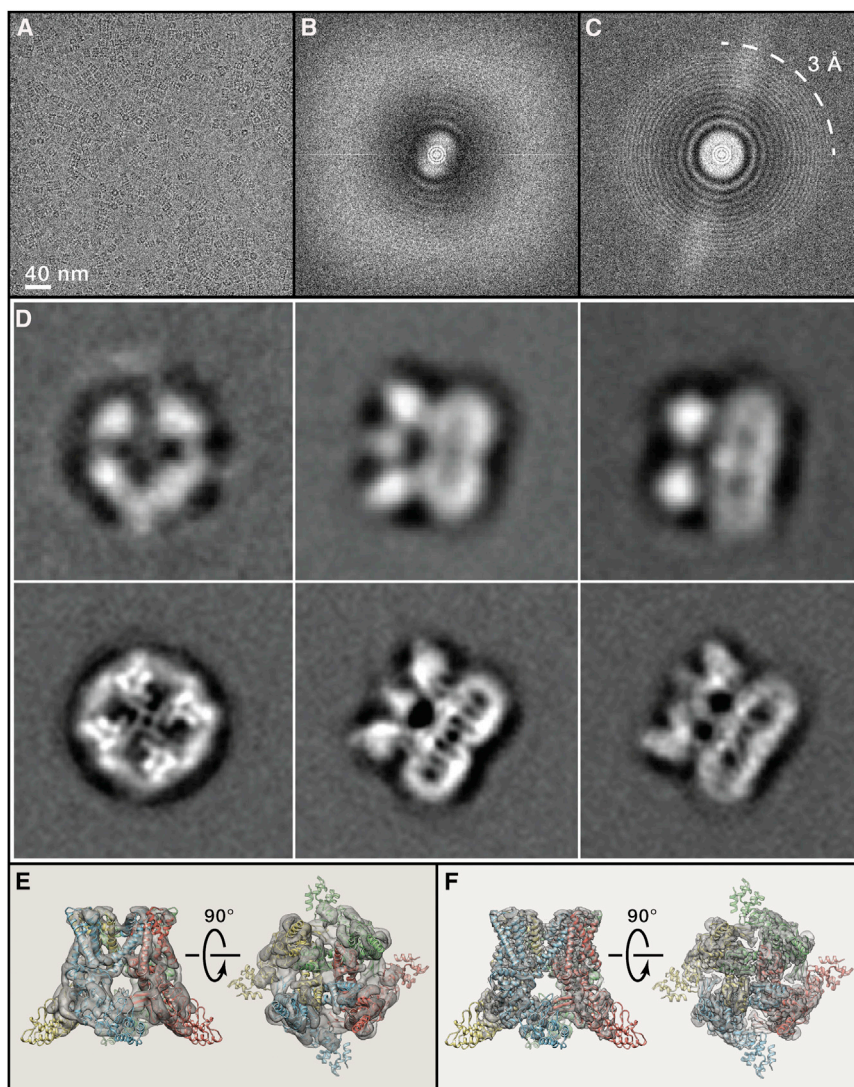


Figure 3. Direct Electron Detection Camera Enabled Major Breakthroughs in Single Particle Cryo-EM

(A) An image of frozen hydrated *T. acidophilum* 20S proteasome recorded using K2 Summit camera with a 300-kV microscope and a defocus of $\sim 0.9 \mu\text{m}$.

(B) Fourier transform of a typical imperfect image of frozen hydrated 20S proteasome, showing a predominant resolution cutoff caused by beam-induced motion.

(C) Fourier transform of the same image after motion correction. Thin ring is restored to resolution of $\sim 3 \text{ \AA}$.

(D) 2D class averages of TRPV1 ion channel calculated from images recorded with a scintillator camera (left) and K2 Summit camera (right) (Liao et al., 2013).

(E) Two different views of TRPV1 3D reconstruction determined from a dataset collected with a scintillator camera.

(F) Same views of the TRPV1 3D reconstruction determined from a dataset collected with a K2 Summit camera. (A–C) are reproduced from (Li et al., 2013).

spatial frequency, leading to poor image contrast. Thus, recording on photographic film typically requires imaging at a higher defocus to ensure sufficient contrast for reliable particle picking and accurate image alignment. Scintillator-based cameras have a better low-frequency DQE than photographic film, resulting in a better image contrast. However, the high-frequency DQE of these cameras is significantly poorer than that of film, making them less suitable for high-resolution imaging (Booth et al., 2006; Meyer et al., 2000).

As their name suggests, the new direct electron detection cameras no longer convert electron signals to light signals

validating the methodological advancements (Bartesaghi et al., 2014; Li et al., 2013). Others were determined ab initio for proteins that resisted crystallization for years (Liao et al., 2013; Lu et al., 2014). Here, I will briefly summarize the recent technological advancements and how they enabled a “resolution revolution” (Kühlbrandt, 2014).

Camera Technology

Image-recording devices are characterized by the detective quantum efficiency (DQE), which describes the signal and noise performance in a digitally recorded image over the spatial frequency range (McMullan et al., 2009a; Mooney, 2007). Traditionally, EM images were recorded on photographic film that was subsequently digitized or with scintillator-based digital cameras, such as charge-coupled device (CCD) or complementary metal-oxide semiconductor (CMOS) cameras. These cameras use a thin layer of phosphor scintillator to convert electron signals to photons, which are coupled through fiber optics to the camera sensor. Photographic film has a relative poor DQE at low

but detect the electrons directly (McMullan et al., 2009b; McMullan et al., 2009c). All commercially available direct detection cameras have significantly higher DQEs than photographic film and scintillator-based cameras in both the low- and high-resolution regimes (Li et al., 2013; McMullan et al., 2014; Ruskin et al., 2013). These cameras typically operate in two distinct modes, the linear charge-integration mode or the electron-counting mode. In the linear mode, charges generated from electrons striking the detector are integrated, while in the counting mode individual electron events are identified and counted. An advantage of operating in the counting mode is that both Landau noise (i.e., the fluctuation in energies generated by each electron striking the camera sensor) and readout noise are removed. Combining direct electron detection with single electron counting significantly improves the DQE further, particularly at low frequencies (Li et al., 2013). Electron-counting cameras thus enable recording low-dose cryo-EM images of small particles with much smaller defocus values (Figure 3A), providing a much

better balance between the requirements for both image contrast and high-resolution signal (Li et al., 2013; Liao et al., 2013; Lu et al., 2014).

Another important feature of the newly developed direct detection cameras is their fast frame readout rate. It enables the already low total electron dose used to image biological samples to be fractionated into many subframes. Computational alignment of these subframes before averaging them can correct for motion-induced image blurring, which results from beam-induced image motion and mechanical instability of the specimen holder (Bai et al., 2013; Brilot et al., 2012; Campbell et al., 2012; Li et al., 2013). The combination of dose fractionation and motion correction greatly improves the efficiency of data acquisition, because nearly all images can be corrected to recover high-resolution information (Figures 3B and 3C). It also provides novel means to optimize usage of the total electron dose (Baker and Rubinstein, 2010). The contrast can be maximized by using a higher total dose and using all frames for particle alignment. However, the later frames that record images of molecules with higher accumulated electron dose and thus more severe radiation damage can later be eliminated or properly down-weighted so as to minimize the effect of radiation damage on the final 3D reconstruction (Li et al., 2013; Scheres, 2014). These novel technologies are now being applied in many cryo-EM laboratories. They marked the beginning of a new era in single-particle cryo-EM, in which atomic structures of a broad range of biological macromolecules can be determined *de novo* and without crystallization (Figures 3D–3F).

Maximum Likelihood-Based Classification

A major advantage of single-particle cryo-EM is that it does not require absolute sample homogeneity. Computational image analysis can deal with a certain level of heterogeneity, both conformational and compositional. Such heterogeneity may prevent crystallization, but in single-particle EM, particles can be computationally sorted into different classes, some of which may contain relatively homogeneous subsets of particles. Single-particle cryo-EM datasets consist of 2D projection images. As determining the orientation parameters of these 2D projections is intertwined with the classification of a heterogeneous dataset into homogeneous subsets, it is always challenging to distinguish whether different 2D projection images represent different views of the same molecule or views of molecules with different conformations or compositions. While there are many ways to classify particles according to their conformations or functional states, a particularly powerful approach is to use a maximum likelihood-based method for classification and refinement (Scheres et al., 2007). Implementing sophisticated maximum likelihood-based classification and refinement algorithms (Sigworth, 1998; Sigworth et al., 2010) into user-friendly software packages (Lyumkis et al., 2013; Scheres, 2010, 2012) made this method easy to use in practice. It has become routine now to classify particle images into different 3D classes, each of which may be amenable to refinement into higher-resolution reconstructions than the global ensemble. The process of 3D classification may separate a number of conformations of the molecule being studied, or separate fully intact particles or complexes from incomplete, truncated or fragmented complexes, or from those damaged during vitrification (Fernández et al., 2013;

Liao et al., 2014). Note that the better image quality provided by direct detection cameras and motion correction enabled success of these classification procedures. Almost all newly published near-atomic resolution 3D reconstructions, in one way or another, utilized such classification procedures.

The use of automated data acquisition (Suloway et al., 2005) with automated particle-picking procedures enables collecting very large datasets with millions of particle images in relatively short periods of time. With large numbers of particles it will be possible to classify particle images with very subtle conformational differences and thus to detect and quantify even subtle conformational states that exist within a population. This has been achieved at somehow moderate resolution (Fischer et al., 2010). It is only a matter of resources and time before single-particle cryo-EM is able to provide solution structures of molecules in multiple conformations at near-atomic resolution and to provide quantitative comparisons of population occupancies under different conditions.

Single-Particle Cryo-EM Is Complementary to X-Ray Crystallography

There are many large protein assemblies and dynamic complexes that are difficult or may even be impossible to crystallize. Thus, single-particle cryo-EM has always been viewed as a supplementary method to X-ray crystallography for studying such assemblies or complexes, such as clathrin coats (Fotin et al., 2004), the 26S proteasome (da Fonseca et al., 2012; Lander et al., 2012; Lasker et al., 2012), the anaphase promoting complex (Chang et al., 2014; da Fonseca et al., 2011), and chromatin fibers (Song et al., 2014), to name just a few. In these studies, structures were typically determined by single-particle methods to subnanometer resolution. Crystal structures of domains and fragments or sequence-based homology models were then fitted into the cryo-EM density maps by molecular dynamic simulations or other computational methods (DiMaio et al., 2015; Seidelt et al., 2009; Trabuco et al., 2009; Zhao et al., 2013). Such hybrid approaches made, for example, subnanometer-resolution structures of integral membrane proteins very meaningful in providing rich structural insights into large membrane protein complexes (Efremov et al., 2015; Vinothkumar et al., 2014) or for dissecting function-related conformational changes (Kim et al., 2014; Meyerson et al., 2014).

With the resolution improved to a level sufficient for sequence-based *de novo* model building, structures determined by single-particle cryo-EM are comparable to those determined from crystals (Bartesaghi et al., 2014; Li et al., 2013). Therefore, for many difficult crystallographic targets, either because they are refractory to crystallization or difficult to express and purify in sufficient quantities for crystallization, single-particle cryo-EM is becoming the *method-of-choice* for structure determination. Recent successes in structure determination of mammalian integral membrane proteins clearly demonstrated this capability (Liao et al., 2013; Lu et al., 2014; Yan et al., 2015; Zalk et al., 2015). Even for those targets that could be crystallized, it is now feasible to use single-particle cryo-EM to determine high-resolution structures of the targets in specific functional states or in complexes with co-factors. We can anticipate that such successes will continue rapidly, with many more structures of

various types of biological molecules being determined to near-atomic resolution. Besides large complexes such as ribosome and icosahedral viruses, integral membrane proteins or membrane protein complexes will be a major area in which single-particle cryo-EM will play a role that is equally significant as X-ray crystallography. Another class of targets that is difficult to crystallize but suitable for single-particle cryo-EM is chromatin in complex with its modifiers, which is essential for understanding the complexities of gene expression. Progress of crystallographic studies in this area has been slow with only a few atomic structures available for nucleosomes alone or in complex with modifiers, each having led to major discoveries in chromatin biology (Cramer, 2014). Recent work, although still limited to nanometer resolution, has shown the tremendous promise of single-particle cryo-EM in this important structural biology field (Song et al., 2014).

Future Perspectives for Single-Particle Cryo-EM

Without a doubt, single-particle cryo-EM is no longer “blobology” but is now a method that can provide resolutions comparable with X-ray crystallography. However, unlike X-ray crystallography, which often ends up with a binary result of either having or not having a diffracting crystal, single-particle cryo-EM always yields some information (although not always at atomic resolution). Even a reconstruction at a modest resolution provides information of how to improve the preparation as well as valuable biological insights. Thus, single-particle cryo-EM is probably even more attractive than X-ray crystallography in studying macromolecules.

However, the technology of single-particle cryo-EM is still far from perfect and technological developments are still moving forward rapidly. The current resolution is still unsatisfactory in many ways. For example, extending the achievable resolution to beyond 3 Å is necessary to convincingly visualize the location of ions, or to visualize not only where but also how small ligand molecules bind to target proteins. The latter is of particular interest for the pharmaceutical industry because it can facilitate structure-based drug design and optimization. A recent review discusses in detail the current technical limitations of single-particle cryo-EM, particularly in achieving higher resolution, and possible solutions (Agard et al., 2014). Related to insufficient resolution, time spent on de novo model building and refinement is often far more than that used to determine the reconstruction itself. While many tools from X-ray crystallography can be applied to cryo-EM density map-based model building and refinement, it requires significant modifications (Amunts et al., 2014; Brown et al., 2015). Also, the traditional validation criterion in X-ray crystallography, such as the free R-factor, is no longer valid for models built into cryo-EM density maps. Therefore, tools and methodologies for efficient model building, refinement, and validation all need further developments.

In addition to improving the technology itself, there are other factors that limit the wide application of single-particle cryo-EM. First, the method itself is not yet a “turnkey” method. Even with automated data acquisition technology and streamlined data processing, image acquisition, and processing is still too complex for a novice to learn with minimal training or by studying manuals. Second, the needed infrastructure, including

fully functional cryo-EM equipment and computational resources for data processing and storage, requires significant financial investment. In addition to the initial investment, the ongoing costs required to maintain and operate a high-end cryo-EM facility are significant. Third, there are currently too few synchrotron-like cryo-EM facilities dedicated for high-throughput cryo-EM data acquisition for the community at large. These limitations set the threshold for entering the field far too high, and improving access will require efforts from multiple parties. Therefore, making the technology robust and relatively easy to learn, reducing the equipment and operational costs, and providing access to ready-to-use facilities staffed with experts will all be important steps toward making cryo-EM as widely used as X-ray crystallography. While the future of single-particle cryo-EM is bright, it requires strong support from the scientific community as well as from funding agencies to make the single particle cryo-EM as popular as X-ray crystallography.

ACKNOWLEDGMENTS

I thank T. Walz, T. Gonen, A. Frost, and members of my laboratory for critical reading of the manuscript. Cryo-EM work in the Cheng laboratory is supported by grants from the NIH (R01GM098672, R01GM082893 and S10RR026814 to Y.C. and P50GM082250 to A. Frankel), the NSF (DBI-0960271 to D.A.A. and Y.C.), which in part funded the development of the K2 camera in association with Gatan and P. Denes at Lawrence Berkeley Laboratory, and the University of California San Francisco Program for Breakthrough Biomedical Research (to Y.C.). Note that the goal of this review is to introduce single-particle cryo-EM to a broad audience by comparing it with the well-established method of X-ray crystallography; it is not meant to be a comprehensive review of single-particle cryo-EM, nor of the history of its methodological developments. I apologize to the many colleagues whose important contributions I was unable to cite due to space limitations.

REFERENCES

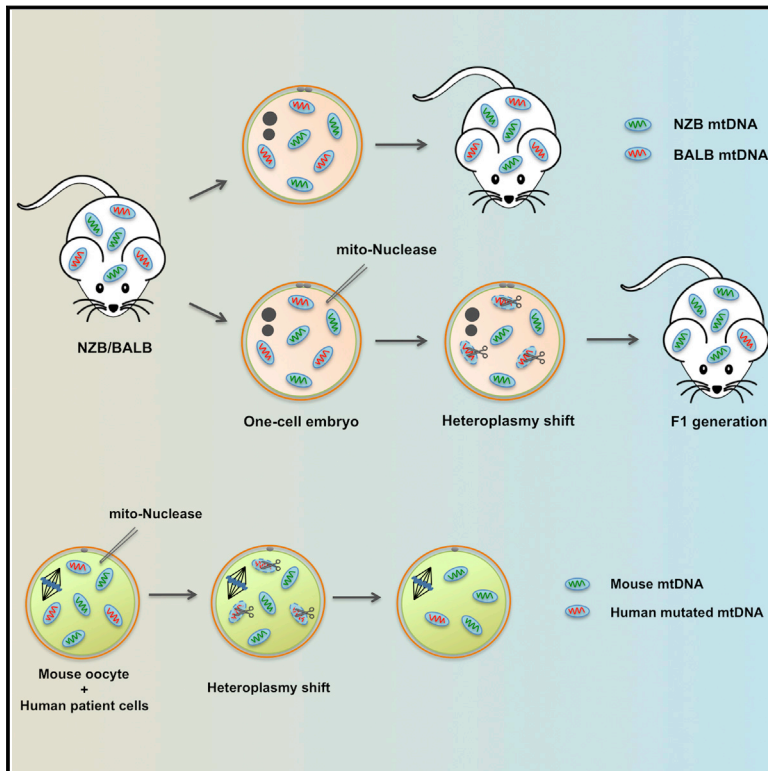
- Agard, D.A., Cheng, Y., Glaeser, R.M., and Subramaniam, S. (2014). Chapter Two – Single-particle cryo-electron microscopy (cryo-EM): progress, challenges, and perspectives for future improvement. *Adv. Imaging Electron Phys.* 185, 113–137.
- Allegretti, M., Mills, D.J., McMullan, G., Kühlbrandt, W., and Vonck, J. (2014). Atomic model of the F420-reducing [NiFe] hydrogenase by electron cryo-microscopy using a direct electron detector. *eLife* 3, e01963.
- Amunts, A., Brown, A., Bai, X.C., Llácer, J.L., Hussain, T., Emsley, P., Long, F., Murshudov, G., Scheres, S.H., and Ramakrishnan, V. (2014). Structure of the yeast mitochondrial large ribosomal subunit. *Science* 343, 1485–1489.
- Bai, X.C., Fernandez, I.S., McMullan, G., and Scheres, S.H. (2013). Ribosome structures to near-atomic resolution from thirty thousand cryo-EM particles. *eLife* 2, e00461.
- Baker, L.A., and Rubinstein, J.L. (2010). Radiation damage in electron cryomicroscopy. *Methods Enzymol.* 481, 371–388.
- Bartesaghi, A., Matthies, D., Banerjee, S., Merk, A., and Subramaniam, S. (2014). Structure of β -galactosidase at 3.2-Å resolution obtained by cryo-electron microscopy. *Proc. Natl. Acad. Sci. USA* 111, 11709–11714.
- Booth, C.R., Jakana, J., and Chiu, W. (2006). Assessing the capabilities of a 4kx4k CCD camera for electron cryo-microscopy at 300kV. *J. Struct. Biol.* 156, 556–563.
- Böttcher, B., Wynne, S.A., and Crowther, R.A. (1997). Determination of the fold of the core protein of hepatitis B virus by electron cryomicroscopy. *Nature* 386, 88–91.

- Brilot, A.F., Chen, J.Z., Cheng, A., Pan, J., Harrison, S.C., Potter, C.S., Carragher, B., Henderson, R., and Grigorieff, N. (2012). Beam-induced motion of vitrified specimen on holey carbon film. *J. Struct. Biol.* **177**, 630–637.
- Brown, A., Long, F., Nicholls, R.A., Toots, J., Emsley, P., and Murshudov, G. (2015). Tools for macromolecular model building and refinement into electron cryo-microscopy reconstructions. *Acta Crystallogr. D Biol. Crystallogr.* **71**, 136–153.
- Campbell, M.G., Cheng, A., Brilot, A.F., Moeller, A., Lyumkis, D., Veesler, D., Pan, J., Harrison, S.C., Potter, C.S., Carragher, B., and Grigorieff, N. (2012). Movies of ice-embedded particles enhance resolution in electron cryo-microscopy. *Structure* **20**, 1823–1828.
- Chang, L., Zhang, Z., Yang, J., McLaughlin, S.H., and Barford, D. (2014). Molecular architecture and mechanism of the anaphase-promoting complex. *Nature* **513**, 388–393.
- Chen, J.Z., Settembre, E.C., Aoki, S.T., Zhang, X., Bellamy, A.R., Dormitzer, P.R., Harrison, S.C., and Grigorieff, N. (2009). Molecular interactions in rotavirus assembly and uncoating seen by high-resolution cryo-EM. *Proc. Natl. Acad. Sci. USA* **106**, 10644–10648.
- Cheng, Y., Zak, O., Aisen, P., Harrison, S.C., and Walz, T. (2004). Structure of the human transferrin receptor-transferrin complex. *Cell* **116**, 565–576.
- Conway, J.F., Cheng, N., Zlotnick, A., Wingfield, P.T., Stahl, S.J., and Steven, A.C. (1997). Visualization of a 4-helix bundle in the hepatitis B virus capsid by cryo-electron microscopy. *Nature* **386**, 91–94.
- Cramer, P. (2014). A tale of chromatin and transcription in 100 structures. *Cell* **159**, 985–994.
- da Fonseca, P.C., Kong, E.H., Zhang, Z., Schreiber, A., Williams, M.A., Morris, E.P., and Barford, D. (2011). Structures of APC/C(Cdh1) with substrates identify Cdh1 and Apc10 as the D-box co-receptor. *Nature* **470**, 274–278.
- da Fonseca, P.C., He, J., and Morris, E.P. (2012). Molecular model of the human 26S proteasome. *Mol. Cell* **46**, 54–66.
- De Rosier, D.J., and Klug, A. (1968). Reconstruction of three dimensional structures from electron micrographs. *Nature* **217**, 130–134.
- DiMaio, F., Song, Y., Li, X., Brunner, M.J., Xu, C., Conticello, V., Egelman, E., Marlovits, T.C., Cheng, Y., and Baker, D. (2015). Atomic-accuracy models from 4.5-Å cryo-electron microscopy data with density-guided iterative local refinement. *Nat. Methods* **12**, 361–365.
- Dubochet, J., Chang, J.J., Freeman, R., Lepault, J., and McDowell, A.W. (1982). Frozen aqueous suspensions. *Ultramicroscopy* **10**, 55–61.
- Eftremov, R.G., Leitner, A., Aebersold, R., and Raunser, S. (2015). Architecture and conformational switch mechanism of the ryanodine receptor. *Nature* **517**, 39–43.
- Fernández, I.S., Bai, X.C., Hussain, T., Kelley, A.C., Lorsch, J.R., Ramakrishnan, V., and Scheres, S.H. (2013). Molecular architecture of a eukaryotic translational initiation complex. *Science* **342**, 1240585.
- Fischer, N., Konevega, A.L., Wintermeyer, W., Rodnina, M.V., and Stark, H. (2010). Ribosome dynamics and tRNA movement by time-resolved electron cryomicroscopy. *Nature* **466**, 329–333.
- Fotin, A., Cheng, Y., Sliz, P., Grigorieff, N., Harrison, S.C., Kirchhausen, T., and Walz, T. (2004). Molecular model for a complete clathrin lattice from electron cryomicroscopy. *Nature* **432**, 573–579.
- Frank, J. (1996). Three-dimensional electron microscopy of macromolecular assembly, 2 edn (Oxford University Press).
- Frank, J., Goldfarb, W., Eisenberg, D., and Baker, T.S. (1978). Reconstruction of glutamine synthetase using computer averaging. *Ultramicroscopy* **3**, 283–290.
- Glaeser, R.M., Typke, D., Tiemeijer, P.C., Pulokas, J., and Cheng, A. (2011). Precise beam-tilt alignment and collimation are required to minimize the phase error associated with coma in high-resolution cryo-EM. *J. Struct. Biol.* **174**, 1–10.
- Henderson, R. (1995). The potential and limitations of neutrons, electrons and X-rays for atomic resolution microscopy of unstained biological molecules. *Q. Rev. Biophys.* **28**, 171–193.
- Henderson, R. (2013). Avoiding the pitfalls of single particle cryo-electron microscopy: Einstein from noise. *Proc. Natl. Acad. Sci. USA* **110**, 18037–18041.
- Henderson, R., and Glaeser, R.M. (1985). Quantitative analysis of image contrast in electron micrographs of beam-sensitive crystals. *Ultramicroscopy* **16**, 139–150.
- Jones, N. (2014). Crystallography: Atomic secrets. *Nature* **505**, 602–603.
- Kim, J., Wu, S., Tomasiak, T., Mergel, C.M., Winter, M.B., Stiller, S.B., Robles-Colmanares, Y., Stroud, R.M., Tampe, R., Craik, C.S., et al. (2014). Subnanometre-resolution electron cryomicroscopy structure of a heterodimeric ABC exporter. *Nature* **517**, 396–400.
- Kühlbrandt, W. (2014). Biochemistry. The resolution revolution. *Science* **343**, 1443–1444.
- Lander, G.C., Estrin, E., Matyskiela, M.E., Bashore, C., Nogales, E., and Martin, A. (2012). Complete subunit architecture of the proteasome regulatory particle. *Nature* **482**, 186–191.
- Lasker, K., Förster, F., Bohn, S., Walzthoeni, T., Villa, E., Unverdorben, P., Beck, F., Aebersold, R., Sali, A., and Baumeister, W. (2012). Molecular architecture of the 26S proteasome holocomplex determined by an integrative approach. *Proc. Natl. Acad. Sci. USA* **109**, 1380–1387.
- Li, X., Mooney, P., Zheng, S., Booth, C.R., Braunfeld, M.B., Gubbens, S., Agard, D.A., and Cheng, Y. (2013). Electron counting and beam-induced motion correction enable near-atomic-resolution single-particle cryo-EM. *Nat. Methods* **10**, 584–590.
- Liao, M., Cao, E., Julius, D., and Cheng, Y. (2013). Structure of the TRPV1 ion channel determined by electron cryo-microscopy. *Nature* **504**, 107–112.
- Liao, M., Cao, E., Julius, D., and Cheng, Y. (2014). Single particle electron cryomicroscopy of a mammalian ion channel. *Curr. Opin. Struct. Biol.* **27**, 1–7.
- Lu, P., Bai, X.C., Ma, D., Xie, T., Yan, C., Sun, L., Yang, G., Zhao, Y., Zhou, R., Scheres, S.H., and Shi, Y. (2014). Three-dimensional structure of human γ -secretase. *Nature* **512**, 166–170.
- Lyumkis, D., Brilot, A.F., Theobald, D.L., and Grigorieff, N. (2013). Likelihood-based classification of cryo-EM images using FREALIGN. *J. Struct. Biol.* **183**, 377–388.
- Mao, Y., Wang, L., Gu, C., Herschhorn, A., Désormeaux, A., Finzi, A., Xiang, S.H., and Sodroski, J.G. (2013). Molecular architecture of the uncleaved HIV-1 envelope glycoprotein trimer. *Proc. Natl. Acad. Sci. USA* **110**, 12438–12443.
- McMullan, G., Chen, S., Henderson, R., and Faruqi, A.R. (2009a). Detective quantum efficiency of electron area detectors in electron microscopy. *Ultramicroscopy* **109**, 1126–1143.
- McMullan, G., Clark, A.T., Turchetta, R., and Faruqi, A.R. (2009b). Enhanced imaging in low dose electron microscopy using electron counting. *Ultramicroscopy* **109**, 1411–1416.
- McMullan, G., Faruqi, A.R., Henderson, R., Guerrini, N., Turchetta, R., Jacobs, A., and van Hoften, G. (2009c). Experimental observation of the improvement in MTF from backthinning a CMOS direct electron detector. *Ultramicroscopy* **109**, 1144–1147.
- McMullan, G., Faruqi, A.R., Clare, D., and Henderson, R. (2014). Comparison of optimal performance at 300keV of three direct electron detectors for use in low dose electron microscopy. *Ultramicroscopy* **147**, 156–163.
- Meyer, R.R., Kirkland, A.I., Dunin-Borkowski, R.E., and Hutchison, J.L. (2000). Experimental characterisation of CCD cameras for HREM at 300 kV. *Ultramicroscopy* **85**, 9–13.
- Meyerson, J.R., Kumar, J., Chittori, S., Rao, P., Pierson, J., Bartesaghi, A., Mayer, M.L., and Subramaniam, S. (2014). Structural mechanism of glutamate receptor activation and desensitization. *Nature* **514**, 328–334.
- Mooney, P. (2007). Optimization of image collection for cellular electron microscopy. *Methods Cell Biol.* **79**, 661–719.
- Ruskin, R.S., Yu, Z., and Grigorieff, N. (2013). Quantitative characterization of electron detectors for transmission electron microscopy. *J. Struct. Biol.* **184**, 385–393.

- Scheres, S.H. (2010). Classification of structural heterogeneity by maximum-likelihood methods. *Methods Enzymol.* **482**, 295–320.
- Scheres, S.H. (2012). RELION: implementation of a Bayesian approach to cryo-EM structure determination. *J. Struct. Biol.* **180**, 519–530.
- Scheres, S.H. (2014). Beam-induced motion correction for sub-megadalton cryo-EM particles. *eLife* **3**, e03665.
- Scheres, S.H., Gao, H., Valle, M., Herman, G.T., Eggermont, P.P., Frank, J., and Carazo, J.M. (2007). Disentangling conformational states of macromolecules in 3D-EM through likelihood optimization. *Nat. Methods* **4**, 27–29.
- Seidelt, B., Innis, C.A., Wilson, D.N., Gartmann, M., Armache, J.P., Villa, E., Trabuco, L.G., Becker, T., Mielke, T., Schulten, K., et al. (2009). Structural insight into nascent polypeptide chain-mediated translational stalling. *Science* **326**, 1412–1415.
- Shi, Y. (2014). A glimpse of structural biology through X-ray crystallography. *Cell* **159**, 995–1014.
- Sigworth, F.J. (1998). A maximum-likelihood approach to single-particle image refinement. *J. Struct. Biol.* **122**, 328–339.
- Sigworth, F.J., Doerschuk, P.C., Carazo, J.M., and Scheres, S.H. (2010). An introduction to maximum-likelihood methods in cryo-EM. *Methods Enzymol.* **482**, 263–294.
- Song, F., Chen, P., Sun, D., Wang, M., Dong, L., Liang, D., Xu, R.M., Zhu, P., and Li, G. (2014). Cryo-EM study of the chromatin fiber reveals a double helix twisted by tetranucleosomal units. *Science* **344**, 376–380.
- Stark, H., Zemlin, F., and Boettcher, C. (1996). Electron radiation damage to protein crystals of bacteriorhodopsin at different temperatures. *Ultramicroscopy* **63**, 75–79.
- Suloway, C., Pulokas, J., Fellmann, D., Cheng, A., Guerra, F., Quispe, J., Stagg, S., Potter, C.S., and Carragher, B. (2005). Automated molecular microscopy: the new Legimon system. *J. Struct. Biol.* **151**, 41–60.
- Taylor, K.A., and Glaeser, R.M. (1974). Electron diffraction of frozen, hydrated protein crystals. *Science* **186**, 1036–1037.
- Trabuco, L.G., Villa, E., Schreiner, E., Harrison, C.B., and Schulten, K. (2009). Molecular dynamics flexible fitting: a practical guide to combine cryo-electron microscopy and X-ray crystallography. *Methods* **49**, 174–180.
- Typke, D., Downing, K.H., and Glaeser, R.M. (2004). Electron microscopy of biological macromolecules: bridging the gap between what physics allows and what we currently can get. *Microsc. Microanal.* **10**, 21–27.
- Urban, K.W. (2011). Electron microscopy: The challenges of graphene. *Nat. Mater.* **10**, 165–166.
- Vinothkumar, K.R., Zhu, J., and Hirst, J. (2014). Architecture of mammalian respiratory complex I. *Nature* **515**, 80–84.
- Wolf, M., Garcea, R.L., Grigorieff, N., and Harrison, S.C. (2010). Subunit interactions in bovine papillomavirus. *Proc. Natl. Acad. Sci. USA* **107**, 6298–6303.
- Yan, Z., Bai, X.C., Yan, C., Wu, J., Li, Z., Xie, T., Peng, W., Yin, C.C., Li, X., Scheres, S.H., et al. (2015). Structure of the rabbit ryanodine receptor RyR1 at near-atomic resolution. *Nature* **517**, 50–55.
- Yu, X., Jin, L., and Zhou, Z.H. (2008). 3.88 Å structure of cytoplasmic polyhedrosis virus by cryo-electron microscopy. *Nature* **453**, 415–419.
- Yu, X., Ge, P., Jiang, J., Atanasov, I., and Zhou, Z.H. (2011). Atomic model of CPV reveals the mechanism used by this single-shelled virus to economically carry out functions conserved in multishelled reoviruses. *Structure* **19**, 652–661.
- Zalk, R., Clarke, O.B., des Georges, A., Grassucci, R.A., Reiken, S., Mancina, F., Hendrickson, W.A., Frank, J., and Marks, A.R. (2015). Structure of a mammalian ryanodine receptor. *Nature* **517**, 44–49.
- Zhang, X., Settembre, E., Xu, C., Dormitzer, P.R., Bellamy, R., Harrison, S.C., and Grigorieff, N. (2008). Near-atomic resolution using electron cryomicroscopy and single-particle reconstruction. *Proc. Natl. Acad. Sci. USA* **105**, 1867–1872.
- Zhang, X., Jin, L., Fang, Q., Hui, W.H., and Zhou, Z.H. (2010). 3.3 Å cryo-EM structure of a nonenveloped virus reveals a priming mechanism for cell entry. *Cell* **141**, 472–482.
- Zhao, G., Perilla, J.R., Yufenyuy, E.L., Meng, X., Chen, B., Ning, J., Ahn, J., Gronenborn, A.M., Schulten, K., Aiken, C., and Zhang, P. (2013). Mature HIV-1 capsid structure by cryo-electron microscopy and all-atom molecular dynamics. *Nature* **497**, 643–646.
- Zhou, Z.H., and Chiu, W. (1993). Prospects for using an IVEM with a FEG for imaging macromolecules towards atomic resolution. *Ultramicroscopy* **49**, 407–416.
- Zhou, Z.H., Dougherty, M., Jakana, J., He, J., Rixon, F.J., and Chiu, W. (2000). Seeing the herpesvirus capsid at 8.5 Å. *Science* **288**, 877–880.

Selective Elimination of Mitochondrial Mutations in the Germline by Genome Editing

Graphical Abstract



Authors

Pradeep Reddy, Alejandro Ocampo, ..., Carlos T. Moraes, Juan Carlos Izpisua Belmonte

Correspondence

belmonte@salk.edu

In Brief

Using mitochondria-targeted nucleases, mtDNA mutations are specifically eliminated in the germline to prevent their transgenerational transmission. This strategy represents a potential therapeutic avenue for preventing the transmission of human mitochondrial diseases.

Highlights

- Mitochondria-targeted nucleases selectively reduce mtDNA haplotypes in germline
- Germline heteroplasmy shift prevents transmission of mtDNA haplotypes to offspring
- Human mutated mtDNA can be reduced in oocytes by mitochondria-targeted nucleases

Accession Numbers

GSE67371
SRP056327



Reddy et al., 2015, Cell 161, 459–469

April 23, 2015 ©2015 Elsevier Inc.

<http://dx.doi.org/10.1016/j.cell.2015.03.051>

Selective Elimination of Mitochondrial Mutations in the Germline by Genome Editing

Pradeep Reddy,^{1,14} Alejandro Ocampo,^{1,14} Keiichiro Suzuki,¹ Jinping Luo,¹ Sandra R. Bacman,² Sion L. Williams,² Atsushi Sugawara,¹ Daiji Okamura,¹ Yuji Tsunekawa,³ Jun Wu,¹ David Lam,¹ Xiong Xiong,⁴ Nuria Montserrat,⁵ Concepcion Rodriguez Esteban,¹ Guang-Hui Liu,^{6,7,8} Ignacio Sancho-Martinez,¹ Dolors Manau,⁹ Salva Civico,⁹ Francesc Cardellach,¹⁰ Maria del Mar O'Callaghan,¹¹ Jaime Campistol,¹¹ Huimin Zhao,⁴ Josep M. Campistol,¹² Carlos T. Moraes,^{2,13} and Juan Carlos Izpisua Belmonte^{1,*}

¹Gene Expression Laboratory, Salk Institute for Biological Studies, La Jolla, CA 92037, USA

²Department of Neurology, University of Miami Miller School of Medicine, Miami, FL 33136, USA

³Laboratory for Cell Asymmetry, RIKEN Center for Developmental Biology, Kobe, Hyogo 650-0047, Japan

⁴Department of Chemical and Biomolecular Engineering, University of Illinois at Urbana-Champaign, Urbana, IL 61801, USA

⁵Pluripotent Stem Cells and Organ Regeneration, Institute for Bioengineering of Catalonia (IBEC), Barcelona 08028, Spain

⁶National Laboratory of Biomacromolecules, Institute of Biophysics, Chinese Academy of Sciences, Beijing 100101, China

⁷Center for Molecular and Translational Medicine (CMTM), Beijing 100101, China

⁸Beijing Institute for Brain Disorders, Beijing 100069, China

⁹Institut Clínic of Gynecology, Obstetrics and Neonatology (ICGON), Hospital Clinic, University of Barcelona, Barcelona 08036, Spain

¹⁰Mitochondrial Research Laboratory, IDIBAPS/CIBER on Rare Diseases, University of Barcelona and Internal Medicine Department, Hospital Clínic, University of Barcelona, Barcelona 08036, Spain

¹¹Neuropediatric Department/CIBERER, Hospital Universitari Sant Joan de Déu, Esplugues de Llobregat 08950, Spain

¹²Renal Division, Hospital Clinic, University of Barcelona, IDIBAPS, Barcelona 08036, Spain

¹³Department of Cell Biology, University of Miami Miller School of Medicine, Miami, FL 33136, USA

¹⁴Co-first author

*Correspondence: belmonte@salk.edu

<http://dx.doi.org/10.1016/j.cell.2015.03.051>

SUMMARY

Mitochondrial diseases include a group of maternally inherited genetic disorders caused by mutations in mtDNA. In most of these patients, mutated mtDNA coexists with wild-type mtDNA, a situation known as mtDNA heteroplasmy. Here, we report on a strategy toward preventing germline transmission of mitochondrial diseases by inducing mtDNA heteroplasmy shift through the selective elimination of mutated mtDNA. As a proof of concept, we took advantage of NZB/BALB heteroplasmic mice, which contain two mtDNA haplotypes, BALB and NZB, and selectively prevented their germline transmission using either mitochondria-targeted restriction endonucleases or TALENs. In addition, we successfully reduced human mutated mtDNA levels responsible for Leber's hereditary optic neuropathy (LHON), and neurogenic muscle weakness, ataxia, and retinitis pigmentosa (NARP), in mammalian oocytes using mitochondria-targeted TALEN (mito-TALENs). Our approaches represent a potential therapeutic avenue for preventing the transgenerational transmission of human mitochondrial diseases caused by mutations in mtDNA.

INTRODUCTION

Mitochondria are double-membrane cellular organelles of bacterial origin that play fundamental roles in multiple cellular

processes including energy production, calcium homeostasis, cellular signaling, and apoptosis (Dyall et al., 2004). Mitochondria contain their own mtDNA encoding 13 polypeptides of the mitochondrial respiratory chain as well as tRNAs and rRNAs necessary for their synthesis (Anderson et al., 1981). mtDNA is present in multiple copies per cell, ranging from approximately 1,000 copies in somatic cells to several 100,000 copies in oocytes, with an average 1–10 copies per organelle (Shoubridge and Wai, 2007). In contrast to nuclear DNA, mtDNA is exclusively transmitted through maternal inheritance. Diseases resulting from mitochondrial dysfunction caused by mtDNA mutations affect 1 in 5,000 children (Haas et al., 2007), and it is estimated that 1 in 200 women could be a mitochondrial disease carrier. Due to the fundamental role of mitochondria in energy production, mitochondrial diseases correlate with degeneration of tissues and organs with high-energy demands. This leads to myopathies, cardiomyopathies, and encephalopathies, among other phenotypes (Taylor and Turnbull, 2005). Currently, there is no cure for mitochondrial diseases. Genetic counseling and pre-implantation genetic diagnosis (PGD) represent the only therapeutic options for preventing transmission of mitochondrial diseases caused by mtDNA mutations. However, due to the non-Mendelian segregation of mtDNA, PGD can only partially reduce the risk of transmitting the disease (Brown et al., 2006). Moreover, analysis of multiple blastomeres may compromise embryo viability. Recently, mitochondrial replacement techniques by spindle, pronuclear, or polar body genome transfer into healthy enucleated donor oocytes or embryos have been reported (Craven et al., 2010; Paull et al., 2013; Tachibana et al., 2013; Wang et al., 2014). Application of these techniques implies combining genetic material from three different individuals, which has

raised ethical, safety, and medical concerns (Hayden, 2013; Vogel, 2014). Therefore, alternative and complementary approaches that alleviate or eliminate these concerns should be investigated when devising feasible clinical paths toward preventing the transmission of mitochondrial diseases caused by mtDNA mutations.

Due to the thousands of copies of mtDNA contained within a cell, the levels of mutated mtDNA can vary. The term homoplasmmy refers to the presence of a single mtDNA haplotype in the cell, whereas heteroplasmmy refers to the coexistence of more than one mtDNA haplotype. When the percentage of mutated mtDNA molecules exceeds a threshold that compromises mitochondrial function, a disease state may ensue (Taylor and Turnbull, 2005; Wallace and Chalkia, 2013). Threshold levels for biochemical and clinical defects are generally in the range of 60%–95% mutated mtDNA depending on the severity of the mutation (Russell and Turnbull, 2014). Changes in the relative levels of heteroplasmic mtDNA can be referred to as mtDNA heteroplasmmy shifts. Despite the fact that mitochondria possess all the necessary machinery for homologous recombination and non-homologous end joining, they do not seem to represent the major pathway for mtDNA repair in mammalian mitochondria (Alexeyev et al., 2013). Previous studies have demonstrated that the relative levels of mutated and wild-type mtDNA can be altered in patient somatic cells containing the m.8993T>G mtDNA mutation responsible for the NARP and MILS syndromes, where elimination of mutated mtDNA led to the restoration of normal mitochondrial function (Alexeyev et al., 2008). Similarly, using the heteroplasmic NZB/BALB mouse model that carries two different mtDNA haplotypes (NZB and BALB), BALB mtDNA, which contains a unique ApaLI site, has been specifically reduced in vivo using a mitochondria-targeted ApaLI (Bacman et al., 2012; 2010). Recently, transcription activator-like effector nucleases (TALENs) and zinc finger nucleases (ZFNs) targeted to mitochondria have been utilized for the specific elimination of mitochondrial genomes carrying mutations responsible for mitochondrial diseases (Bacman et al., 2013; Gammage et al., 2014; Minczuk et al., 2006; 2008). These novel approaches allow for the targeting of a wider spectrum of mutations against which restriction endonucleases could not be used. However, these approaches do not provide mechanisms for preventing the transmission of mutated mtDNA nor do they allow for a complete systemic clearance of mtDNA mutations in subsequent generations.

Here, we report on the specific reduction of mitochondrial genomes in the germline for preventing transmission of mitochondrial diseases. As a proof of concept, and by using the heteroplasmic NZB/BALB mouse model, we specifically reduced BALB or NZB mitochondrial genomes in the germline using mitochondria-targeted restriction endonucleases and TALENs and prevented their transmission to the next generation. Moreover, we successfully reduced mutated mitochondrial genomes responsible for human mitochondrial diseases in mouse oocytes using mitochondria-targeted nucleases. The approaches presented here may be applied and developed to prevent the transgenerational transmission of human mitochondrial diseases.

RESULTS

Specific Reduction of Mitochondrial Genomes in Oocytes and Embryos Using Restriction Endonucleases

With the goal of establishing an alternative therapeutic approach for preventing the germline transmission of mitochondrial diseases caused by mtDNA mutations, we tested the specific elimination of BALB mtDNA in NZB/BALB oocytes and one-cell embryos. For this purpose, we generated a mammalian codon optimized ApaLI targeted to mitochondria by the ATP5B mitochondria targeting sequence and the ATP5B 5' and 3' UTRs to promote co-translational import from mitochondrial associated ribosomes (Marc et al., 2002). An enhanced GFP (EGFP) reporter was also included in the construct to monitor expression (Figure 1A). First, we tested the mitochondrial localization of the ApaLI protein generated from the construct by immunostaining in NZB/BALB tail tip fibroblasts (TTFs) and observed robust co-localization of mitochondria-targeted ApaLI (mito-ApaLI) with the mitochondrial dye Mitotracker (Figure S1A). In contrast, we failed to observe mitochondrial localization of non-mitochondria-targeted ApaLI (Figure S1A). Analysis of mtDNA by “last-cycle hot” PCR and restriction fragment length polymorphism (RFLP) demonstrated induction of heteroplasmmy shift by specific reduction of BALB mtDNA in cells transfected with mito-ApaLI compared to control cells transfected with mito-GFP after 72 hr (Figure S1B). In addition, we found normal mtDNA copy number in mito-ApaLI transfected cells, which resulted from the replication of the remaining NZB mtDNA that compensated for the reduction of BALB mtDNA (Figure S1C).

We next decided to test whether a similar approach could be used in oocytes to specifically eliminate BALB mtDNA (Figure 1A). First, we confirmed the mitochondrial localization of mito-ApaLI in NZB/BALB metaphase II (MII) oocytes injected with mRNA encoding mito-ApaLI by immunostaining (Figure 1B). As expected, mito-ApaLI co-localized with Mitotracker in MII oocytes (Figure 1B). RFLP analysis 48 hr after mito-ApaLI mRNA injection demonstrated the specific reduction of BALB mtDNA and a consequential increase in the relative NZB mtDNA levels (Figure 1C). In agreement with the lack of mtDNA replication in mature oocytes and pre-implantation embryos (Wai et al., 2010), analysis of mtDNA copy number by qPCR revealed a decrease in mtDNA copy number following mito-ApaLI injection proportional to the initial levels of BALB mtDNA (Figure 1D). To verify the reduction of BALB mtDNA, we performed RFLP and qPCR analyses by amplification of an independent region of the mtDNA containing a unique HindIII site, exclusively present in BALB mtDNA. These analyses confirmed the specific reduction of BALB mtDNA upon injection of mito-ApaLI in NZB/BALB MII oocytes (Figure S1D and S1E). Injection of mito-ApaLI in BALB or NZB single haplotype oocytes resulted in complete depletion of mtDNA in BALB oocytes and did not affect mtDNA levels in NZB oocytes reinforcing the specificity of mito-ApaLI (Figure S1F). Collectively, these results suggest the potential of this approach for the specific reduction of mtDNA in the germline.

In addition to oocytes, we tested whether mtDNA heteroplasmmy shift could be applied to one-cell embryos without affecting their normal development until the blastocyst stage (Figure 2A). For this purpose, NZB/BALB one-cell embryos

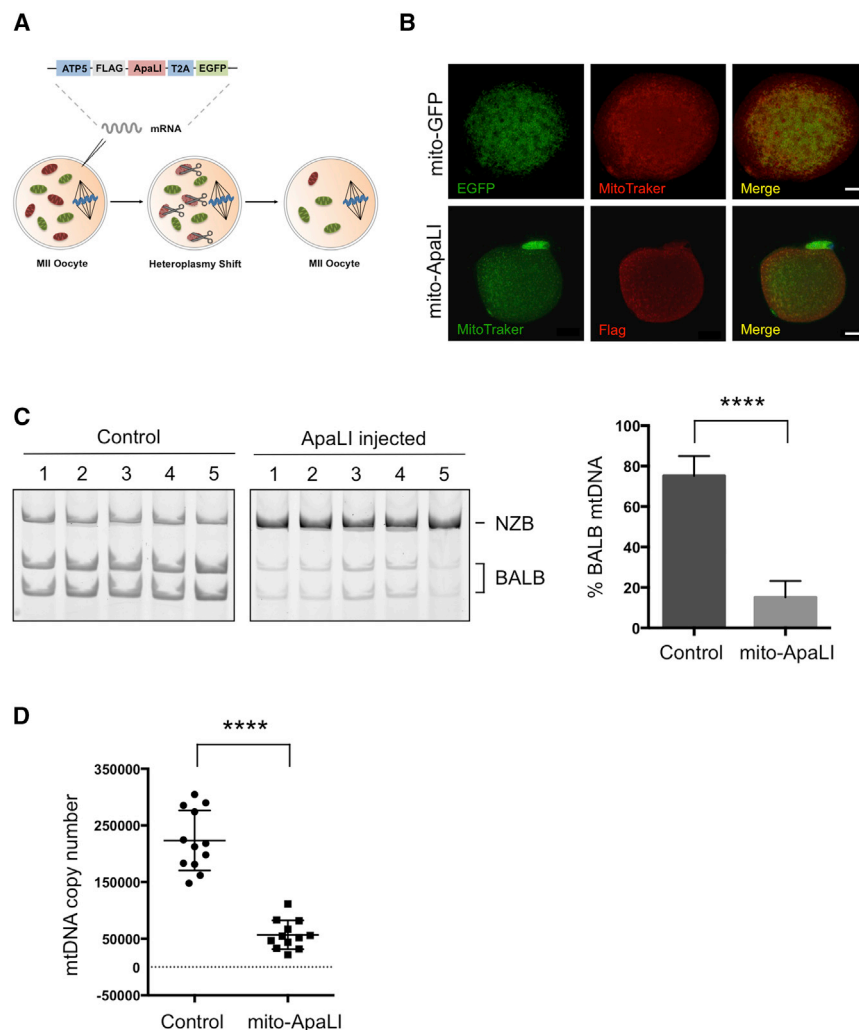


Figure 1. Heteroplasmy Shift in NZB/BALB MII Oocytes Using mito-ApaLI

(A) Injection of mito-ApaLI mRNA in oocytes for induction of heteroplasmy shift.

(B) Mitochondrial co-localization of mito-GFP and mito-ApaLI with Mitotracker in injected oocytes by immunofluorescence. Scale bars, 10 μ m.

(C) RFLP analysis and quantification of mtDNA heteroplasmy in control and mito-ApaLI injected MII oocytes after 48 hr (Control n = 16; mito-ApaLI n = 12). Representative gel.

(D) Quantification of mtDNA copy number by qPCR in control and mito-ApaLI-injected oocytes MII after 48 hr (Control n = 12; mito-ApaLI n = 12). Error bars represent \pm SEM. ****p < 0.0001. See also Figure S1.

chondrial diseases to the next generation. NZB/BALB one-cell embryos injected with mito-ApaLI mRNA were cultured in vitro until the blastocyst stage and transferred to pseudopregnant mice (Figure 3A). After a standard gestation period, pseudopregnant mice gave birth to live pups through natural delivery (Figure 3B). Most importantly, RFLP analysis of total DNA from F1 mito-ApaLI animals revealed a significant reduction of BALB mtDNA (Figure 3C). Further analysis demonstrated reduction of BALB mtDNA in the brain, muscle, heart, and liver. These data indicate the systemic clearance of a specific mtDNA in the offspring of heteroplasmic mothers (Figure 3D). Similarly, analysis at the HindIII region confirmed the specific reduction of BALB mtDNA in F1 mito-ApaLI animals

were injected with mito-ApaLI mRNA. Time-lapse fluorescent microscopy images revealed the expression of mito-ApaLI indicated by EGFP expression, and more importantly, normal development of mito-ApaLI-injected embryos through the different developmental stages analyzed (Figure 2B). Similarly to the results observed in oocytes, RFLP analysis of mito-ApaLI blastocysts demonstrated specific reduction of BALB mtDNA and an increase in the relative levels of NZB mtDNA (Figure 2C). Moreover, due to the lack of mtDNA replication until the blastocyst stage (Wai et al., 2010), analysis of mtDNA copy number by qPCR showed a decrease in mtDNA levels proportional to the BALB mtDNA levels (Figure 2D). RFLP and qPCR analyses at the HindIII region confirmed the specific reduction of BALB mtDNA upon injection of mito-ApaLI in NZB/BALB embryos (Figures S2A and S2B).

Preventing the Transmission of Mitochondrial Genomes Using Mitochondria-Targeted Restriction Endonucleases

Next, we investigated whether induction of mtDNA heteroplasmy shift could be utilized for preventing the transmission of mito-

(Figures S3A and S3B). Furthermore, analysis of mtDNA copy number showed normal mtDNA levels resulting from NZB mtDNA replication upon embryo implantation (Figure 3E). Comprehensive characterization of mito-ApaLI animals, both males and females, showed normal development, weight gain (Figure 4A), complete blood count (Table S1) as well as normal blood levels of glucose and lactate, all potential indicators of mitochondrial dysfunction (Haas et al., 2007) (Figure 4B). Moreover, typical behavioral studies indicative of CNS defects (Ross et al., 2013), including open field, rotor-rod, grip strength, and sensory neuron screening, showed normal performance of mito-ApaLI animals (Figures 4C–4E).

To assess potential off-target effects on the nuclear genome, we performed comparative hybridization genomic (CHG) array and exome sequencing. CGH array indicated normal genomic integrity of mito-ApaLI animals (Figure S3C). Confirming this result, exome sequencing demonstrated variant rates in ApaLI containing exomic regions comparable to non-ApaLI exomic regions, excluding the possibility of off-target effects of mito-ApaLI (0.0014 versus 0.0047 variants per hundred base pairs, respectively). Furthermore, mito-ApaLI animals were fertile, and RFLP

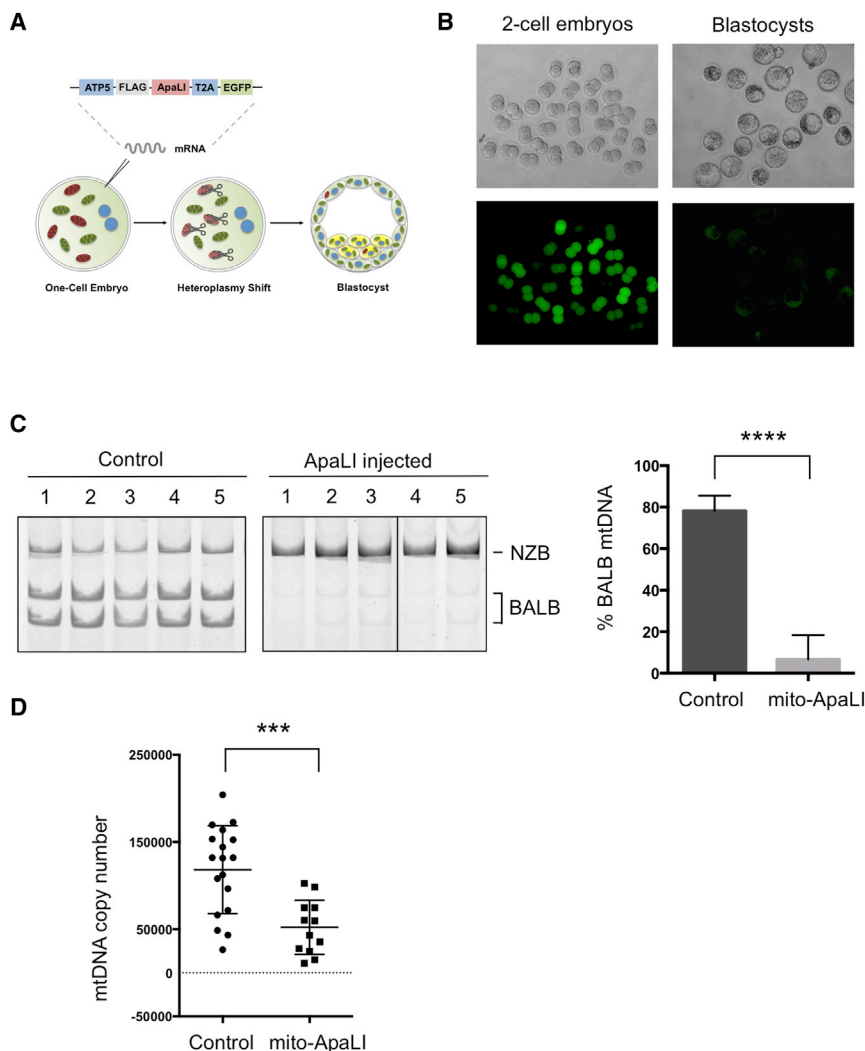


Figure 2. Heteroplasmy Shift in NZB/BALB Embryos Using mito-ApaLI

(A) Injection of mito-ApaLI mRNA in one-cell embryos for induction of heteroplasmy shift.

(B) In vitro development of mito-ApaLI-injected embryos to blastocyst stage. Time-lapse images of EGFP reporter expression at different developmental stages.

(C) RFLP analysis and quantification of mtDNA heteroplasmy in control and mito-ApaLI-injected embryos (Control $n = 10$; mito-ApaLI $n = 8$). Representative gel.

(D) Quantification of mtDNA copy number by qPCR in control and mito-ApaLI-injected embryos (Control $n = 18$; mito-ApaLI $n = 12$).

Error bars represent \pm SEM. *** $p < 0.001$. **** $p < 0.0001$. See also Figure S2.

analyses showed barely detectable levels of BALB mtDNA in the F2 generation (Figures 4F and S4). These results confirm the feasibility of mtDNA heteroplasmy shift to prevent the transgenerational transmission of mitochondrial diseases.

Preventing the Transmission of Mitochondrial Genomes Using Mito-TALENs

Despite the broad range of over 200 mtDNA mutations associated with mitochondrial diseases, only the human mutation m8993T>G responsible for two mitochondrial diseases: neurogenic muscle weakness, ataxia, and retinitis pigmentosa (NARP) and maternally inherited Leigh syndrome (MILS) generates a unique restriction site that can be targeted using the naturally occurring restriction endonuclease XmaI. For these reasons, alternative approaches to induce heteroplasmy shift based on the use of mitochondria-targeted transcription activator-like effector nucleases (TALENs) and zinc finger nucleases (ZFNs), which could be designed against virtually any mutation, have been recently developed by us and other groups (Bacman et al., 2013; Gammage et al., 2014; Minczuk et al., 2006;

2008). In order to evaluate the use of mito-TALENs to prevent the transmission of mitochondrial diseases, we tested the specific elimination of NZB mtDNA in NZB/BALB oocytes. For this purpose, we first generated a collection of TALENs against NZB mtDNA and screened for a TALEN with the highest specificity against NZB mtDNA (Figures S5A–S5C). Under our design, the left monomer of the TALEN will bind to the common sequence of NZB and BALB mtDNA while the right monomer will preferentially recognize and bind to NZB mtDNA, dictating the specific cleavage of NZB mtDNA upon dimerization of the FokI nuclease (Figure S5A). NZB TALEN monomers were targeted to mitochondria by the human ATP5B and SOD2 mitochondria targeting sequence and the ATP5B and SOD2 5'

and 3' UTRs to promote co-translational import from mitochondrial associated ribosomes (Marc et al., 2002). In addition, an EGFP or mCherry reporter was also included in the constructs encoding each TALEN monomer (Figure 5A). Once again, we tested the mitochondrial localization of the NZB TALEN by immunostaining in NZB/BALB tail tip fibroblasts (TTFs) and observed robust co-localization of mitochondria-targeted NZB TALEN monomers (hereafter NZB mito-TALEN) with the Mitotracker (Figure S5D). Analysis of mtDNA by RFLP demonstrated induction of heteroplasmy shift in NZB/BALB cells by a specific reduction of NZB mtDNA after 72 hr in cells transfected with NZB mito-TALENs compared to control cells transfected with mito-GFP (Figure S5E). In addition, similar to mito-ApaLI, we found normal mtDNA copy number in NZB mito-TALEN transfected cells resulting from the replication of the remaining BALB mtDNA that compensated for the reduction of NZB mtDNA (Figure S5F).

We next decided to test whether mito-TALENs could be used in oocytes to specifically eliminate NZB mtDNA (Figure 5A). Fluorescent microscopy images revealed the expression of both

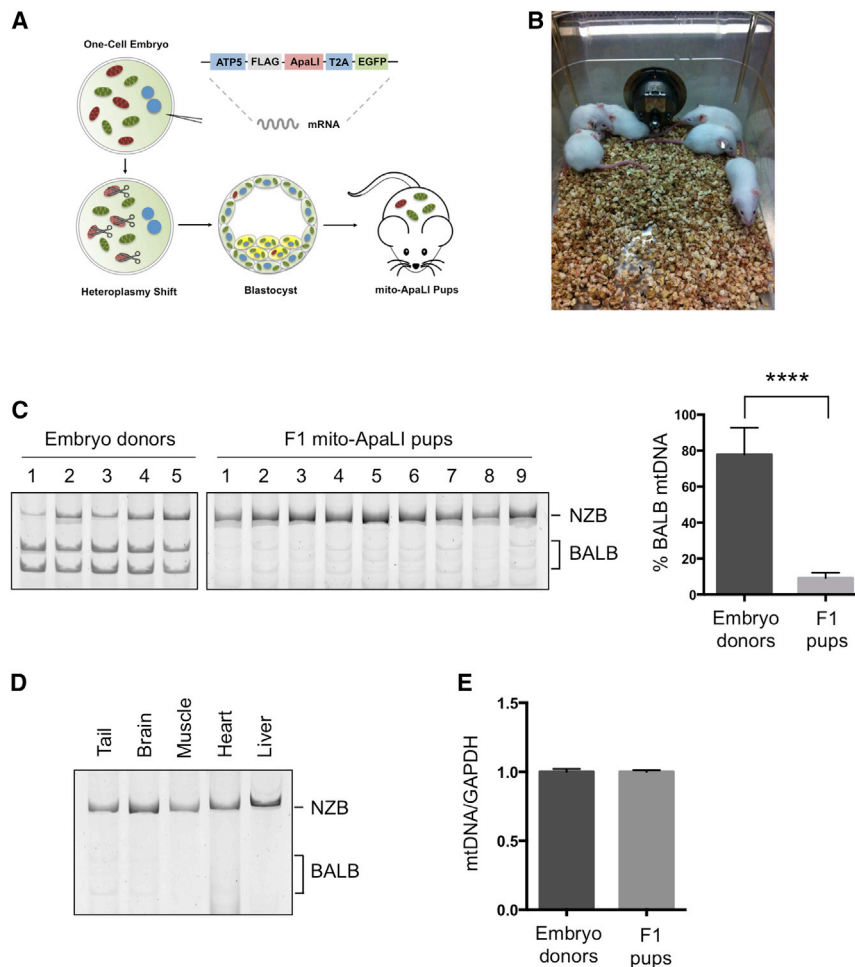


Figure 3. Generation of Live Animals after Induction of Heteroplasmy Shift in NZB/BALB Embryos Using mito-ApaLI

(A) Outline for the generation of live animals after injection of mito-ApaLI mRNA in one-cell embryos. (B) Representative photograph of F1 mito-ApaLI mice.

(C) RFLP analysis and quantification of mtDNA heteroplasmy in tail tip biopsies of embryo donors and generated F1 mito-ApaLI pups. (Donor $n = 10$; mito-ApaLI $n = 9$).

(D) RFLP analysis and quantification of mtDNA heteroplasmy in tail, brain, muscle, heart, and liver of F1 mito-ApaLI mice.

(E) Quantification of mtDNA copy number by qPCR in F1 mito-ApaLI pups (Donor $n = 10$; F1 mito-ApaLI $n = 9$).

Error bars represent \pm SEM. **** $p < 0.0001$. See also Figure S3.

(LHOND) and NARP (Jun et al., 1994; Taylor and Turnbull, 2005). Due to the limited number of available patients and the difficulty in obtaining oocytes from these patients, we generated artificial mammalian oocytes carrying mutated genomes by cellular fusion of patient cells and mouse oocytes using Sendai virus (Figure 6A). Although this model has limitations compared to patient oocytes, it helped us to test the potential of our methodology for the specific elimination of pathogenic human mtDNAs in mammalian oocytes.

For this purpose, we first tested the fusion of 143B osteosarcoma cybrid cells

NZB mito-TALEN monomers as indicated by EGFP and mCherry expression in oocytes (Figure 5B). RFLP analysis 48 hr after NZB mito-TALEN mRNA injection demonstrated the specific decrease of NZB mtDNA and a consequential increase in the relative BALB mtDNA levels (Figure 5C). RFLP analysis at the HindIII region confirmed the specific reduction of NZB mtDNA upon injection of NZB mito-TALEN in NZB/BALB MII oocytes (Figure S5G). Analysis of mtDNA copy number by qPCR revealed a decrease in mtDNA copy number following NZB mito-TALEN injection in oocytes in agreement with the lack of mtDNA replication in oocytes (Figure 5D). These results demonstrate the potential of custom designed mito-TALENs for the specific elimination of mitochondrial genomes in the germline aimed at preventing the transmission of mitochondrial diseases.

Specific Reduction of Human Mutated Mitochondrial Genomes Responsible for Mitochondrial Diseases in Mammalian Oocytes

In order to evaluate the potential of our approach to prevent the transmission of human mitochondrial diseases we decided to test the use of mitochondria-targeted nucleases against mutated mitochondrial genomes responsible for two mitochondrial diseases: Leber's hereditary optic neuropathy and dystonia

harboring the LHOND m.14459G>A mutation to mouse MII oocytes (Figure 6B). After 3 hr, complete fusion was observed and no individual cells were detected under the zona pellucida of oocytes (Figure 6B). LHOND-fused oocytes were incubated for 48 hr and collected for analysis. PCR analysis using primers specific against the human mtDNA region containing the LHOND m.14459G>A mutation allowed for the detection of LHOND mtDNA in fused oocytes (Figure S6A). Next, we tested whether the LHOND mito-TALEN that we have recently reported could be used for the specific elimination of LHOND mtDNA in oocytes (Bacman et al., 2013). For this purpose, MII oocytes harboring LHOND mtDNA were injected with mRNA encoding the LHOND mito-TALEN 3 hr after cell fusion. Fluorescent microscopy images revealed the expression of both LHOND mito-TALEN monomers as indicated by EGFP and mCherry expression (Figure S6B). RFLP analysis 48 hr after mRNA injection demonstrated the specific reduction of LHOND mtDNA in fused oocytes (Figure 6C). Analysis of mtDNA copy number by qPCR confirmed a significant reduction of human mutated LHOND mtDNA upon injection of LHOND mito-TALENs in fused oocytes (Figure 6D). Finally, to demonstrate the potential of this approach against other mitochondrial diseases we decided to use a similar strategy to test the elimination of human mitochondrial genomes

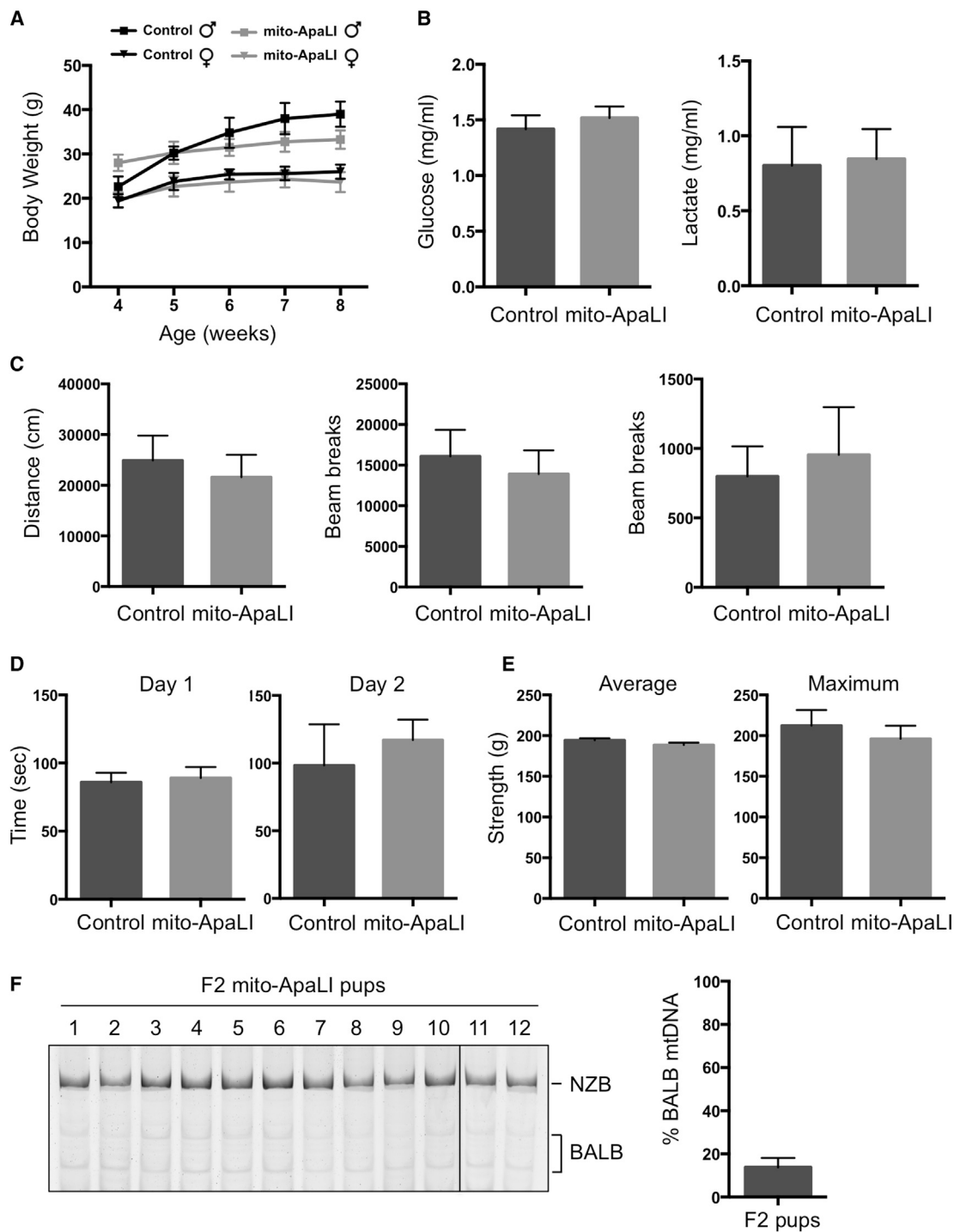


Figure 4. Characterization of F1 mito-ApaLI Mice

(A) Body weight of mito-ApaLI males (Control $n = 5$ and mito-ApaLI $n = 3$) and mito-ApaLI females (Control $n = 5$ and mito-ApaLI $n = 6$) at different time points. ns, non-significant.

(B) Biochemical analysis of glucose and lactate in blood of control ($n = 10$) and mito-ApaLI ($n = 9$) mice. ns, non-significant.

(C) Open field test measuring baseline levels of locomotor activity in freely moving mice quantifying distance traveled, ambulatory counts, and vertical counts.

(D) Rotarod test evaluating locomotor coordination based on the latency at which a fall occurs on a gradually accelerating spinning rod.

(E) Grip strength test measuring average and maximum grip force in the forelimbs.

(F) RFLP analysis and quantification of mtDNA heteroplasmy in tail tip biopsies of F2 mito-ApaLI pups. (F2 mito-ApaLI $n = 12$).

Error bars represent \pm SEM. See also [Figure S4](#) and [Table S1](#).

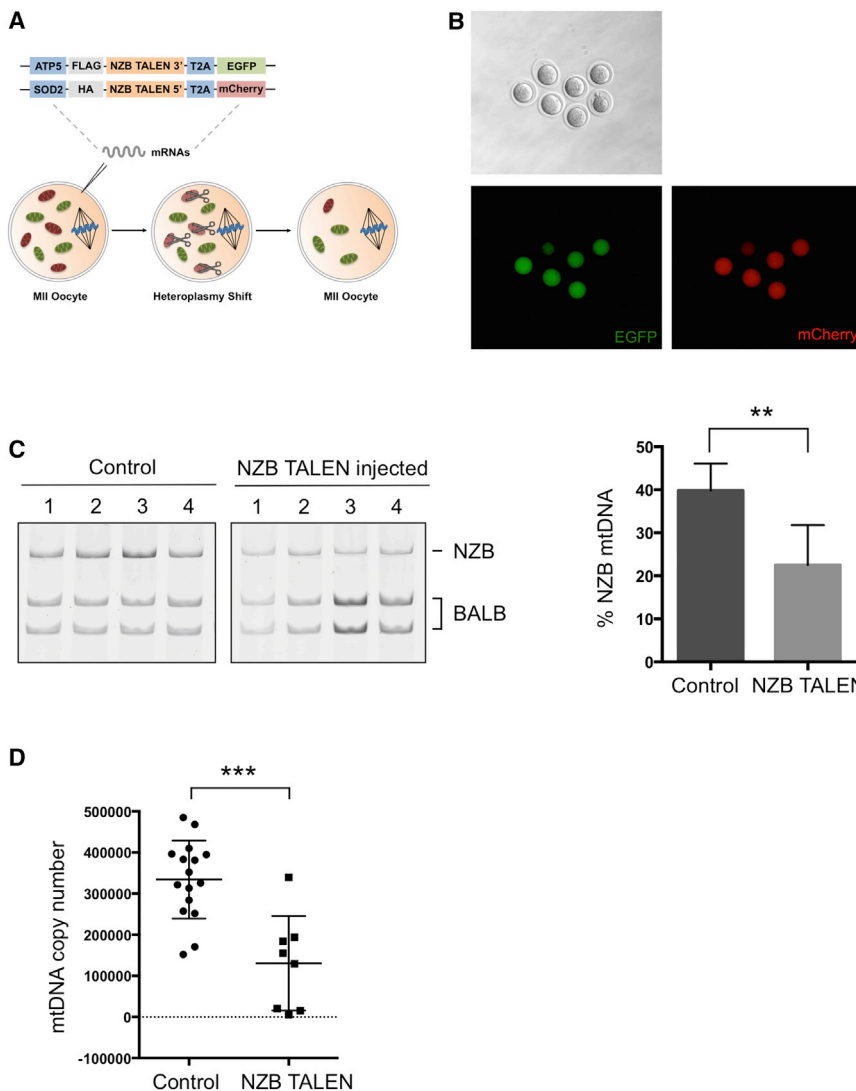


Figure 5. Heteroplasmy Shift in NZB/BALB MII Oocytes Using NZB Mito-TALEN

(A) Injection of NZB mito-TALEN mRNA in oocytes for induction of heteroplasmy shift.

(B) Expression of fluorescent reporters of NZB TALEN monomer in MII oocytes.

(C) RFLP analysis and quantification of mtDNA heteroplasmy in control and NZB TALEN-injected oocytes after 48 hr (Control n = 9; NZB TALEN n = 7). Representative gel.

(D) Quantification of mtDNA copy number by qPCR in control and NZB TALEN-injected oocytes after 48 hr (Control n = 16; NZB TALEN n = 8).

Error bars represent \pm SEM. **p < 0.01. ***p < 0.001. See also Figure S5.

NARP mitochondrial genomes in oocytes. As before, patient cells harboring the NARP m.9176T>C mutation were fused to MII oocytes using Sendai virus and injected with NARP mito-TALEN 3 hr after fusion. Fluorescent reporters for both NARP mito-TALEN monomers were observed in oocytes as indicated by EGFP and mCherry expression (Figure S6I). RFLP analysis 48 hr after mRNA injection demonstrated the specific reduction of NARP mtDNA in fused oocytes (Figure 6E). Analysis of mtDNA copy number by qPCR confirmed a significant reduction of human mutated NARP mtDNA upon injection of NARP mito-TALENs in fused oocytes (Figure 6F). We speculate that the low levels of wild-type mtDNA carried by the NARP patient cells, together with the lack of mtDNA replication in oocytes, might be the reason why we fail to detect a significant increase in wild-type human mtDNA upon NARP

carrying the mutation NARP m.9176T>C. For this purpose, we first generated a collection of TALENs against NARP mtDNA and screened for a TALEN with the highest specificity against the mutation NARP m.9176T>C (Figures S6C–S6E). NARP mito-TALEN monomers were targeted to mitochondria by the ATP5B and SOD2 mitochondria targeting sequence and the ATP5B and SOD2 5' and 3' UTRs (Figure 6A). Immunostaining in NARP patient cells revealed a robust co-localization of mitochondria-targeted NARP mito-TALEN monomers with the mitochondrial dye Mitotracker (Figure S6F). Subsequently, we tested the induction of heteroplasmy shift by NARP mito-TALEN using immortalized NARP patient cells. Analysis of mtDNA by RFLP demonstrated induction of heteroplasmy shift in NARP cells with a reduction in NARP mtDNA after 72 hr in cells transfected with the NARP mito-TALEN compared to cells transfected with mito-GFP (Figure S6G). In addition, we found normal mtDNA copy numbers in NARP mito-TALEN transfected cells resulting from the replication of the remaining mtDNA (Figure S6H). Next, similar to LHOND, we tested the specific elimination of

mito-TALEN injection. Collectively, these results confirm the potential of custom-designed mito-TALENs for the specific elimination of clinically relevant mutated mitochondrial genomes responsible for human mitochondrial diseases in the germline.

DISCUSSION

In summary, we report here on novel strategies for preventing germline transmission of mitochondrial diseases through the induction of mtDNA heteroplasmy shift in oocytes and embryos. As a proof of concept, we used a heteroplasmic mouse model carrying two different mtDNA haplotypes: NZB and BALB. First, we demonstrated that injection of mRNA encoding mitochondria-targeted ApaI restriction enzyme into oocytes, as well as into one-cell embryos, led to the generation of live animals with significantly reduced levels of the BALB mtDNA haplotype. These animals displayed normal behavior, development, gross genomic integrity and fertility. Moreover, their progeny (F2 generation) maintained significantly reduced levels of BALB mtDNA. These results

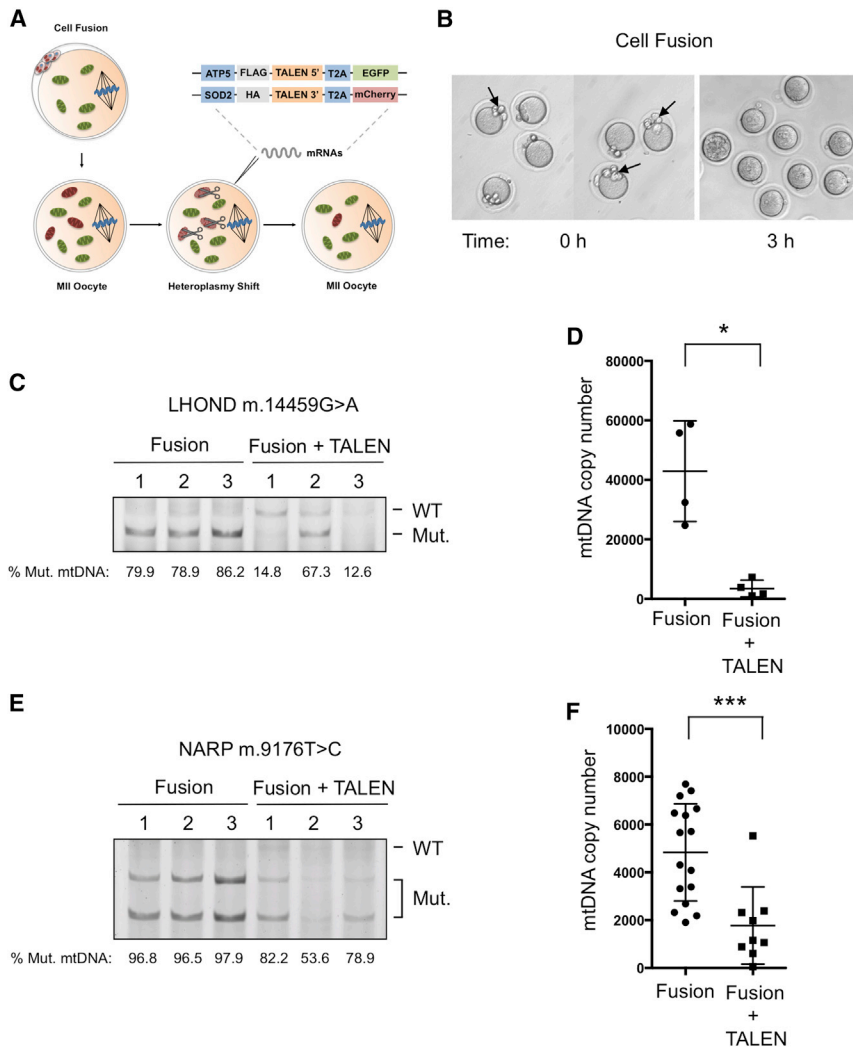


Figure 6. Specific Elimination of Human LHOND m.14459G>A and NARP m.9176T>C Mutations in Mammalian Oocytes Using Mito-TALENs

(A) Fusion of human cells harboring LHOND m.14459G>A and NARP m.9176T>C mutations with mouse MII oocytes followed by the injection of mito-TALENs for induction of heteroplasmy shift. (B) Representative images of MII oocytes before and after cell fusion.

(C) RFLP analysis and quantification of LHOND heteroplasmy in individual MII oocytes with and without LHOND TALEN injection after 48 hr (Fusion n = 3; Fusion + TALEN n = 3).

(D) Quantification of human mtDNA copy number by qPCR in individual MII oocytes with and without LHOND TALEN injection after 48 hr (Fusion n = 4; Fusion + TALEN n = 4).

(E) RFLP analysis and quantification of NARP heteroplasmy in individual MII oocytes with and without NARP TALEN injection after 48 hr (Fusion n = 7; Fusion + TALEN n = 3).

(F) Quantification of human mtDNA copy number by qPCR in individual MII oocytes with and without NARP TALEN injection after 48 hr (Fusion n = 17; Fusion + TALEN n = 9).

Error bars represent \pm SEM. * $p < 0.05$. *** $p < 0.001$. See also Figure S6.

demonstrate the potential of germline heteroplasmy shift to prevent the transgenerational transmission of mitochondrial genomes. In addition, injection of mRNA encoding mitochondria-targeted NZB mito-TALEN into oocytes led to a significant reduction of NZB mtDNA levels. Finally, fusion of human patient cells carrying mtDNA mutations to mouse oocytes followed by injection of mito-TALENs against these mutations demonstrated a specific reduction in the levels of mutated mtDNA.

The use of restriction nucleases for the induction of heteroplasmy shift has been previously demonstrated in the NZB/BALB mouse as well as in patient somatic cells by us and other groups (Alexeyev et al., 2008; Bacman et al., 2010; 2012). However, the application of restriction enzymes to target clinically relevant mutations is limited to only m8993T>G, which is responsible for some cases of NARP and MILS, a mutation that generates a unique restriction site that can be targeted using the restriction endonuclease XmaI (Alexeyev et al., 2008). The use of other approaches using different types of nucleases including TALENs might allow for the custom-designed targeting of a wider range of human mitochondrial mutations responsible for mito-

chondrial diseases. Along this line, several reports have recently demonstrated the use of mitochondria-targeted TALENs and zinc finger nucleases (ZFNs) for the specific elimination of mutated mitochondrial genomes in somatic cells (Bacman et al., 2013; Gammage et al., 2014; Miniczuk et al., 2006; 2008). When compared to mitochondria-targeted restriction endonucleases, the use of mito-TALENs for

preventing transmission of mitochondrial diseases in the germline may be less robust. However, we speculate that their therapeutic use will achieve specific reduction of mutated mitochondrial genomes below the threshold levels (60%–95%) required for biochemical and clinical defects to manifest (Russell and Turnbull, 2014). In addition, we anticipate that the future development and application of more specific and efficient gene editing technologies will allow for a greater reduction of mutated mtDNA levels in the germline.

Transmission of mitochondrial diseases by female carriers directly correlates with the levels of mutated mtDNA present in oocytes. In many cases, asymptomatic female carriers with intermediate levels of mutant load may produce oocytes with different ranges of mutated mtDNA (Chinnery et al., 2000; Cree et al., 2009). Due to the lack of mtDNA replication in oocytes and pre-implantation embryos, targeting of mutated mtDNA in oocytes with high mutant loads using the approach presented here may lead to a dramatic reduction in mtDNA copy number. In mice, embryos with mtDNA levels below a specific threshold develop normally during the pre-implantation stages but subsequently fail to

implant in the uterus or undergo development arrest (Wai et al., 2010). Consequently, oocytes containing high levels of mutated mtDNA that are subjected to heteroplasmy shift may result in embryos with low mtDNA copy number that may fail to implant in the uterine wall. In this case, though heteroplasmy shift may not result in a viable embryo, it would attain the goal of hampering the development and implantation of embryos with high mutant loads, thereby preventing the transmission of mitochondrial diseases to the next generation. In this scenario, PGD could be used as a complementary approach to select embryos with mtDNA copy numbers sufficient for implantation.

Due to the non-Mendelian segregation of mtDNA, current therapeutic approaches, including genetic counseling and PGD, can only partially reduce, but not eliminate, the risk of transmission of mitochondrial diseases (Brown et al., 2006). The recent development of mitochondrial replacement techniques based on spindle, pronuclear, or polar body transfer into healthy enucleated donor oocytes or embryos, soon to be allowed in the UK and currently under review by US regulatory agencies, represent a valid and powerful alternative to current approaches (Craven et al., 2010; Paull et al., 2013; Tachibana et al., 2013; Wang et al., 2014). Mitochondrial replacement techniques involve a series of complex technical manipulations of nuclear genome between patient and donor oocytes that will result in the generation of embryos carrying genetic material from three different origins. For these reasons, mitochondrial replacement techniques have raised biological, medical, and ethical concerns (Hayden, 2013; Reinhardt et al., 2013). Despite their great potential, more studies are still required to show that these techniques are safe in human oocytes. The approach presented here relies on a single injection of mRNA into patient oocytes, which is technically simpler and less traumatic to the oocyte compared to mitochondrial replacement techniques (Craven et al., 2010; Paull et al., 2013; Tachibana et al., 2013; Wang et al., 2014). Importantly, it does not require healthy donor oocytes, thus avoiding ethical issues related to the presence of donor mtDNA.

Induction of mtDNA heteroplasmy shift using restriction endonucleases or TALENs has the potential to eliminate mutated mitochondrial genomes in the germline, and consequently, prevent the transgenerational transmission of mitochondrial diseases. In addition, since mtDNA mutations in the germline have been recently linked to aging (Ross et al., 2013), this strategy could also be applied to prevent the transmission of mtDNA variants with potential roles in aggravating aspects of human aging and age-associated diseases.

EXPERIMENTAL PROCEDURES

Plasmids

A synthetic gene coding for the ApaLI restriction endonuclease with a C-terminal HA (Hemagglutinin antigen) tag was purchased from Integrated DNA Technologies (Coralville) with codon usage optimized for mammalian translation. For the generation of the mito-ApaLI construct, ApaLI was subcloned into the pVAX plasmid containing the mitochondria localization signal derived from ATP5B, a unique Flag immunotag in the N terminus, 5' and 3' UTR from ATP5B to localize the mRNA to ribosomes associated with mitochondria, an independent fluorescent marker to select for expression (enhance GFP [EGFP]) and a recoded picornaviral 2A-like sequence (T2A') between the

mito-ApaLI and the fluorescent marker. Subsequently, the fragment described was subcloned into the pcDNA3 plasmid containing a T7 promoter for in vitro transcription. For the generation of the mito-GFP construct, EGFP was subcloned into the previously described pVAX construct lacking the independent fluorescent marker and the recoded picornaviral 2A-like sequence (T2A') but containing a T7 promoter. For the generation of ApaLI construct, ApaLI RE was subcloned into the previously described pVAX plasmid lacking the N terminus mitochondria localization signal derived from ATP5B and the 5' and 3' UTRs from ATP5B with a T7 promoter. Cloning was done using the In-Fusion HD cloning kit (Clontech Laboratories).

Construction of Mito-TALENs

TALEN target sites for NZB and NARP m.9176T>C were identified using the TAL effector-Nucleotide Targeter (TALE-NT) software (Christian et al., 2010). To increase TALEN specificity, TALEN with targeting sequences of various lengths ranging from 7.5 to 13.5 base pairs were designed. TALENs were constructed into the TALEN cloning vector of the TALE Toolbox kit from Addgene (cat#1000000019) (Sanjana et al., 2012), and the TALENs recognizing the target sites were constructed using the Golden Gate Assembly method. Mito-TALEN, were constructed by addition of mitochondria localization signals derived from ATP5B or SOD2 mitochondria localization signal, inclusion of a unique immuno-tag in the N terminus of the mature protein (hemagglutinin [HA] or Flag), inclusion of the 5' and 3' UTRs from ATP5B or SOD2, inclusion of an independent fluorescent marker to select for expression (EGFP in one monomer and mCherry in the other) and inclusion of a recoded picornaviral 2A-like sequence (T2A') between the mito-TALEN and the fluorescent marker.

Animals

All animal procedures were performed according to NIH guidelines and approved by the Committee on Animal Care at Salk Institute. NZB/BALB heteroplasmic founder females were originally generated (Jenuth et al., 1996). NZB/BALB colony was maintained by breeding the females with BALB/cByJ males. Tail tip genotyping was routinely performed in order to exclude females carrying low levels of one of the two mtDNA haplotypes. BALB/c, BALB/cByJ and NZB mice were obtained from Jackson laboratory.

Cells, Transfection, and Sorting

Simian virus 40 (SV40) immortalized NZB/BALB fibroblasts containing NZB and BALB mtDNA were derived from tail tip of NZB/BALB mice. Human patient cells harboring the NARP m.9176T>C mutation were obtained by skin biopsy after signed informed consent of the donor and with the approval of the Institutional Review Board of the Hospital Clinic, Spain. Cells were immortalized using SV40 and cultured at 37 °C in DMEM (Invitrogen) containing GlutaMAX, non-essential amino acids and 10% fetal bovine serum (FBS). 143B osteosarcoma cybrid cells harboring the LHOND m.14459G>A mutation were obtained and cultured as previously described (Bacman et al., 2013). Cells were transfected with Lipofectamine 2000 (Invitrogen) according to the manufacturer's instructions. After 72 hr, cells were sorted using a BD Influx (Becton, Dickinson and Company) by gating on single-cell fluorescence using a 488-nm laser with a 505LP, 530/40 filter set for EGFP and a 561-nm laser with a 600LP, 610/20 filter set for mCherry. Total DNA was extracted from sorted cells using the DNeasy Blood and Tissue Kit (QIAGEN) following the protocol suggested by the manufacturer.

Single Strand Annealing Reporter Assay

Please refer to [Extended Experimental Procedures](#).

Production of mRNA

In vitro transcription of mRNA was performed using mMESSAGE mMACHINE T7 ULTRA kit (Life Technologies) according to the manufacturer's instructions using linearized and gel purified (QIAGEN) plasmid template. The mRNA was purified using MEGAclear kit (Life Technologies) and quantified using NanoDrop 8000 (Thermo Scientific).

Oocyte Collection and mRNA Injection

Female mice were superovulated with pregnant mares serum gonadotropin (PMSG) and human chorionic gonadotropin (hCG). MII oocytes were

collected 14 hr after hCG injection in M2 medium (Millipore) and freed of cumulus cells using hyaluronidase. For collection of 1-cell embryos, superovulated female mice were mated to BALB/c males and fertilized embryos were collected 18–20 hr after hCG injection from oviduct. mRNA (50–250 ng/ μ l) was injected into the cytoplasm of MII oocytes and fertilized embryos in M2 medium using Eppendorf micromanipulator. The injected MII oocytes were in vitro cultured in KSOM (Millipore) for 48 hr before analysis. The injected embryos were cultured in KSOM at 37°C under 5% CO₂ in air until blastocyst stage. Subsequently, blastocysts were collected for analysis or transferred to BALB/c pseudopregnant females. Live pups were obtained by natural delivery.

Cell Fusion

Cell fusion was achieved by using inactivated Sendai virus (GenomeOne, Cosmo Bio). Sendai virus stock solutions were prepared according to the manufacturer instructions and further diluted 1:20 in cell fusion buffer. The 143B osteosarcoma cybrid cells harboring LHON m.14459G>A mutation and patient cells harboring NARP m9176T>C mutation were used for fusion with mature MII oocytes. Cells were cultured for 48 hr in DMEM no glucose medium supplemented with galactose before using for cell fusion to increase mtDNA content. On the day of fusion, cells were trypsinized and re-suspended in M2 medium. For each MII oocyte, five cells briefly placed in Sendai virus were injected under the zona pellucida. After 3 hr successfully fused oocytes were selected for mito-TALEN mRNA injection. Lastly, surviving oocytes were cultured in KSOM for 48 hr before analysis.

Immunofluorescence

Cells were seeded on coverslips before transfection. Forty-eight hours after transfection cells were incubated in the presence of 350 nM Mitotracker (Invitrogen) for 30 min. Subsequently, cells were fixed and permeabilized with 4% PFA and 0.1% Triton X-100, respectively. After fixation, cells were blocked for 1 hr at room temperature with 1% BSA/PBS. Next, cells were incubated with an anti-Flag M2 primary antibody (Sigma) or anti-HA antibody (Millipore) overnight at 4°C. The next day, cells were washed three times with PBS and incubated for 1 hr at room temperature with Alexa Fluor 488-conjugated donkey antibodies to goat IgG (Molecular Probes) or Alexa Fluor 647-conjugated donkey antibodies to mouse IgG and 10 min with Hoechst 33342 (0.5 μ g ml⁻¹ in PBS) (Invitrogen). Finally, cells were washed three times with PBS and mounted using Fluoromount-G (Southernbiotech). Confocal image acquisition was performed using a Zeiss LSM 780 laser-scanning microscope (Carl Zeiss Jena).

“Last-Cycle Hot” PCR and RFLP

Total DNA from cells, tail biopsies, and oocytes/embryos were used to determine mtDNA heteroplasmy by “Last-cycle hot” PCR using the mtDNA 5′ Fluorescein amidite (FAM) labeled primers as listed in Table S2. NZB/BALB PCR products were digested with ApaI or HindIII, which digests BALB mtDNA at positions 5461 (ApaI targeting site) and 9136 respectively. NARP PCR products were digested with BsrI which digest mutated NARP mtDNA at position 9176. The levels of LHON m.14459G>A were determined as previously reported (Bacman et al., 2013). Digested PCR products were subjected to electrophoresis in a 12% polyacrylamide gel. The fluorescein signal was quantified using a Typhoon 8600 system (Molecular Dynamics) and gels were quantified using ImageQuant 5.2 (Molecular Dynamics).

Quantification of mtDNA Copy Number

Absolute mtDNA copy numbers were quantified by real-time PCR using iQSyber Green on Bio-Rad iCycler (Bio-Rad). Individual oocytes and embryos were transferred into lysis buffer (200 mM KOH) and incubated for 10 min at 65°C. The reaction was neutralized by addition of 200 mM HCl. Absolute mtDNA copy number per 1 μ l of lysate was calculated using a standard curve derived from the Q-PCR amplification of a fragment of mtDNA genome. First, a standard curve was generated by a 10-fold serial dilution of a PCR product obtained using Standard curve primers for the different regions of mtDNA analyzed. Subsequently, to quantify the absolute levels of mtDNA, quantitative real-time PCR was performed using qPCR primers listed in Table S2.

Blood and Plasma Parameters

Blood collection was performed by sub-mandibular bleeding. Whole EDTA blood samples were analyzed in duplicates for Complete Blood Count (CBC) on a Hemavet 950FS Multi Species Hematology System (Drew Scientific). Plasma glucose concentration was determined using the Glucose (GO) Assay Kit (Sigma) according to the manufacturer's instructions. Plasma lactate concentration was determined using the Lactate Assay Kit (Sigma) according to the manufacturer's instructions. Please refer to Extended Experimental Procedures.

Behavioral Analysis

Behavioral testing was carried out at the Salk Institute for Biological Studies Behavioral Testing Core. Basic sensorimotor function was assessed in the Open Field Test, Rotarod, Grip Strength, and Neurological Screen. Please refer to Extended Experimental Procedures.

Array Comparative Genomic Hybridization

aCGH was performed following Agilent Oligonucleotide Array-Based CGH for Genomic DNA Analysis (Agilent Technologies, Santa Clara, CA). Please refer to Extended Experimental Procedures.

Exome Capture and High-Throughput Sequencing

Exome capture was using the SeqCap EZ Mouse Exome Design probe pool (54 Mb, NimbleGen) according to the manufacturer's protocol. Please refer to Extended Experimental Procedures.

Statistical Evaluation

Statistical analyses were performed by using standard unpaired Student's *t* test with Welch's correction using Prism 6 software (GraphPad). All data are presented as mean \pm SEM and represent a minimum of two independent experiments. Statistical significance is displayed as **p* < 0.05, ***p* < 0.01, ****p* < 0.001, and *****p* < 0.0001.

ACCESSION NUMBERS

The GEO database accession number for the aCGH data sets reported in this paper is GSE67371. The GEO accession number for the exome sequencing data sets reported in this paper is SRP056327.

SUPPLEMENTAL INFORMATION

Supplemental Information includes Extended Experimental Procedures, six figures, and two tables and can be found with this article online at <http://dx.doi.org/10.1016/j.cell.2015.03.051>.

AUTHORS CONTRIBUTIONS

P.R., A.O., C.T.M., and J.C.I.B. designed all experiments. P.R., A.O., I.S.-M., and J.C.I.B. prepared the figures and wrote the manuscript. P.R., A.O., K.S., S.R.B., Y.T., J.W., D.L., X.X., N.M., and C.R.E., performed and analyzed all in vitro experiments. P.R., A.O., J.L., A.S., and D.O. performed and analyzed all in vivo experiments. S.R.B., S.L.W., G.H.L., D.M., S.C., M.d.M.O'., H.Z., and C.T.M. provided reagents. F.C., J.C., and J.M.C. contributed to the design of the project.

ACKNOWLEDGMENTS

We thank M. Schwarz for administrative support. We thank S. Heinz and M.M. Ku from H.A. and Mary K. Chapman Charitable Foundations Genomic Sequencing Core at the Salk Institute for help with sequencing analysis. We thank M. Chang from the Integrative Genomics and Bioinformatics Core at the Salk Institute for sequencing data analysis. We thank C.B. Farrokhi from the Behavioral Testing Core at the Salk Institute for help with behavioral studies. We thank Eric Shoubridge from McGill University, Montreal, Canada for sharing with us the NZB/BALB/c heteroplasmic mice. We thank Julio Montoya Villarroja from the University of Zaragoza, Zaragoza, Spain, and M^a Ángeles Ruiz Gómez from the Hospital de Son Espases, Palma de Mallorca,

Spain. Financial support: M.M. Ku and S. Heinz are supported by the Leona M. and Harry B. Helmsley Charitable Trust. A.O. was partially supported by an NIH Ruth L. Kirschstein National Research Service Award Individual Postdoctoral Fellowship. G.-H.L. was supported by National Basic Research Program of China (973 Program, 2015CB964800; 2014CB964600), the Strategic Priority Research Program of the Chinese Academy of Sciences (XDA01020312), National Natural Science Foundation of China (NSFC: 81271266; 31222039; 31201111; 81371342). C.T.M. was supported by NIH grants 5R01EY010804, 1R01AG036871, the JDM Fund, the Muscular Dystrophy Association and the United Mitochondrial Disease Foundation. S.L.W. is supported by Florida Department of Health Grant 3KN09. Work in the laboratory of J.C.I.B. was supported by the G. Harold and Leila Y. Mathers Charitable Foundation and the Leona M. and Harry B. Helmsley Charitable Trust (2012-PG-MED002).

Received: February 2, 2015

Revised: March 5, 2015

Accepted: March 25, 2015

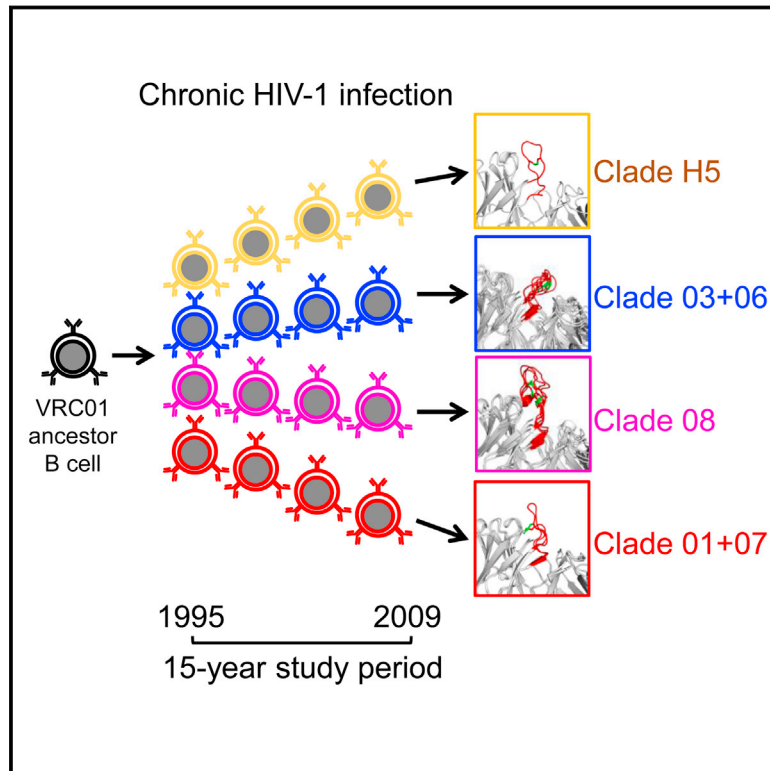
Published: April 23, 2015

REFERENCES

- Alexeyev, M.F., Venediktova, N., Pastukh, V., Shokolenko, I., Bonilla, G., and Wilson, G.L. (2008). Selective elimination of mutant mitochondrial genomes as therapeutic strategy for the treatment of NARP and MILS syndromes. *Gene Ther.* 15, 516–523.
- Alexeyev, M., Shokolenko, I., Wilson, G., and LeDoux, S. (2013). The maintenance of mitochondrial DNA integrity—critical analysis and update. *Cold Spring Harb. Perspect. Biol.* 5, a012641–a012641.
- Anderson, S., Bankier, A.T., Barrell, B.G., de Bruijn, M.H., Coulson, A.R., Drouin, J., Eperon, I.C., Nierlich, D.P., Roe, B.A., Sanger, F., et al. (1981). Sequence and organization of the human mitochondrial genome. *Nature* 290, 457–465.
- Bacman, S.R., Williams, S.L., Garcia, S., and Moraes, C.T. (2010). Organ-specific shifts in mtDNA heteroplasmy following systemic delivery of a mitochondria-targeted restriction endonuclease. *Gene Ther.* 17, 713–720.
- Bacman, S.R., Williams, S.L., Duan, D., and Moraes, C.T. (2012). Manipulation of mtDNA heteroplasmy in all striated muscles of newborn mice by AAV9-mediated delivery of a mitochondria-targeted restriction endonuclease. *Gene Ther.* 19, 1101–1106.
- Bacman, S.R., Williams, S.L., Pinto, M., Peralta, S., and Moraes, C.T. (2013). Specific elimination of mutant mitochondrial genomes in patient-derived cells by mitoTALENs. *Nat. Med.* 19, 1111–1113.
- Brown, D.T., Herbert, M., Lamb, V.K., Chinnery, P.F., Taylor, R.W., Lightowlers, R.N., Craven, L., Cree, L., Gardner, J.L., and Turnbull, D.M. (2006). Transmission of mitochondrial DNA disorders: possibilities for the future. *Lancet* 368, 87–89.
- Chinnery, P.F., Thorburn, D.R., Samuels, D.C., White, S.L., Dahl, H.M., Turnbull, D.M., Lightowlers, R.N., and Howell, N. (2000). The inheritance of mitochondrial DNA heteroplasmy: random drift, selection or both? *Trends Genet.* 16, 500–505.
- Christian, M., Cermak, T., Doyle, E.L., Schmidt, C., Zhang, F., Hummel, A., Bogdanove, A.J., and Voytas, D.F. (2010). Targeting DNA double-strand breaks with TAL effector nucleases. *Genetics* 186, 757–761.
- Craven, L., Tuppen, H.A., Greggains, G.D., Harbottle, S.J., Murphy, J.L., Cree, L.M., Murdoch, A.P., Chinnery, P.F., Taylor, R.W., Lightowlers, R.N., et al. (2010). Pronuclear transfer in human embryos to prevent transmission of mitochondrial DNA disease. *Nature* 465, 82–85.
- Cree, L.M., Samuels, D.C., and Chinnery, P.F. (2009). The inheritance of pathogenic mitochondrial DNA mutations. *Biochim. Biophys. Acta* 1792, 1097–1102.
- Dyall, S.D., Brown, M.T., and Johnson, P.J. (2004). Ancient invasions: from endosymbionts to organelles. *Science* 304, 253–257.
- Gammage, P.A., Rorbach, J., Vincent, A.I., Rebar, E.J., and Minczuk, M. (2014). Mitochondrially targeted ZFNs for selective degradation of pathogenic mitochondrial genomes bearing large-scale deletions or point mutations. *EMBO Mol. Med.* 6, 458–466.
- Haas, R.H., Parikh, S., Falk, M.J., Saneto, R.P., Wolf, N.I., Darin, N., and Cohen, B.H. (2007). Mitochondrial disease: a practical approach for primary care physicians. *Pediatrics* 120, 1326–1333.
- Hayden, E.C. (2013). Regulators weigh benefits of ‘three-parent’ fertilization. *Nature* 502, 284–285.
- Jenuth, J.P., Peterson, A.C., Fu, K., and Shoubridge, E.A. (1996). Random genetic drift in the female germline explains the rapid segregation of mammalian mitochondrial DNA. *Nat. Genet.* 14, 146–151.
- Jun, A.S., Brown, M.D., and Wallace, D.C. (1994). A mitochondrial DNA mutation at nucleotide pair 14459 of the NADH dehydrogenase subunit 6 gene associated with maternally inherited Leber hereditary optic neuropathy and dystonia. *Proc. Natl. Acad. Sci. USA* 91, 6206–6210.
- Marc, P., Margeot, A., Devaux, F., Blugeon, C., Corral-Debrinski, M., and Jacq, C. (2002). Genome-wide analysis of mRNAs targeted to yeast mitochondria. *EMBO Rep.* 3, 159–164.
- Minczuk, M., Papworth, M.A., Kolasinska, P., Murphy, M.P., and Klug, A. (2006). Sequence-specific modification of mitochondrial DNA using a chimeric zinc finger methylase. *Proc. Natl. Acad. Sci. USA* 103, 19689–19694.
- Minczuk, M., Papworth, M.A., Miller, J.C., Murphy, M.P., and Klug, A. (2008). Development of a single-chain, quasi-dimeric zinc-finger nuclease for the selective degradation of mutated human mitochondrial DNA. *Nucleic Acids Res.* 36, 3926–3938.
- Paull, D., Emmanuele, V., Weiss, K.A., Treff, N., Stewart, L., Hua, H., Zimmer, M., Kahler, D.J., Golland, R.S., Noggle, S.A., et al. (2013). Nuclear genome transfer in human oocytes eliminates mitochondrial DNA variants. *Nature* 493, 632–637.
- Reinhardt, K., Dowling, D.K., and Morrow, E.H. (2013). Medicine. Mitochondrial replacement, evolution, and the clinic. *Science* 341, 1345–1346.
- Rogers, D.C., Fisher, E.M., Brown, S.D., Peters, J., Hunter, A.J., and Martin, J.E. (1997). Behavioral and functional analysis of mouse phenotype: SHIRPA, a proposed protocol for comprehensive phenotype assessment. *Mamm. Genome* 8, 711–713.
- Ross, J.M., Stewart, J.B., Hagström, E., Brené, S., Mourier, A., Coppotelli, G., Freyer, C., Lagouge, M., Hoffer, B.J., Olson, L., and Larsson, N.G. (2013). Germline mitochondrial DNA mutations aggravate ageing and can impair brain development. *Nature* 501, 412–415.
- Russell, O., and Turnbull, D. (2014). Mitochondrial DNA disease—molecular insights and potential routes to a cure. *Exp. Cell Res.* 325, 38–43.
- Sanjana, N.E., Cong, L., Zhou, Y., Cunniff, M.M., Feng, G., and Zhang, F. (2012). A transcription activator-like effector toolbox for genome engineering. *Nat. Protoc.* 7, 171–192.
- Shoubridge, E.A., and Wai, T. (2007). Mitochondrial DNA and the mammalian oocyte. *Curr. Top. Dev. Biol.* 77, 87–111.
- Tachibana, M., Amato, P., Sparman, M., Woodward, J., Sanchis, D.M., Ma, H., Gutierrez, N.M., Tippner-Hedges, R., Kang, E., Lee, H.-S., et al. (2013). Towards germline gene therapy of inherited mitochondrial diseases. *Nature* 493, 627–631.
- Taylor, R.W., and Turnbull, D.M. (2005). Mitochondrial DNA mutations in human disease. *Nat. Rev. Genet.* 6, 389–402.
- Vogel, G. (2014). Assisted reproduction. FDA considers trials of ‘three-parent embryos’. *Science* 343, 827–828.
- Wai, T., Ao, A., Zhang, X., Cyr, D., Dufort, D., and Shoubridge, E.A. (2010). The role of mitochondrial DNA copy number in mammalian fertility. *Biol. Reprod.* 83, 52–62.
- Wallace, D.C., and Chalkia, D. (2013). Mitochondrial DNA genetics and the heteroplasmy conundrum in evolution and disease. *Cold Spring Harb. Perspect. Biol.* 5, a012220.
- Wang, T., Sha, H., Ji, D., Zhang, H.L., Chen, D., Cao, Y., and Zhu, J. (2014). Polar body genome transfer for preventing the transmission of inherited mitochondrial diseases. *Cell* 157, 1591–1604.

Maturation and Diversity of the VRC01-Antibody Lineage over 15 Years of Chronic HIV-1 Infection

Graphical Abstract



Authors

Xueling Wu, Zhenhai Zhang, ..., John R. Mascola, Lawrence Shapiro

Correspondence

pdkwong@nih.gov (P.D.K.),
jmascola@nih.gov (J.R.M.),
lss8@columbia.edu (L.S.)

In Brief

The longitudinal analysis of antibody response in a patient during 15 years of HIV-1 infection shows how the VRC01 broadly neutralizing antibody lineage evolved from a single B cell. Antibody maturation occurs with high, but slowing, evolutionary rate over many years, providing a mechanism to achieve extraordinary antibody diversity during chronic infections.

Highlights

- A diverse multi-clade antibody repertoire can develop from a single B cell
- Rate of antibody evolution in long-lived lineages is similar to that of HIV-1
- High lineage evolutionary rate over years enables extraordinary antibody diversity
- An antibody lineage can encompass divergent loop and disulfide structures

Accession Numbers

4XVS, 4XVT, 4S1Q,
4S1R, 4S1S, 4XNZ,
4XMP, 4XNY,
KP840719–KP841751,
KP840592–KP840624,
KP841752–KP842237,
KP840625–KP840656,
KP840657–KP840687,
KP840688–KP840718



Maturation and Diversity of the VRC01-Antibody Lineage over 15 Years of Chronic HIV-1 Infection

Xueling Wu,^{1,2,8} Zhenhai Zhang,^{1,3,4,5,8} Chaim A. Schramm,^{3,8} M. Gordon Joyce,^{1,8} Young Do Kwon,^{1,8} Tongqing Zhou,^{1,8} Zizhang Sheng,^{3,8} Baoshan Zhang,¹ Sijy O'Dell,¹ Krisha McKee,¹ Ivelin S. Georgiev,¹ Gwo-Yu Chuang,¹ Nancy S. Longo,¹ Rebecca M. Lynch,¹ Kevin O. Saunders,¹ Cinque Soto,¹ Sanjay Srivatsan,¹ Yongping Yang,¹ Robert T. Bailer,¹ Mark K. Louder,¹ NISC Comparative Sequencing Program,⁶ James C. Mullikin,⁶ Mark Connors,⁷ Peter D. Kwong,^{1,*} John R. Mascola,^{1,*} and Lawrence Shapiro^{1,3,*}

¹Vaccine Research Center, National Institute of Allergy and Infectious Diseases, National Institutes of Health, Bethesda, MD 20892, USA

²Aaron Diamond AIDS Research Center, Rockefeller University, New York, NY 10016, USA

³Department of Biochemistry and Molecular Biophysics and Department of Systems Biology, Columbia University, New York, NY 10032, USA

⁴State Key Laboratory of Organ Failure Research

⁵National Clinical Research Center for Kidney Disease

Nanfang Hospital, Southern Medical University, Guangzhou, Guangdong 510515, China

⁶NIH Intramural Sequencing Center, National Human Genome Research Institute, National Institutes of Health, Bethesda, MD 20892, USA

⁷Laboratory of Immunoregulation, National Institute of Allergy and Infectious Diseases, National Institutes of Health, Bethesda, MD 20892, USA

⁸Co-first author

*Correspondence: pdkwong@nih.gov (P.D.K.), jmascola@nih.gov (J.R.M.), lss8@columbia.edu (L.S.)

<http://dx.doi.org/10.1016/j.cell.2015.03.004>

SUMMARY

HIV-1-neutralizing antibodies develop in most HIV-1-infected individuals, although highly effective antibodies are generally observed only after years of chronic infection. Here, we characterize the rate of maturation and extent of diversity for the lineage that produced the broadly neutralizing antibody VRC01 through longitudinal sampling of peripheral B cell transcripts over 15 years and co-crystal structures of lineage members. Next-generation sequencing identified VRC01-lineage transcripts, which encompassed diverse antibodies organized into distinct phylogenetic clades. Prevalent clades maintained characteristic features of antigen recognition, though each evolved binding loops and disulfides that formed distinct recognition surfaces. Over the course of the study period, VRC01-lineage clades showed continuous evolution, with rates of ~2 substitutions per 100 nucleotides per year, comparable to that of HIV-1 evolution. This high rate of antibody evolution provides a mechanism by which antibody lineages can achieve extraordinary diversity and, over years of chronic infection, develop effective HIV-1 neutralization.

INTRODUCTION

HIV-1-neutralizing antibodies to autologous virus develop within weeks or months of infection (Albert et al., 1990; Richman et al., 2003; Wei et al., 2003), with serum neutralization generally evolving over time to gain increased potency and breadth (Gray et al., 2011; Mikell et al., 2011). In a study of ~200 chronically

HIV-1-infected individuals, serum from ~50% of studied donors contained antibodies capable of neutralizing ~50% of HIV-1 strains (Hraber et al., 2014). A subset of these individuals develops potent and broadly reactive antibodies (Gray et al., 2011; Li et al., 2007; Mikell et al., 2011; Walker et al., 2010; Wu et al., 2006). Isolation and characterization reveal these broadly neutralizing antibodies to have one or more unusual features including long or protruding heavy-chain third complementarity-determining regions (CDR H3s) (Burton et al., 1994; Walker et al., 2009; Zhou et al., 2007), domain swapping (Calarese et al., 2003), unusual post-translational modifications such as tyrosine sulfation (TyrS) (Huang et al., 2004; Pancera et al., 2010; Pejchal et al., 2010), poly or autoreactivity (Haynes et al., 2005), extensive somatic hypermutation (SHM) (Scheid et al., 2011; Walker et al., 2011; Wu et al., 2010, 2011), or dependence on framework region contacts (Klein et al., 2013). These characteristics highlight the extensive maturation process necessary for most antibodies to achieve effective HIV-1 neutralization (Burton et al., 2005; Klein et al., 2013; Mascola and Haynes, 2013; Scheid et al., 2009).

To understand how effective neutralization develops, we and others have investigated the ontogenies of neutralizing antibody lineages using monoclonal antibodies (mAbs) isolated from individual B cells (Bonsignori et al., 2012; Scheid et al., 2011; Walker et al., 2011), next-generation sequencing (NGS) of cross-sectional samples (Wu et al., 2011; Zhou et al., 2013; Zhu et al., 2012, 2013), and NGS of longitudinal samples studied from time of infection (Doria-Rose et al., 2014; Liao et al., 2013). While these studies often focused on revealing the unmutated common ancestors (UCAs) of neutralizing antibody lineages and early antibody maturation, questions remain about the long-term and continuing development of antibody lineages. What is the scope of B cell development in a broadly neutralizing antibody lineage? What are the rates, compositions, extents, and continuities of lineage evolution? What biological mechanisms underlie the development of HIV-1 neutralization?

Here, we investigate the VRC01-antibody lineage, which targets the site of CD4 engagement on HIV-1 (Wu et al., 2010; Zhou et al., 2010) and is a member of a class of antibodies (the VRC01 class), which share similar structural and genetic characteristics (West et al., 2012; Wu et al., 2011; Zhou et al., 2013). We identified dozens of VRC01-lineage antibodies from one donor and describe characteristics of this lineage as it evolved over the course of 15 years. Overall, these results delineate the scope of evolutionary diversity for a persistent antibody lineage. Antibody lineage characteristics identified here—such as multi-clade divergence and a high rate of evolution—may be common to effective HIV-1-neutralizing antibodies and provide insights into the immunological mechanisms that enable their development.

RESULTS

39 Probe-Identified Antibodies Define Three VRC01-Lineage Clades

The broadly neutralizing antibodies VRC01, VRC02, and VRC03 were previously isolated from an August 2008 sample of donor 45 peripheral blood mononuclear cells (PBMCs), using the resurfaced stabilized core 3 (RSC3) probe (Wu et al., 2010). From additional 2008 samples, other probes were subsequently used to isolate five more VRC01-class antibodies: NIH45-46, NIH45-177, NIH45-243, VRC06, and VRC06b (Li et al., 2012; Scheid et al., 2011). All eight of these antibodies appeared to be somatic variants from a single VRC01 lineage (Zhou et al., 2013).

To gain insight into the scope of the VRC01 lineage, we performed RSC3-specific B cell sorting on PBMCs from April 2002 and August 2008 time points to identify additional lineage members (Figure 1A, left and right). We also performed B cell sorting with a modified gp120 outer-domain probe (Joyce et al., 2013) on PBMCs from January 2008 (Figure 1A, middle). Five antibodies were recovered from the 2002 sample, including a new VRC01-lineage antibody, VRC08, which was substantially different from those identified previously. The CDR H3 of VRC08 was 23 amino acids in length by Kabat definition, substantially longer than those of VRC01 and VRC07 (12 and 16 amino acids, respectively) or VRC03 and VRC06 (14 and 15 amino acids, respectively) (Figure 1B). We assessed neutralization by VRC08 against 195 Env pseudoviruses. VRC08 displayed breadth and potency similar to VRC01 (Figure 1C; Table S1). In addition to VRC08, several other closely related antibodies were identified. In all, we identified 31 new neutralizing antibodies from donor 45, all with naturally paired heavy and light chains and derived from the same origin genes (Figure 1B; Figure S1).

A maximum-likelihood phylogenetic tree was constructed from the concatenated heavy- and light-chain nucleotide sequences of the 39 VRC01-lineage antibodies (Figure 1D); they segregated into three major clades, termed clade 01+07, clade 03+06, and clade 08. Sequence differences within clades were under 25%, while differences exceeded 50% between clades (Figure 1E), and CDR H3 lengths varied from 12 to 23 amino acids.

Tracking Potential VRC01-Lineage Sequences in Longitudinal Samples

To gain a more complete understanding of the VRC01 lineage and its development, we used NGS to identify potential lineage

members over 15 years. The first sample available was from March 1995, well after the diagnosis of HIV-1 infection in 1990. Ten samples were analyzed, extending to December 2009. During this 15-year period, donor 45 maintained a relatively stable plasma viral load of around 10,000 copies/ml and a CD4⁺ T cell count >500 cells/ μ l without anti-retroviral therapy (Table S2A). cDNA libraries from each time point, corresponding to the transcripts of 3–5 million PBMCs, were used as templates, and 5' gene family-specific primers were used to amplify VH1 genes or V κ 3 genes, with 3' primers for both immunoglobulin M (IgM) and immunoglobulin G (IgG) or immunoglobulin κ (Ig κ) constant regions. We estimate that each longitudinal sample contained 75–125,000 VH1-family-derived B cells and 100–160,000 V κ 3-family-derived B cells. 454 pyrosequencing, with either a half- or full-454 chip, generally yielded between a quarter million to a million raw reads for each heavy- or light-chain reaction, for each time point (Figure 2).

A heavy-chain-specific bioinformatics pipeline with multiple computational sieves was used to identify VRC01-lineage transcripts and to classify them into closely related groups of sequences based on CDR H3 identity (Figure S2A, bottom panels). We utilized a modified cross-donor analysis algorithm and applied several levels of data quality filtering and de-replication with a 97.25% identity threshold (Extended Experimental Procedures). These quality filters ameliorated known 454 errors and reduced the number of unique sequences. The effect of each data-filtering step on the number of retained sequences is shown in Table S2B. Similarly, a light-chain-specific pipeline was used to identify and classify VRC01-lineage light-chain transcripts (Figure S2B, bottom panels). As with the heavy chains, we applied data-quality filters (Figure 2B, bottom panels, and Table S2B).

We were able to track the evolution of each clade of the VRC01 lineage through the positions of clusters of closely related sequences on identity/divergence (I-D) plots over time (Figure 2; Figures S2C–S2F). The positions of these clusters at successive time points revealed the persistence and continued SHM of each clade, with a typical increase of 5%–10% in divergence over 10 years and a maximal sequence identity around the time of isolation of the referent antibody.

Validation of Functional Antibody Clades and Definition of the VRC01 Lineage

For both heavy and light chains, we found large groups of sequences that were divergent from all probe-isolated antibodies but shared VRC01-lineage origin genes. We previously used functional complementation between heavy and light chains to confirm functionality and membership in the VRC01 class (Wu et al., 2011; Zhu et al., 2013). Importantly, reconstitution of unrelated antibody heavy chains with a VRC01 light chain, even using heavy chains with high predicted VRC01 structural compatibility, failed to neutralize HIV-1 in ten out of ten trials (Wu et al., 2011). To assess the thousands of divergent B cell transcripts from NGS, we clustered them into groups: heavy chains were clustered based on CDR H3 identity into CDR H3 groups; light chains, which have short CDR L3s, were clustered based on overall sequence identity into light-chain variable region (VL) groups. We focused on the most populous groups (those

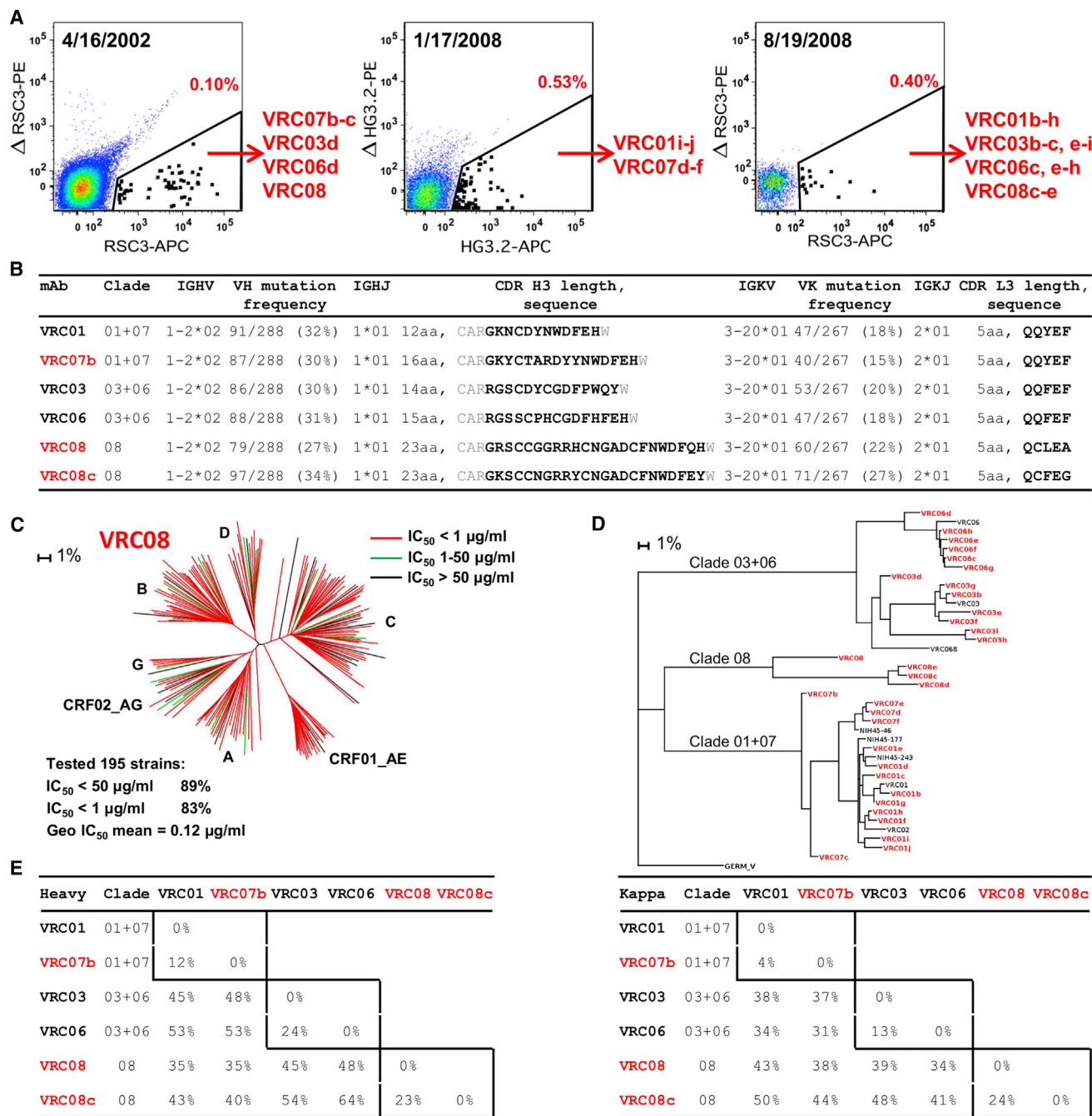


Figure 1. VRC01-Antibody Lineage: 39 Probe-Identified Antibodies Define Three Distinct Clades
(A) Isolation of antigen-specific antibodies by sorting of donor 45. B cells were probed either with RSC3 and its ΔI371 mutant ΔRSC3 or with a modified outer domain OD4.2 protein HG3.2 and its D368R mutant ΔHG3.2. Indicated in red is the percentage of total IgG⁺ B cells defined as probe-specific in each gate.
(B) Heavy- and light-chain sequence analysis for six representative antibodies, two from each clade. Residues flanking the CDR H3 are shown in gray.
(C) VRC08 neutralization dendrogram of 195 HIV-1 Env pseudoviruses with branches colored by potency.
(D) Maximum-likelihood tree of VRC01-lineage antibodies from donor 45, rooted on the germline V gene sequence. Antibody clades, 01+07, 03+06, and 08 are indicated.
(E) Pairwise sequence difference of heavy- (left) and light- (right) chain variable domains for the six representative antibodies. Intra-clade differences are boxed. See also Figure S1 and Table S1.

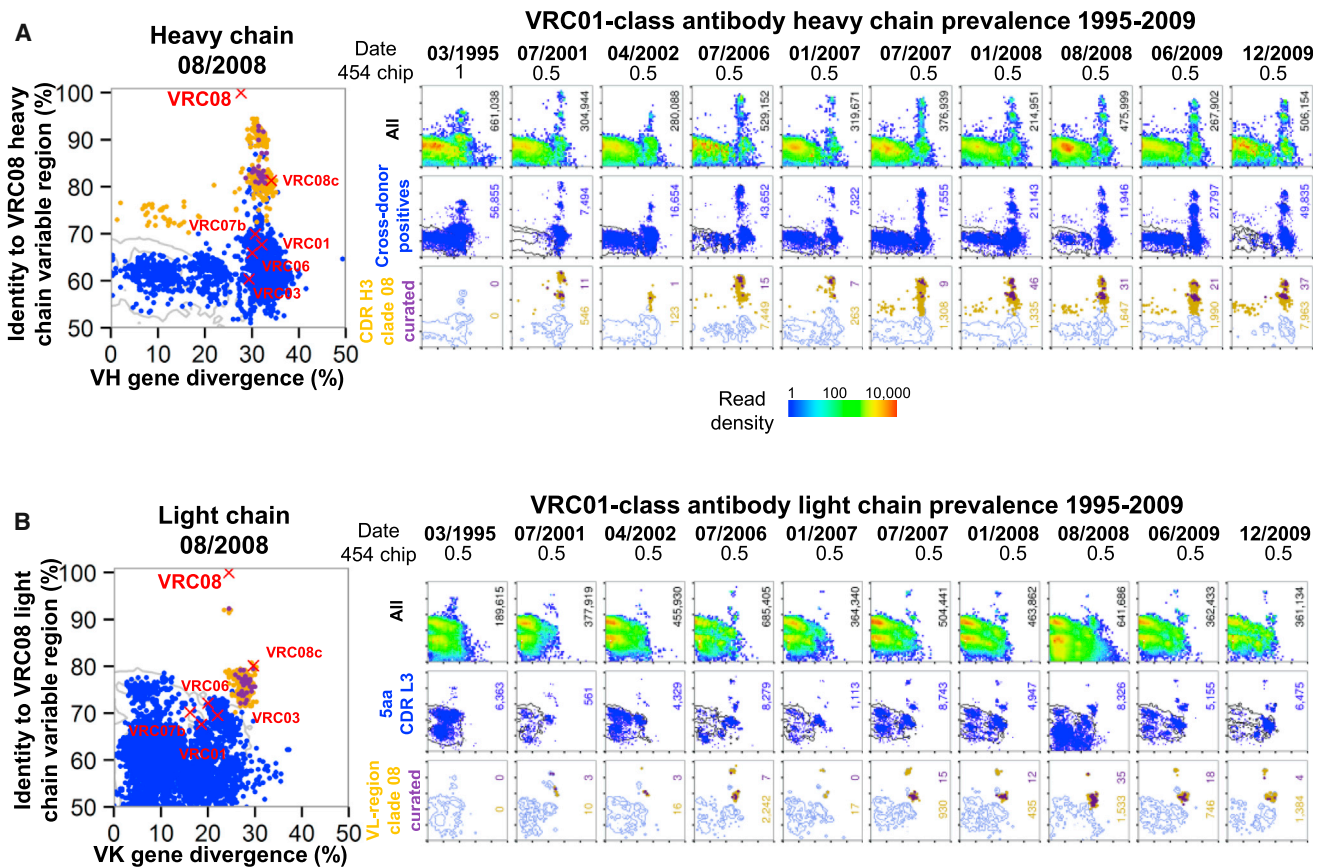


Figure 2. NGS-Identified VRC01-Lineage Transcripts in Donor 45 over 15 Years

(A) Clade-specific identity-divergence plots from heavy-chain longitudinal samples. Large example plot is shown at left for clade 08. Sequence divergence from the assigned germline V gene (x axis) and sequence identity to the VRC08 heavy-chain variable domain (y axis). Positions of the six representative antibodies from Figures 1D and 1E are shown as red X's. Identity-divergence plots for ten longitudinal time points (right). Time points and fraction of a 454 chip used for NGS are indicated at the top. The top row shows a heatmap for positions of all 454 sequences. The total number of sequences is indicated at the right borders. The middle row shows the distribution of cross-donor positive sequences as blue dots, with gray contours indicating raw sequences. The total number of cross-donor positives is displayed in blue. The bottom row shows the distribution of sequences in the same CDR H3 group as any probe-isolated antibody from that clade. Yellow dots indicate raw sequences within the CDR H3 groups, while purple dots show the subset of those sequences that survived quality-control filtering. The total numbers of raw and curated sequences in the CDR H3 groups are indicated in yellow and purple, respectively; blue contours indicate cross-donor positives.

(B) Clade-specific identity-divergence plots from light-chain longitudinal samples. The same analyses are shown as for (A), except that the middle row shows the distribution of sequences with a 5-amino-acid CDR L3. Because sequences are clustered across all ten time points to determine the final curated sequences (Extended Experimental Procedures), groups of in-clade sequences (yellow dots) with high identity to the referent antibody (e.g., in the 01/2007, 07/2007, and 01/2008 time points) may appear to have resulted in no surviving high-quality sequences (no purple dots). In actuality, the representative sequence in the final curated set has simply been chosen from a different time point (e.g., 07/2006).

See also Figure S2 and Table S2.

containing at least 300 raw heavy-chain sequences or 75 raw light-chain sequences) and chose two representative sequences for testing from each heavy- and light-chain group (Figure 3; Tables S3A and S3B) (Extended Experimental Procedures). Many of these selected sequences were observed at multiple time points (Tables S3C and S3D). For heavy chains, representative sequences from 19 CDR H3 groups neutralized HIV-1 when reconstituted with VRC01 or VRC03 light chain (Figure 3A; Table S3A). Two of these groups, H.I and H.N, appeared to use non-lineage matching JH genes (Extended Experimental Procedures), though the identity of the JH gene was uncertain due to the high level of SHM (~35% and ~25% diverged from VH1-2, respectively). These ambiguous groups were analyzed sepa-

rately from the rest of the VRC01 lineage. For light chains, 18 VL groups neutralized HIV-1 when reconstituted with VRC01 or VRC03 heavy chain (Figure 3B; Table S3B). One group, L.C, was composed of multiple unrelated lineages using various V_{κ} and J_{κ} genes and was not included in analysis of the VRC01 lineage.

Although they shared the same germline origin genes (VH1-2 and JH1), the diverse heavy-chain sequences identified could derive from a single lineage or multiple lineages. We observed that the 39 probe-identified antibodies from donor 45 all contained a cysteine at position 98 (99 in some sequences due to a 1-aa insertion). This cysteine is not a required feature of the VRC01 class, as VRC01-class antibodies from other donors do

A Identification and function of heavy chain neutralizing groups

CDR H3 group	Raw & curated reads	Assigned V-gene	Assigned J-gene	Probe-identified mAb	Representative sequence & CDR H3	Heavy chain clade	Light chain pair	Breadth	Neutralization (IC50)										
									HIV clade A					HIV clade B					HIV clade C
									GEO mean	Q23.17	Q842.d12	UG037.8	45.01 dG5	45.01 dH5	45.01 dH1	YU2	JR-FL	DU156.12	ZM109.4
H.A	34,600 158	IGHV1-2*02	IGHJ1*01	VRC03	45-VRC01.H3.A-022283 GRSCGQDCYHWDFQL	H3	01	70%	0.72	0.76	0.06	0.21	0.002	0.05	>50	0.07	>50	>50	4.62
								40%	6.41	>50	>50	>50	0.003	0.05	>50	11.20	4.74	>50	>50
								90%	0.03	0.01	0.01	0.01	0.01	0.01	0.35	0.004	0.001	0.35	>50
H.B	24,167 204	IGHV1-2*02	IGHJ1*01	VRC03	45-VRC01.H03+06.C-000427 RGPCDYCGDFVWQH	03+06	03	60%	0.40	1.23	>50	>50	0.001	0.01	0.30	0.01	0.002	>50	>50
								100%	0.06	0.09	0.03	0.04	0.002	0.03	2.59	0.01	0.35	0.08	0.14
								40%	7.85	>50	>50	>50	0.003	0.04	13.40	39.20	>50	>50	>50
H.C	22,624 178	IGHV1-2*02	IGHJ1*01	VRC08	45-VRC01.H08.F-117225 GKSCCGRRYCGADCFNWFHEH	08	01	10%	42.41	>50	>50	>50	>50	>50	9.64	>50	>50	>50	>50
								40%	17.66	>50	>50	>50	3.77	1.38	5.96	>50	6.09	>50	>50
								100%	0.24	0.80	0.11	0.34	0.01	0.04	13.90	0.27	0.09	0.41	0.38
H.D	12,451 177	IGHV1-2*02	IGHJ1*01	VRC03	45-VRC01.H4.H-015736 RDYCPDDNCNRWDLRH	H4	01	10%	42.41	>50	>50	>50	>50	>50	9.64	>50	>50	>50	>50
								40%	17.66	>50	>50	>50	3.77	1.38	5.96	>50	6.09	>50	>50
								100%	0.24	0.80	0.11	0.34	0.01	0.04	13.90	0.27	0.09	0.41	0.38
H.E	7,238 56	IGHV1-2*02	IGHJ1*01	VRC03	45-VRC01.H5.F-185917 TADCDERDPCGWVFPFH	H5	01	100%	0.24	0.80	0.11	0.34	0.01	0.04	13.90	0.27	0.09	0.41	0.38
								30%	8.85	>50	>50	>50	0.01	0.04	>50	10.50	>50	>50	>50
								40%	12.08	>50	>50	>50	0.19	0.47	>50	18.80	2.59	>50	>50
H.F	6,914 56	IGHV1-2*02	IGHJ1*01	VRC03	45-VRC01.H03+06.E-010699 RGFCDHCSKWTFEH	03+06	03	20%	19.99	>50	>50	>50	1.60	0.16	>50	>50	>50	>50	>50
								80%	0.15	0.05	0.04	0.06	0.003	0.04	0.71	0.03	0.01	>50	>50
								60%	1.17	4.47	>50	>50	0.003	0.06	1.72	0.04	0.01	>50	>50
H.G	4,613 50	IGHV1-2*02	IGHJ1*01	VRC06	45-VRC01.H03+06.G-022172 RGSSCPHCGDFHFEH	03+06	01	100%	0.04	0.09	0.03	0.08	0.002	0.02	1.82	0.05	0.01	0.06	0.06
								50%	3.57	>50	>50	>50	0.01	0.06	10.70	>50	2.61	>50	0.12
								10%	47.96	>50	>50	>50	33.00	>50	>50	>50	>50	>50	>50
H.H	4,171 54	IGHV1-2*02	IGHJ1*01	VRC06	45-VRC01.H08.H-000826 GKSCCAGRRFCGPTDCYNWDFAH	08	01	100%	0.04	0.09	0.03	0.08	0.002	0.02	1.82	0.05	0.01	0.06	0.06
								50%	3.57	>50	>50	>50	0.01	0.06	10.70	>50	2.61	>50	0.12
								10%	47.96	>50	>50	>50	33.00	>50	>50	>50	>50	>50	>50
H.I	2,300 n/a	IGHV1-2*02	IGHJ2*01	VRC06b	45-H.G-267276 GRTCCGDCYFWDLEF	Lineage 2	01	10%	47.96	>50	>50	>50	33.00	>50	>50	>50	>50	>50	>50
								10%	43.35	>50	>50	>50	12.00	>50	>50	>50	>50	>50	>50
								90%	0.17	>50	0.01	0.67	0.01	0.04	8.83	0.16	0.01	0.04	1.10
H.J	2,011 13	IGHV1-2*03	IGHJ1*01	VRC06b	45-VRC01.H03+06.B-033346 RGHCDHCYQWTLQH	03+06	03	20%	8.86	>50	>50	>50	0.004	0.02	>50	>50	>50	>50	>50
								80%	0.21	0.05	0.02	0.07	0.011	0.04	>50	0.10	0.17	0.19	>50
								30%	6.50	>50	>50	>50	0.004	0.02	>50	2.06	>50	>50	>50
H.K	1,192 22	IGHV1-2*02	IGHJ1*01	VRC06b	45-VRC01.H03+06.O-914954 RAVCDHCGNHFHQQ	03+06	01	60%	4.15	0.17	0.02	0.13	>50	32.80	>50	0.77	>50	23.30	>50
								20%	41.26	>50	>50	>50	32.70	11.20	>50	>50	>50	>50	>50
								100%	0.03	0.03	0.01	0.03	0.003	0.03	4.31	0.02	0.01	0.03	0.07
H.L	999 23	IGHV1-2*03	IGHJ1*01	VRC01	45-VRC01.H01+07.E-217618 GKNCDDNWDFEH	01+07	01	100%	0.03	0.03	0.01	0.03	0.003	0.03	4.31	0.02	0.01	0.03	0.07
								40%	2.51	>50	>50	>50	0.002	0.04	>50	0.04	0.25	>50	>50
								10%	38.08	>50	>50	>50	>50	>50	>50	>50	>50	>50	>50
H.M	935 n/a	IGHV1-2*02	IGHJ4*01	VRC01	45-H.B-049559 DGGPVFEFH	Lineage 3	01	10%	38.08	>50	>50	>50	>50	>50	>50	>50	>50	>50	>50
								No Expression											
								100%	0.03	0.02	0.01	0.02	0.001	0.02	0.71	0.01	0.001	0.03	43.60
H.N	808 18	IGHV1-2*02	IGHJ1*01	VRC06b	45-VRC01.H03+06.G-011493 KGPSCPHCGDFHWQY	03+06	01	100%	0.03	0.02	0.01	0.02	0.001	0.02	0.71	0.01	0.001	0.03	43.60
								60%	0.39	0.07	>50	>50	0.001	0.01	0.64	0.01	0.002	>50	>50
								100%	0.03	0.07	0.01	0.04	0.002	0.02	2.00	0.03	0.01	0.05	0.06
H.O	671 9	IGHV1-2*02	IGHJ1*01	VRC07b	45-VRC01.H01+07.C-120417 GKYCTARDYNNWDFEH	01+07	01	100%	0.03	0.07	0.01	0.04	0.002	0.02	2.00	0.03	0.01	0.05	0.06
								30%	6.25	>50	>50	>50	0.002	0.02	>50	3.06	>50	>50	>50
								80%	0.23	0.06	0.02	0.11	0.01	0.04	>50	0.05	0.27	0.29	>50
H.P	593 6	IGHV1-2*02	IGHJ1*01	VRC06b	45-VRC01.H03+06.O-004620 RGLCDHCGNHFHQQ	03+06	01	80%	0.23	0.06	0.02	0.11	0.01	0.04	>50	0.05	0.27	0.29	>50
								30%	5.48	>50	>50	>50	0.00	0.01	>50	0.61	>50	>50	>50
								10%	7.99	>50	2.63	>50	0.01	0.06	>50	>50	>50	>50	>50
H.Q	414 11	IGHV1-2*02	IGHJ1*01	VRC06b	45-VRC01.H03+06.A-144779 RGHCDHCDFTWLQH	03+06	01	30%	7.99	>50	2.63	>50	0.01	0.06	>50	>50	>50	>50	>50
								20%	30.31	>50	>50	>50	8.43	1.99	>50	>50	>50	>50	>50
								100%	0.06	0.03	0.01	0.11	0.02	0.03	2.03	0.08	0.01	0.08	0.05
H.R	371 0	IGHV1-2*02	IGHJ1*01	VRC06b	45-VRC01.H08.O-909912 GRSCCAGRRFCSTDCYNWDFEH	08	03	30%	9.69	>50	>50	>50	0.02	0.03	>50	>50	21.60	>50	>50

B Identification and function of light chain neutralizing groups

Vr region group	Raw & curated reads	Assigned V-gene	Assigned J-gene	Probe-identified mAb	Representative sequence & CDR L1	Light chain clade	Heavy chain pair	Breadth
-----------------	---------------------	-----------------	-----------------	----------------------	----------------------------------	-------------------	------------------	---------

not contain such a residue. We therefore used this signature cysteine to assess membership in the VRC01 lineage. Of 1,041 curated NGS sequences assigned to the VRC01 lineage, six did not contain the cysteine while 1,035 did (99.4%). By contrast, of the remaining VH1-2-derived NGS reads from this donor not assigned to the VRC01 lineage, 104,223 sequences did not have this signature cysteine, while 4,641 did (4.3%; $p < 0.0001$) (Figure S3B).

To examine the relationship among the neutralizing groups with VRC01-lineage origin genes, we calculated the full-length pairwise identities of the validated representative sequences and probe-identified antibodies. Pairwise identity matrices, grouped by similarity, are shown as heatmaps for heavy and light chains in Figures 4A and 4B, respectively. The CDR H3 and VL groups clustered into higher-order units. Critically, correspondence with maximum-likelihood phylogenetic trees (Figure 4C) confirmed that the clusters of neutralizing groups define phylogenetic clades similar to the three originally defined by the probe-isolated antibodies (Figure S4).

Known heavy- and light-chain pairings from the probe-identified antibodies were used to approximately align the heavy and light maximum-likelihood phylogenetic trees. Temporal prevalence was calculated from the number of non-redundant NGS reads assigned to each of the clades (Figure 4C, middle) (Extended Experimental Procedures). For each clade, prevalence of reads waxed and waned independently over time. For example, clades H5 and L3 remained at a fairly constant level, while clade 01+07 was more prevalent at intermediate time points, and clades H3, H4, and 08 increased in prevalence at later time points. For the three probe-identified clades (01+07, 03+06, and 08), heavy- and light-chain prevalence should correlate temporally; in practice, these correlations ranged from 0.05 to 0.91, suggesting possible sampling issues for clade 03+06. Overall, the NGS of peripheral VRC01-lineage transcripts provided a large number of sequences (Table S2B), allowing for much greater definition of VRC01-lineage diversity than was possible with the 39 probe-identified antibodies (Figure 1). Multiple branches surround and embed the original three clades in a more diverse phylogenetic tree with three additional heavy-chain clades and two additional light-chain clades (Figure 4C). The greater number of NGS sequences permitted quantification of the initial and newly identified clades over time, thus illuminating the scope, diversity, and development of the lineage.

Conservation of Antigen-Binding Mode within the 01+07 Clade of the VRC01 Lineage

The extraordinary sequence diversity of the VRC01 lineage revealed by NGS could represent possibilities ranging from significant changes in mode of antigen recognition to sequence alteration with a conserved binding mode. To delineate between these two extremes, we evaluated the longitudinal maintenance

of a previously defined set of VRC01 signature residues (Zhou et al., 2013) and the structural conservation of recognition by a clade over time. While only 60%–70% of unrelated VH1-2 sequences conserved at least eight of ten positions in the signature, nearly all sequences from four of the six heavy-chain clades did so (Figures 5A and 5B; Figure S5A). For clade 01+07, we determined co-crystal structures of an antibody from 1995 and compared these to the co-crystal structure of an antibody identified from the 2008 time point (Figures 5C–5F) (Diskin et al., 2011). For the 1995 antibody, co-crystal structures were determined with extended cores both from the autologous gp120 (from donor 45) and from a heterologous gp120. By contrast, the antibody from the 2008 time point was determined in complex only with a heterologous gp120 extended core (Figure 5E; Table S4). We calculated the root-mean-square deviations (rmsds) for the variable domains in the various crystal structures: there was a 0.38 Å rmsd on C α of the variable domains between the two 1995 antibody structures; between the 1995 structures and 2008 structure, the rmsd was 0.45 and 0.50 Å for the same gp120 and different gp120s, respectively. Epitope recognition was highly conserved between the 1995 and 2008 antibodies, which interact with a similarly sized area of gp120 (1,185 Å² and 1,166 Å² for the 1995 antibody, and 1,247 Å² for the 2008 antibody) with approximately 95% of the contact area conserved (Figure S5B). The antibody paratope was also highly similar but showed an increase in size for the 2008 antibody compared to the 1995 antibody (1,177 Å² and 1,136 Å² for the 1995 antibody, and 1,458 Å² for the 2008 antibody). This difference in the paratope was largely due to reduced inner domain and bridging sheet interactions for the 1995 antibody compared to the 2008 antibody, and the increase in recognized surface could be attributed to SHM, especially Ser74Tyr and Ser99BArg in the heavy chain.

We assessed gp120 binding of a VRC01 variant with the germline sequence in the heavy- and light-chain variable regions, but mature CDR3 regions (since the original unmutated versions of the CDR3 junctions cannot be accurately inferred). Such germline-reverted variants of VRC01-class antibodies have been reported to lack gp120 binding activity (Jardine et al., 2013; McGuire et al., 2013; Zhou et al., 2010). Nonetheless, here we show binding to the early autologous gp120 molecule, d45-01dG5 (GenBank accession number JQ609687) (Wu et al., 2012) (Figure S5C) with affinity in the micromolar range. The affinity of the VRC01 lineage for this gp120 improved to sub-nanomolar levels for the 1995 and 2008 antibodies. These later antibodies were also able to interact with many more autologous and heterologous gp120 strains. Overall, the structures indicate that the 20 changes in amino acid sequence due to SHM between 1995 and 2008 antibodies enhance antibody-antigen interactions. However, antibody recognition over the 13-year time period remains highly similar, with core interactive residues

Two groups with non-matching J gene assignments (gray rows) were excluded from further analysis. Total sequences in each group, probe-identified representative (if any), assigned V and J genes, and the most neutralizing representative and its CDR H3 sequence (left columns) are shown. Neutralization breadth and potency for both VRC01 and VRC03 light-chain pairings are provided against selected HIV-1 viruses from clades A, B, and C (right columns).

(B) The same information as shown in (A), for the most prevalent light-chain-variable region groups tested for neutralization after reconstitution with the heavy chains from VRC01 and VRC03. Group L.C., shown in gray, consisted of multiple unrelated clones and was excluded from further analysis.

See also Figure S3 and Table S3.

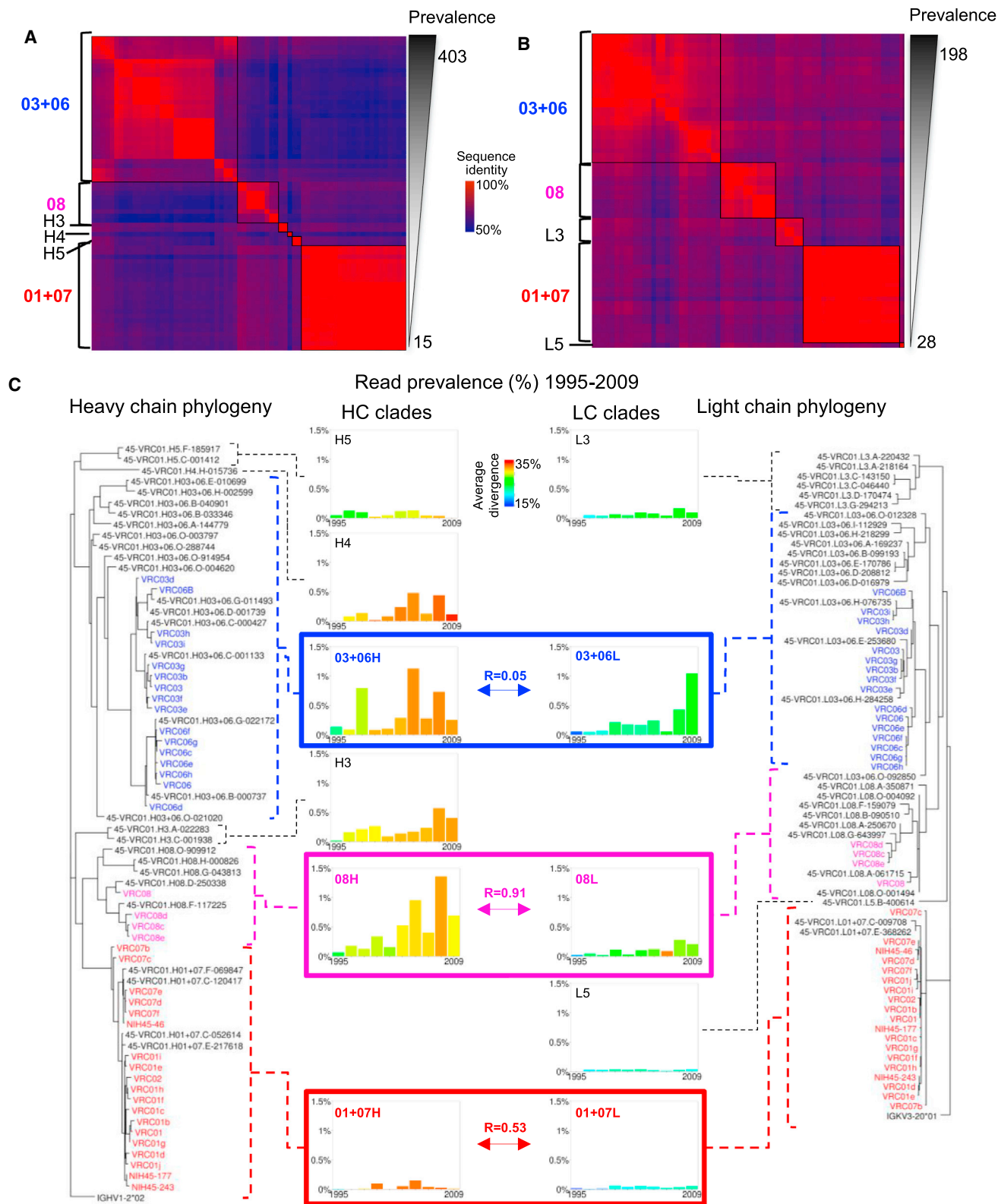


Figure 4. Heavy and Light Chain of the VRC01 Lineage Exhibit Multi-Clade Phylogenetic Organization and Concordance

(A) Heatmap showing pairwise sequence identities for heavy chains of probe-identified antibodies and validated neutralizing heavy-chain sequences sorted by overall prevalence (among final curated sequences). Groups with high identity and similar prevalences were merged into clades, shown at left.

(legend continued on next page)

mostly unchanged. Thus, despite extraordinary sequence variation, the VRC01 lineage maintains a largely conserved binding mode.

Rate of VRC01-Lineage Evolution

Since somatic variants of the VRC01 lineage derived from a common precursor B cell, it is possible to determine evolutionary rates for the maturation of the lineage as well as for each clade. To quantify the rate of lineage evolution, we used BEAST v1.8 (Drummond and Rambaut, 2007), which has been used previously to estimate evolutionary rates for sequences from various population types, including HIV (Alizon and Fraser, 2013; Vrancken et al., 2014). It is important to note that evolutionary rate is not equivalent to the increase in germline divergence, as it describes the overall rate of substitutions, not all of which result in increased germline divergence. For example, the same site can mutate multiple times, including reverting to the original nucleotide.

Over the entire time period of the study, VRC01-lineage heavy and light chains had similar evolutionary rates of 2.1 and 1.6 substitutions per 100 nucleotides per year, respectively (Figure 6A, green and blue panels). This rate of mutation was similar to the rate of 1.5 substitutions per 100 nucleotides per year that we determined for the Env gene in this donor (Figure 6A, red panel) based on previously determined viral genome sequences (Wu et al., 2012), and the rate of 1.9 substitutions per 100 nucleotides per year determined for previously reported Env sequences from donor CH505 (Liao et al., 2013). These results are also consistent with previous estimations of Env evolution rates, which have ranged from 0.69 to 1.4 substitutions per 100 nucleotides per year (Alizon and Fraser, 2013; Chaillon et al., 2012; Vrancken et al., 2014). We also calculated evolutionary rates for each clade independently (Figure 6A, green and blue panels). Although clades H4 and L3 showed rates somewhat higher than the other clades, evolutionary rates for all of the VRC01 clades were similar at approximately two substitutions per 100 nucleotides per year.

To provide an overview of the VRC01 lineage and its development, we produced maximum-likelihood phylogenetic trees with curated sequences, annotated with evolutionary rates for the VRC01-lineage clades (Figure 6B). Each sequence is colored based on its apparent “birthday”—the time point from which it was first identified in the NGS data. Importantly, advancing time (indicated by the progression of colors) and advancing maturation (indicated by branch positions) were consistent, in that later transcripts appeared at greater radial distances on the tree.

Evolutionary Rate of the VRC01 Lineage Appears to Slow

To compare the evolutionary rates of the VRC01 lineage with other broadly HIV-1-neutralizing antibody lineages, we retrieved CAP256-VRC26 (Doria-Rose et al., 2014) and CH103 (Liao et al., 2013) lineage NGS sequences from GenBank. Average germline

divergence for these lineages increased more rapidly than for the VRC01 lineage (Figure S6A). We also found an evolutionary rate of 11 and 9.3 substitutions per 100 nucleotides per year, respectively, for the CAP256-VRC26 lineage heavy and light chains, and 13 and eight substitutions per 100 nucleotides per year, respectively, for the CH103 lineage (from donor CH505) heavy and light chains (Figure 6C, purple panel). Each of these early rates was ~5-fold higher than that observed for the VRC01 lineage, which was at a much later stage in its development.

Since these rate differences in principle could arise from differences between the donors, we undertook direct rate calculations on donor 45 datasets comprising the beginning (1995–2002) and end (2006–2009) of the study period (Figure 6C, green and blue panels). For aggregate data, including all clades, the evolutionary rate was higher for the early time period than the later one (2.1 versus 1.6 substitutions per 100 nucleotides per year). Although this difference was not statistically significant, it is consistent with the hypothesis that antibody SHM occurs at a faster rate during the early phase of lineage development. Similarly, when data from each clade were considered separately, the calculated rate was in all cases higher for the early time period than the later one, further supporting the idea that evolutionary rates slowed over time.

As a third test for the slowing of evolutionary rates, we used the BEAST package to infer the date of the most recent common ancestor sequence for each lineage. If evolutionary rate were stable over time, we would expect this extrapolation to give a reasonable estimate (Smith et al., 2009). For the VRC01 lineage, the most recent common ancestor was estimated to have occurred for heavy chain in 1971 and for light chain in 1979 (Figure S6B). Although the exact date at which donor 45 was infected is unknown, the inferred dates are implausible, as the AIDS epidemic began in the early 1980s. Similarly, the most recent common ancestor of the CAP256-VRC26 lineage was calculated to have occurred in early 2005 (Figure S6C), although the UCA of that lineage is known to have appeared sometime in March 2006 (Doria-Rose et al., 2014). The same inconsistency is also observed for the CH103 lineage (Liao et al., 2013) (Figure S6D). The consistent prediction of common ancestors at impossibly or implausibly early dates suggests that the evolutionary rate was faster earlier in lineage development. The fact that this was observed for the younger CAP256-VRC26 and CH103 lineages, as well, implies that this slowing begins almost immediately.

Thus, three distinct lines of evidence support the idea that SHM persists over an extended period of time, but evolutionary rate slows as an antibody lineage matures. Overall, clades within the VRC01 lineage had similar evolutionary rates. Rates for other lineages are not similar and varied over at least a factor of 5 between fast-early and slower-late lineage development. Studies

(B) Heatmap for light chains of probe-identified antibodies and validated neutralizing light-chain sequences, produced as in (A).

(C) Maximum-likelihood phylogenetic trees for heavy-chain (left) and light-chain (right) sequences. The clades described in (A) and (B) can be clearly seen in the structure of the trees, which have similar overall topology. Temporal prevalence (middle) is charted for each clade as the fraction of unique sequences with an in-frame junction and no stop codons (but without manual curation) at each time point, which are assigned to that clade. For clades 01+07, 03+06, and 08, which are anchored by probe-identified antibodies, the correlation of heavy- and light-chain temporal prevalence is shown (boxes). The average divergence for each clade at each time point is calculated from curated sequences.

See also Figure S4.

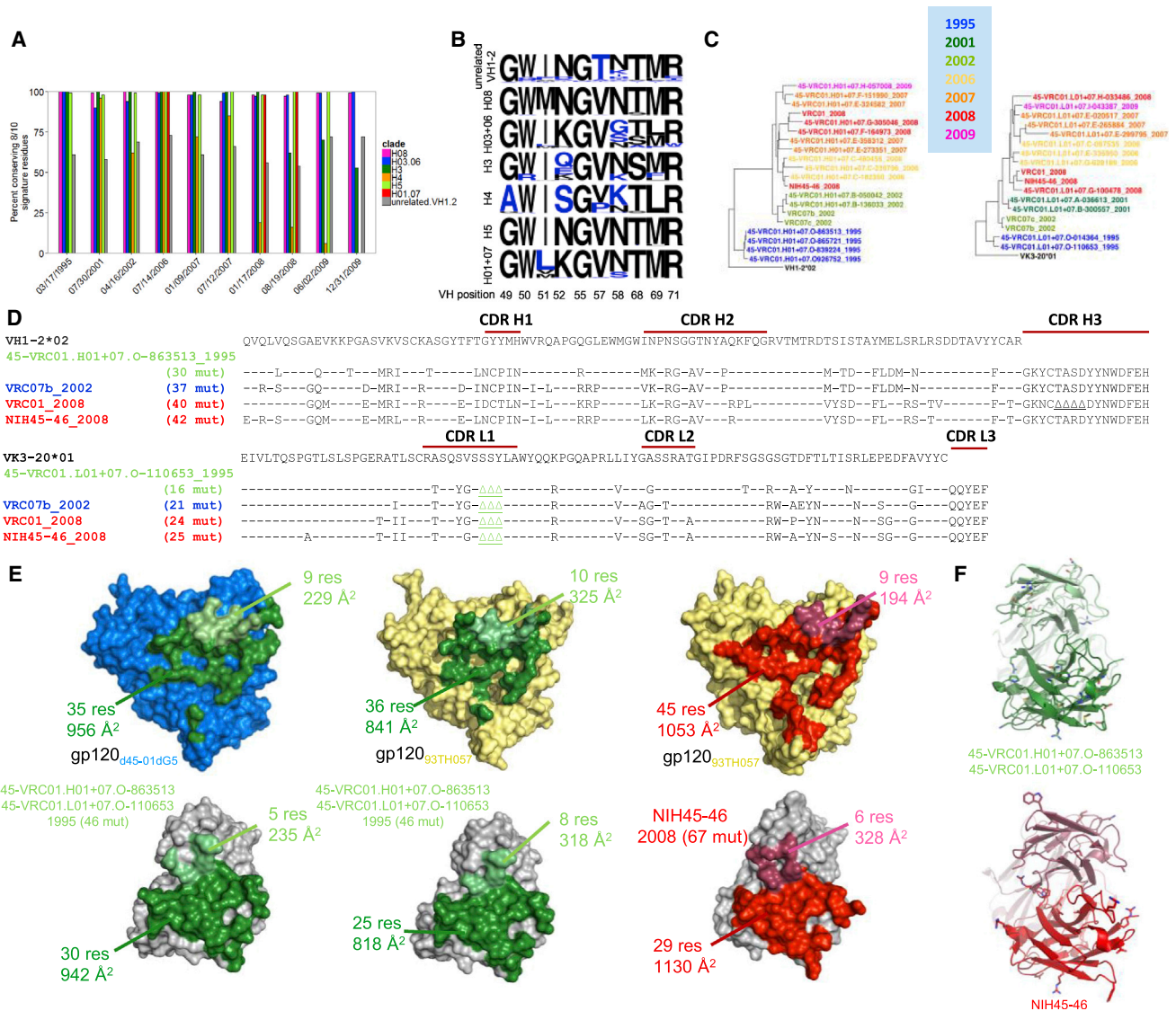


Figure 5. Conservation of VRC01+07 Clade Recognition over 15 Years of Chronic Maturation

(A) Percentage of curated sequences in each clade conserving at least eight of the ten-residue heavy-chain signature amino acids of VRC01-class antibodies. Bars are not shown where data were unavailable for a particular clade and time point. Nearly all sequences in four of six heavy-chain clades conserve at least eight of the ten positions, compared to only 60%–70% of unrelated VH1.2-derived sequences (gray bars). Clades H3 (dark green) and H4 (orange) mutate away from the signature over the course of the study.

(B) Sequence logos of the VRC01 class signature positions for each clade. Residues colored in blue do not match the defined signature. Note, nine of the ten signature residues are contained in the VH1.2 germline. Thus, although in the non-VRC01-lineage sequences the dominant residue at each position matches the signature, there is variation at almost every position, and any individual read is likely to have more than two residues mutated (A). For VRC01 sequences, by contrast, there is strong conservation at any given position (even those that are mutated away from the signature), and relatively few positions have any variation at all.

(C) Longitudinal phylogenetic trees of clade 01+07 sequences for heavy chain (left) and light chain (right). The color of each sequence corresponds to the date at which it is first identified in the NGS data.

(D) Sequence alignment of heavy-chain (top) and light-chain (bottom) sequences from temporally diverse members of the 01+07 clade showing mutation from the germline V gene.

(E) Crystal structures of autologous (blue, top left) or heterologous (pale yellow, top middle and top right) gp120s determined in complex with clade 01+07 antibodies (bottom). The complexes have been rotated to show the interacting surfaces on each molecule. Contacts made by 45-VRC01.H01+07.O-863513/45-VRC01.L01+07.O-110653 (NGS-derived sequences from 1995, bottom left and bottom middle) are colored in green, while those made by NIH45-46 (isolated from 2008, bottom right) are shown in red. Heavy-chain contacts are in the darker shade. These structures show a common binding mode, with a modest increase in buried surface area from the 1995 to the 2008 antibodies when bound to heterologous gp120.

(F) Antibody structures from (E) shown in ribbon format, with residues mutated from the germline V gene (top) or the 1995 sequence (bottom) shown in stick representation.

See also Figure S5 and Table S4.

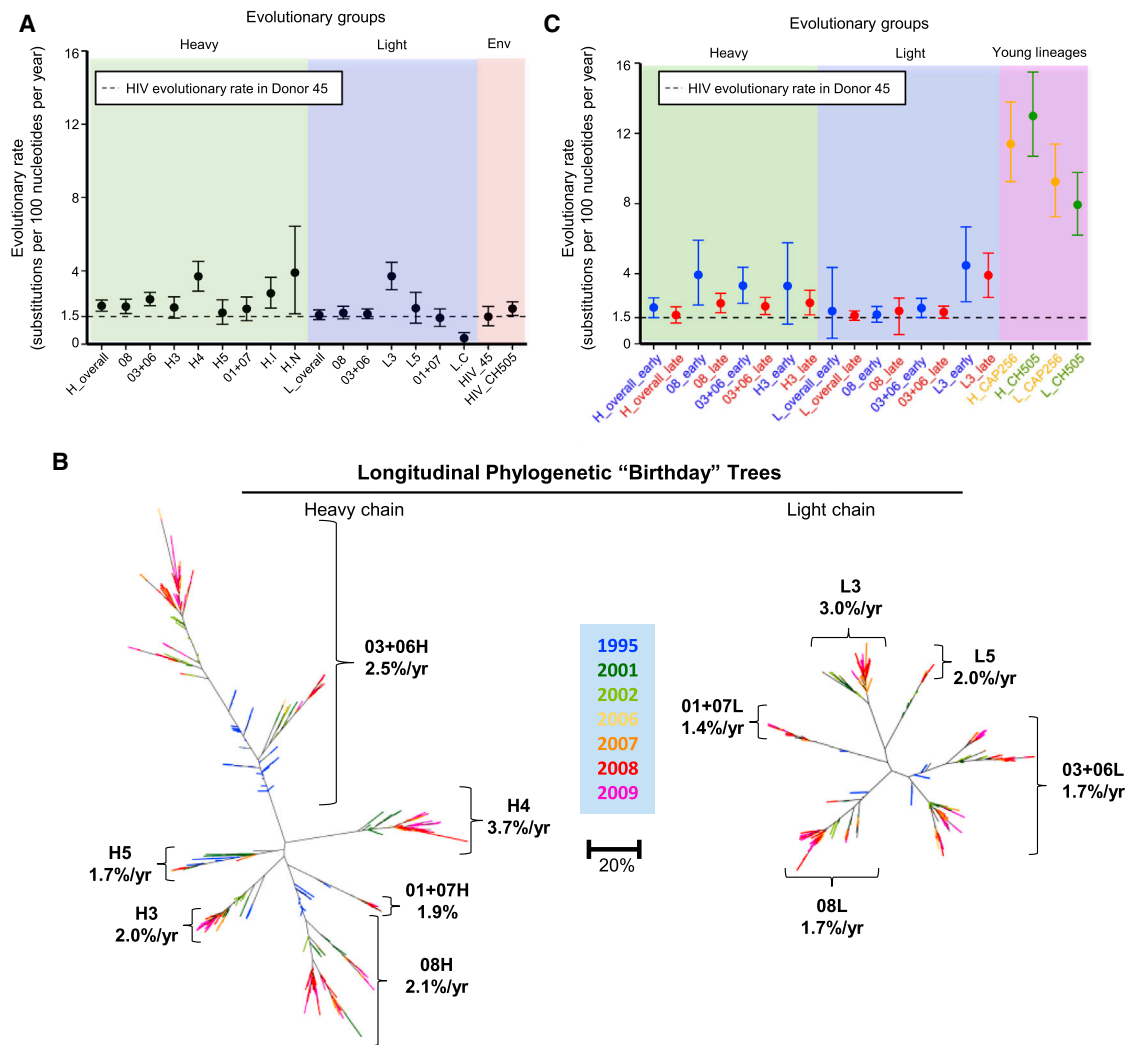


Figure 6. Rates of Evolution and Extents of Divergence for Clades of the VRC01 Lineage over 15 Years of Chronic Infection

(A) Point estimates and 95% highest probability density of evolutionary rates for heavy- (green panel) and light-chain (blue panel) transcripts of the VRC01 lineage, shown for the lineage overall and individual clades, calculated from subsets of the curated sequence set. Dashed line represents the rate calculated for HIV-1 Env in donor 45. Evolutionary rates for Env for HIV genomes isolated from both donor 45 and donor CH505 (red panel) are comparable to the evolutionary rate of the VRC01 lineage, calculated from deposited sequences for those datasets.

(B) Heavy- (left) and light-chain (right) phylogenetic trees for curated sequences from the VRC01 lineage annotated to show point estimates of evolutionary rate for each clade. Trees are shown as “birthday” trees, with each sequence colored to show the time point at which it was first observed. Later observation times (warmer colors) and greater maturation (larger radial distances) were consistent.

(C) Point estimates and 95% confidence intervals of evolutionary rate for VRC01 lineage transcripts calculated separately for the beginning (1995–2002) and end (2006–2009) of the study period (green and blue panels). Sequences used are subsets of those described for (A). In each case, the earlier rate is faster than the later one, though the differences do not reach statistical significance. For comparison, evolutionary rates of early HIV-1-neutralizing antibody lineages from donors CH505 and CAP256 (purple panel) are ~5-fold higher, as calculated from deposited sequences of those. Additionally estimation of least common ancestors for each lineage are consistently earlier than known or plausible dates (Figure S6), suggesting that evolutionary rates were faster earlier in the history of each lineage.

See also Figure S6.

of the early lineages CAP256-VRC26 and CH103 suggested that this slowing begins very early in lineage development.

VRC01-Lineage Recognition: Epitope Variation, Disulfide Patterns, and Probed Surfaces

The continuous mutation observed over years of chronic infection provides a means to achieve the extraordinary levels

of SHM observed with many of the anti-HIV-1 broadly neutralizing antibodies. For the VRC01 lineage, this divergence reaches over 30% for individual lineage members relative to the germline genes, although the variance between individual members of the lineage is considerably greater, with multiple clades evolving in a multiplexed manner (Figure 6B).

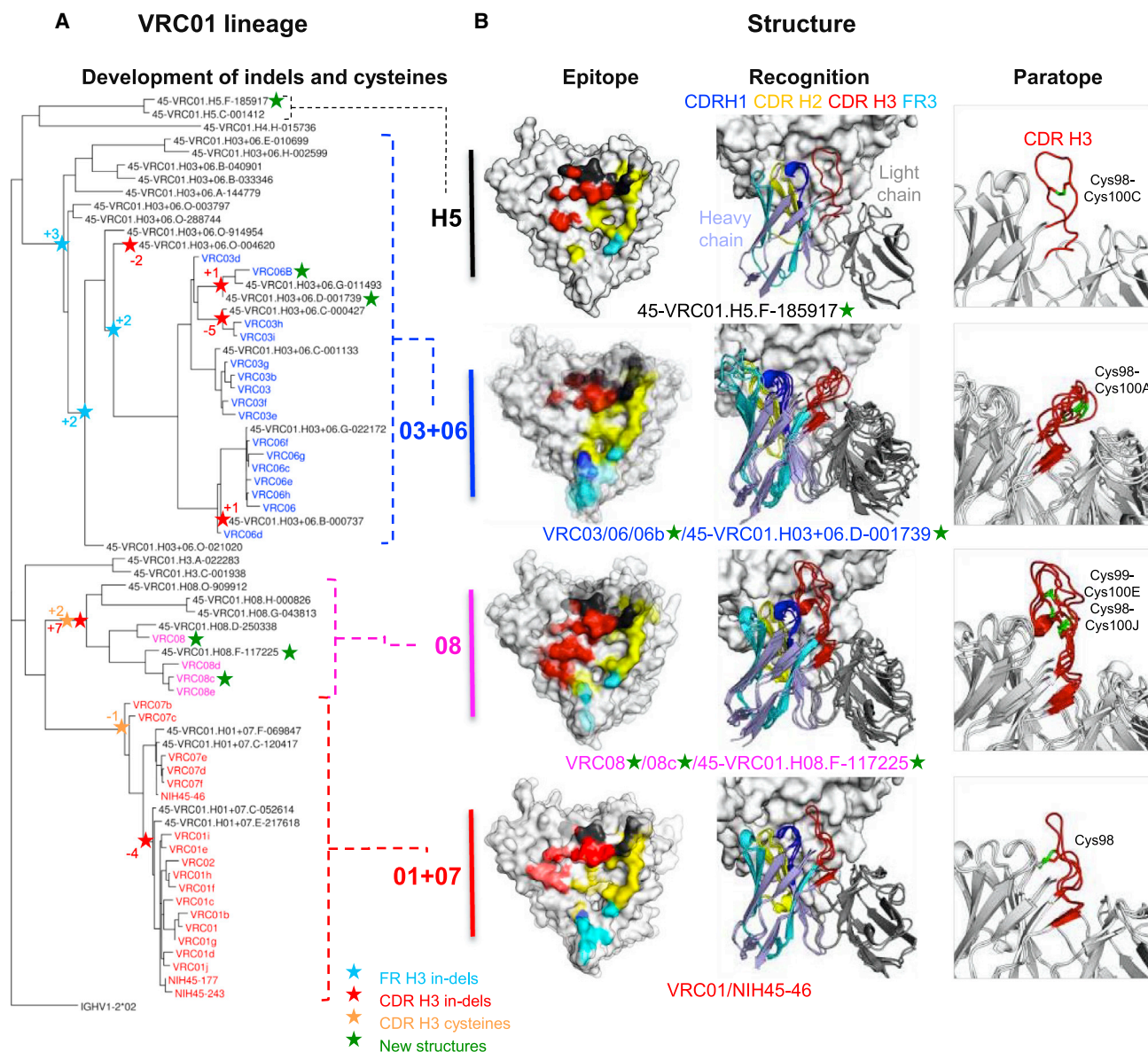


Figure 7. The VRC01 Lineage Evolves Divergent Recognition Loops and CDR H3 Disulfides

(A) Heavy-chain phylogenetic tree for probe-identified antibodies and validated neutralizing sequences of the VRC01 lineage annotated for the acquisition of molecular features.

(B) Epitope, recognition, and paratope for representative VRC01 clades. Structures of VRC01-lineage antibodies in complex with gp120 are shown with CDR H1 in blue, CDR H2 in yellow, CDR H3 in red, FR3 in cyan, and light chain in dark gray. These are displayed on the gp120 surface for epitope (left column), as colored regions of a ribbon diagram for recognition (middle column), and the CDR H3 and associated cysteines are highlighted in paratope (right column). For clade H5 (top row), the NGS-identified heavy chain 45-VRC01.H5.F-185917 paired with the light chain from VRC01 is shown. NGS-derived heavy chains in clades 03+06 and 08 were paired with VRC03 and VRC08 light chains, respectively.

See also Figure S7 and Table S5.

Several of the newly identified VRC01-lineage clades showed remarkable differences. For example, the VRC08 CDR H3 is 11 residues longer than that of VRC01 and contains three additional cysteines. To understand the variation of structural recognition of VRC01-lineage antibodies between different clades, we crystallized the antigen-binding fragments (Fabs) of representative antibodies from each clade in complex with HIV-1 gp120. Repre-

sentative antibodies were chosen based on their expression level (>5 mg/l), neutralization potency (Figure 3), and phylogenetic placement (Figure 7A). From a total of ten antibodies, six formed crystals with extended core gp120, which diffracted beyond 3.5 Å; structures of these were solved by molecular replacement, and structural features of their recognition were analyzed.

New structures included two from the 03+06 heavy-chain clade (VRC06b and 45-VRC01.H03+06.D-001739; for NGS-defined antibodies we use the nomenclature “donor-lineage.[H/L]clade.time-point.read_number” for heavy and light chains), three from the 08 heavy-chain clade (VRC08, VRC08c, and 45-VRC01.H08.F-117225), and one from the H5 heavy-chain clade (45-VRC01.H5.F-185917). We analyzed these structures along with previously determined antibody-gp120 structures from donor 45 comprising those of VRC01, VRC03, NIH45-46, and VRC06 (Diskin et al., 2011; Georgiev et al., 2013; Wu et al., 2011; Zhou et al., 2010). When gp120s were superimposed, modes of gp120 recognition by the variable domains of the donor 45 antibodies resembled each other, with the consensus/shared framework region of heavy chains (rmsds = 0.46–2.41 Å) (Table S5) showing moderately greater diversity than that of light-chain-variable domains (rmsds = 0.36–1.65 Å) (Table S5). While intra-donor differences between common/consensus framework regions were not significantly different from the inter-donor differences for VRC01-class antibodies from different donors, two antibody heavy-chain regions showed substantial clade diversity: the CDR H3 and the heavy-chain-framework region 3 (FR3) (Figure 7B). The clade 08 CDR H3 loop (23 amino acids) extends toward the inner domain of gp120 and contributes ~35% and ~70% more binding surfaces on gp120 than CDR H3 loops of 01+07 and 03+06 clades, respectively (Figure 7B; Table S5). Unlike the CDR H3 of clade 08, the CDR H3s of clade 03+06 and clade H5 make substantially less contact with the inner domain of gp120 (~130 Å² for clade 03+06, ~200 Å² for clade H5, and ~450 Å² for clade 08). Meanwhile, clade 03+06 antibodies are unique among antibodies of the lineage for their extended FR3s, the result of a seven amino acid insertion. These extended FR3s provide ~1.5-, ~2.5-, and ~4.5-fold more binding surface on gp120 V1/V2 stem region than FR3s of clades 01+07, 08, and H5, respectively (Table S5), and induce conformation of the V1/V2 region different from that of other antibody-gp120 structures (Figure S7A). Because antibody-Env complexes determined here were in the monomeric gp120 core context, we docked antibodies in the recently determined structure of trimeric BG505 SOSIP (Julien et al., 2013; Lyumkis et al., 2013; Pancera et al., 2014). The extended FR3s were spatially proximal in the trimeric context to V1/V2 (residues 203–206) and V3 (residues 314–318) of the neighboring protomer (Figure S7B). Small rearrangements could potentially allow for energetically favorable contact, with positive V3 interacting electrostatically with negatively charged FR3 insertions. In terms of the large CDR H3 alterations, these projected onto the inner domain and did not interact with neighboring protomers. However, the CDR H3 of VRC08c makes potential contacts with helix- α 0 of the neighboring gp120 (Figure S7C).

Notably, the disulfide bonding patterns in the CDR H3 loops vary between clades (Figure 7B). 01+07 clades have an interloop disulfide bond between Cys98 (CDR H3) and Cys32 (CDR H1). Clade 03+06 and clade H5 have a single disulfide bond between Cys98 and Cys100A, Cys98 and Cys100C, respectively. Clade 08 has two pairs of intra disulfide bonds (Cys98-Cys100J and Cys99-Cys100E) within the CDR H3 loop, which likely adds structural rigidity to this CDR H3, which is approximately ten residues longer than observed in most of the other clades.

Although CDR H3 cysteine diversity has been observed before with bovine antibodies (Wang et al., 2013), the bovine mechanism depends on specific D genes optimized for cysteine pairing, whereas, in the present case, cysteine diversity derives from SHM within a single lineage.

To investigate the functional consequences of the clade diversity, we analyzed neutralization fingerprints for a representative selection of VRC01-lineage antibodies. Remarkably, a dendrogram built to represent the neutralization (functional) features mirrors dendrograms based on sequence phylogeny, and, in particular, replicated the overall clade structure (Figure S7D). Thus, the diverse clades do have functional differences that reflect their divergent sequences and the clade organization.

Despite originating from a single ancestor B cell, different clades of the VRC01 lineage have evolved substantial differences in disulfide-bonding patterns and sequence lengths for some of their antigen-binding loops. The CDR H2—the central contact surface of the antibody lineage with gp120—does not vary in this manner, nor do other loops of the variable domains. The peripheral role of both the CDR H3 and the FR3 region in gp120 recognition may allow for extraordinary variation as different antibody variants evolve to probe the gp120 surface in distinctive ways.

DISCUSSION

It has been unclear how antibody lineages achieve the unusually high levels of mutation commonly found for broadly HIV-1-neutralizing antibodies. This led us to investigate the evolutionary history of B cell lineages that produce such antibodies. SHM and B cell selection are a form of “accelerated evolution” that generates high-affinity antibodies. In most cases, this process takes a few weeks and involves only a handful of mutations, averaging about 5% nucleotide difference from the originating antibody genes. However, some broadly HIV-1-neutralizing antibodies are characterized by extraordinary levels of SHM where >30% of nucleotides in the antibody variable region differ from the germline-encoded sequence (Burton et al., 2012; Kwong and Mascola, 2012; Mascola and Haynes, 2013). One such antibody, VRC01 (Wu et al., 2010), was isolated approximately two decades after the donor was diagnosed with HIV-1 infection. Here, we used antibody isolation, NGS, and crystal structures to characterize the VRC01 lineage from 1995–2009. We observed extraordinary diversity, a result of a high rate of SHM over years of chronic infection. Of note, several prior studies indicated germline-reverted variants of VRC01-class antibodies not to bind HIV-1 gp120, raising the question of how they arise (Jardine et al., 2013; McGuire et al., 2013; Zhou et al., 2010); our results indicate germline-reverted VRC01 to bind an early autologous Env (d45-01dG5) (Wu et al., 2012), suggesting the VRC01 lineage to have been initiated by interaction with a specific autologous Env sequence (Figure S5C).

The NGS-derived sequences determined here are expected to contain errors arising from cDNA preparation, PCR amplification, and 454 sequencing platform. We used the 454 pyrosequencing platform because its read lengths allowed identification of full variable region sequences. Unfortunately, the

sequencing reactions were error prone. We implemented quality-control procedures to reduce errors ([Extended Experimental Procedures](#)) and to parse the NGS-derived data into three levels of experimental certainty. First, “raw” VRC01-lineage sequences, from all ten time points, comprise 124,834 heavy-chain and 28,500 light-chain sequences. Based on prior published data, these sequences are expected to have an RMS error in sequence of 1.38% ([Zhu et al., 2012](#)). Second, “curated” sequences comprise 1,041 heavy- and 492 light-chain sequences, and, of these, 162 heavy-chain and 119 light-chain sequences were observed to have biological replicates at the 97.25% level in other time points. Third, “confirmed neutralizers” comprise the closest to consensus or most highly represented sequences, and these are expected to have median accuracy in sequence of 98.9% identity based on the accuracy of VRC01-class plasmids ([Extended Experimental Procedures](#)). Additionally, 36% of the confirmed neutralizing sequences had temporal biological replicates at >97.25% identity. Finally, we note that evolutionary rate calculations were performed with curated sequences, and the results were similar over multiple bootstraps, suggesting that these calculated rates were not substantially affected by NGS-sequence errors. Thus, the “leaves” of the VRC01-lineage phylogenetic tree and raw data ([Figure 2](#)) contain substantial uncertainty, while the overall clade structure ([Figures 4 and 7](#)) (which is defined by the confirmed neutralizers and probe-identified antibodies and consists of clades that differ on average by 40%–50% in sequence) and overall rate of evolution ([Figure 6](#)) should not be substantially affected by errors in the NGS data.

Despite the substantial differences between clades of the VRC01 lineage, their average divergences were similar at each time point, and they also showed similar evolutionary rates ([Figure 6A](#)). Antibody lineages unrelated to the VRC01 lineage, however, showed substantially different evolutionary rates. Thus, each member of a lineage appeared to share common rate characteristics. Notably, this rate does not appear to be influenced by the differing neutralization of the individual clades on autologous virus ([Wu et al., 2012](#)), as might be expected from the co-evolution of virus and neutralizing antibody ([Richman et al., 2003; Wei et al., 2003](#)). These findings suggest that the criteria for continued maturation may be less stringent than the criteria for effective neutralization and that the rate of antibody evolution may depend on the number of cell divisions from the single originating common ancestor B cell.

Our data suggest that the evolutionary rate of an antibody lineage slows as it matures. Importantly, even the lowest rates of antibody evolution that we observed were comparable to the evolutionary rate of HIV-1 Env. For the 01+07 clade, heavy chains had already mutated to 20% divergence at the earliest study time point, and we observed continuous SHM to >30% at the end study point ([Figure S6A](#)). Likewise, the levels of SHM for other heavy-chain and light-chain clades of the lineage also increased over time, despite high initial divergence. These data suggest that SHM may continue for as long as antigen persists in long-term chronic infection. The rapid evolutionary rates described here, combined with persistent antigen due to chronic infection over years, provide a mechanism to explain how antibodies can develop the high levels of SHM

and lineage diversity required for broad and potent neutralization of HIV-1.

Previously described antibodies from the VRC01 lineage of donor 45 were diverse enough that they appeared to represent several separate lineages ([Wu et al., 2010, 2011](#)). Here, we show that the diversity of the VRC01 lineage extends far beyond what has generally been thought possible, comprising at least six distinct heavy-chain clades and five light-chain clades. The curated deep-sequencing data fill in details of this clade structure, without deviating from the outlines provided by functionally validated sequences and antibodies ([Figure S7E](#)). Each clade had distinctive sequence and structure characteristics. CDR H3 length within the lineage ranged from 9 to 23 residues, and CDR H3 cysteines ranged from a single cysteine, which formed an interloop disulfide with another CDR, to four cysteines, which formed two intraloop disulfides ([Figure 7B](#)). This diversity and its continued evolution present a picture of antibody immunity in which extraordinary variation within just a few antibody lineages—or even a single lineage—may be of critical importance for opposing HIV-1.

EXPERIMENTAL PROCEDURES

Human Specimens

Recovery of PBMCs from donor 45 ([Li et al., 2007; Wu et al., 2010](#)) has been described previously. Donor 45 samples from different time points were collected with informed consent under clinical protocols approved by the appropriate institutional review board (IRB).

Isolation of Donor 45 Antibodies

Fluorescence-activated cell sorting of antigen-specific IgG⁺ B cells from donor 45 PBMC and the amplification and cloning of immunoglobulin genes were carried out using previously described protocols ([Wu et al., 2010](#)).

Expression and Purification of Antibodies and Fab Fragments

Expression plasmids for heavy and kappa chains were constructed as described previously ([Zhou et al., 2010](#)). The expression and purification of antibody IgGs and preparation of Fab fragments were carried out as described in [Extended Experimental Procedures](#).

Neutralization Assessment

Neutralization of donor 45 antibodies were measured using single-round-of-infection HIV-1 Env pseudoviruses and TZM-bl target cells using protocols described in [Extended Experimental Procedures](#).

Crystallization, X-Ray Data Collection, Structure Determination, and Refinement of Donor 45 Antibodies in Complex with HIV-1 gp120

Purification, crystallization of antibody-gp120 complexes, and data collection are described in [Extended Experimental Procedures](#). All diffraction data were integrated and scaled with the HKL2000 suite ([Otwinowski and Minor, 1997](#)). Structure solution, refinement, and analysis are described in [Extended Experimental Procedures](#).

454 Pyrosequencing

454 pyrosequencing libraries from donor 45 were prepared and 454 pyrosequencing of the PCR products were performed with modifications to those described previously ([Wu et al., 2011](#)) and in [Extended Experimental Procedures](#).

Bioinformatics Analysis

Bioinformatics analyses of the longitudinal 454 data were performed using algorithms similar to those described previously ([Zhu et al., 2013](#)), implemented

in a new Python code base. Data-quality filtering and other new bioinformatics methods are described in [Extended Experimental Procedures](#).

ACCESSION NUMBERS

Coordinates and structure factors for the eight antibody-HIV-1 gp120 complex structures have been deposited in the Protein Data Bank with accession numbers 4XVS, 4XVT, 4S1Q, 4S1R, 4S1S, 4XNZ, 4XMP, and 4XNY. Raw 454 data have been deposited in the NCBI Short Reads Archive with accession number SRP052625. In addition, 1,041 curated heavy-chain sequences (accession numbers KP840719–KP841751), 33 functionally validated NGS-derived heavy-chain sequences (accession numbers KP840592–KP840624), 492 curated light-chain sequences (accession numbers KP841752–KP842237), 32 functionally validated NGS-derived light-chain sequences (accession numbers KP840625–KP840656), and 31 new probe-identified antibodies with both heavy- and light-chain sequences (accession numbers KP840657–KP840687 and KP840688–KP840718, respectively) have been deposited in GenBank.

SUPPLEMENTAL INFORMATION

Supplemental Information includes Extended Experimental Procedures, seven figures, and five tables and can be found with this article online at <http://dx.doi.org/10.1016/j.cell.2015.03.004>.

CONSORTIA

The NISC Comparative Sequencing Program includes Betty Benjamin, Robert Blakesley, Gerry Bouffard, Shelise Brooks, Holly Coleman, Mila Dekhtyar, Michael Gregory, Xiaobin Guan, Jyoti Gupta, Joel Han, April Hargrove, Shiling Ho, Richelle Legaspi, Quino Maduro, Cathy Masiello, Baishali Maskeri, Jenny McDowell, Casandra Montemayor, James Mullikin, Morgan Park, Nancy Riebow, Karen Schandler, Brian Schmidt, Christina Sison, Mal Stantripop, James Thomas, Pam Thomas, Meg Vemulapalli, and Alice Young.

AUTHOR CONTRIBUTIONS

X.W., Z.Z., C.A.S., M.G.J., Y.D.K., T.Z., Z.S., P.D.K., J.R.M., and L.S. designed research, analyzed data, and wrote and edited the paper. X.W. isolated and characterized antibodies, prepared samples for 454 pyrosequencing, and performed functional characterization. Z.Z. and C.A.S. designed and carried out bioinformatics analyses. M.G.J., Y.D.K., and T.Z. determined and analyzed structures of VRC01-lineage antibodies with gp120. Z.S. performed the evolutionary rate analysis. B.Z. produced recombinant antibodies and gp120 core proteins. S.O., K.M., and R.T.B. performed neutralization assays. I.S.G. conducted computational analyses of neutralization fingerprinting, and G.-Y.C. conducted statistical analyses of lineage membership. C.S. and N.S.L. contributed additional bioinformatics analyses. R.M.L. tested germline reverted antibody variants. K.O.S. isolated antibodies, S.S. assisted with crystallization, Y.Y. expressed proteins for crystallization, R.T.B. and M.K.L. defined neutralization on 195-isolate panel, J.C.M. and NISC performed next-generation sequencing and bioinformatics analysis, and M.C. contributed donor 45 samples.

ACKNOWLEDGMENTS

We thank E. Turk and C.-L. Lin for technical assistance with large neutralization panels. We thank members of the Structural Biology Section, Structural Bioinformatics Core Section, and Humoral Immunology Core Section, Vaccine Research Center (VRC), NIAID, NIH, for comments and suggestions on the manuscript. We thank J. Baalwa, D. Ellenberger, F. Gao, B. Hahn, K. Hong, J. Kim, F. McCutchan, D. Montefiori, L. Morris, J. Overbaugh, E. Sanders-Buell, G. Shaw, R. Swanstrom, M. Thomson, S. Tovanabutra, C. Williamson, and L. Zhang for contributing the HIV-1 Envelope plasmids used in our neutralization panel. The sequences of NIH45-177 and NIH45-243 were kindly provided by J. Scheid and M. Nussenzweig. We thank F. Alt for helpful discus-

sions on antibody lineage development and rates. Support for this work was provided by the Intramural Research Program of the VRC and the NHGRI and by NIH grant P01-AI104722. Use of sector 22 at the Advanced Photon Source was supported by the US Department of Energy, Basic Energy Sciences, Office of Science, under contract number W-31-109-Eng-38.

Received: September 12, 2014

Revised: December 1, 2014

Accepted: February 9, 2015

Published: April 9, 2015

REFERENCES

- Albert, J., Abrahamsson, B., Nagy, K., Aurelius, E., Gaines, H., Nyström, G., and Fenyö, E.M. (1990). Rapid development of isolate-specific neutralizing antibodies after primary HIV-1 infection and consequent emergence of virus variants which resist neutralization by autologous sera. *AIDS* 4, 107–112.
- Alizon, S., and Fraser, C. (2013). Within-host and between-host evolutionary rates across the HIV-1 genome. *Retrovirology* 10, 49.
- Bonsignori, M., Montefiori, D.C., Wu, X., Chen, X., Hwang, K.K., Tsao, C.Y., Kozink, D.M., Parks, R.J., Tomaras, G.D., Crump, J.A., et al. (2012). Two distinct broadly neutralizing antibody specificities of different clonal lineages in a single HIV-1-infected donor: implications for vaccine design. *J. Virol.* 86, 4688–4692.
- Burton, D.R., Pyati, J., Koduri, R., Sharp, S.J., Thornton, G.B., Parren, P.W., Sawyer, L.S., Hendry, R.M., Dunlop, N., Nara, P.L., et al. (1994). Efficient neutralization of primary isolates of HIV-1 by a recombinant human monoclonal antibody. *Science* 266, 1024–1027.
- Burton, D.R., Stanfield, R.L., and Wilson, I.A. (2005). Antibody vs. HIV in a clash of evolutionary titans. *Proc. Natl. Acad. Sci. USA* 102, 14943–14948.
- Burton, D.R., Poignard, P., Stanfield, R.L., and Wilson, I.A. (2012). Broadly neutralizing antibodies present new prospects to counter highly antigenically diverse viruses. *Science* 337, 183–186.
- Calarese, D.A., Scanlan, C.N., Zwick, M.B., Deechongkit, S., Mimura, Y., Kunert, R., Zhu, P., Wormald, M.R., Stanfield, R.L., Roux, K.H., et al. (2003). Antibody domain exchange is an immunological solution to carbohydrate cluster recognition. *Science* 300, 2065–2071.
- Chaillon, A., Braibant, M., Hué, S., Bencharif, S., Enard, D., Moreau, A., Samri, A., Agut, H., and Barin, F. (2012). Human immunodeficiency virus type-1 (HIV-1) continues to evolve in presence of broadly neutralizing antibodies more than ten years after infection. *PLoS ONE* 7, e44163.
- Diskin, R., Scheid, J.F., Marcovecchio, P.M., West, A.P., Jr., Klein, F., Gao, H., Gnanapragasam, P.N., Abadir, A., Seaman, M.S., Nussenzweig, M.C., and Bjorkman, P.J. (2011). Increasing the potency and breadth of an HIV antibody by using structure-based rational design. *Science* 334, 1289–1293.
- Doria-Rose, N.A., Schramm, C.A., Gorman, J., Moore, P.L., Bhiman, J.N., DeKosky, B.J., Erandes, M.J., Georgiev, I.S., Kim, H.J., Pancera, M., et al.; NISC Comparative Sequencing Program (2014). Developmental pathway for potent V1V2-directed HIV-neutralizing antibodies. *Nature* 509, 55–62.
- Drummond, A.J., and Rambaut, A. (2007). BEAST: Bayesian evolutionary analysis by sampling trees. *BMC Evol. Biol.* 7, 214.
- Georgiev, I.S., Doria-Rose, N.A., Zhou, T., Kwon, Y.D., Staupe, R.P., Moquin, S., Chuang, G.Y., Louder, M.K., Schmidt, S.D., Altae-Tran, H.R., et al. (2013). Delineating antibody recognition in polyclonal sera from patterns of HIV-1 isolate neutralization. *Science* 340, 751–756.
- Gray, E.S., Madiga, M.C., Hermanus, T., Moore, P.L., Wibmer, C.K., Tumba, N.L., Werner, L., Mlisana, K., Sibeko, S., Williamson, C., et al.; CAPRISA002 Study Team (2011). The neutralization breadth of HIV-1 develops incrementally over four years and is associated with CD4+ T cell decline and high viral load during acute infection. *J. Virol.* 85, 4828–4840.
- Haynes, B.F., Fleming, J., St Clair, E.W., Katinger, H., Stiegler, G., Kunert, R., Robinson, J., Searce, R.M., Plonk, K., Staats, H.F., et al. (2005). Cardiophilic autophagy in two broadly neutralizing HIV-1 antibodies. *Science* 308, 1906–1908.

- Hraber, P., Seaman, M.S., Bailer, R.T., Mascola, J.R., Montefiori, D.C., and Korber, B.T. (2014). Prevalence of broadly neutralizing antibody responses during chronic HIV-1 infection. *AIDS* 28, 163–169.
- Huang, C.C., Venturi, M., Majeed, S., Moore, M.J., Phogat, S., Zhang, M.Y., Dimitrov, D.S., Hendrickson, W.A., Robinson, J., Sodroski, J., et al. (2004). Structural basis of tyrosine sulfation and VH-gene usage in antibodies that recognize the HIV type 1 coreceptor-binding site on gp120. *Proc. Natl. Acad. Sci. USA* 101, 2706–2711.
- Jardine, J., Julien, J.P., Menis, S., Ota, T., Kalyuzhnyi, O., McGuire, A., Sok, D., Huang, P.S., MacPherson, S., Jones, M., et al. (2013). Rational HIV immunogen design to target specific germline B cell receptors. *Science* 340, 711–716.
- Joyce, M.G., Kanekiyo, M., Xu, L., Bertiumpfel, C., Boyington, J.C., Moquin, S., Shi, W., Wu, X., Yang, Y., Yang, Z.Y., et al. (2013). Outer domain of HIV-1 gp120: antigenic optimization, structural malleability, and crystal structure with antibody VRC-PG04. *J. Virol.* 87, 2294–2306.
- Julien, J.P., Cupo, A., Sok, D., Stanfield, R.L., Lyumkis, D., Deller, M.C., Klasse, P.J., Burton, D.R., Sanders, R.W., Moore, J.P., et al. (2013). Crystal structure of a soluble cleaved HIV-1 envelope trimer. *Science* 342, 1477–1483.
- Klein, F., Diskin, R., Scheid, J.F., Gaebler, C., Mouquet, H., Georgiev, I.S., Pancera, M., Zhou, T., Incesu, R.B., Fu, B.Z., et al. (2013). Somatic mutations of the immunoglobulin framework are generally required for broad and potent HIV-1 neutralization. *Cell* 153, 126–138.
- Kwong, P.D., and Mascola, J.R. (2012). Human antibodies that neutralize HIV-1: identification, structures, and B cell ontogenies. *Immunity* 37, 412–425.
- Li, Y., Migueles, S.A., Welcher, B., Sveha, K., Phogat, A., Louder, M.K., Wu, X., Shaw, G.M., Connors, M., Wyatt, R.T., and Mascola, J.R. (2007). Broad HIV-1 neutralization mediated by CD4-binding site antibodies. *Nat. Med.* 13, 1032–1034.
- Li, Y., O'Dell, S., Wilson, R., Wu, X., Schmidt, S.D., Hogerkorp, C.M., Louder, M.K., Longo, N.S., Poulsen, C., Guenaga, J., et al. (2012). HIV-1 neutralizing antibodies display dual recognition of the primary and coreceptor binding sites and preferential binding to fully cleaved envelope glycoproteins. *J. Virol.* 86, 11231–11241.
- Liao, H.X., Lynch, R., Zhou, T., Gao, F., Alam, S.M., Boyd, S.D., Fire, A.Z., Roskin, K.M., Schramm, C.A., Zhang, Z., et al.; NISC Comparative Sequencing Program (2013). Co-evolution of a broadly neutralizing HIV-1 antibody and founder virus. *Nature* 496, 469–476.
- Lyumkis, D., Julien, J.P., de Val, N., Cupo, A., Potter, C.S., Klasse, P.J., Burton, D.R., Sanders, R.W., Moore, J.P., Carragher, B., et al. (2013). Cryo-EM structure of a fully glycosylated soluble cleaved HIV-1 envelope trimer. *Science* 342, 1484–1490.
- Mascola, J.R., and Haynes, B.F. (2013). HIV-1 neutralizing antibodies: understanding nature's pathways. *Immunol. Rev.* 254, 225–244.
- McGuire, A.T., Hoot, S., Dreyer, A.M., Lippy, A., Stuart, A., Cohen, K.W., Jardine, J., Menis, S., Scheid, J.F., West, A.P., et al. (2013). Engineering HIV envelope protein to activate germline B cell receptors of broadly neutralizing anti-CD4 binding site antibodies. *J. Exp. Med.* 210, 655–663.
- Mikell, I., Sather, D.N., Kalams, S.A., Altfeld, M., Alter, G., and Stamatatos, L. (2011). Characteristics of the earliest cross-neutralizing antibody response to HIV-1. *PLoS Pathog.* 7, e1001251.
- Otwinowski, Z., and Minor, W. (1997). Processing of X-ray diffraction data collected in oscillation mode. *Methods Enzymol.* 276, 307–326.
- Pancera, M., McLellan, J.S., Wu, X., Zhu, J., Changela, A., Schmidt, S.D., Yang, Y., Zhou, T., Phogat, S., Mascola, J.R., and Kwong, P.D. (2010). Crystal structure of PG16 and chimeric dissection with somatically related PG9: structure-function analysis of two quaternary-specific antibodies that effectively neutralize HIV-1. *J. Virol.* 84, 8098–8110.
- Pancera, M., Zhou, T., Druz, A., Georgiev, I.S., Soto, C., Gorman, J., Huang, J., Acharya, P., Chuang, G.Y., Ofek, G., et al. (2014). Structure and immune recognition of trimeric pre-fusion HIV-1 Env. *Nature* 514, 455–461.
- Pejchal, R., Walker, L.M., Stanfield, R.L., Phogat, S.K., Koff, W.C., Poignard, P., Burton, D.R., and Wilson, I.A. (2010). Structure and function of broadly reactive antibody PG16 reveal an H3 subdomain that mediates potent neutralization of HIV-1. *Proc. Natl. Acad. Sci. USA* 107, 11483–11488.
- Richman, D.D., Wrin, T., Little, S.J., and Petropoulos, C.J. (2003). Rapid evolution of the neutralizing antibody response to HIV type 1 infection. *Proc. Natl. Acad. Sci. USA* 100, 4144–4149.
- Scheid, J.F., Mouquet, H., Feldhahn, N., Seaman, M.S., Velinzon, K., Pietzsch, J., Ott, R.G., Anthony, R.M., Zebroski, H., Hurley, A., et al. (2009). Broad diversity of neutralizing antibodies isolated from memory B cells in HIV-infected individuals. *Nature* 458, 636–640.
- Scheid, J.F., Mouquet, H., Ueberheide, B., Diskin, R., Klein, F., Oliveira, T.Y., Pietzsch, J., Fenyo, D., Abadir, A., Velinzon, K., et al. (2011). Sequence and structural convergence of broad and potent HIV antibodies that mimic CD4 binding. *Science* 333, 1633–1637.
- Smith, G.J., Vijaykrishna, D., Bahl, J., Lycett, S.J., Worobey, M., Pybus, O.G., Ma, S.K., Cheung, C.L., Raghwani, J., Bhatt, S., et al. (2009). Origins and evolutionary genomics of the 2009 swine-origin H1N1 influenza A epidemic. *Nature* 459, 1122–1125.
- Vrancken, B., Rambaut, A., Suchard, M.A., Drummond, A., Baele, G., Derdelinckx, I., Van Wijngaerden, E., Vandamme, A.M., Van Laethem, K., and Lemey, P. (2014). The genealogical population dynamics of HIV-1 in a large transmission chain: bridging within and among host evolutionary rates. *PLoS Comput. Biol.* 10, e1003505.
- Walker, L.M., Phogat, S.K., Chan-Hui, P.Y., Wagner, D., Phung, P., Goss, J.L., Wrin, T., Simek, M.D., Fling, S., Mitcham, J.L., et al.; Protocol G Principal Investigators (2009). Broad and potent neutralizing antibodies from an African donor reveal a new HIV-1 vaccine target. *Science* 326, 285–289.
- Walker, L.M., Simek, M.D., Priddy, F., Gach, J.S., Wagner, D., Zwick, M.B., Phogat, S.K., Poignard, P., and Burton, D.R. (2010). A limited number of antibody specificities mediate broad and potent serum neutralization in selected HIV-1 infected individuals. *PLoS Pathog.* 6, e1001028.
- Walker, L.M., Huber, M., Doores, K.J., Falkowska, E., Pejchal, R., Julien, J.P., Wang, S.K., Ramos, A., Chan-Hui, P.Y., Moyle, M., et al.; Protocol G Principal Investigators (2011). Broad neutralization coverage of HIV by multiple highly potent antibodies. *Nature* 477, 466–470.
- Wang, F., Ekiert, D.C., Ahmad, I., Yu, W., Zhang, Y., Bazirgan, O., Torkamani, A., Raudsepp, T., Mwangi, W., Criscitiello, M.F., et al. (2013). Reshaping antibody diversity. *Cell* 153, 1379–1393.
- Wei, X., Decker, J.M., Wang, S., Hui, H., Kappes, J.C., Wu, X., Salazar-Gonzalez, J.F., Salazar, M.G., Kilby, J.M., Saag, M.S., et al. (2003). Antibody neutralization and escape by HIV-1. *Nature* 422, 307–312.
- West, A.P., Jr., Diskin, R., Nussenzweig, M.C., and Bjorkman, P.J. (2012). Structural basis for germ-line gene usage of a potent class of antibodies targeting the CD4-binding site of HIV-1 gp120. *Proc. Natl. Acad. Sci. USA* 109, E2083–E2090.
- Wu, L., Yang, Z.Y., Xu, L., Welcher, B., Winfrey, S., Shao, Y., Mascola, J.R., and Nabel, G.J. (2006). Cross-clade recognition and neutralization by the V3 region from clade C human immunodeficiency virus-1 envelope. *Vaccine* 24, 4995–5002.
- Wu, X., Yang, Z.Y., Li, Y., Hogerkorp, C.M., Schief, W.R., Seaman, M.S., Zhou, T., Schmidt, S.D., Wu, L., Xu, L., et al. (2010). Rational design of envelope identifies broadly neutralizing human monoclonal antibodies to HIV-1. *Science* 329, 856–861.
- Wu, X., Zhou, T., Zhu, J., Zhang, B., Georgiev, I., Wang, C., Chen, X., Longo, N.S., Louder, M., McKee, K., et al.; NISC Comparative Sequencing Program (2011). Focused evolution of HIV-1 neutralizing antibodies revealed by structures and deep sequencing. *Science* 333, 1593–1602.
- Wu, X., Wang, C., O'Dell, S., Li, Y., Keele, B.F., Yang, Z., Imamichi, H., Doria-Rose, N., Hoxie, J.A., Connors, M., et al. (2012). Selection pressure on HIV-1 envelope by broadly neutralizing antibodies to the conserved CD4-binding site. *J. Virol.* 86, 5844–5856.
- Zhou, T., Xu, L., Dey, B., Hessel, A.J., Van Ryk, D., Xiang, S.H., Yang, X., Zhang, M.Y., Zwick, M.B., Arthos, J., et al. (2007). Structural definition of a conserved neutralization epitope on HIV-1 gp120. *Nature* 445, 732–737.

Zhou, T., Georgiev, I., Wu, X., Yang, Z.Y., Dai, K., Finzi, A., Kwon, Y.D., Scheid, J.F., Shi, W., Xu, L., et al. (2010). Structural basis for broad and potent neutralization of HIV-1 by antibody VRC01. *Science* 329, 811–817.

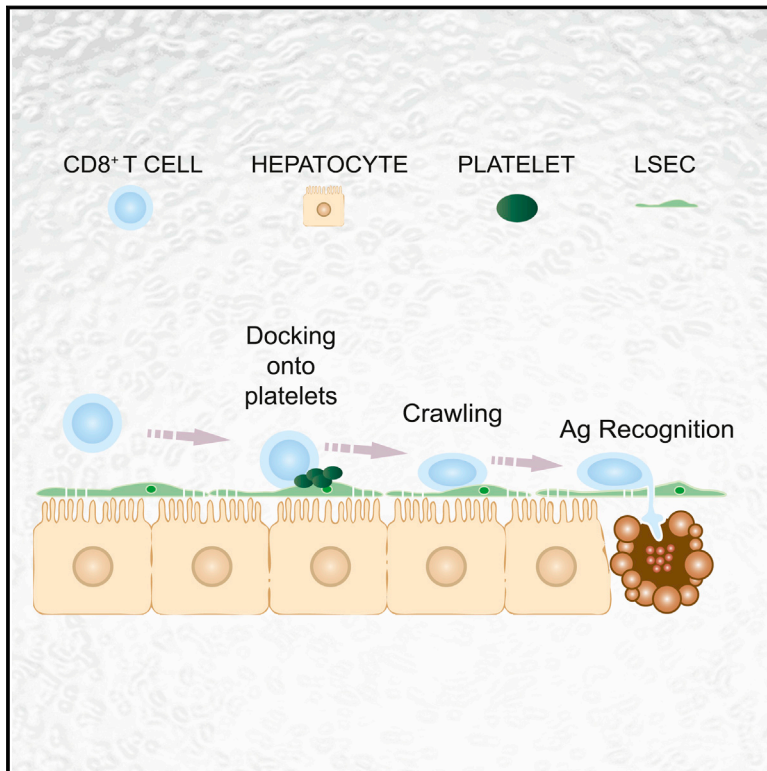
Zhou, T., Zhu, J., Wu, X., Moquin, S., Zhang, B., Acharya, P., Georgiev, I.S., Altae-Tran, H.R., Chuang, G.Y., Joyce, M.G., et al.; NISC Comparative Sequencing Program (2013). Multidonor analysis reveals structural elements, genetic determinants, and maturation pathway for HIV-1 neutralization by VRC01-class antibodies. *Immunity* 39, 245–258.

Zhu, J., O'Dell, S., Ofek, G., Pancera, M., Wu, X., Zhang, B., Zhang, Z., Mullikin, J.C., Simek, M., Burton, D.R., et al.; NISC Comparative Sequencing Program (2012). Somatic Populations of PGT135-137 HIV-1-Neutralizing Antibodies Identified by 454 Pyrosequencing and Bioinformatics. *Front Microbiol* 3, 315.

Zhu, J., Wu, X., Zhang, B., McKee, K., O'Dell, S., Soto, C., Zhou, T., Casazza, J.P., Mullikin, J.C., Kwong, P.D., et al.; NISC Comparative Sequencing Program (2013). De novo identification of VRC01 class HIV-1-neutralizing antibodies by next-generation sequencing of B-cell transcripts. *Proc. Natl. Acad. Sci. USA* 110, E4088–E4097.

Immunosurveillance of the Liver by Intravascular Effector CD8⁺ T Cells

Graphical Abstract



Authors

Luca G. Guidotti, Donato Inverso, ..., Giovanni Sitia, Matteo Iannacone

Correspondence

guidotti.luca@hsr.it (L.G.G.),
iannacone.matteo@hsr.it (M.I.)

In Brief

Circulating effector cytotoxic T cells recognize antigen and kill virus-infected hepatocytes without need to migrate into the tissue. Rather, they arrest within liver sinusoids, docking onto platelets, from where they probe hepatocytes for the presence of antigens, a process that is inhibited during liver fibrosis.

Highlights

- Circulating CD8 T_E arrest in liver sinusoids by docking onto platelet aggregates
- CD8 T_E crawl along liver sinusoids in search of hepatocellular antigen
- Cytokine production and hepatocyte killing occur in a diapedesis-independent manner
- Liver fibrosis impairs antigen recognition by intravascular CD8 T_E



Immunosurveillance of the Liver by Intravascular Effector CD8⁺ T Cells

Luca G. Guidotti,^{1,2,9,*} Donato Inverso,^{1,3,9} Laura Sironi,^{1,4} Pietro Di Lucia,¹ Jessica Fioravanti,¹ Lucia Ganzer,^{1,4} Amleto Fiocchi,¹ Maurizio Vacca,¹ Roberto Aiolfi,^{1,3} Stefano Sammiceli,¹ Marta Mainetti,¹ Tiziana Cataudella,¹ Andrea Raimondi,⁵ Gloria Gonzalez-Aseguinolaza,⁶ Ulrike Protzer,⁷ Zaverio M. Ruggeri,⁸ Francis V. Chisari,² Masanori Isogawa,² Giovanni Sitia,¹ and Matteo Iannacone^{1,3,5,*}

¹Division of Immunology, Transplantation and Infectious Diseases, IRCCS San Raffaele Scientific Institute, 20132 Milan, Italy

²Department of Immunology and Microbial Sciences, The Scripps Research Institute, La Jolla, CA 92037, USA

³Vita-Salute San Raffaele University, 20132 Milan, Italy

⁴Department of Physics, University of Milano Bicocca, 20126 Milan, Italy

⁵Experimental Imaging Center, IRCCS San Raffaele Scientific Institute, 20132 Milan, Italy

⁶Gene Therapy and Gene Regulation Program, Center for Applied Medical Research, 31008 Pamplona, Spain

⁷Institute of Virology, Technical University of Munich, 81675 Munich, Germany

⁸Department of Molecular and Experimental Medicine, The Scripps Research Institute, La Jolla, CA 92037, USA

⁹Co-first author

*Correspondence: guidotti.luca@hsr.it (L.G.G.), iannacone.matteo@hsr.it (M.I.)

<http://dx.doi.org/10.1016/j.cell.2015.03.005>

SUMMARY

Effector CD8⁺ T cells (CD8 T_E) play a key role during hepatotropic viral infections. Here, we used advanced imaging in mouse models of hepatitis B virus (HBV) pathogenesis to understand the mechanisms whereby these cells home to the liver, recognize antigens, and deploy effector functions. We show that circulating CD8 T_E arrest within liver sinusoids by docking onto platelets previously adhered to sinusoidal hyaluronan via CD44. After the initial arrest, CD8 T_E actively crawl along liver sinusoids and probe sub-sinusoidal hepatocytes for the presence of antigens by extending cytoplasmic protrusions through endothelial fenestrae. Hepatocellular antigen recognition triggers effector functions in a diapedesis-independent manner and is inhibited by the processes of sinusoidal defenestration and capillarization that characterize liver fibrosis. These findings reveal the dynamic behavior whereby CD8 T_E control hepatotropic pathogens and suggest how liver fibrosis might reduce CD8 T_E immune surveillance toward infected or transformed hepatocytes.

INTRODUCTION

The capacity of CD8⁺ T cells to protect against intracellular pathogens is mediated by antigen (Ag)-experienced effector cells that migrate to infected organs, recognize pathogen-derived Ags, and perform effector functions. Priming of adaptive immune responses during infection with intracellular bacteria or viruses results in extensive reprogramming of T cell trafficking so that effector cells can deal with pathogens that are located in peripheral compartments (Masopust et al., 2001). Understanding of the dynamic events leading to generation and expansion of effector

CD8⁺ T cells (CD8 T_E) within lymphoid organs has rapidly improved in recent years, particularly with the use of intravital microscopy (IVM) (Germain et al., 2012). By contrast, less is known on the spatiotemporal aspects that govern CD8 T_E migration and function at peripheral infection sites. As a general rule, CD8 T_E are thought to recognize pathogen-infected parenchymal cells and perform effector functions in the brain, skin, or gut following extravasation from post-capillary venules mediated by different combinations of inflammation-regulated selectins, integrins, and chemokines (Mueller, 2013).

The liver is a vital organ in which pathogenesis and outcome of infection by clinically relevant noncytotoxic viruses, such as hepatitis B virus (HBV) or hepatitis C virus (HCV), is determined by CD8 T_E (Guidotti and Chisari, 2006). Several observations suggest that the liver may be an exception to the classic multi-step leukocyte migration paradigm involving rolling, adhesion, and extravasation from postcapillary venules. First, leukocyte adhesion is not restricted to the endothelium of post-capillary venules and occurs also in sinusoids (Lee and Kubes, 2008). Second, leukocyte adhesion to liver sinusoidal endothelial cells (LSEC) often occurs independent of any notable rolling (Lee and Kubes, 2008). Furthermore, in contrast to vascular beds in most organs—where a continuous endothelial cell layer and a basal membrane physically separate parenchymal cells from circulating leukocytes—LSEC lack tight junctions as well as a basal membrane and contain numerous fenestrae of up to 200 nm in diameter (Jacobs et al., 2010). Thus, the fenestrated endothelial barrier of sinusoids provides the opportunity for direct interaction of circulating cells with underlying hepatocytes. For all these reasons, the pathways directing the spatiotemporal regulation of CD8 T_E migration and function in the liver may differ from those in other vascular districts.

Here, we have used advanced imaging methodologies in mouse models of HBV pathogenesis to show that hepatic CD8 T_E homing is indeed independent of selectins, β2- and α4-integrins, PECAM-1, VAP-1, Gαi-coupled chemokine receptors, or Ag recognition, all previously thought to be variably relevant for

leukocyte trafficking in other organs (von Andrian and Mackay, 2000; Mueller, 2013). Rather, circulating CD8 T_E initially arrest within liver sinusoids by docking onto platelets in turn adherent to sinusoidal hyaluronan via CD44. After the initial platelet-dependent arrest, CD8 T_E actively crawl along liver sinusoids and extend cellular protrusions through endothelial fenestrae to probe underlying hepatocytes for the presence of Ag. Hepato-cellular Ag recognition leading to cytokine production and hepatocyte killing occurs in a diapedesis-independent manner, i.e., before CD8 T_E extravasation into the parenchyma, and it is inhibited by experimental sinusoidal defenestration and capillarization, both of which are characteristic of liver fibrosis.

RESULTS

CD8 T_E Arrest within Liver Sinusoids Independently of Ag Recognition

To study how CD8 T_E traffic within the liver and recognize Ag, we made use of two transgenic mouse strains whose CD8⁺ T cells express H2^b- or H2^d-restricted T cell receptors (TCRs) specific for the HBV nucleocapsid (Cor) or envelope (Env) proteins, respectively (Isogawa et al., 2013). Naive CD8⁺ T cells from these TCR transgenic mice (referred to as Cor93 and Env28 CD8⁺ T cells, respectively) could be differentiated in vitro into bona fide CD8 T_E (data not shown) that, when transferred into HBV replication-competent transgenic mice (Guidotti et al., 1995), caused liver disease and inhibited viral replication (data not shown) as much as previously reported polyclonal memory HBV-specific CD8⁺ T cells (Iannacone et al., 2005). Further analyses in HBV replication-competent transgenic mice revealed that (1) passively transferred Cor93 and Env28 CD8 T_E accumulate at peak levels in the liver (see quantification of flow cytometric data in Figure 1A) and no longer circulate throughout the hepatic vasculature by 2 hr of intravenous injection (see quantification of epifluorescence IVM data in Figure 1B), and (2) virtually all CD8 T_E that arrested within the 2 hr time frame (~30% of visualized CD8 T_E, Figure 1C) adhered to hepatic sinusoids and not to post-sinusoidal venules (Figures 1D and 1E; Movie S1). The transfer of HBV-specific CD8 T_E into wild-type (WT) mice, previously injected with a reporter adenovirus (Ad-HBV-GFP) rendering HBV-replicating hepatocytes fluorescent (Sprinzl et al., 2001), revealed that CD8 T_E adhere to liver sinusoids regardless of the location of HBV Ag-producing hepatocytes (Movie S1). Consistent with these results, the overall accumulation of CD8 T_E in the liver was independent of Ag recognition, as virtually identical numbers of co-transferred Cor93 and Env28 CD8 T_E were isolated by 2 hr of injection from the same liver of transgenic and nontransgenic MHC-matched and MHC-mismatched recipients (Figure 1F; Movie S1).

Adhesion Molecules that Govern Leukocyte Trafficking in Other Organs Are Not Required for CD8 T_E Accumulation in the Liver

Next, we investigated whether the hepatic CD8 T_E accumulation observed within 2 hr of transfer involves the same adhesion molecules known to govern leukocyte trafficking in vascular locations of other organs (von Andrian and Mackay, 2000). Blocking PSGL-1, CD62L, CD62E, VLA-4, LFA-1, PECAM-1, and VAP-1

expressed by CD8⁺ T cells or LSEC (data not shown) had no impact on hepatic CD8 T_E accumulation (Figures 2A–2C) and neither did CD8 T_E expression of CD44 (Figure 2D), which has been implicated in hepatic neutrophil recruitment (McDonald et al., 2008). Pertussis toxin (PTX) treatment of CD8 T_E, which inhibited chemokine-mediated in vitro migration (data not shown), also did not alter the in vivo hepatic homing capacity of these cells (Figure 2E). Of note, the expression of selectins, integrin ligands, and chemokines is relatively low in the liver of HBV replication-competent transgenic mice prior to CD8 T_E transfer (Figures S1A and S1B), consistent with the uninfamed environment seen in experimentally infected chimpanzees prior to HBV-specific CD8⁺ T cell arrival (Wieland and Chisari, 2005). Increasing the hepatic expression of selectins, integrin ligands, and chemokines via Env28 CD8 T_E injection (Figures S1A and S1B) did not affect the liver homing potential of subsequently injected Cor93 CD8 T_E either PTX-treated or not (Figures 2F and 2G). To ascertain that the results shown in Figure 2 were not limited to in vitro differentiated CD8 T_E, we verified that the liver homing potential of in vivo generated CD8 T_E isolated from the spleen of lymphocytic choriomeningitis virus (LCMV)-infected mice and injected into recipient mice was not affected by blocking the above-mentioned adhesion molecules, even when multiple ligand-receptor pairs were blocked at one time (Figures S1C–S1G). Thus, hepatic accumulation of in vitro or in vivo differentiated CD8 T_E is independent of PSGL-1, CD62L, CD62E, VLA-4, LFA-1, PECAM-1, VAP-1, their CD44 expression and Gαi-coupled receptor signaling capability, and the degree of liver inflammation.

Hepatic CD8 T_E Accumulation Requires Platelet Adherence to Sinusoidal Hyaluronan via CD44

We previously showed that platelets facilitate the hepatic accumulation of CD8 T_E observed in HBV replication-competent mice at 1–2 days post transfer (Iannacone et al., 2005). However, it remained to be determined whether a platelet-specific pathway could influence the early adhesion of CD8 T_E to liver sinusoids. To address this question, we crossed two transgenic mouse strains, one HBV replication-competent and the other with platelets in which the human glycoprotein (GP) Ibα subunit replaced the mouse homolog in the GPIb-IX-V complex (mGPIbα^{null};hGPIbα^{Tg} mice) (Ware et al., 2000). The resulting HBV replication-competent mGPIbα^{null};hGPIbα^{Tg} mice can be depleted of endogenous platelets by specific anti-hGPIbα monoclonal antibodies and subsequently reconstituted with mouse platelets lacking reactivity with the depleting antibodies (Iannacone et al., 2008). Platelet depletion per se reduced the hepatic accumulation of CD8 T_E by ~50% by 2 hr after transfer (Figure 3A), and this reduction was associated with diminished CD8 T_E adhesion to LSEC (Figure 3B; Movie S2) and higher number of CD8 T_E circulating throughout the liver microvasculature (Figure 3C; Movie S2). Notably, platelets frequently adhered to LSEC prior to CD8 T_E transfer, forming small and transient aggregates of up to 10–15 platelets (Movie S3). Although these aggregates covered a minute fraction of the LSEC surface area (<3%, data not shown), circulating CD8 T_E docked preferentially to these sites (Movie S3), so that up to 30% of intrasinusoidal CD8 T_E were found attached to platelets at the 2 hr time point by static

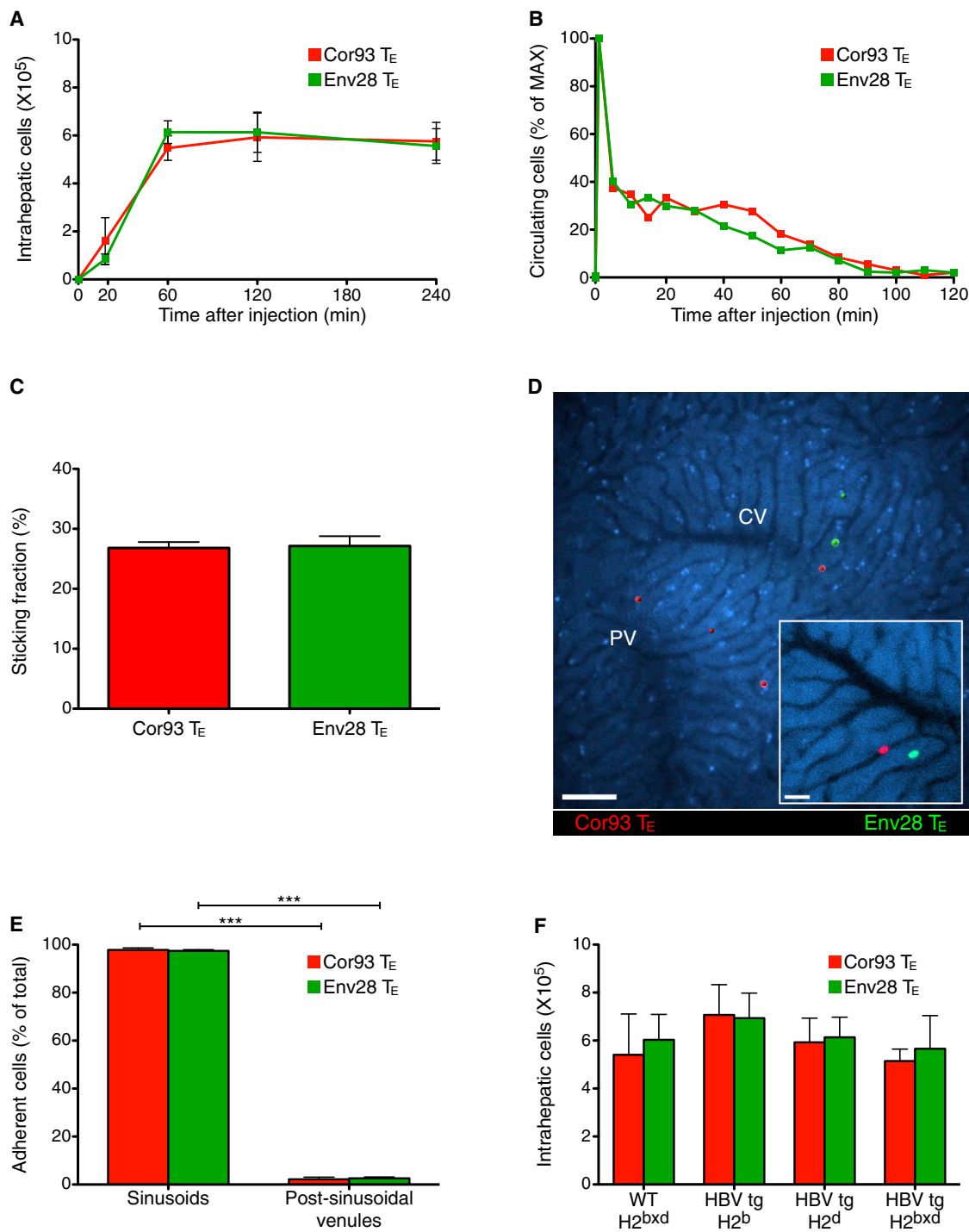


Figure 1. CD8 T_E Arrest within Liver Sinusoids Independently of Ag Recognition

Cor93 (10⁷) CD8 T_E (red) and Env28 (10⁷) CD8 T_E (green) were intravenously injected into HBV replication-competent transgenic mice (H₂^{bxd}) or into the indicated mouse strains.

(A) Absolute number of hepatic Cor93 (red) and Env28 (green) CD8 T_E recovered at the indicated time points after injection. *n* = 8; results are representative of three independent experiments.

(B) Quantification of the number of circulating Cor93 (red) and Env28 (green) CD8 T_E detected at the indicated time points within the field of a view (see [Experimental Procedures](#)). Results are representative of at least five experiments.

(C) Quantification of the sticking fractions for Cor93 (red) and Env28 (green) CD8 T_E. *n* = 5.

(legend continued on next page)

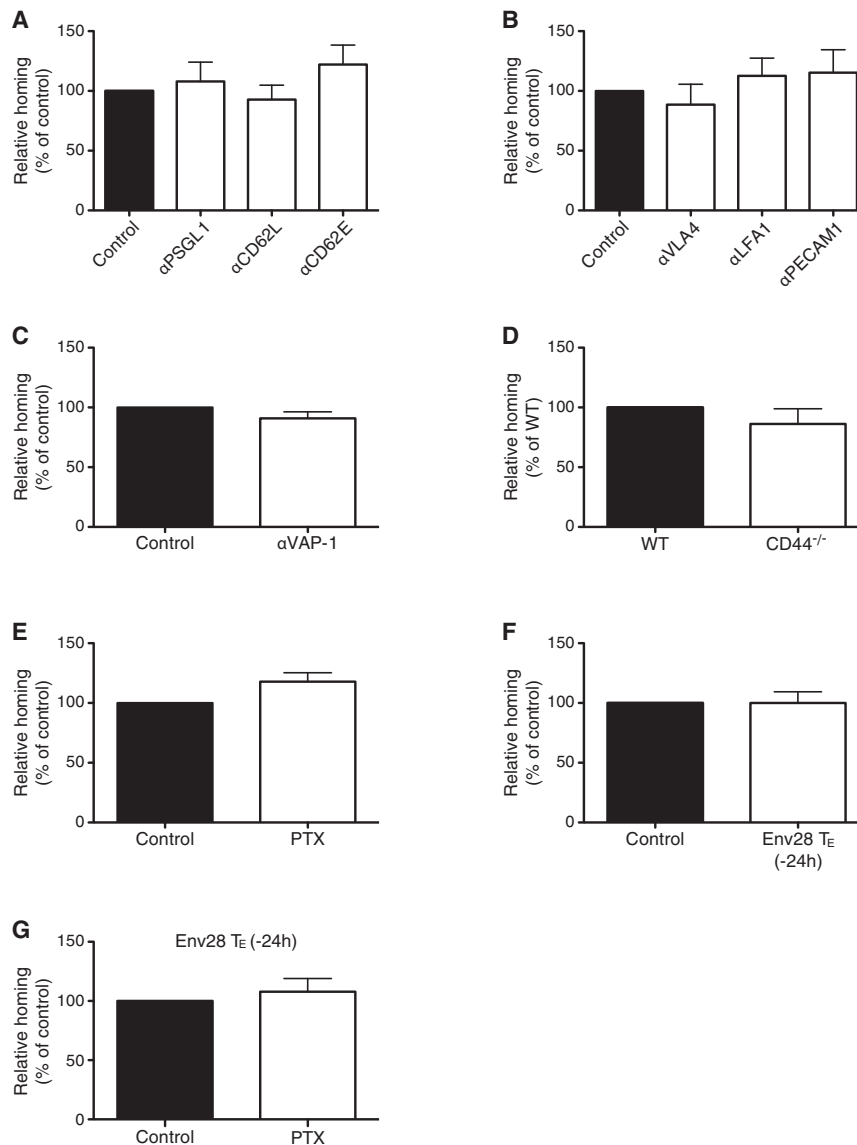


Figure 2. Adhesion Molecules that Govern Leukocyte Trafficking in Other Organs Are Not Required for CD8 T_E Accumulation in the Liver

(A) Percentage of Cor93 CD8 T_E that accumulated within the liver 2 hr upon transfer into HBV replication-competent transgenic mice (H2^{bxd}) that were previously treated with anti-PSGL1, anti-CD62L or anti-CD62E Abs relative to control (control = 100%). n = 5; results are representative of two independent experiments. Similar results were obtained with Env28 CD8 T_E (data not shown).

(B) Percentage of Cor93 CD8 T_E that accumulated within the liver 2 hr upon transfer into HBV replication-competent transgenic mice (H2^{bxd}) that were previously treated with anti-VLA-4, anti-LFA-1 or anti-PECAM-1 Abs relative to control (control = 100%). n = 8; results are representative of two independent experiments. Similar results were obtained with Env28 CD8 T_E (data not shown).

(C) Percentage of Cor93 CD8 T_E that accumulated within the liver 2 hr upon transfer into HBV replication-competent transgenic mice (H2^{bxd}) that were previously treated with anti-VAP-1 Abs relative to control (control = 100%). n = 5; results are representative of two independent experiments. Similar results were obtained with Env28 CD8 T_E (data not shown).

(D) Percentage of CD44^{-/-} Cor93 CD8 T_E that accumulated within the liver 2 hr upon transfer into HBV replication-competent transgenic mice (H2^{bxd}) relative to WT Cor93 CD8 T_E (WT = 100%). n = 10; results are representative of two independent experiments.

(E) Percentage of PTX-treated Cor93 CD8 T_E that accumulated within the liver 2 hr upon transfer into HBV replication-competent transgenic mice (H2^{bxd}) relative to control Cor93 CD8 T_E (control = 100%). n = 5; results are representative of two independent experiments. Similar results were obtained with Env28 CD8 T_E (data not shown).

(F) Percentage of Cor93 CD8 T_E that accumulated within the liver 2 hr upon transfer into HBV replication-competent transgenic mice (H2^{bxd}) that were injected 24 hr earlier with 5×10^6 Env28 CD8 T_E relative to control (control = 100%). n = 5; results are representative of two independent experiments.

(G) Percentage of PTX-treated Cor93 CD8 T_E (relative to untreated Cor93 CD8 T_E controls) that accumulated within the liver 2 hr upon transfer into HBV replication-competent transgenic mice (H2^{bxd}) that were treated 24 hr earlier with Env28 CD8 T_E. n = 5; results are representative of two independent experiments. Results are expressed as mean ± SEM.

See also [Figure S1](#).

confocal immunofluorescence analysis ([Figures 3D and 3E](#)). Dynamic epifluorescence IVM analysis of platelet-CD8 T_E interaction revealed that 30 out of 48 arrested CD8 T_E (>60%) docked onto platelets that were already adherent to liver sinusoids

(data not shown). Using reconstitution experiments and genetic approaches to identify molecules that might mediate the capacity of platelets to support early hepatic CD8 T_E accumulation, we found that platelet-derived CD44 (but not platelet-derived

(D) Representative images of Cor93 (red) and Env28 (green) CD8 T_E within the liver vasculature. Images are representative of at least ten experiments. Scale bars represent 50 μm and 20 μm (inset).

(E) Quantification of the localization (sinusoids versus post-sinusoidal venules) of adherent Cor93 (red) and Env28 (green) CD8 T_E. Cells were defined as adherent when they arrested for >30 s. n = 5.

(F) Absolute number of hepatic Cor93 (red) and Env28 (green) CD8 T_E recovered 2 hr after injection from the livers of WT or HBV replication-competent transgenic mice (H2^b, H2^d or H2^{bxd}). n = 8; results are representative of two independent experiments.

Results are expressed as mean ± SEM. ***p < 0.001.

See also [Movie S1](#).

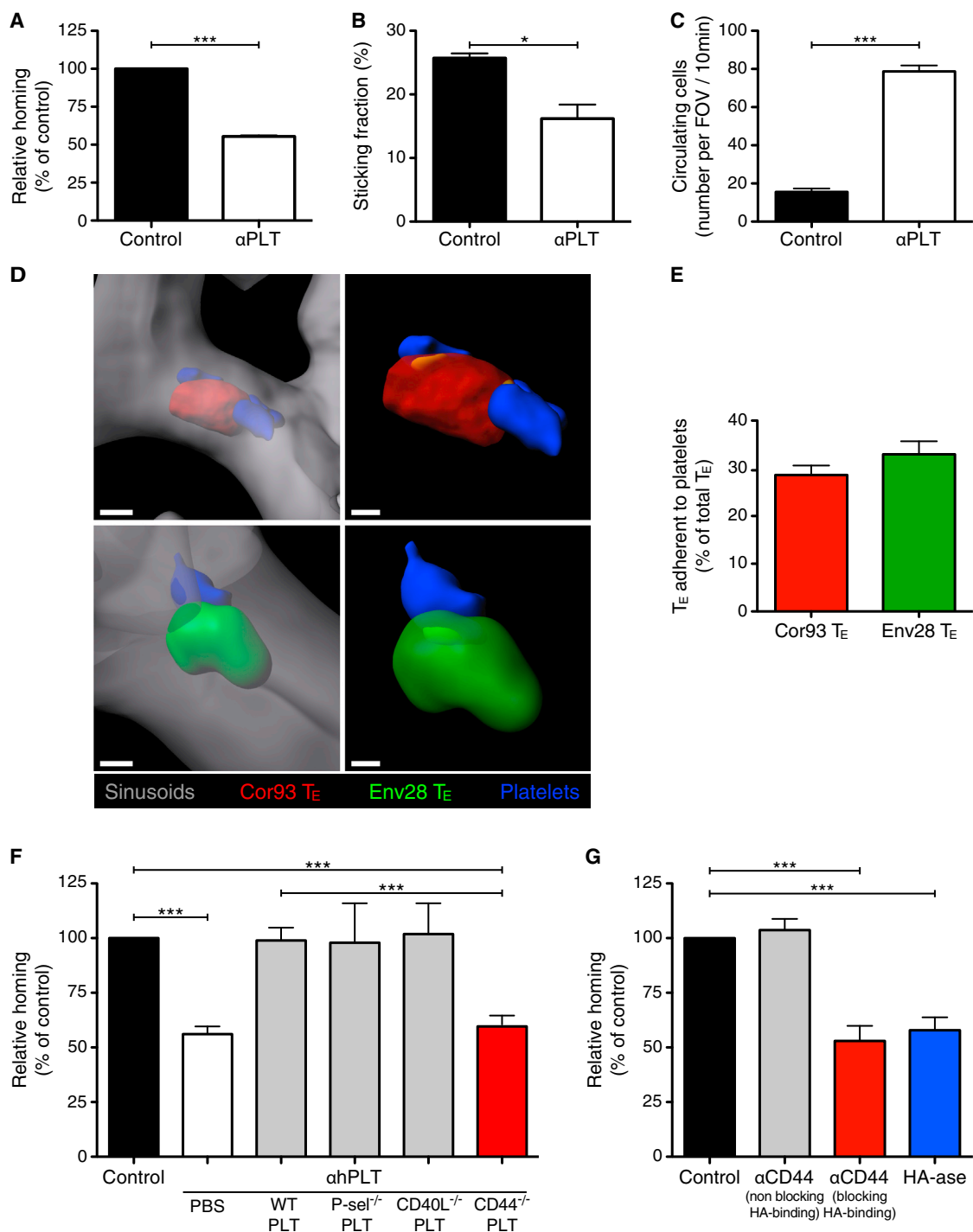


Figure 3. Hepatic CD8 T_E Accumulation Requires Platelets that Have Adhered to Sinusoidal Hyaluronan via CD44

(A) Percentage of Cor93 CD8 T_E that accumulated within the liver 2 hr upon transfer into HBV replication-competent × mGP-Ib α^{null} ;hGP-Ib α^{Tg} mice that were previously depleted of platelets (αPLT) relative to control (control = 100%). n = 4; results are representative of three independent experiments.

(B) Quantification of the sticking fraction for Cor93 CD8 T_E injected into HBV replication-competent × mGP-Ib α^{null} ;hGP-Ib α^{Tg} mice that were platelet-depleted (αPLT) or left untreated (control). Results are representative of three experiments.

(C) Quantification of the number of Cor93 CD8 T_E that were still circulating 2 hr after transfer into HBV replication-competent × mGP-Ib α^{null} ;hGP-Ib α^{Tg} mice that were platelet-depleted (αPLT) or left untreated (control). Results are representative of three experiments.

(D) Representative confocal micrographs of the liver of a HBV replication-competent × mGP-Ib α^{null} ;hGP-Ib α^{Tg} mouse (H2^b) that was injected 2 hr earlier with Cor93 (red) and Env28 (green) CD8 T_E. Platelets are shown in blue and sinusoids in gray. To allow visualization of intravascular event and to enhance image clarity,

(legend continued on next page)

P-selectin, CD40L, or serotonin) facilitated CD8 T_E homing to the liver (Figures 3F and S2A). Of note, CD44—expressed by CD8 T_E (data not shown) and platelets (Figure S2B)—has the capacity to bind to hyaluronan on liver sinusoids (McDonald et al., 2008). Accordingly, platelet adhesion to liver sinusoids occurred less efficiently in CD44^{-/-} mice than wild-type (WT) controls (Figure S2C; note that CD44^{-/-} mice have normal blood platelet counts and normal in vitro platelet aggregation capacity, data not shown); moreover, in vivo blockade of CD44-hyaluronan interaction or removal of sinusoidal hyaluronan decreased early hepatic CD8 T_E accumulation and the attendant liver disease (Figures 3G, S2D, and S2E). Similar results (i.e., reduced hepatic CD8 T_E accumulation and reduced liver disease severity) were obtained when CD44-hyaluronan interaction was blocked in a different model of acute viral hepatitis (Iannacone et al., 2005) that relies on endogenous, rather than adoptively transferred, CD8 T_E (Figures S2F and S2G). Altogether, these results indicate that CD8 T_E adhesion within liver sinusoids and the attendant immunopathology require platelet-expressed CD44 interacting with hyaluronan.

CD8 T_E Crawl along Liver Sinusoids until Hepatocellular Ags Are Recognized

We next took advantage of multiphoton IVM to study events that follow the initial platelet-dependent sinusoidal CD8 T_E arrest and eventually lead to cognate recognition of hepatocellular Ag. To this end, HBV-specific CD8 T_E were infused into mice that had been previously injected with either Ad-HBV-GFP or with adeno-associated viral vectors encoding for GFP and for specific HBV Ags (AAV-HBcAg-GFP or AAV-HBsAg-GFP), using experimental conditions whereby fewer than 5% of hepatocytes are transduced (data not shown). Dynamic imaging revealed that CD8 T_E not adjacent to Ag-expressing hepatocytes crawl upstream and downstream in the liver sinusoids at an average speed of ~10 μm/min (note that blood flows in liver sinusoids at 100–400 μm/s) (Sironi et al., 2014). By contrast, CD8 T_E migrating in close proximity to Ag-expressing hepatocytes slowed down and eventually arrested (Figures 4A and S3A–S3E; Movie S4). To confirm that cessation of intrasinusoidal CD8 T_E crawling is dictated by proximity to HBV Ag-expressing hepatocytes and by capacity to recognize cognate Ag, Cor93 and Env28 CD8 T_E were co-transferred into a lineage of HBV transgenic mice that express HBcAg (but not HBsAg) in 100% of hepatocytes (Guidotti et al., 1994). While Env28 CD8 T_E crawled within liver sinusoids of HBcAg transgenic mice at an

average speed of ~10 μm/min, the vast majority of Cor93 CD8 T_E remained immotile, or moved much more slowly and had a confined motility (Figures 4B–4F, S3F, and S3G; Movie S5). Altogether, these observations indicate that CD8 T_E exhibit an intrasinusoidal crawling behavior that halts when hepatocellular Ags are recognized.

Of note, HBV Ag expression in HBcAg transgenic mice, as in HBV replication-competent mice, is restricted to hepatocytes (Isogawa et al., 2013); in keeping with this, only hepatocytes isolated from these HBV transgenic mouse lineages presented Ag in vitro to HBV-specific CD8 T_E, in contrast to LSECs, Kupffer cells and dendritic cells isolated from their livers or liver-draining lymph nodes, which did not (Figure S4 and data not shown). These results are consistent with recent reports showing that HLA class I restricted HBV epitopes are exclusively expressed by human hepatocytes during natural HBV infection (Ji et al., 2012).

CD8 T_E Recognize Hepatocellular Ags and Perform Effector Functions in a Diapedesis-Independent Manner

The foregoing results suggest that CD8 T_E may recognize hepatocellular Ag while still in the intravascular space. To test this hypothesis, we set up an immunofluorescence staining method allowing the detection of Ag-recognizing (i.e., IFN-γ producing) cells with respect to their localization within the liver. Two hours after the co-transfer of Cor93 and Env28 CD8 T_E in H2^b-restricted HBV replication-competent or HBcAg transgenic mice, both populations were contained within the hepatic sinusoidal lumen but only MHC-matched Cor93 CD8 T_E expressed IFN-γ (Figures 5A, S5A, and S5B; Movie S6; data not shown). IFN-γ expression by intravascular CD8 T_E adjacent to hepatocyte expressing cognate Ag was also confirmed in WT mice that were injected with Ad-HBV-GFP prior to Cor93 CD8 T_E transfer (Figures S5C and S5D). That CD8 T_E performed effector functions without extravasating is further indicated by the detection of apoptotic hepatocytes preferentially juxtaposed to intravascular MHC-matched—rather than MHC-mismatched—CD8 T_E (Figure 5B; Movie S6; quantification in Figure S6). Confocal 3D reconstructions of these experiments occasionally revealed the presence of small CD8 T_E protrusions appearing to penetrate the sinusoidal wall in order to gain contact with underlying hepatocytes (Figure 5B; Movie S6). Analysis of the hepatic localization of CD8 T_E in transgenic and nontransgenic MHC-matched and MHC-mismatched recipients at 2 and 4 hr after CD8 T_E transfer revealed that only CD8 T_E capable of recognizing Ag eventually

the transparency of the sinusoidal rendering was set to 45% (left panels) and the transparency of the cell rendering to 48% (right panels). Scale bars represent 3 μm (left panels) and 1.5 μm (right panels).

(E) Percentage of Cor93 (red) and Env28 (green) CD8 T_E that were adherent to endogenous platelets in the liver of a HBV replication-competent × mGP-Ibα^{null};hGP-Ibα^{Tg} mouse (H2^b) that was injected 2 hr earlier with these cells. 300 of each cell type from 30 random 40× fields of view were analyzed. Results are representative of two independent experiments.

(F) Percentage of Cor93 CD8 T_E that accumulated within the liver 2 hr upon transfer into HBV replication-competent × mGP-Ibα^{null};hGP-Ibα^{Tg} mice that were previously depleted of platelets (αPLT) and then injected with PBS, WT platelets, P-selectin^{-/-} platelets, CD40L^{-/-} platelets, or CD44^{-/-} platelets relative to control (control = 100%). n = 6; results are representative of three independent experiments. For the role of platelet-derived serotonin see Figure S2.

(G) Percentage of Cor93 CD8 T_E that accumulated within the liver 2 hr upon transfer into HBV replication-competent × mGP-Ibα^{null};hGP-Ibα^{Tg} mice that were previously injected with anti-CD44 Abs (clones KM81 or IM7 that either block or not the capacity of CD44 to bind to hyaluronan [HA], respectively) or hyaluronidase (HA-ase) relative to control (control = 100%). n = 7; results are representative of two independent experiments.

Results are expressed as mean ± SEM. *p < 0.05, ***p < 0.001.

See also Figure S2 and Movies S2 and S3.

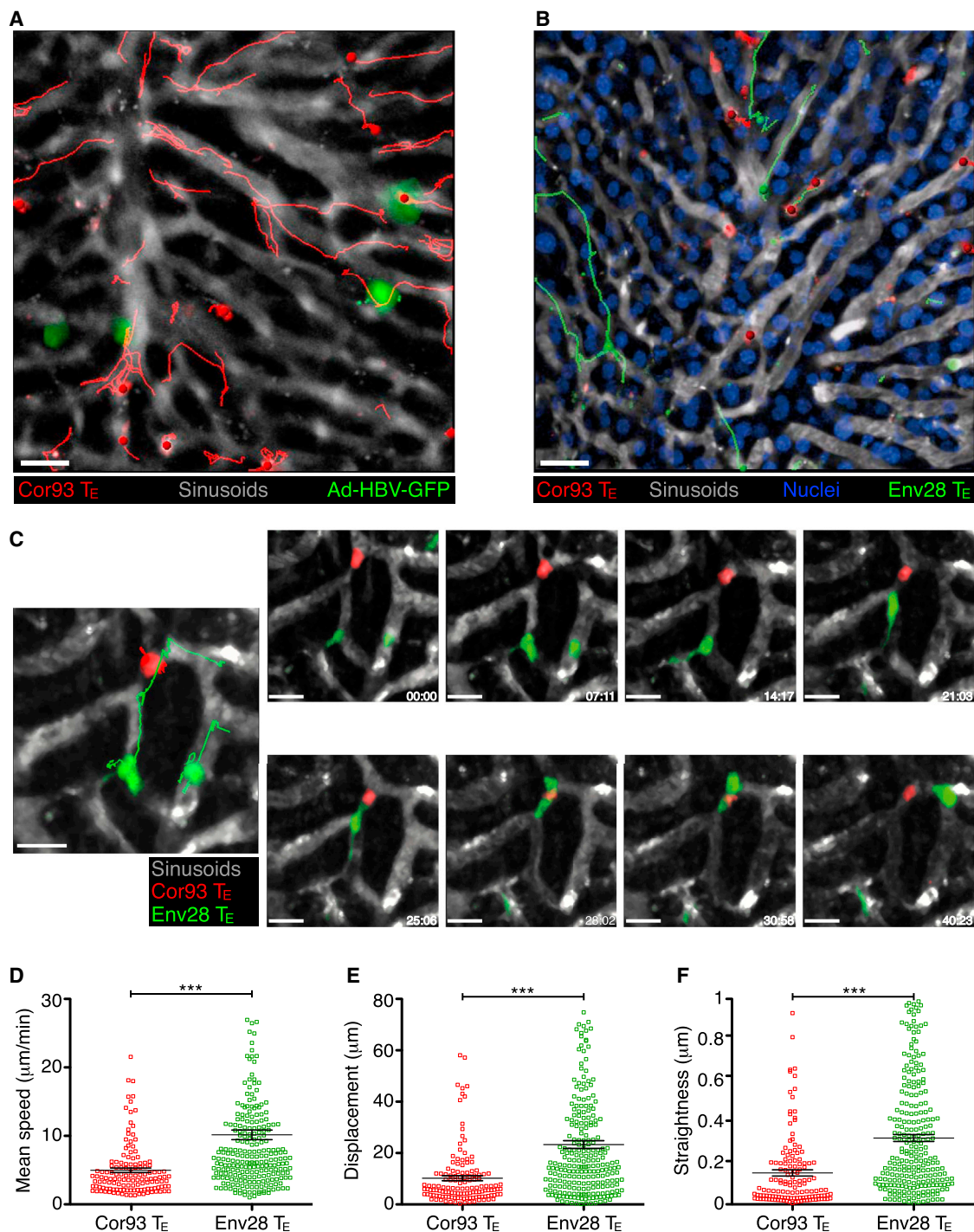


Figure 4. CD8 T_E Crawl along Liver Sinusoids until Hepatocellular Ags Are Recognized

(A) Intrasinusoidal crawling of CD8 T_E visualized by multiphoton IVM (still image from [Movie S4](#)) in the liver of a WT mouse that was injected with Ad-HBV-GFP 2 days prior to Cor93 CD8 T_E transfer. The movie was recorded ~1 hr after Cor93 CD8 T_E transfer. Red lines denote tracks of individual Cor93 CD8 T_E. Sinusoids are in gray. Scale bar represents 50 μ m. Similar results were obtained when Env28 CD8 T_E were transferred into Ad-HBV-GFP-injected mice or when Cor93 or Env28 CD8 T_E were transferred into WT mice previously injected with AAV-HBcAg-GFP or AAV-HBsAg-GFP, respectively (data not shown).

(B) Intrasinusoidal crawling of CD8 T_E visualized by multiphoton IVM (still image from [Movie S5](#)) in the liver of a HBcAg transgenic mouse (H2^b) that was injected with H2^b-restricted Cor93 (red) and H2^d-restricted Env28 (green) CD8 T_E. Red and green lines denote tracks of individual Cor93 and Env28 CD8 T_E, respectively. Sinusoids are in gray and hepatocellular nuclei are in blue. Scale bar represents 50 μ m.

(legend continued on next page)

extravasate (Figures S7A–S7C). These observations, coupled with the notion that the ratio between intravascular and extravascular CD8 T_E performing effector functions (i.e., expressing IFN- γ or triggering hepatocellular apoptosis) decreases over time (Figures S7D and S7E), indicate that extravasation follows rather than precedes Ag recognition. Together, the above results indicate that CD8 T_E do not need to extravasate in order to recognize hepatocellular Ags and to perform effector functions.

CD8 T_E Recognize Hepatocellular Ags through Fenestrations in Liver Sinusoidal Endothelial Cells

The above-mentioned results and the unique anatomy of the liver microvasculature suggest that CD8 T_E cellular protrusions might reach underlying hepatocytes through anatomical discontinuities in the hepatic sinusoid created by fenestrae that penetrate the endothelial cell lining. To test this hypothesis, we established a correlative technique that combines the specificity of 3D confocal fluorescence microscopy with the resolution of transmission electron tomography; this was carried out on liver sections from HBcAg transgenic mice whose LSEC are fluorescent (see [Experimental Procedures](#)). While confirming at higher resolution that CD8 T_E protrusions penetrate the sinusoidal wall, we found that these structures correspond to cytoplasmic CD8 T_E extensions that protrude through the LSEC fenestrae and contact the hepatocyte membrane over relatively large surface areas (Figures 5C and 5D; [Movie S7](#)). Although the fixation procedure of this correlative technique does not permit Ab staining (thus it cannot detect Ag recognition markers), these results are compatible with the formation of an immunological synapse between intravascular CD8 T_E and hepatocytes. The notion that CD8 T_E extend cytoplasmic protrusions penetrating the sinusoidal barrier of WT mice as well (data not shown) suggests that contacts with sub-sinusoidal hepatocytes might be the mechanism whereby CD8 T_E crawling intravascularly probe the liver for the presence of hepatocellular Ag.

To test the biological significance of CD8 T_E-mediated Ag recognition through sinusoidal fenestrae, HBV replication-competent transgenic mice were chronically exposed to low doses of arsenite ([Straub et al., 2007](#)), a treatment that reduces liver porosity (i.e., number and size of sinusoidal endothelial cell fenestrae) recapitulating the sinusoidal defenestration that characterizes liver fibrosis ([Friedman, 2004](#)). Arsenite treatment decreased liver porosity by ~5-fold (Figures 6A–6C) without affecting neither hepatic HBV Ag expression nor the capacity of hepatocytes to present Ag to CD8 T_E in vitro (data not shown). This same treatment did not alter the hepatic homing of CD8 T_E, which is platelet-dependent, but it reduced their in vivo Ag recognition capacity, as evidenced by the reduction of both IFN- γ expression and sALT elevation (Figures 6D–6J). To rule out off-target effects of arsenite treatment, we infected arse-

nite-treated mice with LCMV, a virus whose tropism in the liver is mostly restricted to intravascular Kupffer cells ([Guidotti et al., 1999](#)) and where, therefore, subsequently transferred LCMV-specific CD8 T_E should recognize infected cells independent of contacts through sinusoidal endothelial fenestrae. Indeed, arsenite exposure impacted neither the homing nor the Ag-recognition capacity of LCMV-specific CD8 T_E (Figures 6K and 6L).

Next, we evaluated whether the deposition of extracellular matrix in the space of Disse—a process known as liver capillarization, which creates a physical barrier between sinusoidal fenestrae and hepatocellular membranes and is frequently found in fibrotic livers ([Friedman, 2004](#))—could also limit Ag recognition by intravascular CD8 T_E. To this end, we transferred HBV-specific CD8 T_E to HBV replication-competent transgenic mice with liver fibrosis as a consequence of chronic exposure to carbon tetrachloride (Figures 7A–7C). This treatment did not alter the capacity of CD8 T_E to home to the liver, while significantly impaired CD8 T_E ability to recognize Ag on hepatocytes but not on intravascular Kupffer cells (Figures 7D–7H).

Altogether, these results indicate that CD8 T_E recognize hepatocellular Ags through sinusoidal endothelial fenestrations and suggest a mechanism whereby liver fibrosis reduces T cell immune-surveillance toward infected or transformed hepatocytes.

DISCUSSION

In this study, we coupled advanced imaging techniques and models of HBV pathogenesis to reveal previously unappreciated determinants that regulate the migration, Ag recognition, and effector function of CD8 T_E within the liver. In contrast to most other organs—where CD8 T_E arrest is mainly restricted to post-capillary venules and promoted by inflammation ([von Andrian and Mackay, 2000](#))—CD8 T_E circulating through the liver initially arrest within sinusoids and they do so independently of selectins, G α i-coupled chemokine receptors, β 2- and α 4-integrins, PECAM-1, and VAP-1. Furthermore, sinusoidal arrest and early accumulation of CD8 T_E occurs independently of their capacity to recognize hepatocellular Ag.

We previously used similar models of HBV pathogenesis to show that platelets are involved in hepatic CD8 T_E accumulation occurring 1–2 days post transfer ([Iannacone et al., 2005](#)), but the molecular mechanisms and spatiotemporal dynamics underlying these observations have remained elusive. Herein, we extended these observations by showing that (1) platelets adhere to LSEC even under steady-state conditions, leading to the transient formation of small intrasinusoidal aggregates on LSECs; (2) this process is mediated by platelet-expressed CD44 interacting with LSEC hyaluronan; and (3) intrasinusoidal platelet aggregates function as preferential docking sites for

(C) Still image (large left panel) and time lapse recording (small right panels) in the liver of a HBcAg transgenic mouse (H2^b) that was injected with Cor93 (red) and Env28 (green) CD8 T_E. Red and green lines denote tracks of individual Cor93 and Env28 CD8 T_E, respectively. Sinusoids are in gray. Elapsed time in minutes:seconds. Scale bar represents 15 μ m (left) and 10 μ m (right).

(D–F) Mean speed (D), displacement (E), and straightness (F) (see [Experimental Procedures](#)) of individual Cor93 (red) and Env28 (green) CD8 T_E in the liver of a HBcAg transgenic mouse (H2^b). Data are representative of two independent experiments.

Results are expressed as mean \pm SEM. ***p < 0.001.

See also [Figures S3 and S4](#) and [Movies S4 and S5](#).

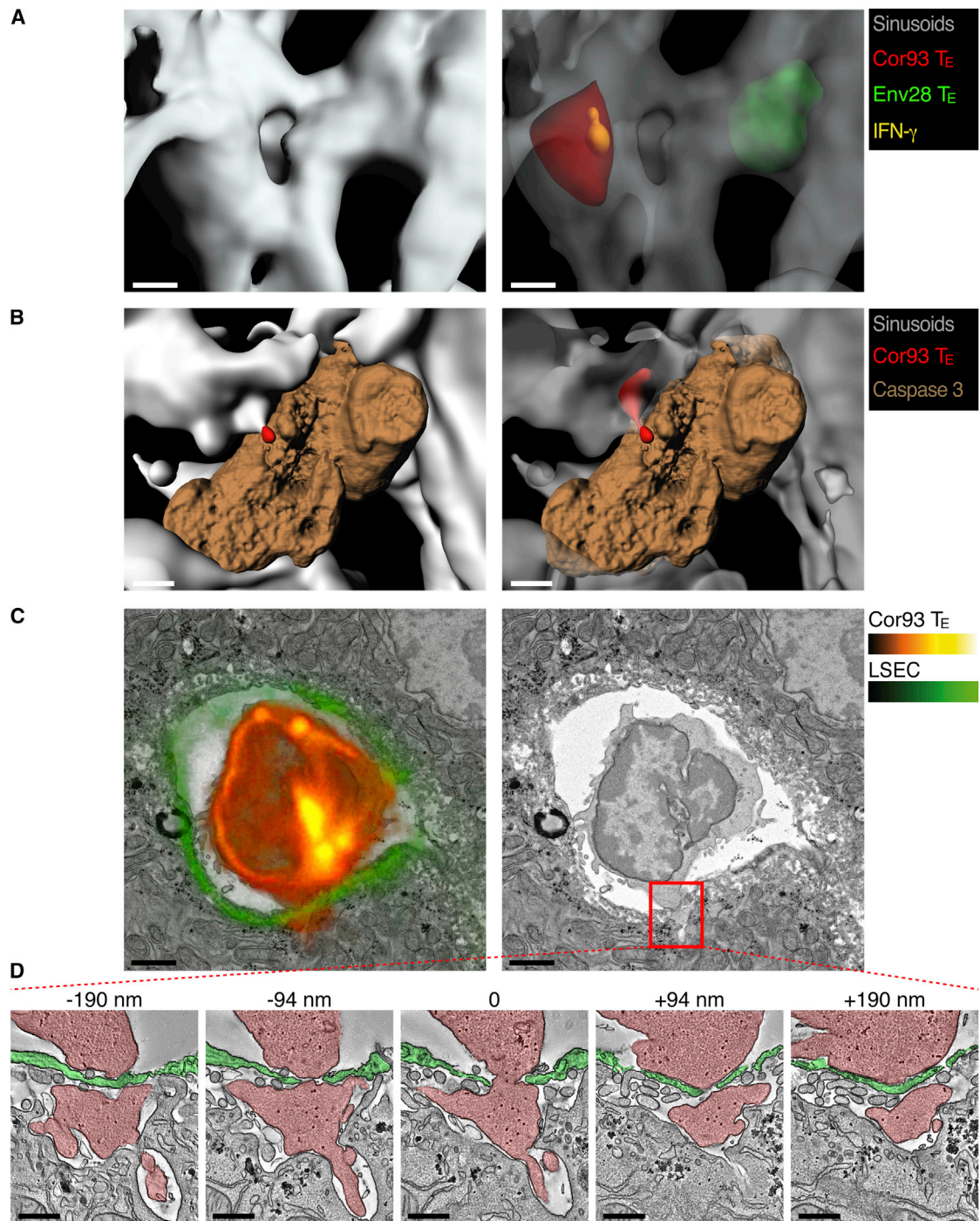


Figure 5. CD8 T_E Recognize Hepatocellular Ags and Perform Effector Functions in a Diapedesis-Independent Manner

(A) Representative confocal micrographs of the liver of a HBV replication-competent transgenic mouse (H2^b) that was injected 2 hr earlier with Cor93 (red) and Env28 (green) CD8 T_E. Sinusoids are shown in gray and IFN- γ in yellow. To allow visualization of intravascular events and to enhance image clarity, the transparency of the sinusoidal rendering in the right panel was set to 70% and that of T cells to 60%. Scale bars represent 4 μ m. See also [Movie S6](#) and [Figure S5](#). Similar results were obtained in similarly treated HBcAg transgenic mice (data not shown).

(B) Representative confocal micrographs of the liver of a HBV replication-competent transgenic mouse (H2^b) that was injected 2 hr earlier with Cor93 CD8 T_E (red). Sinusoids are shown in gray and caspase 3 in brown. To allow visualization of intravascular events and to enhance image clarity, the transparency of the sinusoidal rendering in the right panel was set to 50%. Scale bars represent 5 μ m. See also [Movie S6](#) and [Figure S6](#). Similar results were obtained in similarly treated HBcAg transgenic mice (data not shown).

(legend continued on next page)

circulating CD8 T_E. Other platelet molecules that had been previously implicated in the cross-talk between platelets and adaptive immunity, such as CD40L (Iannacone et al., 2008) or serotonin (Lang et al., 2008) were shown to be dispensable for these processes. Notably, platelets have been shown to form intrasinusoidal aggregates on the surface of bacterially infected Kupffer cells, possibly as a pathogen-trapping mechanism promoting immune-mediated clearance (Wong et al., 2013). In contrast to this study, we saw no evidence for a preferential formation of platelet aggregates on Kupffer cells in our system (data not shown), where Kupffer cells are neither infected with bacteria nor targeted by CD8 T_E. These results, together with the notion that Kupffer cell depletion does not affect hepatic CD8 T_E accumulation in these mouse models (Sitia et al., 2011), indicate that platelet-Kupffer cell interaction does not play a role in the hepatic homing of CD8 T_E targeting hepatocellular Ags.

It is noteworthy that experiments using anti-GP-Ib α Abs to deplete circulating platelets by roughly 50-fold (reducing normal platelet counts from $\sim 10^6$ platelets/ μ L to $\sim 2 \times 10^4$ platelets/ μ L) decreased the early hepatic accumulation of CD8 T_E only 2-fold. These results suggest that either the number of circulating platelets vastly exceeds the number required to efficiently arrest CD8 T_E in the liver or that a fraction of CD8 T_E home to the liver independently of platelets. Although the failure to further reduce hepatic CD8 T_E accumulation by treating platelet-depleted animals with CD44 blocking Abs supports the latter hypothesis, future studies are needed to settle this issue definitively.

Although our data have unambiguously identified the molecular interaction by which platelets adhere to LSEC, the mechanism(s) supporting CD8 T_E docking onto platelet aggregates remains unexplained. Of note, platelets possess a large array of surface molecules mediating adhesion to endothelial cells, and, among these, only P-selectin has a known ligand (i.e., PSGL-1) expressed also by CD8 T_E (Borges et al., 1997). As passive PSGL-1 neutralization or reconstitution with P-selectin-deficient platelets did not alter the capacity of CD8 T_E to accumulate intrahepatically, it appears that the interaction between P-selectin on platelets and PSGL-1 on CD8 T_E is not operative in our system. Whether other constitutively expressed or activation-induced platelet molecules directly or indirectly (via the formation of molecular bridges with CD8 T_E ligands) contribute to the process of CD8 T_E docking onto platelet aggregates remains to be determined. An attractive alternative hypothesis, which is currently under investigation, is that intrasinusoidal platelet aggregates alter local flow dynamics in ways that force CD8 T_E to slow down and then engage platelets and/or LSEC via non-covalent interactions.

Following the initial interaction with platelets, CD8 T_E were shown to crawl along liver sinusoids independently of blood direction and at a speed that was 500- to 1,000-fold slower than

sinusoidal flow (Sironi et al., 2014). This multi-directional intrasinusoidal crawling behavior is reminiscent of what has been observed for CD1d-restricted NKT cells patrolling the liver microvasculature (Geissmann et al., 2005). While the molecular mechanisms mediating CD8 T_E crawling are unknown, preliminary data show that chemokine cues might not be involved in this process (unpublished data). Whether hepatic CD8 T_E crawl along physical structures—as described for naive T cells migrating along the fibroblastic reticular cell network in the T cell area of lymph nodes (Bajénoff et al., 2006) or for effector T cells migrating along the myeloid scaffold delineating hepatic granulomas (Egen et al., 2008)—or whether noradrenergic neurotransmitters from sympathetic nerves can also modulate intrasinusoidal CD8 T_E motility—as described for intrasinusoidal hepatic NKT cells (Wong et al., 2011)—remains to be determined.

Importantly, our data show that the intrasinusoidal crawling behavior represents a form of immune surveillance, since it occurs independently of the presence of cognate Ag and it ceases following hepatocellular Ag recognition. Indeed, virus-specific CD8 T_E were shown to recognize hepatocellular Ags and to perform pathogenic functions (i.e., they produced IFN- γ and they killed HBV-expressing hepatocytes) while still in the intravascular space. These processes were mediated by the extension of cellular protrusions through sinusoidal endothelial cell fenestrae by CD8 T_E, producing contact sites with the hepatocyte membrane that are compatible with the establishment of an immunological synapse (Dustin and Groves, 2012). Of note, this Ag probing activity by intravascular CD8 T_E would require the formation and retraction of cellular protrusions, events that might seem at odds with average CD8 T_E migration rates of ~ 10 μ m/min. The high variability among CD8 T_E velocities (between 1 and up to 30 μ m/min, see Figure 4D) is compatible with the hypothesis that slower cells are more active in extending and retracting trans-endothelial protrusions than faster-moving ones. The notion that circulating leukocytes can interact with hepatocytes through endothelial fenestrations has been proposed in previous studies (Ando et al., 1994; Geissmann et al., 2005; Warren et al., 2006). Our results revealed that this process has functional significance, as reducing sinusoidal porosity or creating a physical barrier between sinusoidal fenestrae and hepatocellular membranes inhibited hepatocellular Ag recognition by CD8 T_E. These results also suggest a potential mechanism whereby liver fibrosis (a condition promoting both sinusoidal defenestration and capillarization) might reduce CD8 T_E immune surveillance toward infected or transformed hepatocytes and, in the latter case, favor the development and progression of hepatocellular carcinoma.

Another novel finding from our studies is that CD8 T_E extravasation from the liver microcirculation follows, rather than

(C) Correlative confocal and transmission electron microscopy of the liver of an HBcAg transgenic mouse whose LSEC express membrane-targeted tdTomato (see Experimental Procedures) that was injected 30 min earlier with Cor93 CD8 T_E. Left: overlay of the Cor93 CD8 T_E and LSEC fluorescence (red and green, respectively) with the electron micrograph of the same section. Right: electron micrograph alone. Scale bars represent 2 μ m.

(D) Transmission electron tomograms of five selected serial slices from the area delineated by the red inset in (C). The numbers indicate the z-distance from the middle section. Cor93 CD8 T_E and LSEC are indicated by the red and green overlay, respectively. Scale bars represent 500 nm. See Movie S7 for the complete tomographic reconstruction of 289 sections with a 1.95 nm z-step.

See also Figures S5, S6, and S7 and Movies S6 and S7.

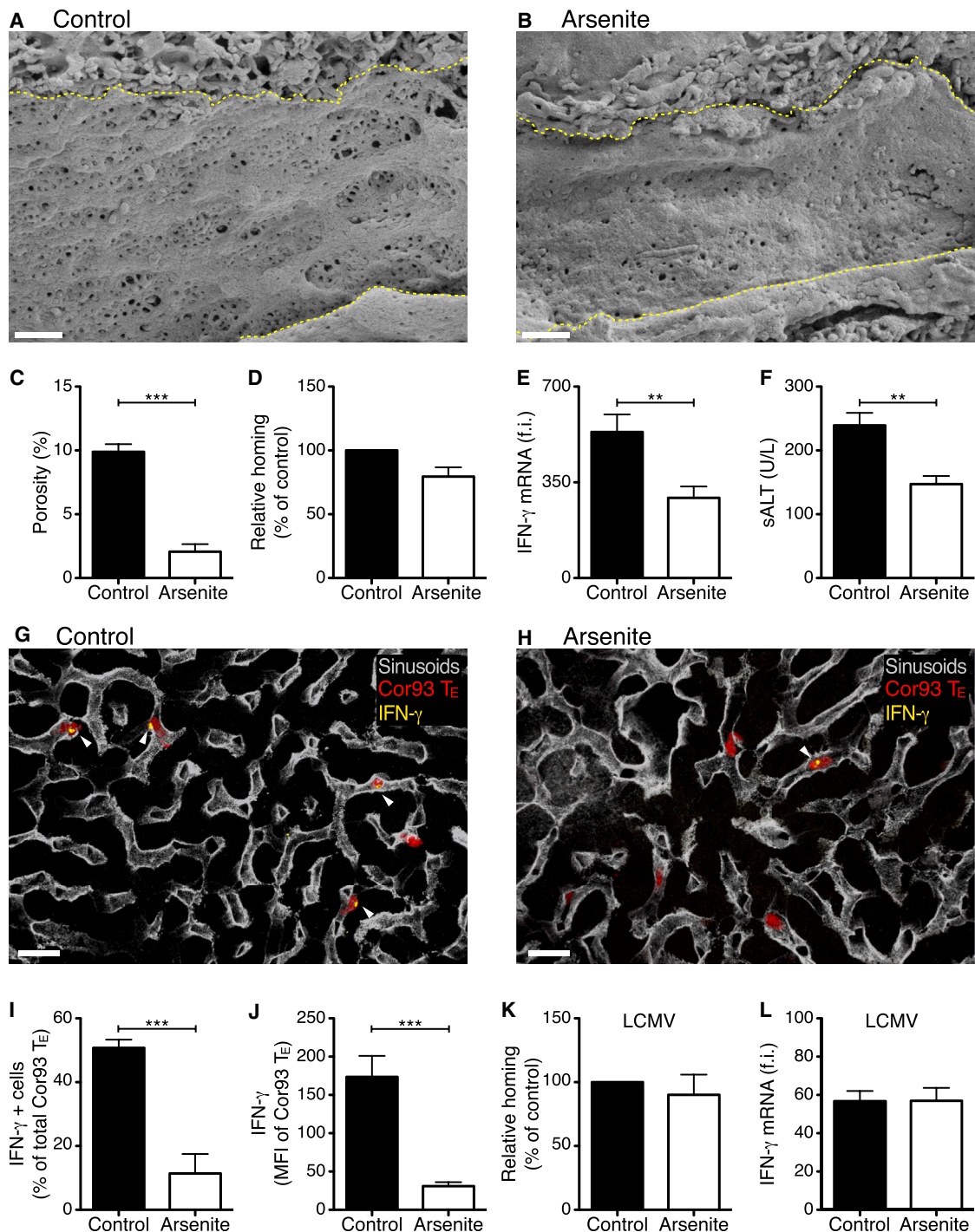


Figure 6. Reducing Sinusoidal Porosity Limits Hepatocellular Ag Recognition by CD8 T_E

(A and B) Representative scanning electron micrographs from liver sections of control (A) or arsenite-treated (B) HBV replication-competent transgenic mice (H2^{bxd}) mice. Yellow dotted lines denote sinusoidal edges. Scale bars represent 1 μ m.

(C) Porosity (the percentage of liver endothelial surface area occupied by fenestrae) was measured in control and arsenite-treated mice. $n = 3$; results are representative of two independent experiments.

(D) Percentage of Cor93 CD8 T_E that accumulated within the liver 2 hr upon transfer into HBV replication-competent transgenic mice (H2^{bxd}) that were previously treated with arsenite relative to control (control = 100%). $n = 20$; results are representative of two independent experiments. Similar results were obtained with Env28 CD8 T_E (data not shown).

(E) Total hepatic RNA from the same mice described in (D) was analyzed for the expression of IFN- γ by qPCR. Results are expressed as fold induction (f.i.) over HBV replication-competent transgenic mice injected with PBS, after normalization to the housekeeping gene GAPDH.

(legend continued on next page)

precedes, hepatocellular Ag recognition and effector function. The fate of extravasated CD8 T_E remains ill defined. One possibility is that they invade hepatocytes, enter endosomal/lysosomal compartments and are degraded, a process of suicidal emperipolesis that was recently described for naive CD8⁺ T cells undergoing primary activation in the liver (Benseler et al., 2011). We are attracted by the hypothesis that CD8 T_E extravasation into the liver parenchyma (whether through emperipolesis or other yet undefined mechanisms) might actually represent a way to limit Ag recognition and, therefore, to regulate excessive liver damage caused by CD8 T_E. This concept is supported by the notion that hepatocellular MHC-I expression is polarized and localized predominantly to the portion of the basolateral membrane facing the sinusoidal lumen (Warren et al., 2006), so that MHC-I-peptide complexes might be less accessible to CD8 T_E residing in extravascular spaces.

In summary, the data presented here reveal novel dynamic determinants regulating trafficking and effector function of CD8 T_E after hepatocellular Ag recognition. This is particularly relevant for the pathogenesis of viral infections such as those caused by HBV and HCV, noncytopathic pathogens that replicate selectively in the hepatocyte and cause acute or chronic liver disease that are triggered by virus-specific CD8 T_E (Guidotti and Chisari, 2006). By extension, it is conceivable that similar mechanisms may also be operative for bacterial and parasitic infections that target hepatocytes.

EXPERIMENTAL PROCEDURES

Mice

Mice were obtained from various sources and maintained in SPF conditions. All experimental animal procedures were approved by the Institutional Animal Committee of the San Raffaele Scientific Institute. For details on mouse lines and BM chimera generation, see the [Extended Experimental Procedures](#).

Viruses and Vectors

For details on adenoviral vectors, adeno-associated viruses and LCMV, see the [Extended Experimental Procedures](#). All infectious work was performed in designated BSL-2 or BSL-3 workspaces, in accordance with institutional guidelines.

Generation of Effector CD8⁺ T Cells and Adoptive Transfer

In vitro generation of CD8⁺ T cells (CD8 T_E) was performed basically as described (Manjunath et al., 2001). A total of 10⁷ cells of each cell type were injected intravenously (i.v.) into recipient animals. In imaging experiments, CD8 T_E were labeled with 2.5 μM CMFDA, 2.5 μM CFSE, 7.5 μM CMTPIX, 10 μM CMTMR, or 2.5 μM BODIPY 630/650-X (Life Technologies) for 20 min at 37°C in plain RPMI prior to adoptive transfer. For details, see the [Extended Experimental Procedures](#).

Blocking Abs and Hyaluronidase Treatment

The following blocking Abs were injected i.v. 2 hr prior to T cell transfer: anti-PSGL-1 (clone 4RA10; BioXCell; 200 μg/mouse), anti-CD62L (clone MEL-14; BioXCell; 100 μg/mouse), anti-CD62E (clone 10E9.6; BD Pharmingen; 100 μg/mouse), anti-VLA-4 (clone PS/2; BioXCell; 100 μg/mouse), anti-LFA-1 (clone M17/4; BioXCell; 100 μg/mouse and clone GAME46; BD Pharmingen; 25 μg/mouse), anti-PECAM-1 (clone MEC13.3; BioLegend; 100 μg/mouse), anti-VAP-1 (80 μg of clone 7-88 + 80 μg of clone 7-106/mouse, both provided by S. Jalkanen), anti-CD44 (clone KM81, blocking CD44 binding to hyaluronan [Zheng et al., 1995]; Cedarlane; 20 μg/mouse), anti-CD44 (clone IM7, not interfering with CD44 binding to hyaluronan [Zheng et al., 1995]; BioXCell; 100 μg/mouse). In indicated experiments mice were injected intraperitoneally (i.p.) with 20 U/g hyaluronidase type-IV (Sigma-Aldrich), as described (Johnsson et al., 1999).

Env28 CD8 T_E-Mediated Induction of Liver Inflammation

In order to increase the hepatic expression of selectins, integrin ligands and chemokines (experiments described in [Figures 2F, 2G, and S1](#)), HBV replication-competent transgenic mice were injected i.v. with 5 × 10⁶ Env28 CD8 T_E 24 hr prior to the injection of 10⁷ Cor93 CD8 T_E.

Treatment with Pertussis Toxin and Chemotaxis Assay

The role of G_αi signaling was assessed by incubating CD8 T_E (10⁷ cells/ml) for 2 hr at 37°C with 100 ng/ml pertussis toxin (Merck). For details on chemotaxis assay see the [Extended Experimental Procedures](#).

Depletion and Transfusion of Platelets

HBV replication-competent x mGP-Ibα^{null};hGP-Ibα^{Tg} mice were injected i.v. with 80 μg of clone LJ-P3 (a monoclonal Ab that recognizes the platelet-specific human GP-Ibα) at least 3 hr prior to further experimental manipulation, as described (Iannacone et al., 2008). Platelet transfusion was performed as described (Iannacone et al., 2008), with each mouse receiving a single i.v. injection of 6 × 10⁸ platelets.

Treatment with Sodium Arsenite or Carbon Tetrachloride

In indicated experiments, mice were treated with sodium arsenite (250 ppb in drinking water ad libitum) for 10 weeks. In other experiments mice were fed by oral gavage with a solution of carbon tetrachloride (CCl₄) in peanut oil (Sigma-Aldrich) at a final dose of 0.7 mg/g of body weight. CCl₄ was administered twice a week for 12 weeks, after which the treatment was suspended for a washout period of 4 weeks.

Cell Isolation and Flow Cytometry

Single-cell suspensions of livers, spleens, and lymph nodes were generated as described (Iannacone et al., 2005; Tonti et al., 2013). For details on flow cytometric analyses see the [Extended Experimental Procedures](#).

Isolation of Primary Hepatocytes, LSEC, Kupffer Cells, Intrahepatic Dendritic Cells, and Dendritic Cells from Liver-Draining Lymph Nodes

Primary hepatocytes, LSEC, Kupffer cells, and dendritic cells were isolated essentially as described (Isogawa et al., 2013). Hepatic lymph node dendritic cells were isolated by positive selection using biotinylated CD11c and streptavidin Magnetic Particles (BD Biosciences). For details see the [Extended Experimental Procedures](#).

(F) ALT activity measured in the serum of the same mice described in (D).

(G and H) Representative confocal micrographs from the same mice described in (D). Cor93 CD8 T_E are shown in red, sinusoids in gray and IFN-γ in yellow. Arrowheads denote IFN-γ⁺ cells. Scale bars represent 20 μm.

(I) The percentage of Cor93 CD8 T_E that stained positive for IFN-γ was quantified in liver sections from the same mice described in (D). n = 90.

(J) IFN-γ mean fluorescence intensity (MFI) of Cor93 CD8 T_E was quantified in liver sections from the same mice described in (D). n = 90.

(K) Percentage of GP33 CD8 T_E that accumulated within the liver 2 hr upon transfer into LCMV-infected mice that were previously treated with arsenite, relative to control (control = 100%). n = 5; results are representative of two independent experiments.

(L) Total hepatic RNA from the same mice described in (K) was analyzed for the expression of IFN-γ by qPCR. Results are expressed as fold induction (f.i.) over LCMV-infected mice injected with PBS, after normalization to the housekeeping gene GAPDH.

Results are expressed as mean ± SEM. **p < 0.01, ***p < 0.001.

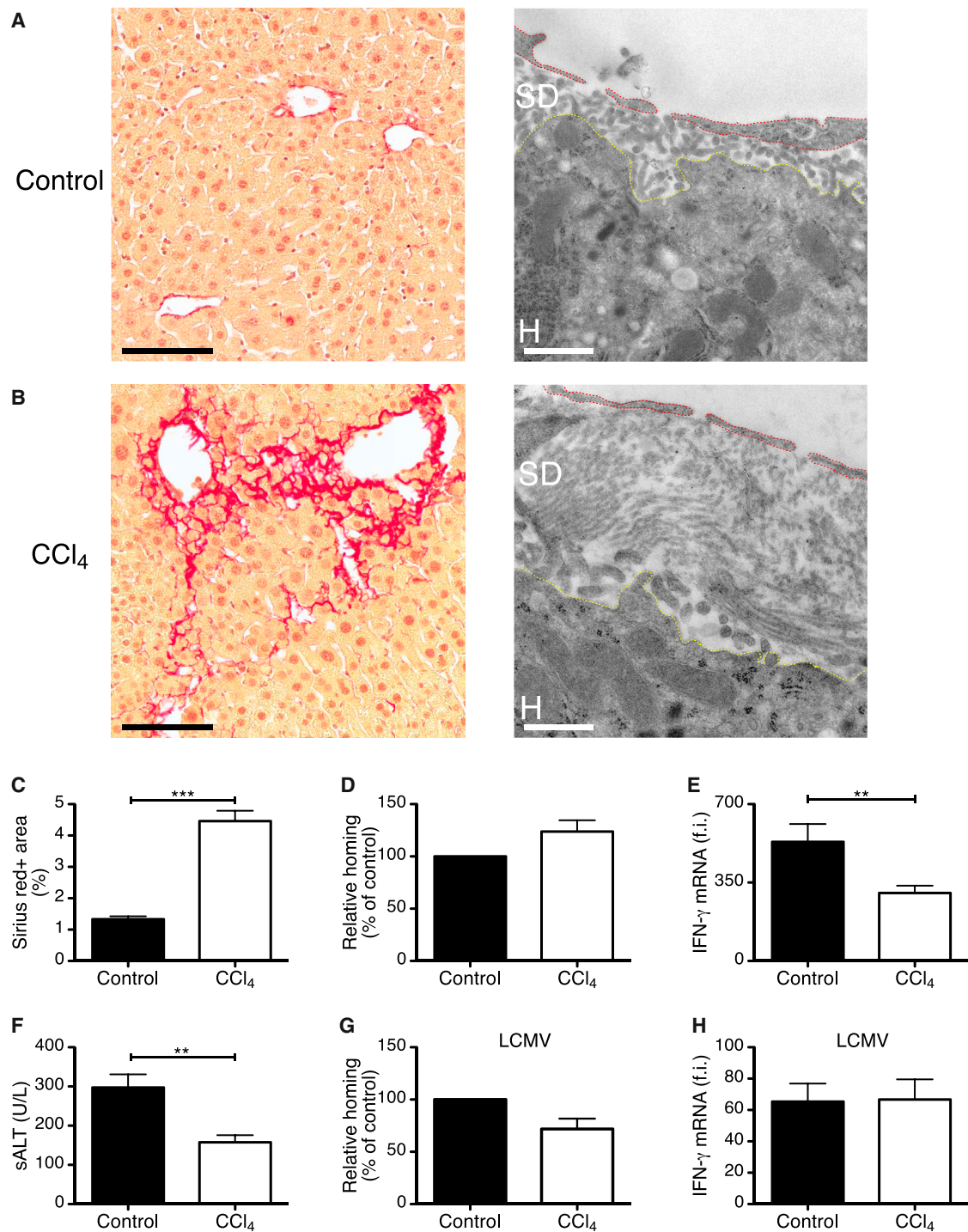


Figure 7. Liver Fibrosis Limits Hepatocellular Ag Recognition by CD8 T_E

(A and B) Representative Sirius Red (left) or transmission electron (right) micrographs from liver sections of control (A) or carbon tetrachloride (CCl₄)-treated (B) HBV replication-competent transgenic mice. Sirius Red staining is shown in red. Scale bars represent 100 μ m (Sirius Red) and 1.5 μ m (transmission electron micrographs). Red and yellow dotted lines denote LSEC and the hepatocyte body, respectively. SD, space of Disse; H, hepatocyte.

(C) Quantification of Sirius red staining in HBV replication-competent transgenic mice that were treated or not with CCl₄. n = 3; results are representative of two independent experiments.

(D) Percentage of Cor93 CD8 T_E that accumulated within the liver 2 hr upon transfer into HBV replication-competent transgenic mice (H2^{bxd}) that were previously treated with carbon tetrachloride (CCl₄) relative to control (control = 100%). n = 15; results are representative of two independent experiments.

(legend continued on next page)

Imaging Studies

For details on histochemistry, confocal immunofluorescence histology, intravital epifluorescence, and multiphoton microscopy, electron microscopy, and correlative light and electron tomography, see the [Extended Experimental Procedures](#).

DNA, RNA, and Biochemical Analyses

For details on molecular and biochemical analyses, see the [Extended Experimental Procedures](#).

Statistical Analyses

Results are expressed as mean \pm SEM. All statistical analyses were performed in Prism 5 (GraphPad Software). Means between two groups were compared with two-tailed t test. Means among three or more groups were compared with one-way or two-way ANOVA with Bonferroni post-test.

SUPPLEMENTAL INFORMATION

Supplemental Information includes Extended Experimental Procedures, seven figures, and seven movies and can be found with this article online at <http://dx.doi.org/10.1016/j.cell.2015.03.005>.

AUTHOR CONTRIBUTIONS

L.G.G. and M. Iannacone designed and supervised the study. L.G.G., D.I., L.S., P.D.L., J.F., L.G., A.F., M.V., S.S., M.M., G.S., and M. Iannacone performed experiments. R.A. helped with platelet transfusions and aggregations. T.C. helped with the isolation of liver cell populations. L.G.G., D.I., L.S., P.D.L., J.F., L.G., and M. Iannacone analyzed the data. D.I. and A.R. performed the correlative confocal and transmission electron microscopy analysis. L.S. wrote the scripts for the IVM analyses. D.I. and L.S. performed the quantitative confocal microscopy analysis. L.G. helped with the computational analyses of the imaging data. G.G.-A. generated recombinant adeno-associated viruses. U.P. provided recombinant adenoviruses. Z.M.R. provided mGP-Ib α^{null} ;hGP-Ib α^{Tg} mice and gave conceptual advice. F.V.C. and M. Isogawa provided HBV-specific TCR transgenic mice and gave conceptual advice. D.I. and L.S. prepared the figures and movies. L.G.G., Z.M.R., F.V.C., and M. Iannacone wrote the manuscript.

ACKNOWLEDGMENTS

We thank M. Raso for technical support; R. Serra for secretarial assistance; S. Jaikonen for providing anti-VAP-1 Abs; S. Wieland for providing pCMV- β -gal; M. Bader for providing TPH-1 $^{-/-}$ mice; J. Egen for advice on the liver surgical preparation for the inverted microscope setup; C. Tacchetti for advice on correlative microscopy; L. Suarez-Amarán for help with the generation of recombinant adeno-associated viruses; P. Dellabona and R. Pardi for critical reading of the manuscript and the members of the M. Iannacone and L.G.G. laboratories for helpful discussions. We would like to acknowledge the PhD program in Basic and Applied Immunology at San Raffaele University, as D.I. conducted this study as partial fulfillment of his PhD in Molecular Medicine within that program. This work was supported by European Research Council (ERC) grants 250219 (to L.G.G.) and 281648 (to M. Iannacone); NIH RO1 grant AI40696 (to L.G.G.) and HL-42846 (to Z.M.R.); Italian Association for Cancer Research (AIRC) grant 9965 (to M. Iannacone); and a Career Development Award from the Giovanni Armenise-Harvard Foundation (to M. Iannacone).

Received: September 24, 2014

Revised: December 18, 2014

Accepted: February 24, 2015

Published: April 16, 2015

REFERENCES

- Ando, K., Guidotti, L.G., Cerny, A., Ishikawa, T., and Chisari, F.V. (1994). CTL access to tissue antigen is restricted in vivo. *J. Immunol.* **153**, 482–488.
- Bajénoff, M., Egen, J.G., Koo, L.Y., Laugier, J.P., Brau, F., Glaichenhaus, N., and Germain, R.N. (2006). Stromal cell networks regulate lymphocyte entry, migration, and territoriality in lymph nodes. *Immunity* **25**, 989–1001.
- Benseler, V., Warren, A., Vo, M., Holz, L.E., Tay, S.S., Le Couteur, D.G., Breen, E., Allison, A.C., van Rooijen, N., McGuffog, C., et al. (2011). Hepatocyte entry leads to degradation of autoreactive CD8 T cells. *Proc. Natl. Acad. Sci. USA* **108**, 16735–16740.
- Borges, E., Tietz, W., Steegmaier, M., Moll, T., Hallmann, R., Hamann, A., and Vestweber, D. (1997). P-selectin glycoprotein ligand-1 (PSGL-1) on T helper 1 but not on T helper 2 cells binds to P-selectin and supports migration into inflamed skin. *J. Exp. Med.* **185**, 573–578.
- Dustin, M.L., and Groves, J.T. (2012). Receptor signaling clusters in the immune synapse. *Annu. Rev. Biophys.* **41**, 543–556.
- Egen, J.G., Rothfuchs, A.G., Feng, C.G., Winter, N., Sher, A., and Germain, R.N. (2008). Macrophage and T cell dynamics during the development and disintegration of mycobacterial granulomas. *Immunity* **28**, 271–284.
- Friedman, S.L. (2004). Mechanisms of disease: Mechanisms of hepatic fibrosis and therapeutic implications. *Nat. Clin. Pract. Gastroenterol. Hepatol.* **1**, 98–105.
- Geissmann, F., Cameron, T.O., Sidobre, S., Manlongat, N., Kronenberg, M., Briskin, M.J., Dustin, M.L., and Littman, D.R. (2005). Intravascular immune surveillance by CXCR6 $^{+}$ NKT cells patrolling liver sinusoids. *PLoS Biol.* **3**, e113.
- Germain, R.N., Robey, E.A., and Cahalan, M.D. (2012). A decade of imaging cellular motility and interaction dynamics in the immune system. *Science* **336**, 1676–1681.
- Guidotti, L.G., and Chisari, F.V. (2006). Immunobiology and pathogenesis of viral hepatitis. *Annu. Rev. Pathol.* **1**, 23–61.
- Guidotti, L.G., Martinez, V., Loh, Y.T., Rogler, C.E., and Chisari, F.V. (1994). Hepatitis B virus nucleocapsid particles do not cross the hepatocyte nuclear membrane in transgenic mice. *J. Virol.* **68**, 5469–5475.
- Guidotti, L.G., Matzke, B., Schaller, H., and Chisari, F.V. (1995). High-level hepatitis B virus replication in transgenic mice. *J. Virol.* **69**, 6158–6169.
- Guidotti, L.G., Borrow, P., Brown, A., McClary, H., Koch, R., and Chisari, F.V. (1999). Noncytotoxic clearance of lymphocytic choriomeningitis virus from the hepatocyte. *J. Exp. Med.* **189**, 1555–1564.
- Iannacone, M., Sitia, G., Isogawa, M., Marchese, P., Castro, M.G., Lowenstein, P.R., Chisari, F.V., Ruggeri, Z.M., and Guidotti, L.G. (2005). Platelets mediate cytotoxic T lymphocyte-induced liver damage. *Nat. Med.* **11**, 1167–1169.
- Iannacone, M., Sitia, G., Isogawa, M., Whitmire, J.K., Marchese, P., Chisari, F.V., Ruggeri, Z.M., and Guidotti, L.G. (2008). Platelets prevent IFN- α /beta-induced lethal hemorrhage promoting CTL-dependent clearance of lymphocytic choriomeningitis virus. *Proc. Natl. Acad. Sci. USA* **105**, 629–634.

(E) Total hepatic RNA from the same mice described in (D) was analyzed for the expression of IFN- γ by qPCR. $n = 15$; results are representative of two independent experiments.

(F) ALT activity measured in the serum of the same mice described in (D). $n = 15$; results are representative of two independent experiments.

(G) Percentage of GP33 CD8 T $_E$ that accumulated within the liver 2 hr upon transfer into LCMV-infected mice that were previously treated with CCl $_4$ relative to control (control = 100%). $n = 7$; results are representative of two independent experiments.

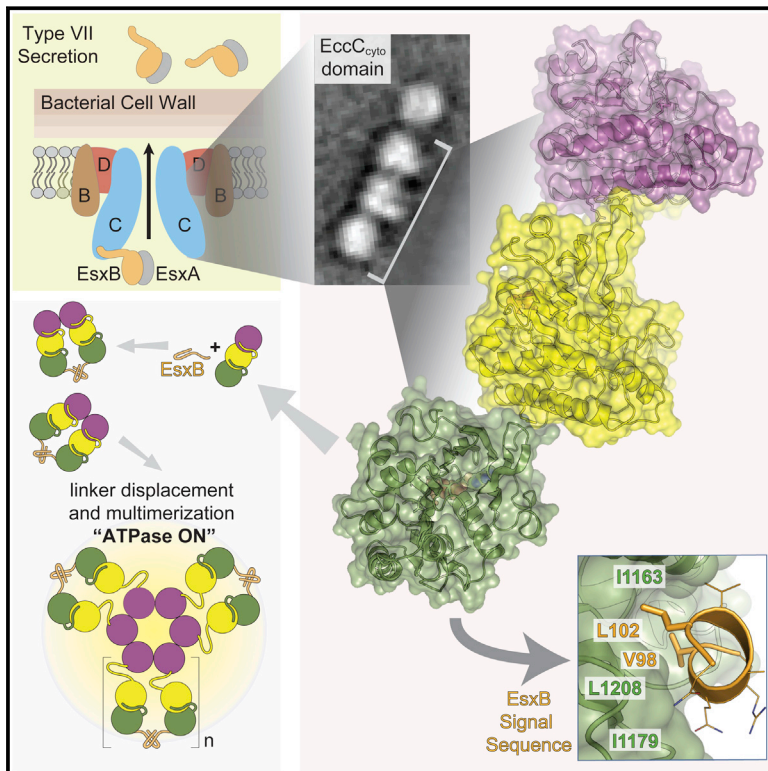
(H) Total hepatic RNA from the same mice described in (G) was analyzed for the expression of IFN- γ by qPCR. Results are expressed as fold induction (f.i.) over LCMV-infected mice injected with PBS, after normalization to the housekeeping gene GAPDH.

Results are expressed as mean \pm SEM. ** $p < 0.01$, *** $p < 0.001$.

- Isogawa, M., Chung, J., Murata, Y., Kakimi, K., and Chisari, F.V. (2013). CD40 activation rescues antiviral CD8⁺ T cells from PD-1-mediated exhaustion. *PLoS Pathog.* 9, e1003490.
- Jacobs, F., Wisse, E., and De Geest, B. (2010). The role of liver sinusoidal cells in hepatocyte-directed gene transfer. *Am. J. Pathol.* 176, 14–21.
- Ji, C., Sastry, K.S.R., Tiefenthaler, G., Cano, J., Tang, T., Ho, Z.Z., Teoh, D., Bohini, S., Chen, A., Sankuratri, S., et al. (2012). Targeted delivery of interferon- α to hepatitis B virus-infected cells using T-cell receptor-like antibodies. *Hepatology* 56, 2027–2038.
- Johnsson, C., Hällgren, R., Elvin, A., Gerdin, B., and Tufveson, G. (1999). Hyaluronidase ameliorates rejection-induced edema. *Transpl. Int.* 12, 235–243.
- Lang, P.A., Contaldo, C., Georgiev, P., El-Badry, A.M., Recher, M., Kurrer, M., Cervantes-Barragan, L., Ludewig, B., Calzascia, T., Bolinger, B., et al. (2008). Aggravation of viral hepatitis by platelet-derived serotonin. *Nat. Med.* 14, 756–761.
- Lee, W.-Y., and Kubes, P. (2008). Leukocyte adhesion in the liver: distinct adhesion paradigm from other organs. *J. Hepatol.* 48, 504–512.
- Manjunath, N., Shankar, P., Wan, J., Weninger, W., Crowley, M.A., Hieshima, K., Springer, T.A., Fan, X., Shen, H., Lieberman, J., and von Andrian, U.H. (2001). Effector differentiation is not prerequisite for generation of memory cytotoxic T lymphocytes. *J. Clin. Invest.* 108, 871–878.
- Masopust, D., Vezys, V., Marzo, A.L., and Lefrançois, L. (2001). Preferential localization of effector memory cells in nonlymphoid tissue. *Science* 291, 2413–2417.
- McDonald, B., McAvoy, E.F., Lam, F., Gill, V., de la Motte, C., Savani, R.C., and Kubes, P. (2008). Interaction of CD44 and hyaluronan is the dominant mechanism for neutrophil sequestration in inflamed liver sinusoids. *J. Exp. Med.* 205, 915–927.
- Mueller, S.N. (2013). Effector T-cell responses in non-lymphoid tissues: insights from in vivo imaging. *Immunol. Cell Biol.* 91, 290–296.
- Sironi, L., Bouzin, M., Inverso, D., D'Alfonso, L., Pozzi, P., Cotelli, F., Guidotti, L.G., Iannacone, M., Collini, M., and Chirico, G. (2014). In vivo flow mapping in complex vessel networks by single image correlation. *Sci. Rep.* 4, 7341.
- Sitia, G., Iannacone, M., Aiolfi, R., Isogawa, M., van Rooijen, N., Scozzesi, C., Bianchi, M.E., von Andrian, U.H., Chisari, F.V., and Guidotti, L.G. (2011). Kupffer cells hasten resolution of liver immunopathology in mouse models of viral hepatitis. *PLoS Pathog.* 7, e1002061.
- Sprinzi, M.F., Oberwinkler, H., Schaller, H., and Protzer, U. (2001). Transfer of hepatitis B virus genome by adenovirus vectors into cultured cells and mice: crossing the species barrier. *J. Virol.* 75, 5108–5118.
- Straub, A.C., Stolz, D.B., Ross, M.A., Hernández-Zavala, A., Soucy, N.V., Klei, L.R., and Barchowsky, A. (2007). Arsenic stimulates sinusoidal endothelial cell capillarization and vessel remodeling in mouse liver. *Hepatology* 45, 205–212.
- Tonti, E., Jiménez de Oya, N., Galliverti, G., Moseman, E.A., Di Lucia, P., Amabile, A., Sammiceli, S., De Giovanni, M., Sironi, L., Chevrier, N., et al. (2013). Bisphosphonates target B cells to enhance humoral immune responses. *Cell Rep.* 5, 323–330.
- von Andrian, U.H., and Mackay, C.R. (2000). T-cell function and migration. Two sides of the same coin. *N. Engl. J. Med.* 343, 1020–1034.
- Ware, J., Russell, S., and Ruggeri, Z.M. (2000). Generation and rescue of a murine model of platelet dysfunction: the Bernard-Soulier syndrome. *Proc. Natl. Acad. Sci. USA* 97, 2803–2808.
- Warren, A., Le Couteur, D.G., Fraser, R., Bowen, D.G., McCaughan, G.W., and Bertolino, P. (2006). T lymphocytes interact with hepatocytes through fenestrations in murine liver sinusoidal endothelial cells. *Hepatology* 44, 1182–1190.
- Wieland, S.F., and Chisari, F.V. (2005). Stealth and cunning: hepatitis B and hepatitis C viruses. *J. Virol.* 79, 9369–9380.
- Wong, C.H.Y., Jenne, C.N., Lee, W.Y., Léger, C., and Kubes, P. (2011). Functional innervation of hepatic iNKT cells is immunosuppressive following stroke. *Science* 334, 101–105.
- Wong, C.H.Y., Jenne, C.N., Petri, B., Chrobok, N.L., and Kubes, P. (2013). Nucleation of platelets with blood-borne pathogens on Kupffer cells precedes other innate immunity and contributes to bacterial clearance. *Nat. Immunol.* 14, 785–792.
- Zheng, Z., Katoh, S., He, Q., Oritani, K., Miyake, K., Lesley, J., Hyman, R., Hamik, A., Parkhouse, R.M., Farr, A.G., and Kincade, P.W. (1995). Monoclonal antibodies to CD44 and their influence on hyaluronan recognition. *J. Cell Biol.* 130, 485–495.

Substrates Control Multimerization and Activation of the Multi-Domain ATPase Motor of Type VII Secretion

Graphical Abstract



Authors

Oren S. Rosenberg, Dustin Dovala, ..., Robert M. Stroud, Jeffery S. Cox

Correspondence

jeffery.cox@ucsf.edu

In Brief

To be translocated by the bacterial type VII secretion apparatus, the virulence protein EsxB first has to help to assemble and activate the secretion structure.

Highlights

- X-ray and EM structures reveal the structure of the type VII secretion ATPase EccC
- EccC is a unique, linear array of three interlocking ATPase domains
- The secretion substrate EsxB binds to an unexpected pocket on the third ATPase domain
- Binding of substrates controls multimerization and activation of EccC



Substrates Control Multimerization and Activation of the Multi-Domain ATPase Motor of Type VII Secretion

Oren S. Rosenberg,^{1,7} Dustin Dovala,^{2,7} Xueming Li,³ Lynn Connolly,^{1,5} Anastasia Bendebury,² Janet Finer-Moore,⁴ James Holton,^{4,6} Yifan Cheng,⁴ Robert M. Stroud,⁴ and Jeffery S. Cox^{2,*}

¹Division of Infectious Diseases, Department of Medicine, UCSF Medical Center, University of California, San Francisco, San Francisco, CA 94143-0654, USA

²Department of Microbiology and Immunology, Program in Microbial Pathogenesis and Host Defense, University of California, San Francisco, San Francisco, CA 94158, USA

³School of Life Sciences, Tsinghua University, Beijing 100084, China

⁴Department of Biophysics and Biochemistry, University of California, San Francisco, San Francisco, CA 94158, USA

⁵Achaogen, Inc., South San Francisco, CA 94080, USA

⁶Lawrence Berkeley National Laboratory, MS6-2100, Berkeley, CA 94720, USA

⁷Co-first author

*Correspondence: jeffery.cox@ucsf.edu

<http://dx.doi.org/10.1016/j.cell.2015.03.040>

SUMMARY

Mycobacterium tuberculosis and *Staphylococcus aureus* secrete virulence factors via type VII protein secretion (T7S), a system that intriguingly requires all of its secretion substrates for activity. To gain insights into T7S function, we used structural approaches to guide studies of the putative translocase EccC, a unique enzyme with three ATPase domains, and its secretion substrate EsxB. The crystal structure of EccC revealed that the ATPase domains are joined by linker/pocket interactions that modulate its enzymatic activity. EsxB binds via its signal sequence to an empty pocket on the C-terminal ATPase domain, which is accompanied by an increase in ATPase activity. Surprisingly, substrate binding does not activate EccC allosterically but, rather, by stimulating its multimerization. Thus, the EsxB substrate is also an integral T7S component, illuminating a mechanism that helps to explain interdependence of substrates, and suggests a model in which binding of substrates modulates their coordinate release from the bacterium.

INTRODUCTION

While all cells secrete proteins through the conserved Sec system, bacteria also utilize specialized secretion systems to interact with their environment (Waksman, 2012). These systems are particularly important for bacterial pathogens, as they allow for regulated secretion of virulence factors into eukaryotic cells during infection. The type VII secretion (T7S) system, the only specialized secretion system found exclusively in Gram-positive bacteria (Huppert et al., 2014; Waksman, 2012), is required for virulence of several bacterial pathogens, including *Mycobacte-*

rium tuberculosis (Guinn et al., 2004; Houben et al., 2014; Hsu et al., 2003; Stanley et al., 2003), *Mycobacterium marinum* (Davis and Ramakrishnan, 2009; Gao et al., 2004), and *Staphylococcus aureus* (Burts et al., 2005). The significance of this secretion system is further highlighted by the fact that loss of the ESX-1 T7S system in *M. tuberculosis* is the most important genetic difference between virulent strains that cause tuberculosis and the live attenuated vaccine strain, BCG (Brodin et al., 2006; Mahairas et al., 1996; Pym et al., 2003). However, despite its medical importance and its broad evolutionary conservation, the molecular architecture, mechanism of secretion, and regulation of T7S are unknown.

T7S systems have been identified in many Gram-positive organisms and are defined by the presence of two conserved elements: EccC, a membrane-bound protein with three predicted ATPase domains, and EsxB, a small secretion substrate containing a WXG motif (Bitter et al., 2009; Pallen, 2002). Other components have been genetically linked to T7S, but these are not universally conserved (Abdallah et al., 2007). EccC and EsxB interact physically (Stanley et al., 2003), and the last seven amino acids of EsxB constitute a “signal sequence” that is necessary and sufficient for secretion through the ESX-1 system (Champion et al., 2006), although additional signals adjacent to these sequences are also required for full secretion (Daleke et al., 2012; Sysoeva et al., 2014). The molecular basis of T7S substrate-targeting selection is not known, and our understanding of substrate recognition has been mostly limited to yeast two-hybrid and genetic studies. One interesting feature of T7S is that substrates are co-dependent for secretion (Fortune et al., 2005), in that genetic removal of one substrate abrogates secretion of all other substrates through a specific T7S system. This unique feature of T7S has complicated the study of individual virulence factors in the context of infection and has thwarted attempts to genetically engineer these systems to secrete heterologous proteins.

EccC has a unique multi-domain structure consisting of a two-pass transmembrane domain, a short domain of unknown function (DUF), and three P loop NTPase domains that share ~20%

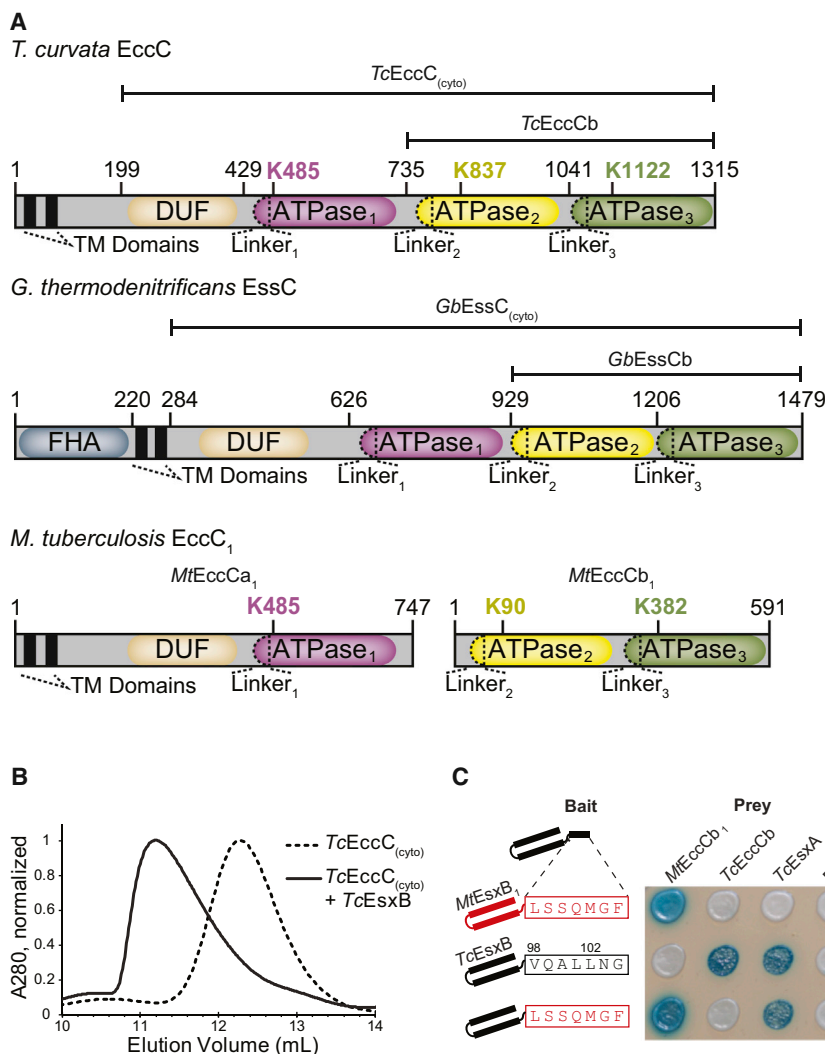


Figure 1. The EccC ATPase Has a Unique, Conserved Domain Structure and Binds to the EsxB Signal Sequence

(A) Domain structure of the EccC and EssC ATPases.

(B) Size exclusion chromatography showing that *TcEsxB* binds to *TcEccC*_(cyto) and induces a large shift in elution volume.

(C) Yeast two-hybrid analysis of interactions between EccC and EsxB. Wild-type *TcEsxB* and *MtEsxB*₁ are directed specifically to their cognate ATPase via the last seven amino acids (boxed), which are not required for interaction with EsxA. See also Figure S1.

the cell, are also necessary components of the secretion apparatus itself, and provide a mechanistic explanation for the unique interdependence of substrate secretion in T7S.

RESULTS

The EsxB Signal Sequence Binds the EccC Translocase but Does Not Activate Its ATPase Activity

To understand the nature of the interaction between EccC and EsxB using an in vitro system, we screened a panel of EccC/EsxB pairs from various bacterial species and found robust expression in *E. coli* of the cytoplasmic portion of EccC from the thermophilic actinobacterium *Thermomonospora curvata* (*TcEccC*_(cyto)) and its cognate EsxB partner (*TcEsxB*). The *T. curvata* secretion system shares close homology with other actinomycete T7S systems and contains all of the conserved

identity to one another (Figure 1A). The ATPase domains are evolutionarily related to the ASCE (additional strand conserved glutamate) fold family that includes protein and DNA-directed mechanoenzymes such as FtsK, VirD4 (TrwB), and VirB4 (TrwK) (Erzberger and Berger, 2006). These motor proteins generally assemble into hexameric rings with the ATPase activity dependent on “arginine finger” residues that extend into adjacent monomers to form the active site (Ahmadian et al., 1997). The individual ATPase domains of EccC are unique in that each has a long N-terminal linker that is of unknown function but contains several motifs that are highly conserved among all of the EccC proteins.

We present here a series of structures of EccC, both with and without the EsxB signal sequence, that reveal that EccC exists in an autoinhibited state as a tightly integrated set of three ATPase domains joined to one another through specific linker/pocket interactions. We show that EccC activity is activated by disruption of one of these linker interactions and is further activated through substrate-mediated multimerization of the enzyme. Our findings suggest that substrates, in addition to serving roles outside of

components identified in the *M. tuberculosis* Esx systems, including EsxA, EsxB, EccC, EccD, EccB, and MycP1 (Bitter et al., 2009) (Figure S1A). *TcEccC*_(cyto), *TcEsxA*, and *TcEsxB* were all stable in isolation and strongly bound one another to form an EccC:EsxB:EsxA complex (Figure 1B; Figures S1B and S1C). Similar to yeast two-hybrid studies with *M. tuberculosis* proteins (Champion et al., 2006), the last seven amino acids of *TcEsxB* specifically targeted the substrate to *TcEccC*, and swapping this sequence with the C terminus of *MtEsxB*₁ completely reversed the specificity (Figure 1C). Thus, the known EccC interactions of the virulence-associated ESX-1 system of *M. tuberculosis* are recapitulated in our model system.

In the ESX-1 system in *M. tuberculosis*, *MtEccC* is split into two polypeptides, *MtEccCa* (containing the trans- and juxta-membrane regions and ATPase₁) and *MtEccCb* (containing ATPase₂ and ATPase₃), which interact with one another to form a complete *MtEccCab* complex (Stanley et al., 2003). The substrate *MtEsxB* interacts exclusively with *MtEccCb* and not with *MtEccCa*, and we found this feature was conserved in our *T. curvata* system. When we artificially split *TcEccC*

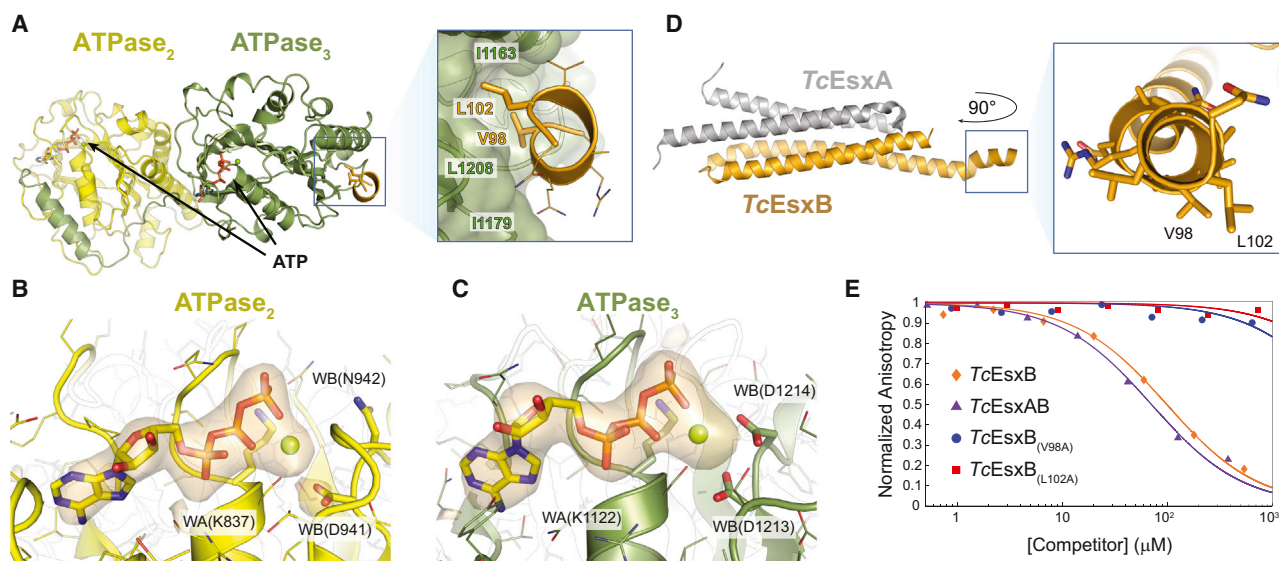


Figure 2. Co-Crystal Structure Reveals Signal-Sequence Binding Pocket in TcEccCb

(A) The crystal structure of TcEccCb (ATPase domains colored as in Figure 1A) bound to the C-terminal signal sequence of TcEsxB (gold). Binding of the C-terminal amino acids of TcEsxB to ATPase₃ is mediated by interactions with two conserved hydrophobic residues that bind in a hydrophobic binding pocket. Only the C-terminal signal-sequence residues are interpretable in the electron density (Figure S2A), and the Y-X-X-X-D/E motif implicated in secretion (Daleke et al., 2012) appears disordered in the crystal.

(B and C) The orange volume represents the simulated-annealing difference-density map calculated for ATPase₂ (B) and ATPase₃ (C) without nucleotide and contoured at 4 σ .

(D) X-ray structure of the TcEsxAB heterodimer with a close-up view of the C-terminal signal-sequence helix. V98 and L102, which are necessary for binding to TcEccC, are labeled.

(E) Binding of a fluorescently labeled signal-sequence peptide (5-FAM-VNVRVQALLNG) to TcEccC_(cyto) monitored in the presence of increasing concentrations of unlabeled competing full-length TcEsxB. Wild-type TcEsxB and TcEsxAB heterodimer compete with the peptide. Mutations in L102 or V98 prevent competition with the wild-type peptide, indicating that they do not bind. Presented data are representative experiments.

See also Figure S2.

into “TcEccCa” and “TcEccCb” fragments orthologous to the tuberculosis ESX-1 proteins, these fragments interacted robustly in the two-hybrid assay (Figure S1B). Likewise, EsxB interacted directly with TcEccCb, but not TcEccCa, which parallels the ESX-1 system (Figures S1B and S1D).

In analogy with other phylogenetically related translocases (Guglielmini et al., 2013), which are often strongly activated by their substrates (Massey et al., 2006), we hypothesized that binding of TcEccC_(cyto) to the substrate TcEsxB would activate its ATPase domains. However we could not measure any ATPase activity in the TcEccC_(cyto) or TcEccCb proteins, either in the presence or absence of TcEsxB (Figure S1E). Likewise, the nucleotide binding state of EccC had no effect on the apparent K_D of signal-sequence binding (Figure S1F). This unexpected result suggested that the binding to EccC does not immediately lead to work being done on the substrate.

The Structure of TcEccCb Bound to the Signal Sequence

In order to understand the interaction between EsxB and EccC, we solved the structure of TcEccCb (containing ATPase₂ and ATPase₃) using data to 3.24 Å resolution, in combination with a peptide containing the last 23 residues of the TcEsxB substrate, including the C-terminal signal sequence (Figure 2A; Figure S2A and Table S2). Both ATPase₂ and ATPase₃ are clearly bound to ATP in the structure (Figures 2B and 2C), suggesting that the

ATPase activity of these domains is indeed extremely low, even in the presence of saturating amounts of EsxB signal-sequence peptide. This ATPase-inactivated state appears to be evolutionarily conserved, as a high-resolution crystal structure of a fragment of the related EssC ATPase from *Geobacillus thermodenitrificans* (“GbEssCb”) has a very similar structure, with both domains bound to ATP (Figure S2B).

The C terminus of the signal-sequence peptide, which was previously thought to be unstructured (Renshaw et al., 2005), forms a short amphipathic helix (residues 96–103) that interacts exclusively with the hydrophobic pocket on ATPase₃ (pocket₃) (Figure 2A). This C-terminal helix is likely a common feature of all EsxB homologs (Poulsen et al., 2014). The helix was also present in a higher-resolution structure of the full-length TcEsxBA complex in the absence of ATPase₃ (Figure 2D and Table S2). Here, we observed the characteristic helical hairpin seen in all EsxB homolog proteins; however, in our structure, the chain makes a turn through a short extended region (residues 93–95) before ending in a helix that matches the length of helix observed in the ATPase complex structure. Of note, this helix is found in a crystal contact with an adjacent symmetry related molecule, which could artificially stabilize the helical structure. Although present in the EsxB fragment crystallized with EccC, the Y-X-X-X-D/E motif implicated in secretion (Daleke et al., 2012; Sysoeva et al., 2014) was disordered in our crystal, suggesting that it is

not involved in recognition of the signal-sequence motif. Importantly, pocket₃ is distant from the ATP catalytic site, and binding of the peptide does not appear to alter the ATP binding ability of ATPase₃. Mutation of any of the EsxB interaction residues on either EsxB or EccC completely abrogated the interaction, demonstrating the specificity of its binding to pocket₃ (Figures 2E and S2C). Together, these data show that TcEsxB is targeted to TcEccCb through specific binding to the hydrophobic pocket₃ on ATPase₃, but binding of the C terminus of TcEsxB neither requires nor enhances nucleotide hydrolysis or exchange.

Because EccC lacked ATPase activity with or without substrate, we examined the evolutionary conservation of each ATPase domain among many unique EccC orthologs to determine whether the residues required for ATPase activity are conserved. We found that the catalytic residues of ATPase₂ and ATPase₃ are highly degenerate with respect to other related ATPases, especially in the catalytic glutamate of the Walker B motif (Figure S2D). Such changes might be expected to greatly reduce or eliminate ATP hydrolysis (Wendler et al., 2012), which is consistent with the presence of ATP in these domains observed in our crystal structures. In contrast, ATPase₁ is highly conserved with its closest known homolog, the motor protein FtsK, suggesting that ATPase₁ may serve as the active motor domain for EccC. Thus, ATPase₂ and ATPase₃ appear to be naturally suboptimal ATPases, similar to the catalytically inactive domains of other multimeric ATPases such as dynein (Carter et al., 2011) and the F₁-ATPase (Walker, 2013).

ATPase₁ Is Inhibited by Its Interaction with ATPase₂

To understand the structure of ATPase₁ and its relationship to ATPase₂ and ATPase₃, we solved the crystal structure of the full cytoplasmic domain of TcEccC, “TcEccC_(cyto),” using data to 2.9 Å resolution (Figure 3A; Figures S3A and S3B; Table S3). Although the full protein is present in the crystal (Figure S3C), the N-terminal “DUF” domain and linker₁ are disordered in the structure and could not be modeled. The structure is monomeric, as it is in solution (Figure S3D), and ATPase₂ and ATPase₃ are very similar in both their conformation and nucleotide binding state compared to the TcEccCb structure (RMSD 0.7 Å), showing that binding of the signal sequence does not alter EccC’s structure in these domains. The interface between ATPase₁ and ATPase₂ is remarkably similar to the interface between ATPase₂ and ATPase₃, joining together the three domains in a direct translation where the only interfaces between the domains are mediated by the inter-domain linkers. Highlighting the general importance of these linker interactions, removal of the N-terminal 34 amino acids homologous to linker₂ on MtEccCb completely blocked binding to MtEccCa (Figures S3E and S3F). Single-particle electron microscopy and 3D reconstruction of TcEccC_(cyto) and a related ATPase from *Geobacillus thermodenitrificans* revealed a similar monomeric structure that was remarkably rigid, as illustrated in the homogeneity of the class averages (Figures 3B and 3C; Figures S3G, S3H, S3I, and S3J). The DUF domain, which is required for secretion in vivo (Figure S3K), is also visible in these images, though its density is reduced, likely due to averaging of multiple flexible states.

In ATPase₁, the nucleotide binding residues and nucleotide loading are strikingly different from the other two domains (Fig-

ures 3D and 3E). Despite the high ATP concentration in the crystallization solution (5 mM), ATPase₁ contains a sulfate ion in the active site (Figure 3A), whereas ATPase₂ and ATPase₃ are bound to ATP as they were in the signal-sequence-bound structure (Figure 2). Several structural features of the ATPase₁ catalytic site are strongly reminiscent of the ATP “empty” (β_E) subunit of the F₁-ATPase (Figures 3D and 3E), which is known to have a very low affinity for nucleotide (Menz et al., 2001; Senior, 2012). In particular, the Walker A lysine is rotated into an unfavorable rotamer and is bound to the Walker B aspartate, displacing the binding of magnesium in the active site and likely preventing binding of ATP. An analysis of all P loop ATPases in the Protein Data Bank (Berman et al., 2002) that contain both ATP-bound and ATP-unbound subunits in the asymmetric unit found that this configuration of the enzymatic residues in the ATP binding site is very unusual under these conditions and is essentially restricted to structural models of the empty state of the F₁-ATPase (Figures 3F and 3G and Table S4).

Despite the low-affinity state in the crystal, the ability of ATPase₁ to bind ATP is required in vivo (Figures 3H and Figures S3L, S3M, and S3N), showing that cycling of ATPase₁ into an ATP avid conformation is required for the function of the secretion system. We conclude that we have captured a low-nucleotide-affinity state of ATPase₁ that must be reversed during the EccC catalytic cycle.

Overlaying the three ATPase domains revealed that the linker-pocket interactions of ATPase₁ and ATPase₂ are analogous to signal-sequence binding of ATPase₃ (Figure 4A). In particular, the important residues for signal-sequence binding in pocket₃ have clear homologs in the linker₂-pocket₁ interaction (Figure 4B). Since ATPases are often modulated by the effect of N- and C-terminal appendages (Besprozvannaya et al., 2013; Karamanou et al., 1999; Peña et al., 2011), we hypothesized that the attachment between pocket₁ and linker₂ might allosterically regulate ATPase₁, locking it into the low-affinity form seen in the crystal structure and leading to the low catalytic rate we observed in vitro. Much of the interface between ATPase₁ and linker₂ is mediated by a 100% conserved arginine in pocket₁, R543, that interacts with W762 and L763 in linker₂ (Figures 5A and 5B). We reasoned that loss of this interaction might mimic an allosteric effector binding in pocket₁ in a manner analogous to signal-sequence binding to ATPase₃ and might modulate the activity of ATPase₁. Indeed, mutation of R543 to alanine resulted in a sharp increase in EccC ATPase activity (Figure 5C). Additional mutation of an ATPase₁ catalytic residue (E593Q) completely inhibited this activation, suggesting that this increase in ATPase activity is dependent on the activity of ATPase₁. Because R543 does not make any direct interactions with the ATP binding or catalytic residues, these results strongly suggest that the activity of ATPase₁ is modulated allosterically by its interaction with the linker. Mutation of the equivalent residue at the ATPase₂-ATPase₃ interface had no significant effect on the activity of the enzyme. Therefore, we conclude that the activity of ATPase₁ is controlled through its pocket-linker interaction with ATPase₂. Importantly, mutation of R543 to alanine in MtEccCa₁ severely reduced secretion of EsxB by *M. tuberculosis* (Figures S4A and S4B), indicating that the interface between ATPase₁ and ATPase₂ is critical for the secretion process. This is consistent with a model in which this

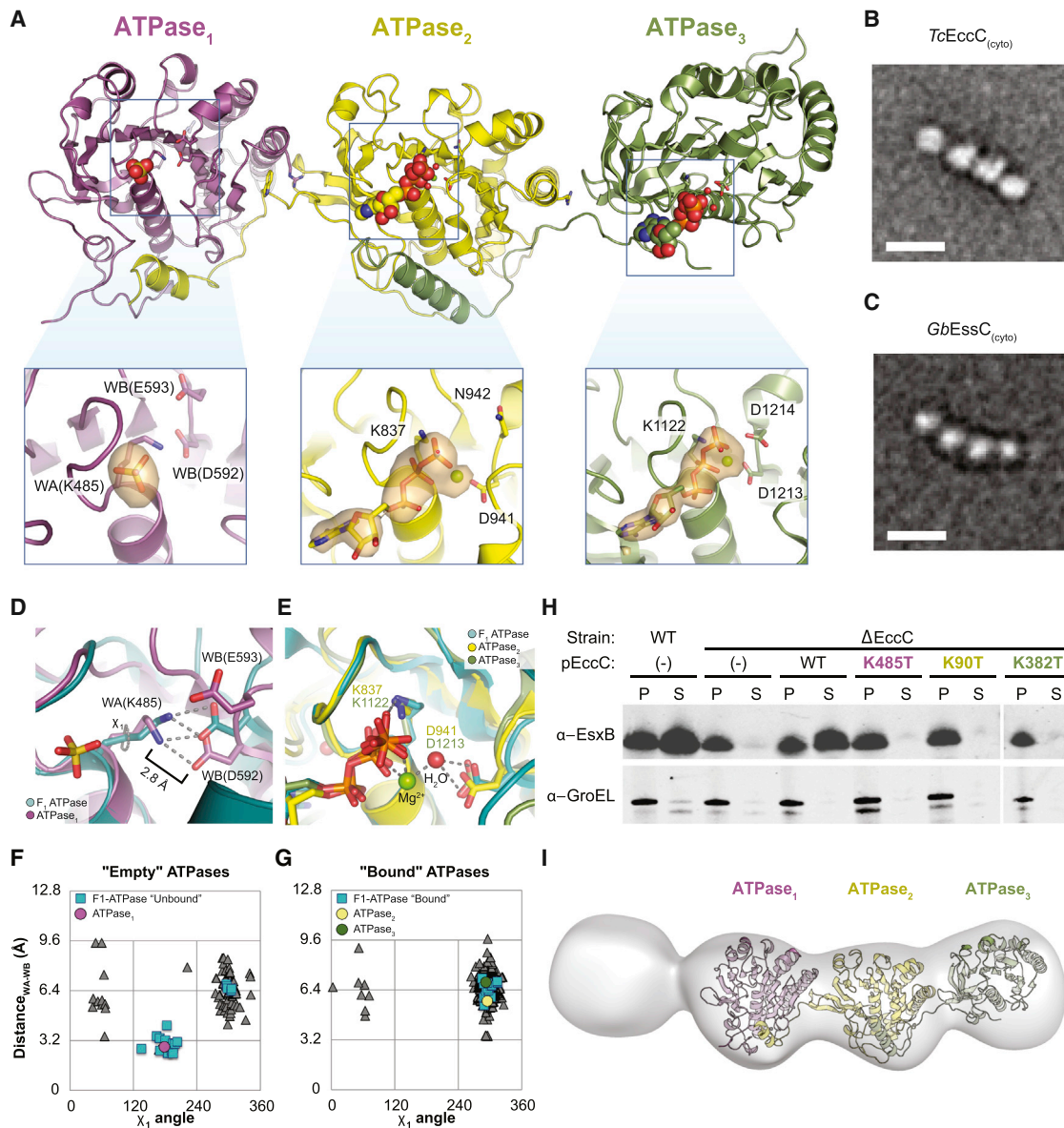


Figure 3. ATPase₁ Is Autoinhibited and Integrated into a Ridged Array of ATPase Domains

(A) The crystal structure of TcEccC_(cyto) highlighting the differences between the ATP-bound catalytic sites of ATPase₂ and ATPase₃ and the nucleotide-free site of ATPase₁. The orange volume represents a simulated-annealing difference-density map calculated without nucleotide or sulfate and contoured at 3 σ . Note that the ATPase₃ insert has been rotated slightly to allow for comparison between the ATPase active sites.

(B and C) Representative EM class average of (B) TcEccC_(cyto) and (C) GbEssC_(cyto) showing the linear structure of EccC. Scale bars, 100 Å.

(D) ATPase₁ (purple), with the "empty" subunit of F₁-ATPase (PDB 1H8H) overlaid in cyan and (E) ATPase₂ (yellow) and ATPase₃ (green) overlaid with the AMP-PNP-bound subunit of F₁-ATPase (cyan) from 1H8H.

(F) A graph representing the distance between the Walker A lysine amino group and the closest Walker B carboxylate oxygen, as a function of the rotameric position of the Walker A lysine. Each triangle represents one of 311 PDB chains of an ATP bound, P loop ATPase identified by our protocol (see [Extended Experimental Procedures](#)). The orientation of the Walker A lysine was confirmed in simulated annealing difference density maps with the lysine residue removed.

(G) A similar graph to (F) except the triangle represents the residues of "empty" ATPases from PDB entries that contain both a bound and unbound P loop ATPase domain in the same file.

(H) Western blot detection of MtEsxB₁ and GroEL from cell supernatants (S) and cell pellet lysate (P) fractions of MtEccC₁ knockout and complemented cells.

(I) Three-dimensional reconstruction at an estimated resolution of 23 Å, based on 1,634 images in the presence of 1 mM ATP- γ S and 10 mM MgCl₂. The model has been contoured to fit the crystal structure. Though it is impossible to resolve the difference between the first and fourth domains, the electron density of one is much lower than the other three, suggesting that this domain is the DUF domain, which is disordered in the crystal structure.

See also [Figure S3](#).

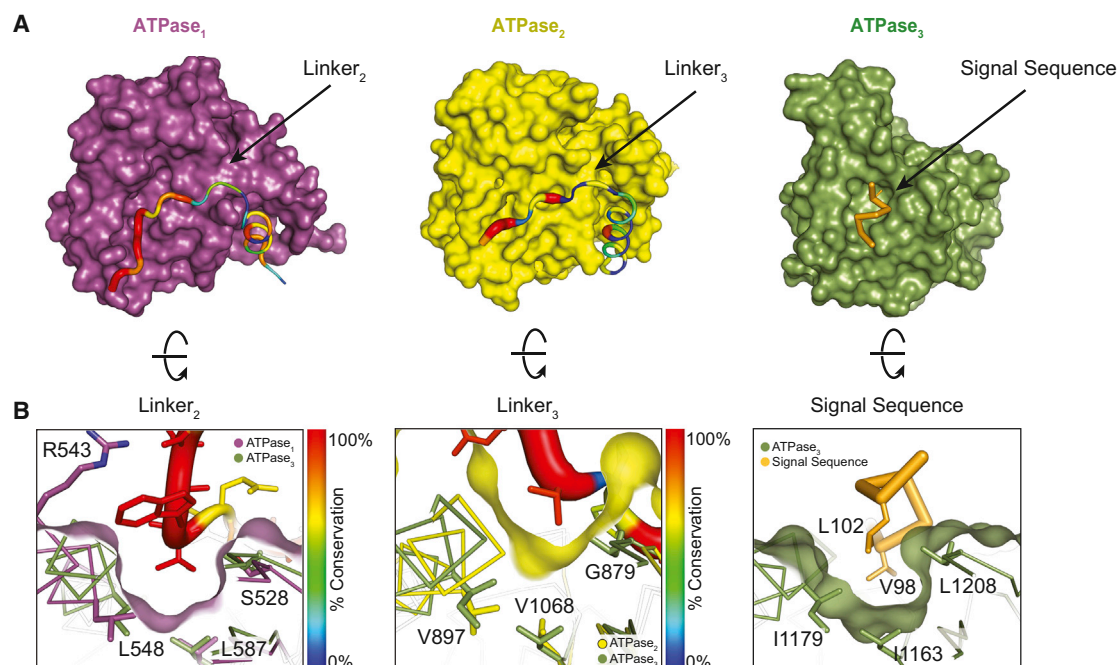


Figure 4. Residues in Linker₂ and Linker₃ Mimic the Substrate and Bind to Pocket₁ and Pocket₂ on TcEccC

(A) The individual ATPase domains are shown and have been rotated to reveal the path of the linker across the ATPase domain. The linker is colored and weighted in diameter according to the degree of conservation across 142 unique EccC sequences.

(B) The surface has been rotated to highlight the linker groove. ATPase₃ and the pocket residues (Figure S2C) overlay ATPase₁ and ATPase₂ to highlight the homologies in the linker binding and signal-sequence binding pockets. The ATPase₂ pocket is significantly shallower than ATPase₁ and ATPase₃.

interface couples substrate recognition in EccCb (ATPase₂ and ATPase₃) with EccCa (ATPase₁) activity.

EccC ATPase Activation by Substrate Binding

In contrast to the wild-type enzyme, addition of TcEsxB to the TcEccC_(cyto, R543A)-activated mutant led to a 5-fold saturating increase in the ATPase activity (Figure 6A), revealing that substrates can contribute to EccC activation if the autoinhibitory interaction between ATPase₁ and ATPase₂ is removed. Mutation of TcEsxB residues responsible for the interaction with ATPase₃ abrogated stimulation, demonstrating that the effect is specific to signal-sequence binding (Figure S4C). However, mutation of the Y-X-X-X-D/E motif in EsxB did not change stimulation by EsxB (Figure S4D), suggesting that these residues likely play a role at a different stage in the secretion cycle. The additional stimulation in response to TcEsxB required ATPase₁ activity, while mutation of the catalytic residues in ATPase₂ and ATPase₃ significantly reduced but did not eliminate overall ATPase activity (Figure S4E). In accord with this finding, ATP binding by ATPase₂ and ATPase₃ is also required for secretion in vivo (Figure 3H). In contrast, ATPase₂ and ATPase₃ alone had no activity and were not stimulated by TcEsxB (Figure 6A). Thus, although binding of ATP by ATPase₂ and ATPase₃ is required for full activity of EccC, these domains act to regulate the activity of ATPase₁ rather than additively contribute to overall ATPase activity. This is consistent with recent genetic evidence that the different ATPase domains play distinct roles during secretion in vivo (Ramsdell et al., 2014).

EccC Activity Is Controlled by Multimerization

Binding of the EsxB signal sequence to ATPase₃ appears to be a simple molecular recognition event (Figure 2), and our results suggest that binding is unlikely to change the conformation of ATPase₁. We thus reasoned that substrate binding could activate EccC via regulating multimerization. Indeed, the related FtsK and TrwB ATPases form multimers during their catalytic cycle in which arginine residues (“R fingers”) complete the active site of neighboring subunits (Gomis-Rüth et al., 2001; Massey et al., 2006; Wendler et al., 2012). ATPase₁ has a completely conserved R finger (Figure S4G and S4H) that is required for secretion in vivo (Figure S4I), implying that formation of the active site of ATPase₁ also involves multimerization. Furthermore, expression of ATPase-deficient versions of EccC in wild-type bacteria has a dominant-negative effect on secretion, consistent with this notion (Ramsdell et al., 2014).

In order to investigate the role of multimerization in the activation of EccC, we measured the dependence of k_{cat} on increasing concentrations of enzyme. In the absence of multimerization, the k_{cat} should be a constant property of the enzyme, but if the catalytic pocket of one ATPase molecule is assembled in *trans* with an arginine donated by a different ATPase molecule, the k_{cat} of the enzyme should increase, as more arginine fingers become available with increasing concentration of enzyme. In the absence of TcEsxB, neither TcEccC_(cyto) nor TcEccC_(cyto, R543A) exhibited concentration-dependent ATPase activation (Figure 6B), suggesting that their

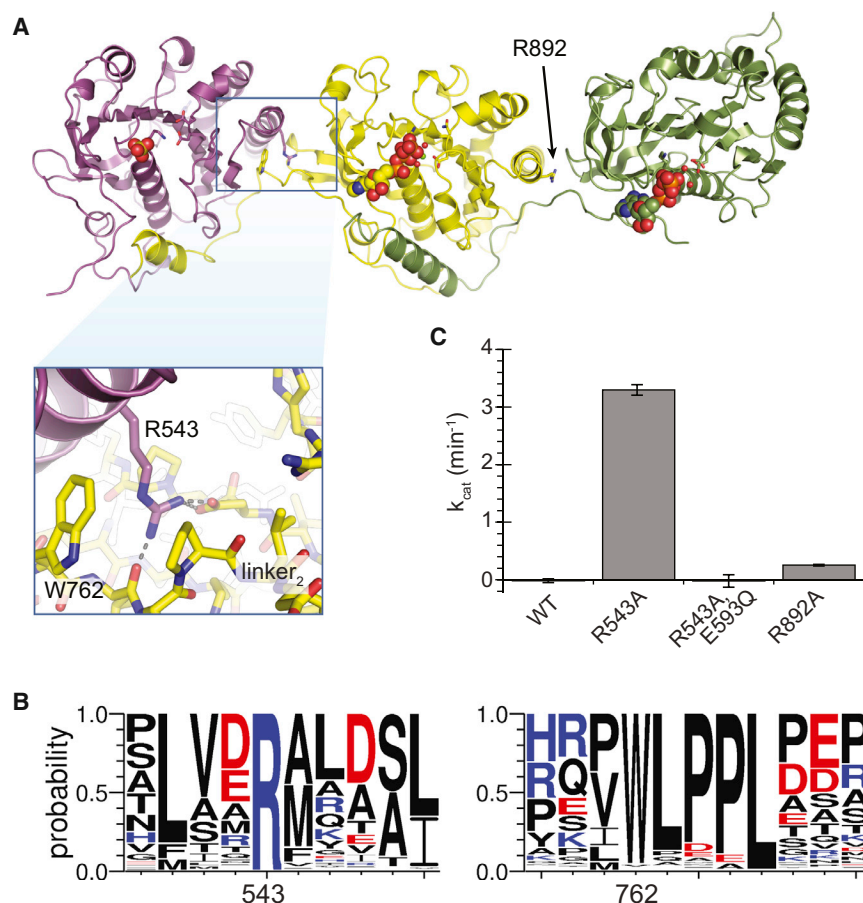


Figure 5. ATPase₁ Is Held in an Autoinhibited State by Inter-ATPase Interactions

(A) Crystal structure of *TcEccC*_(cyto) with inset highlighting the interface between ATPase₁ and ATPase₂.

(B) Logo diagram representing the alignment of 142 unique EccC sequences.

(C) Disruption of ATPase₁-ATPase₂ interface by R543A mutation activates the ATPase activity of *TcEccC*, which requires the Walker B catalytic residue in ATPase₁ (E593Q). An analogous mutation between ATPase₂ and ATPase₃, R892A, led to a small increase in activity. ATPase activity from three independent enzyme preparations was measured in triplicate, and the mean of the means was plotted on the graph. Error bars represent SD of the means. The enzyme concentration was 1 μM ATPase, with saturating ATP \cdot MgCl₂ (10 mM).

See also Figure S4.

EsxB, but Not EsxA or EsxBA, Directly Multimerizes EccC Translocase

To probe the multimeric state of *TcEccC*_(cyto) during active catalysis, we used glutaraldehyde crosslinking to capture higher-order multimers. Crosslinking of *TcEccC*_(cyto, R543A) in the presence of native *TcEsxB* or with the *TcEsxB*-*TcEccC*_(cyto, R543A) fusion revealed both dimer and higher-order oligomeric states that are strongly correlated with activity

(Figure 6A). These oligomers were specific to EccC and did not form with the substrate alone (Figure S5A) or when ATPase was incubated with a signal-sequence mutant, *TcEsxB*_(V98A) (Figures S5C and S5D). Importantly, while *TcEsxB* binding was insufficient to activate ATPase activity of the wild-type enzyme (Figure 6A), it effectively drove *TcEccC*_(cyto) into higher-order complexes (Figures S5B and S5D), indicating that substrate-mediated multimerization is not sufficient to override autoinhibition mediated by ATPase₂. We found that EsxB exists as a homodimer in isolation (Figure S5E), and thus the substrate likely stabilizes multimers by first forming EccC:EsxB:EsxB:EccC complexes. Although the addition of EsxB leads to a clear increase in multimerization of the ATPase, it appears to stabilize a state that occurs in the absence of EsxB, as both crosslinking (Figure S5B) and analytical ultracentrifugation (Figure S4F) experiments revealed a low level of EccC multimerization without EsxB.

Surprisingly, addition of *TcEsxA*, another substrate that forms a tight 1:1 complex with *TcEsxB* (Figure 2D; Figure S5F; Renshaw et al., 2002) but does not directly bind to EccC (Figures S1B and S5G), strongly inhibited ATPase activity in a cooperative manner (Hill coefficient > 2, Figure 6C), suggesting that each *TcEsxA* molecule affects the activity of more than two *TcEccC*_(cyto, R543A)-*TcEsxB* molecules. The higher-order multimer concentration decreased with increasing *TcEsxA* in a pattern that directly mirrored the cooperative decrease in

activity was not dependent on multimerization. In contrast, in the presence of a 10-fold excess of *TcEsxB* (*TcEsxB*+*TcEccC*_(cyto, R543A)), the ATPase activity was strongly concentration dependent. To guarantee a one-to-one molar ratio between *TcEsxB* and *TcEccC*, we fused *TcEsxB* via a flexible 14 amino acid linker to the C terminus of *TcEccC*_(cyto, R543A). This protein was dimeric, as determined by analytical ultracentrifugation (Figure S4F), and similarly to the *TcEsxB*+*TcEccC*_(cyto, R543A) complex, the k_{cat} of this chimera was highly concentration dependent (Figure 6B), with a maximal activity similar to the saturated *TcEsxB*:*TcEccC*_(cyto, R543A) complex (>100-fold over wild-type). Mutation of the R-finger residue in the activated, substrate-ATPase fusion protein (*TcEsxB*-*TcEccC*_(cyto, R543A, R616Q)) reduced its activity down to the baseline activity level of the R543A mutant (Figure S4J). Thus, the R543A mutant does not exhibit concentration-dependent activation in the absence of the substrate and also does not require the R-finger residue for its baseline activity. These data strongly support the idea that the active form of EccC is multimeric, but this state is sparsely populated in the absence of the EsxB substrate. However, the activity of this multimeric form is only manifest in the setting of the permissive R543A mutation. These experiments define a hierarchy of activation where both the effect of the R543A mutation and the multimerization are required for appreciable ATPase activity.

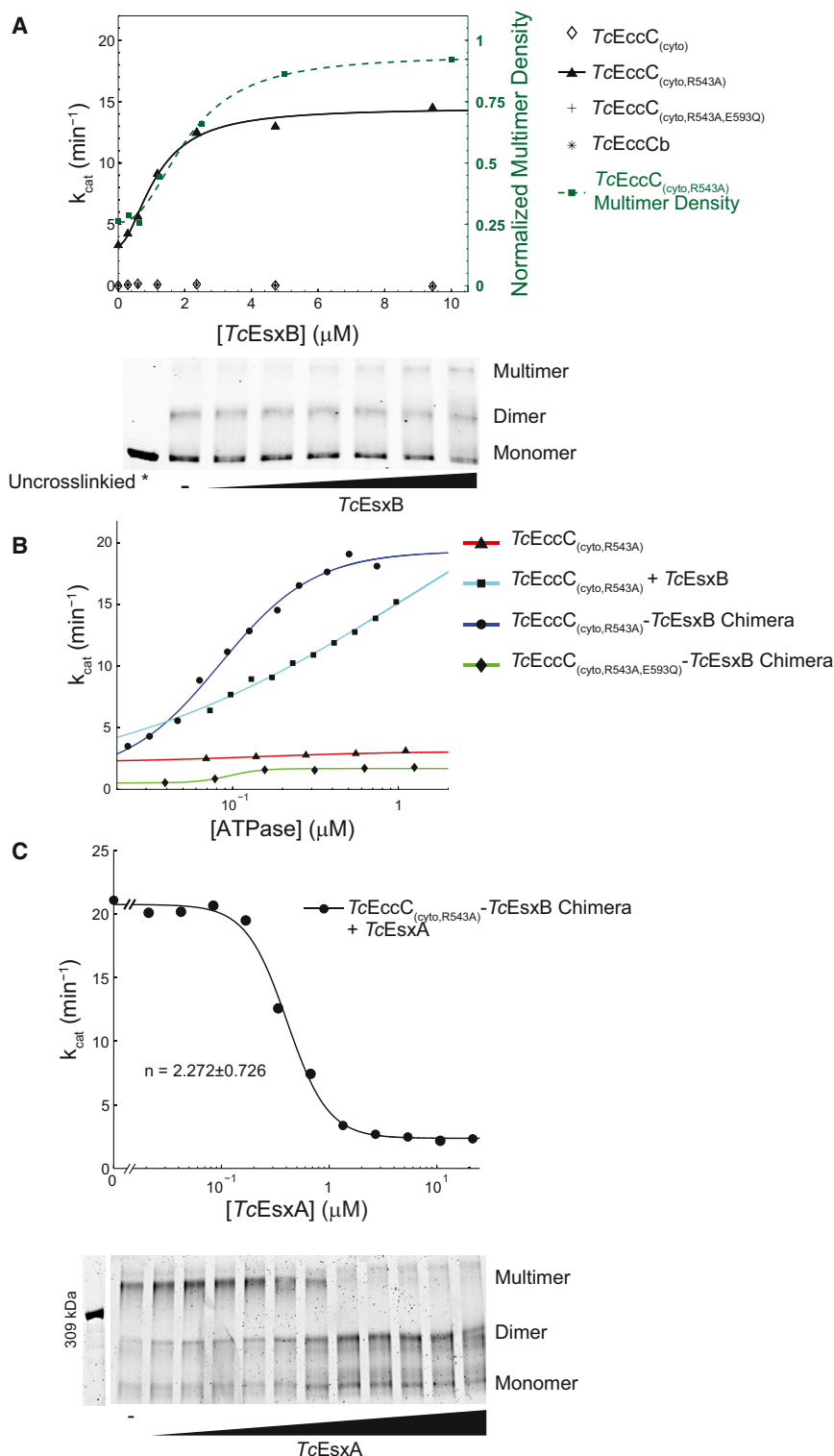


Figure 6. EsxB and EsxA Substrates Control EccC Activity via Regulating Enzyme Multimerization

(A) The ATPase activity of the indicated *TcEccC* proteins was measured at different concentrations of *TcEsxB*. Multimerization of *TcEccC*_(cyto, R543A), detected by glutaraldehyde crosslinking (bottom) increases with addition of *TcEsxB* (0–10 μM). Quantification of the multimer band is also indicated on the ATPase activity graph (green dotted line with squares) to demonstrate correlation between multimer concentration and activity.

(B) ATPase activity of the indicated proteins, either *TcEccC*_(cyto, R543A) +/- *TcEsxB* or *TcEccC*_(cyto, R543A)-*TcEsxB* chimeras, was measured as a function of enzyme concentration. In (B) and (C), each point represents the mean of three independent measurements.

(C) ATPase activity of the *TcEccC*_(cyto, R543A)-*TcEsxB* chimera was measured at different concentrations of *TcEsxA* (top), and multimerization of the enzyme in these reactions was assessed by glutaraldehyde crosslinking followed by SDS-PAGE (bottom, top concentration of *TcEsxA* is 22 μM and concentrations are reduced 2-fold in each lane to the left).

See also Figure S5.

while EsxB homodimers promote assembly and activation of EccC, EsxA binding to EsxB-bound EccC leads to cooperative disassembly and inhibition of the multimeric ATPase.

To test whether EsxA-induced inhibition was due to disruption of the EsxB:EsxB dimerization event, we measured inhibition of ATPase activity in the *TcEsxB-TcEccC*_(cyto, R543A) chimera with increasing concentrations of the signal-sequence mutant *TcEsxB*_(V98A), which can still form homodimers but cannot bind to EccC. We found that *TcEsxB*_(V98A) also inhibits activity (Figure S5K), supporting the notion that EsxA inactivates EccC by removing the stabilizing effect of the EsxB:EsxB interaction, presumably by forming EccC:EsxB:EsxA trimers instead of EccC:EsxB:EsxB:EccC tetramers.

DISCUSSION

In this work we have developed a thermophilic model system that allowed for the detailed dissection of the only two components of T7S conserved in all Gram-

positive bacteria: EccC and EsxB. Based on our findings, we posit a model in which secretory substrates play an active regulatory role in T7S by modulating the activity of EccC (Figure 7). In the absence of EsxB, EccC is monomeric and tightly inactivated

positive bacteria: EccC and EsxB. Based on our findings, we posit a model in which secretory substrates play an active regulatory role in T7S by modulating the activity of EccC (Figure 7). In the absence of EsxB, EccC is monomeric and tightly inactivated

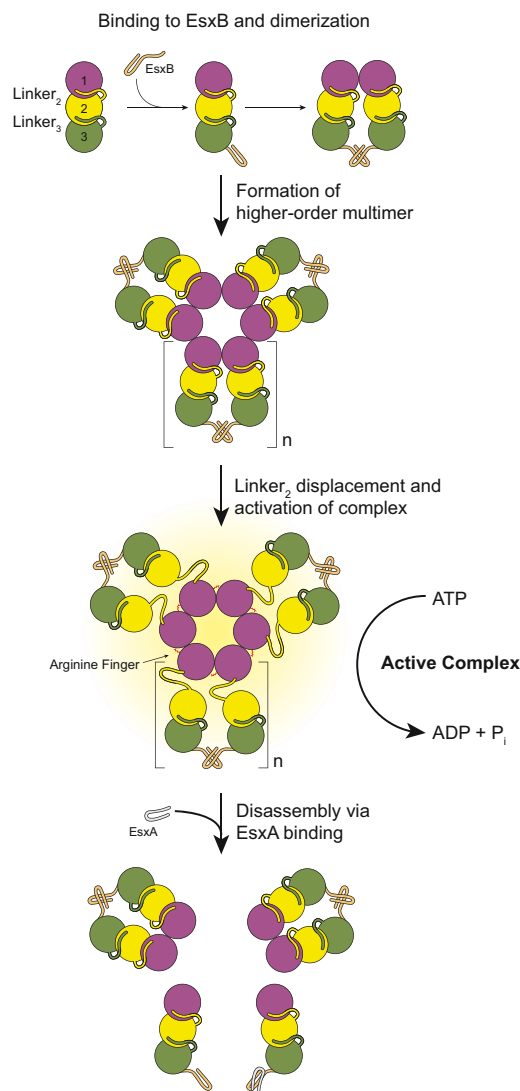


Figure 7. Model of Substrate-Mediated Activation of EccC

In the absence of substrates, EccC is monomeric. Interaction with EsxB leads to dimerization of the ATPase and then higher-order multimerization but cannot activate the enzyme. In this study, we used the R543A mutation to disrupt the interaction between ATPase₁ and ATPase₂, although in vivo this role may be played by other proteins that bind to ATPase₁ analogously to the binding of EsxB to ATPase₃ or other signals. Once ATPase₁ is displaced, EccC is activated further by multimerization mediated by a conserved R finger. EsxA can disrupt the EsxB:EsxB interaction and disassemble the multimer. We have no evidence for the structure of the EccC:EsxB dimer or stoichiometry and structure of the multimeric form. Thus, both of these aspects of the model are speculative, though based on prior structures of related substrate proteins (i.e., 3GVM) and the FtsK-like ATPases (i.e., 2IUU). We have indicated this ambiguity with the variable “n” for the number of subunits in the multimer.

via interactions between ATPase₁ and ATPase₂. EsxB binding to ATPase₃, which is relatively weak ($\sim 10 \mu\text{M}$), drives EccC multimerization but is not sufficient for activation. Allosteric interactions through displacement of linker₂ from pocket₁, which relieves the inhibitory interaction with ATPase₂, are also required to permit activation of EccC. While we do not yet know the nature

of these activation signals, given the linker-pocket architecture found in each ATPase domain, we suspect that other substrates and/or T7S components bind to these pockets to create an “AND” logic gate by which secretion of multiple substrates is coordinated, explaining the phenomenon of mutually dependent type VII secretion (Fortune et al., 2005). The DUF and the transmembrane domains also play an important role in secretion (Figure S3K), and full delineation of their contribution to the process awaits further experimentation.

This model suggests that T7S activity may be governed by a simple, “just-in-time” post-translational control mechanism in which energy is expended only when key substrates are recognized by EccC (Bozdech et al., 2003). T7S may be poised for secretion under all conditions, with EccC waiting for delivery of complete sets of substrates, which would explain why removal of one substrate would inhibit secretion of others. In this way, T7S may not be directly regulated by environmental stimuli but, rather, actuated by signal transduction pathways that regulate synthesis of substrates, such as PhoP/R (Ryndak et al., 2008) and EspR (Raghavan et al., 2008). Although other control mechanisms may be in play, this mode of regulation would not only conserve ATP consumption until it is needed, but would also allow for coordinate secretion of multiple substrates, a function that may be beneficial for the organism.

Our results also suggest that EsxB homodimers, in addition to EsxAB heterodimers (Renshaw et al., 2002), play an important role in type VII secretion, a notion supported by the observation that ancestral T7S systems, such as those found in the phylum firmicutes, lack EsxA homologs and EsxB exists solely as a homodimer (Poulsen et al., 2014). Experimental evidence from the literature also supports the idea that EsxB dimers have an important physiological role. For example, recent work shows that EsxB in *Bacillus subtilis* is secreted as a dimer (Sysoeva et al., 2014). Likewise, at least four unique crystal structures of different EsxB homodimers from various bacterial species have been deposited in the Protein Data Bank, including 2VRZ (Sundaramoorthy et al., 2008), 3GVM (Poulsen et al., 2014), 3ZBH, and 3O9O. Taken together, we believe that these results provide compelling evidence for the role of EsxB homodimers in vivo and support a model that one role of EsxA is to antagonize the stimulatory effects of EsxB on EccC. How substrates are actually translocated out of the cell upon binding EccC, the oligomeric state of substrates during translocation, and how EccC and/or other T7S proteins modify substrates before export remain important questions that require further study.

Most motor proteins only display maximal ATPase activity in the presence of a mechanical load. Indeed, the activity of EccC, even when activated by the substrate and the R543A mutation, is relatively low. We believe that the activity we measure likely represents a basal ATPase rate without the “load” of substrates to be translocated across a membrane. A graded activation of ATPase function is reminiscent of the activation of SecA translocase. In this case, SecA is nearly inactive when cytosolic (Lill et al., 1990) but is partially activated by its interaction with SecYEG, which releases an interdomain, allosteric inhibition in SecA leading to an increase in ATPase activity (Karamanou et al., 2007). The motor is thus primed for the translocation

reaction, which is stimulated by its interaction with the signal-sequence-bearing protein (Chatzi et al., 2014).

Our structural analysis shows other intriguing similarities to the Sec translocation system. The Sec translocase binds to a similar, small helical peptide using mixed electrostatic and hydrophobic interactions. In both cases, the binding occurs in a specialized groove that is distant from the ATPase active site (Gelís et al., 2007), suggesting a role in targeting and orientation of substrates. There are also similarities to targeting of substrates in other secretion systems. For example, in the type III secretion system, a targeting sequence on a chaperone protein, CesAB, is required for interaction with the type III ATPase; however, the actual translocation is mediated by an entirely different signal (Chen et al., 2013). Given that several other regions of the EsxB and EsxA proteins have been implicated in translocation (Daleke et al., 2012; Sysoeva et al., 2014), we suspect that a similar division between targeting and substrate orientation is also present in the type VII system.

The EccC ATPase is phylogenetically related to the T4 secretion system coupling proteins, typified by the VirD4 ATPase in *Agrobacterium tumefaciens* (Guglielmini et al., 2013). These proteins also bind to a C-terminal sequence on substrate proteins that is necessary for secretion, but the molecular interactions and biochemical effects of substrate binding in these systems is unknown (Trokter et al., 2014). In the *A. tumefaciens* system, three monomeric ATPases (VirB4, VirD4 and VirB11) are required for secretion of substrates by the system. It is intriguing to speculate that these three ATPases, which all appear to serve very different mechanistic purposes, may carry out functions analogous to the three ATPase domains of EccC, but this hypothesis awaits further structural information about the assembly and function of EccC and of the T4 secretion ATPases.

Targeting T7S for inhibition is an attractive antibacterial strategy, given the centrality of these systems to pathogenesis in *M. tuberculosis* and *S. aureus* and their wide distribution among Gram-positive bacteria (Chen et al., 2010). Our work suggests two unexpected targets for disruption of the function of T7 secretion. First, small molecules targeted to the inactive state of ATPase_i may stabilize its autoinhibition (Schindler et al., 2000). Second, the interaction pocket for the substrate is quite deep and may be amenable to small molecule targeting. Additionally, knowing the molecular determinants of signal-sequence recognition may also allow us to design improved vaccine strains, which export subsets of immunodominant virulence factors but do not cause disease.

EXPERIMENTAL PROCEDURES

A full description of the methods, reagents, and crystallographic statistics is included in the Extended Experimental Procedures.

Mycobacterial Mutants and Secretion Assays

The $\Delta eccCa_{1M}-\Delta eccCb_{1M}$ deletion strain was created by homologous recombination using specialized transducing phage, as previously described (Glickman et al., 2000). Complementation of the eccC null mutant was carried out by cloning the entire *M. tuberculosis* rv3870-rv3871 locus into an integrating vector containing a C-terminal flag tag and under the control of the predicted native promoter. Secretion assays were performed as described previously (Ohol et al., 2010).

Protein Expression and Purification

Recombinant proteins were subcloned by PCR into a pET vector system and expressed and purified from C41(DE3) strain *E. coli* using standard techniques. Details are available in the Extended Experimental Procedures.

Electron Microscopy

Single particles were picked from uranyl acetate-stained images and processed into classes containing ~60 images. Reconstructions were accomplished as described in the Extended Experimental Procedures.

Crystallization and Structure Solution

Crystallization and structure solution are described in detail in the Extended Experimental Procedures. For the EccC_{TC(199-1315)} structure, initial phases were determined with SAD phasing of a Ta₆Br₁₂ derivative at ~7.5 Å and were then improved by MIR phasing with Pt and Hg derivatives. An anomalous difference map determined by comparison to a selenomethionine derivative assisted model building. The other structures were solved using standard methods.

Biochemical Assays

Steady-state ATPase activity was analyzed using a continuously coupled assay (Kornberg and Pricer, 1951) adapted to a 96 well format.

Fluorescence anisotropy was performed using a 5-FAM-VNRVQALLNG peptide interacting with the EccC_{TC(199-1315)} construct, as described in the Extended Experimental Procedures.

For crosslinking assays, 2–5 µg of total protein was incubated with 0.2% glutaraldehyde for 10 min and then quenched with 1 M Tris (pH 8.0). Denaturing gels were stained with Coomassie or were western blotted. A full description is available in the Extended Experimental Procedures.

Bioinformatics

We attempted to identify all P loop ATPases in the PDB on a per chain basis and then analyzed the position of the Walker A lysine side chain relative to the position of the Walker B aspartic acid using programs designed by the authors. The initial list and the sorted lists described in the text are available in Table S4. Please see the Extended Experimental Procedures for full details.

Genetic Interaction Studies

Directed yeast two-hybrid studies were performed using a LacZ reporter system, as described previously (Champion et al., 2006). Strain names and additional procedures are available in the Extended Experimental Procedures.

SUPPLEMENTAL INFORMATION

Supplemental Information includes Extended Experimental Procedures, five figures, and four tables and can be found with this article online at <http://dx.doi.org/10.1016/j.cell.2015.03.040>.

AUTHOR CONTRIBUTIONS

O.S.R. and D.D. contributed equally to this work. O.S.R. and J.S.C. conceived the research; O.S.R., D.D., X.L., Y.C., R.M.S., and J.S.C. designed experiments; O.S.R., D.D., X.L., L.C., and A.B. collected data; O.S.R., D.D., X.L., J.H., J.F.-M., Y.C., R.M.S., and J.S.C. analyzed data; O.S.R., D.D., and J.S.C. wrote the manuscript. All authors commented on the scientific content of the manuscript.

ACKNOWLEDGMENTS

We acknowledge support from the NIH (K08AI091656 to O.S.R., R01AI081727 and P01AI063302 to J.S.C., and U54GM094625 to R.M.S.) and the NSF (grant no. 1144247 to D.D.). For technical assistance, we thank Rebecca Robbins, Peter Bieling, Jennifer Du Mond, Lara Koehler, R. Stefan Isaac, Yaneth Robles, Diana Romero, Spencer Alexander, and Andrew Rodriguez. For helpful discussions, we thank Ron Vale, John Kuriyan, James Berger, Bennett Penn, Matt Lohse, and Damian Ekiert. We thank R. Rajashankar at the APS beamline

NE-CAT 24ID; George Meigs and Jane Tanamachi at ALS BL 8.3.1; and Tzanko Doukov and Lisa Dunn at SSRL. APS is supported by the U.S. DOE Contract DE-AC02-06CH11357. ALS is supported by the U.S. DOE Contract DE-AC02-05CH11231. The SSRL Structural Molecular Biology Program is supported by the U.S. DOE Office of Biological and Environmental Research and by the NIH-GMS (including P41GM103393).

Received: July 16, 2014

Revised: November 10, 2014

Accepted: February 11, 2015

Published: April 9, 2015

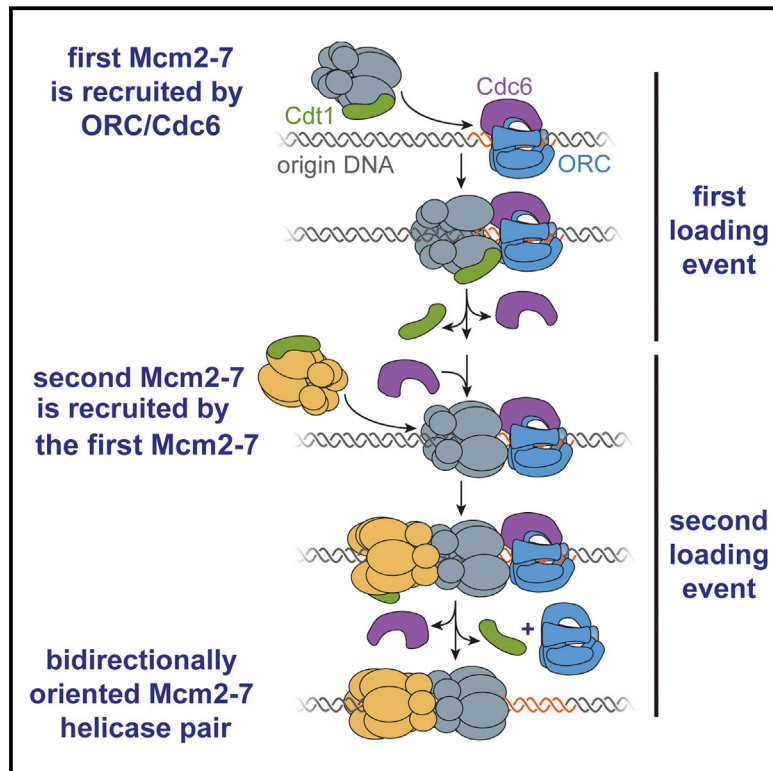
REFERENCES

- Abdallah, A.M., Gey van Pittius, N.C., Champion, P.A.D., Cox, J., Luirink, J., Vandenbroucke-Grauls, C.M.J.E., Appelmek, B.J., and Bitter, W. (2007). Type VII secretion—mycobacteria show the way. *Nat. Rev. Microbiol.* 5, 883–891.
- Ahmadian, M.R., Stege, P., Scheffzek, K., and Wittinghofer, A. (1997). Confirmation of the arginine-finger hypothesis for the GAP-stimulated GTP-hydrolysis reaction of Ras. *Nat. Struct. Biol.* 4, 686–689.
- Berman, H.M., Battistuz, T., Bhat, T.N., Bluhm, W.F., Bourne, P.E., Burkhardt, K., Feng, Z., Gilliland, G.L., Iype, L., Jain, S., et al. (2002). The Protein Data Bank. *Acta Crystallogr. D Biol. Crystallogr.* 58, 899–907.
- Besprozvannaya, M., Pivorunas, V.L., Feldman, Z., and Burton, B.M. (2013). SpoIIIE protein achieves directional DNA translocation through allosteric regulation of ATPase activity by an accessory domain. *J. Biol. Chem.* 288, 28962–28974.
- Bitter, W., Houben, E.N.G., Bottai, D., Brodin, P., Brown, E.J., Cox, J.S., Derbyshire, K., Fortune, S.M., Gao, L.-Y., Liu, J., et al. (2009). Systematic genetic nomenclature for type VII secretion systems. *PLoS Pathog.* 5, e1000507.
- Bozdech, Z., Llinás, M., Pulliam, B.L., Wong, E.D., Zhu, J., and DeRisi, J.L. (2003). The transcriptome of the intraerythrocytic developmental cycle of *Plasmodium falciparum*. *PLoS Biol.* 1, E5.
- Brodin, P., Majlessi, L., Marsollier, L., de Jonge, M.I., Bottai, D., Demangel, C., Hinds, J., Neyrolles, O., Butcher, P.D., Leclerc, C., et al. (2006). Dissection of ESAT-6 system 1 of *Mycobacterium tuberculosis* and impact on immunogenicity and virulence. *Infect. Immun.* 74, 88–98.
- Burts, M.L., Williams, W.A., DeBord, K., and Missiakas, D.M. (2005). EsxA and EsxB are secreted by an ESAT-6-like system that is required for the pathogenesis of *Staphylococcus aureus* infections. *Proc. Natl. Acad. Sci. USA* 102, 1169–1174.
- Carter, A.P., Cho, C., Jin, L., and Vale, R.D. (2011). Crystal structure of the dynein motor domain. *Science* 331, 1159–1165.
- Champion, P.A.D., Stanley, S.A., Champion, M.M., Brown, E.J., and Cox, J.S. (2006). C-terminal signal sequence promotes virulence factor secretion in *Mycobacterium tuberculosis*. *Science* 313, 1632–1636.
- Chatzi, K.E., Sardis, M.F., Economou, A., and Karamanou, S. (2014). SecA-mediated targeting and translocation of secretory proteins. *Biochim. Biophys. Acta* 1843, 1466–1474.
- Chen, J.M., Pojer, F., Blasco, B., and Cole, S.T. (2010). Towards anti-virulence drugs targeting ESX-1 mediated pathogenesis of *Mycobacterium tuberculosis*. *Drug Discov. Today Dis. Mech.* 7, e25–e31.
- Chen, L., Ai, X., Portaliou, A.G., Minetti, C.A.S.A., Remeta, D.P., Economou, A., and Kalodimos, C.G. (2013). Substrate-activated conformational switch on chaperones encodes a targeting signal in type III secretion. *Cell Rep.* 3, 709–715.
- Daleke, M.H., Ummels, R., Bawono, P., Heringa, J., Vandenbroucke-Grauls, C.M., Luirink, J., and Bitter, W. (2012). General secretion signal for the mycobacterial type VII secretion pathway. *Proc. Natl. Acad. Sci. USA* 109, 11342–11347.
- Davis, J.M., and Ramakrishnan, L. (2009). The role of the granuloma in expansion and dissemination of early tuberculous infection. *Cell* 136, 37–49.
- Erzberger, J.P., and Berger, J.M. (2006). Evolutionary relationships and structural mechanisms of AAA+ proteins. *Annu. Rev. Biophys. Biomol. Struct.* 35, 93–114.
- Fortune, S.M., Jaeger, A., Sarracino, D.A., Chase, M.R., Sassetti, C.M., Sherman, D.R., Bloom, B.R., and Rubin, E.J. (2005). Mutually dependent secretion of proteins required for mycobacterial virulence. *Proc. Natl. Acad. Sci. USA* 102, 10676–10681.
- Gao, L.-Y., Guo, S., McLaughlin, B., Morisaki, H., Engel, J.N., and Brown, E.J. (2004). A mycobacterial virulence gene cluster extending RD1 is required for cytotoxicity, bacterial spreading and ESAT-6 secretion. *Mol. Microbiol.* 53, 1677–1693.
- Gelis, I., Bonvin, A.M.J.J., Keramisanou, D., Koukaki, M., Gouridis, G., Karamanou, S., Economou, A., and Kalodimos, C.G. (2007). Structural basis for signal-sequence recognition by the translocase motor SecA as determined by NMR. *Cell* 131, 756–769.
- Gomis-Rüth, F.X., Moncalián, G., Pérez-Luque, R., González, A., Cabezon, E., de la Cruz, F., and Coll, M. (2001). The bacterial conjugation protein TrwB resembles ring helicases and F1-ATPase. *Nature* 409, 637–641.
- Guglielmini, J., de la Cruz, F., and Rocha, E.P. (2013). Evolution of conjugation and type IV secretion systems. *Mol. Biol. Evol.* 30, 315–331.
- Guinn, K.M., Hickey, M.J., Mathur, S.K., Zakel, K.L., Grotzke, J.E., Lewinsohn, D.M., Smith, S., and Sherman, D.R. (2004). Individual RD1-region genes are required for export of ESAT-6/CFP-10 and for virulence of *Mycobacterium tuberculosis*. *Mol. Microbiol.* 51, 359–370.
- Houben, E.N.G., Korotkov, K.V., and Bitter, W. (2014). Take five - Type VII secretion systems of Mycobacteria. *Biochim. Biophys. Acta* 1843, 1707–1716.
- Hsu, T., Hingley-Wilson, S.M., Chen, B., Chen, M., Dai, A.Z., Morin, P.M., Marks, C.B., Padiyar, J., Goulding, C., Gingery, M., et al. (2003). The primary mechanism of attenuation of bacillus Calmette-Guérin is a loss of secreted lytic function required for invasion of lung interstitial tissue. *Proc. Natl. Acad. Sci. USA* 100, 12420–12425.
- Huppert, L.A., Ramsdell, T.L., Chase, M.R., Sarracino, D.A., Fortune, S.M., and Burton, B.M. (2014). The ESX system in *Bacillus subtilis* mediates protein secretion. *PLoS ONE* 9, e96267.
- Karamanou, S., Vrontou, E., Sianidis, G., Baud, C., Roos, T., Kuhn, A., Politou, A.S., and Economou, A. (1999). A molecular switch in SecA protein couples ATP hydrolysis to protein translocation. *Mol. Microbiol.* 34, 1133–1145.
- Karamanou, S., Gouridis, G., Papanikou, E., Sianidis, G., Gelis, I., Keramisanou, D., Vrontou, E., Kalodimos, C.G., and Economou, A. (2007). Preprotein-controlled catalysis in the helicase motor of SecA. *EMBO J.* 26, 2904–2914.
- Kornberg, A., and Pricer, W.E., Jr. (1951). Enzymatic phosphorylation of adenosine and 2,6-diaminopurine riboside. *J. Biol. Chem.* 193, 481–495.
- Lill, R., Dowhan, W., and Wickner, W. (1990). The ATPase activity of SecA is regulated by acidic phospholipids, SecY, and the leader and mature domains of precursor proteins. *Cell* 60, 271–280.
- Mahairas, G.G., Sabo, P.J., Hickey, M.J., Singh, D.C., and Stover, C.K. (1996). Molecular analysis of genetic differences between *Mycobacterium bovis* BCG and virulent *M. bovis*. *J. Bacteriol.* 178, 1274–1282.
- Massey, T.H., Mercogliano, C.P., Yates, J., Sherratt, D.J., and Löwe, J. (2006). Double-stranded DNA translocation: structure and mechanism of hexameric FtsK. *Mol. Cell* 23, 457–469.
- Menz, R.I., Walker, J.E., and Leslie, A.G. (2001). Structure of bovine mitochondrial F(1)-ATPase with nucleotide bound to all three catalytic sites: implications for the mechanism of rotary catalysis. *Cell* 106, 331–341.
- Ohl, Y.M., Goetz, D.H., Chan, K., Shiloh, M.U., Craik, C.S., and Cox, J.S. (2010). *Mycobacterium tuberculosis* MycP1 protease plays a dual role in regulation of ESX-1 secretion and virulence. *Cell Host Microbe* 7, 210–220.
- Pallen, M.J. (2002). The ESAT-6/WXG100 superfamily — and a new Gram-positive secretion system? *Trends Microbiol.* 10, 209–212.
- Peña, A., Ripoll-Rozada, J., Zunzunegui, S., Cabezon, E., de la Cruz, F., and Arechaga, I. (2011). Autoinhibitory regulation of TrwK, an essential VirB4 ATPase in type IV secretion systems. *J. Biol. Chem.* 286, 17376–17382.

- Poulsen, C., Panjikar, S., Holton, S.J., Wilmanns, M., and Song, Y.-H. (2014). WXG100 protein superfamily consists of three subfamilies and exhibits an α -helical C-terminal conserved residue pattern. *PLoS ONE* 9, e89313.
- Pym, A.S., Brodin, P., Majlessi, L., Brosch, R., Demangel, C., Williams, A., Griffiths, K.E., Marchal, G., Leclerc, C., and Cole, S.T. (2003). Recombinant BCG exporting ESAT-6 confers enhanced protection against tuberculosis. *Nat. Med.* 9, 533–539.
- Raghavan, S., Manzanillo, P., Chan, K., Dovey, C., and Cox, J.S. (2008). Secreted transcription factor controls *Mycobacterium tuberculosis* virulence. *Nature* 454, 717–721.
- Ramsdell, T.L., Huppert, L.A., Sysoeva, T.A., Fortune, S.M., and Burton, B.M. (2014). Linked domain architectures allow for specialization of function in the FtsK/SpoIIIE ATPases of ESX secretion systems. *J. Mol. Biol.* 427, 1119–1132.
- Renshaw, P.S., Panagiotidou, P., Whelan, A., Gordon, S.V., Hewinson, R.G., Williamson, R.A., and Carr, M.D. (2002). Conclusive evidence that the major T-cell antigens of the *Mycobacterium tuberculosis* complex ESAT-6 and CFP-10 form a tight, 1:1 complex and characterization of the structural properties of ESAT-6, CFP-10, and the ESAT-6*CFP-10 complex. Implications for pathogenesis and virulence. *J. Biol. Chem.* 277, 21598–21603.
- Renshaw, P.S., Lightbody, K.L., Veverka, V., Muskett, F.W., Kelly, G., Frenkiel, T.A., Gordon, S.V., Hewinson, R.G., Burke, B., Norman, J., et al. (2005). Structure and function of the complex formed by the tuberculosis virulence factors CFP-10 and ESAT-6. *EMBO J.* 24, 2491–2498.
- Ryndak, M., Wang, S., and Smith, I. (2008). PhoP, a key player in *Mycobacterium tuberculosis* virulence. *Trends Microbiol.* 16, 528–534.
- Schindler, T., Bornmann, W., Pellicena, P., Miller, W.T., Clarkson, B., and Kurtyan, J. (2000). Structural mechanism for STI-571 inhibition of abelson tyrosine kinase. *Science* 289, 1938–1942.
- Senior, A.E. (2012). Two ATPases. *J. Biol. Chem.* 287, 30049–30062.
- Stanley, S.A., Raghavan, S., Hwang, W.W., and Cox, J.S. (2003). Acute infection and macrophage subversion by *Mycobacterium tuberculosis* require a specialized secretion system. *Proc. Natl. Acad. Sci. USA* 100, 13001–13006.
- Sundaramoorthy, R., Fyfe, P.K., and Hunter, W.N. (2008). Structure of *Staphylococcus aureus* EsxA suggests a contribution to virulence by action as a transport chaperone and/or adaptor protein. *J. Mol. Biol.* 383, 603–614.
- Sysoeva, T.A., Zepeda-Rivera, M.A., Huppert, L.A., and Burton, B.M. (2014). Dimer recognition and secretion by the ESX secretion system in *Bacillus subtilis*. *Proc. Natl. Acad. Sci. USA* 111, 7653–7658.
- Trocter, M., Felisberto-Rodrigues, C., Christie, P.J., and Waksman, G. (2014). Recent advances in the structural and molecular biology of type IV secretion systems. *Curr. Opin. Struct. Biol.* 27, 16–23.
- Waksman, G. (2012). Bacterial secretion comes of age. *Philos. Trans. R. Soc. Lond. B Biol. Sci.* 367, 1014–1015.
- Walker, J.E. (2013). The ATP synthase: the understood, the uncertain and the unknown. *Biochem. Soc. Trans.* 41, 1–16.
- Wendler, P., Ciniawsky, S., Kock, M., and Kube, S. (2012). Structure and function of the AAA+ nucleotide binding pocket. *Biochim. Biophys. Acta* 1823, 2–14.

Single-Molecule Studies of Origin Licensing Reveal Mechanisms Ensuring Bidirectional Helicase Loading

Graphical Abstract



Authors

Simina Ticau, Larry J. Friedman, ..., Jeff Gelles, Stephen P. Bell

Correspondence

gelles@brandeis.edu (J.G.),
spbell@mit.edu (S.P.B.)

In Brief

Single-molecule assays reveal that loading of the two replicative helicase complexes at eukaryotic origins depends on two distinct mechanisms and that helicase-helicase interactions ensure their proper orientation to initiate bidirectional replisome assembly.

Highlights

- Single-molecule studies of origin licensing reveal new steps in helicase loading
- Two rounds of ordered Cdc6 and Cdt1 DNA binding and release direct helicase loading
- One ORC protein sequentially loads two Mcm2-7 to form a head-to-head double hexamer
- Distinct mechanisms load the two Mcm2-7 complexes, ensuring bidirectional assembly



Single-Molecule Studies of Origin Licensing Reveal Mechanisms Ensuring Bidirectional Helicase Loading

Simina Ticau,¹ Larry J. Friedman,² Nikola A. Ivica,¹ Jeff Gelles,^{2,*} and Stephen P. Bell^{1,*}

¹Howard Hughes Medical Institute, Department of Biology, Massachusetts Institute of Technology, Cambridge, MA 02139, USA

²Department of Biochemistry, Brandeis University, Waltham, MA 02454, USA

*Correspondence: gelles@brandeis.edu (J.G.), spbell@mit.edu (S.P.B.)

<http://dx.doi.org/10.1016/j.cell.2015.03.012>

SUMMARY

Loading of the ring-shaped Mcm2–7 replicative helicase around DNA licenses eukaryotic origins of replication. During loading, Cdc6, Cdt1, and the origin-recognition complex (ORC) assemble two heterohexameric Mcm2–7 complexes into a head-to-head double hexamer that facilitates bidirectional replication initiation. Using multi-wavelength single-molecule fluorescence to monitor the events of helicase loading, we demonstrate that double-hexamer formation is the result of sequential loading of individual Mcm2–7 complexes. Loading of each Mcm2–7 molecule involves the ordered association and dissociation of distinct Cdc6 and Cdt1 proteins. In contrast, one ORC molecule directs loading of both helicases in each double hexamer. Based on single-molecule FRET, arrival of the second Mcm2–7 results in rapid double-hexamer formation that anticipates Cdc6 and Cdt1 release, suggesting that Mcm-Mcm interactions recruit the second helicase. Our findings reveal the complex protein dynamics that coordinate helicase loading and indicate that distinct mechanisms load the oppositely oriented helicases that are central to bidirectional replication initiation.

INTRODUCTION

Eukaryotic DNA replication must occur faithfully each cell cycle to maintain genomic stability. Initiation of replication occurs at genomic sites called origins. To ensure that no origin initiates replication more than once per cell cycle, the cell restricts the DNA loading and activation of the Mcm2–7 replicative helicase to distinct cell-cycle stages (Siddiqui et al., 2013). Importantly, helicase loading (also known as pre-RC formation) licenses origins of replication by establishing the correct architecture for helicase activation and bidirectional replication initiation.

Three helicase-loading proteins direct Mcm2–7 loading: the origin recognition complex (ORC), Cdc6, and Cdt1 (reviewed in Yardimci and Walter, 2014). ORC binds origins of replication and recruits Cdc6 at the M/G1 transition. Cdc6-bound ORC recruits Mcm2–7 in complex with Cdt1 to origin DNA. In an ATP-

hydrolysis-dependent reaction, recruited Mcm2–7 complexes are loaded around the origin DNA (Coster et al., 2014; Kang et al., 2014). Helicase loading requires opening and closing of the toroidal Mcm2–7 ring between the Mcm2 and Mcm5 subunits (Bochman and Schwacha, 2008; Costa et al., 2011; Samel et al., 2014). The product of helicase loading is a pair of tightly interacting Mcm2–7 complexes that encircle the double-stranded origin DNA in a head-to-head conformation, with staggered Mcm2/5 gates (Costa et al., 2014; Evrin et al., 2009; Remus et al., 2009; Sun et al., 2014).

Although the structure of the double-hexamer product of helicase loading is clear, important questions remain about how the helicase-loading proteins achieve this outcome. In particular, the mechanisms that load the first and second Mcm2–7 complex in opposite orientations are unclear (reviewed in Yardimci and Walter, 2014). Do the two Mcm2–7 complexes associate and load simultaneously or in an ordered fashion? Do the same or different ORC and Cdc6 proteins load each Mcm2–7 complex? To address these questions, we have developed single-molecule assays to monitor helicase loading.

Single-molecule studies are a powerful tool to address questions of stoichiometry and dynamics during DNA replication events. Studies of this type have led to important insights including the dynamics and number of DNA polymerases acting at the replication fork (reviewed in Stratmann and van Oijen, 2014). Extending these approaches to replication initiation has the potential for additional discovery. Unlike current ensemble helicase loading assays, which can only detect events that survive multiple washes, single-molecule approaches readily detect short-lived interactions during cycles of enzymatic function. Single-molecule approaches also allow stoichiometric determinations that are difficult with ensemble helicase loading assays due to DNA-to-DNA asynchrony and heterogeneity. Finally, although multi-step reactions are frequently asynchronous, post hoc synchronization of single-molecule data allows precise kinetic analysis of reaction pathways.

We have developed single-molecule assays that monitor the DNA association of eukaryotic helicase-loading proteins using colocalization single-molecule spectroscopy (CoSMoS) (Friedman et al., 2006; Hoskins et al., 2011). We show that the two Mcm2–7 hexamers are recruited and loaded in separate events that require distinct Cdc6 and Cdt1 molecules. In contrast, one ORC molecule directs loading of both Mcm2–7 complexes present in a double hexamer. Consistent with distinct mechanisms loading the two hexamers, we observe kinetic differences between events associated with loading the first and second

helicase. By combining CoSMoS with fluorescence resonance energy transfer (FRET), we demonstrate that formation of the Mcm2–7 double-hexamer interface precedes dissociation of Cdc6 and Cdt1, suggesting interactions with the first Mcm2–7, rather than ORC, drive recruitment of the second helicase. Our observations reveal both the complex protein coordination required to assemble Mcm2–7 double hexamers and the mechanisms ensuring the two Mcm2–7 molecules are loaded in the opposite orientations required for bidirectional replication initiation.

RESULTS

A Single-Molecule Assay for Helicase Loading

To develop a single-molecule assay for eukaryotic helicase loading, we used CoSMoS to monitor the origin-DNA association of the proteins required for this process (ORC, Cdc6, Cdt1, Mcm2–7). First, we immobilized origin-containing DNA by coupling it to microscope slides. We determined the location of surface-attached DNA on the slide using a DNA-coupled fluorophore (Figure 1A). We monitored associations of one or two proteins (labeled with distinguishable fluorophores) with origin DNA using colocalization of the protein- and DNA-associated fluorophores (Figure S1A). Fluorescent labeling of ORC, Cdc6, Cdt1, and Mcm2–7 was accomplished using a SNAP-tag or sortase-mediated coupling of fluorescent peptides (Gendreizig et al., 2003; Popp et al., 2007). In each case, the fluorescent tags did not interfere with protein function in ensemble helicase-loading reactions (Figure S1B). After imaging the locations of slide-coupled DNA molecules, purified ORC, Cdc6, and Cdt1/Mcm2–7 were added (one or two of which were fluorescently labeled), and the location of each DNA molecule was continuously monitored for labeled protein colocalization in 1-s intervals for 20 min.

Multiple observations indicated that Mcm2–7-DNA colocalizations represented events of helicase loading (Table S1; Movies S1, S2, and S3). First, colocalizations of Mcm2–7 with the DNA were dramatically reduced in the absence of ORC or Cdc6, proteins required for helicase loading (Yardimci and Walter, 2014). Second, stable association (>30 s) of Mcm2–7 was dependent on the presence of the ORC DNA binding site (the ARS-consensus sequence, ACS). Third, ORC, Cdc6, origin DNA, and ATP hydrolysis were each required to form Mcm2–7 molecules that were resistant to a high-salt wash (Table S1), a biochemical test for loaded helicases encircling double-stranded DNA (dsDNA) independently of helicase-loading proteins (Donovan et al., 1997; Randell et al., 2006).

Mcm2–7 Association and Loading Occurs in a One-at-a-Time Manner

Our initial studies monitored Mcm2–7 association with origin DNA. We performed CoSMoS helicase-loading experiments using Mcm2–7 containing SNAP-tagged Mcm4 labeled with 549 fluorophore (Mcm2–7^{4SNAP549}; Figure 1) and unlabeled ORC, Cdc6, and Cdt1. Over the course of 20 min, we observed both single- and double-stepwise increases in Mcm2–7-associated fluorescence intensity at origin DNAs (Figures 1B and S1C). Mcm2–7 dwell-time distributions were multi-exponential with

many short-lived (<30 s) and fewer longer-lived (>30 s) relative increases in fluorescent intensity, suggesting at least two distinct types of Mcm2–7 association with the DNA (Figure 1C).

There are two possible explanations for the multiple stepwise increases in DNA-colocalized Mcm2–7-coupled fluorescence. The simplest interpretation of this data is that Mcm2–7 hexamers associate with origin DNA in a one-at-a-time manner, with multiple hexamers accumulating over time. Alternatively, it was possible that each increase in fluorescence was due to the simultaneous association of a Mcm2–7 multimer (e.g., a pre-formed dimer of two Mcm2–7 hexamers). To distinguish between these possibilities, we used photobleaching to count the number of DNA-associated Mcm2–7 hexamers. To this end, we first observed Mcm2–7^{4SNAP549} associations with DNA and then washed the surface-tethered DNA molecules with reaction buffer, removing unbound proteins. Then, to promote photobleaching, we increased laser excitation power and removed oxygen scavengers. Comparison of the number of Mcm2–7^{4SNAP549} photobleaching steps after the wash with the number of association steps that accumulated before the wash showed no single-step increase in fluorescence before the wash resulted in a two-step photobleaching afterward (Figure 1D, top). We confirmed that loss of fluorescence was due to photobleaching and not dissociation of Mcm2–7 by observing previously non-illuminated microscope fields of view. These data eliminate models in which multiple Mcm2–7 complexes are recruited simultaneously. We conclude that Mcm2–7 association occurs in a one-at-a-time manner.

We next asked whether loading of salt-resistant Mcm2–7 hexamers around origin DNA occurred sequentially or simultaneously. We used the same photobleaching assay (described above) except a high-salt wash was used to remove any incompletely loaded Mcm2–7 complexes prior to photobleaching. If loading of both Mcm2–7 hexamers occurs simultaneously, we should observe only even numbers of high-salt-resistant hexamers. In contrast, if loading occurs sequentially, we should observe even and odd numbers of high-salt-resistant hexamers. At low protein concentrations, we observed both one- and two-step photobleaching events (Figures 1D, bottom, and 1E). Roughly half (79/160) of all single Mcm2–7-associated fluorophores that colocalized with origin DNA before the high-salt wash were high-salt resistant, and 67% (40/60) of the double-Mcm2–7-associated fluorophores were high-salt resistant. When we increased protein concentrations, we also observed DNA molecules with three and four origin-dependent, high-salt-resistant Mcm2–7 complexes (Figure S1D), indicating that more than one double-hexamer loading event occurred at a single origin.

We considered the possibility that the apparent colocalization of odd numbers of loaded Mcm2–7 complexes was due to incomplete fluorescent labeling of Mcm2–7. For example, a single salt-resistant Mcm2–7-associated fluorophore could be the result of loading two Mcm2–7 complexes, only one of which is fluorescently labeled. To address this possibility, we purified Mcm2–7 complexes that were labeled on two subunits with different fluorophores (Mcm2–7^{4SNAP549/7SORT649}). Because the SNAP-tag and sortase labeling approaches are independent of each other, we could use single-molecule imaging to determine

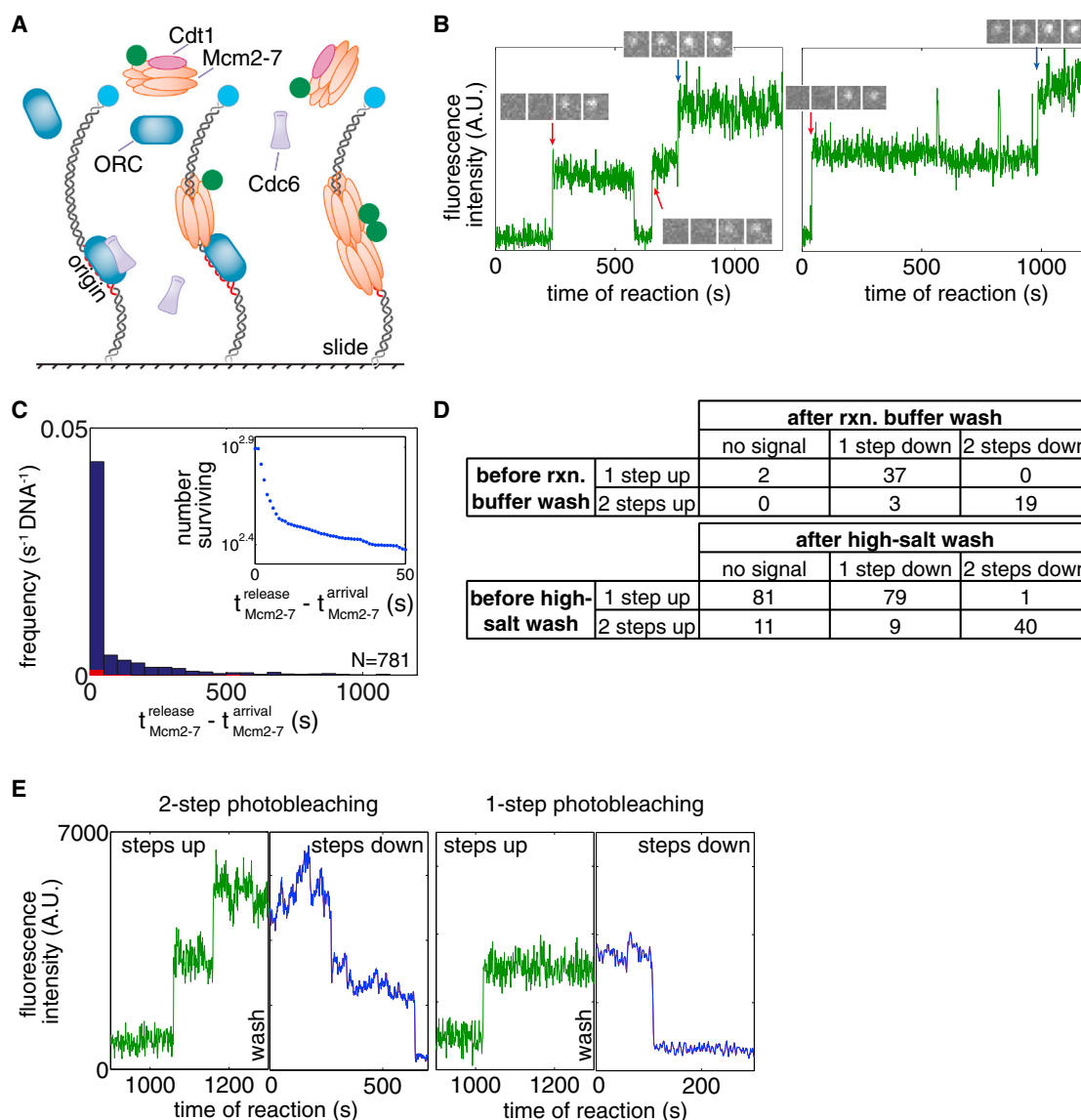


Figure 1. Mcm2-7 Hexamers Associate with and Are Loaded on DNA in a One-at-a-Time Manner

(A) Schematic for the single-molecule helicase-loading assay. Alexa-Fluor-488-labeled (blue circle) 1.3 kb origin DNAs were coupled to microscope slides. Purified ORC, Cdc6, and Cdt1/Mcm2-7 (at least one fluorescently labeled, Mcm2-7 in this illustration) were incubated with slide-coupled DNA, and colocalization of the fluorescently labeled protein with the DNA was monitored.

(B) Mcm2-7 complexes sequentially associate with origin DNA. Plots display the Mcm2-7^{4SNAP549} fluorescence intensity recorded at two representative DNA molecules. Insets show fluorescence images (4 × 1 s) taken during the sequential association of first (red arrow) and second (blue arrow) Mcm2-7.

(C) Mcm2-7 dwell times on DNA have a multiexponential distribution. Mcm2-7 dwell times were plotted as a histogram. Combined data from first and second Mcm2-7 associations are included; vertical axis represents the number of dwells of the specified duration per second per DNA molecule. Red bars are results from a separate experiment using mutant origin DNA. Inset shows the distribution of Mcm2-7 dwell times on DNA molecules as a semilogarithmic cumulative survival plot; only a portion of the entire plot is shown to emphasize that the distribution has at least two exponential components.

(D) Mcm2-7 associates with DNA one at a time. The number of associations present at standard protein concentrations before a reaction buffer (top) or high-salt buffer (0.5 M NaCl; bottom) wash is compared to the number of fluorophores that are detected by photobleaching immediately after the wash.

(E) Two representative traces before and after a high-salt wash and photobleaching. Reactions were washed twice with a high-salt buffer and imaged at higher laser power in the absence of an oxygen scavenging system until all fluorophores were photobleached. Traces of Mcm2-7^{4SNAP549} associations during the reaction (green) are plotted adjacent to photobleaching steps after a high-salt wash (blue).

the efficiency of each labeling protocol (79% for SNAP and 77% for sortase). This labeling protocol also increased the proportion of Mcm2-7 complexes that have at least one coupled fluoro-

phore to 95%. Using the measured labeling efficiencies, we determined the number of high-salt-resistant Mcm2-7 complexes with no more than one of each fluorophore that would

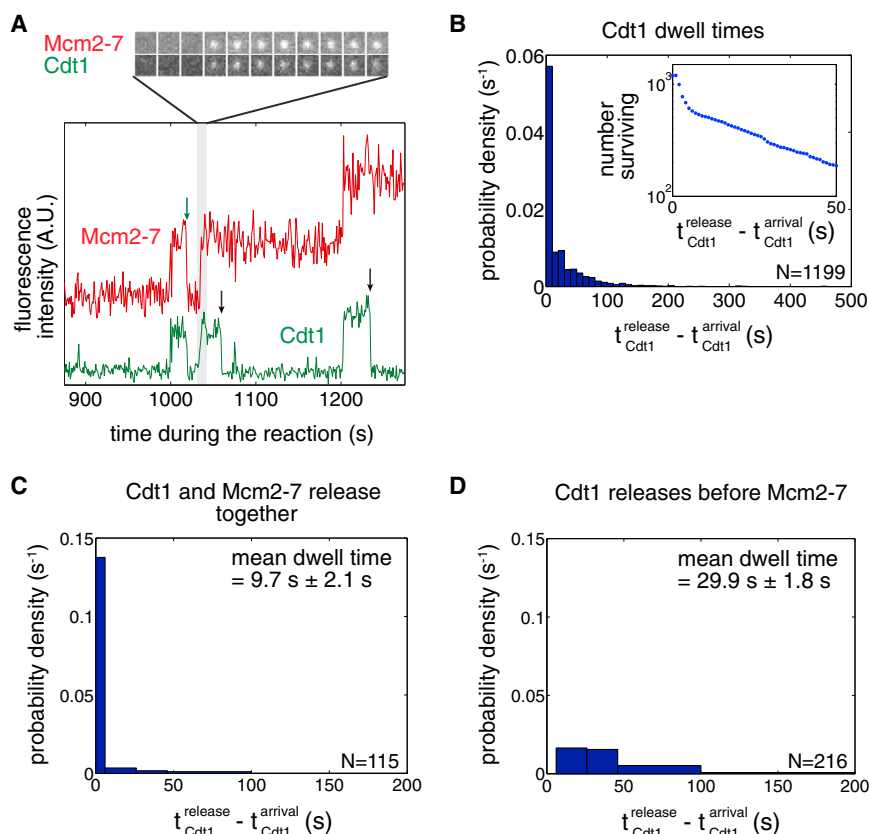


Figure 2. Distinct Cdt1 Molecules Load the First and the Second Mcm2-7 Hexamer

(A) Cdt1 molecules arrive with Mcm2-7 but release quickly after the complex arrives. A representative two-color recording of Mcm2-7^{4SNAPJF646} and Cdt1^{SORT549} fluorescence at an origin-DNA location is shown. The baseline of the red plot (Mcm2-7) is shifted up relative to the green plot (Cdt1) throughout when two-color recordings are displayed together. The sequence of single-frame images of the Cdt1- and Mcm2-7-fluorescent spots illustrates the concurrent arrival of Cdt1 and Mcm2-7. Cdt1 release occurs either with (green arrow) or without (black arrows) concurrent Mcm2-7 release.

(B) Cdt1 dwell times on DNA have a multi-exponential distribution. Cdt1 dwell times were plotted as a histogram. Inset shows semi-logarithmic cumulative survival plot as in Figure 1C.

(C and D) There are two types of Cdt1 release events. (C) Histogram shows the duration of Cdt1 origin-DNA associations when Cdt1 releases with Mcm2-7. The mean dwell time \pm SEM is reported. (D) Histogram shows the duration of Cdt1 origin-DNA associations when Cdt1 releases before Mcm2-7. The mean dwell time \pm SEM is reported.

be expected if only double hexamers were loaded (Figure S1E, model II). Assays with Mcm2-7^{4SNAP549/7SORT649} yielded single, salt-resistant fluorophores in a proportion that is inconsistent with this model. Instead, our data are consistent with a model where both single and double hexamers are loaded (in a 52:48 ratio based on our data; Figure S1E, model I). We conclude that Mcm2-7 complexes are both recruited and loaded onto origin DNA in a sequential manner.

Distinct Cdc6 and Cdt1 Molecules Load the First and Second Mcm2-7

We investigated the number of Cdt1 and Cdc6 molecules required for helicase loading and their relative times of DNA association. Both proteins are essential for loading but show little or no association with DNA in bulk assays (Coster et al., 2014; Kang et al., 2014), suggesting that their protein and/or DNA associations during helicase loading are transient. To detect these associations, we simultaneously monitored the binding of two different protein pairs labeled with distinguishable fluorophores: either Cdt1^{SORT549} with Mcm2-7^{4SNAPJF646} or Cdc6^{SORT549} with Mcm2-7^{4SNAPJF646}. The associations of both fluorophores with origin DNA were monitored simultaneously, revealing relative times of arrival and departure for the two molecules in each pair.

Consistent with being recruited to origins as a complex, we typically observed that Cdt1 and Mcm2-7 associated with origin DNA simultaneously (Figure 2A; Figures S2A–S2C). Uncommon instances where Cdt1 or Mcm2-7 are seen associating sepa-

ately (Cdt1 alone: 11.4%, Mcm2-7 alone: 18.6%) are likely caused by incomplete dye labeling of the other protein because the frequencies of these events are similar to the fractions of unlabeled Mcm2-7 or Cdt1 (14% and 20%, respectively). Like Mcm2-7, Cdt1 dwell times followed a multi-exponential distribution, indicating the presence of at least two types of Cdt1-containing complexes on the DNA (Figure 2B). Consistent with this interpretation, we identified two classes of Mcm2-7/Cdt1 dwell-time and departure behaviors. In many instances, Cdt1 and Mcm2-7 were released simultaneously (i.e., within 1 s, see Figures S2B and S2C). This release pattern occurs whether or not the DNA molecule already had an associated Mcm2-7. These associations were typically short lived (Figure 2C) and represent non-productive binding events. Interestingly, these events were less frequent if the Mcm2-7/Cdt1 was the second (29%) rather than the first (53%) to arrive at the DNA. In the remaining cases, Cdt1 was typically longer lived (Figure 2D) and was released from origin DNA by itself, leaving behind an associated Mcm2-7. Clearly, only instances when Cdt1 is released independently of Mcm2-7 can be on the pathway for double-hexamers formation. Because Cdt1-associated fluorophore photobleaching was much slower than Cdt1 dissociation (Figure S2D; Table S2), nearly all loss of fluorescent colocalization was due to dissociations, not photobleaching.

Like Cdt1, Cdc6 association with the DNA is dynamic with distinct molecules acting during loading of the first and second Mcm2-7 (Figure 3A; Figure S3A). Simultaneous analysis of Mcm2-7 and Cdc6 DNA association showed short Cdc6-DNA associations (mean lifetime $27.8 \pm 1.5 \text{ s}$; Figure S3B), a subset of which directed Mcm2-7 recruitment (35.8%, $n = 514$;

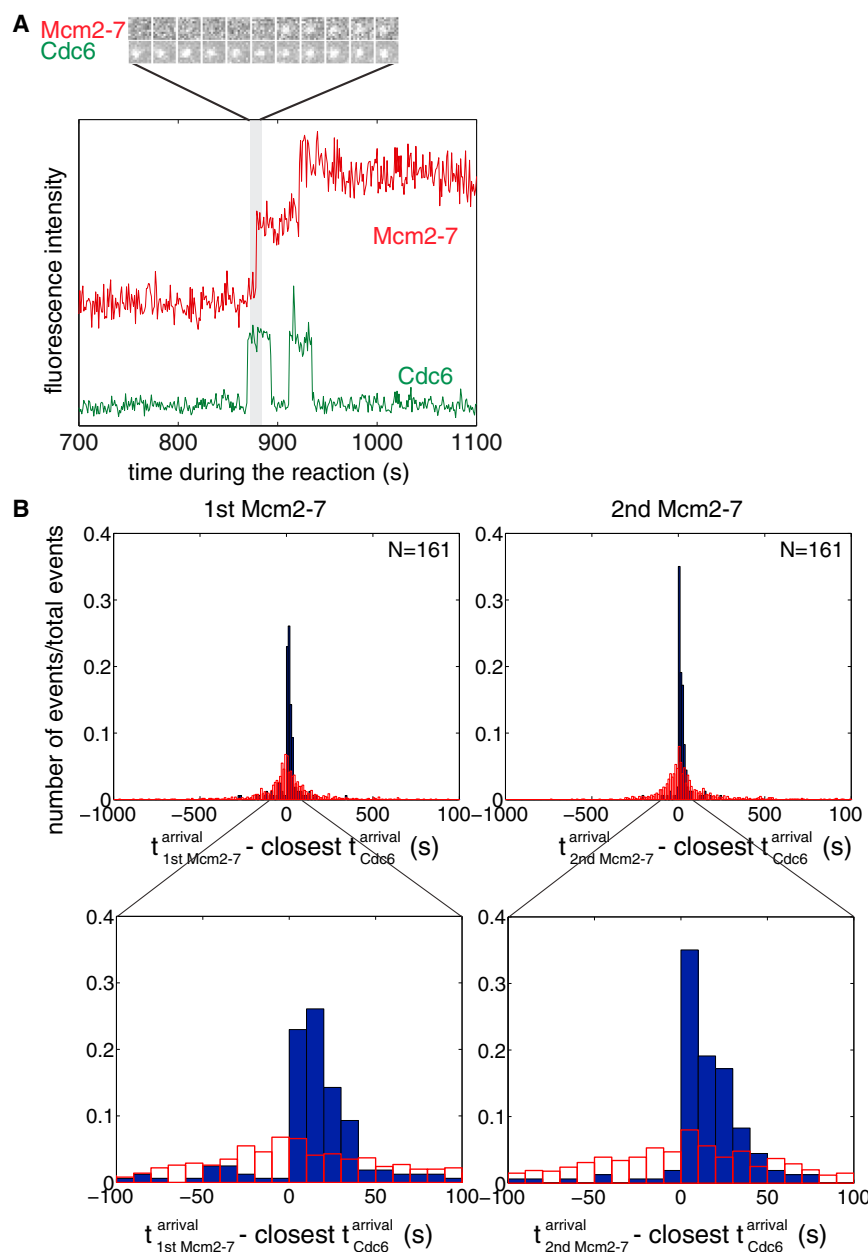


Figure 3. Distinct Cdc6 Molecules Recruit and Load the First and the Second Mcm2-7 Hexamer

(A) Distinct Cdc6 molecules anticipate each Mcm2-7 association. A representative fluorescence intensity record for Mcm2-7^{4SNAPJF646} and Cdc6^{SORT549} at origin DNA. Images of the Cdc6- and Mcm2-7-associated fluorescent spots show Cdc6 binds before the arrival of the first Mcm2-7 complex.

(B) Cdc6 association anticipates binding of the first and second Mcm2-7. Full histogram (top) and expanded view (bottom) of Mcm2-7 arrival time minus the closest Cdc6 arrival time on the same DNA molecule (blue bars). Data are separated into Mcm2-7 complexes arriving at the DNA first (left) or second (right). In >85% of the observations the difference was greater than zero, indicating that Cdc6 arrived before Mcm2-7; in the remaining <15%, Mcm2-7 arrived before Cdc6 (likely due to an unlabeled Cdc6 molecule). Red bars show a control analysis in which each Mcm2-7 arrival time was paired with the closest Cdc6 arrival time on a different, randomly selected DNA molecule. The randomized control does not show the prominent peak at differences between 0 and +50 s indicating the sequential association of Cdc6 and Mcm2-7 was not coincidental.

question: (1) we performed experiments in which Cdc6 and Cdt1 were labeled with different fluorophores, and (2) we compared the times of Cdc6 and Cdt1 release relative to the time of the corresponding Mcm2-7 association in the previously described double-labeled experiments (Mcm2-7^{4SNAPJF646} with either Cdt1^{SORT549} or Cdc6^{SORT549}).

When Cdc6 and Cdt1 were labeled in the same experiment, we consistently saw Cdc6 associating with and releasing from origin DNA before Cdt1 (Figure 4A; Figure S4A). Because only non-productive Cdt1-DNA interactions had dwell times less than 6 s (see Figure 2C), we excluded these molecules from our analysis. Cdc6^{SORT649} is released before

Figures 3A and S3A). Cdc6 consistently anticipated Mcm2-7 arrival at the DNA (>85%; Figures 3A and S3A). The remaining cases likely reflected the action of unlabeled Cdc6. We observed distinct Cdc6 proteins direct recruitment of the first and second Mcm2-7 with a similar rate constant (Figure S3C). The high frequency of Cdc6 DNA associations led us to test and confirm that sequential binding of Cdc6 and Mcm2-7 was not coincidental for either Mcm2-7 loading event (Figure 3B).

Release of Cdc6 and Cdt1 Is Sequential during Helicase Loading

We next asked whether helicase loading led to a defined order of Cdc6 and Cdt1 release. We took two approaches to address this

Cdt1^{SORT549} in >95% of cases when Cdt1 and Cdc6 were co-localized on a DNA (Figure 4B). When the fluorophores coupled to the proteins were swapped (Cdc6^{SORT549} and Cdt1^{SORT649}), >90% of observations showed Cdc6 dissociates from origin DNA before Cdt1 (Figure S4B). This lower percentage is likely due to the higher photobleaching rate of the 649 dye (Table S2). These results suggest that Cdc6 is released prior to Cdt1 during helicase loading.

Because Mcm2-7 was unlabeled in the previous experiments, we did not know which of the Cdc6-Cdt1 DNA co-localization events directed double-hexamer formation. To address whether Cdc6 is released before Cdt1 during double-hexamer formation, we analyzed the time that each Cdc6 or Cdt1 spent on the DNA

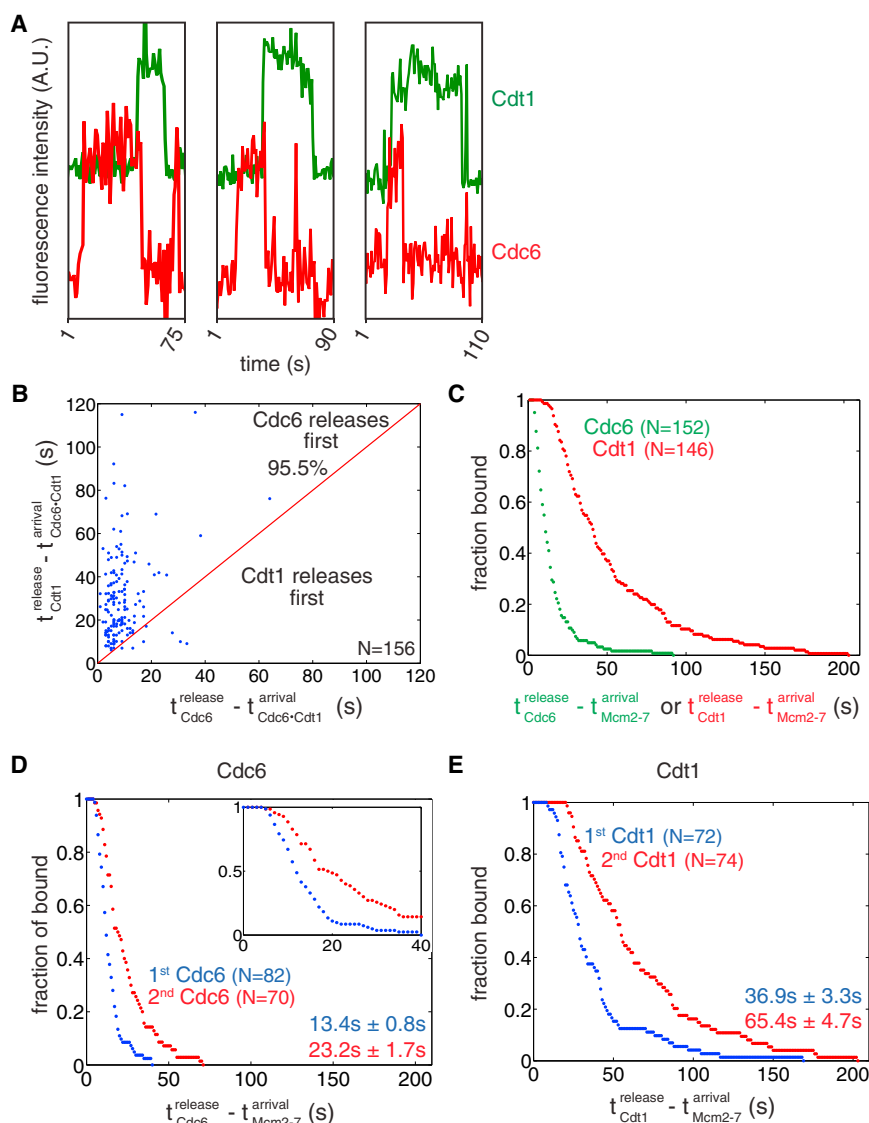


Figure 4. Cdc6 Release Occurs before Cdt1 Release

(A) Three representative fluorescence intensity records for Cdc6^{SORT649} and Cdt1^{SORT549} showing arrival and departure of Cdc6 before Cdt1.

(B) Release of Cdc6 anticipates Cdt1 release in a majority of cases. Time of Cdt1 release (y axis) is plotted against time of Cdc6 release (x axis, both times are measured from start of simultaneous presence of Cdc6 and Cdt1). The red line represents where points would fall if Cdc6 and Cdt1 released simultaneously. The fraction of measurements in which Cdc6 is released before Cdt1 is reported.

(C) Release of Cdc6 occurs before release of Cdt1 during double hexamer formation. Survival function for Cdc6^{SORT549} and Cdt1^{SORT549} dwell times after the first or second Mcm2-7 associates with origin DNA. The y axis represents the fraction of Cdc6 or Cdt1 molecules that are still associated after the time represented on the x axis.

(D and E) Cdc6 and Cdt1 release events are slower for the second versus the first Mcm2-7 loading events. (D) The time of Cdc6 release after Mcm2-7 association is plotted for the first (blue) and second (red) Mcm2-7 association as a survival plot (the fraction of Cdc6 molecules that remain DNA associated is plotted against time). Inset shows the first 40 s of the entire plot to emphasize the presence of a lag prior to DNA release. Numbers are mean release times \pm SEM for the first or second Mcm2-7-associated Cdc6 molecule. (E) Cdt1 release after the first (blue) and second Mcm2-7 association (red) as a survival plot as described for (D).

with Mcm2-7. Consistent with the Cdc6-Cdt1 double-labeling experiments, the average time between Mcm2-7 arrival and Cdc6 release is significantly shorter than the corresponding time before Cdt1 release (Figure 4C). Both the Cdc6^{SORT549} and Cdt1^{SORT549} release times are >50-fold shorter than the fluorescent dye lifetimes calculated from photobleaching rates (Table S2), verifying that these are dissociation events and not due to photobleaching. We conclude that each Mcm2-7 loading event is associated with the ordered release of Cdc6 followed by Cdt1 from the DNA.

Kinetic Evidence for Distinct Mechanisms Loading the First and Second Helicase

We reasoned that if loading of the first and second helicases occurred by different mechanisms, the time that Cdc6 and Cdt1 would spend associated with the first versus the second Mcm2-7 would differ. The resulting survival curves showed de-

longer for the second Mcm2-7 loading event for both Cdc6 ($p < 0.003$; Figure 4D) and Cdt1 ($p < 0.001$; Figure 4E). These kinetic data suggest that loading of the first and second helicase occurs through distinct mechanisms.

A Single ORC Directs Formation of the Mcm2-7 Double Hexamer

There are multiple models for the stoichiometry of ORC during helicase loading (Figure S5A). One ORC molecule could direct both helicase loading events (model I). Alternatively, two ORC molecules could be present throughout the loading reaction (model II). Finally, it is possible that distinct ORC molecules direct each loading event, but both ORC molecules are only present for the second loading event (model III), or, like Cdc6 and Cdt1, each ORC is only present during loading of one Mcm2-7 (model IV). To distinguish between these models, we performed CoSMoS with simultaneous labeling of ORC and Mcm2-7.

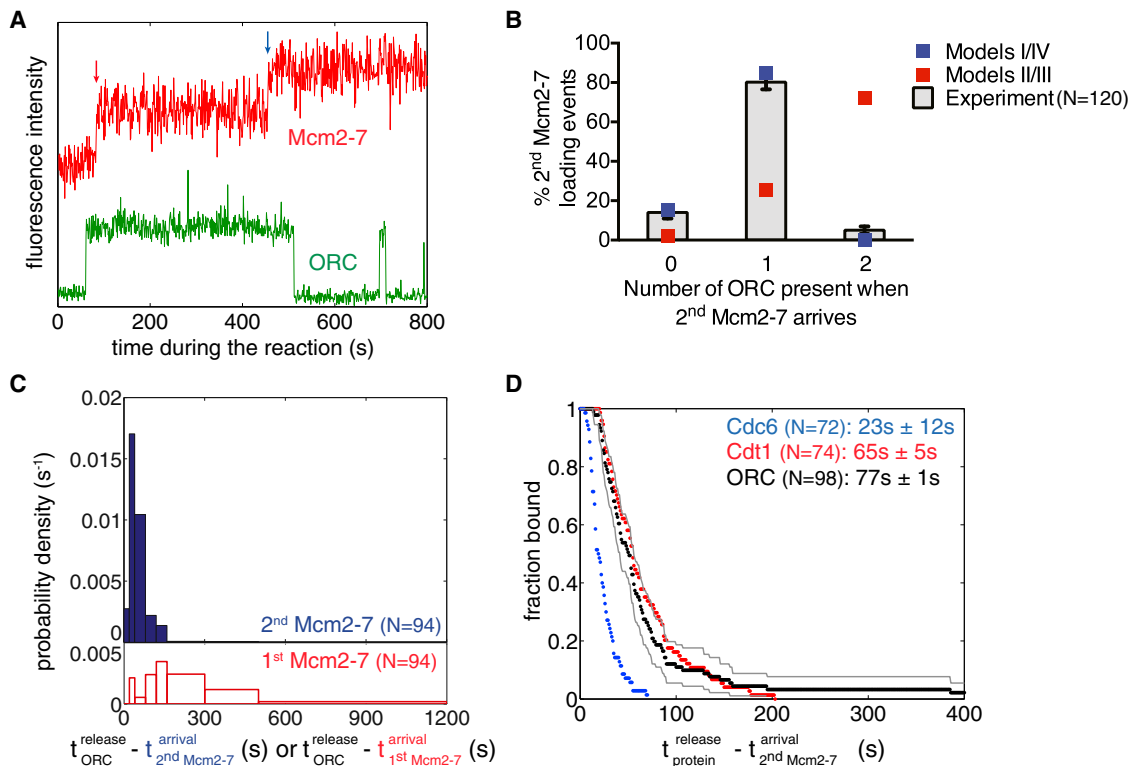


Figure 5. A Single ORC Complex Directs Recruitment and Loading of the First and Second Mcm2-7 Hexamer

(A) Representative fluorescence intensity record for ORC^{1SORT549} and Mcm2-7^{4SNAPJF646} at an origin-DNA location. Association of first and second Mcm2-7 are marked with red and blue arrows, respectively.

(B) A single ORC complex directs recruitment of two hexamers. The fraction (\pm SE) of DNA molecules observed to have zero, one or two ORC fluorophores bound when the second Mcm2-7 was recruited, is plotted (bars) together with the predicted number of associated fluorophores (red and blue squares) of different models (see Figure S5A).

(C) ORC is released rapidly after recruitment of the second Mcm2-7 hexamer. Histograms showing the time between the association of the second Mcm2-7 and ORC release (top) or association of the first Mcm2-7 and ORC release (bottom).

(D) Release of Cdc6^{SORT549} (blue), Cdt1^{SORT549} (red), and ORC^{1SORT549} (black) after the association of the second Mcm2-7^{4SNAPJF646} complex is plotted as a survival function. There are two ORC molecules that associate for >400 s (1,033.8 s and 709.6 s) that are not shown and disproportionately affect the mean dwell time. Gray lines represent a 95% confidence interval for the ORC data set showing that there is no significant difference between Cdt1 and ORC release time distributions. Numbers in parentheses represent the mean release times \pm SEM.

Initially, we fluorescently labeled ORC on the Orc1 subunit (ORC^{1SORT549}) and observed associations with DNA in the presence of unlabeled Cdc6, Cdt1, and Mcm2-7. ORC DNA binding showed a broad distribution of dwell times (Figure S5B, left panel). Consistent with the long-lived associations reflecting ORC binding to the ACS, mutation of this element resulted in >94% of ORC DNA associations being short lived (<10 s; Figure S5B, right panel). The associations of ORC are shorter than the calculated fluorescent dye lifetimes confirming that we are observing dissociations and not photobleaching (Figure S5C; Table S2).

To identify ORC molecules involved in helicase loading, we simultaneously monitored ORC and Mcm2-7 DNA associations (Figure 5A). As expected, ORC associates with DNA and Cdt1/Mcm2-7. Unlike Cdc6 and Cdt1, we consistently observed a single increase in ORC fluorescence that remained present continuously during recruitment of the first and second Mcm2-7 complexes (Figures 5A and S5D).

Because ORC multimers have been detected (Sun et al., 2012), we addressed whether ORC complexes dimerize in solution prior to DNA binding by counting the number of photobleaching steps associated with single increases in ORC-associated fluorescence (as was described for Mcm2-7). The large majority of cases were consistent with ORC binding as a single complex (67 of 69; Figure S5E). These data confirmed that the single increases in ORC-associated fluorescence were due to single ORC molecules associating with origin DNA during loading.

Although the majority of observations involved a single ORC directing loading of two Mcm2-7 hexamers, occasionally we observed the presence of multiple DNA-bound ORC molecules at the time of a Mcm2-7 association. To address which models for ORC function during helicase loading were possible, we counted the number of DNA-associated ORC molecules (by counting stepwise increases in ORC fluorescence) during the second Mcm2-7 hexamer association (Figure 5B). Models II

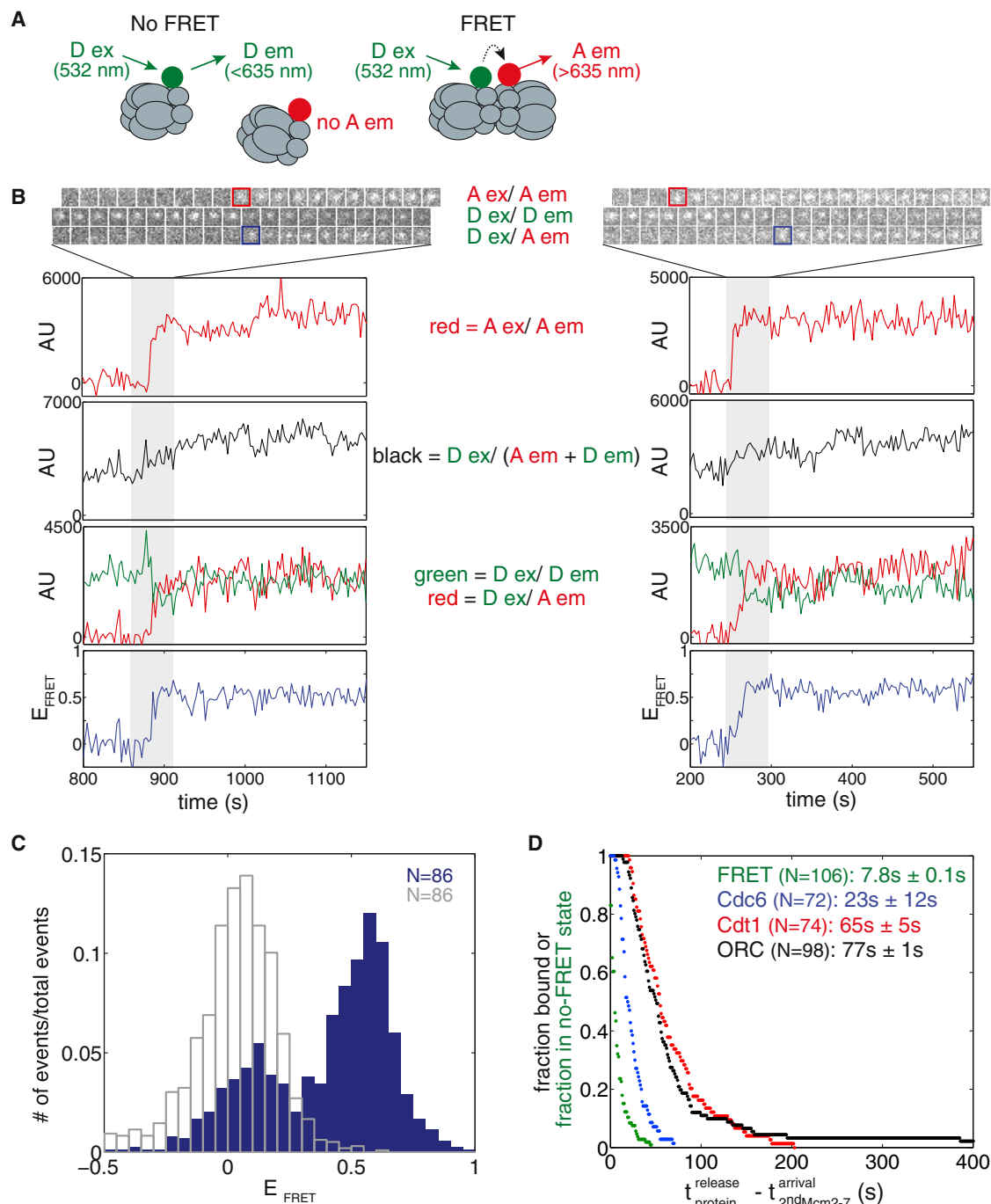


Figure 6. Double-Hexamer Formation Occurs Quickly upon Recruitment of the Second Mcm2-7 Hexamer

(A) When the two fluorophores (green circle = Dy549, red circle = Dy649) are not associated, excitation of the donor (D ex) will only yield emission from the donor (D em). However, when the two fluorophores are in close proximity, we observe acceptor emission (A em) upon D ex, and a weaker D em signal. Wavelengths represent laser excitation and emissions that were monitored.

(B) Representative fluorescence records for experiments using a mixture of Mcm2-7^{SORT549} and Mcm2-7^{SORT649} showing FRET upon arrival of the second Mcm2-7. Red squares highlight when Mcm2-7^{SORT649} associates with DNA (Mcm2-7^{SORT549} is already present), and blue squares highlight when FRET occurs. Images and records of fluorescence intensity for D ex/D em (Mcm2-7^{SORT549}), A ex/A em (Mcm2-7^{SORT649}), total emission (D ex / (D em + A em)), and FRET (D ex/A em) are shown together with calculated E_{FRET} .

(C) Histogram of E_{FRET} is plotted for times when a single Mcm2-7^{SORT549} and a single Mcm2-7^{SORT649} are present (blue bars) or when only Mcm2-7^{SORT549} is associated with the DNA (unfilled gray bars). The histogram displays the first ten consecutive E_{FRET} measurements after arrival of the second Mcm2-7 for 86 DNA

(legend continued on next page)

and III predict two ORC molecules bound to DNA when the second Mcm2–7 is recruited. In contrast to these models, we observed two ORC molecules associated during loading of the second hexamer only 5% of the time (as opposed to 70% predicted by model II or III using the measured ORC labeling efficiency; 85%; see [Extended Experimental Procedures](#)). Instead, we observe a single ORC present during association of the second helicase 80% (96/120) of the time, very close to the percentage expected if a single ORC is responsible for loading the second Mcm2–7 (85%). To distinguish between models I and IV, we asked whether the same or different ORC molecules directed the first and second helicase-loading events. Consistent with model I, 94% ($n = 96$) of observations showed a single ORC complex continuously present during both Mcm2–7 recruitment events. Thus, our data indicate one ORC molecule directs loading of both the first and the second Mcm2–7 hexamer (model I).

Interestingly, in most traces where two Mcm2–7 associate with the DNA, we observed dissociation of ORC from origin DNA soon after binding of the second Mcm2–7 hexamer (see [Figures 5A and S5D](#)). Plotting the times between the association of the second Mcm2–7 hexamer and ORC release ([Figure 5C](#), blue bars), we observed only one instance where ORC released from DNA in <15 s (13.1 s), followed by a short time interval (15–90 s) during which 87% of the ORC complexes were released. The shape of this distribution suggests that, like Cdc6 and Cdt1, release of ORC is a multi-step process. In contrast, a much broader distribution was observed when ORC release was measured relative to DNA association of the first Mcm2–7 hexamer ([Figure 5C](#), red bars), suggesting ORC release is independent of this event. To investigate the order of ORC release relative to the other helicase-loading proteins, we compared the distribution of ORC, Cdc6, and Cdt1 dwell times after binding of the second Mcm2–7 complex ([Figure 5D](#)), using data from two-color experiments with Mcm2–7^{4SNAPJF646} and 549-labeled ORC, Cdt1, or Cdc6. Photobleaching of the 549-labeled proteins was insignificant relative to their observed dwell times ([Table S2](#)). Although there is a significant difference between release of Cdc6 and ORC ($p < 0.001$), we saw no significant difference in the distributions of Cdt1 and ORC release ([Figure 5D](#)). Thus, loading of the first Mcm2–7 allows ORC retention, whereas loading of the second Mcm2–7 appears to induce the linked release of ORC and the second Cdt1.

Recruitment of a Second Mcm2–7 Results in Rapid Double-Hexamer Formation

The interactions that drive recruitment of the second Mcm2–7 remain unclear ([Yardimci and Walter, 2014](#)). To gain insight into this event, we used fluorescence resonance energy transfer (FRET)-CoSMoS ([Crawford et al., 2013](#)) to detect the proximity of the Mcm7 N-terminal domains upon double-hexamer formation ([Costa et al., 2014; Sun et al., 2014](#)). To this end, we labeled the

Mcm7 subunit in separate preparations of Mcm2–7 with either 549 (Mcm2–7^{7SORT549}, donor) or 649 (Mcm2–7^{7SORT649}, acceptor) fluorophore ([Figure 6A](#)). When mixed in an equimolar ratio, the differently labeled Mcm2–7 should be in the same double hexamer $\sim 50\%$ of the time, and those molecules should exhibit substantial FRET efficiency (E_{FRET}) because the Mcm7 N-terminal regions are in close proximity in the double hexamer ([Sun et al., 2014](#)). We alternated between 633 and 532 nm laser excitation to monitor both arrival of each Mcm2–7 and E_{FRET} . Importantly, when Mcm2–7^{7SORT549} and Mcm2–7^{7SORT649} were sequentially recruited to the origin DNA (in either order), we observed rapid development of a high $E_{\text{FRET}} \approx 0.53$ state ([Figures 6B and 6C](#), blue bars; [Figure S6](#)). A second peak at $E_{\text{FRET}} \approx 0.02$ was also observed in the absence of acceptor ([Figure 6C](#), unfilled gray bars) and thus represents state(s) with no detectable FRET. Consistent with the detected FRET signal occurring as a consequence of double-hexamer formation, the high E_{FRET} state was stable for hundreds of seconds, and 95% (55/58) of the complexes that exhibited $E_{\text{FRET}} \approx 0.53$ were high-salt resistant.

To determine when double-hexamer formation occurs relative to binding of the second Mcm2–7, we compared the time of FRET formation to the time of arrival of the second Mcm2–7 ([Figure 6D](#)). We found the mean time between recruitment of the second Mcm2–7 hexamer until formation of FRET was 7.8 ± 0.1 s. This time is significantly shorter than release of Cdc6 after arrival of the second Mcm2–7 hexamer (23.2 ± 1.7 s, $p < 0.001$), indicating that formation of the N-terminal-to-N-terminal interactions anticipates, and is therefore independent of, Cdc6 and Cdt1 release ([Figure 6D](#)).

DISCUSSION

By determining precise protein/DNA stoichiometry and real-time dynamics, the single-molecule observations of helicase loading described here provide important insights into this event. Together, our findings strongly support a model in which the first and second helicase are loaded by distinct mechanisms and the second Mcm2–7 complex is recruited through interactions with the first. Accordingly, we propose a new model for helicase loading that is consistent with our current data and is described below ([Figure 7](#)).

Recruitment and Loading of Mcm2–7 Helicases Occur in a One-at-a-Time Manner

Monitoring associations in real-time reveals sequential recruitment and loading of Mcm2–7 helicases to origin DNA. One-at-a-time recruitment is consistent with an initial complex containing a single Mcm2–7 associated with the three helicase-loading proteins ([Sun et al., 2013](#)) and ensemble assays that show temporal separation of Mcm2–7 recruitment ([Fernández-Cid et al., 2013](#)). Recent structural observations indicate that the Mcm2/5

molecules (the same number of molecules and time points were used for the control). E_{FRET} data below -0.5 were excluded from the plot (3/860 signal points and 17/860 control points).

(D) Double-hexamer formation anticipates Cdc6, Cdt1, and ORC release. Survival after the association of the second Mcm2–7 complex of the no-FRET state (green) and of DNA-bound Cdc6⁵⁴⁹ (blue), Cdt1⁵⁴⁹ (red), and ORC⁵⁴⁹ (black). Mean times \pm SEM until FRET increase and ORC, Cdt1, Cdc6 release are reported for comparison.

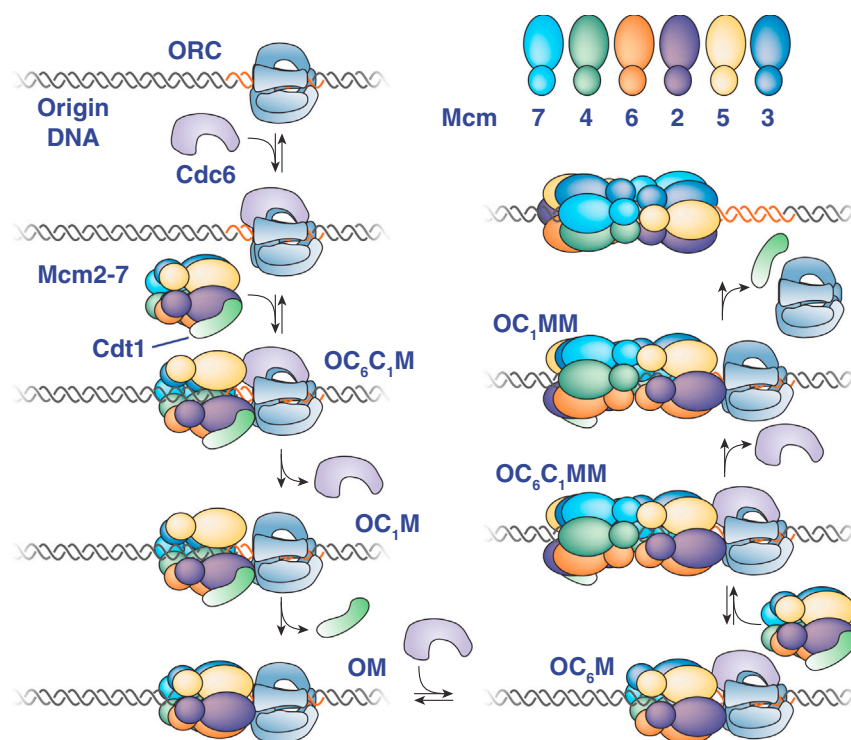


Figure 7. Proposed Model for Helicase Loading

Proteins present are indicated adjacent to each illustration (O = ORC, C₆ = Cdc6, C₁ = Cdt1, M = Mcm2-7). Reversible steps that are observed are indicated. See text for details.

gates, which must open to provide DNA access to the Mcm2-7 central channel (Samel et al., 2014), are staggered in the double hexamer (Costa et al., 2014; Sun et al., 2014). Concerted Mcm2-7 loading would require alignment of the two Mcm2/5 gates to allow simultaneous DNA entry into the central channels of both hexamers. In contrast, sequential Mcm2-7 loading can readily accommodate the formation of a staggered-gate double-hexamer structure.

Although high-salt-resistant single hexamers have been detected after artificially closing the Mcm2/5 gate (Samel et al., 2014), previous studies have not detected single loaded (high-salt resistant) Mcm2-7 complexes in unperturbed helicase-loading reactions (Evrin et al., 2009; Kang et al., 2014; Remus et al., 2009). This difference may be due to the higher protein concentrations used in these ensemble reactions. Alternatively, the high-salt-resistant single hexamers may be less stable than the double hexamers resulting in their loss during sample preparation for chromatography or EM. Indeed, a higher percentage of double hexamers showed high-salt resistance relative to single hexamers (74% versus 49%; see Figure 1D). The high-salt wash is effective in the single-molecule assay setting, however, as this treatment efficiently releases incompletely loaded Mcm2-7 formed in the absence of ATP hydrolysis (Table S1, ATP_γS).

Ordered Release of Cdc6 and Cdt1 Molecules during Double-Hexamer Loading

Our studies provide insights into Cdc6 and Cdt1 function during helicase loading. Previously, robust DNA association of these proteins was only observed when helicase-loading reactions

were arrested at an early ATP-dependent step. We found that the initial ORC-Cdc6-Cdt1-Mcm2-7 (OC₆C₁M) complex has two possible fates (Figure 7, left): (1) simultaneous release of Mcm2-7 and Cdt1 or (2) sequential release of Cdc6 and Cdt1 with retention of Mcm2-7. The former is most likely the reversal of the initial Mcm2-7/Cdt1 association, whereas the latter pathway leads to sequential formation of OC₁M and OM complexes and Mcm2-7 loading. Based on this distinction, we propose that release of Cdt1 independent of Mcm2-7 is coupled to successful helicase loading (illustrated as closing of the Mcm2/5 gate; Figure 7). Consistent with this hypothesis, treatments (e.g., ATP_γS) or mutations (e.g., Mcm2-7 ATPase mutations, Coster et al., 2014; Kang et al., 2014) that lead to

Cdt1 retention prevent helicase loading. We note that other times of ring closure (and opening) than those illustrated in the model are possible.

Electron microscopic (EM) and ensemble assays suggest the existence of helicase loading intermediates with ORC-Cdc6-Mcm2-7 (OC₆M) and ORC-Cdc6-Mcm2-7-Mcm2-7 (OC₆MM, Sun et al., 2014). Our findings suggest that the OC₆M complex is a short-lived intermediate formed prior to recruitment of the second Mcm2-7/Cdt1 complex rather than being formed by release of Cdt1 from the OC₆C₁M (Fernández-Cid et al., 2013). We do not see evidence of an OC₆MM complex during helicase loading, and there is no direct evidence that Cdc6 is present in the 2D class averages used in these studies (Sun et al., 2014). Given their relatively lower resolution, these studies could have detected either the OC₆C₁MM or OC₁MM complexes that we observe (Figure 7, right). Our previous studies found an intermediate with two Cdt1 complexes that is not detected in the current studies (Takara and Bell, 2011). During efforts to reconcile these findings, we found the Mcm2-7 protein used in the previous studies contained a non-lethal mutation in the C terminus of Mcm3 that is predicted to inhibit Cdc6 interactions (Frigola et al., 2013). We suspect that this mutant enhanced dependence on other interactions leading to the detection of two Cdt1 associations.

Loading of the First and Second Mcm2-7 Occurs by Distinct Mechanisms

In addition to answering a long-standing question about ORC function, our data indicating that one ORC molecule directs Mcm2-7 double-hexamer formation strongly suggest that

different mechanisms direct loading of the first and second Mcm2–7. EM studies suggest that during helicase loading ORC interacts with the C-terminal end of the first Mcm2–7 on adjacent DNA (Sun et al., 2014; 2013). Assuming this configuration, direct recruitment of the second Mcm2–7 complex by the same ORC would load the two Mcm2–7 molecules in a head-to-tail fashion (Figure S7, top). Even if ORC had a second binding site for Mcm2–7 on its opposite side, a similar direct interaction with Mcm2–7 could not load two Mcm2–7 complexes with adjacent N-terminal domains (Figure S7, bottom). Further evidence in favor of distinct mechanisms loading the first and second Mcm2–7 include (1) the two loading events show different Cdc6, Cdt1, and ORC release kinetics; (2) Cdt1 associated with the second loading event shows an increased propensity to release without Mcm2–7.

We considered the possibility that a second ORC binds DNA in the opposite orientation and loads the second helicase by the same mechanism as the first. Several observations argue against this model. First, because we do not consistently detect a second ORC during recruitment of the second Mcm2–7, the average dwell time for this second ORC would have to be below our detection limit (~0.5 s). This limit is >10-fold shorter than the average dwell time observed for ORC on non-origin DNA (Figure S5B). Second, in contrast to a model in which a short-lived second ORC directs loading of the second Mcm2–7, the Cdc6 protein associated with loading the second Mcm2–7 is easily detected (23.2 s average dwell time; Figure 4D). Third, even at diffusion-limited binding rates the sequential association of Cdc6 and Mcm2–7/Cdt1 with such a short-lived ORC is improbable. Finally, experiments showing that soluble ORC is not required for helicase loading if ORC is pre-loaded onto DNA (Bowers et al., 2004; Fernández-Cid et al., 2013; Duzdevich et al., 2015) are not consistent with a role for a short-lived second ORC.

Recruitment of the Second Mcm2–7

Instead of ORC and Cdc6 directly recruiting the second Mcm2–7/Cdt1 complex, our findings suggest that interactions involved in stabilizing the Mcm2–7 double hexamer mediate the recruitment of the second Mcm2–7/Cdt1. We detect these interactions prior to Cdc6 or Cdt1 release (Figure 6), suggesting that formation of double-hexamer interactions anticipates loading of the second helicase. Recent EM studies of a complex between one ORC and a head-to-head Mcm2–7 double hexamer are consistent with this hypothesis (Sun et al., 2014). Because FRET is not observed immediately upon recruitment of the second Mcm2–7, an intervening event (e.g., a Mcm2–7 conformational change or ATP hydrolysis) may be required to bring the Mcm7 N-terminal domains into close proximity. We do not know which parts of the Mcm2–7 N-terminal domains drive the proposed interactions. For simplicity, the model (Figure 7) illustrates interactions consistent with those observed in EM studies of Mcm2–7 double hexamers (Costa et al., 2014; Sun et al., 2014). One argument against a model in which Mcm2–7 N-terminal domains drive recruitment of the second Mcm2–7 is the observation that a C-terminal mutation in Mcm3 that interferes with recruitment of the first Mcm2–7 also inhibits recruitment of the second Mcm2–7 (Frigola et al., 2013). This mutant has additional defects in Mcm2–7 ATP hydrolysis, how-

ever, which could explain a loading defect for the second Mcm2–7 (Coster et al., 2014; Kang et al., 2014; Sun et al., 2014).

Because purified Mcm2–7 complexes do not show affinity for one another in solution (Evrin et al., 2009), the first Mcm2–7 must be altered to facilitate interactions with a second Mcm2–7. A likely possibility is that ORC and Cdc6 alter the conformation of the first Mcm2–7 to facilitate these interactions (shown as separation of the Mcm2/Mcm5 N-terminal regions, Sun et al., 2013). In support of a role for Cdc6, although we observe an ORC-Mcm2–7 (OM) intermediate after the first loading event, this complex is unable to recruit a second Mcm2–7 until a second Cdc6 protein associates (OC₆M).

The model for helicase loading presented here has several advantageous features. Because Cdc6 ATPase activity is required to remove incorrectly or incompletely loaded Mcm2–7 (Coster et al., 2014; Frigola et al., 2013; Kang et al., 2014), the use of different Cdc6 proteins to load the first and second Mcm2–7 would allow each event to be evaluated separately. More importantly, the use of Mcm2–7 N-terminal domain interactions to recruit the second Mcm2–7 ensures the establishment of a head-to-head double hexamer. This conformation is the first step in the establishment of bidirectional replication initiation and could be essential for initial DNA melting. Finally, the retention of ORC after the first loading event coupled with the release of ORC after the second loading event has the advantage of promoting the formation of double hexamers while inhibiting repeated loading of single hexamers.

EXPERIMENTAL PROCEDURES

Protein Purification and Labeling

Wild-type Mcm2–7/Cdt1 and ORC complexes were purified as described previously (Kang et al., 2014). Wild-type Cdc6 was purified as described in Frigola et al. (2013). We used a variety of protein fusions to fluorescently label ORC (Ubiquitin-GGG-Flag at the N terminus of Orc1), Cdc6 (GST-SUMO-GGG tag at the N terminus), and Cdt1/Mcm2–7 (Ubiquitin-GGG-Flag at the N terminus of Mcm7 or Cdt1, and/or a SNAP-tag (NEB) at the N terminus of Mcm4). The Ubiquitin (in vivo) and GST-SUMO (using Ulp1 protease) fusions were removed to reveal three N-terminal glycines required for sortase labeling. Sortase was used to couple fluorescently labeled peptide (DY549P1- or DY649P1-CHHHHHHHHLPETGG; referred to as SORT549 and SORT649, respectively) to the N terminus of these proteins. SNAP-Surface549 (NEB, SNAP549) or SNAP-Janelia Fluor 646 (SNAPJF646; Grimm et al., 2015) was coupled to SNAP-tagged Mcm2–7 (See Extended Experimental Procedures for these purification protocols). For sortase labeling, peptide-coupled proteins were separated from uncoupled proteins using Complete-His-Tag Resin (Roche). See Extended Experimental Procedures for these purification protocols. Yeast strains and plasmids used are listed in Tables S3 and S4, respectively.

Single-Molecule Microscopy

The micro-mirror total internal reflection (TIR) microscope used for multi-wavelength single-molecule using excitation wavelengths 488, 532, and 633 nm has been previously described (Friedman and Gelles, 2012; Friedman et al., 2006). Biotinylated Alexa-Fluor-488-labeled, 1.3-kb-long DNA molecules containing an origin were coupled to the surface of a reaction chamber through streptavidin. Briefly, the chamber surface was cleaned and derivatized using a 200:1 ratio of silane-NHS-PEG and silane-NHS-PEG-biotin (see Extended Experimental Procedures). We identified DNA molecule locations by acquiring four to seven images with 488 nm excitation at the beginning of the experiment. Unless otherwise noted, helicase loading reactions contained 0.25 nM ORC, 1 nM Cdc6, and 2.5 nM Cdt1/Mcm2–7. Reaction buffer was as previously

described (Kang et al., 2014) except without any glycerol and with the addition of 2 mM dithiothreitol, 2 mg/ml bovine serum albumin (EMD Chemicals), and an oxygen scavenging system (glucose oxidase/catalase) to minimize photobleaching (Friedman et al., 2006). After addition of protein to the DNA-coupled chamber, frames of 1-s duration were acquired according to the following protocol: (1) a single-image frame visualizing the DNA positions (488 excitation), (2) 60 frames monitoring both the 549 and 649 fluorophores (simultaneous 532 and 633 excitation), and (3) a computer-controlled focus adjustment (using a 785-nm laser). This cycle was repeated roughly 20 times in the course of an experiment (~20 min). Chambers were then washed with either three chamber volumes of reaction buffer or two volumes of the same buffer with 0.5 M NaCl in place of 300 mM K-glutamate and 1 volume reaction buffer. For photobleaching, laser power(s) were increased, and one or multiple fluorophores were imaged simultaneously until no visible spots remained. Typically, photobleaching was also examined in a second field of view that was not imaged during the loading reaction.

FRET Experiments

The conditions for monitoring FRET were similar to the other experiments, with a few exceptions. Typical reactions contained 0.75 nM ORC, 3 nM Cdc6, 5 nM Cdt1/Mcm2-7^{7SORT549}, and 5 nM Cdt1/Mcm2-7^{7SORT649}. DNA was imaged before and immediately after adding the reaction to the slide but not throughout the experiment. The imaging protocol alternated between 1-s frames with the 532 laser on and 1-s frames with the 633 laser on over 20–30 min. Apparent E_{FRET} was calculated as described (Crawford et al., 2013).

SUPPLEMENTAL INFORMATION

Supplemental Information includes Extended Experimental Procedures, seven figures, three movies, and four tables and can be found with this article online at <http://dx.doi.org/10.1016/j.cell.2015.03.012>.

AUTHOR CONTRIBUTIONS

S.T. designed and conducted experiments with feedback from L.J.F., J.G., and S.P.B. S.T. and L.J.F. analyzed data. N.A.I. developed labeling strategies, and S.T. and N.A.I. generated proteins. S.T. and S.P.B. composed the paper with input from all authors, and S.P.B. and J.G. directed the project.

ACKNOWLEDGMENTS

We are grateful to members of the Bell laboratory for useful discussions. We thank Daniel Duzdevich and Eric C. Greene for comments on the manuscript and helpful discussions. We thank Jonathan B. Grimm and Luke D. Lavis for graciously providing the Janelia Fluors. This work was supported by NIH grants GM52339 (S.P.B.) and R01 GM81648 (J.G.) and a grant from the G. Harold and Leila Y. Mathers Foundation (J.G.). S.T. was supported in part by an NIH Pre-Doctoral Training Grant (GM007287). S.P.B. is an investigator with the Howard Hughes Medical Institute.

Received: November 13, 2014

Revised: January 26, 2015

Accepted: March 2, 2015

Published: April 16, 2015

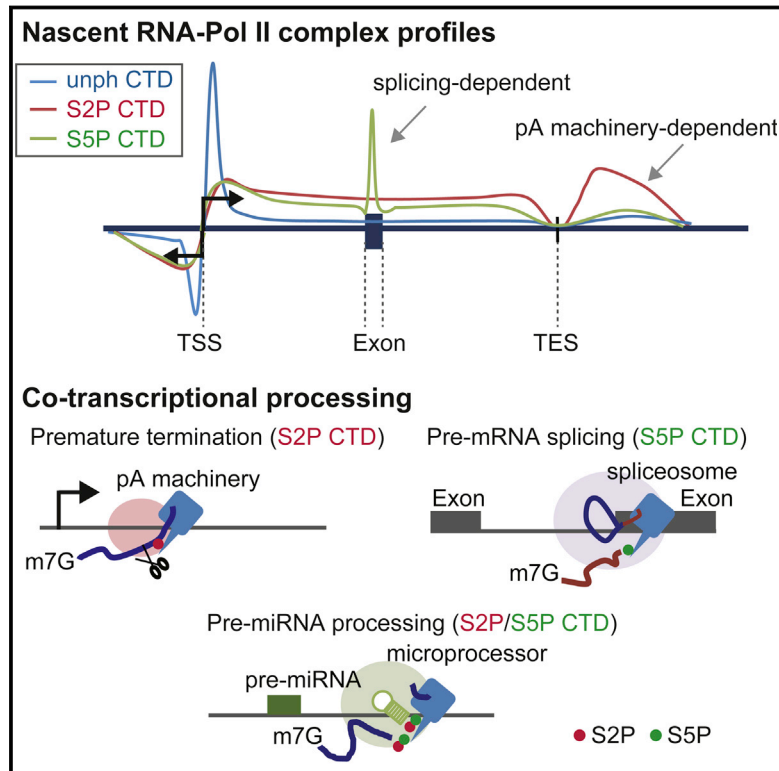
REFERENCES

- Bochman, M.L., and Schwacha, A. (2008). The Mcm2-7 complex has in vitro helicase activity. *Mol. Cell* 31, 287–293.
- Bowers, J.L., Randell, J.C.W., Chen, S., and Bell, S.P. (2004). ATP hydrolysis by ORC catalyzes reiterative Mcm2-7 assembly at a defined origin of replication. *Mol. Cell* 16, 967–978.
- Costa, A., Ilves, I., Tamberg, N., Petojevic, T., Nogales, E., Botchan, M.R., and Berger, J.M. (2011). The structural basis for MCM2-7 helicase activation by GINS and Cdc45. *Nat. Struct. Mol. Biol.* 18, 471–477.
- Costa, A., Renault, L., Swuec, P., Petojevic, T., Pesavento, J.J., Ilves, I., MacLellan-Gibson, K., Fleck, R.A., Botchan, M.R., and Berger, J.M. (2014). DNA binding polarity, dimerization, and ATPase ring remodeling in the CMG helicase of the eukaryotic replisome. *eLife* 3, e03273.
- Coster, G., Frigola, J., Beuron, F., Morris, E.P., and Diffley, J.F.X. (2014). Origin licensing requires ATP binding and hydrolysis by the MCM replicative helicase. *Mol. Cell* 55, 666–677.
- Crawford, D.J., Hoskins, A.A., Friedman, L.J., Gelles, J., and Moore, M.J. (2013). Single-molecule colocalization FRET evidence that spliceosome activation precedes stable approach of 5' splice site and branch site. *Proc. Natl. Acad. Sci. USA* 110, 6783–6788.
- Donovan, S., Harwood, J., Drury, L.S., and Diffley, J.F.X. (1997). Cdc6p-dependent loading of Mcm proteins onto pre-replicative chromatin in budding yeast. *Proc. Natl. Acad. Sci. USA* 94, 5611–5616.
- Duzdevich, D., Warner, M.D., Tica, S., Ivica, N.A., Bell, S.P., and Greene, E.C. (2015). The dynamics of eukaryotic replication initiation: Origin specificity, licensing, and firing at the single-molecule level. *Mol. Cell* 58. Published online April 23, 2015. <http://dx.doi.org/10.1016/j.molcel.2015.03.017>.
- Evrin, C., Clarke, P., Zech, J., Lurz, R., Sun, J., Uhle, S., Li, H., Stillman, B., and Speck, C. (2009). A double-hexameric MCM2-7 complex is loaded onto origin DNA during licensing of eukaryotic DNA replication. *Proc. Natl. Acad. Sci. USA* 106, 20240–20245.
- Fernández-Cid, A., Riera, A., Tognetti, S., Herrera, M.C., Samel, S., Evrin, C., Winkler, C., Gardenal, E., Uhle, S., and Speck, C. (2013). An ORC/Cdc6/MCM2-7 complex is formed in a multistep reaction to serve as a platform for MCM double-hexamer assembly. *Mol. Cell* 50, 577–588.
- Friedman, L.J., and Gelles, J. (2012). Mechanism of transcription initiation at an activator-dependent promoter defined by single-molecule observation. *Cell* 148, 679–689.
- Friedman, L.J., Chung, J., and Gelles, J. (2006). Viewing dynamic assembly of molecular complexes by multi-wavelength single-molecule fluorescence. *Biophys. J.* 91, 1023–1031.
- Frigola, J., Remus, D., Mehanna, A., and Diffley, J.F.X. (2013). ATPase-dependent quality control of DNA replication origin licensing. *Nature* 495, 339–343.
- Gendreizig, S., Kindermann, M., and Johnsson, K. (2003). Induced protein dimerization in vivo through covalent labeling. *J. Am. Chem. Soc.* 125, 14970–14971.
- Grimm, J.B., English, B.P., Chen, J., Slaughter, J.P., Zhang, Z., Revyakin, A., Patel, R., Macklin, J.J., Normanno, D., Singer, R.H., et al. (2015). A general method to improve fluorophores for live-cell and single-molecule microscopy. *Nat. Methods* 12, 244–250.
- Hoskins, A.A., Friedman, L.J., Gallagher, S.S., Crawford, D.J., Anderson, E.G., Wombacher, R., Ramirez, N., Cornish, V.W., Gelles, J., and Moore, M.J. (2011). Ordered and dynamic assembly of single spliceosomes. *Science* 331, 1289–1295.
- Kang, S., Warner, M.D., and Bell, S.P. (2014). Multiple functions for Mcm2-7 ATPase motifs during replication initiation. *Mol. Cell* 55, 655–665.
- Popp, M.W., Antos, J.M., Grotenbreg, G.M., Spooner, E., and Ploegh, H.L. (2007). Sortagging: a versatile method for protein labeling. *Nat. Chem. Biol.* 3, 707–708.
- Randell, J.C.W., Bowers, J.L., Rodríguez, H.K., and Bell, S.P. (2006). Sequential ATP hydrolysis by Cdc6 and ORC directs loading of the Mcm2-7 helicase. *Mol. Cell* 21, 29–39.
- Remus, D., Beuron, F., Tolun, G., Griffith, J.D., Morris, E.P., and Diffley, J.F.X. (2009). Concerted loading of Mcm2-7 double hexamers around DNA during DNA replication origin licensing. *Cell* 139, 719–730.
- Samel, S.A., Fernández-Cid, A., Sun, J., Riera, A., Tognetti, S., Herrera, M.C., Li, H., and Speck, C. (2014). A unique DNA entry gate serves for regulated loading of the eukaryotic replicative helicase MCM2-7 onto DNA. *Genes Dev.* 28, 1653–1666.
- Siddiqui, K., On, K.F., and Diffley, J.F.X. (2013). Regulating DNA replication in eukarya. *Cold Spring Harb. Perspect. Biol.* 5, a012930.

- Stratmann, S.A., and van Oijen, A.M. (2014). DNA replication at the single-molecule level. *Chem. Soc. Rev.* *43*, 1201–1220.
- Sun, J., Kawakami, H., Zech, J., Speck, C., Stillman, B., and Li, H. (2012). Cdc6-induced conformational changes in ORC bound to origin DNA revealed by cryo-electron microscopy. *Structure* *20*, 534–544.
- Sun, J., Evrin, C., Samel, S.A., Fernández-Cid, A., Riera, A., Kawakami, H., Stillman, B., Speck, C., and Li, H. (2013). Cryo-EM structure of a helicase loading intermediate containing ORC-Cdc6-Cdt1-MCM2-7 bound to DNA. *Nat. Struct. Mol. Biol.* *20*, 944–951.
- Sun, J., Fernandez-Cid, A., Riera, A., Tognetti, S., Yuan, Z., Stillman, B., Speck, C., and Li, H. (2014). Structural and mechanistic insights into Mcm2-7 double-hexamer assembly and function. *Genes Dev.* *28*, 2291–2303.
- Takara, T.J., and Bell, S.P. (2011). Multiple Cdt1 molecules act at each origin to load replication-competent Mcm2-7 helicases. *EMBO J.* *30*, 4885–4896.
- Yardimci, H., and Walter, J.C. (2014). Prereplication-complex formation: a molecular double take? *Nat. Struct. Mol. Biol.* *21*, 20–25.

Mammalian NET-Seq Reveals Genome-wide Nascent Transcription Coupled to RNA Processing

Graphical Abstract



Authors

Takayuki Nojima, Tomás Gomes, ..., Maria Carmo-Fonseca, Nicholas J. Proudfoot

Correspondence

carmo.fonseca@medicina.ulisboa.pt (M.C.-F.),
nicholas.proudfoot@path.ox.ac.uk (N.J.P.)

In Brief

Sequencing nascent transcripts from the active site of mammalian RNA polymerase II by a technique called mNET-seq unravels dynamic insights into the transcription cycle, including co-transcriptional splicing and RNA microprocessing.

Highlights

- Development of mammalian native elongating transcript sequencing (mNET-seq)
- Dynamic Pol II CTD phosphorylation during transcription cycle
- Co-transcriptional splicing and microprocessing detected by mNET-seq
- Termination factors are associated with Pol II pausing at both TES and TSS

Accession Numbers

GSE60358



Mammalian NET-Seq Reveals Genome-wide Nascent Transcription Coupled to RNA Processing

Takayuki Nojima,^{1,4} Tomás Gomes,^{2,4} Ana Rita Fialho Grosso,² Hiroshi Kimura,³ Michael J. Dye,¹ Somdutta Dhir,¹ Maria Carmo-Fonseca,^{2,*} and Nicholas J. Proudfoot^{1,*}

¹Sir William Dunn School of Pathology, University of Oxford, South Parks Road, Oxford OX1 3RE, UK

²Instituto de Medicina Molecular, Faculdade de Medicina, Universidade de Lisboa, 1649-028 Lisboa, Portugal

³Department of Biological Sciences, Graduate School of Bioscience and Biotechnology, Tokyo Institute of Technology, 226-8501 Yokohama, Japan

⁴Co-first author

*Correspondence: carmo.fonseca@medicina.ulisboa.pt (M.C.-F.), nicholas.proudfoot@path.ox.ac.uk (N.J.P.)

<http://dx.doi.org/10.1016/j.cell.2015.03.027>

This is an open access article under the CC BY-NC-ND license (<http://creativecommons.org/licenses/by-nc-nd/4.0/>).

SUMMARY

Transcription is a highly dynamic process. Consequently, we have developed native elongating transcript sequencing technology for mammalian chromatin (mNET-seq), which generates single-nucleotide resolution, nascent transcription profiles. Nascent RNA was detected in the active site of RNA polymerase II (Pol II) along with associated RNA processing intermediates. In particular, we detected 5' splice site cleavage by the spliceosome, showing that cleaved upstream exon transcripts are associated with Pol II CTD phosphorylated on the serine 5 position (S5P), which is accumulated over downstream exons. Also, depletion of termination factors substantially reduces Pol II pausing at gene ends, leading to termination defects. Notably, termination factors play an additional promoter role by restricting non-productive RNA synthesis in a Pol II CTD S2P-specific manner. Our results suggest that CTD phosphorylation patterns established for yeast transcription are significantly different in mammals. Taken together, mNET-seq provides dynamic and detailed snapshots of the complex events underlying transcription in mammals.

INTRODUCTION

Virtually all transcripts synthesized by RNA polymerase II (Pol II) from protein-coding genes are co-transcriptionally processed to generate the final functional mRNA (Moore and Proudfoot, 2009). First, a Cap structure (^m7Gppp) is added to the transcript 5' end soon after transcriptional initiation, which ultimately earmarks transcripts for efficient cytoplasmic translation. Then as the polymerase proceeds to elongate through the gene body (GB), intronic RNA, which often constitutes the majority of the primary transcript in mammalian genes, is removed by a splicing mechanism involving the stepwise assembly of a complex set of small

RNA (snRNA) and associated proteins that together make up the spliceosome (Wahl et al., 2009). In outline, U1snRNA-protein complex (U1snRNP) identifies the intron 5' splice site (SS) as soon as it is transcribed by Pol II, and then on reaching the 3' end of the intron multiple snRNPs, U2, U4, U5, and U6 recognize the 3' SS and proximal intronic branch point on the nascent transcript. Following reorganization of snRNP/intron interactions, the branch point A nucleotide carries out a 2'OH nucleophilic attack on the 5' SS, resulting in cleavage of the intron from the upstream exon. The newly formed upstream exon 3' OH then undergoes a second nucleophilic attack on the 3' SS, resulting in precise fusion of adjacent exons and release of the intron. Prior to intron splicing, hairpin structures embedded within some introns are excised by the double-strand RNA-specific microprocessor complex. This comprises an RNA-binding protein DGCR8 together with the endonuclease Drosha, which facilitate release of pre-microRNA (miRNA) hairpins from the nascent transcript. These pre-miRNA go on to form cytoplasmic miRNA, which are critical for the translational regulation of many mRNA (Krol et al., 2010). Finally at gene 3' ends, a further RNA-processing reaction involving cleavage of the nascent transcript at a specific poly(A) signal (PAS) occurs. This RNA cleavage reaction is mediated by an endonuclease (CPSF73) that is part of a large multimeric cleavage and polyadenylation complex. A poly(A) tail is then added to the mRNA 3' end, promoting rapid release of mRNA from the chromatin template (Proudfoot, 2011). Although these individual RNA-processing mechanisms are well characterized, their interconnections with transcription remain enigmatic. We describe in this study a method to investigate these interconnections, genome wide.

The above outlined co-transcriptional pre-mRNA-processing reactions are precisely coordinated with the Pol II transcription cycle that proceeds from initiation at the transcription start site (TSS), leading on to elongation through the GB and ending with release of the mRNA at the PAS, also called the transcription end site (TES). Finally, termination occurs whereby Pol II separates from the DNA template. Both the Pol II transcription cycle and coupled pre-mRNA-processing reactions are orchestrated by a unique structural feature of Pol II. This comprises an extended C-terminal domain (CTD) of the large subunit (Rpb1) that has a heptad structure YSPTSPS repeated 52 times with

some variation in mammals and 26 times in budding yeast. This CTD is separate from the main globular enzyme, being positioned close to the RNA exit channel. It is relatively unstructured (Meinhart and Cramer, 2004) and subject to extensive post-translational modification, especially phosphorylation of S2 and S5 but also Y1, T4, and S7 (Heidemann et al., 2013; Hsin and Manley, 2012). This combined but differential CTD phosphorylation is often considered to be a molecular code that acts to orchestrate transcription and coupled pre-mRNA processing. Especially in simpler eukaryotes, such as budding yeast, CTD S5P is correlated with TSS-associated events, whereas S2P is thought to correlate with TES events (Buratowski, 2009). However in the larger and more complex genes of mammals, this CTD code may be less clear-cut and vary between different gene classes.

To gain a more complete understanding of the Pol II transcription cycle and how this is coordinated with co-transcriptional pre-mRNA processing, genome-wide analysis of nascent RNA has been undertaken. For example, global nuclear run on-sequencing (GRO-seq) and precision nuclear run on-sequencing (PRO-seq) with modified nucleotides (Core et al., 2008; Kwak et al., 2013) provide a way to study Pol II profiles associated with nascent transcription. Similarly, 5' capped nascent RNA isolated from insoluble chromatin can be sequenced at high resolution (3'NT-seq) (Weber et al., 2014). These approaches generated detailed maps of Pol II nascent transcription in mammals and flies, which accumulates at promoters, providing a regulated transition from initiation into productive elongation (Adelman and Lis, 2012; Core and Lis, 2008; Gilchrist et al., 2010; Rahl et al., 2010). Precise maps of PRO-seq reads identified two different types of Pol II pausing at the TSS, referred to as proximal and distal TSS pausing. PRO-seq additionally showed Pol II accumulation near 3'SS, possibly important for the selection of active exons (Kwak et al., 2013). GRO-seq has also shown a correlation between Pol II density and nucleosome occupancy as observed at the TES of many genes, suggesting a connection with transcription termination (Grosso et al., 2012). A significant limitation to these above nascent RNA-mapping techniques is that the relationship between Pol II CTD modification and nascent RNA was not established.

Precise maps of Pol II nascent RNA have also been generated by native elongating transcript sequencing (NET-seq) in yeast (Churchman and Weissman, 2011). Here, endogenous Pol II is flag tagged by genomic integration allowing immunoprecipitation (IP) of Pol II nascent RNA complexes. However, again connections between Pol II CTD modifications and nascent RNA could not be determined. In contrast, we establish mammalian NET-seq technology (mNET-seq) using a selection of CTD phosphorylation-specific Pol II antibodies to IP Pol II-associated transcripts. In detail, we have compared low or unphosphorylated (unph), S2P, S5P, and total (unph+ph) CTD mNET-seq profiles and show that unph CTD Pol II-nascent RNA are accumulated over the TSS, whereas S2P Pol II-nascent RNA are spread throughout the GB and TES. Remarkably S5P profiles precisely correlate with active splicing on protein-coding genes. An important feature of our analysis is that we are able to directly detect the initial 5'SS cleavage step in intron splicing and can also observe active Drosha cleavage of pre-miRNA hairpin structures

present in gene introns. In effect, our extensive mNET-seq data sets provide a "treasure trove" of detailed information on nascent transcription and co-transcriptional RNA processing in mammalian cells.

RESULTS

mNET-Seq Strategy

To detect unstable nascent RNA across the human genome, we isolated a nuclear chromatin fraction from HeLa cells enriched in transcriptionally active Pol II (Pol Ilo) and associated nascent RNA (Figure 1A) (Nojima et al., 2013). This chromatin-bound RNA was fragmented to 150–200 nt and ligated to adaptors for strand-specific paired-end deep sequencing (Figure S1A, top; Experimental Procedures). ChrRNA-seq detects unstable RNA, such as promoter upstream transcripts (PROMPTs), introns, and read-through transcripts (Figures 1D and S1B). For mNET-seq, chromatin was digested with micrococcal nuclease (MNase) to release Pol II from insoluble chromatin. Note that accessible RNA will also be digested (Figure S1A, bottom; Experimental Procedures). Western blot analysis using Pol II 8WG16 antibody confirmed that both phosphorylated (Pol Ilo) and unphosphorylated (Pol Ila) forms were released in a MNase dose-dependent manner (Figure 1B). Nascent RNA distribution was also tested after cell fractionation and MNase digestion, by using nuclear run on (NRO) nuclei, labeled with [α - 32 P] UTP (Figure 1C). The nucleoplasmic (Np) fraction contained long 32 P-RNA (over 600 nt). However, after MNase digestion (40 U/ μ l), the residual chromatin pellet (P) contained RNA of 10–600 nt, whereas the chromatin supernatant (S) had shorter RNA of 10–200 nt. This supernatant fraction was then IPed using Pol II 8WG16 antibody, which efficiently precipitated this shorter RNA. Although the predominant size of the IPed RNA was 20–45 nt, we selected a longer RNA fraction (35–100 nt) to obtain unique alignment with the human genome after deep sequencing. In this method, the Pol II complex will protect nascent RNA from MNase digestion. The hydroxylated 3' end (3'OH) of the nascent RNA corresponds to the terminal nucleotide synthesized by Pol II (Figure 1A, asterisk). The 5' end of the cleaved Pol II-associated RNA is also hydroxylated after MNase digestion. To achieve strand-specific RNA sequencing, we carried out a kinase reaction on the IP beads to phosphorylate all nascent RNA 5' ends but leave the Pol II-embedded 3'OH intact (Figure S1A). Illumina adapters were then ligated onto gel-purified RNA, and Illumina high-throughput paired-end sequencing was carried out and generated $\sim 10^8$ reads for each mNET-seq sample. For library construction, we omitted the NRO step because the NRO reaction may perturb the native Pol II distribution. The above Pol II IP from MNase-treated chromatin coupled with isolation and sequencing of the associated RNA constitutes a refined mammalian NET-seq protocol.

Finally, libraries were prepared from two biological replicates of HeLa native chromatin after Pol II 8WG16 IP. Deep sequencing was conducted using a reverse sequence primer to read the 3' ends of the RNA insert, which corresponds to the RNA synthesis site in the Pol II active site (Figure 1A). mNET-seq data aligned to the human genome (hg19) was compared to 8WG16 chromatin IP (ChIP-seq) and ChrRNA-seq as shown for *ATP5G1*, a typical

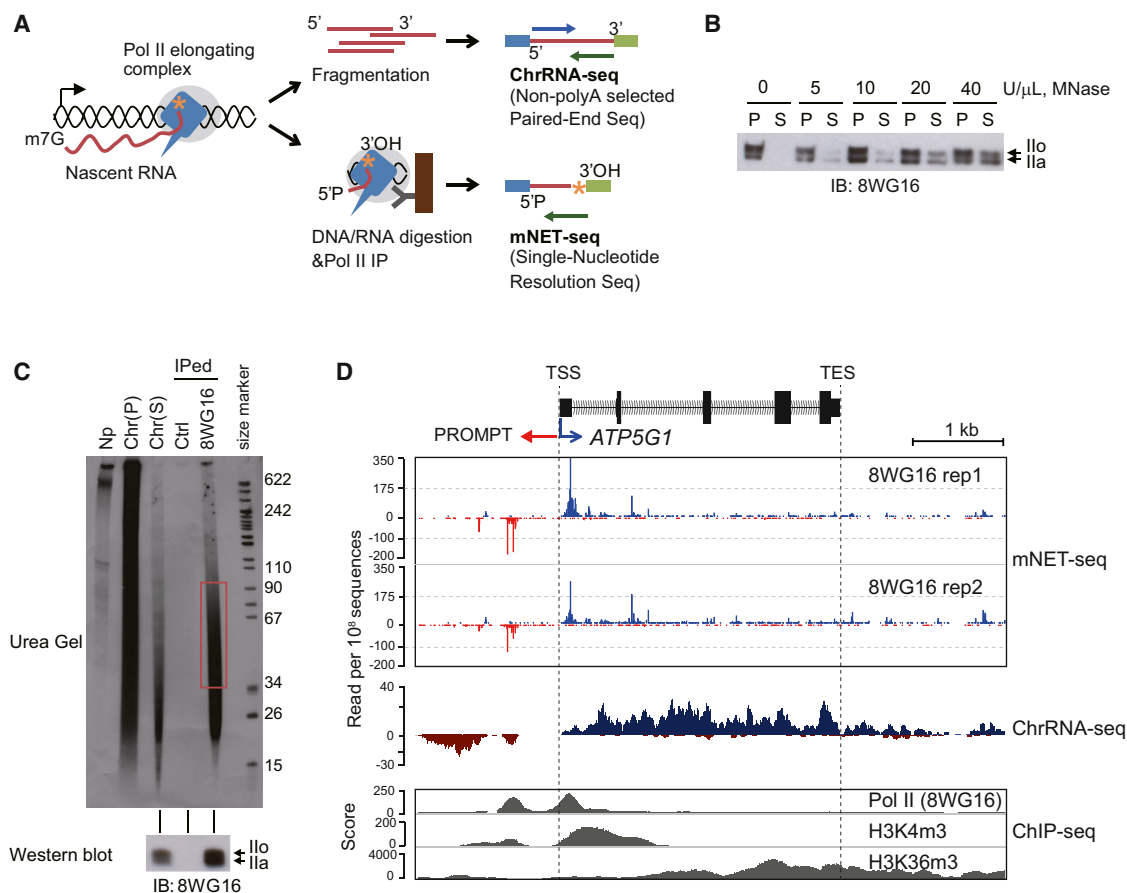


Figure 1. mNET-Seq Methodology

(A) ChrRNA-seq and mNET-seq strategies. Pol II (blue) elongating complex (gray circle) and associated nascent RNA (red line) in chromatin. Orange asterisk depicts the 3'OH of nascent RNA. For ChrRNA-seq (top), fragmented nascent RNA is subjected to directional paired-end deep sequencing. For mNET-seq (bottom), DNA and RNA are digested with MNase and Pol II-nascent RNA complex precipitated with Pol II antibody. Isolated RNA is deep sequenced, and the 3' end nucleotide uniquely mapped on the human genome.

(B) Pol II release from insoluble chromatin DNA. Chromatin DNA was digested with increasing amounts of MNase. Western blot used 8WG16 Pol II antibody. P; pellet, S; supernatant. Ilo and Ila indicate phosphorylated and unphosphorylated Pol II.

(C) Nascent RNA distribution in mNET-seq method. Nascent RNA was 32 P-labeled by NRO reaction. Fractionated nascent RNA are nucleoplasm (Np), chromatin pellet (Chr(P)) and supernatant (Chr(S)). IP was with 8WG16 Pol II antibody. 35–100 nt RNA purified from gel (red box). IPed Pol II was detected by western blot (bottom).

(D) *ATP5G1* mNET-seq. Two biological replicates of mNET-seq/unph using 8WG16 Pol II antibody. ChrRNA-seq shown as mNET-seq input. ChIP-seq (Pol II [8WG16], H3K4m3, and H3K36m3) data are from ENCODE project data sets (Consortium et al., 2012).

example of an actively expressed gene in HeLa cells (Figure 1D). A lower-resolution cluster of genes expressed at varying levels is also presented (Figure S1B). Note that as mNET-seq identifies the 3' end of transcript within the Pol II active site, TSS-associated reads will only be detected 30 nt or beyond the exact TSS. Modifications of histone H3, H3K4m3 and H3K36m3, reflect active promoters and gene bodies, respectively. Strand-specific transcription activity was revealed by ChrRNA-seq. As expected, both replicates of mNET-seq/8WG16 (unph) display strong peaks at the active TSS, consistent with the previously described ChIP-seq/unph profiles. We therefore predict that this TSS-accumulated mNET-seq signal reflects Pol II pausing. Additionally, mNET-seq data revealed both sense and antisense transcription on active genes, as previously shown by GRO-seq and PRO-seq (Core et al., 2008; Kwak et al., 2013).

Pol II CTD Phosphorylation-Specific Nascent RNA Profiles at TSS and TES

A major benefit of our mNET-seq procedure is that it allows the use of different Pol II antibodies to precipitate modified Pol II-associated nascent transcripts. We elected to employ newly described specific monoclonal antibodies to detect CTD phosphorylation-dependent nascent RNA profiles for S2P, S5P, and all CTD isoforms (Figure 2A) (Stasevich et al., 2014). We carried out further tests to confirm the specificity of these antibodies versus 8WG16. First we performed ELISA assays (Figure S2A) with synthetic peptides of 15 amino acids, containing two adjacent heptad repeats, either singly or doubly phosphorylated on S2P, S5P, and S7P. As expected, 8WG16 bound with relative specificity to unphosphorylated or singly phosphorylated CTD peptides. CMA601 bound all CTD peptides with or without serine

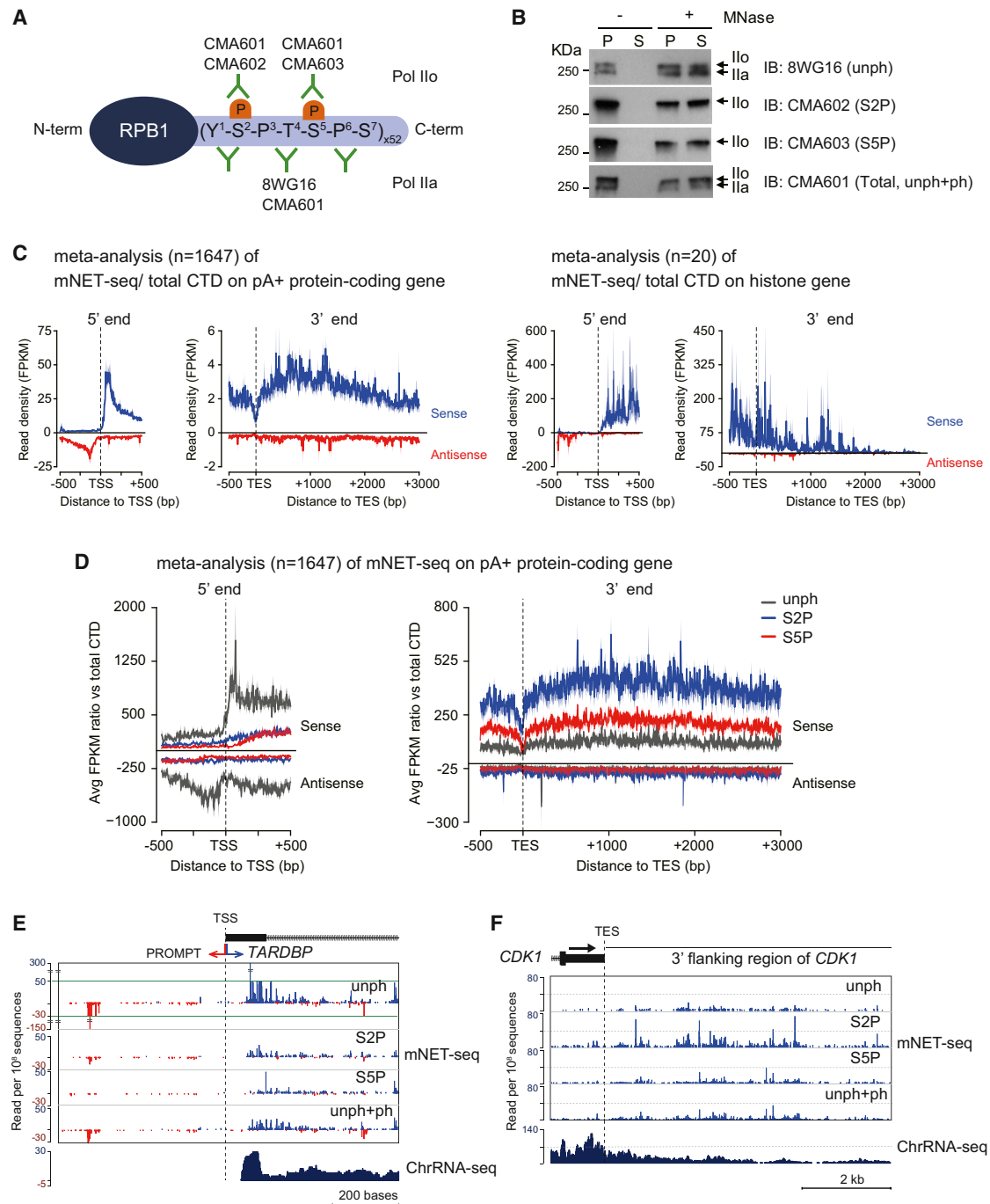


Figure 2. mNET-Seq with Different Phospho-CTD Modifications

(A) Diagram showing different Pol II antibody epitopes on CTD (Stasevich et al., 2014).

(B) Specificity of Pol II phosphorylation released from chromatin following MNase treatment with indicated Pol II antibodies.

(C) Meta-analyses of mNET-seq/unph+ph on TSS and TES of pA⁺ protein-coding genes (left) and histone genes (right). Read density (FPKM) of mNET-seq data were plotted around TSS (± 0.5 kb) and TES (-0.5 k \sim +3 kb). Data on pA⁺ and histone genes are represented as mean \pm SEM. mNET-seq sense strand, blue; antisense strand, red.

(D) Meta-analyses of mNET-seq on TSS and TES of pA⁺ protein-coding genes. Ratio of read density (FPKM) of indicated mNET-seq data to mNET-seq/unph+ph data was plotted around TSS (± 0.5 kb) and TES (-0.5 k \sim +3 kb). unph, dark gray; S2P, blue; S5P, red. Line and shading represent mean \pm SEM for each bin.

(E and F) mNET-seq profiles over TSS of *TARDBP* (E) and TES of *CDK1* (F). Read density, read per 10⁸ sequences.

phosphorylation, whereas CMA602 and CMA603 bound CTD peptides containing S2P and S5P, respectively. We also performed IP Pol II western blots (Figure S2B) with these four antibodies under mNET-seq conditions and confirmed their specificity and IP efficiency. We finally performed Pol II ChIP analysis on three specific genes comparing our monoclonal antibodies to commercial polyclonal antibodies (ab5095 [S2P] and ab5131 [S5P], respectively) that are widely used for ChIP-seq assays (Pérez-Lluch et al., 2011) (Figure S2C). Notably, matching ChIP profiles were observed for the different S2P- and S5P-specific antibodies. A potential concern with our mNET-seq protocol was that, as we only partially solubilize the chromatin pellet by MNase treatment, there may be selective release of different Pol II modifications. However, the chromatin pellet and supernatant following MNase treatment gave very similar patterns of Pol IIo and Pol IIa with all four antibodies arguing against selective release of differentially modified Pol II (Figure 2B).

Based on previously published RNA-seq data (Lacoste et al., 2014), we found 11,560 (45%) RefSeq genes actively transcribed in HeLa cells. However, to avoid over-representation of ncRNA (such as rRNA, tRNA, snoRNA, and snRNA) in the mNET-seq meta-analysis, we excluded genes overlapping these sequences. We also excluded overlapping transcription units as these might bias average profiles (see Extended Experimental Procedures). We initially looked at meta-profiles over TSS and TES regions for all Pol II isoforms (unph+ph antibody). As expected, bidirectional TSS mNET-seq peaks were detected and a wider, mainly sense peak beyond the TES. In contrast, the histone genes gave a flatter mNET-seq profile across these short poly(A) minus genes and diminished TSS antisense reads (Figure 2C). This clearly shows the specificity of our mNET-seq profiles. We next analyzed meta-profiles using the CTD phospho-specific Pol II antibodies (Figure 2D). To allow cross-comparison between the different antibodies, the data are presented as a ratio with mNET-seq reads obtained for total Pol II (unph+ph). Remarkably, only mNET-seq/unph gave a bidirectional TSS profile, whereas S2P and S5P show a gradual increase from low TSS signals to higher signals in the GB. The TES meta-profiles revealed the expected dominance of S2P. Single-gene TSS and TES mNET-seq profiles (*TARDBP* and *CDK1*, respectively) were consistent with the meta-profiles. The marked differences in mNET-seq profiles observed for specific CTD phosphorylation were not seen for histone genes, which showed little difference other than higher unph reads across the genes (Figure S2D). Overall, mNET-seq profiles reveal remarkable CTD phosphorylation specificity for poly(A)⁺ protein-coding genes.

Exon Tethering to Pol II with CTD S5P for Co-Transcriptional Splicing

The coupling of Pol II transcription to splicing is well established (Moore and Proudfoot, 2009). For example, altered Pol II elongation speed can affect alternative splicing patterns (Ip et al., 2011; Muñoz et al., 2009), indicating that Pol II slows down near splice sites to promote spliceosome assembly. In particular, genome-wide analysis of nascent RNA by high-resolution tiling arrays in yeast showed that Pol II is paused over terminal exons but only for co-transcriptionally spliced genes (Carrillo Oesterreich et al., 2010). Additionally, precisely timed ChIP analysis in yeast

revealed that Pol II CTD S5P accumulates over the 3'SS of intron-containing genes (Alexander et al., 2010). Furthermore, this splicing-dependent Pol II pausing requires pre-spliceosome assembly (Chathoth et al., 2014).

We were interested to determine whether our mNET-seq profiles reflect the co-transcriptionality of splicing, but we observed unexpected patterns. First, we present the mNET-seq profile of a specific gene, *TARS*, comparing the four different Pol II antibody profiles (Figure 3A). Surprisingly, mNET-seq/S5P selectively detected prominent exon peaks. We have reasoned that mNET-seq will specifically identify the nascent transcript 3'OH in the Pol II active site. However, as previously noted (Churchman and Weissman, 2011), co-precipitated spliceosomes contain 3'OH RNA derived from splicing intermediates that also yield NET-seq signal. Remarkably, single-nucleotide analysis of *TARS* exon 9 reveals that the major S5P peaks exactly match the 5'SS (Figure 3A, lower panel). These observations suggest that S5P detects the initial 5'SS cleavage intermediate, indicating that spliceosome complex C is associated with Pol II CTD S5P. We next performed meta-analysis of mNET-seq comparing all four antibodies over gene regions that are co-transcriptionally spliced as judged by fused exon reads (Figure 3B). As for *TARS*, these actively spliced introns give a strong 5'SS S5P-specific signal indicative of co-precipitated spliceosome C complex. Significantly, we also detect selective accumulation of S5P reads over the downstream exon. Apparently, Pol II CTD S5P pauses over exon sequences and so allows time for the spliceosome to perform the first catalytic step. This will generate intronic lariats and cleaved upstream exons, which remain tethered to the downstream positioned Pol II. To further substantiate this mechanism, we carried out additional meta-analysis of predicted included or excluded exons from final spliced mRNA in HeLa cells by analyzing total poly(A)⁺ RNA-seq data (Katz et al., 2010). Again, we demonstrate a strong 5'SS S5P signal for included but not excluded exons (Figure 3C). We finally present mNET-seq analysis for five intronless genes that show no clear S5P peaks (Figure S3).

The surprising observation that mNET-seq/S5P profiles show a strong 5'SS signal merited further experimental validation. We therefore employed the splicing inhibitor pladienolide B (Pla-B), which is known to inactivate the SF3b sub-complex of U2 snRNP (Kotake et al., 2007), required for intronic branch point recognition as a prelude to the first catalytic step of intron splicing. We initially confirmed the effect of Pla-B treatment on two specific genes (*BRD2* and *BZW1*). First, nucleoplasmic RNA from control DMSO or Pla-B-treated cells was sequenced (NpRNA-seq), and the patterns obtained across these two genes showed a clear increase in intron retention (Figure 4A). This was confirmed by RT-PCR with specific exon primers (Figure 4B) where Pla-B treatment enhanced intron retention in both cases. Notably, mNET-seq/S5P analysis across these same two genes showed the usual high 5'SS peaks for the control but not Pla-B-treated cells (Figure 4A). To establish generality, we performed meta-analysis over 1,051 actively spliced introns (Figure 4C). As before, we saw the high 5'SS peak and enrichment of S5P reads over the downstream exon. Dramatically, Pla-B treatment eradicated the 5'SS signal and substantially reduced downstream exon pausing. These results confirm that the 5'SS

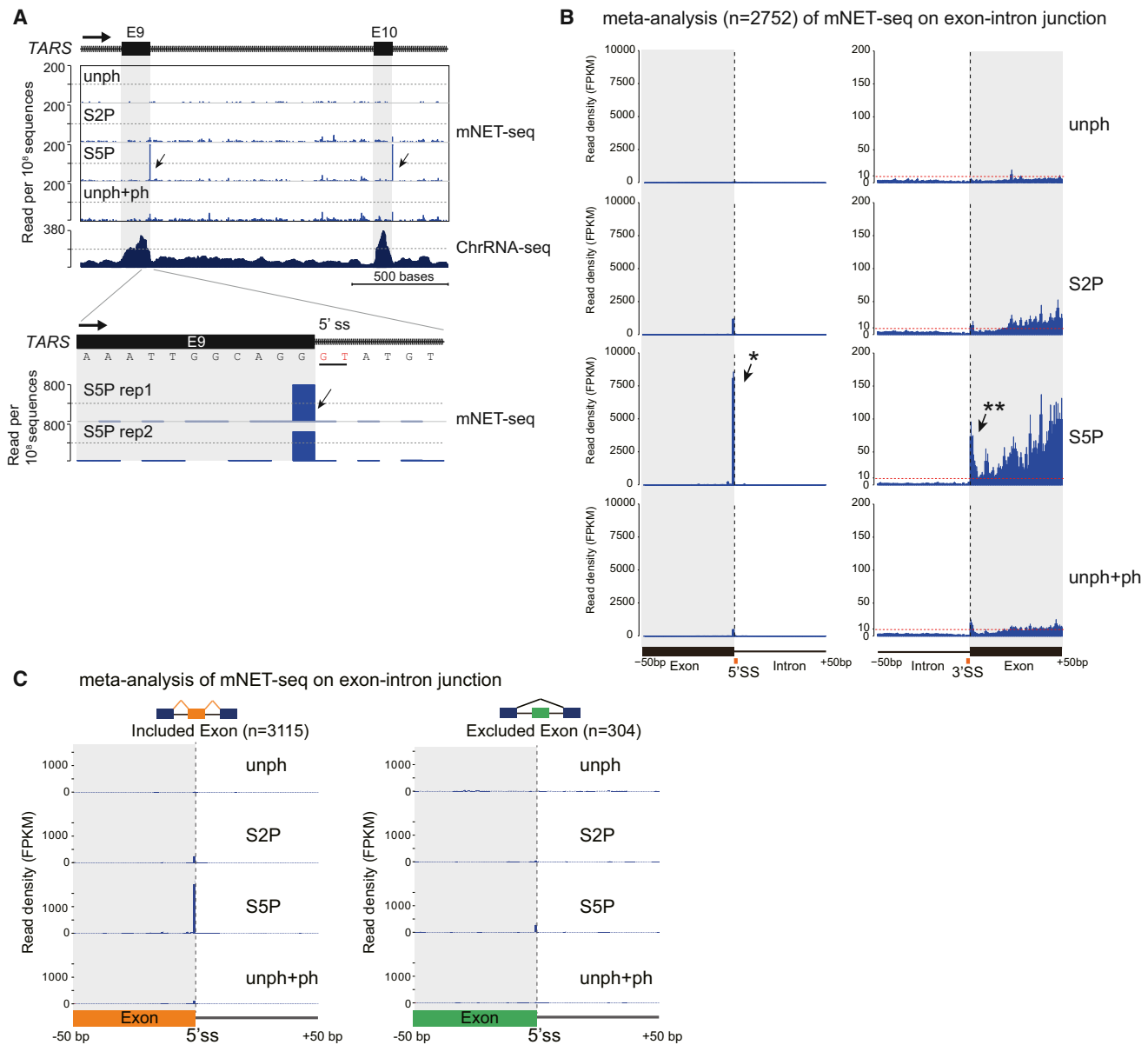


Figure 3. Exon Tethering to Ser5-Phosphorylated Pol II Complex

(A) TARS mNET-seq profile with different antibodies, followed by expanded view of exon 9 5' SS. S5P-dominant peaks are indicated by black arrows.

(B) Meta-analysis of mNET-seq profiles over 3' ends (left) and 5' ends (right) of co-transcriptionally spliced exons. Single asterisk, peak at 3' end of spliced exon; double asterisk, accumulation of Pol II at 5' end of spliced exon.

(C) Meta-analysis of mNET-seq data over 5' SS of included exons (orange) and excluded exons (green).

For (B) and (C), bars represent mean \pm SEM for each base.

mNET-seq/S5P signal that we detect genome wide for spliced exons is indeed a bona fide splicing intermediate.

We also studied the mutually exclusive exons 9 and 10 of *PKM*. RT-PCR and ChrRNA-seq analyses show that exon 10 is predominantly included in mature *PKM* transcripts in HeLa cells (Figures S4A and S4B) (David et al., 2010). Furthermore the mNET-seq/S5P profile gave the characteristic 5' SS signal at the end of exon 10 but not exon 9 of *PKM* (Figure S4B). To experimentally manipulate this well-known case of alternative splicing,

we performed S5P analysis on chromatin from cells with the splicing-regulatory protein PTBP1 depleted by siRNA treatment (Figure S4C), which is known to be required for the alternative splicing of *PKM* exon 10 (David et al., 2010). As shown by a lower-resolution and then single-nucleotide resolution mNET-seq profile, the 5' SS peak is reduced at the end of exon 10 but enhanced at the end of exon 9 after depletion of PTBP1 (Figure S4E). Again, this splice-site switch is confirmed by RT-PCR analysis (Figure S4D). Overall, these data on *PKM* exon 9 and

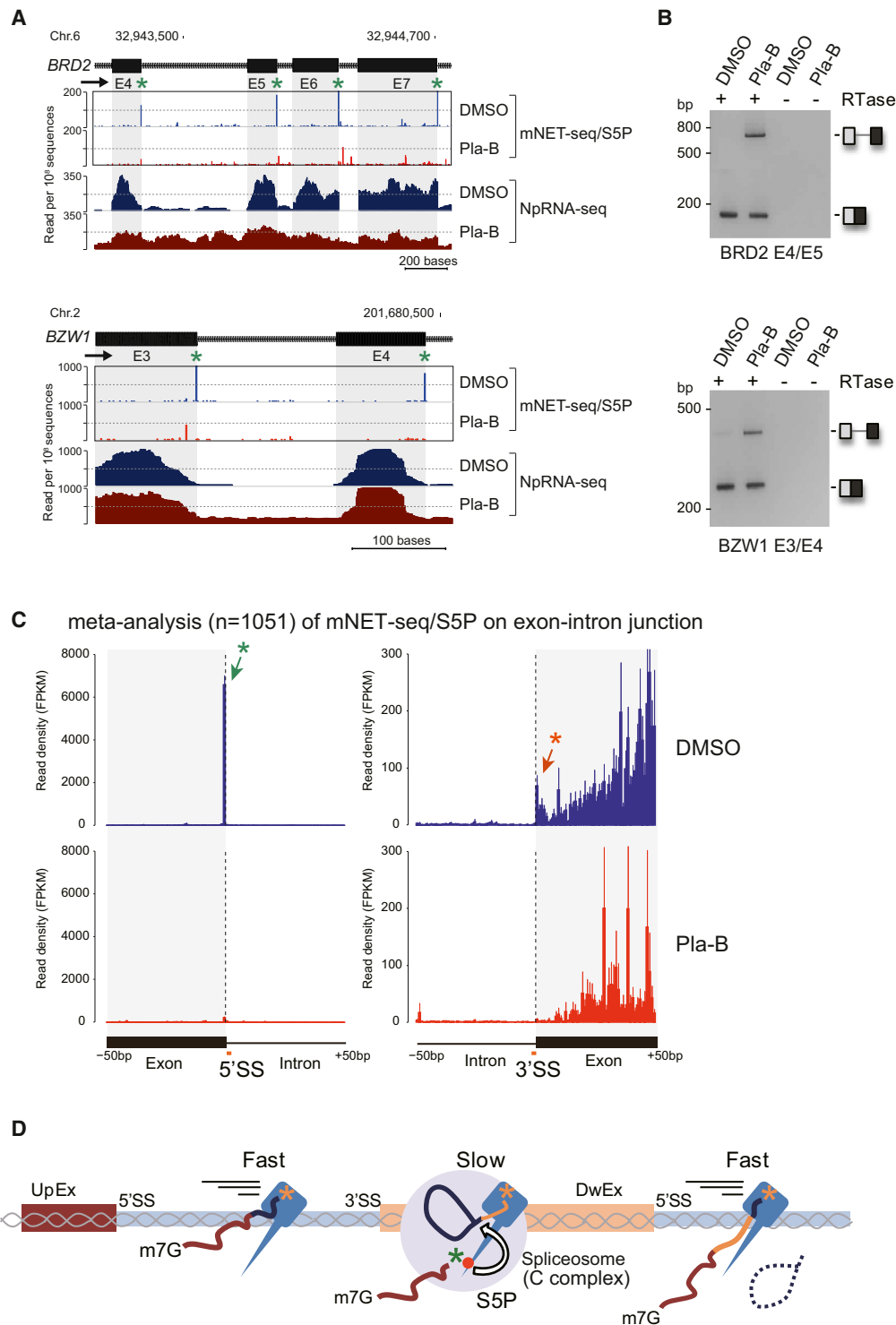


Figure 4. Effect of Splicing Inhibition on mNET-Seq and ChrRNA-Seq Profiles

(A) mNET-seq and NpRNA-seq on *BRD2* and *BZW1* from HeLa cell treated with DMSO (blue) or splicing inhibitor Pla-B (red). Green asterisks denote 5' SS peaks. (B) RT-PCR analysis of indicated exon splicing showing unspliced and spliced RNA products. (C) Meta-analysis of mNET-seq/S5P around exon 5'SS and 3'SS from DMSO (blue) and Pla-B (red) treated HeLa cells. S5P-peaks at 5' and 3' ends of spliced exons are shown by orange and green asterisks, respectively. Bars represent mean \pm SEM for each base. (D) Co-transcriptional splicing model. 3'OH of upstream exon (UpEx, dark red) and RNA in Pol II catalytic site are shown as green and orange asterisks, respectively. 3'OH of the UpEx RNA is protected in S5P Pol II-spliceosome C complex (gray circle). S5P Pol II pauses over DwEx.

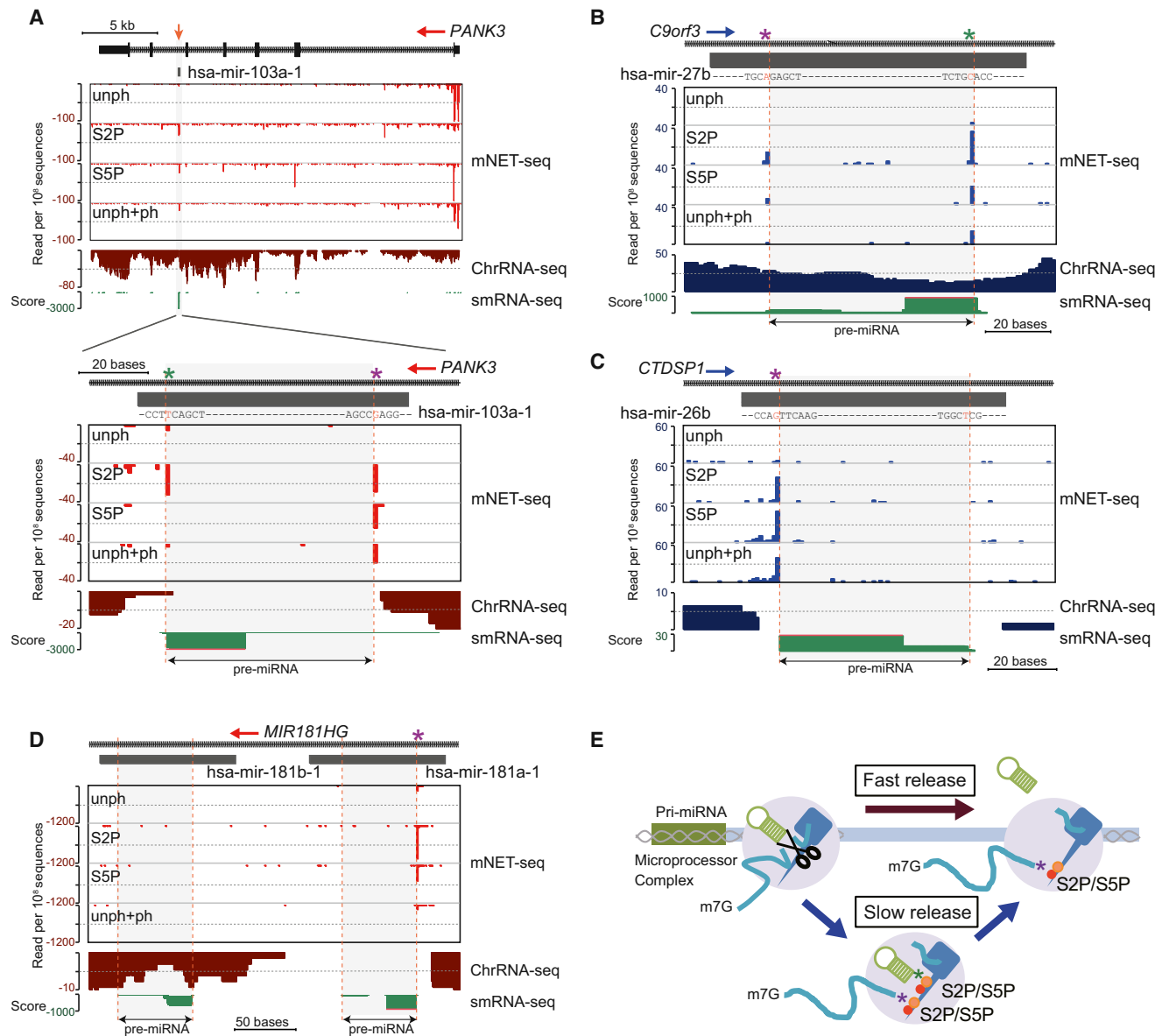


Figure 5. Pre-miRNA Biogenesis from Protein-Coding Gene Introns

(A–D) mNET-seq with different Pol II antibodies versus ChrRNA-seq over intronic pre-miRNAs. (A) mNET-seq data on *PANK3* with magnified view over hsa-mir-103a-1 denoted by a black rectangle. The pre-miRNA is indicated by an orange arrow (top). Three other pre-miRNAs are also shown: hsa-mir-27b (B), hsa-mir-26b (C), and hsa-mir181a/b-1 (D). Drosha cleavage sites are identified by dashed orange lines, and asterisks indicate frequent cleavage sites (5' end, purple; 3' end, green). Small RNA-seq data are shown below (green).

(E) Model of co-transcriptional pre-miRNA biogenesis. Pre-miRNA DNA and hairpin RNA are shown in green. Co-transcriptional Drosha cleavage (scissors) and spliceosome (gray) shown with 3' ends of cleaved RNA (purple asterisk) and pre-miRNA (green asterisk) tethered to phosphorylated CTD. Pre-miRNA release may occur from the transcription complex, fast (dark red arrow) or slow (blue arrows).

10 alternative splicing fully corroborate the general upstream exon-tethering pattern for actively spliced exons as demonstrated by our mNET-seq analysis.

Co-Transcriptional Pre-miRNA Biogenesis

Most pre-miRNA are present within the introns of protein-coding genes and are excised co-transcriptionally by the microprocessor complex, containing Drosha and DGCR8 (Morlando

et al., 2008; Pawlicki and Steitz, 2008). Drosha cleavage generates 3'OH ends that have the potential for mNET-seq detection. Because RNA cleavage sites on pre-miRNA generated by the microprocessor complex are quite variable, we individually checked the mNET-seq profiles for highly expressed pri-miRNA in HeLa cells. Our analysis began with *PANK3*, which harbors hsa-mir-103a-1 in its penultimate intron (Figure 5A). Its mNET-seq profiles show high S5P 5'SS peaks indicative of exon

tethering for each exon except exon 5, before the pre-miRNA-containing intron 5. Instead a peak is detected with S5P- and S2P-specific antibodies over the pre-miRNA within this intron. The single-nucleotide resolution profile over hsa-mir-103a-1 (Figure 5A, bottom) shows two peaks by mNET-seq/S2P defining the pre-miRNA 5' and 3' ends. Notably, only the 5' end is detected by mNET-seq/S5P. Similarly hsa-mir-27b in an intron of *C9orf3* gives S5P and S2P peaks at both ends of the pre-miRNA (Figure 5B). In contrast, for intronic hsa-mir-26b (*CTDSP1*), only a 5' peak is detectable (Figure 5C). A further three examples of intronic pre-miRNAs show both 5' and 3' pre-miRNA peaks detectable by either mNET-seq/S5P or S2P (Figures S5A–S5C). These specific 5' and 3' end pre-miRNA peaks correspond to the 3' ends of the cleaved intron and the pre-miRNA, which reaffirms the co-transcriptionality of pre-miRNA processing. As with spliceosomes, we suggest that microprocessor is co-precipitated with Pol II so that 3'OH intermediates of Drosha cleavage are detected by mNET-seq. Two pre-miRNAs (hsa-mir181a-1 and hsa-mir181b-1) are located in the *MIR181A1HG* intron (Figure 5D). Although the ENCODE project data (Consortium et al., 2012) show that both mature miRNAs are expressed in HeLa cells, only hsa-mir181a-1 yields significant mNET-seq peaks. This correlates with ChrRNA-seq analysis showing a signal window over hsa-mir181a-1, but not hsa-mir181b-1. We infer that only hsa-mir181a-1 is co-transcriptionally processed. Evidently, mNET-seq distinguishes co-transcriptional and post-transcriptional pre-miRNA processing. We also note that the variable mNET-seq double peaks (i.e., hsa-mir-27b) and single peaks (i.e., hsa-mir-26b) suggest kinetic differences in pre-miRNA biogenesis. Some pre-miRNAs (such as pre-miRNA-26b and 181a-1) may be released immediately from the Pol II elongation complex after microprocessor cleavage. Other pre-miRNAs (such as pre-miRNA-27b and let-7g) may be more slowly released with the 3' ends of the pre-miRNA still tethered to the Pol II elongation complex (Figure 5E, model). Significantly, S2P and S5P generally show larger peaks than unph for pre-miRNA processing, suggesting that CTD phosphorylation is important for co-transcriptional pre-miRNA biogenesis. For the *MIR17HG* locus containing six tandem pre-miRNA (Figure S5D), Drosha co-transcriptionally cleaves the outer pre-miRNA. However, more inner pre-miR18a and pre-miR19a appear to be processed post-transcriptionally, as judged by a lack of mNET-seq peaks and the absence of a hole in the ChrRNA-seq profile over these sequences (Conrad et al., 2014).

Pol II Pausing Regulated by CPA Factors at TES

To establish the impact of CPA factors on mNET-seq profiles over and 3' to TES, we depleted CPA (CPSF73 and CstF64+ CstF64t) and Xrn2 by siRNA treatment (Figure S6A, left panels). ChrRNA-seq analyses for specific genes demonstrated clear Pol II termination defects after depletion of CPA factors (Figure S6A, right panels). Double-knockdown of CstF64+CstF64t proteins was necessary to see a full termination defect, presumably due to their functional redundancy in HeLa cells (Yao et al., 2012). Xrn2 knockdown showed no significant termination defect as suggested previously (Brannan et al., 2012). Possibly like CstF64, this factor acts redundantly with other termination factors. Interestingly, Xrn2 depletion increased transcript levels

within the GB, suggesting a major role for Xrn2 in nuclear turnover (Davidson et al., 2012). We also performed ChrRNA-seq analysis for histone genes (Figure S6B). Here, CPSF73 still showed a clear termination defect consistent with the known association of CPSF with the histone 3' processing machinery (Kolev and Steitz, 2005). In contrast, CstF64+CstF64t or Xrn2 knockdowns showed no termination defect. Notably, loss of Xrn2 significantly increased histone gene reads, again indicating a major role in histone mRNA turnover.

To extend our termination studies to mNET-seq, we principally analyzed CTD S2P profiles as these are most likely to show effects on 3' end processing (Ahn et al., 2004; Hirose and Manley, 1998; McCracken et al., 1997). However, we also performed S5P and unph meta-analyses in CPSF73-depleted cells. Interestingly, depletion of CPSF73 substantially reduced Pol II unph, S2P, and S5P pausing over the TES (Figure 6A). Similarly CstF64+CstF64t double-knockdown reduced TES pausing. In contrast, Xrn2 knockdown showed no significant difference to the siLuc control (Figure 6B). We also observe that S2P profiles upon knockdown of CPA factors crossed over the siLuc control profile approximately 2.5 kb downstream of the TES, reflecting expected transcriptional termination defects (Figures 6A and 6B). These mNET-seq meta-analyses were complemented by ChrRNA-seq (Figure 6C) where meta-analysis of CPSF73 knockdown gave clear a termination defect immediately following the TES, whereas CstF64+CstF64t double-knockdown showed a termination defect further downstream. Again, specific genes are shown from both our mNET-seq and ChrRNA-seq data sets and show similar trends to those seen in meta-analyses after CPA knockdown (Figures S6C and S6D).

3' End Termination Machinery Regulates Levels of Promoter-Associated RNA

Although RNA cleavage sites have been previously identified near TSS (Almada et al., 2013), which factors are involved in this process has not been determined. Because CPSF73 contains the endonuclease activity, it could potentially cleave nascent RNA near the TSS by recognition of cryptic PAS. We therefore performed meta-analysis across TSS using the mNET-seq data obtained from knockdown of CPA factors and Xrn2. Interestingly, we observe an equivalent increase in TSS-associated S2P Pol II pausing on both mRNA and PROMPT strands after depletion of CPA factors and Xrn2 (Figures 7A and 7B). Notably, this effect is specific for S2P as S5P or unph meta-analysis following CPSF73 knockdown did not show a change in TSS pausing (Figure 7A). S2P meta-analysis of CstF64+CstF64t double-knockdown shows an average 3.6-fold increase as compared to siLuc (Figure 7B, top). Also, CPSF73 and Xrn2 knockdowns both show an average 2.3-fold increase in Pol II pausing (Figures 7A, middle and 7B, bottom). The extent of pausing varies with a more focused effect for CPSF73 and Xrn2 but more prolonged for CstF64+CstF64t on both mRNA and PROMPT strands (Figures 7A and 7B). We also present gene-specific examples to validate our TSS mNET-seq meta-analysis. *FUS* shows enhanced levels of TSS mNET-seq reads following CPSF73 knockdown, but only for S2P (Figure 7C). *SLC30A6* also shows similar enhanced levels of TSS reads for S2P following each termination factor knockdown (Figure 7D).

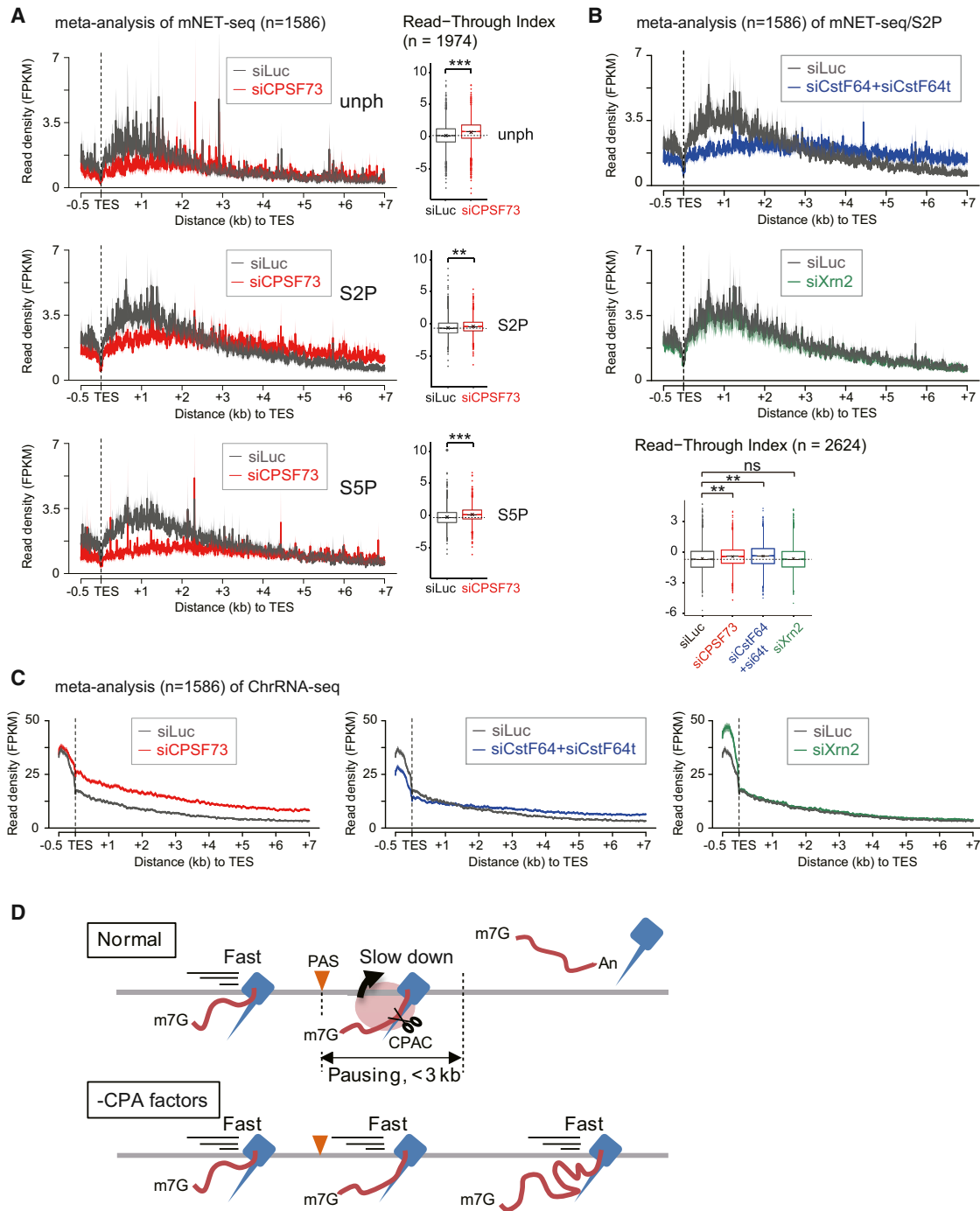


Figure 6. Nascent RNA within Pol II Complex at TES

(A) Meta-analysis of mNET-seq with indicated Pol II antibodies over TES regions (−0.5 kb~+7kb) from siLuc (dark gray) and siCPSF73 (red) treated HeLa cells (left) is shown. Also shown are RTIs of mNET-seq following CPSF73 knockdown (right). GB signals were divided by signals in a 2 kb region from TES (TES+2kb) for RTI (see [Extended Experimental Procedures](#)). Dashed line is median of siLuc. (**) p value < 8.52×10^{-11} , and (***) p value < 2.17×10^{-35} by two-sided Mann-Whitney test. (B) Meta-analysis of mNET-seq/S2P following termination factor knockdown over TES regions (top). siLuc (dark gray), siCstF64+siCstF64t (blue), and siXrn2 (green). RTI of mNET-seq following indicated knockdown (bottom) is shown. (**) p value < 1.94×10^{-15} by two-sided Mann-Whitney test; ns indicates no difference between samples (p value = 0.9894 by two-sided Mann-Whitney test).

(C) Meta-profiles of ChrRNA-seq following indicated knockdown over TES. siLuc (dark gray), siCPSF73 (red), siCstF64+siCstF64t (blue), and siXrn2 (green).

(D) Model correlating Pol II pausing and PAS-dependent transcription termination at TES. RNA cleavage (scissors) by CPA complex (red circle) at PAS (orange triangle). Pol II elongation speed over 3' flank region is regulated by PAS recognition on average over a 3 kb region from TES.

For (A)–(C), line and shading represent mean \pm SEM for each bin.

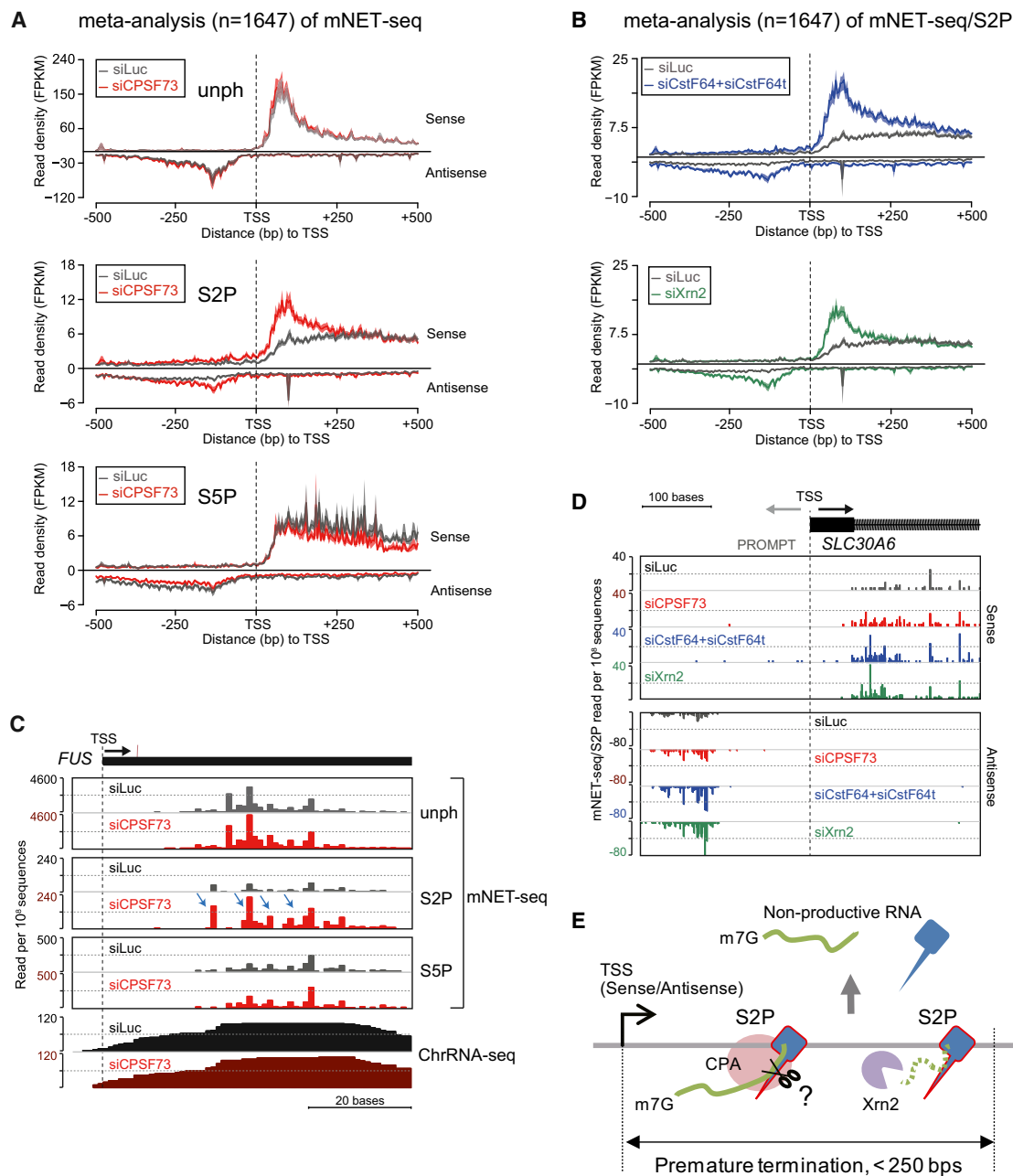


Figure 7. Promoter-Associated RNA Turnover Regulated by Termination Factors

(A) Meta-analysis of mNET-seq with indicated Pol II antibodies over TSS regions (−0.5k~+0.5 kb) from siLuc (dark gray) and siCPSF73 (red) treated HeLa cells (left).

(B) Meta-analyses of mNET-seq/S2P following knockdown of CstF64t+CstF64t (blue) and Xrn2 (green) at TSS (left).

(C) mNET-seq of *FUS* with indicated Pol II antibodies and ChrRNA-seq from siLuc (dark gray) and siCPSF73 (red) treated HeLa cells. Increased mNET-seq/S2P signals following depletion of CPSF73 are denoted by blue arrows.

(D) mNET-seq/S2P maps with indicated knockdowns around TSS of *SLC30A6* on both mRNA and PROMPT strands.

(E) Model showing effects of CPA and Xrn2 at TSS. S2P Pol II-CPA complex (red circle) cleaves TSS-associated nascent RNA, and Xrn2 (purple) degrades cleaved RNA from 5' end to 3' end over a region of 250 bp from TSS.

For (A) and (B), line and shading represent mean ± SEM for each bin.

We quantitated the effects of termination factor knockdown by measuring the ratio change between mNET-seq reads over the TSS as compared to the GB; we refer to this as the Escaping

Index (EI). We also calculated any changes in read values across the GB (Figure S7; Extended Experimental Procedures). The distribution of EI values clearly shows that depletion of all three

factors increases promoter-associated S2P Pol II pausing but has no effect on S2P Pol II distribution across the GB. These results indicate that CPA factors and Xrn2 are involved in restricting the levels of promoter-associated non-productive transcripts.

In order to examine whether CPA factors could directly bind to nascent RNA near TSS, we analyzed *in vivo* cross-linking and immunoprecipitation (CLIP) data for genome-wide alternative polyadenylation at TES (Martin et al., 2012). Surprisingly, all CPA factors, including CPSF73, CstF64, CstF64t, CPSF160, CPSF30, and CFIIm25 proteins, are significantly detected on both strands within 500 nt of the TSS. Especially CPSF73 shows a substantial peak 160 nt upstream and 80 nt downstream of TSS (Figure S7C and Table S1). Together with our mNET-seq/S2P results, we conclude that the CPA complex cleaves not only pre-mRNA at the PAS to promote 3' end termination but also promotes promoter-associated premature termination (Figure 7E). Notably, Xrn2 plays a unique role in TSS but not in TES termination.

DISCUSSION

Our mNET-seq analysis reveals precise maps of both nascent RNA and the associated Pol II "CTD code." We employed recently evaluated high-affinity and specificity monoclonal antibodies to Pol II CTD S5P, S2P, unph, and unph+ph (Figure S2; Stasevich et al., 2014) in our mNET-seq analysis. Interestingly, our mNET-seq data reveal significant differences in CTD modification profiles across mammalian protein-coding genes as compared to previous studies. In particular, we detect predominantly low or unphosphorylated CTD over the TSS region (at least lacking S5P and S2P modification). Furthermore, most detected S5P signal is found in the GBs, where it is particularly associated with actively spliced exons. Finally, although we find that S2P signal is more associated with TES regions (consistent with previous studies), we demonstrate a redistribution of this CTD mark to TSS following CPA depletion. Several explanations may account for the differences between our mNET-seq data and previous studies. Thus, mNET-seq does not involve cross-linking (by formaldehyde), which is by necessity used in ChIP analysis. The possibility that cross-linking distorts the native chromatin structure remains a concern. Similarly, mNET-seq detects nascent transcripts at single-nucleotide resolution, which cannot be achieved by GRO-seq analysis. Even though PRO-seq analysis does give single-nucleotide resolution, the act of isolating nuclei, treating with sarcosyl, and then carrying out an *in vitro* transcription reaction (using modified nucleotides) as in both GRO-seq and PRO-seq protocols may distort the native transcription profiles of genes. Clearly, in the future, we can extend our analysis to include other CTD phosphorylation marks using appropriate Pol II antibodies. For example, the CTD S7P mark is important to recruit Integrator complex to snRNA genes, which regulates 3' end processing and termination (Egloff et al., 2007). Mutation of CTD T4 specifically represses histone gene expression by blocking 3' end processing (Hsin et al., 2011). Another CTD modification, Y1P, stimulates the binding of elongation factor Spt6 and blocks recruitment of termination factors in yeast (Mayer et al., 2012).

It remains a possibility that the mammalian CTD code may be significantly different than the likely simplified code for budding yeast. Notably, yeast CTD has only 26 heptad repeats in its CTD, and these are near identical, unlike the more variable mammalian heptad repeats. Possibly, the high S5P TSS signals observed in yeast are replaced by other CTD or indeed histone marks in higher eukaryotes. Furthermore, few yeast genes possess introns so that the dominant presence of S5P marks over mammalian exons would be less quantitatively significant in yeast. Even so, it has been shown that yeast introns display high S5P signals near their 3' ends (Alexander et al., 2010), similarly to the mammalian S5P splicing association, described here.

A remarkable feature of our mNET-seq data is that we readily detect RNA 3' ends formed as RNA-processing intermediates through co-association of RNA-processing complexes with elongating Pol II. In particular, the Pol II CTD S5P mark, previously thought to be mainly associated with TSS events such as co-transcriptional capping and early transcriptional elongation (Hsin and Manley, 2012), plays a major role in splicing. Thus, 5'SS peaks of mNET-seq/S5P are detected at the end of co-transcriptionally spliced exons (Figure 3), indicating that the 3' cleaved upstream exon within the spliceosome is associated with Pol II elongation complexes in an S5P-dependent manner. We also note that the mNET-seq S5P reads are particularly high over spliced exons, suggesting that S5P Pol II pauses over functional exons allowing time for U2 snRNP-mediated activation of 5'SS cleavage. Indeed, we demonstrate this by directly inhibiting U2 snRNP function (Figures 4 and S4). Overall, we find that the 5'SS cleavage intermediate is retained within the spliceosome C complex associated with Pol II S5P until subsequent ligation with the downstream exon can occur (Figure 4D, model). In effect, we provide genome-wide support for exon tethering to Pol II as previously predicted from studies on transfected gene constructs wherein co-transcriptional intron cleavage did not prevent exon splicing across a discontinuous intron (Dye et al., 2006). We anticipate that our mNET-seq technology will provide new ways to unravel the complexity of the co-transcriptional splicing mechanism.

A surprising aspect of our mNET-seq analysis is that we do not detect a peak of signal associated with pre-mRNA 3' end processing (TES meta-analysis in Figure 2C and Figures 6A and 6B). This contrasts the splicing-associated 5'SS and Drosha cleavage sites that are highly prevalent in our data (Figures 3, 4, and 5). We predict that 3' end cleavage (coupled with polyadenylation) may cause rapid mRNA release from the Pol II complex and so escape mNET-seq detection, like in the pre-miRNA fast-release model (Figure 5E). Although 3' end processing is known to be required for Pol II termination (Proudfoot, 2011), it is also thought that Pol II pausing at TES regulates both 3' end processing and subsequent transcription termination (Gromak et al., 2006; Nag et al., 2007). We examined the effect on Pol II pausing at TES following depletion of CPA components. Consistent with previous reports, ChrRNA-seq reveals that CPSF73 and CstF64 depletion cause transcriptional termination defects on protein-coding genes (Figure 6). Interestingly, our mNET-seq data also reveal that depletion of CPA factors causes significantly less pausing immediately downstream of TES (<3 kb from TES) and then more Pol II occupancy at further downstream regions

(>3 kb from TES) compared to control cells. This indicates that Pol II elongation speed is regulated by the CPA complex, which may be an important factor in mediating transcription termination (Figure 6D). We also demonstrate that no significant termination defect occurs following the TES upon knockdown of Xrn2 (Figure 6A, bottom). This observation contrasts our previous reports based on plasmid transfection studies (West et al., 2004). However, it has been shown more recently that Xrn2 has a required partner protein, TTF2, for transcription termination (Brannan et al., 2012). It seems likely that Xrn2-associated termination is redundant with other termination factors.

Unexpectedly, mNET-seq analysis showed a significant increase specifically in S2P Pol II pausing at the TSS (<250 base) for both mRNA and PROMPT transcription upon CPA factor and Xrn2 depletion. This suggests that CPA and Xrn2 are involved in premature termination at the TSS, consistent with a previous report (Brannan et al., 2012). Although CPA factors and Xrn2 affect S2P Pol II occupancy at TSS, they show no difference in S2P Pol II distribution across the GB. Recent studies have pointed toward differences between promoter-proximal termination for mRNA sense or antisense RNA (Almada et al., 2013; Ntini et al., 2013). Antisense TSS transcripts (PROMPTs) are thought to utilize cryptic PAS close to the TSS, whereas sense TSS transcripts may have reduced occurrence of cryptic PAS. Those that are present may be blocked by nearby 5' SSU1 snRNP recruitment (Kaida et al., 2010). These apparent differences in cryptic PAS usage between PROMPTs and sense TSS-associated transcripts may favor productive sense over non-productive antisense transcription. However, our mNET-seq data suggest that CPA factors and Xrn2 play equivalent roles in restricting sense and antisense TSS transcription. Thus, their depletion causes an equivalent increase in S2P Pol II pausing in both transcriptional directions. Also, we show by CLIP analysis that CPA factors are directly and equally associated with these two transcript classes (Martin et al., 2012). Our data suggest that transcriptional directionality at TSS is unlikely to be regulated by CPA-mediated termination. Rather both sense and antisense TSS-associated transcripts are restricted by normally TES-associated termination factors. Indeed, we observe a redistribution of S2P Pol II from the TES to the TSS following CPA factor and Xrn2 knockdown. This argues for close interconnections between both ends of the Pol II transcription unit, as previously demonstrated by 3C analysis (Ansari and Hampsey, 2005; O'Sullivan et al., 2004; Tan-Wong et al., 2012). Several gene-specific analyses in mammals have reported the co-association of CPA with transcription initiation factors. Thus, CPSF is a known component of some TFIID complexes (Dantonel et al., 1997), and CstF has been shown to associate with TFIIB (Wang et al., 2010). Also, mutating the PAS depleted promoter-associated transcription factors and increased promoter-associated Pol II CTD S2P (Mapendano et al., 2010). Finally, the elongation factor TFIIS has been shown to promote release of paused TSS transcripts in *Drosophila* (Adelman et al., 2005), and this may in turn relate to CPA promoter effects.

Overall, mNET-seq maps nascent transcription at single-nucleotide resolution, showing both Pol II pausing and associated co-transcriptional RNA cleavage. Importantly, this method

can be applied genome wide to check for modified polymerase occupancy (even Pol I and Pol III) by selecting a range of different antibodies. We anticipate that mNET-seq will expand our knowledge of how different nascent RNA are associated with specific "CTD codes."

EXPERIMENTAL PROCEDURES

Antibodies and siRNA

Antibodies and siRNA information are available in the [Extended Experimental Procedures](#). In outline, siRNA treatment was carried out for 3 days prior to cell harvesting. The efficiency of protein depletion was confirmed by western blot with appropriate antibodies.

Cell Culture, NRO Assay, and RT-PCR

Cell culture and NRO assay were as previously described (Nojima et al., 2013). RT-PCR and primers are described in the [Extended Experimental Procedures](#).

In Vivo Splicing Inhibition

HeLa cells were treated with either DMSO (0.1%) or Pla-B (1 μ M) for 4 hr. Pla-B was purchased from Santa Cruz (sc-391691).

RNA-Seq Methods

Preparation of chromatin and nucleoplasmic RNA was previously described (Nojima et al., 2013). For mNET-seq, isolated chromatin was incubated with MNase (40 u/ μ l). MNase was inactivated by EGTA, and the insoluble chromatin removed by centrifugation. IP was performed from the supernatant using specific Pol II antibody-conjugated beads for 1 hr. IPed RNA was 5' end phosphorylated by polynucleotide kinase treatment of the washed beads. Purified RNA was fractionated on denaturing acrylamide gels, and a 35–100 nt fraction was isolated. RNA libraries were prepared according to the manual of Truseq small RNA library prep kit (Illumina). The reads were generated in Hiseq2000/2500 (Illumina). For full methods, see the [Extended Experimental Procedures](#).

Data Pre-Processing

mNET-seq data adaptors were trimmed using Cutadapt (v1.1) (Martin, 2011). The remaining paired reads were aligned to the reference human genome (hg19) using TopHat (v2.0.9) (Kim et al., 2013) only allowing for one alignment to the reference. The last nucleotide incorporated by the polymerase was defined as the 5' end of read two (green arrow, Figure 1A) of the pair, with the directionality indicated by read one (blue arrow, Figure 1A), and then the properly aligned read pairs were trimmed to solely keep the 5' nucleotide of read two. ChrRNA-seq and nucleoplasmic RNA-seq data were aligned using the same version of TopHat but allowing for the read pairs to be separated by 3 kb. Further details of data pre-processing and bioinformatic analysis are available in the [Extended Experimental Procedures](#).

ACCESSION NUMBERS

The data present in this work are deposited in NCBI's Gene Expression Omnibus (GEO) database (www.ncbi.nlm.nih.gov/geo) under the accession number GSE60358.

SUPPLEMENTAL INFORMATION

Supplemental information includes Extended Experimental Procedures, seven figures, and one table and can be found with this article online at <http://dx.doi.org/10.1016/j.cell.2015.03.027>.

AUTHOR CONTRIBUTIONS

T.N. performed all molecular biology and genomic analyses, except that M.J.D. performed NRO. T.G. carried out all bioinformatic analyses aided by

ARFG, except that S.D. analyzed CLIP-seq data. H.K. generated Pol II antibodies. T.N., M.C.-F., and N.J.P. designed the project and wrote the paper.

ACKNOWLEDGMENTS

We thank the N.J.P. lab and Dr. M. Dienstbier for critical discussion. T.N. was supported by the KANAE foundation. H.K. was supported by JSPS KAKENHI and JST CREST. This work was supported by funding to N.J.P. (Wellcome Trust Programme [091805/Z/10/Z] and ERC Advanced [339270] Grants) and to M.C.-F. (Fundação Ciência e Tecnologia, Portugal).

Received: August 12, 2014

Revised: December 24, 2014

Accepted: February 25, 2015

Published: April 23, 2015

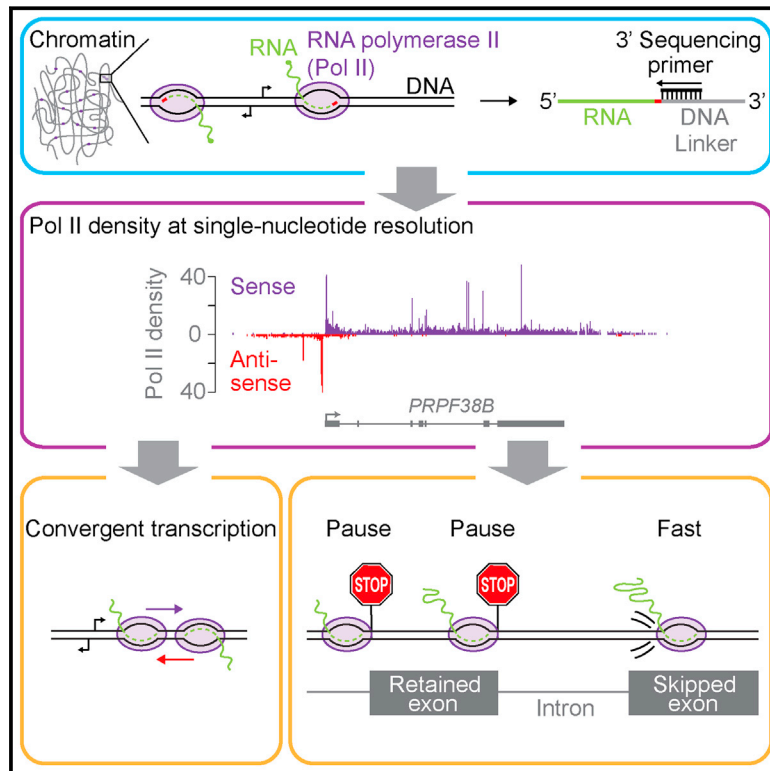
REFERENCES

- Adelman, K., and Lis, J.T. (2012). Promoter-proximal pausing of RNA polymerase II: emerging roles in metazoans. *Nat. Rev. Genet.* **13**, 720–731.
- Adelman, K., Marr, M.T., Werner, J., Saunders, A., Ni, Z., Andrulis, E.D., and Lis, J.T. (2005). Efficient release from promoter-proximal stall sites requires transcript cleavage factor TFIIS. *Mol. Cell* **17**, 103–112.
- Ahn, S.H., Kim, M., and Buratowski, S. (2004). Phosphorylation of serine 2 within the RNA polymerase II C-terminal domain couples transcription and 3' end processing. *Mol. Cell* **13**, 67–76.
- Alexander, R.D., Innocente, S.A., Barrass, J.D., and Beggs, J.D. (2010). Splicing-dependent RNA polymerase pausing in yeast. *Mol. Cell* **40**, 582–593.
- Almada, A.E., Wu, X., Kriz, A.J., Burge, C.B., and Sharp, P.A. (2013). Promoter directionality is controlled by U1 snRNP and polyadenylation signals. *Nature* **499**, 360–363.
- Ansari, A., and Hampsey, M. (2005). A role for the CPF 3'-end processing machinery in RNAP II-dependent gene looping. *Genes Dev.* **19**, 2969–2978.
- Brannan, K., Kim, H., Erickson, B., Glover-Cutter, K., Kim, S., Fong, N., Kie-mele, L., Hansen, K., Davis, R., Lykke-Andersen, J., and Bentley, D.L. (2012). mRNA decapping factors and the exonuclease Xrn2 function in widespread premature termination of RNA polymerase II transcription. *Mol. Cell* **46**, 311–324.
- Buratowski, S. (2009). Progression through the RNA polymerase II CTD cycle. *Mol. Cell* **36**, 541–546.
- Carrillo Oesterreich, F., Preibisch, S., and Neugebauer, K.M. (2010). Global analysis of nascent RNA reveals transcriptional pausing in terminal exons. *Mol. Cell* **40**, 571–581.
- Chathoth, K.T., Barrass, J.D., Webb, S., and Beggs, J.D. (2014). A splicing-dependent transcriptional checkpoint associated with prespliceosome formation. *Mol. Cell* **53**, 779–790.
- Churchman, L.S., and Weissman, J.S. (2011). Nascent transcript sequencing visualizes transcription at nucleotide resolution. *Nature* **469**, 368–373.
- Conrad, T., Marsico, A., Gehre, M., and Orom, U.A. (2014). Microprocessor activity controls differential miRNA biogenesis in vivo. *Cell Rep* **9**, 542–554.
- Consortium, E.P., Bernstein, B.E., Birney, E., Dunham, I., Green, E.D., Gunter, C., and Snyder, M.; ENCODE Project Consortium (2012). An integrated encyclopedia of DNA elements in the human genome. *Nature* **489**, 57–74.
- Core, L.J., and Lis, J.T. (2008). Transcription regulation through promoter-proximal pausing of RNA polymerase II. *Science* **319**, 1791–1792.
- Core, L.J., Waterfall, J.J., and Lis, J.T. (2008). Nascent RNA sequencing reveals widespread pausing and divergent initiation at human promoters. *Science* **322**, 1845–1848.
- Dantoni, J.C., Murthy, K.G., Manley, J.L., and Tora, L. (1997). Transcription factor TFIID recruits factor CPSF for formation of 3' end of mRNA. *Nature* **389**, 399–402.
- David, C.J., Chen, M., Assanah, M., Canoll, P., and Manley, J.L. (2010). HnRNP proteins controlled by c-Myc deregulate pyruvate kinase mRNA splicing in cancer. *Nature* **463**, 364–368.
- Davidson, L., Kerr, A., and West, S. (2012). Co-transcriptional degradation of aberrant pre-mRNA by Xrn2. *EMBO J.* **31**, 2566–2578.
- Dye, M.J., Gromak, N., and Proudfoot, N.J. (2006). Exon tethering in transcription by RNA polymerase II. *Mol. Cell* **21**, 849–859.
- Egloff, S., O'Reilly, D., Chapman, R.D., Taylor, A., Tanzhaus, K., Pitts, L., Eick, D., and Murphy, S. (2007). Serine-7 of the RNA polymerase II CTD is specifically required for snRNA gene expression. *Science* **318**, 1777–1779.
- Gilchrist, D.A., Dos Santos, G., Fargo, D.C., Xie, B., Gao, Y., Li, L., and Adelman, K. (2010). Pausing of RNA polymerase II disrupts DNA-specified nucleosome organization to enable precise gene regulation. *Cell* **143**, 540–551.
- Gromak, N., West, S., and Proudfoot, N.J. (2006). Pause sites promote transcriptional termination of mammalian RNA polymerase II. *Mol. Cell. Biol.* **26**, 3986–3996.
- Grosso, A.R., de Almeida, S.F., Braga, J., and Carmo-Fonseca, M. (2012). Dynamic transitions in RNA polymerase II density profiles during transcription termination. *Genome Res.* **22**, 1447–1456.
- Heidemann, M., Hintermair, C., Voß, K., and Eick, D. (2013). Dynamic phosphorylation patterns of RNA polymerase II CTD during transcription. *Biochim. Biophys. Acta* **1829**, 55–62.
- Hirose, Y., and Manley, J.L. (1998). RNA polymerase II is an essential mRNA polyadenylation factor. *Nature* **395**, 93–96.
- Hsin, J.P., and Manley, J.L. (2012). The RNA polymerase II CTD coordinates transcription and RNA processing. *Genes Dev.* **26**, 2119–2137.
- Hsin, J.P., Sheth, A., and Manley, J.L. (2011). RNAP II CTD phosphorylated on threonine-4 is required for histone mRNA 3' end processing. *Science* **334**, 683–686.
- Ip, J.Y., Schmidt, D., Pan, Q., Ramani, A.K., Fraser, A.G., Odom, D.T., and Blencowe, B.J. (2011). Global impact of RNA polymerase II elongation inhibition on alternative splicing regulation. *Genome Res.* **21**, 390–401.
- Kaida, D., Berg, M.G., Younis, I., Kasim, M., Singh, L.N., Wan, L., and Dreyfuss, G. (2010). U1 snRNP protects pre-mRNAs from premature cleavage and polyadenylation. *Nature* **468**, 664–668.
- Katz, Y., Wang, E.T., Airolidi, E.M., and Burge, C.B. (2010). Analysis and design of RNA sequencing experiments for identifying isoform regulation. *Nat. Methods* **7**, 1009–1015.
- Kim, D., Pertea, G., Trapnell, C., Pimentel, H., Kelley, R., and Salzberg, S.L. (2013). TopHat2: accurate alignment of transcriptomes in the presence of insertions, deletions and gene fusions. *Genome Biol.* **14**, R36.
- Kolev, N.G., and Steitz, J.A. (2005). Symplekin and multiple other polyadenylation factors participate in 3'-end maturation of histone mRNAs. *Genes Dev.* **19**, 2583–2592.
- Kotake, Y., Sagane, K., Owa, T., Mimori-Kiyosue, Y., Shimizu, H., Uesugi, M., Ishihama, Y., Iwata, M., and Mizui, Y. (2007). Splicing factor SF3b as a target of the antitumor natural product pladienolide. *Nat. Chem. Biol.* **3**, 570–575.
- Krol, J., Loedige, I., and Filipowicz, W. (2010). The widespread regulation of microRNA biogenesis, function and decay. *Nat. Rev. Genet.* **11**, 597–610.
- Kwak, H., Fuda, N.J., Core, L.J., and Lis, J.T. (2013). Precise maps of RNA polymerase reveal how promoters direct initiation and pausing. *Science* **339**, 950–953.
- Lacoste, N., Woolfe, A., Tachiwana, H., Gareau, A.V., Barth, T., Cantaloube, S., Kurumizaka, H., Imhof, A., and Almouzni, G. (2014). Mislocalization of the centromeric histone variant CenH3/CENP-A in human cells depends on the chaperone DAXX. *Mol. Cell* **53**, 631–644.
- Mapendano, C.K., Lykke-Andersen, S., Kjems, J., Bertrand, E., and Jensen, T.H. (2010). Crosstalk between mRNA 3' end processing and transcription initiation. *Mol. Cell* **40**, 410–422.
- Martin, M. (2011). Cutadapt removes adapter sequences from high-throughput sequencing reads. *EMBnet. J.* **17**, 10–12.

- Martin, G., Gruber, A.R., Keller, W., and Zavolan, M. (2012). Genome-wide analysis of pre-mRNA 3' end processing reveals a decisive role of human cleavage factor I in the regulation of 3' UTR length. *Cell Rep.* 1, 753–763.
- Mayer, A., Heidemann, M., Lidschreiber, M., Schreieck, A., Sun, M., Hintermair, C., Kremmer, E., Eick, D., and Cramer, P. (2012). CTD tyrosine phosphorylation impairs termination factor recruitment to RNA polymerase II. *Science* 336, 1723–1725.
- McCracken, S., Fong, N., Yankulov, K., Ballantyne, S., Pan, G., Greenblatt, J., Patterson, S.D., Wickens, M., and Bentley, D.L. (1997). The C-terminal domain of RNA polymerase II couples mRNA processing to transcription. *Nature* 385, 357–361.
- Meinhart, A., and Cramer, P. (2004). Recognition of RNA polymerase II carboxy-terminal domain by 3'-RNA-processing factors. *Nature* 430, 223–226.
- Moore, M.J., and Proudfoot, N.J. (2009). Pre-mRNA processing reaches back to transcription and ahead to translation. *Cell* 136, 688–700.
- Morlando, M., Ballarino, M., Gromak, N., Pagano, F., Bozzoni, I., and Proudfoot, N.J. (2008). Primary microRNA transcripts are processed co-transcriptionally. *Nat. Struct. Mol. Biol.* 15, 902–909.
- Muñoz, M.J., Pérez Santangelo, M.S., Paronetto, M.P., de la Mata, M., Pelisch, F., Boireau, S., Glover-Cutter, K., Ben-Dov, C., Blaustein, M., Lozano, J.J., et al. (2009). DNA damage regulates alternative splicing through inhibition of RNA polymerase II elongation. *Cell* 137, 708–720.
- Nag, A., Narsinh, K., and Martinson, H.G. (2007). The poly(A)-dependent transcriptional pause is mediated by CPSF acting on the body of the polymerase. *Nat. Struct. Mol. Biol.* 14, 662–669.
- Nojima, T., Dienstbier, M., Murphy, S., Proudfoot, N.J., and Dye, M.J. (2013). Definition of RNA polymerase II CoTC terminator elements in the human genome. *Cell Rep.* 3, 1080–1092.
- Ntini, E., Järvelin, A.I., Bornholdt, J., Chen, Y., Boyd, M., Jørgensen, M., Andersson, R., Hoof, I., Schein, A., Andersen, P.R., et al. (2013). Polyadenylation site-induced decay of upstream transcripts enforces promoter directionality. *Nat. Struct. Mol. Biol.* 20, 923–928.
- O'Sullivan, J.M., Tan-Wong, S.M., Morillon, A., Lee, B., Coles, J., Mellor, J., and Proudfoot, N.J. (2004). Gene loops juxtapose promoters and terminators in yeast. *Nat. Genet.* 36, 1014–1018.
- Pawlicki, J.M., and Steitz, J.A. (2008). Primary microRNA transcript retention at sites of transcription leads to enhanced microRNA production. *J. Cell Biol.* 182, 61–76.
- Pérez-Lluch, S., Blanco, E., Carbonell, A., Raha, D., Snyder, M., Serras, F., and Corominas, M. (2011). Genome-wide chromatin occupancy analysis reveals a role for ASH2 in transcriptional pausing. *Nucleic Acids Res.* 39, 4628–4639.
- Proudfoot, N.J. (2011). Ending the message: poly(A) signals then and now. *Genes Dev.* 25, 1770–1782.
- Rahl, P.B., Lin, C.Y., Seila, A.C., Flynn, R.A., McQuine, S., Burge, C.B., Sharp, P.A., and Young, R.A. (2010). c-Myc regulates transcriptional pause release. *Cell* 141, 432–445.
- Stasevich, T.J., Hayashi-Takanaka, Y., Sato, Y., Maehara, K., Ohkawa, Y., Sakata-Sogawa, K., Tokunaga, M., Nagase, T., Nozaki, N., McNally, J.G., and Kimura, H. (2014). Regulation of RNA polymerase II activation by histone acetylation in single living cells. *Nature* 516, 272–275.
- Tan-Wong, S.M., Zaugg, J.B., Camblong, J., Xu, Z., Zhang, D.W., Mischo, H.E., Ansari, A.Z., Luscombe, N.M., Steinmetz, L.M., and Proudfoot, N.J. (2012). Gene loops enhance transcriptional directionality. *Science* 338, 671–675.
- Wahl, M.C., Will, C.L., and Lührmann, R. (2009). The spliceosome: design principles of a dynamic RNP machine. *Cell* 136, 701–718.
- Wang, Y., Fairley, J.A., and Roberts, S.G. (2010). Phosphorylation of TFIIB links transcription initiation and termination. *Curr. Biol.* 20, 548–553.
- Weber, C.M., Ramachandran, S., and Henikoff, S. (2014). Nucleosomes are context-specific, H2A.Z-modulated barriers to RNA polymerase. *Mol. Cell* 53, 819–830.
- West, S., Gromak, N., and Proudfoot, N.J. (2004). Human 5' → 3' exonuclease Xrn2 promotes transcription termination at co-transcriptional cleavage sites. *Nature* 432, 522–525.
- Yao, C., Biesinger, J., Wan, J., Weng, L., Xing, Y., Xie, X., and Shi, Y. (2012). Transcriptome-wide analyses of CstF64-RNA interactions in global regulation of mRNA alternative polyadenylation. *Proc. Natl. Acad. Sci. USA* 109, 18773–18778.

Native Elongating Transcript Sequencing Reveals Human Transcriptional Activity at Nucleotide Resolution

Graphical Abstract



Authors

Andreas Mayer, Julia di Iulio, ...,
John A. Stamatoyannopoulos,
L. Stirling Churchman

Correspondence

churchman@genetics.med.harvard.edu

In Brief

Native elongating transcript sequencing in human uncovers convergent sense and antisense transcription within promoter-proximal regions of lower-expressed genes and unravels details about Pol II pausing.

Highlights

- Human NET-seq maps global RNA polymerase II (Pol II) density at high resolution
- Widespread convergent transcription occurs near promoters of lower-expressed genes
- Strong Pol II pausing at sites of occupied transcription factors, including YY1 and CTCF
- NET-seq reveals pronounced Pol II pausing at the boundaries of retained exons

Accession Numbers

GSE61332



Native Elongating Transcript Sequencing Reveals Human Transcriptional Activity at Nucleotide Resolution

Andreas Mayer,^{1,4} Julia di Iulio,^{1,4} Seth Maleri,¹ Umut Eser,¹ Jeff Vierstra,² Alex Reynolds,² Richard Sandstrom,² John A. Stamatoyannopoulos,^{2,3} and L. Stirling Churchman^{1,*}

¹Department of Genetics, Harvard Medical School, Boston, MA 02115, USA

²Department of Genome Sciences, University of Washington, Seattle, WA 98104, USA

³Department of Medicine, Division of Oncology, University of Washington, Seattle, WA 98104, USA

⁴Co-first author

*Correspondence: churchman@genetics.med.harvard.edu

<http://dx.doi.org/10.1016/j.cell.2015.03.010>

SUMMARY

Major features of transcription by human RNA polymerase II (Pol II) remain poorly defined due to a lack of quantitative approaches for visualizing Pol II progress at nucleotide resolution. We developed a simple and powerful approach for performing native elongating transcript sequencing (NET-seq) in human cells that globally maps strand-specific Pol II density at nucleotide resolution. NET-seq exposes a mode of antisense transcription that originates downstream and converges on transcription from the canonical promoter. Convergent transcription is associated with a distinctive chromatin configuration and is characteristic of lower-expressed genes. Integration of NET-seq with genomic footprinting data reveals stereotypic Pol II pausing coincident with transcription factor occupancy. Finally, exons retained in mature transcripts display Pol II pausing signatures that differ markedly from skipped exons, indicating an intrinsic capacity for Pol II to recognize exons with different processing fates. Together, human NET-seq exposes the topography and regulatory complexity of human gene expression.

INTRODUCTION

High-throughput sequencing analyses of transcription have discovered new classes of RNAs and new levels of regulatory complexity. Many of these results were obtained with two experimental strategies to measure RNA polymerase density genome wide. The first, RNA polymerase II (Pol II) ChIP-seq or ChIP-chip, identifies DNA bound to RNA polymerase. The second set of approaches, global run-on sequencing (GRO-seq) and precision nuclear run-on and sequencing (PRO-seq), restarts RNA polymerase in vitro with labeled nucleotides to purify and sequence nascent RNA (Core et al., 2008; Kwak et al., 2013). GRO-seq and

Pol II ChIP detect strong transcriptional pauses ~50 bp downstream of many transcription start sites, demonstrating that promoter-proximal pausing is more prevalent than initially observed (Core et al., 2008; Krumm et al., 1992; Kwak et al., 2013; Muse et al., 2007; Rahl et al., 2010; Rougvie and Lis, 1988; Strobl and Eick, 1992; Zeitlinger et al., 2007). Abundant unstable transcripts upstream of and antisense to promoters revealed that divergent transcription is a common feature of eukaryotic promoters (Core et al., 2008; Neil et al., 2009; Preker et al., 2008; Seila et al., 2008; Xu et al., 2009). Despite progress in understanding how these transcripts are terminated and degraded (Almada et al., 2013; Ntini et al., 2013; Preker et al., 2008; Schulz et al., 2013), their roles remain unknown (Wu and Sharp, 2013). Finally, recent studies confirm that splicing is largely co-transcriptional and splicing outcome is kinetically tied to elongation rate (Bhatt et al., 2012; Davis-Turak et al., 2015; Dujardin et al., 2014; Fong et al., 2014; Ip et al., 2011; de la Mata et al., 2003; Roberts et al., 1998; Shukla et al., 2011; Tilgner et al., 2012). However, it has been impossible to determine whether such kinetic coupling in human cells is mediated by pausing events genome wide, due to the high resolution required to measure pausing on short human exons.

The strongly stereotyped locations of promoter-proximal pauses and divergent antisense transcription can be exposed by averaging Pol II density from many genes (metagene analysis) obtained at low resolution (Core et al., 2008; Neil et al., 2009; Preker et al., 2008; Rahl et al., 2010; Seila et al., 2008; Xu et al., 2009). Yet, the precise architecture of promoter-associated transcriptional activity and of pausing outside of promoter regions has been obscured by the resolution limitations of current methodologies, preventing deeper insight into the underlying regulatory mechanisms. Indeed, the interplay between chromatin structure, transcription factors, and the transcription machinery is largely undefined. Pol II ChIP-seq is typically limited in its resolution to >200 bp resolution and lacks strand specificity. GRO-seq is similarly limited to ~50 bp resolution, and although PRO-seq has higher resolution, both run-on methods require transcription elongation complexes to resume polymerization in vitro, a variable process sensitive to the experimental conditions and the Pol II pausing state (Core et al., 2008; Weber et al., 2014). Recently, we showed that

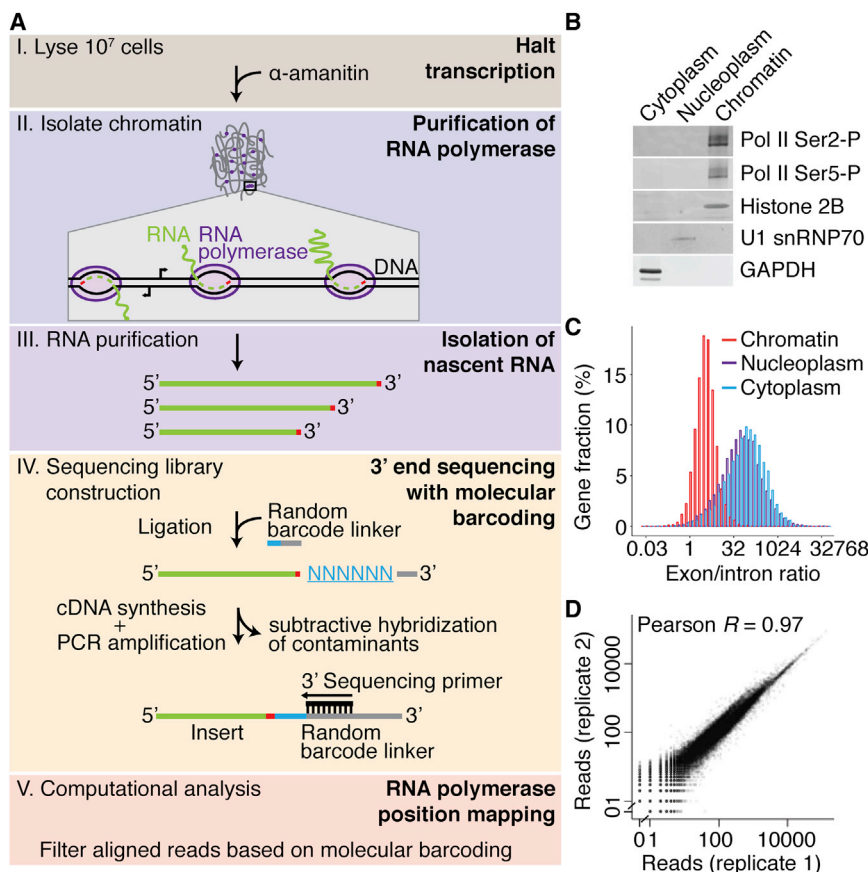


Figure 1. A Robust and Simplified NET-Seq Approach for Human Cells

(A) Schematic view of the key steps of the human NET-seq approach. The transcription inhibitor, α -amanitin, is introduced at cell lysis and is maintained through all purification steps. Engaged RNA polymerase is purified through the isolation of chromatin. The 3' end of the co-purified nascent RNA (red) is ligated to a linker containing a mixed random hexameric sequence (blue) that serves as a molecular barcode. After cDNA synthesis, contaminant species are removed by hybridization. PCR amplification results in a DNA-sequencing library with the sequencing primer binding site proximal to the random hexamer barcode. Finally, the 3' ends of the sequenced nascent RNA are aligned to the human genome, yielding RNA polymerase density at nucleotide resolution. Analysis of the molecular barcode allows reads arising from DNA library construction artifacts to be filtered out. (B) Representative western blot analysis of cellular fractions in HeLa S3 cells. Subcellular localization markers were also probed (chromatin marker, histone 2B; nucleoplasm marker, U1 snRNP70; cytoplasm marker, GAPDH).

(C) Histograms of the size-normalized ratio of subcellular RNA-seq reads that map to exons versus introns for each gene.

(D) Number of uniquely aligned reads per Pol II gene for two biological replicates from HeLa S3 cells (Pearson's correlation, $R = 0.97$). 0.5 pseudocounts were added to genes with zero counts in one of the replicates. The data set with higher coverage was randomly downsampled to match the total number of reads of the other data set. See also Figure S1 and Table S1.

the extraordinary stability of the RNA-DNA-RNA polymerase ternary complex can be exploited to capture nascent RNA (Churchman and Weissman, 2011). Native elongating transcript sequencing (NET-seq) quantitatively purifies Pol II complexes and sequences the 3' end of nascent RNA to reveal the strand-specific position of Pol II with single-nucleotide resolution. NET-seq detects all transcriptionally engaged Pol II, including productively transcribing Pol II, paused Pol II, and Pol II recovering from pausing (Churchman and Weissman, 2011).

Here, we develop a NET-seq approach that quantitatively defines the full spectrum of transcriptional activity in a strand-specific manner and at nucleotide resolution in human cells. We find that many promoters display antisense transcription downstream of a promoter-proximal pause, resulting in convergent sense and antisense transcriptional activities that face one another in close proximity. Convergent transcription is associated with a distinct chromatin conformation and is a feature of lower-expressed genes, suggesting a possible regulatory role. NET-seq reveals that Pol II density profiles differ between retained exons, skipped exons, and introns in human cells, indicating generalized kinetic coupling of transcription and splicing. Human NET-seq is readily applicable to diverse cell types and provides a general strategy to study transcriptional complexity.

RESULTS

A Robust Human NET-Seq Methodology

The first step of NET-seq purifies nascent RNA through its tight interaction with RNA polymerase. In yeast, this is achieved through an epitope-tagged Pol II subunit that enables highly quantitative purification and specific elution (Churchman and Weissman, 2011). In adapting NET-seq to human cells, we biochemically purify >99% of all engaged RNA polymerase in a highly specific manner that can be applied to any mammalian cell line or tissue without genetic modification (Figure 1A). This method avoids using Pol II antisera, which could bias the population of isolated Pol II complexes due to posttranslational modifications and epitope masking by heterogeneous Pol II binding partners and structural conformations. Instead, human NET-seq exploits the high stability of the RNA-DNA-RNA polymerase ternary complex, even in the presence of high salt and urea (Cai and Luse, 1987; Wuarin and Schibler, 1994), to purify engaged RNA polymerase, along with its nascent RNA, through an association with chromatin after cellular fractionation into cytoplasm, nucleoplasm, and chromatin (Bhatt et al., 2012; Pandya-Jones and Black, 2009; Wuarin and Schibler, 1994). To prevent transcriptional run-on during fractionation, lysate is kept at $\leq 4^\circ\text{C}$, and α -amanitin, a potent transcriptional inhibitor (Lindell et al., 1970), is included in every step. Through optimization of current

fractionation approaches, we identified buffers and washing conditions that cleanly purify >99% of elongating RNA polymerase II (C-terminal domain [CTD] Ser2-P, Ser5-P, and the general CTD hyper-phosphorylated form of Pol II) in the chromatin fraction (see [Experimental Procedures](#) and [Figures 1B](#) and [S1A](#)). Western blot analyses of Pol II isoforms and factors with well-defined subcellular localizations verify the stringency of our fractionation conditions ([Figure 1B](#)).

To confirm that our purification strategy specifically isolates nascent RNA, we sequenced the RNA in each fraction. Unprocessed RNA species, such as intron-containing Pol II transcripts and spacer-containing Pol I transcripts ([Figures 1C](#) and [S1B](#)), are heavily enriched in the chromatin fraction. Importantly, the large majority of intron-containing RNAs observed in the nucleoplasm persist to the cytoplasm, indicating that these RNAs are products of intron-retaining alternative splicing and not nascent transcripts ([Figure S1C](#)). Together, these results demonstrate that RNA polymerase and nascent RNA are quantitatively purified through the isolation of chromatin.

The second step of the NET-seq approach requires sequencing the 3' ends of the nascent RNA, which localizes Pol II genome wide at nucleotide resolution ([Churchman and Weissman, 2011](#); [Ferrari et al., 2013](#); [Weber et al., 2014](#)). In large part, our yeast library construction protocol is used ([Churchman and Weissman, 2012](#)), with two important changes to account for the increased complexity of the human genome. First, we addressed reverse transcription (RT) artifacts that arise from the significant size of human nascent RNA. We found that reverse transcription frequently initiates within the RNA if there are stretches as short as six nucleotides of complementarity to the RT primer ([Figure S1D](#)). When the 3' ends of the nascent RNA are ligated to a linker pool, consisting of a random hexamer at the 5' end followed by a common sequence, ligation efficiency increases and mispriming events are dramatically reduced ([Figure S1D](#)). Furthermore, the hexamer serves as a molecular barcode for each molecule and enables the computational removal of reads arising from residual mispriming events and PCR duplicates. Second, we deplete abundant mature snRNAs, snoRNAs, rRNA, and others through subtractive hybridization targeting their 3' ends ([Figure S1E](#), [Table S1](#)) to increase sequencing coverage for nascent transcripts. Finally, library construction steps are optimized to be highly efficient (>90%) and are continually monitored through quality controls to minimize bias. Together, our optimized library construction protocol faithfully converts the 3' ends of nascent human RNA to a DNA sequencing library that allows the high-fidelity mapping of strand-specific Pol II density.

To observe genome-wide transcriptional activity, a NET-seq library was prepared from HeLa S3 cells and sequenced to high coverage (768 million total reads, 360 million uniquely aligned). Each sequencing read was aligned to the human genome, and the genomic location of the 3' end of the nascent RNA was recorded to map RNA polymerase density with nucleotide resolution. As expected, we recovered nascent RNA from all three nuclear RNA polymerases (Pol I, Pol II, Pol III), as well as mature chromatin-associated RNAs, such as snRNAs, and splicing intermediates ([Figures S1F](#) and [S1G](#)). Here, we focused our analysis on Pol-II-synthesized RNAs, but our results suggest

that the NET-seq approach is amenable to the study of other RNA polymerases. Importantly, comparison of a biological replicate library (175 million total reads, 83 million uniquely aligned) shows strong agreement, indicating the robustness of the approach (Pearson's coefficient, 0.97, [Figure 1D](#)). To demonstrate that NET-seq is easily adaptable to other cell lines, we applied our approach to HEK293T cells and obtained data from two replicates with similar reproducibility (replicate 1: 1.203 billion total reads, 555 million uniquely aligned; replicate 2: 358 million total reads, 135 million uniquely aligned; [Figure S1H](#)). From these analyses, we conclude that human NET-seq is capable of quantitatively monitoring transcriptional activity across the human genome and adaptation to new cell lines is straightforward.

NET-Seq Reveals Transcriptional Activity at Nucleotide Resolution Genome Wide

The resolution afforded by NET-seq and the sequencing coverage obtained provide an in-depth view of genome-wide transcriptional activity. The highest coverage is observed across promoter-proximal regions, which we conservatively defined as the region between the earliest annotated transcription start site and +1 kb. Within this region, >50% of genes have coverage of >1 read per kb per million uniquely aligned reads (RPKM) in both HeLa S3 ([Figures 2A](#) and [2B](#)) and HEK293T cells ([Figure S2C](#)). When coverage is calculated across entire genes, the percentage decreases to <30% in both cell lines due to the prevalence of promoter-proximal pausing ([Figures 2A](#) and [2B](#)). Indeed, most (89% in HeLa S3 cells and 94% in HEK293T cells) expressed genes display promoter-proximal pausing defined by a traveling ratio (coverage ratio between a narrow promoter-proximal region and the gene body) of ≥ 2 , consistent with earlier observations in mouse embryonic stem cells ([Figures 2C](#) and [S2D](#)) ([Rahl et al., 2010](#)). Furthermore, we detect unstable RNA production, antisense transcription upstream of many promoters (89% in HeLa S3 cells and 82% in HEK293T cells), transcription downstream of many polyadenylation sites (95% in HeLa S3 cells and 88% in HEK293T cells), and enhancer RNAs ([Figures S2A](#), [S2B](#), [S2E](#), and [S2F](#)).

NET-seq data describe transcriptional activity at many length scales. At the single-gene level, strong signal is observed at promoter regions and across introns ([Figure 2D](#), top and middle). Signal variation across the gene body suggests that transcription elongation is discontinuous following release from promoter-proximal regions and that pausing is a general feature during productive Pol II transcription. Near transcription start sites (TSSs), NET-seq detects sense and antisense transcription of divergent promoters at single-nucleotide resolution, revealing that promoter-proximal pausing does not occur at only one position; instead, there are narrow regions of high Pol II density ([Figure 2D](#), bottom). Together, NET-seq data uncover key features of human transcription activity, and the high resolution and the coverage of the data provide deeper insight into these complexities.

Widespread Convergent Transcription in Promoter-Proximal Regions

Several previous studies showed widespread divergent transcription at eukaryotic promoters ([Churchman and Weissman,](#)

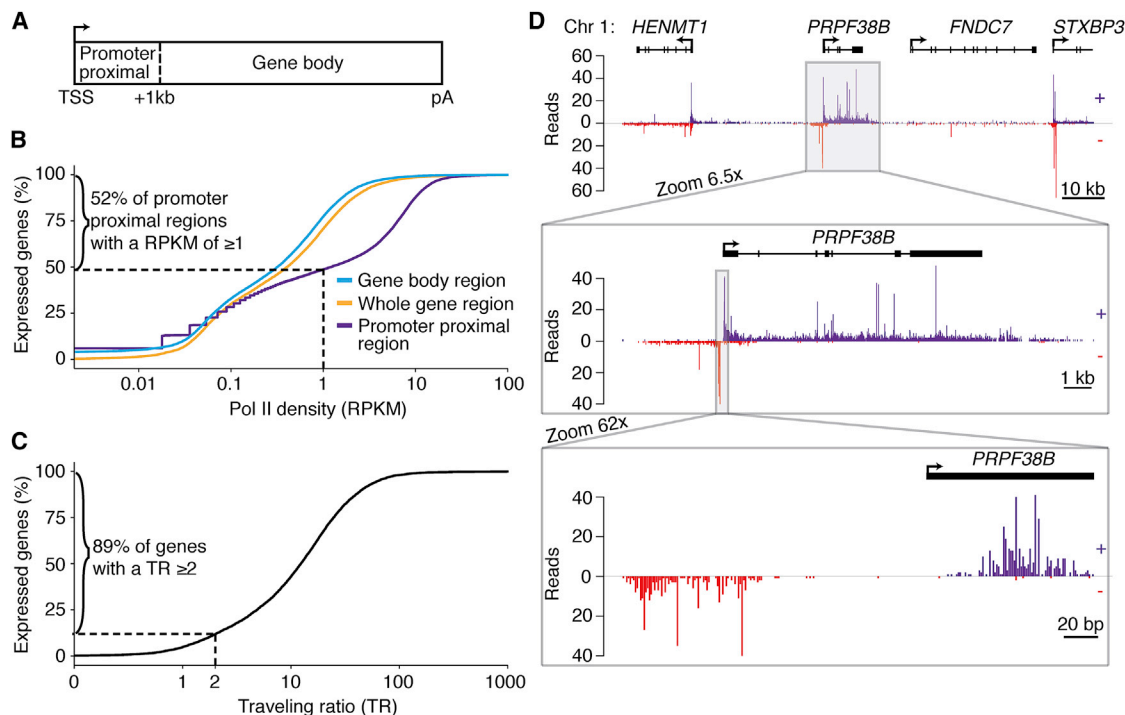


Figure 2. NET-Seq Reports on Transcription Globally and Locally

(A) Schematic defining gene regions used in analysis of NET-seq data.

(B) Distributions of the percent of expressed Pol-II-transcribed protein-coding genes ($n = 19,108$), with a given Pol II coverage for different gene regions as defined in Figure 2A.

(C) Distributions of the percent of well-expressed Pol II protein-coding genes ($n = 8,912$) with a given traveling ratio. Well-expressed Pol II genes are defined as those genes with an RPKM of 1 or greater in a tight promoter-proximal region (-30 bp to $+300$ bp of the TSS). Traveling ratio (TR) is defined as the RPKM of the tight promoter-proximal region divided by the RPKM of the gene body region.

(D) Number of NET-seq reads at three zoom levels around the *PRPF38B* locus for HeLa S3 cells. Reads that aligned to the positive strand (+) are in violet, and reads that aligned to the negative strand (-) are in red. The TSS and the direction of transcription are indicated by an arrow. Annotation of exonic and intronic regions is shown as boxes and lines, respectively.

RPKM, reads per kb per million uniquely aligned reads at Pol-II-transcribed genes; TSS, transcription start site; pA, polyadenylation site. See also Figure S2.

2011; Core et al., 2008; Neil et al., 2009; Seila et al., 2008; Xu et al., 2009). We analyzed this phenomenon for a stringently defined set of Pol-II-transcribed genes that do not overlap other genes within 2.5 kb of the TSS and polyadenylation site and are longer than 2 kb to avoid misinterpreting transcription from other genes as antisense transcription ($n = 3,937$ genes). Analysis of regions 2 kb upstream and downstream of transcription start sites with broad coverage and no sign of missing overlapping annotation ($n = 1,488$; see Experimental Procedure) reveals divergent transcription in 77% of promoter-proximal regions, consistent with other studies (Figure 3A, left) (Core et al., 2008; Seila et al., 2008). Surprisingly, close inspection of our data revealed an unappreciated form of antisense transcription near promoters. At 25% of promoter-proximal regions, we observe antisense transcription originating downstream of sense transcription (Figure 3A, right), which we term convergent transcription. Convergent transcription is clearly observed at single-promoter regions (Figures 3B and 3C), and in most cases, such as near the *KLHL9* promoter, convergent transcription is accompanied by divergent transcription (Figure 3B). However, it also occurs in the absence of divergent transcription (for example,

FAM133B, Figure 3C). Furthermore, GRO-seq also detects these transcripts. A re-analysis of mouse embryonic stem cell data reveals convergent antisense transcription (Jonkers et al., 2014) (Figure S3A).

To characterize the structural attributes on these modes of transcriptional activity, distances between sense and antisense peaks were determined for each promoter-proximal region (Figure 3D). A stereotypical distance (250 ± 50 bp) separates the sense and antisense peaks in divergent transcription, while the sense and antisense peaks in convergent transcription are also separated by a stereotypical distance ($150 \text{ bp} \pm 50 \text{ bp}$), indicating that convergent antisense transcription is not simply the result of spurious antisense transcription initiation events across the promoter-proximal region (Figure 3D).

A Distinct Chromatin Structure Associated with Convergent Transcription

Many chromatin modifiers control antisense transcription (Churchman and Weissman, 2011; DeGennaro et al., 2013; Kim et al., 2012; Marquardt et al., 2014; Whitehouse et al., 2007), and we asked how promoter-proximal transcriptional

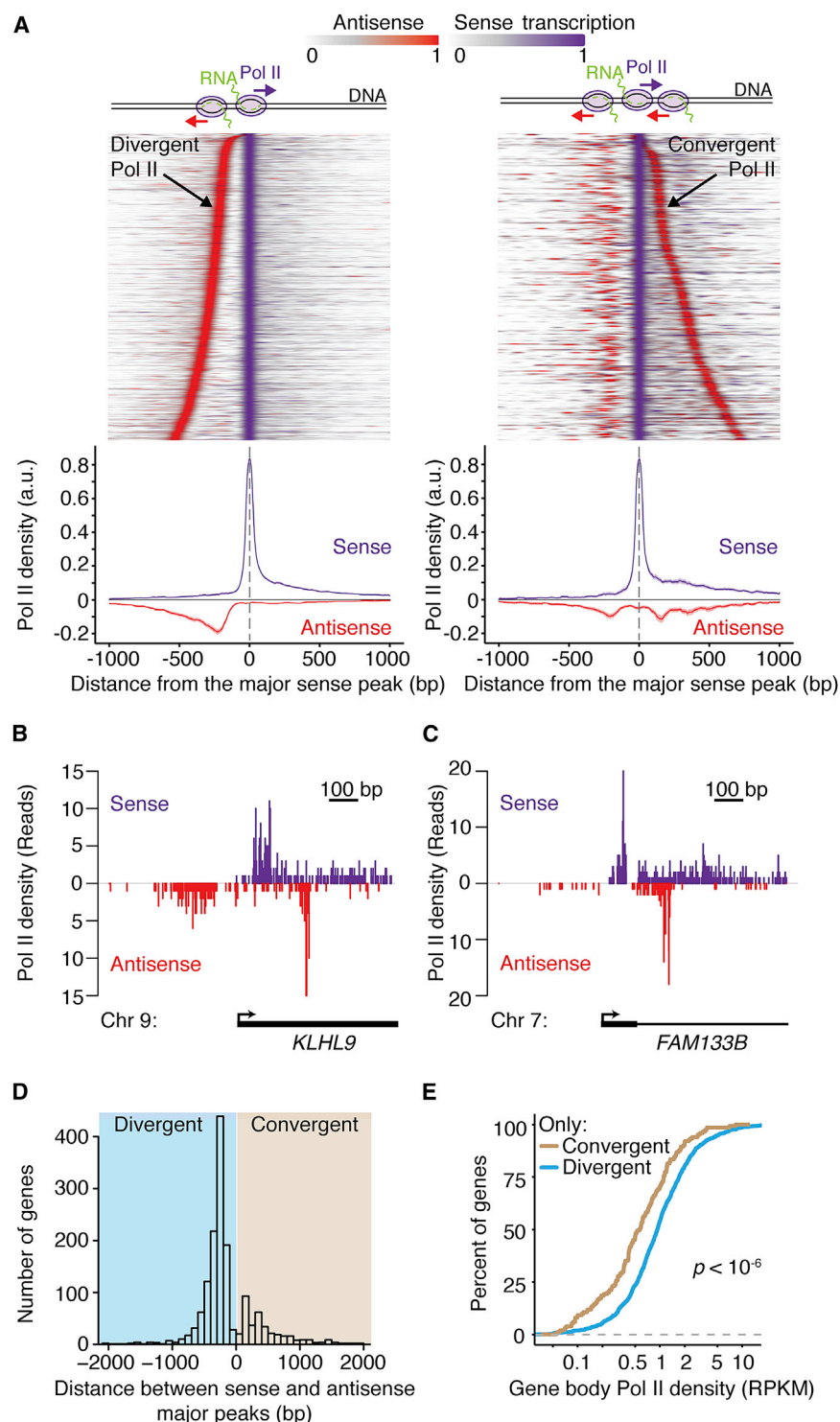


Figure 3. Convergent Transcription Observed at the Promoter-Proximal Regions of Lower-Expressed Genes

(A) Promoters are classified depending on whether they contain a peak of convergent antisense Pol II transcription, as illustrated by the cartoon above the heat maps. A stringent set of promoter-proximal regions was selected for analysis to ensure that transcription arising from other transcription units would not bias classification (see [Experimental Procedures](#)). Heatmaps of Pol II scaled density are displayed for each class (left, no convergent peak, $n = 931$ genes; right, convergent peak, $n = 373$). For each gene, the sense (violet) and antisense (red) raw signal is analyzed separately and normalized to vary from 0 to 1. Both signals are superposed, centered on the major sense transcription peak. Genes are sorted by the distance between the sense and antisense peaks. Mean Pol II density profile is displayed below the heatmaps, where raw sense and antisense data are normalized together to vary between 0 and 1 and smoothed with a 50 bp sliding window average. Solid lines indicate the mean values, and shading shows the 95% confidence interval. Sense transcription is shown in violet, and antisense transcription is shown in red.

(B and C) Examples of NET-seq reads in two promoter-proximal regions that display convergent Pol II transcription.

(D) Histogram of distances between the major peak of Pol II density in the sense direction and the peak(s) in the antisense direction for all promoters with convergent and/or divergent peaks ($n = 1,304$).

(E) Distributions of the percentage of genes with a given Pol II density in the gene body region, as defined in [Figure 2A](#). Genes with only convergent transcription (yellow, $n = 151$) or only divergent transcription (blue, $n = 931$) in their promoter-proximal regions are compared. The p value is calculated by the Kolmogorov-Smirnov test.

RPKM, reads per kb per million uniquely aligned reads at Pol-II-transcribed genes. See also [Figure S3](#).

activity relates to local chromatin structure. We used DNase-seq to map regions of open chromatin and highly positioned nucleosomes in the same HeLa S3 cells used for NET-seq ([Thurman et al., 2012](#)). We examined the distribution of DNase I accessibility relative to promoter-proximal peaks in NET-seq data

relative to the divergent antisense peak shows that this transcriptional activity originates from the 5' side of the promoter hypersensitivity region, consistent with the model that divergent antisense transcription is a consequence of an open chromatin region ([Seila et al., 2009](#)) ([Figure 4C](#)). In contrast, genes with

([Figure 4](#)). At genes that have a sense Pol II peak (representing promoter-proximally paused Pol II), we observe strong DNase I hypersensitivity upstream of the peak, determining the canonical promoter ([Figure 4A](#)), and reduced DNase sensitivity downstream of the peak corresponding to the +1 nucleosome. Thus, promoter-proximal pausing occurs prior to the +1 nucleosome in mammalian cells. Comparison of DNase I data rela-

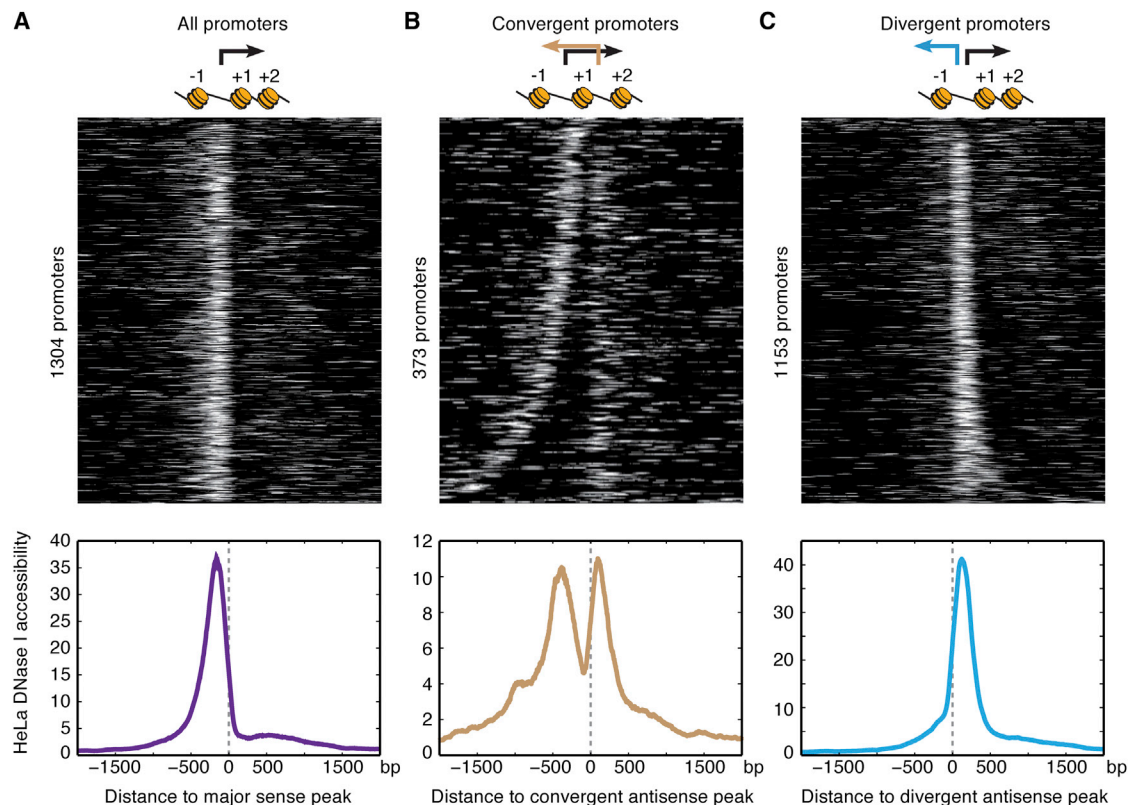


Figure 4. Convergent Transcription Is Associated with a Distinct Chromatin Structure

(A–C) Heatmaps showing DNase I accessibility in HeLa S3 cells surrounding all (A) promoters ($n = 1,304$) aligned to the sense NET-seq peak, (B) promoters that have convergent transcription ($n = 373$) aligned to the antisense convergent NET-seq peak, and (C) promoters that have divergent transcription ($n = 1,153$) aligned to the antisense divergent peak. Below each heatmap is the mean DNase I accessibility profile of the region shown in the heatmap. The raw data are smoothed with a 150 bp sliding window in 20 bp steps. Solid lines indicate the trimmed mean (removing 5% of extreme data points). Above each heatmap are arrows showing the transcriptional activity observed in each promoter-proximal region. A cartoon displays the chromatin structure determined by analysis of the DNase-seq data.

convergent transcription show two distinct peaks in DNase I hypersensitivity: a canonical promoter peak and a downstream peak located proximal to the antisense convergent peak (Figure 4B). Thus, convergent antisense transcription likely originates locally. Furthermore, the dip between the two peaks of DNase I hypersensitivity likely represents the +1 nucleosome, consistent with the ~ 150 bp spacing between the sense and convergent antisense Pol II peaks (Figures 3D and 4B). These results indicate that convergent transcription reflects sense and antisense transcription that initiates locally and undergoes promoter-proximal pausing flanking the +1 nucleosome.

Convergent Transcription Is a Feature of Lower-Expressed Genes

Convergent transcription can regulate gene expression through transcriptional interference mechanisms (Callen et al., 2004; Elledge and Davis, 1989; Gullerova and Proudfoot, 2012; Hobson et al., 2012; Martens et al., 2004; Prescott and Proudfoot, 2002; Shearwin et al., 2005). Thus, we considered whether promoter-proximal convergent transcription may be involved in release of Pol II from promoter-proximal pausing into productive elonga-

tion. We compared Pol II density within the gene body (+1 kb after the transcription start site to the polyadenylation site, illustrated in Figure 2A) at genes that display only convergent transcription to genes that display only divergent transcription. Notably, genes with only convergent transcription near their promoters show consistently less transcription downstream of their promoter regions (Figure 3E) (1.8-fold less on average, Kolmogorov–Smirnov test, $p < 10^{-6}$). Comparison of less stringently defined sets of genes, such as all genes with convergent transcription to all genes without convergent transcription, showed a similar effect (Figure S3B). In agreement with this observation, analysis of ENCODE HeLa S3 ChIP-seq data reveals that H3K79me2 histone marks, which correlate with transcription elongation, occur at significantly lower levels in the gene bodies of genes with convergent antisense transcription (Figure S3C) (Consortium, 2012; Guenther et al., 2007; Wozniak and Strahl, 2014). Thus, convergent antisense transcription could interfere with productive transcription elongation or could be a consequence of less-productive elongation. Either of these possibilities could be directly mediated by Pol II or by another factor, such as chromatin.

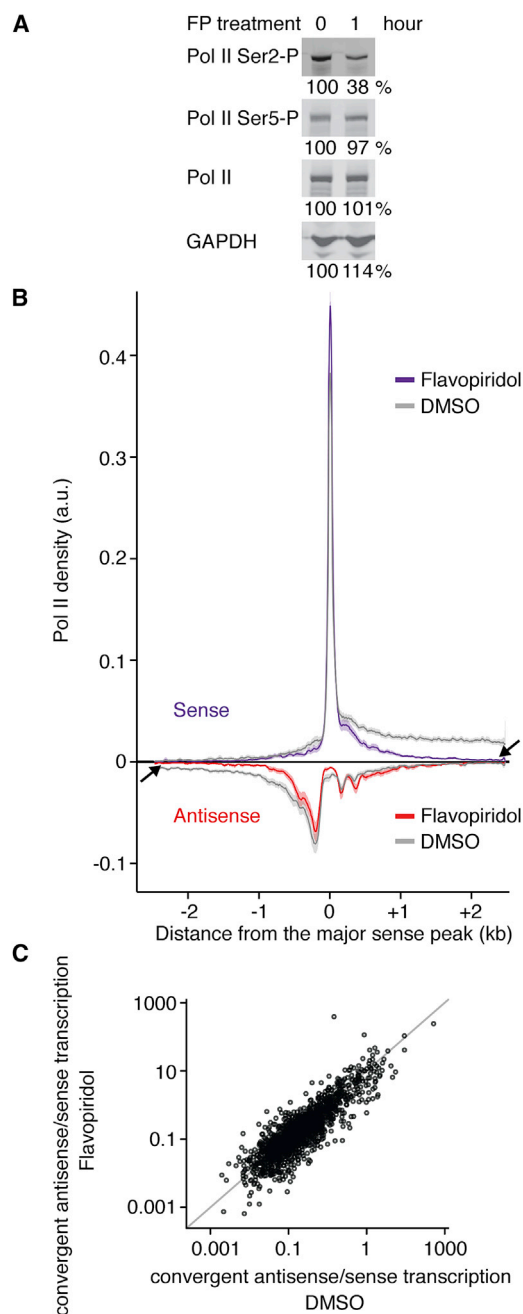


Figure 5. P-TEFb Inhibition Proportionally Affects Levels of Sense Transcription and Convergent Antisense Transcription

(A) Western blot analysis of whole-cell extract of HeLa S3 cells with flavopiridol (FP) treatment (1 hr). The percentage at the bottom of each lane is the amount of the respective protein (as determined by image quantification) before and after FP treatment. GAPDH serves as a loading control.

(B) Meta-gene analysis of NET-seq data from HeLa S3 cells treated with 1 μ M FP (purple and red) or DMSO control (gray) for 1 hr. Arrows indicate regions where transcription is affected by FP treatment. Genes that had convergent and/or divergent peaks (described in [Experimental Procedures](#)) in both data sets are included in the analysis ($n = 615$). NET-seq signal from each promoter region (± 2.5 kb centered at the sense transcription peak) are binned into 10 bp windows. For each sample, sense and antisense signal are normalized together to vary between

To test whether convergent antisense transcription is a consequence of reduced sense transcription elongation, we globally suppressed productive elongation by inhibiting positive transcription elongation factor b (P-TEFb). Most promoter-proximally paused Pol II are released through recruitment of P-TEFb that phosphorylates multiple proteins, including Ser2 residues of the Pol II CTD (Kim and Sharp, 2001; Peterlin and Price, 2006). Therefore, active P-TEFb greatly facilitates the transition to productive elongation but does not affect transcription initiation (Lis et al., 2000; Peterlin and Price, 2006; Rahl et al., 2010). We performed NET-seq analysis on HeLa S3 cells exposed to the P-TEFb inhibitor flavopiridol (FP) (Chao and Price, 2001) or DMSO alone. As expected, after 60 min, FP reduced Pol II CTD Ser2 phosphorylation, but phosphorylation of Ser5 residues and overall Pol II levels remained unchanged (Figures 5A and S4). We generated NET-seq libraries from HeLa S3 cells after a 1 hr FP treatment or DMSO control (FP treatment NET-seq data set, 486 million total reads, 262 uniquely mapped reads; DMSO control NET-seq data set, 491 million total reads, 263 million uniquely mapped). In agreement with previous studies, we observe a global decrease in Pol II density outside of promoter-proximal regions compared to the DMSO control (Figure 5B, arrows) (Flynn et al., 2011; Jonkers et al., 2014; Rahl et al., 2010). Thus, FP treatment reduces productive elongation of most genes. To quantify the effect of FP treatment on convergent transcription, we calculated the ratio of convergent antisense to sense transcription at all promoter-proximal regions. If convergent transcription were a simple consequence of lower expression, it should not only be increased proportionally to promoter-proximal sense transcription following FP treatment, but importantly, it should appear in genes where it was not detected before. We observe that the convergent antisense-to-sense transcription ratio remains constant following FP treatment, indicating that sense and convergent antisense transcription levels covary, and we do not detect a new subpopulation of genes with convergent transcription in their promoter-proximal regions (Figure 5C). This result suggests that the lack of sense-productive transcription elongation is not sufficient to induce convergent transcription. Thus, if convergent antisense transcription is not a simple consequence of low sense expression, then it may contribute to the cause.

Impact of Transcription Factor Occupancy on Pol II Elongation

DNA-bound transcription factors (TFs) have the potential to obstruct elongating Pol II. To investigate the relationship between TF occupancy and Pol II progress, we expanded our

0 and 1 and then smoothed with a 50 bp sliding window. Solid lines indicate the mean normalized Pol II density, and shading shows the 95% confidence interval.

(C) A scatterplot comparing the convergent-to-sense ratio after treatment with DMSO (control) and after FP treatment for a stringent subset of non-overlapping genes with at least 10 reads across the 500 bp region after TSS in both samples ($n = 1,667$). The ratio is the sum of NET-seq signal on the antisense strand versus the sense strand across the 500 bp region after the TSS. The handful of genes with a ratio of 0 are not plotted.

TSS, transcription start site. See also Figure S4.

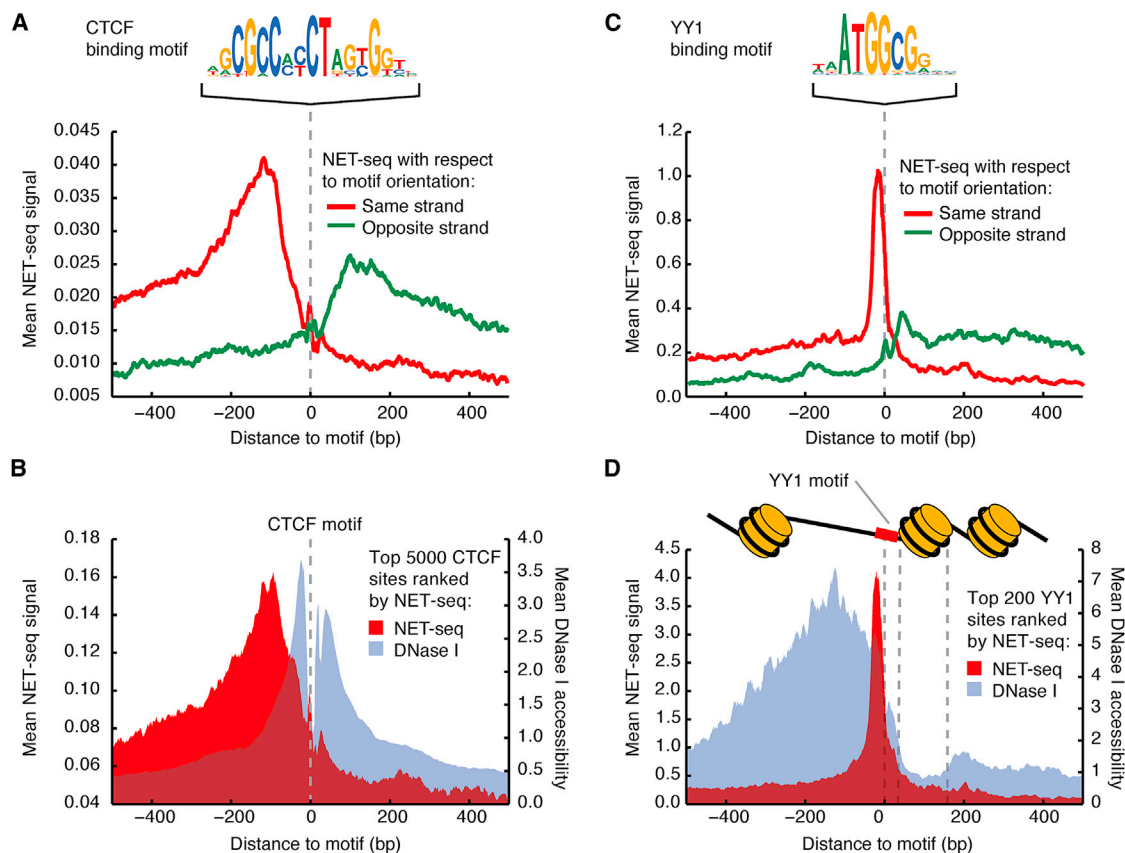


Figure 6. Pol II Pausing Associated with Transcription Factor Occupancy

(A) Average NET-seq signal around 16,339 CTCF motifs with accessible chromatin. In red is NET-seq signal oriented to the strand of the motif (Pol II transcription from left to right), and in green is NET-seq on the other strand (Pol II transcription from right to left). The CTCF binding motif is pictured above. The NET-seq data were smoothed by a 10 bp sliding window average.

(B) Mean NET-seq (red) and DNase I cleavage (gray) signal (10 bp windowed averages) surrounding the top 5,000 CTCF motifs sorted by NET-seq signal.

(C) Average NET-seq signal (smoothed by a 10 bp sliding window average) around 731 YY1 motifs with accessible chromatin. In red is NET-seq signal oriented to the strand of the motif (Pol II transcription from left to right), and in green is NET-seq on the other strand (Pol II transcription from right to left). The YY1 binding motif is pictured above.

(D) Mean per nucleotide NET-seq (red) and DNase I cleavage (gray) signal surrounding the top 200 YY1 motifs sorted by NET-seq signal. Both signals are presented as 10 bp windowed averages. Schematic of nucleosome positioning relative to YY1 inferred from DNase I accessibility is above plot.

DNase-seq data from HeLa S3 cells to genomic footprinting depth (269 million uniquely mapped genomic reads), enabling detailed mapping of the occupancy of TF recognition sites within DNase I hypersensitivity sites (DHSs). As CTCF is implicated in Pol II pausing in vitro and within the cell (Shukla et al., 2011), we quantified NET-seq signal and DNase-seq signal around CTCF recognition sites within DHSs on both strands. We observed higher Pol II density just upstream of the CTCF sites, suggesting that CTCF might represent a barrier to Pol II elongation genome wide (Figures 6A and 6B). Interestingly, the NET-seq signal around these sites differs in magnitude for each strand, indicating that CTCF may pose strand-specific obstacles (Figure 6A).

As transcriptional pausing has been seen upstream of nucleosomes in yeast and *Drosophila* cells (Churchman and Weissman, 2011; Mavrich et al., 2008; Weber et al., 2014), we investigated Pol II density around YY1, a canonical promoter-

centric transcription factor (Xi et al., 2007) thought to position +1 nucleosomes (Vierstra et al., 2014). Thus, we speculated that YY1 occupancy might impact Pol II elongation. Given that poly-zinc finger TFs engage DNA asymmetrically, we also speculated that any impact on Pol II might also be strand specific. We observed a peak in NET-seq signal precisely at YY1 sites in DHSs, consistent with YY1-directed pausing (Figures 6C and 6D). Strikingly, this effect was highly directional and is predominant when Pol II engages YY1 from the upstream direction (Figure 6D). These results indicate that TFs might directly regulate Pol II elongation in direction- or strand-specific ways.

Fine Structure of Pol II Pausing along Constitutive and Alternative Exons

Alteration to transcription elongation rates affects splicing outcomes, which has led to the proposal of the kinetic model of transcription and splicing coupling (Dujardin et al., 2014; Fong et al.,

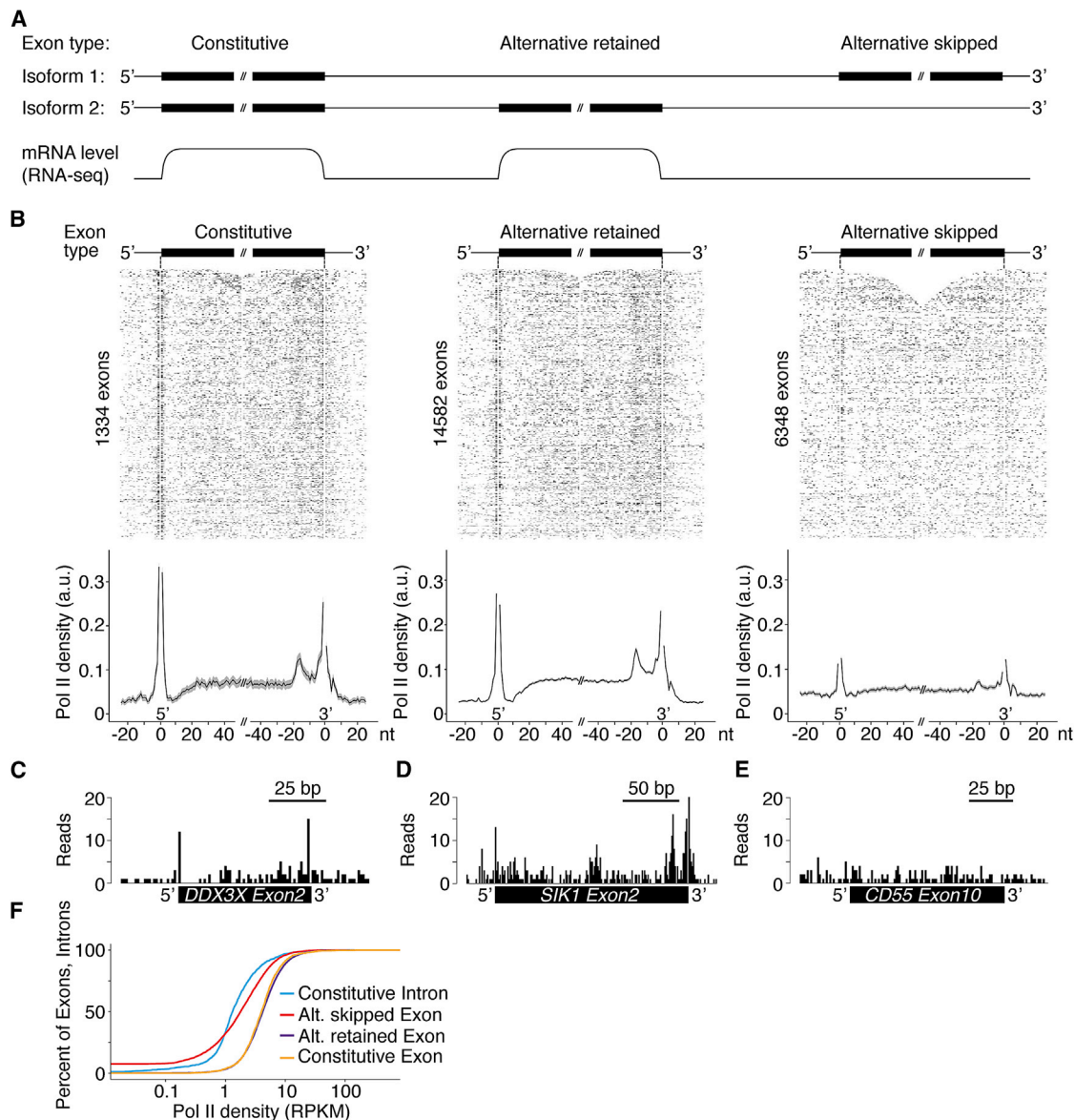


Figure 7. Pol II Density across Exons Reveals a Stereotypical Pausing Pattern that Depends on Splicing Outcome

(A) Schematic of the classification of constitutive, alternative retained, and alternative skipped exons based on annotated isoforms and detected levels in cytosolic RNA-seq data.

(B) A stringent set of exons was selected for analysis from genes containing NET-seq signal of ≥ 1 RPKM (B, see [Experimental Procedures](#)). Heatmaps and meta-exon analysis of HeLa S3 Pol II density across each type of exon, as defined in (A) (left to right: constitutive exons, $n = 1,334$; alternative retained, $n = 14,582$; and alternative skipped, $n = 6,348$). NET-seq signal from each exon (± 25 bp) is normalized to vary from 0 to 1 (white to black scale in the heatmaps). Solid lines on the meta-exon plots indicate the mean values, and the gray shading represents the 95% confidence interval. The single-nucleotide positions where splicing intermediates align (3' ends of introns and exons) were entirely removed from analysis (see [Experimental Procedures](#)) and appear as a blank position in the figures.

(C-E) Raw NET-seq reads across the constitutive exon 2 within the *DDX3X* gene (C), alternative retained exon 2 within the *SIK1* gene (D), and the alternative skipped exon 10 within the *CD55* gene (E).

(F) Distribution of the percent of exons or introns with a given Pol II density.

RPKM, reads per kb per million Pol II uniquely aligned reads. See also [Figure S5](#).

2014; Ip et al., 2011; de la Mata et al., 2003; Roberts et al., 1998). However, the degree to which transcription rate is modulated locally around exons is unclear. Higher Pol II density at human exons versus introns was reported using Pol II ChIP-seq and ChIP-chip (Brodsky et al., 2005; Schwartz et al., 2009), but in

another study, no significant difference was observed (Spies et al., 2009). Furthermore, the precise pattern across individual exons could not be resolved. In *Drosophila* cells, PRO-seq observed high Pol II density across exons and detected a high enrichment of Pol II density at the 5' ends (Kwak et al., 2013).

We analyzed NET-seq data at constitutive exons and revealed significantly higher coverage than at introns in both HeLa S3 (2.4 × higher) and HEK293T cells (2.2 × higher) ($p < 10^{-15}$, Kolmogorov–Smirnov test), suggesting that transcription elongation is slower at exons in human cells (Figures 7A, 7B, 7F and S5A). Any contamination from processed mRNA would inflate these differences; however, our quality controls (Figures 1B, 1C, and S1A) suggest that this is a small effect, if at all. Strikingly, NET-seq signal across exons is not uniform: sharp increases in Pol II density occur in the few base pairs surrounding the 5′ and 3′ ends of constitutive exons, indicating strong Pol II pausing at exon boundaries (Figure 7B). As splicing intermediates are known NET-seq contaminants (Figure S1G), we removed the single bp positions where they align from analysis. Furthermore, a broader peak of RNA polymerase density is present ~17 nt before the 3′ end of exons. The general features of this pattern are observed at single exons, for example, exons 2 of the *DDX3X* and *SIK1* genes (Figures 7C and 7D). Finally, we observe similar trends in the NET-seq data from HEK293T cells (Figure S5B). This analysis suggests that exon borders impose a structured barrier to Pol II elongation.

Most human exons can be alternatively spliced, with retained exons varying between cell types (Pan et al., 2008; Wang et al., 2008). We expanded our analysis to alternatively spliced exons and investigated whether transcriptional pausing varies at exons with different splicing outcomes. We focused our analysis on genes with a NET-seq RPKM of >1 in the gene body (Figure S5A) and defined skipped exons as those undetected in the cytoplasmic RNA-seq data (Figure 7A). As for constitutive exons, retained alternative exons have higher Pol II density compared to the density across introns (Figure 7F). These exons also have a similar pausing pattern as constitutive exons, which is visible by meta-exon analysis and at the single exon (Figures 7B and 7D). Interestingly, Pol II density is lower at skipped exons than at alternative retained exons (Figure 7F). Strikingly, the Pol II density pattern is similarly shaped across skipped and retained exons, albeit significantly different in amplitude (Figures 7B and 7E). The residual pausing pattern at skipped exons could be due to the small number of retained exons that are misannotated as skipped. Finally, the same differences in the Pol II density patterns across retained and skipped exons are observed in HEK293T cells (Figure S5B). Together, these data show that Pol II recognizes exon structures with different processing fates, suggesting that alternative splicing is kinetically coupled to transcription elongation genome wide.

DISCUSSION

Here, we demonstrate that human NET-seq provides complete, strand-specific maps of transcription at single-nucleotide resolution. NET-seq thereby defines transcriptional pausing sites and directly measures unstable transcripts. Finally, NET-seq instantaneously reports the transcription status of genes, in contrast to RNA-seq, which reports the balance between RNA synthesis and degradation.

Our work describes an unappreciated aspect of promoter-proximal transcription: the presence of convergent transcription

at many human genes. Importantly, we show that convergent transcription is characteristic of lower-expressed genes, suggesting a potential role in the regulation of promoter-proximal pausing. Prominent DNase I hypersensitivity sites flanking the convergent antisense peak indicate that promoter-proximal convergent transcription reflects initiation at a defined promoter located a characteristic distance from the canonical sense promoter.

Other than expression level, only one commonality is found between the genes with convergent transcription: the dinucleotide CC occurs slightly more frequently in regions displaying convergent transcription ($12.4\% \pm 0.4\%$ for convergent, $11.1\% \pm 0.2\%$ for not convergent). Thus, it appears that convergent transcription is a prevalent phenomenon that is not restricted to a specific class of genes. An intriguing possibility is that paused antisense Pol II directly blocks or clashes with sense transcription, as can occur in yeast (Prescott and Proudfoot, 2002). The sense and convergent antisense peaks are too far apart (~150 bp) to reflect direct contact of paused polymerases, but the DNase-seq data reveal that this distance likely represents the +1 nucleosome that is positioned between them. Interference could arise through positioning of the +1 nucleosome or indirect mechanisms such as transcription-induced changes in DNA topology, chromatin modifications, or transcription factor occupancy. In any event, NET-seq data do not resolve whether sense and antisense transcription occur simultaneously, as the approach requires averaging over a population of cells. Therefore, potential roles of convergent transcription during initiation, elongation, and termination will have to be investigated within cell populations and at the single-cell level.

Our study yields a global picture of how transcription elongation is altered at alternatively spliced exons in human cells. Changes in transcription elongation influence alternative splicing, which is thought to be mediated either by the differential recruitment of splicing factors (recruitment model) or by biasing kinetic competition between multiple splicing outcomes (kinetic model) (Bentley, 2014; Dujardin et al., 2013; Kornblihtt et al., 2004). Here, we show that alternative splicing outcomes in human cells are associated with Pol II exon density and strong pauses at the 5′ and 3′ ends, consistent with the kinetic model. What causes pauses at exons is an important question. Nucleosomes can influence transcriptional pausing (Churchman and Weissman, 2011; Hodges et al., 2009; Izban and Luse, 1991; Skene et al., 2014), and, importantly, nucleosome occupancy and histone modifications transition at exon boundaries according to splice site strength (Andersson et al., 2009; Chodavarapu et al., 2010; Huff et al., 2010; Schwartz et al., 2009; Spies et al., 2009; Tilgner et al., 2009). DNA sequence and DNA methylation at exon boundaries could contribute to pausing because sequence elements have been shown to cause transcriptional pausing (Gelfman et al., 2013; Herbert et al., 2006; Kassavetis and Chamberlin, 1981; Larson et al., 2014; Maizels, 1973; Vvedenskaya et al., 2014). Additionally, transcription factors could underlie pausing at retained exons, as is the case with CTCF binding at exon 5 of the *CD45* gene (Shukla et al., 2011). The broad peak of Pol II density 17 bp from the 3′ end of the exon may reflect Pol II backtracking during the recovery from the strong pause at the 3′ end of the exon. Backtracking would

produce small cleavage products, consistent with the population of tiny RNAs that were previously identified in this region (Taft et al., 2009).

We expect adaptation of human NET-seq to any human cell type to be straightforward, resulting in a tool to illuminate a variety of biological processes. Future applications include high-resolution analyses of transcription regulation across cell types, responses to signaling pathways, and cellular differentiation.

EXPERIMENTAL PROCEDURES

Cell Fractionation and RNA Purification

Cell fractionation is performed as described by (Bhatt et al., 2012; Pandya-Jones and Black, 2009) and based on (Wuarin and Schibler, 1994) with modifications. All steps are conducted on ice or at 4°C and in the presence of 25 μ M α -amanitin, 50 units/ml SUPERaseIN and Protease inhibitors cOmplete. HeLa S3 cells and HEK293T cells are grown in DMEM containing 10% FBS, 100 U/ml penicillin, and 100 μ g/ml streptomycin to a confluency of 90%. Following lysis of 1×10^7 cells, the nuclei are washed with the nuclei wash buffer (0.1% Triton X-100, 1 mM EDTA, in $1 \times$ PBS) to remove cytoplasmic remnants. Nuclei lysis is performed without $MgCl_2$ (1% NP-40, 20 mM HEPES [pH 7.5], 300 mM NaCl, 1 M Urea, 0.2 mM EDTA, 1 mM DTT). The success of cell fractionation is monitored by western blot analysis and subcellular RNA-seq.

Sequencing Library Constructions

For NET-seq, the library preparation is performed as described by Churchman and Weissman (2011, 2012) with modifications. For 3' RNA ligation, a pre-adenylated DNA linker with a mixed random hexameric barcode sequence at its 5' end is used. cDNA containing the 3' end sequences of a subset of mature and heavily sequenced snRNAs, snoRNAs, rRNAs, and mitochondrial tRNAs are specifically depleted using biotinylated DNA oligos (Table S1), as described by Ingolia et al. (2012). For subcellular RNA-seq, the sequencing libraries are prepared as described in Churchman and Weissman (2012), with the ribosomal RNA removed using the Ribo-Zero Magnetic Kit (Epicentre). DNA libraries are sequenced by the NextSeq 500 and HiSeq 2000 Illumina platforms.

Processing and Alignment of Sequencing Reads

Reads are trimmed and aligned using STAR (v2.4.0) (Dobin et al., 2013). For NET-seq data, only the position matching the 5' end of the sequencing read (after removal of the barcode), corresponding to the 3' end of the nascent RNA fragment, is recorded with a Python script using HTSeq package (Anders et al., 2015). Reverse transcription mispriming events are identified and removed when molecular barcode sequences match exactly to the genomic sequence adjacent to the aligned read. Reads that align to the same genomic position and contain identical barcodes are considered PCR duplication events and are removed. Splicing intermediates have 3' hydroxyls and will enter NET-seq libraries and contribute to the reads aligning to the exact single-nucleotide 3' ends of introns and 3' ends of exons (Figure S1G). Therefore, reads that map precisely at the exact single-nucleotide ends of introns and exons are discarded, and the single 1 bp genomic positions are not considered in subsequent analysis.

Annotation of Exons and Introns

Clear exonic regions are identified by determining the minimum overlapping exonic region of all isoforms that have an exon at that position. If the region is present in all isoforms, it is considered a constitutive exon; otherwise, it is labeled alternative. Alternative skipped exons are classified by those alternative exons that are entirely undetected in the cytoplasm RNA-seq data, and the rest of the alternative exons are classified as retained. Constitutive intronic regions are identified as the minimum intronic overlapping regions present in all isoforms.

NET-Seq Exon Metagene and Heatmap Analysis

The set of exons included in the analysis are required to be within genes of an RPKM >1 in gene bodies (defined in Figure 2A) and not overlapping any other annotated exon. They are required to begin and end at the same position in all isoforms that contain the exon. First and last exons of genes are removed from analysis. NET-seq signal across each exon ± 25 bp is normalized to range between 0 and 1 so that each exon contributes to the analysis with the same weight. Precise single-nucleotide genomic loci where splicing intermediates map (exact 3' ends of introns and exons) are not included in the analysis, and those locations are left blank in any plots.

Analysis of Promoter-Proximal Regions

Promoter-proximal regions were carefully selected for analysis to ensure that there is minimal contamination from transcription arising from other transcription units. Starting with genes that are Pol II protein coding, non-overlapping within a region of 2.5 kb upstream of the TSS and 2.5 kb downstream of the polyA site, and longer than 2 kb, NET-seq data at promoter-proximal regions are required to have a coefficient of variation >0.5 and have at least 40 positions covered in the sense strand. Within a 4 kb window surrounding the TSS, peaks were identified in the sense from these genes. If >40 bases on the antisense strand have NET-seq signal, peaks were also identified on the antisense strand. Promoter regions with an antisense peak located downstream of the sense major peak are classified as displaying convergent transcription. Promoter regions with an antisense peak located upstream of the sense major peak are classified as displaying divergent transcription.

ACCESSION NUMBERS

All NET-seq and RNA-seq data sets are available at GEO under the accession number GSE61332. DNase-seq data sets are available at ENCODE under the ENCODE DCC accession number ENCBS229UDI.

SUPPLEMENTAL INFORMATION

Supplemental Information includes Extended Experimental Procedures, five figures, and one table and can be found with this article online at <http://dx.doi.org/10.1016/j.cell.2015.03.010>.

AUTHOR CONTRIBUTIONS

A.M., J.d.I. and L.S.C. designed the NET-seq experiments; A.M. established NET-seq and subcellular RNA-seq experimental protocols, with input from J.d.I.; A.M. and S.M. carried out experiments; J.d.I. developed a bioinformatics analysis pipeline for human NET-seq and subcellular RNA-seq, with input from A.M.; A.R., J.V., R.S., and J.A.S. generated and analyzed the DNase-seq data; J.d.I., U.E., and L.S.C. analyzed NET-seq data; A.M., J.d.I., J.A.S., and L.S.C. wrote the manuscript.

ACKNOWLEDGMENTS

We thank F. Winston, J. Gray, M. Couvillion, S. Doris, and E. Feinberg for critical comments on the manuscript. We thank J. Gray and A. Snively for help with eRNA analysis. We thank F. Winston, K. Struhl, S. Buratowski, A. Ciuffi, and A. Regev for advice and discussions. We thank M. Gebremeskel for tissue culture support; K. Waraska at the HMS Biopolymers Facility and Z. Herbert at the DFCI Molecular Biology Core Facilities for sequencing; and N. Pho and B.D. Kim at HMS Research Computing for computing support. This work was supported by US National Institutes of Health NHGRI grants R01HG007173 to L.S.C. and U54HG007010 to J.A.S.; a Damon Runyon Dale F. Frey Award for Breakthrough Scientists (to L.S.C.); and a Burroughs Wellcome Fund Career Award at the Scientific Interface (to L.S.C.). A.M. was supported by Long-Term Postdoctoral Fellowships of the Human Frontier Science Program (LT000314/2013-L) and EMBO (ALTF858-2012). J.d.I. was supported by the Swiss National Science Foundation Postdoc Mobility

Fellowship. J.V. was supported by US National Science Foundation Graduate Research Fellowship under grant DGE-071824.

Received: October 8, 2014

Revised: November 26, 2014

Accepted: February 18, 2015

Published: April 23, 2015

REFERENCES

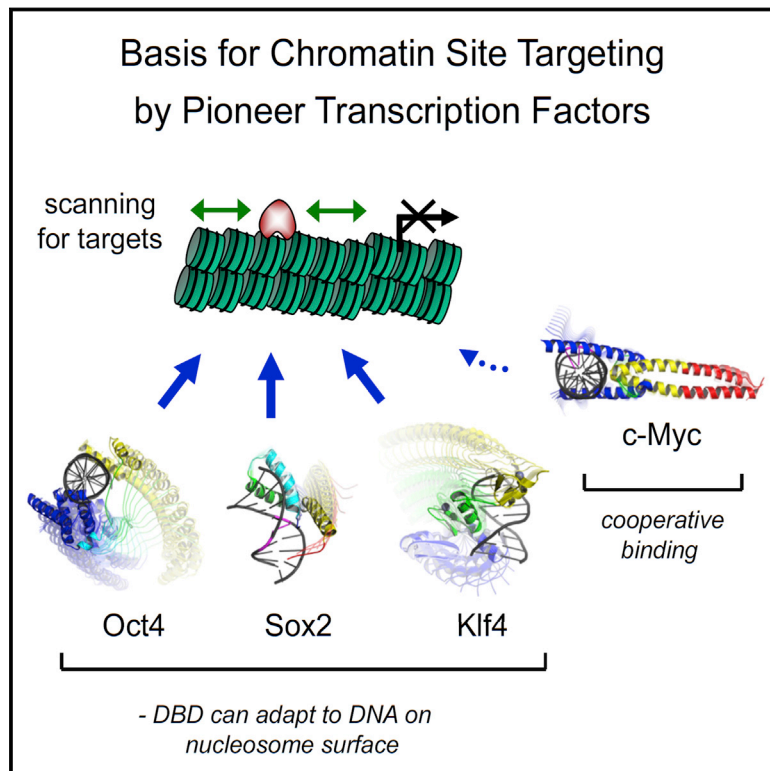
- Almada, A.E., Wu, X., Kriz, A.J., Burge, C.B., and Sharp, P.A. (2013). Promoter directionality is controlled by U1 snRNP and polyadenylation signals. *Nature* 499, 360–363.
- Anders, S., Pyl, P.T., and Huber, W. (2015). HTSeq—a Python framework to work with high-throughput sequencing data. *Bioinformatics* 31, 166–169.
- Andersson, R., Enroth, S., Rada-Iglesias, A., Wadelius, C., and Komorowski, J. (2009). Nucleosomes are well positioned in exons and carry characteristic histone modifications. *Genome Res.* 19, 1732–1741.
- Bentley, D.L. (2014). Coupling mRNA processing with transcription in time and space. *Nat. Rev. Genet.* 15, 163–175.
- Bhatt, D.M., Pandya-Jones, A., Tong, A.-J., Barozzi, I., Lissner, M.M., Natoli, G., Black, D.L., and Smale, S.T. (2012). Transcript dynamics of proinflammatory genes revealed by sequence analysis of subcellular RNA fractions. *Cell* 150, 279–290.
- Brodsky, A.S., Meyer, C.A., Swinburne, I.A., Hall, G., Keenan, B.J., Liu, X.S., Fox, E.A., and Silver, P.A. (2005). Genomic mapping of RNA polymerase II reveals sites of co-transcriptional regulation in human cells. *Genome Biol.* 6, R64.
- Cai, H., and Luse, D.S. (1987). Transcription initiation by RNA polymerase II in vitro. Properties of preinitiation, initiation, and elongation complexes. *J. Biol. Chem.* 262, 298–304.
- Callen, B.P., Shearwin, K.E., and Egan, J.B. (2004). Transcriptional interference between convergent promoters caused by elongation over the promoter. *Mol. Cell* 14, 647–656.
- Chao, S.H., and Price, D.H. (2001). Flavopiridol inactivates P-TEFb and blocks most RNA polymerase II transcription in vivo. *J. Biol. Chem.* 276, 31793–31799.
- Chodavarapu, R.K., Feng, S., Bernatavichute, Y.V., Chen, P.-Y., Stroud, H., Yu, Y., Hetzel, J.A., Kuo, F., Kim, J., Cokus, S.J., et al. (2010). Relationship between nucleosome positioning and DNA methylation. *Nature* 466, 388–392.
- Churchman, L.S., and Weissman, J.S. (2011). Nascent transcript sequencing visualizes transcription at nucleotide resolution. *Nature* 469, 368–373.
- Churchman, L.S., and Weissman, J.S. (2012). Native elongating transcript sequencing (NET-seq). *Curr. Protoc. Mol. Biol. Chapter 4*, 1–17.
- Consortium, T.E.P.; ENCODE Project Consortium (2012). An integrated encyclopedia of DNA elements in the human genome. *Nature* 489, 57–74.
- Core, L.J., Waterfall, J.J., and Lis, J.T. (2008). Nascent RNA sequencing reveals widespread pausing and divergent initiation at human promoters. *Science* 322, 1845–1848.
- Davis-Turak, J.C., Allison, K., Shokhirev, M.N., Ponomarenko, P., Tsimring, L.S., Glass, C.K., Johnson, T.L., and Hoffmann, A. (2015). Considering the kinetics of mRNA synthesis in the analysis of the genome and epigenome reveals determinants of co-transcriptional splicing. *Nucleic Acids Res.* 43, 699–707.
- de la Mata, M., Alonso, C.R., Kadener, S., Fededa, J.P., Blaustein, M., Pelisch, F., Cramer, P., Bentley, D., and Kornblitt, A.R. (2003). A slow RNA polymerase II affects alternative splicing in vivo. *Mol. Cell* 12, 525–532.
- DeGennaro, C.M., Alver, B.H., Marguerat, S., Stepanova, E., Davis, C.P., Bähler, J., Park, P.J., and Winston, F. (2013). Spt6 regulates intragenic and antisense transcription, nucleosome positioning, and histone modifications genome-wide in fission yeast. *Mol. Cell Biol.* 33, 4779–4792.
- Dobin, A., Davis, C.A., Schlesinger, F., Drenkow, J., Zaleski, C., Jha, S., Batut, P., Chaisson, M., and Gingeras, T.R. (2013). STAR: ultrafast universal RNA-seq aligner. *Bioinformatics* 29, 15–21.
- Dujardin, G., Lafaille, C., Petrillo, E., Buggiano, V., Gómez Acuña, L.I., Fiszbein, A., Godoy Herz, M.A., Nieto Moreno, N., Munoz, M.J., Alló, M., et al. (2013). Transcriptional elongation and alternative splicing. *Biochim. Biophys. Acta* 1829, 134–140.
- Dujardin, G., Lafaille, C., de la Mata, M., Marasco, L.E., Muñoz, M.J., Le Josic-Corcos, C., Corcos, L., and Kornblitt, A.R. (2014). How slow RNA polymerase II elongation favors alternative exon skipping. *Mol. Cell* 54, 683–690.
- Elledge, S., and Davis, R. (1989). Position and density effects on repression by stationary and mobile DNA-binding proteins. *Genes Dev.* 3, 185–197.
- Ferrari, F., Plachetka, A., Alekseyenko, A.A., Jung, Y.L., Oszolák, F., Kharchenko, P.V., Park, P.J., and Kuroda, M.I. (2013). “Jump start and gain” model for dosage compensation in *Drosophila* based on direct sequencing of nascent transcripts. *Cell Rep.* 5, 629–636.
- Flynn, R.A., Almada, A.E., Zamudio, J.R., and Sharp, P.A. (2011). Antisense RNA polymerase II divergent transcripts are P-TEFb dependent and substrates for the RNA exosome. *Proc. Natl. Acad. Sci. USA* 108, 10460–10465.
- Fong, N., Kim, H., Zhou, Y., Ji, X., Qiu, J., Saldi, T., Diener, K., Jones, K., Fu, X.-D., and Bentley, D.L. (2014). Pre-mRNA splicing is facilitated by an optimal RNA polymerase II elongation rate. *Genes Dev.* 28, 2663–2676.
- Gelfman, S., Cohen, N., Yearim, A., and Ast, G. (2013). DNA-methylation effect on cotranscriptional splicing is dependent on GC architecture of the exon-intron structure. *Genome Res.* 23, 789–799.
- Guenther, M.G., Levine, S.S., Boyer, L.A., Jaenisch, R., and Young, R.A. (2007). A chromatin landmark and transcription initiation at most promoters in human cells. *Cell* 130, 77–88.
- Gullerova, M., and Proudfoot, N.J. (2012). Convergent transcription induces transcriptional gene silencing in fission yeast and mammalian cells. *Nat. Struct. Mol. Biol.* 19, 1193–1201.
- Herbert, K.M., La Porta, A., Wong, B.J., Mooney, R.A., Neuman, K.C., Landick, R., and Block, S.M. (2006). Sequence-resolved detection of pausing by single RNA polymerase molecules. *Cell* 125, 1083–1094.
- Hobson, D.J., Wei, W., Steinmetz, L.M., and Svejstrup, J.Q. (2012). RNA polymerase II collision interrupts convergent transcription. *Mol. Cell* 48, 365–374.
- Hodges, C., Bintu, L., Lubkowska, L., Kashlev, M., and Bustamante, C. (2009). Nucleosomal fluctuations govern the transcription dynamics of RNA polymerase II. *Science* 325, 626–628.
- Huff, J.T., Plocik, A.M., Guthrie, C., and Yamamoto, K.R. (2010). Reciprocal intronic and exonic histone modification regions in humans. *Nat. Struct. Mol. Biol.* 17, 1495–1499.
- Ingolia, N.T., Brar, G.A., Rouskin, S., McGeachy, A.M., and Weissman, J.S. (2012). The ribosome profiling strategy for monitoring translation in vivo by deep sequencing of ribosome-protected mRNA fragments. *Nat. Protoc.* 7, 1534–1550.
- Ip, J.Y., Schmidt, D., Pan, Q., Ramani, A.K., Fraser, A.G., Odom, D.T., and Blencowe, B.J. (2011). Global impact of RNA polymerase II elongation inhibition on alternative splicing regulation. *Genome Res.* 21, 390–401.
- Izban, M.G., and Luse, D.S. (1991). Transcription on nucleosomal templates by RNA polymerase II in vitro: inhibition of elongation with enhancement of sequence-specific pausing. *Genes Dev.* 5, 683–696.
- Jonkers, I., Kwak, H., and Lis, J.T. (2014). Genome-wide dynamics of Pol II elongation and its interplay with promoter proximal pausing, chromatin, and exons. *eLife* 3, e02407.
- Kassavetis, G.A., and Chamberlin, M.J. (1981). Pausing and termination of transcription within the early region of bacteriophage T7 DNA in vitro. *J. Biol. Chem.* 256, 2777–2786.
- Kim, J.B., and Sharp, P.A. (2001). Positive transcription elongation factor B phosphorylates hSPT5 and RNA polymerase II carboxyl-terminal domain independently of cyclin-dependent kinase-activating kinase. *J. Biol. Chem.* 276, 12317–12323.
- Kim, T., Xu, Z., Clauder-Münster, S., Steinmetz, L.M., and Buratowski, S. (2012). Set3 HDAC mediates effects of overlapping noncoding transcription on gene induction kinetics. *Cell* 150, 1158–1169.

- Kornblihtt, A.R., de la Mata, M., Fededa, J.P., Munoz, M.J., and Nogues, G. (2004). Multiple links between transcription and splicing. *RNA* 10, 1489–1498.
- Krumm, A., Meulia, T., Brunvand, M., and Groudine, M. (1992). The block to transcriptional elongation within the human c-myc gene is determined in the promoter-proximal region. *Genes Dev.* 6, 2201–2213.
- Kwak, H., Fuda, N.J., Core, L.J., and Lis, J.T. (2013). Precise maps of RNA polymerase reveal how promoters direct initiation and pausing. *Science* 339, 950–953.
- Larson, M.H., Mooney, R.A., Peters, J.M., Windgassen, T., Nayak, D., Gross, C.A., Block, S.M., Greenleaf, W.J., Landick, R., and Weissman, J.S. (2014). A pause sequence enriched at translation start sites drives transcription dynamics in vivo. *Science* 344, 1042–1047.
- Lindell, T.J., Weinberg, F., Morris, P.W., Roeder, R.G., and Rutter, W.J. (1970). Specific inhibition of nuclear RNA polymerase II by alpha-amanitin. *Science* 170, 447–449.
- Lis, J.T., Mason, P., Peng, J., Price, D.H., and Werner, J. (2000). P-TEFb kinase recruitment and function at heat shock loci. *Genes Dev.* 14, 792–803.
- Maizels, N.M. (1973). The nucleotide sequence of the lactose messenger ribonucleic acid transcribed from the UV5 promoter mutant of *Escherichia coli*. *Proc. Natl. Acad. Sci. USA* 70, 3585–3589.
- Marquardt, S., Escalante-Chong, R., Pho, N., Wang, J., Churchman, L.S., Springer, M., and Buratowski, S. (2014). A chromatin-based mechanism for limiting divergent noncoding transcription. *Cell* 157, 1712–1723.
- Martens, J.A., Laprade, L., and Winston, F. (2004). Intergenic transcription is required to repress the *Saccharomyces cerevisiae* SER3 gene. *Nature* 429, 571–574.
- Mavrich, T.N., Jiang, C., Ioshikhes, I.P., Li, X., Venters, B.J., Zanton, S.J., Tomsho, L.P., Qi, J., Glaser, R.L., Schuster, S.C., et al. (2008). Nucleosome organization in the *Drosophila* genome. *Nature* 453, 358–362.
- Muse, G.W., Gilchrist, D.A., Nechaev, S., Shah, R., Parker, J.S., Grissom, S.F., Zeitlinger, J., and Adelman, K. (2007). RNA polymerase is poised for activation across the genome. *Nat. Genet.* 39, 1507–1511.
- Neil, H., Malabat, C., d'Aubenton-Carafa, Y., Xu, Z., Steinmetz, L.M., and Jacquier, A. (2009). Widespread bidirectional promoters are the major source of cryptic transcripts in yeast. *Nature* 457, 1038–1042.
- Ntini, E., Järvelin, A.I., Bornholdt, J., Chen, Y., Boyd, M., Jørgensen, M., Andersson, R., Hoof, I., Schein, A., Andersen, P.R., et al. (2013). Polyadenylation site-induced decay of upstream transcripts enforces promoter directionality. *Nat. Struct. Mol. Biol.* 20, 923–928.
- Pan, Q., Shai, O., Lee, L.J., Frey, B.J., and Blencowe, B.J. (2008). Deep surveying of alternative splicing complexity in the human transcriptome by high-throughput sequencing. *Nat. Genet.* 40, 1413–1415.
- Pandya-Jones, A., and Black, D.L. (2009). Co-transcriptional splicing of constitutive and alternative exons. *RNA* 15, 1896–1908.
- Peterlin, B.M., and Price, D.H. (2006). Controlling the elongation phase of transcription with P-TEFb. *Mol. Cell* 23, 297–305.
- Preker, P., Nielsen, J., Kammler, S., Lykke-Andersen, S., Christensen, M.S., Mapendano, C.K., Schierup, M.H., and Jensen, T.H. (2008). RNA exosome depletion reveals transcription upstream of active human promoters. *Science* 322, 1851–1854.
- Prescott, E.M., and Proudfoot, N.J. (2002). Transcriptional collision between convergent genes in budding yeast. *Proc. Natl. Acad. Sci. USA* 99, 8796–8801.
- Rahl, P.B., Lin, C.Y., Seila, A.C., Flynn, R.A., McGuire, S., Burge, C.B., Sharp, P.A., and Young, R.A. (2010). c-Myc regulates transcriptional pause release. *Cell* 141, 432–445.
- Roberts, G.C., Gooding, C., Mak, H.Y., Proudfoot, N.J., and Smith, C.W. (1998). Co-transcriptional commitment to alternative splice site selection. *Nucleic Acids Res.* 26, 5568–5572.
- Rougvié, A.E., and Lis, J.T. (1988). The RNA polymerase II molecule at the 5' end of the uninduced hsp70 gene of *D. melanogaster* is transcriptionally engaged. *Cell* 54, 795–804.
- Schulz, D., Schwalb, B., Kiesel, A., Baejen, C., Torkler, P., Gagneur, J., Soeding, J., and Cramer, P. (2013). Transcriptome surveillance by selective termination of noncoding RNA synthesis. *Cell* 155, 1075–1087.
- Schwartz, S., Meshorer, E., and Ast, G. (2009). Chromatin organization marks exon-intron structure. *Nat. Struct. Mol. Biol.* 16, 990–995.
- Seila, A.C., Calabrese, J.M., Levine, S.S., Yeo, G.W., Rahl, P.B., Flynn, R.A., Young, R.A., and Sharp, P.A. (2008). Divergent transcription from active promoters. *Science* 322, 1849–1851.
- Seila, A.C., Core, L.J., Lis, J.T., and Sharp, P.A. (2009). Divergent transcription: a new feature of active promoters. *Cell Cycle* 8, 2557–2564.
- Shearwin, K.E., Callen, B.P., and Egan, J.B. (2005). Transcriptional interference—a crash course. *Trends Genet.* 21, 339–345.
- Shukla, S., Kavak, E., Gregory, M., Imashimizu, M., Shutinowski, B., Kashlev, M., Oberdoerffer, P., Sandberg, R., and Oberdoerffer, S. (2011). CTCF-promoted RNA polymerase II pausing links DNA methylation to splicing. *Nature* 479, 74–79.
- Skene, P.J., Hernandez, A.E., Groudine, M., Henikoff, S., and Espinosa, J.M. (2014). The nucleosomal barrier to promoter escape by RNA polymerase II is overcome by the chromatin remodeler Chd1. *eLife* 3, e02042.
- Spies, N., Nielsen, C.B., Padgett, R.A., and Burge, C.B. (2009). Biased chromatin signatures around polyadenylation sites and exons. *Mol. Cell* 36, 245–254.
- Strobl, L.J., and Eick, D. (1992). Hold back of RNA polymerase II at the transcription start site mediates down-regulation of c-myc in vivo. *EMBO J.* 11, 3307–3314.
- Taft, R.J., Glazov, E.A., Cloonan, N., Simons, C., Stephen, S., Faulkner, G.J., Lassmann, T., Forrest, A.R.R., Grimmond, S.M., Schroder, K., et al. (2009). Tiny RNAs associated with transcription start sites in animals. *Nat. Genet.* 41, 572–578.
- Thurman, R.E., Rynes, E., Humbert, R., Vierstra, J., Maurano, M.T., Haugen, E., Sheffield, N.C., Stergachis, A.B., Wang, H., Vernot, B., et al. (2012). The accessible chromatin landscape of the human genome. *Nature* 489, 75–82.
- Tilgner, H., Nikolaou, C., Althammer, S., Sammeth, M., Beato, M., Valcárcel, J., and Guigó, R. (2009). Nucleosome positioning as a determinant of exon recognition. *Nat. Struct. Mol. Biol.* 16, 996–1001.
- Tilgner, H., Knowles, D.G., Johnson, R., Davis, C.A., Chakraborty, S., Djebali, S., Curado, J., Snyder, M., Gingeras, T.R., and Guigó, R. (2012). Deep sequencing of subcellular RNA fractions shows splicing to be predominantly co-transcriptional in the human genome but inefficient for lncRNAs. *Genome Res.* 22, 1616–1625.
- Vierstra, J., Wang, H., John, S., Sandstrom, R., and Stamatoyannopoulos, J.A. (2014). Coupling transcription factor occupancy to nucleosome architecture with DNase-FLASH. *Nat. Methods* 11, 66–72.
- Vvedenskaya, I.O., Vahedian-Movahed, H., Bird, J.G., Knoblauch, J.G., Goldman, S.R., Zhang, Y., Ebright, R.H., and Nickels, B.E. (2014). Transcription. Interactions between RNA polymerase and the “core recognition element” counteract pausing. *Science* 344, 1285–1289.
- Wang, E.T., Sandberg, R., Luo, S., Khrebtkova, I., Zhang, L., Mayr, C., Kingsmore, S.F., Schroth, G.P., and Burge, C.B. (2008). Alternative isoform regulation in human tissue transcriptomes. *Nature* 456, 470–476.
- Weber, C.M., Ramachandran, S., and Henikoff, S. (2014). Nucleosomes are context-specific, H2A.Z-modulated barriers to RNA polymerase. *Mol. Cell* 53, 819–830.
- Whitehouse, I., Rando, O.J., Delrow, J., and Tsukiyama, T. (2007). Chromatin remodelling at promoters suppresses antisense transcription. *Nature* 450, 1031–1035.
- Wozniak, G.G., and Strahl, B.D. (2014). Hitting the ‘mark’: Interpreting lysine methylation in the context of active transcription. *Biochim. Biophys. Acta* 1839, 1353–1361.

- Wu, X., and Sharp, P.A. (2013). Divergent transcription: a driving force for new gene origination? *Cell* 155, 990–996.
- Wuarin, J., and Schibler, U. (1994). Physical isolation of nascent RNA chains transcribed by RNA polymerase II: evidence for cotranscriptional splicing. *Mol. Cell. Biol.* 14, 7219–7225.
- Xi, H., Yu, Y., Fu, Y., Foley, J., Halees, A., and Weng, Z. (2007). Analysis of overrepresented motifs in human core promoters reveals dual regulatory roles of YY1. *Genome Res.* 17, 798–806.
- Xu, Z., Wei, W., Gagneur, J., Perocchi, F., Clauder-Münster, S., Camblong, J., Guffanti, E., Stutz, F., Huber, W., and Steinmetz, L.M. (2009). Bidirectional promoters generate pervasive transcription in yeast. *Nature* 457, 1033–1037.
- Zeitlinger, J., Stark, A., Kellis, M., Hong, J.W., Nechaev, S., Adelman, K., Levine, M., and Young, R.A. (2007). RNA polymerase stalling at developmental control genes in the *Drosophila melanogaster* embryo. *Nat. Genet.* 39, 1512–1516.

Pioneer Transcription Factors Target Partial DNA Motifs on Nucleosomes to Initiate Reprogramming

Graphical Abstract



Authors

Abdenour Soufi,
Meilin Fernandez Garcia, ...,
Matteo Pellegrini, Kenneth S. Zaret

Correspondence

zaret@upenn.edu

In Brief

The pioneer activity of a transcription factor for initiating reprogramming relates to its ability to target partial motifs displayed on the nucleosome surface. For proteins that lack such ability, binding with a pioneer factor allows partial motif recognition and nucleosome binding.

Highlights

- Oct4, Sox2, Klf4, and Myc show a range of affinities to nucleosomes
- Oct4, Sox2, and Klf4 target partial motifs exposed on nucleosomes
- c-Myc recognizes degenerate E-box motifs on nucleosomes with other factors
- DBD recognition of motifs on nucleosome surface determines pioneer activity



Pioneer Transcription Factors Target Partial DNA Motifs on Nucleosomes to Initiate Reprogramming

Abdenour Soufi,^{1,3} Meilin Fernandez Garcia,¹ Artur Jaroszewicz,² Nebiyu Osman,¹ Matteo Pellegrini,² and Kenneth S. Zaret^{1,*}

¹Institute for Regenerative Medicine and Epigenetics Program, Department of Cell and Developmental Biology, University of Pennsylvania Perelman School of Medicine, Smilow Center for Translational Research, Building 421, 3400 Civic Center Boulevard, Philadelphia, PA 19104-5157, USA

²Department of Molecular, Cell and Developmental Biology, UCLA, Box 951606, Los Angeles, CA 90095-1606, USA

³Present address: MRC Centre for Regenerative Medicine, SCRM Building, University of Edinburgh, Edinburgh Bioquarter, 5 Little France Drive, Edinburgh EH16 4UU, UK

*Correspondence: zaret@upenn.edu

<http://dx.doi.org/10.1016/j.cell.2015.03.017>

SUMMARY

Pioneer transcription factors (TFs) access silent chromatin and initiate cell-fate changes, using diverse types of DNA binding domains (DBDs). FoxA, the paradigm pioneer TF, has a winged helix DBD that resembles linker histone and thereby binds its target sites on nucleosomes and in compacted chromatin. Herein, we compare the nucleosome and chromatin targeting activities of Oct4 (POU DBD), Sox2 (HMG box DBD), Klf4 (zinc finger DBD), and c-Myc (bHLH DBD), which together reprogram somatic cells to pluripotency. Purified Oct4, Sox2, and Klf4 proteins can bind nucleosomes *in vitro*, and *in vivo* they preferentially target silent sites enriched for nucleosomes. Pioneer activity relates simply to the ability of a given DBD to target partial motifs displayed on the nucleosome surface. Such partial motif recognition can occur by coordinate binding between factors. Our findings provide insight into how pioneer factors can target naive chromatin sites.

INTRODUCTION

Silent chromatin is packed with nucleosomes, acting as a barrier to targeting by most transcription factors (TFs) (Adams and Workman, 1995; Mirny, 2010). However, a select group of transcription factors (TFs) known as pioneer factors have the combined ability to access their target sites in silent chromatin and initiate cell-fate changes (Iwafuchi-Doi and Zaret, 2014; Zaret and Carroll, 2011). The winged-helix DNA binding domain (DBD) of the pioneer factor FoxA (Clark et al., 1993), which is similar to that of linker histone (Ramakrishnan et al., 1993), allows the protein to bind its DNA motif exposed on a nucleosome and access to silent chromatin (Cirillo and Zaret, 1999; Cirillo et al., 1998, 2002). Such activity is necessary for liver induction (Lee et al., 2005). Other TFs involved in cell reprogramming can target their sites in silent chromatin (Montserrat et al., 2013; Soufi et al.,

2012; Takahashi and Yamanaka, 2006; Wapinski et al., 2013), but they possess DBDs that differ from that of FoxA. Whether such reprogramming factors directly bind nucleosomes and how the structures of their respective DBDs relate to nucleosome binding, and hence pioneer activity, has not been assessed.

Transcription factors containing major structural classes of DBDs, including Pit-Oct-Unc (POU), Sry-related High Mobility Group (HMG), Zinc Fingers (ZF), and basic-helix-loop-helix (bHLH), represented by O, S, K, and M, respectively, have been used in the most dramatic example of cellular reprogramming: the conversion of differentiated cells into induced pluripotent stem cells (Takahashi and Yamanaka, 2006). We previously compared genomic chromatin features of human fibroblasts, prior to the ectopic expression of OSKM, to where the factors first bind the genome during their initial expression (Soufi et al., 2012). This allowed us to assess how OSKM target pre-existing states in chromatin, as opposed to assessing chromatin states after the factors are bound. The data showed that Oct4, Sox2, and Klf4, but not c-Myc, could function as pioneers during reprogramming by virtue of their ability to mostly target “closed” chromatin sites that are DNase I resistant and “naive” by virtue of lacking evident active histone modifications (Soufi et al., 2012). Recently, single-molecule imaging analysis using fluorescently tagged proteins monitored in living cells proposed that Sox2 guides Oct4 to its target sites (Chen et al., 2014); the chromatin status of the sites was unknown. However, we previously found that the ectopic Oct4 and Sox2 bind most extensively to separate sites in chromatin (Soufi et al., 2012), leaving open how the bulk of chromatin targeting is achieved. While many of initial binding events were promiscuous and not retained in pluripotent cells, many others occurred at target genes that are required for conversion to pluripotency.

Ascl1, Pax7, and Pu.1 have emerged as pioneer transcription factors based on targeting closed chromatin and their ability to reprogram cells, though assessments of direct interaction with nucleosomes has been lacking (Barozzi et al., 2014; Budry et al., 2012; Wapinski et al., 2013). In light of the bHLH factor c-Myc being unable to bind closed chromatin on its own (Soufi et al., 2012), it was surprising that Ascl1, another bHLH factor, can bind closed chromatin during reprogramming fibroblasts to neuron-like cells

(Wapinski et al., 2013). Studies that have examined the correlation between co-existing TF binding and nucleosome occupancy, without characterizing the “pre-bound” chromatin state, could not address questions about initial chromatin access.

Generating induced pluripotent stem (iPS) cells, using the OSKM factors, has proved to be highly valuable for research, with great potential for regenerative medicine (Robinton and Daley, 2012). In an attempt to increase the efficiency of reprogramming, efforts have focused on explaining how somatic cells respond to the ectopic expression of OSKM (Buganim et al., 2013; Papp and Plath, 2013; Soufi, 2014). To gain insights into the molecular mechanisms that impart OSKM access to closed chromatin, we measured the fundamental interaction between the factors and nucleosomes, in vivo and in vitro, by three mutually supportive approaches: biochemical assays, genomics, and structural analysis. We find that the inherent ability of DBDs to recognize one face of DNA on nucleosome, as seen by targeting a part of their canonical motif on nucleosome-enriched sequences in chromatin, is the primary determinant of pioneer factor activity. These findings can explain the pioneer activity of a diverse set of reprogramming factors containing different structural classes of DBDs as well as the synergistic behavior of pioneer and non-pioneer factors.

RESULTS

O, S, K, and M Show a Range of Nucleosome Binding In Vitro

The interaction of full-length O, S, K, and M, as used in reprogramming, with nucleosomes is not known. Therefore, we purified and refolded the full-length O, S, and K factors, along with c-Myc and its obligate heterodimerization partner Max from bacterial cells, representing post-translationally unmodified proteins (Figure 1A; Figure S1A). We also obtained the full-length O, S, K, and M expressed in human HEK293 cells and purified under native conditions, representing post-translationally modified versions of the proteins (Figure 1A). To quantify the DNA binding activities of the proteins, the apparent equilibrium dissociation constants (K_D) were determined using two different methods: from the decrement in the amount of free DNA (total K_D) and from the appearance of the first DNA-bound complex (specific K_D), in electrophoretic mobility shift assays (EMSA). As expected, the bacterial (bact.) and the mammalian (mamm.) expressed, recombinant O, S, K, and M proteins bound to DNA probes containing canonical motifs, as previously reported for the purified DBDs (Farina et al., 2004; Nakatake et al., 2006; Rodda et al., 2005) (Figure S1B; Table 1), and bound with much lower affinity to non-specific DNA sequences of the same length (Figure S1C). The bact. reconstituted Myc:Max heterodimers formed a complex that migrated more slowly than Max homodimers, and no protein-DNA complexes with similar mobility to Max homodimers were observed even at the highest concentrations, confirming that the c-Myc:Max preparation did not contain Max homodimers (Figure S1B). The mamm. c-Myc did not show any specific DNA binding activity in the absence of its partner Max, as seen previously (Wechsler et al., 1994). These data demonstrate that the recombinant full-length OSKM proteins were highly active in specific DNA binding.

To measure the direct interactions between OSKM and nucleosomes, we identified a nucleosome-enriched site in the fibroblast genome that is efficiently targeted by OSKM (Soufi et al., 2012), focusing on the *LIN28B* locus that is important for reprogramming and pluripotency (Shyh-Chang et al., 2013; Yu et al., 2007). RNA sequencing (RNA-seq) data showed that *LIN28B* is silent in human fibroblasts and remains silent after 48 hr OSKM induction, revealing that OSKM binding precedes *LIN28B* gene activation (data not shown). We selected a region downstream of the *LIN28B* poly(A) site that is strongly enriched for a nucleosome in pre-induced human fibroblasts, as measured by MNase sequencing (MNase-seq) (Kelly et al., 2012) and was targeted by all four factors at 48 hr post-induction (Figure 1B). We used PCR on human fibroblast DNA to generate a 162-bp, Cy5-labeled *LIN28B*-DNA, which was assembled into nucleosomes (*LIN28B*-nuc) by salt gradient dilution with purified recombinant human histones (Figure S1D). The nucleosomes exhibited protection from low concentrations of DNase I except at the ends of the *LIN28B* fragment, compared to free DNA, indicating translational positioning around the center of the 162-bp *LIN28B* sequence (Figure 1C, top two boxes), similar to the observed position of the center of the MNase-seq peak (Figures 1B and 1C). Ten-fold higher concentrations of DNase generated an approximately 10-bp DNase-cleavage repeat pattern on *LIN28B*-nuc, reflecting rotational positioning of nucleosomes within the population (Figure 1C, bottom).

It is generally accepted that nucleosomes act as a barrier to DNA binding by TFs (see Introduction), though exceptions have been noted (Perlmann and Wrangé, 1988). Interestingly, Oct4, Sox2, and Klf4, but not c-Myc:Max, showed binding to the *LIN28B*-nuc (Figure 1D). Remarkably, both mamm. and bact. Oct4 and Sox2 showed similar or lower apparent K_D values for *LIN28B*-nuc compared to *LIN28B*-DNA, indicating similar or higher affinity to nucleosome than to free DNA (Figure 1D; Table 1). On the other hand, Klf4 was able to bind *LIN28B*-nuc with a higher apparent K_D value compared to free DNA, indicating substantial nucleosome binding, but at a lower affinity than to free DNA (Figure 1D; Table 1). c-Myc:Max did not yield saturated binding to *LIN28B*-nuc, even at the highest concentrations of protein used, and thus the apparent K_D must be in the μ M range (Figure 1D; Table 1). In conclusion, both mammalian and bacterial expressed O, S, K, and M exhibit the same relative range of affinities to *LIN28B*-nuc, and O, S, and K have an independent nucleosome binding activity.

Specific and Non-Specific DNA Interactions Contribute to Nucleosome Binding

It is well recognized that TFs show both sequence-specific and non-specific interactions with their DNA targets (Biggin, 2011). To measure the contribution of specificity on OSK binding to *LIN28B* nucleosomes, we carried out EMSA in the presence of increasing amounts of specific and non-specific DNA sequences that we had already characterized as competitors (Figures S1B and S1C; Table 1). EMSA competition experiments show that a 40-fold molar excess of non-labeled DNA probes containing specific binding sites, but not probes containing non-specific sequences, can displace *LIN28B*-DNA complexes with each of the

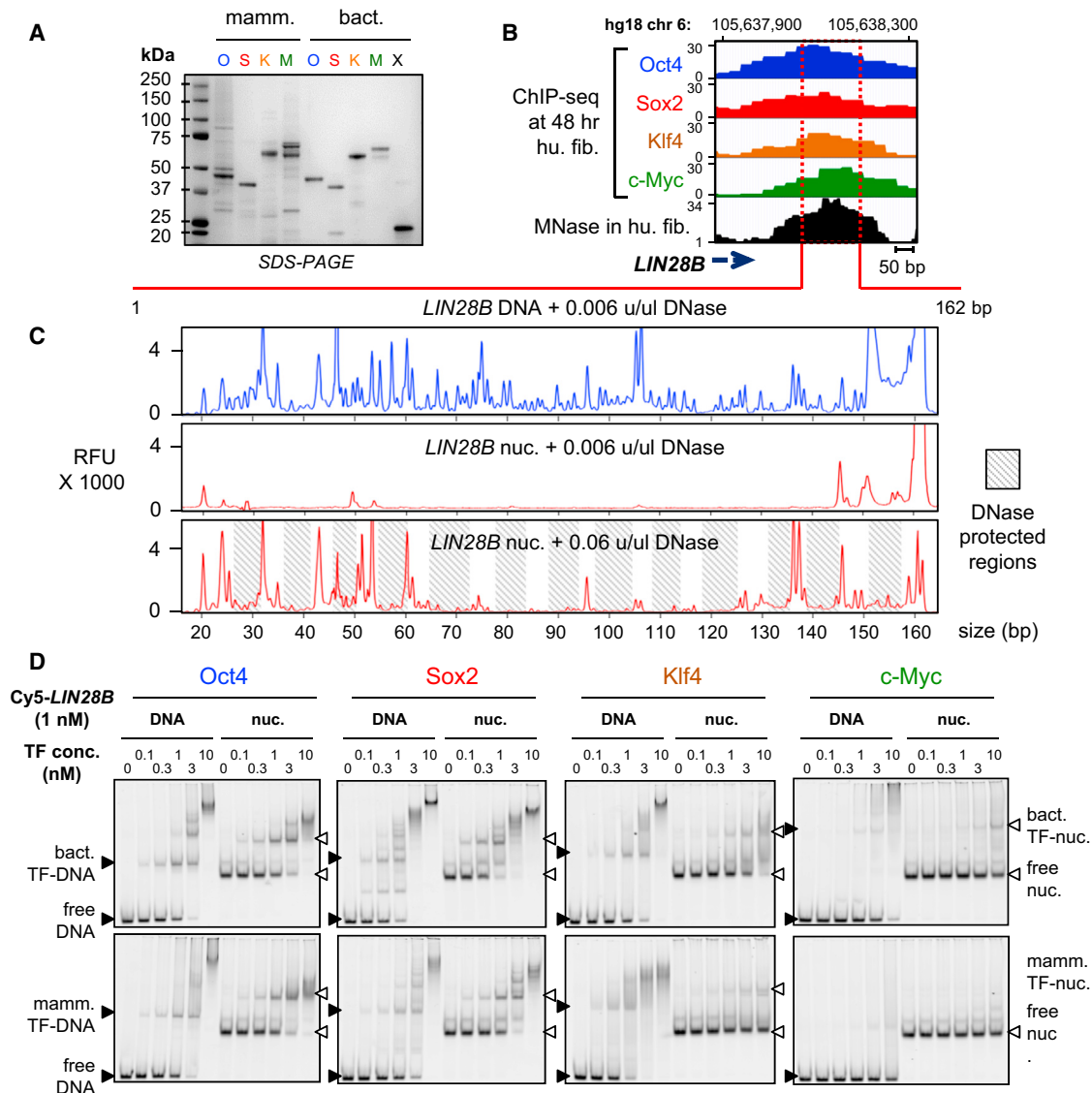


Figure 1. O, S, K, and M Display Differential Affinity to Nucleosomes In Vitro

(A) Recombinant purified mammalian and bacterial O, S, K, M, and bacterial Max (X) proteins analyzed by SDS-PAGE and Coomassie staining. The respective OSKM bands run at the expected sizes when compared to the sizes of protein standards. The OSKM DNA binding activity and specificity are shown in Figures S1A–S1C.

(B) O, S, K, and M ChIP-seq profiles (blue, red, orange, and green, respectively) 48 hr post-induction and MNase-seq profile (black) in fibroblasts across the *LIN28B* locus within the displayed genomic location.

(C) DNase I footprinting showing the protection of *LIN28B*-DNA before and after nucleosome reconstitution in vitro. Electropherograms of 5'-6FAM end-labeled *LIN28B* (top strand) oligonucleotides generated by digesting free DNA (blue) and nucleosomal DNA (red) with DNase I. The amount of DNase I used is indicated on top of each panel. Shaded boxes represent the DNase I-protected regions within *LIN28B*-nuc in the expected ~10-bp pattern. See Figure S1D for details about nucleosome reconstitution.

(D) Representative EMSA showing the affinity of increasing amounts of recombinant O, S, K, and M proteins (bact. top panels and mamm. bottom panels) to Cy5-labeled *LIN28B*-DNA (left panels) and *LIN28B*-nucleosome (right panels). EMSA of O, S, K, and M to DNA probes containing specific and non-specific targets are shown in Figures S1B and S1C.

OSKM proteins, indicating specific interaction with *LIN28B*-DNA (Figure 2A, left panel), similar to OSKM interaction with their canonical sites (Figure S2A). As expected, bact. and mamm. O, S, or K in complexes with *LIN28B*-nuc were displaced in the presence of a 40× molar excess of unlabeled, specific competi-

tors (Figure 2A, lanes 16, 19, and 22). A 40× or lower (range from 5× to 20×) molar excess of non-specific DNA failed to displace bact. and mamm. Oct4 from the *LIN28B*-nuc (Figures 2A, lane 17, and S2B, lanes 14–16), demonstrating specific binding by Oct4 to the nucleosomes in vitro.

Table 1. Recombinant O, S, K, and M Show a Range of Affinities to Nucleosomes

Apparent K_D (nM)	Oct4		Sox2		Klf4		c-Myc	
	bact.	mamm.	bact.	mamm.	bact.	mamm.	bact.	mamm.
Total canonical	0.61	0.64	0.37	0.98	2.49	1.46	1.88	ND
Specific canonical	0.76	1.04	0.45	1.50	3.18	1.95	0.77	ND
Total <i>LIN28B</i> DNA	0.75	0.93	0.38	1.46	1.25	0.41	8.28	ND
Specific <i>LIN28B</i> DNA	0.92	2.05	0.68	3.83	2.26	1.12	6.25	ND
Total <i>LIN28B</i> nuc.	1.09	1.34	0.34	1.06	5.96	3.45	ND	ND
Specific <i>LIN28B</i> nuc.	1.17	1.84	0.39	1.43	7.21	13.97	ND	ND

Apparent dissociation constants (K_D) were derived from EMSA to represent the relative affinities of bacterial (bact.) and mammalian (mamm.) O, S, K, and M to their canonical sites, *LIN28B*-free DNA, and *LIN28B* nucleosomes (nuc.). Apparent K_D were derived from two separate binding curves representing two experimental replicates, fitted to the experimental data within R^2 values of ~ 0.97 , and expressed in nM units. Apparent K_D were quantified from the fractional decrement of free DNA or nuc, designated as “total” binding, or from the first bound-DNA/nuc complexes, representing “specific” binding.

ND, not determined.

By contrast, a 40 \times excess of non-specific DNA competed almost all of Sox2 and Klf4 from binding to *LIN28B*-nuc (Figure 2A, lanes 20 and 23). Importantly, lower levels of non-specific competitor, from 5 \times to 20 \times , did not compete to the same extent as specific competitor with *LIN28B*-nuc for binding either Sox2 or Klf4 (Figures S2C and S2D, compare lanes 10 to 11–13 versus 14–16). Thus, both specific and non-specific interactions contribute to Sox2 and Klf4 binding to nucleosomes in vitro.

DNase footprinting showed that each of the O, S, K, and M factors protect sequences on *LIN28B*-free DNA that resemble their canonical motifs (Figures 2B and 2C, dash boxes). In addition, at the concentrations used for footprinting, Sox2, Klf4, and c-Myc also show non-specific protection of the *LIN28B*-free DNA (Figure 2B, peaks labeled by asterisks). DNase footprinting of *LIN28B*-nuc bound to Oct4 and Sox2 show that the factors protect part of their canonical motifs, agreeing with the specific binding to nucleosomes seen with EMSA competition experiments (Figures 2B and 2C). However, Sox2 and Klf4 protect both specific and non-specific nucleotides on *LIN28B*-nuc, supporting the non-specific contribution of Sox2 and Klf4 to nucleosomes as seen in EMSA competition experiments (Figure 2B). The Klf4 binding site is close to the predicted nucleosome dyad axis, where DNase cleavage is minimal, thus precluding an accurate assessment of specific footprinting. Expectedly, c-Myc showed minimal protection of *LIN28B*-nuc, confirming the weak affinity to nucleosomes. Altogether, the O, S, and K reprogramming factors employ specific and nonspecific nucleosome interactions to different extents.

Range of Nucleosome Binding In Vitro Is Observed in Genome Targeting In Vivo

We assessed whether OSKM, 48 hr post-induction, targeted sites with pre-existing nucleosome enrichment in fibroblast chromatin. Pooling seven replicates from the MNase-seq data set (GSM543311) allowed a high-resolution map of nucleosomes with 6.6-fold genome coverage. First, we curated the sites where O, S, K, or M targeted alone, by identifying O, S, K, or M peaks that are 500 bp or more apart from each other. The sites were arranged in rank order by the number of chromatin immunoprecipitation sequencing (ChIP-seq) tags in the central 200 bp, from

high- to low-affinity sites. This analysis confirms that each of the O, S, K, and M factors is highly enriched at the central 200 bp within a 2-kb region (Figure 3A, blue boxes). Interestingly, Sox2 bound most frequently alone ($n = 41,107$) compared to Oct4 ($n = 22,495$), Klf4 ($n = 28,212$), and c-Myc ($n = 23,885$). Subsequently, MNase tags across the respective 2-kb regions were counted, reflecting local nucleosome enrichment. Read-density heatmaps showed a range of nucleosome enrichment at the central 200-bp regions that were targeted by O, S, K, or M factors alone (Figure 3A, red boxes). Notably, Oct4 targets were the most highly enriched for nucleosomes, followed by Sox2, and then Klf4 throughout the respective TF rank-ordered binding profiles. By contrast, MNase tags in the c-Myc targeted sites were diminished. Also, we did not observe pre-phased arrays of nucleosomes at OSKM target sites, indicating that the initial association with nucleosomes proceeds repositioning, if any. Remarkably, the extent of nucleosome targeting of O, S, K, and M in vivo correlates with the relative abilities of the factors to bind nucleosomes in vitro (Figure 1D; Table 1).

To assess the contribution of non-specific binding in vivo, we counted the number of O, S, K, and M peaks at 48 hr post-induction as function of false discovery rate (FDR) threshold. Remarkably, while O, K, and M peak numbers begin to stabilize above an FDR of 0.5% (used in our study) (slopes of 1.6, 1.5, and 1.3 respectively), the number of Sox2 peaks continues to increase (slope of 2.1) with higher FDR (Figure S3A). Thus, it appears that Sox2 employs a measure of non-specific targeting in vivo, as we observed in vitro.

O, S, K, and/or M Synergistic Targeting of Nucleosomes In Vivo and In Vitro

It has been previously suggested that transcription factors can access nucleosomal DNA by cooperative binding in order to compete with histones (Polach and Widom, 1996). To investigate the contribution of synergy between O, S, K, and/or M to nucleosome targeting, we studied sites that were co-targeted by multiple factors within a range of 100 bp or less from each other, i.e., within one nucleosome. In general, we observed that all possible O, S, K, and/or M combinations targets were enriched for nucleosomes except for KM targets, and the co-bound sites, on

average, were more enriched for nucleosomes than singly bound sites (Figures 3B and S3B). Notably, there were more S, K, and/or M combinations that included Oct4 and showed higher nucleosome enrichment at initially targeted sites, compared to binding combinations lacking Oct4 (Figures 3B and S3, compare C–I to J–M). For example, c-Myc showed the most nucleosome targeting when co-bound with Oct4, followed by with Sox2, while c-Myc showed weak targeting to nucleosomes with Klf4 (Figure S3, compare E to K and M). Interestingly, the KM combination was the most frequent at nucleosome-depleted promoters, similar to KM targeting DNase hypersensitive regions (Soufi et al., 2012) (Figure S3M, red plot). Nevertheless, KM still targeted nucleosome-enriched sites at TSS-distal regions (Figure S3M, blue plot).

To further investigate synergistic targeting with Oct4, we assessed binding by each of the factors Sox2, Klf4, and c-Myc:Max (1 nM) to the reconstituted *LIN28B*-nuc (2 nM) in the presence of low amounts of Oct4 (0.3 nM). EMSA showed that all the three recombinant proteins are able to bind with Oct4 to nucleosomal DNA in vitro, forming higher order complexes (Figure 3C). Notably, c-Myc:Max binding to *LIN28B*-nuc was enabled in the presence of Oct4 (Figure 3C, right panel). To assess the presence of histones in the *LIN28B*-nuc in the complexes, we transferred the proteins from an EMSA gel to a polyvinylidene fluoride (PVDF) membrane and blotted for H3 and H2B (Figure S4). Though the c-Myc antibody was the weakest, all *LIN28B*-nuc-bound complexes showed detectable amounts of H3, and to a lesser extent H2B, indicating the factors bind together to nucleosomes. In summary, Oct4, Sox2, and Klf4 enable c-Myc to target nucleosomal sites both in vivo and in vitro.

O, S, and K Separately Recognize Partial Motifs on Nucleosomes

To identify DNA motifs that are associated with O, S, and K alone targeting to nucleosomes in vivo, the respective targeted sites were rank ordered according to nucleosome enrichment in the central 200 bp. This allowed us to separate nucleosome-enriched from nucleosome-depleted regions that were individually targeted by O, S, or K. By these criteria, 85%, 80%, and 65% of the genomic sites initially targeted by Oct4, Sox2, and Klf4, respectively, were enriched for nucleosomes (Figures 4A–4C, red boxes). We used de novo motif analysis, separately analyzing the targets that were enriched for nucleosomes (Figures 4A–4C, red boxes, upper portion) from those that were depleted of nucleosomes, i.e., free DNA targets (Figures 4A–4C, red boxes, lower portion). While O, S, and K primarily targeted sequences similar to their canonical motifs at nucleosome-depleted and nucleosome-enriched sites, motifs occurring at nucleosome-enriched sites showed distinctive features (Figures 4D–4F).

Strikingly, while Oct4 targeted its canonical octamer sequence at nucleosome-depleted sites (~49% of $n = 3,375$), Oct4 targeted hexameric motifs resembling one or another half of the octamer motif at nucleosome-enriched sites (42% and 28%, respectively, of $n = 19,120$) (Figure 4D). Sox2 targeted its canonical HMG box motif at nucleosome-depleted sites (64% of $n = 8,221$), while targeting a more degenerate motif lacking

the sixth “G” nucleotide in the nucleosomal motif (~74% out of $n = 32,886$) (Figure 4E, arrowhead). Finally, Klf4 alone targeted its nonameric motif at nucleosome-depleted sites (94% of $n = 9,874$), whereas Klf4 targeted a hexameric motif that was missing the three terminal nucleotides at nucleosome-enriched sites (90% of $n = 18,338$) (Figure 4F, see dashed lines).

These findings agree with the above DNase footprinting of *LIN28B*-nuc bound to the factors (Figure 2B, right panels), with Oct4 and Sox2 protecting a part of their canonical motifs on one side of the *LIN28B*-nuc DNA (Figures 2B and 2C; right). On free DNA, Klf4 protected the first three nucleotides of its motif on the upper strand while protecting the remaining six nucleotides of its motif on the bottom strand (Figure S5A). However, Klf4 did not protect the first three nucleotides on the upper strand of *LIN28B*-nuc, as they were not exposed to DNase I digestion, indicating that Klf4 may be interacting with part of its motif exposed on the other strand (Figures 2B and 2C).

These data show that the O, S, and K factors can independently target nucleosomes using partial or degenerate motifs, and that each of the factors targets their full canonical motif in the absence of nucleosomes at a target site. Targeting of partial motifs at nucleosomal sites by OS or OK together also reveals partial motifs for each of the factors (data not shown).

The Molecular Basis for O, S, and K Nucleosomal Targeting

In order to define the molecular basis that govern O, S, and K interactions with nucleosomal DNA, we interrogated the three dimensional structures of O, S, and K DBDs in complexes with their canonical motifs that were deposited in the RCSB Protein Data Bank. Oct4 contains a bipartite POU domain, composed of an N-terminal POU-specific (POU_S) and a C-terminal POU-homeodomain (POU_{HD}), separated by a linker region. The X-ray structure of Oct4-POU-DNA complex confirms that the POU_S and POU_{HD} each bind one-half of the octameric motif on DNA (Esch et al., 2013) (Figure 4G, lower panels). The truncated POU_S and POU_{HD} can bind their respective half motif DNA probes in vitro, independently from each other (Verrijzer et al., 1992). Interestingly, the isolated DNA-bound state of either POU_S or POU_{HD} accommodates less than half of the DNA surface across the circumference of the double helix (DNA surface occupied 606 and 718 Å², respectively), leaving the opposite DNA surface solvent-exposed and potentially free to interact with histones in a nucleosome conformation (Figure 4G, red dashed arrows in upper panels). However, once both POU_S and POU_{HD} are bound to the full motif (1,321 Å²), less than a quarter of the DNA circumference is solvent-exposed and hence would be incompatible with nucleosome binding, due to steric hindrance (Figure 4G, red dashed arrow in lower panel). Thus, the two POU domains do not target directly adjacent half sites on nucleosomes, as seen in free DNA, but the exposure of the separate half sites on nucleosomes is enough for Oct4 initial targeting.

Sox2 binds DNA through its HMG box, inducing a sharp bend and widening of the minor groove (Reményi et al., 2003) (Figure 4H, lower-left panel). Our motif analysis showed that Sox2 targets a degenerate motif within nucleosomes, missing one “G” nucleotide at the sixth position (Figure 4E). This “G”

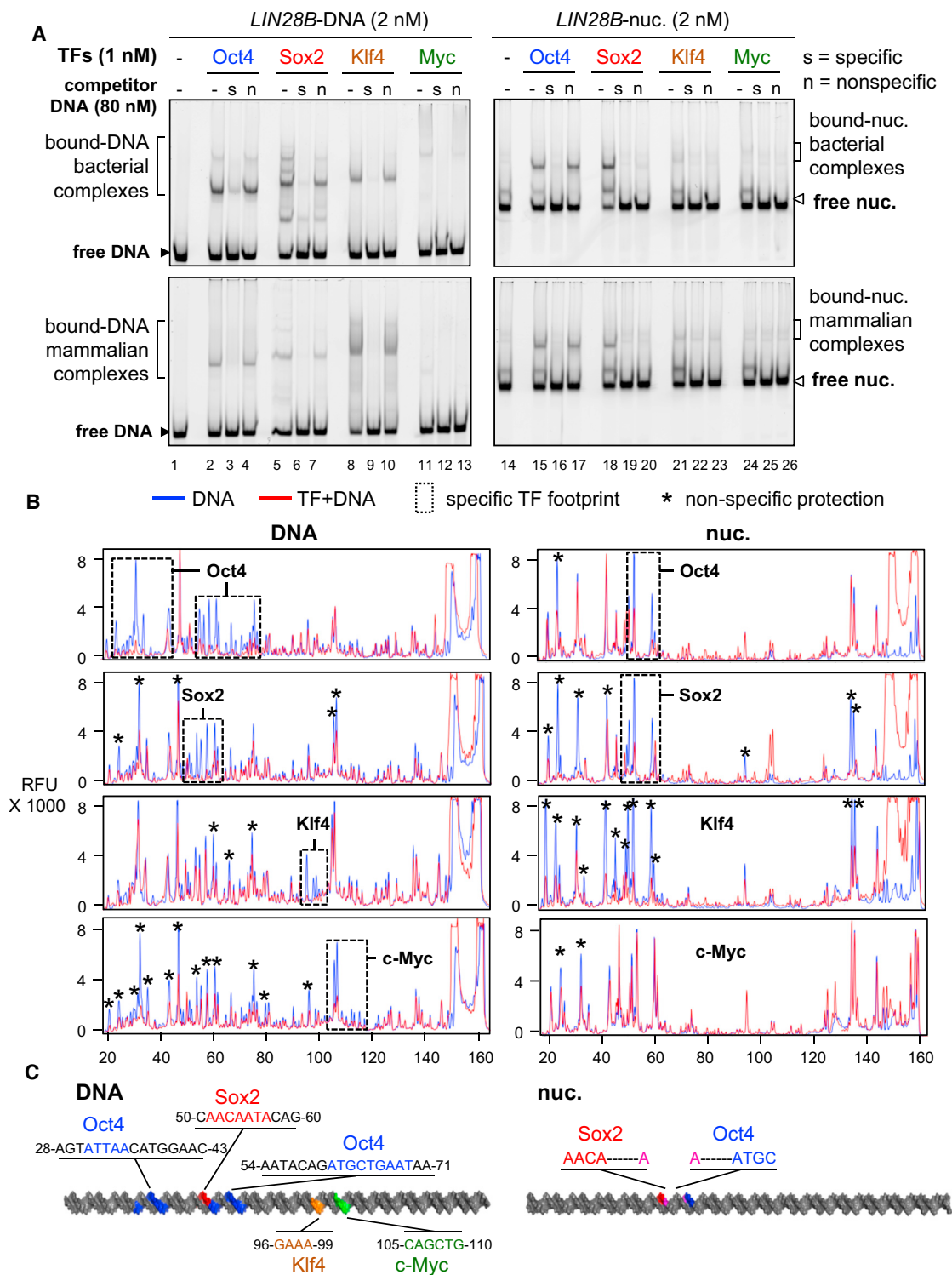


Figure 2. The Contribution of Non-Specific Binding to Nucleosome Targeting In Vitro

(A) Representative EMSA showing the affinity of recombinant O, S, K, and M proteins (bact. top panels and mamm. bottom panels) to *LIN28B*-DNA (left panels) and *LIN28B*-nucleosome (right panels) in the presence of 40-fold molar excess of specific competitor ("s" lanes) or non-specific competitor ("n" lanes) or absence of competitor ("—" lanes). Competition assays showing the specificity of O, S, K, and M to their canonical DNA probes and to *LIN28B* DNA and nucleosome under lower titration of competitor are shown in Figure S2.

(legend continued on next page)

nucleotide is positioned at the angle of the induced bend and makes direct contacts with the N46 residue at the N-terminal tail of Sox2-HMG (Reményi et al., 2003) (Figures 4E and 4H, arrowhead). Remarkably, mutation of this one amino acid (N46Q) within Sox2-HMG results in a significant decrease in DNA-bending ability without affecting DNA binding (Scaffidi and Bianchi, 2001). In transient transfection assays, the Sox2-N46Q mutant displays higher transactivation activity from the *Fgf4* enhancer compared to Sox2 wild-type (Scaffidi and Bianchi, 2001). Furthermore, mutation of the “G” nucleotide in the sixth position of the motif has the unique ability, among all mutations tested, to abolish DNA bending by wild-type Sox2 (Scaffidi and Bianchi, 2001). Together these data indicate that Sox2 would not induce extensive DNA-distortion when targeting the nucleosomal motif, since that motif lacks the “G” nucleotide. To further support these observations we superimposed the 3D structure of DNA bound by wild-type Sox2 and Sox2-N46Q mutant on nucleosomal DNA and after 1,000 cycles refinement we calculated the root-mean-square deviation (RMSD) as a measure of the average distance between the phosphate backbone for the best fit. These analysis reveal that the less distorted DNA is more compatible with nucleosomal DNA (RMSD = 0.86 Å) compared to the extensively distorted DNA (RMSD = 6.83 Å) (Figure 4H, right panel). In conclusion, our data indicate that Sox2 engages nucleosomes by recognizing a degenerate motif that involves less DNA distortion, better filling the curvature and widened minor groove of DNA around the histone octamer.

Klf4 recognizes the nonameric DNA motif using all three C₂H₂-type ZFs (three nucleotides per ZF) located at the C terminus (Schuetz et al., 2011) (Figure 4F). However, we identified a hexameric motif, lacking the last three nucleotides, enriched within nucleosomal targets (Figure 4F, 90%). Mutagenic studies have shown that the hexameric motif represents the minimal essential binding site for Klf4 (Shields and Yang, 1998). Recently, X-ray crystallography has revealed the structures of Klf4 bound to the hexameric and nonameric sites (Schuetz et al., 2011) (Figure 4I). Klf4 uses its two most C-terminal ZFs, out of the three, to recognize the hexameric motif, occupying one side of the DNA double helix (595 Å²) and leaving more than half of the opposite surface potentially free to interact with histones in a nucleosome (Figure 4I, red dashed arrow in upper-right panel). Klf4 bound to the nonameric motif, with all three ZFs, fills up more than half of the DNA surface (847 Å²) and would hinder binding to nucleosomes (Figure 4I, red dashed arrow in lower-right panel). This analysis suggests that Klf4 employs two of its three ZFs to engage nucleosomes.

Interestingly, the observed adaptability of O, S, and K to recognize partial motifs correlates with the apparent flexibility of their respective DBDs that we modeled during their transition from the DNA-free to the DNA-bound states (Figures S5B–S5G).

c-Myc Recognizes a Partial Motif Enriched on Nucleosomes through Co-Binding with Other Factors

Using the partitioning method in Figures 4A–4C, a subset of c-Myc targeted sites (33%, n = 5,494) were enriched for nucleosomal DNA, while the majority of sites (77%, n = 18,391) did not exhibit enrichment (Figure 5A). Motif analysis revealed that c-Myc nucleosomal targets were enriched for an E-box motif that is missing the two central nucleotides (CANNTG) compared to the canonical E-box (CACGTG) (Figure 5B, double arrowheads in top panel). However, nucleosome-depleted targets were enriched for a less degenerate E-box motif that we and others have previously reported to be associated with c-Myc binding at enhancers (Lin et al., 2012; Nie et al., 2012; Soufi et al., 2012) (Figure 5B, single arrowhead in bottom panel). Interestingly, c-Myc-alone (i.e., without OSK) nucleosomal targets were additionally enriched for a homeobox (73%) motif that is highly similar to the POU_{HD} motif, compared to nucleosome-depleted sites (48%) (Figure 5C). Likewise, the majority of c-Myc sites that co-targeted with Oct4 (76%, n = 2,219) that are enriched for nucleosomes contain centrally a degenerate E-box motif similar to that identified in nucleosomal c-Myc-alone targets (Figures 5D and 5E). The separate halves of the POU motif were also enriched at the OM targeted sites, indicating that Oct4 uses one or the other DBD while co-binding with c-Myc (Figure 5F). In conclusion, c-Myc targets nucleosomal sites either with O, S, K, or with endogenous homeodomain factors, recognizing a centrally degenerate E-box motif.

The basic region of bHLH domain, not bound to DNA, appears to be unfolded in solution (Sauvé et al., 2004) (Figure 6A; Figure S6A). Upon DNA binding, the basic region folds as an extension of helix-1 and will be referred to as basic-helix-1 (bH) (Nair and Burley, 2003) (Figures 6D and S6B, blue helices). Notably, the most conserved four nucleotides of the E-box (CANNTG) face toward the interaction interface between bHLH and DNA, while the degenerate central two nucleotides (CANNTG) face the exterior part of the DNA helix (Figure 6B, see cyan and magenta arrowheads). The transition between DNA free and DNA bound by molecular morphing indicates that the bH follows a gradual folding trajectory across the major groove of DNA (Figures 6A–6D and S6B). The interaction between a partially folded bHLH and the CANNTG provides the initial recognition of the E-box without making contacts with the central nucleotides (NN), resulting in the centrally degenerate E-box motif that we observed for c-Myc at the nucleosome-enriched sites (Figure 6B).

Importantly, the partially folded c-Myc only occupies one-half the DNA helix surface, leaving the other half solvent-exposed and potentially nucleosome compatible (Figure 6B, red dashed arrow). Apparently, the partially folded c-Myc-DNA complex requires further assistance from other factors such as Oct4 or other homeodomain-containing proteins to remain associated with DNA. The interaction between a partially folded bHLH and a centrally degenerate E-Box motif has been observed by X-ray

(B) DNase I footprinting showing the protection of *LIN28B*-DNA (left panels) and *LIN28B*-nuc (right panels) in the absence (blue lines) or presence (red lines) of O, S, K, and M. Electropherograms of 5'-6FAM end-labeled *LIN28B* (top strand) oligonucleotides generated by DNase I digestion of DNA (0.006 U) and nucleosomal DNA (0.06 U). Dashed boxes and stars represent specific and non-specific sites protected by O, S, K, and M, respectively.

(C) A cartoon representation of the 162-bp *LIN28B* DNA (left) and nucleosome (right) highlighting the binding sites of O, S, K, and M in vitro in blue, red, orange, and green, respectively, as measured by DNase I footprinting. The protected DNA sequences are indicated.

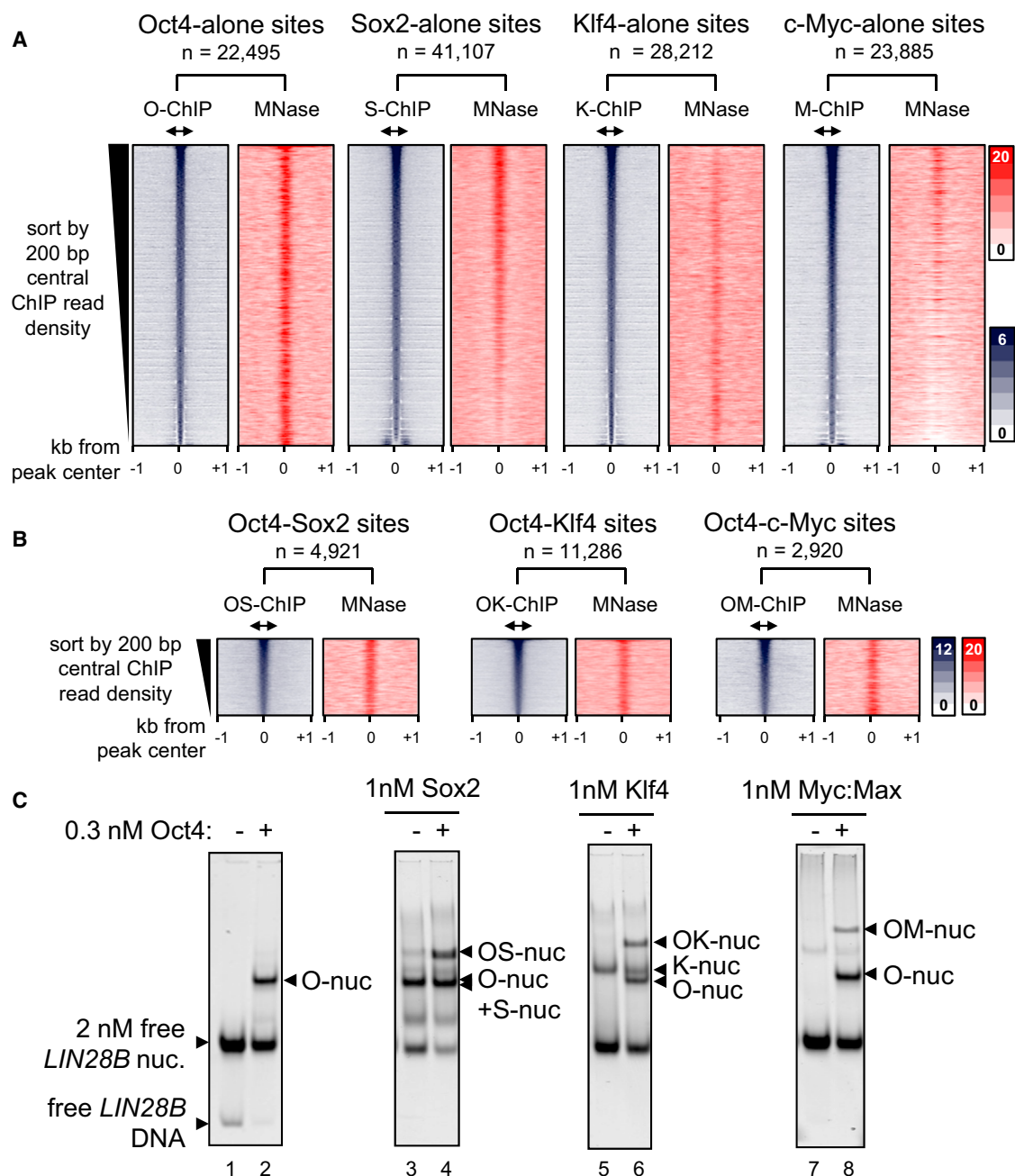


Figure 3. O, S, K, and M Display a Range of Nucleosome Targeting In Vivo

(A) Read density heatmaps (in color scales) showing the intensity of O, S, K, and M ChIP-seq signal (blue) and MNase-seq (red) spanning ± 1 kb from the center of the O, S, K, and M peaks where each factor binds alone within 500-bp threshold. The analyzed sequences were organized in rank order, from high to low number ChIP-seq reads within the central 200 bp (double arrows). The number of targeted sites is indicated.

(B) As in (A), but showing where the OS, OK, and OM factors peaks are within 100 bp or less apart from each other. The full possible OSKM combinations are shown in Figure S3.

(C) The binding affinity of S, K, and M (1 nM) in the presence of Oct4 (0.3 nM) to *LIN28B* nucleosomal DNA (lanes 4, 6, and 8, respectively) or absence of Oct4 (lanes 3, 5, and 7). The binding of Oct4 on its own (lane 2) and free *LIN28B* nucleosomes (lane 1) are indicated. The histone content of the nucleosome bound complexes is shown in Figure S4.

crystallography for Mitf, which shares 86% sequence homology across the basic region with c-Myc (Figure S6C) (Pogenberg et al., 2012). Once fully folded, the c-Myc bHLH adopts a

rigid structure, stabilizing DNA binding and resulting in less-degenerate E-box motif, which would be incompatible with nucleosomes (Figure 6D). We conclude that partially unfolded

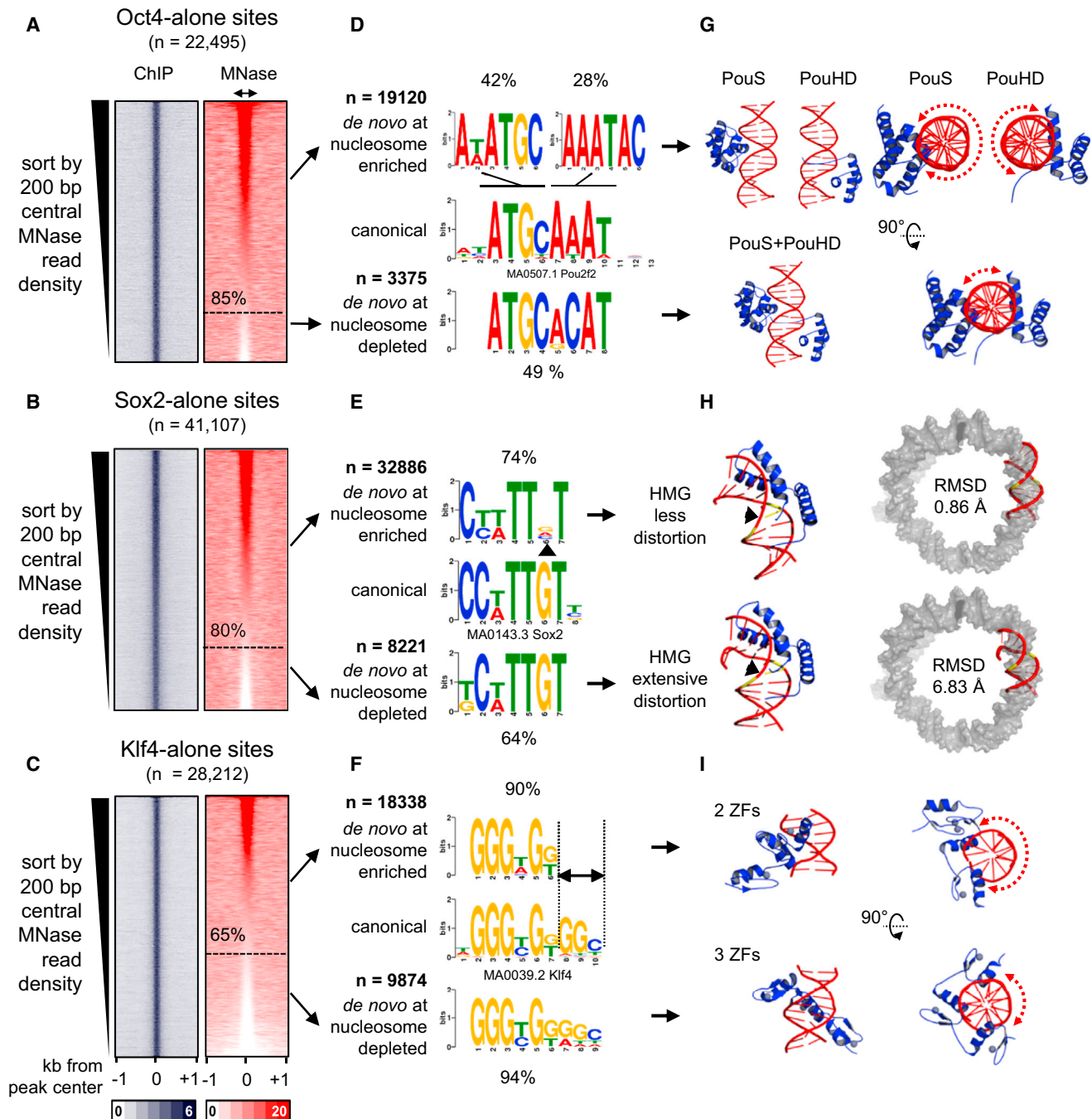


Figure 4. O, S, and K Recognize Partial Motifs on Nucleosomes

(A–C) Same as in Figure 3A, but the sites were organized in a descending rank order according to the MNase-seq tags within the central 200 bp. The nucleosome-enriched sites were separated from the nucleosome-depleted sites (dashed line) for each factor.

(D–F) Logo representations of *de novo* motifs identified in the O, S, and K nucleosome-enriched targets (top) and nucleosome-depleted targets (bottom). The motifs were aligned to canonical motifs (middle). The number of targets analyzed and percentage of motif enrichments are indicated.

(G–I) Cartoon representations of the 3D structures of O (PDB-3L1P), S (PDB-1GT0), and K (PDBs-2WBS and 2WBU) DBDs in complexes with DNA containing canonical motifs. Side and top views are shown for O and K, and dashed curved arrows are shown to represent the extent of exposed DNA surface (G and I). The 3D structure of the less distorted DNA (top) and extensively distorted DNA (bottom) were superimposed on nucleosomal DNA (PDB-3LZ0, gray) to display the extent Sox2-nucleosome binding compatibility by measuring RMSD of the fit.

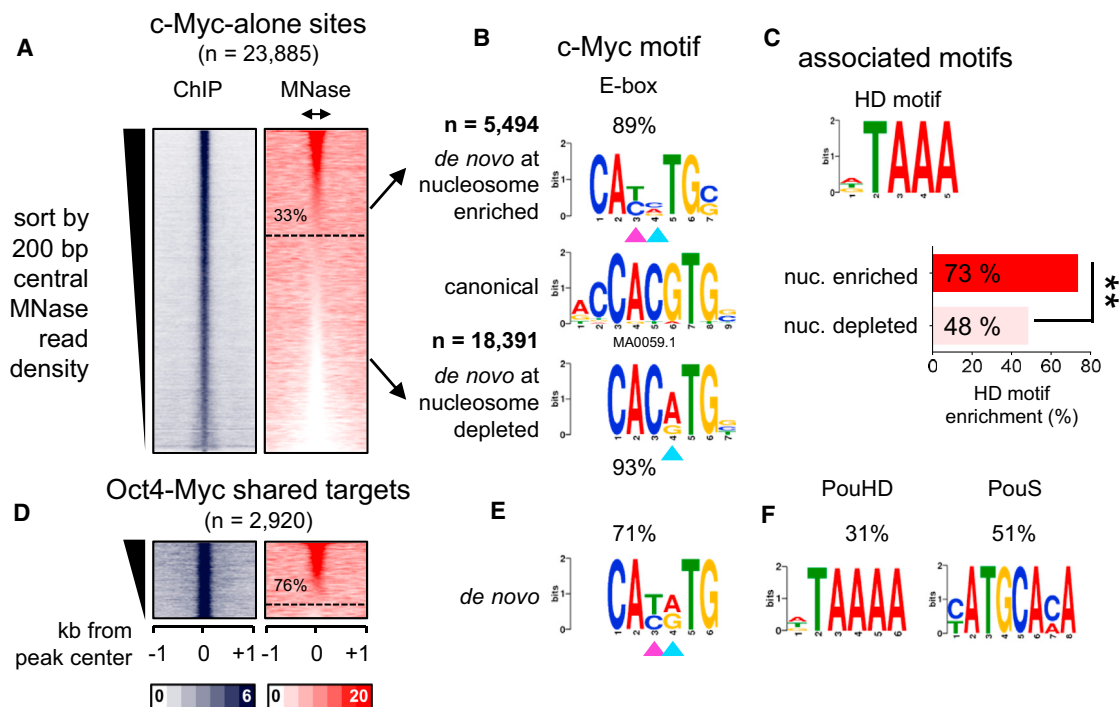


Figure 5. c-Myc Recognition of Degenerate E-Box on Nucleosome Is Assisted by Binding with Co-Factors

(A–F) Same as shown in Figures 4A–4F, but for c-Myc alone and OM targets. (C) The enrichment of an associated motif (HD) is measured within c-Myc alone targets containing or depleted from nucleosomes. The data indicate that c-Myc is driven to a degenerate E-box on nucleosomes, in part, by homeodomain factors ** $p < 0.001$.

c-Myc targets a centrally degenerate E-box motif, thereby adapting to a nucleosome template when assisted by other factors.

Predicting Pioneer Activity among Different bHLH Factors in Reprogramming

To gain insights on how bHLH proteins may differentially target nucleosomes in reprogramming, we examined the 3D structures of a range of bHLH-DNA complexes that have been used in reprogramming experiments (Longo et al., 2008; Ma et al., 1994; El Omari et al., 2013). Interestingly, the basic helix-1 from the different bHLH domains extends across the DNA helix to variable extents (Figures 6E–6I). Motif analysis was also carried out on genomic sites bound by these factors from available ChIP-seq data. Notably, in conjunction with our findings on c-Myc, the length of the bH α helix negatively correlates with the degeneracy of the central nucleotides (CANNTG) of the de novo motifs that we identified for each factor (Figures 6E–6I).

To further test this correlation, we examined the recent findings that the bHLH factor Ascl1 can act as a pioneer factor during reprogramming fibroblasts to neurons (Wapinski et al., 2013). We measured nucleosome enrichment in pre-induced mouse embryonic fibroblasts (MEF) within Ascl1 initial targets in MEFs after 48 hr induction (Teif et al., 2012; Wapinski et al., 2013). Unlike c-Myc, the majority of Ascl1 sites (73%, $n = 3,019$) were enriched for nucleosomes (Figure S6D). Importantly, the basic helix-1 of Ascl1 is considerably shorter compared to that of c-Myc, leaving more of the DNA surface solvent exposed (Figure 6E). Similar to c-Myc, Ascl1 target nucleosomes were enriched (99.3%) for an

E-box motif with degenerate central two nucleotides (CANNTG) compared to the E-box seen in 98.7% of sites depleted from nucleosomes (Figure S6E). Ascl1 nucleosomal targets contain an extra “G” nucleotide at the 3’-end of the E-box motif, which is missing in the nucleosome-depleted sites, resulting in more specific targeting of nucleosomes despite the centrally degenerate E-box (Figures 6E and S6E).

Ascl1 and Olig2 exhibited the shortest bH regions, by molecular modeling, compared to X-ray crystals of NeuroD, MyoD, and Tal1, with longer bHs. To verify that the observed bH lengths were not due to the methodology, we examined the amino-acid composition of the basic regions in all bHLH factors (Figure 6J). The bH-DNA interaction is mainly driven by positively charged residues (and hence the name basic). Interestingly, the Ascl1 bH ends at the last (N-terminal end) basic residue (arginine), which is positioned further upstream (toward the C terminus) compared to the other factors (Figures 6J and 6R, residues in blue boxes). The last basic residue of Olig2-bH falls in between Ascl1 and the rest of the factors. In conclusion, the basic helix-1 of pioneer bHLH factors such as Ascl1 is intrinsically shorter, allowing the factors to bind nucleosomes more efficiently.

DISCUSSION

The introduction of a defined set of TFs, such as OSKM, into differentiated cells can result in cell-fate conversion (Takahashi and Yamanaka, 2006), and yet it has been clear that the different factors have different contributions or “strengths” in cell-type

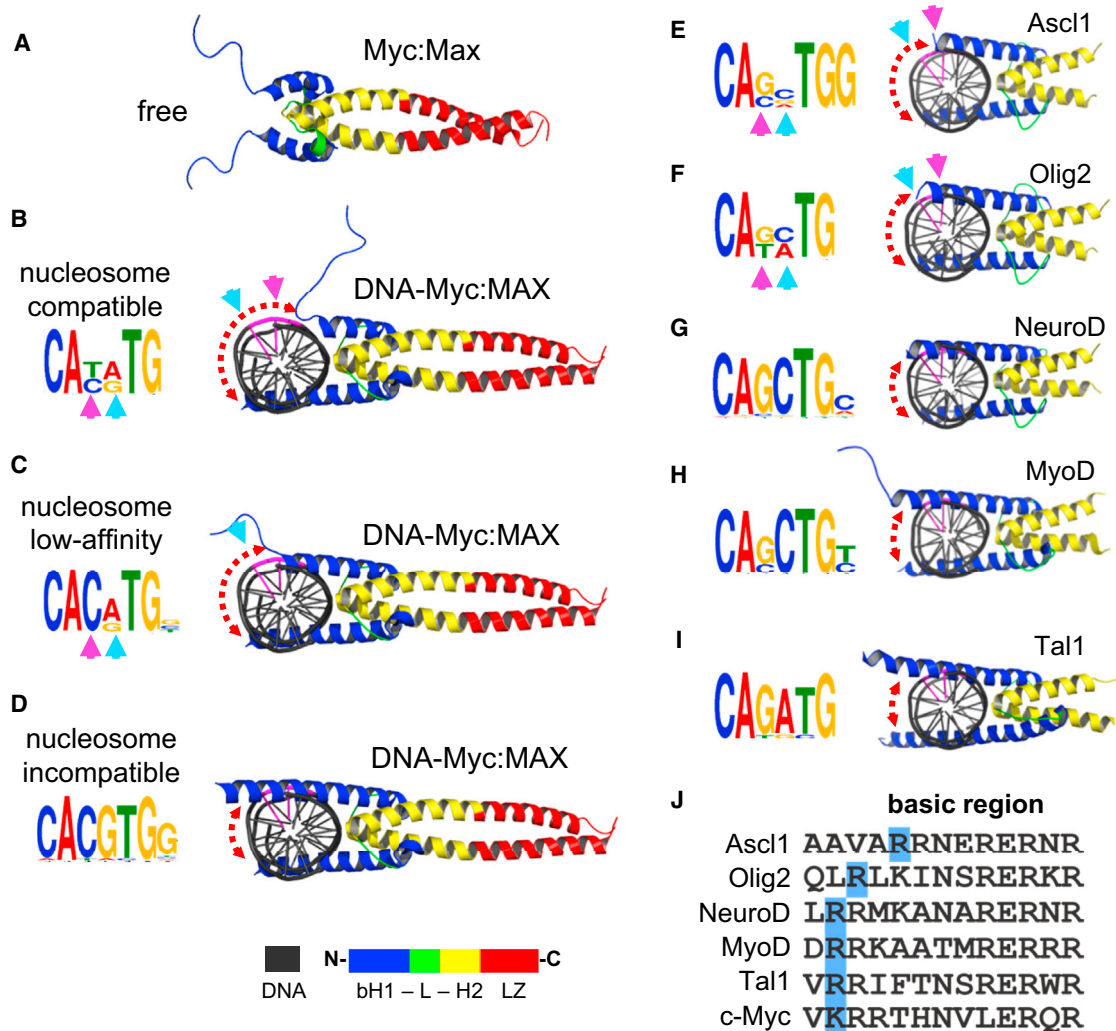


Figure 6. The Folding Extent of bHLH Basic Helix-1 on DNA Anti-Correlates with Targeting Centrally Degenerate E-Box Motifs on Nucleosomes

(A–D) The folding trajectory of basic helix-1 of c-Myc upon DNA binding showing the possible conformations of c-Myc:Max heterodimers (B and C) that are compatible with nucleosome binding. See Figure S6A for c-Myc Morph. The initial DNA-free state (A) and the fully folded DNA-bound state (D), which is incompatible with nucleosome binding, are indicated. The associated motifs for each c-Myc:Max conformation are shown in the left. See Figure S6B for Mitf structure in complexes with E-box with variable central nucleotides.

(E–I) Cartoon representations of various bHLH reprogramming factors in complexes with DNA containing their canonical motifs (right). The de novo motifs identified for each factor from ChIP-seq data are indicated (left). The cyan and pink arrows represent the position of the exposed nucleotides within the central E-box motif not making base-contacts with the relative bHLH conformation. The central two nucleotides (CANNTG) are colored in purple in the DNA cartoon. The color scheme of the bHLH along with leucine zipper (LZ) is shown at the bottom.

(J) Alignment of amino-acid sequences of the basic region of Ascl1, Olig2, NeuroD, MyoD, Tal1, and c-Myc. The last basic residue at the C-terminal end is highlighted in blue. See Figures S6D and S6E for MNase enrichment and motif analysis of Ascl1.

conversion. This provided the basis for our effort to tackle the long-standing problem of how TFs initially target their sites in closed chromatin. The pioneer factor theory partly answers this question by suggesting that a select group of TFs, such as FoxA1, access closed chromatin by a direct interaction with nucleosomal DNA through a DBD that resembles the structure of a linker histone (Zaret and Carroll, 2011, Iwafuchi-Doi and Zaret, 2014). We previously found that the diverse set of DBDs exhibited by O, S, K, and M, which are structurally different from a linker histone, have differential abilities to access closed chromatin (Soufi

et al., 2012). Here, we revealed that the relative tendencies of O, S, K, and M to initially target nucleosomal sites in reprogramming reflect their inherent ability to bind nucleosomes in vitro and their ability to recognize partial motifs on nucleosomes in vivo. This is different from what was observed for FoxA1, which recognizes the same motif on free DNA and nucleosomes (Cirillo et al., 1998; Li et al., 2011). Factors that cannot bind nucleosomes on their own, such as c-Myc, associate with other factors to target degenerate E-boxes on nucleosomes. Our new approach is in contrast to the previous predictions of pioneer factors by fitting

fully folded DBDs, in their naked DNA-bound state, on nucleosomes through a docking mechanism.

We found that the bipartite POU domain of Oct4 can target partial motifs exposed on nucleosomes using separate PouS or PouHD domains. The single motif targeted by each domain is longer than each half of the octamer motif, thus providing greater binding specificity than a half motif. In addition, mass spectroscopy analysis has identified histones as interacting partners of Oct4 in mouse ES cells (Pardo et al., 2010), indicating an additional affinity contribution by protein-histone interactions. The bipartite domain-Pax family of TFs can bind DNA using both domains and still occupy half of the DNA surface and would therefore be compatible with nucleosome binding (Garvie et al., 2001; Xu et al., 1999) (Figure S7, right, compared to POU TFs). This agrees with the finding that Pax7 is a pioneer factor that uses full motif recognition during initial targeting (Budry et al., 2012). Thus, bipartite TFs have to either employ one DBD or position both DBDs on the same surface of DNA in order to interact with nucleosomes. Notably, the pioneer activity of a Zebrafish homolog of an Oct protein was observed during the maternal-to-zygote transition (Lee et al., 2013; Leichsenring et al., 2013), suggesting that targeting nucleosomal sites may be a general method for de novo programming of the genome.

The high affinity of Sox2 for nucleosomes may be due to the pre-bent conformation of DNA, which widens the DNA minor groove and favors initial minor groove sensing. While bending naked DNA by Sox2 requires minimal work (Privalov et al., 2009), the energy cost would impede Sox2 to further bend DNA on nucleosomes. We find that Sox2 would not further bend nucleosomal DNA because it recognizes a partial motif that diminishes the extreme bending of the full motif. Sox family members share the recognition of the core motif but display diverse preferences outside the core in naked DNA (Badis et al., 2009). Our findings reveal greater flexibility with regard to Sox2 core motif preferences on nucleosomes than was previously recognized. In addition, we showed evidence for both specific and nonspecific binding by Sox2 in vitro and in vivo. The stable, motif-driven targeting by Sox2 on nucleosomes in the ChIP-seq data show much lower co-binding with Oct4 (Soufi et al., 2012) than seen in live imaging (Chen et al., 2014), leaving open whether the latter approach depicts nucleosomal or free DNA binding during genome scanning.

Klf4 showed higher affinity to free DNA compared to nucleosomes in vitro, and its initial targets in vivo were enriched for nucleosomes, though less so than compared to Oct4 and Sox2. Klf4 targets nucleosomes in vivo using two out of its three zinc fingers, recognizing a hexameric motif. This explains how the affinity of Klf4 to nucleosomes is lower than that to free DNA. The pioneer factor GATA4 binds nucleosomes modestly in vitro (Cirillo and Zaret, 1999) and targets a hexameric motif in vivo (Zheng et al., 2013). Notably, GATA4 only contains two zinc fingers. The Gils zinc finger family 1 (Gli1) greatly enhances reprogramming when co-expressed with OSK (Maekawa et al., 2011). Interestingly, despite containing five ZFs, Gli1 only employs two ZFs (number four and five) to recognize its targets (Pavletich and Pabo, 1993). The repressor ZFP57/Kap1, which is known to be associated with closed chromatin, also recognizes a hexameric motif despite containing an array of seven zinc fingers (Quenne-

ville et al., 2011). This suggests that zinc finger proteins in general may use two zinc fingers to initially target hexameric motifs exposed on nucleosomes. Klf4 also showed non-specific interactions with nucleosomes, suggesting a similar genome searching mechanism as Sox2.

Various examples have been reported on the overexpression of bHLH factors in cancer, including c-Myc, Tal1, and Olig2 (Lin et al., 2012; Nie et al., 2012; Palii et al., 2011; Sanda et al., 2012; Suvà et al., 2014). In all of these cases, the bHLH factors have been associated with degenerate E-box motifs and co-binding with other factors. We propose that the extent to which basic helix-1 lays on DNA and co-binds with pioneer factors is reflected in the recognized motif, predicting bHLH ability to bind nucleosomes and access closed chromatin. Interestingly, the mutation of two amino acids within the basic helix-1 that interacts with central E-box makes the non-myogenic bHLH factor E12 able to convert fibroblasts to muscle cells (Davis and Weintraub, 1992). The homeodomain factor PBX primes MyoD targets to induce myogenic potential (Maves et al., 2007). Furthermore, the hematopoietic TAL1-E45 heterodimer employs one of the two bHLH domains using LMO2 as an adaptor to interact with GATA1 (El Omari et al., 2013). Hence, in addition to their intrinsic structures, bHLH factors co-binding with DNA-binding and non-DNA binding proteins appear to be involved in stabilizing the interaction of the partially folded bHLH factors to nucleosomes. These features are relevant to the multitude of bHLH factors functioning in development, cancer, and reprogramming experiments.

The differential ability of TFs to recognize their target sites on nucleosomes supports a hierarchical model where pioneer factors are the first to gain access to their targets in silent chromatin. We also observe that the initial targeting can occur for non-pioneer proteins when they bind in conjunction with pioneer factors that allow the former to recognize their DBDs to a reduced motif that is compatible with nucleosome binding. Further studies are needed to understand the secondary events that lead to subsequent changes in local chromatin structure and the formation of large complexes at gene regulatory sequences. By understanding the mechanistic basis by which certain transcription factors are especially capable of initiating cell-fate changes, we hope to modulate the process and ultimately control cell fates at will.

EXPERIMENTAL PROCEDURES

Protein Expression and Purification

We made the bacterial expression plasmids pET-28B-huOct4, pET-28B-huSox2, pET-28B-huKlf4, and pET-28B-huMyc encoding the full-length human O, S, K, M, respectively, fused to an N-terminal 6× histidine tag. The recombinant proteins were expressed in *E. coli* Rosetta (DE3) pLysS (Novagen #70956-3) and purified using a nickel charged column under denaturing conditions. The mammalian expressed human OSKM recombinant proteins were obtained from OriGene (Oct4 #TP311998, Sox2 #TP300757, Klf4 #TP306691, c-Myc #TP301611). See [Extended Experimental Procedures](#) for more details of this and following sections.

Nucleosome Reconstitution

The 162-bp *LIN28B* DNA fragment was created by PCR with end-labeled primers. The fluorescent-tagged DNA fragments were gel extracted and further purified using ion-exchange liquid chromatography by MonoQ (GE Healthcare). The nucleosomes were reconstituted by mixing purified human

H2A/H2B dimers and H3/H4 tetramers with LIN28B-DNA at 1:1 molar ratio of histone octamer:DNA using a salt-urea gradient.

DNA Binding Reactions

Cy5 end-labeled DNA containing specific or non-specific sites, *LIN28B*-DNA, and *LIN28B*-nucleosomes were incubated with recombinant proteins in 10 mM Tris-HCl (pH 7.5), 1 mM MgCl₂, 10 μM ZnCl₂, 1 mM DTT, 10 mM KCl, 0.5 mg/ml BSA, 5% glycerol at room temperature for 60 min. Free and bound DNA were separated on 4% non-denaturing polyacrylamide gels run in 0.5 × Tris borate EDTA and visualized using a PhosphorImager. The intensity of Cy5 fluorescence was quantified using Multi-Gauge software (Fujifilm Science lab) to generate binding curves for K_D analysis.

DNase footprinting was carried out by treating free DNA or nucleosomes, 6FAM 5' end-labeled, with DNase I (Worthington) in the absence or presence of TFs. The end-labeled digested fragments were separated by capillary electrophoresis in ABI 96-capillary 3730XL Sequencer (Applied Biosystems).

Genomic Data Analysis

The O, S, K, and M ChIP-seq aligned data along with the called peaks (FDR-controlled at 0.005) were obtained from GEO (GSE36570) (Soufi et al., 2012). The MNase-seq data (GSM543311) (Kelly et al., 2012) were aligned to build version NCBI36/HG18 of the human genome, and seven replicates were pooled together generating 145,546,004 unique reads. The MNase-seq reads were extended to 150 bp to cover one nucleosome and thus resulting in 6.6-fold genome coverage.

Motif analysis was carried out using the MEME-ChIP suit v.4.9.1 available at <http://meme.nbcr.net> (Machanic and Bailey, 2011).

SUPPLEMENTAL INFORMATION

Supplemental Information includes Extended Experimental Procedures and seven figures and can be found with this article online at <http://dx.doi.org/10.1016/j.cell.2015.03.017>.

AUTHOR CONTRIBUTIONS

A.S. and K.S.Z. conceived the study and designed the experiments. A.S. and M.F.G. carried out EMSA and nucleosome reconstitution. A.S., A.J., and M.P. performed MNase-seq data analysis. A.S. and N.O. carried out the recombinant protein purification experiments. A.S. performed the motif and 3D structure analysis. A.S. and K.S.Z. contributed to supervision of personnel, data interpretation, and writing the manuscript.

ACKNOWLEDGMENTS

We thank G. Donahue for advice and G. Blobel, R. Marmorstein, M. Iwafuchi-Doi, and D. Nicetto for comments on the manuscript. The work was supported by NIH grant P01GM099134 to K.S.Z.

Received: July 31, 2014

Revised: December 24, 2014

Accepted: February 15, 2015

Published: April 16, 2015

REFERENCES

Adams, C.C., and Workman, J.L. (1995). Binding of disparate transcriptional activators to nucleosomal DNA is inherently cooperative. *Mol. Cell. Biol.* 15, 1405–1421.

Badis, G., Berger, M.F., Philippakis, A.A., Talukder, S., Gehrke, A.R., Jaeger, S.A., Chan, E.T., Metzler, G., Vedenko, A., Chen, X., et al. (2009). Diversity and complexity in DNA recognition by transcription factors. *Science* 324, 1720–1723.

Barozzi, I., Simonatto, M., Bonifacio, S., Yang, L., Rohs, R., Ghisletti, S., and Natoli, G. (2014). Coregulation of transcription factor binding and nucleosome occupancy through DNA features of mammalian enhancers. *Mol. Cell* 54, 844–857.

Biggin, M.D. (2011). Animal transcription networks as highly connected, quantitative continua. *Dev. Cell* 21, 611–626.

Budry, L., Balsalobre, A., Gauthier, Y., Khetchoumian, K., L'honoré, A., Vallette, S., Brue, T., Figarella-Branger, D., Meij, B., and Drouin, J. (2012). The selector gene *Pax7* dictates alternate pituitary cell fates through its pioneer action on chromatin remodeling. *Genes Dev.* 26, 2299–2310.

Buganim, Y., Faddah, D.A., and Jaenisch, R. (2013). Mechanisms and models of somatic cell reprogramming. *Nat. Rev. Genet.* 14, 427–439.

Chen, J., Zhang, Z., Li, L., Chen, B.-C., Revyakin, A., Hajj, B., Legant, W., Dahan, M., Lionnet, T., Betzig, E., et al. (2014). Single-molecule dynamics of enhanceosome assembly in embryonic stem cells. *Cell* 156, 1274–1285.

Cirillo, L.A., and Zaret, K.S. (1999). An early developmental transcription factor complex that is more stable on nucleosome core particles than on free DNA. *Mol. Cell* 4, 961–969.

Cirillo, L.A., McPherson, C.E., Bossard, P., Stevens, K., Cherian, S., Shim, E.Y., Clark, K.L., Burley, S.K., and Zaret, K.S. (1998). Binding of the winged-helix transcription factor HNF3 to a linker histone site on the nucleosome. *EMBO J.* 17, 244–254.

Cirillo, L.A., Lin, F.R., Cuesta, I., Friedman, D., Jarnik, M., and Zaret, K.S. (2002). Opening of compacted chromatin by early developmental transcription factors HNF3 (FoxA) and GATA-4. *Mol. Cell* 9, 279–289.

Clark, K.L., Halay, E.D., Lai, E., and Burley, S.K. (1993). Co-crystal structure of the HNF-3/fork head DNA-recognition motif resembles histone H5. *Nature* 364, 412–420.

Davis, R., and Weintraub, H. (1992). Acquisition of myogenic specificity by replacement of three amino acid residues from MyoD into E12. *Science* 256, 1027–1030.

El Omari, K., Hoosdally, S.J., Tuladhar, K., Karia, D., Hall-Ponselé, E., Platonova, O., Vyas, P., Patient, R., Porcher, C., and Mancini, E.J. (2013). Structural basis for LMO2-driven recruitment of the SCL:E47bHLH heterodimer to hematopoietic-specific transcriptional targets. *Cell Rep.* 4, 135–147.

Esch, D., Vahokoski, J., Groves, M.R., Pogenberg, V., Cojocaru, V., Vom Bruch, H., Han, D., Drexler, H.C.A., Araújo-Bravo, M.J., Ng, C.K.L., et al. (2013). A unique Oct4 interface is crucial for reprogramming to pluripotency. *Nat. Cell Biol.* 15, 295–301.

Farina, A., Faiola, F., and Martinez, E. (2004). Reconstitution of an E box-binding Myc:Max complex with recombinant full-length proteins expressed in *Escherichia coli*. *Protein Expr. Purif.* 34, 215–222.

Garvie, C.W., Hagman, J., and Wolberger, C. (2001). Structural studies of Ets-1/Pax5 complex formation on DNA. *Mol. Cell* 8, 1267–1276.

Iwafuchi-Doi, M., and Zaret, K.S. (2014). Pioneer transcription factors in cell reprogramming. *Genes Dev.* 28, 2679–2692.

Kelly, T.K., Liu, Y., Lay, F.D., Liang, G., Berman, B.P., and Jones, P.A. (2012). Genome-wide mapping of nucleosome positioning and DNA methylation within individual DNA molecules. *Genome Res.* 22, 2497–2506.

Lee, C.S., Friedman, J.R., Fulmer, J.T., and Kaestner, K.H. (2005). The initiation of liver development is dependent on Foxa transcription factors. *Nature* 435, 944–947.

Lee, M.T., Bonneau, A.R., Takacs, C.M., Bazzini, A.A., DiVito, K.R., Fleming, E.S., and Giraldez, A.J. (2013). Nanog, Pou5f1 and SoxB1 activate zygotic gene expression during the maternal-to-zygotic transition. *Nature* 503, 360–364.

Leichsenring, M., Maes, J., Mössner, R., Driever, W., and Onichtchouk, D. (2013). Pou5f1 transcription factor controls zygotic gene activation in vertebrates. *Science* 341, 1005–1009.

Li, Z., Schug, J., Tuteja, G., White, P., and Kaestner, K.H. (2011). The nucleosome map of the mammalian liver. *Nat. Struct. Mol. Biol.* 18, 742–746.

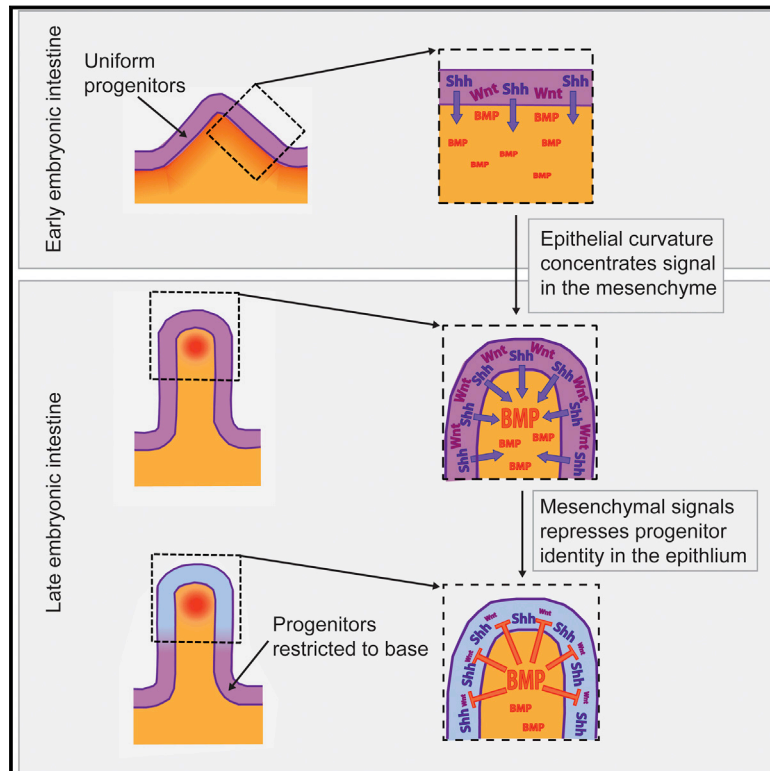
Lin, C.Y., Lovén, J., Rahl, P.B., Paranal, R.M., Burge, C.B., Bradner, J.E., Lee, T.I., and Young, R.A. (2012). Transcriptional amplification in tumor cells with elevated c-Myc. *Cell* 151, 56–67.

Longo, A., Guanga, G.P., and Rose, R.B. (2008). Crystal structure of E47-NeuroD1/beta2 bHLH domain-DNA complex: heterodimer selectivity and DNA recognition. *Biochemistry* 47, 218–229.

- Ma, P.C., Rould, M.A., Weintraub, H., and Pabo, C.O. (1994). Crystal structure of MyoD bHLH domain-DNA complex: perspectives on DNA recognition and implications for transcriptional activation. *Cell* 77, 451–459.
- Machanick, P., and Bailey, T.L. (2011). MEME-ChIP: motif analysis of large DNA datasets. *Bioinformatics* 27, 1696–1697.
- Maekawa, M., Yamaguchi, K., Nakamura, T., Shibukawa, R., Kodanaka, I., Ichisaka, T., Kawamura, Y., Mochizuki, H., Goshima, N., and Yamanaka, S. (2011). Direct reprogramming of somatic cells is promoted by maternal transcription factor Glis1. *Nature* 474, 225–229.
- Maves, L., Waskiewicz, A.J., Paul, B., Cao, Y., Tyler, A., Moens, C.B., and Tapscott, S.J. (2007). Pbx homeodomain proteins direct MyoD activity to promote fast-muscle differentiation. *Development* 134, 3371–3382.
- Mirny, L.A. (2010). Nucleosome-mediated cooperativity between transcription factors. *Proc. Natl. Acad. Sci. USA* 107, 22534–22539.
- Montserrat, N., Nivet, E., Sancho-Martinez, I., Hishida, T., Kumar, S., Miquel, L., Cortina, C., Hishida, Y., Xia, Y., Esteban, C.R., and Izpisua Belmonte, J.C. (2013). Reprogramming of human fibroblasts to pluripotency with lineage specifiers. *Cell Stem Cell* 13, 341–350.
- Nair, S.K., and Burley, S.K. (2003). X-ray structures of Myc-Max and Mad-Max recognizing DNA. Molecular bases of regulation by proto-oncogenic transcription factors. *Cell* 112, 193–205.
- Nakatake, Y., Fukui, N., Iwamatsu, Y., Masui, S., Takahashi, K., Yagi, R., Yagi, K., Miyazaki, J., Matoba, R., Ko, M.S.H., and Niwa, H. (2006). Klf4 cooperates with Oct3/4 and Sox2 to activate the Lefty1 core promoter in embryonic stem cells. *Mol. Cell. Biol.* 26, 7772–7782.
- Nie, Z., Hu, G., Wei, G., Cui, K., Yamane, A., Resch, W., Wang, R., Green, D.R., Tessarollo, L., Casellas, R., et al. (2012). c-Myc is a universal amplifier of expressed genes in lymphocytes and embryonic stem cells. *Cell* 151, 68–79.
- Palii, C.G., Perez-Iratxeta, C., Yao, Z., Cao, Y., Dai, F., Davison, J., Atkins, H., Allan, D., Dilworth, F.J., Gentleman, R., et al. (2011). Differential genomic targeting of the transcription factor TAL1 in alternate haematopoietic lineages. *EMBO J.* 30, 494–509.
- Papp, B., and Plath, K. (2013). Epigenetics of reprogramming to induced pluripotency. *Cell* 152, 1324–1343.
- Pardo, M., Lang, B., Yu, L., Prosser, H., Bradley, A., Babu, M.M., and Choudhary, J. (2010). An expanded Oct4 interaction network: implications for stem cell biology, development, and disease. *Cell Stem Cell* 6, 382–395.
- Pavletich, N.P., and Pabo, C.O. (1993). Crystal structure of a five-finger GLI-DNA complex: new perspectives on zinc fingers. *Science* 261, 1701–1707.
- Perlmann, T., and Wrangé, O. (1988). Specific glucocorticoid receptor binding to DNA reconstituted in a nucleosome. *EMBO J.* 7, 3073–3079.
- Pogenberg, V., Ogmundsdóttir, M.H., Bergsteinsdóttir, K., Schepsky, A., Phung, B., Deineko, V., Milewski, M., Steingrímsson, E., and Wilmanns, M. (2012). Restricted leucine zipper dimerization and specificity of DNA recognition of the melanocyte master regulator MITF. *Genes Dev.* 26, 2647–2658.
- Polach, K.J., and Widom, J. (1996). A model for the cooperative binding of eukaryotic regulatory proteins to nucleosomal target sites. *J. Mol. Biol.* 258, 800–812.
- Privalov, P.L., Dragan, A.I., and Crane-Robinson, C. (2009). The cost of DNA bending. *Trends Biochem. Sci.* 34, 464–470.
- Quenneville, S., Verde, G., Corsinotti, A., Kapopoulou, A., Jakobsson, J., Offner, S., Baglivo, I., Pedone, P.V., Grimaldi, G., Riccio, A., and Trono, D. (2011). In embryonic stem cells, ZFP57/KAP1 recognize a methylated hexanucleotide to affect chromatin and DNA methylation of imprinting control regions. *Mol. Cell* 44, 361–372.
- Ramakrishnan, V., Finch, J.T., Graziano, V., Lee, P.L., and Sweet, R.M. (1993). Crystal structure of globular domain of histone H5 and its implications for nucleosome binding. *Nature* 362, 219–223.
- Reményi, A., Lins, K., Nissen, L.J., Reinbold, R., Schöler, H.R., and Wilmanns, M. (2003). Crystal structure of a POU/HMG/DNA ternary complex suggests differential assembly of Oct4 and Sox2 on two enhancers. *Genes Dev.* 17, 2048–2059.
- Robinton, D.A., and Daley, G.Q. (2012). The promise of induced pluripotent stem cells in research and therapy. *Nature* 481, 295–305.
- Rodda, D.J., Chew, J.-L., Lim, L.-H., Loh, Y.-H., Wang, B., Ng, H.-H., and Robson, P. (2005). Transcriptional regulation of nanog by OCT4 and SOX2. *J. Biol. Chem.* 280, 24731–24737.
- Sanda, T., Lawton, L.N., Barrasa, M.I., Fan, Z.P., Kohlhammer, H., Gutierrez, A., Ma, W., Taterek, J., Ahn, Y., Kelliher, M.A., et al. (2012). Core transcriptional regulatory circuit controlled by the TAL1 complex in human T cell acute lymphoblastic leukemia. *Cancer Cell* 22, 209–221.
- Sauvé, S., Tremblay, L., and Lavigne, P. (2004). The NMR solution structure of a mutant of the Max b/HLH/LZ free of DNA: insights into the specific and reversible DNA binding mechanism of dimeric transcription factors. *J. Mol. Biol.* 342, 813–832.
- Scaffidi, P., and Bianchi, M.E. (2001). Spatially precise DNA bending is an essential activity of the sox2 transcription factor. *J. Biol. Chem.* 276, 47296–47302.
- Schuetz, A., Nana, D., Rose, C., Zocher, G., Milanovic, M., Koenigsmann, J., Blasig, R., Heinemann, U., and Carstanjen, D. (2011). The structure of the Klf4 DNA-binding domain links to self-renewal and macrophage differentiation. *Cell. Mol. Life Sci.* 68, 3121–3131.
- Shields, J.M., and Yang, V.W. (1998). Identification of the DNA sequence that interacts with the gut-enriched Krüppel-like factor. *Nucleic Acids Res.* 26, 796–802.
- Shyh-Chang, N., Zhu, H., Yvanka de Soysa, T., Shinoda, G., Seligson, M.T., Tsanov, K.M., Nguyen, L., Asara, J.M., Cantley, L.C., and Daley, G.Q. (2013). Lin28 enhances tissue repair by reprogramming cellular metabolism. *Cell* 155, 778–792.
- Soufi, A. (2014). Mechanisms for enhancing cellular reprogramming. *Curr. Opin. Genet. Dev.* 25, 101–109.
- Soufi, A., Donahue, G., and Zaret, K.S. (2012). Facilitators and impediments of the pluripotency reprogramming factors' initial engagement with the genome. *Cell* 151, 994–1004.
- Suvà, M.L., Rheinbay, E., Gillespie, S.M., Patel, A.P., Wakimoto, H., Rabkin, S.D., Riggi, N., Chi, A.S., Cahill, D.P., Nahed, B.V., et al. (2014). Reconstructing and reprogramming the tumor-propagating potential of glioblastoma stem-like cells. *Cell* 157, 580–594.
- Takahashi, K., and Yamanaka, S. (2006). Induction of pluripotent stem cells from mouse embryonic and adult fibroblast cultures by defined factors. *Cell* 126, 663–676.
- Teif, V.B., Vainshtein, Y., Caudron-Herger, M., Mallm, J.-P., Marth, C., Höfer, T., and Rippe, K. (2012). Genome-wide nucleosome positioning during embryonic stem cell development. *Nat. Struct. Mol. Biol.* 19, 1185–1192.
- Verrijzer, C.P., Alkema, M.J., van Weperen, W.W., Van Leeuwen, H.C., Strating, M.J., and van der Vliet, P.C. (1992). The DNA binding specificity of the bipartite POU domain and its subdomains. *EMBO J.* 11, 4993–5003.
- Wapinski, O.L., Vierbuchen, T., Qu, K., Lee, Q.Y., Chanda, S., Fuentes, D.R., Giresi, P.G., Ng, Y.H., Marro, S., Neff, N.F., et al. (2013). Hierarchical mechanisms for direct reprogramming of fibroblasts to neurons. *Cell* 155, 621–635.
- Wechsler, D.S., Papoulas, O., Dang, C.V., and Kingston, R.E. (1994). Differential binding of c-Myc and Max to nucleosomal DNA. *Mol. Cell. Biol.* 14, 4097–4107.
- Xu, H.E., Rould, M.A., Xu, W., Epstein, J.A., Maas, R.L., and Pabo, C.O. (1999). Crystal structure of the human Pax6 paired domain-DNA complex reveals specific roles for the linker region and carboxy-terminal subdomain in DNA binding. *Genes Dev.* 13, 1263–1275.
- Yu, J., Vodyanik, M.A., Smuga-Otto, K., Antosiewicz-Bourget, J., Frane, J.L., Tian, S., Nie, J., Jonsdottir, G.A., Ruotti, V., Stewart, R., et al. (2007). Induced pluripotent stem cell lines derived from human somatic cells. *Science* 318, 1917–1920.
- Zaret, K.S., and Carroll, J.S. (2011). Pioneer transcription factors: establishing competence for gene expression. *Genes Dev.* 25, 2227–2241.
- Zheng, R., Rebolledo-Jaramillo, B., Zong, Y., Wang, L., Russo, P., Hancock, W., Stanger, B.Z., Hardison, R.C., and Blobel, G.A. (2013). Function of GATA factors in the adult mouse liver. *PLoS ONE* 8, e83723.

Bending Gradients: How the Intestinal Stem Cell Gets Its Home

Graphical Abstract



Authors

Amy E. Shyer, Tyler R. Huycke, ...,
L. Mahadevan, Clifford J. Tabin

Correspondence

tabin@genetics.med.harvard.edu

In Brief

The buckling of the epithelial surface during the formation of intestinal villi creates pockets under the villus tips that concentrate the morphogen Shh, thereby restricting intestinal stem cells to the base.

Highlights

- The entire embryonic gut epithelium expresses intestinal stem cell (ISC) markers
- As villi form, BMP activity from underlying mesenchyme restricts ISCs to their base
- The mesenchymal Bmp expression is induced at villus tips by Shh from the endoderm
- Uniformly secreted Shh is concentrated by the physically driven villus architecture



Shyer et al., 2015, Cell 161, 569–580

April 23, 2015 ©2015 Elsevier Inc.

<http://dx.doi.org/10.1016/j.cell.2015.03.041>

Bending Gradients: How the Intestinal Stem Cell Gets Its Home

Amy E. Shyer,^{1,8} Tyler R. Huycke,¹ ChangHee Lee,¹ L. Mahadevan,^{2,3,4,5,6,7} and Clifford J. Tabin^{1,*}

¹Department of Genetics, Harvard Medical School, Boston, MA 02115, USA

²School of Engineering and Applied Sciences

³Department of Organismic and Evolutionary Biology

⁴Department of Physics

⁵Wyss Institute for Biologically Inspired Engineering

⁶Kavli Institute for Nanobio Science and Technology

Harvard University, Cambridge, MA 02138, USA

⁷Department of Systems Biology, Harvard Medical School, Boston, MA 02115, USA

⁸Present address: The Miller Institute for Basic Research in Science, Department of Molecular and Cellular Biology, University of California, Berkeley, Berkeley, CA 94720, USA

*Correspondence: tabin@genetics.med.harvard.edu

<http://dx.doi.org/10.1016/j.cell.2015.03.041>

SUMMARY

We address the mechanism by which adult intestinal stem cells (ISCs) become localized to the base of each villus during embryonic development. We find that, early in gut development, proliferating progenitors expressing ISC markers are evenly distributed throughout the epithelium, in both the chick and mouse. However, as the villi form, the putative stem cells become restricted to the base of the villi. This shift in the localization is driven by mechanically influenced reciprocal signaling between the epithelium and underlying mesenchyme. Buckling forces physically distort the shape of the morphogenic field, causing local maxima of epithelial signals, in particular Shh, at the tip of each villus. This induces a suite of high-threshold response genes in the underlying mesenchyme to form a signaling center called the “villus cluster.” Villus cluster signals, notably Bmp4, feed back on the overlying epithelium to ultimately restrict the stem cells to the base of each villus.

INTRODUCTION

Although studies of stem cells have revealed a great deal about maintenance and propagation, the origin of most adult stem cell populations remains an open question. Intestinal stem cells (ISCs) have been particularly well studied. A number of important factors have been described as being produced in the ISC niche to maintain their multipotency and proliferative potential, including canonical Wnt signaling (Spence et al., 2011). The identification of genetic ISC markers in the adult intestine, such as Lgr5, has made it possible to identify the location of these cells. In the adult Lgr5-positive ISCs reside in the intestinal crypt, found below the base of each (Barker et al., 2007). The earliest known expression of Lgr5 is just after birth in mouse (Kim et al., 2012). At

this time, Lgr5 is expressed at the base of each villus, where the crypt will soon form. However, the expression patterns of this and other adult stem cell markers in amniotic embryos have not been systematically studied, and indeed, whether or not Lgr5-positive cells are even present prior to birth has remained uncertain.

It is clear, however, that morphological villi arise before birth (or hatching in birds). Perhaps surprisingly, although stem cell proliferation and differentiation are critical for homeostatic maintenance of the villi, the initial formation of the villi does not appear to be a stem-cell-dependent phenomenon, at least in the chick. Morphogenesis of the lumen of the chick gut occurs in a stepwise progression wherein the initially smooth lining of the primitive gut tube is first transformed by compressive forces into a series of longitudinal parallel ridges. These are then deformed into a series of regular zigzag ridges. Finally, the zigzags segment to give rise to individual villi (Coulombre and Coulombre, 1958; Shyer et al., 2013) (Figure S1A). A similar process occurs in the formation of human villi (Hilton, 1902; Lacroix et al., 1984). The formation of the ridges is driven by the differentiation of the first circumferential smooth muscle layer of the intestine. This forms a barrier restricting further expansion as the inner submucosal and endodermal layers continue to proliferate, resulting in their buckling. Similarly, the zigzags form due to compressive forces generated by further submucosal and endodermal growth when the second longitudinal smooth muscle layer differentiates, creating orthogonal barriers to expansion in both the longitudinal and radial directions. Finally, the arms of the zigzags each give rise to individual villi as the third, innermost layer of longitudinal smooth muscle differentiates in the context of a decrease in proliferation along the top of the zigzags (Shyer et al., 2013). This previous study thus addressed the mechanism by which villi first form in the developing chick gut. However, this work begs the question of why proliferation suddenly drops at the tips of the folds at the zigzag stage and also leaves unanswered the critical question of how stem cells are localized to the base of the villi as they form. These issues are the focus of this current study.

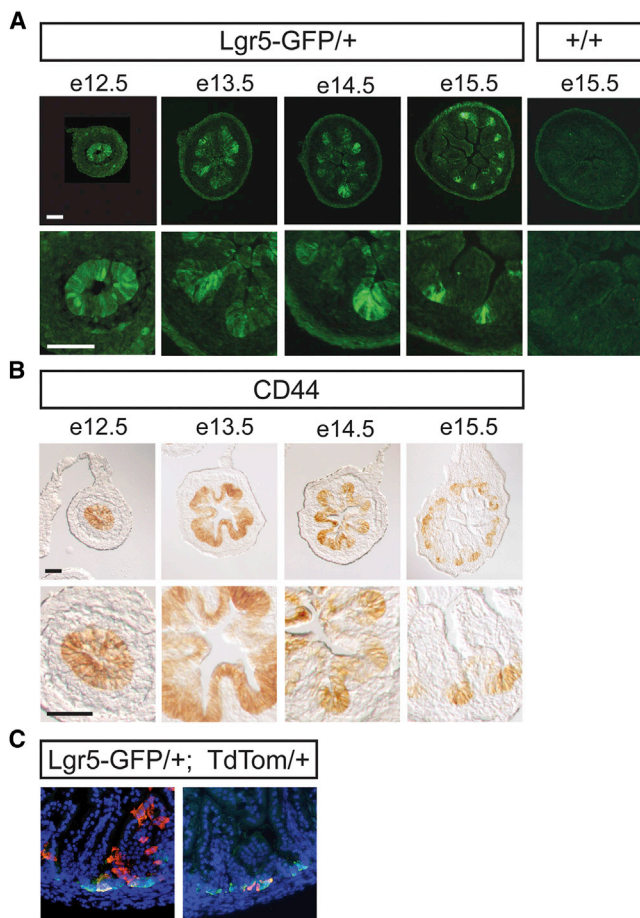


Figure 1. Intestinal Stem Cell Markers Are Expressed Uniformly in the Early Mammalian Embryo and Are Refined during Development

(A) Lgr5-EGFP-positive cells in heterozygous mouse intestines from E12.5 to E15.5. High-magnification views (below) show progressive restriction of expression from the villus tip. Sections from a littermate control lacking the knock-in allele (right column) show no GFP expression.

(B) CD44 immunohistochemistry in mouse intestines from E12.5 to E15.5. High-magnification views (below) show similar progressive restriction of expression from the villus tip.

(C) Sections of the intestine from two different P0 mice that resulted from crossing the Lgr5 knock-in allele containing an inducible Cre with a Rosa26-TdTomato floxed reporter after tamoxifen induction at E13.5. GFP represents Lgr5 expression at P0, and TdTomato indicates the location of cells and their descendants that expressed Lgr5 during induction at E13.5. Scale bars, 50 μ m.

RESULTS

Intestinal Stem Cell Markers Are Expressed Uniformly in the Early Mammalian Gut and Are Refined during Villus Formation

Although the definitive ISCs of the postnatal intestine are derived from the endoderm of the primitive gut tube and the early gut epithelium has been hypothesized to be a uniform stem-cell-like pool (Crosnier et al., 2006), it has remained unclear whether ISC markers are expressed at these early stages. To test this, we took advantage of a murine GFP knock-in allele of the best-stud-

ied ISC marker, Lgr5 (EGFP-IRES-creERT2) (Barker et al., 2007). Strikingly, Lgr5-expressing cells are found throughout the epithelium in the embryonic day 12.5 (E12.5) small intestine, just prior to villus formation (Figure 1A). Over the following days of development, Lgr5 expression is lost in the forming villus tip and is progressively restricted to the space between villi as they form (Figure 1A). A second ISC marker, CD44 (Itzkovitz et al., 2012), follows a similar progression albeit with slightly delayed kinetics (Figure 1B).

In the adult intestine, canonical Wnt signaling is essential for maintaining ISCs. In previous studies, markers for active Wnt signaling, such as Sox9, have been reported to be initially expressed uniformly throughout the embryonic gut but are then restricted to the intervillous space as villi form (Blache et al., 2004; Formeister et al., 2009; Furuyama et al., 2011). Moreover, previous reports have shown that epithelial proliferation follows the same progressive restriction from the tip of forming villi (Crosnier et al., 2006).

These data suggest that the ISCs localized at the base of the villi at birth are remnants of a broader precursor stem cell population found throughout the early gut endoderm. To directly test whether this is the case, we made use of the inducible Cre present in the Lgr5 knock-in allele and crossed it into the background of a Rosa26-TdTomato floxed reporter that is irreversibly activated in the presence of Cre recombinase, marking the cells in which Cre is expressed and also their descendants. We labeled cells by inducing Cre activity at E13.5, a stage when the entire epithelium is proliferative and expresses Lgr5. We then sectioned guts of postnatal animals, a time when stem cells are localized to the base of the villi and to the inter-villus regions, and examined them for TdTomato expression. We observed staining at the base of the villi that colocalized with Lgr5 expression and, in many cases, also saw staining along the sides of the villi (Figure 1C) even though, at this stage, the epithelial cells of the villi do not actively express Lgr5. As the epithelial cells of the villi at this stage are known to be derived from the stem cells at their base, these data indicate that the embryonically labeled Lgr5-positive cells are indeed the progenitors of the post-natal intestinal stem cells.

Although the villi in mouse appear to be established through similar compressive forces as in the chick (Shyer et al., 2013), they arise much more quickly and without the clear stepwise progression seen in the chick (Figure S1B). To investigate when in this process the stem cells are localized, we therefore switched systems to the chick.

Stem Cells Are Restricted Late in Chick Endodermal Morphogenesis as Zigzags Become Compact and Begin to Morph into Pre-villus Bulges

As Lgr5 expression is difficult to detect in the developing chick midgut, we utilized single-molecule fluorescent in situ hybridization (FISH) to locate Lgr5-expressing cells across chick intestinal development. Lgr5 is expressed uniformly throughout the early embryonic intestinal epithelium and continues as such through the early stages of epithelial morphogenesis into ridges and zigzags (Figures 2A and S2A). However, by E15, as the zigzags attain their maximal compaction just before they begin to morph into the bulges that will give rise to villi, Lgr5 expression is diminished in the tip of the epithelial fold. By hatching, expression is

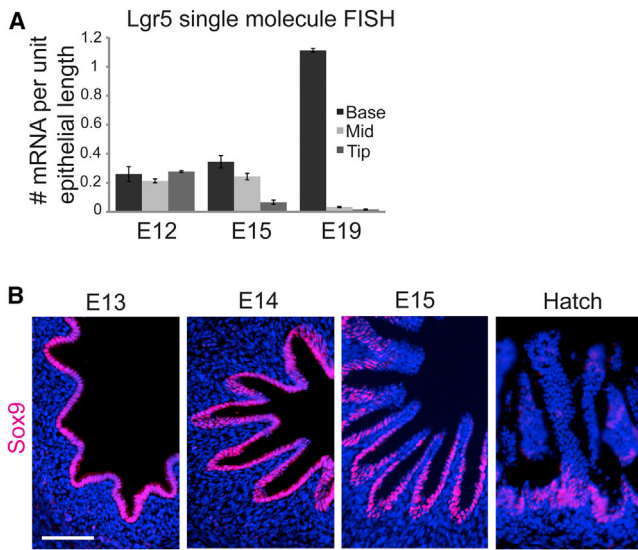


Figure 2. Restriction of Progenitor Identity Is Observed during the Slower Progression of Villus Formation in Chick

(A) Quantification of single LGR5 mRNA molecules per unit length across the base, middle, and tip of epithelial folds over time (quantifications were done on at least three gut samples for each stage). Data are represented as mean \pm 1 SD. See also Figure S2.

(B) Immunofluorescence for Sox9 in the chick intestine across development from E13 when expression is uniform in the epithelium through E15 when Sox9 is restricted from the tips of the folds and at hatch when Sox9 is expressed predominantly in the intervillous space. Scale bars, 50 μ m.

predominantly limited to the intervillous space (Figures 2A and S2A). Similarly, Sox9 is expressed uniformly in the early chick intestinal epithelium and is lost at the tips of the folds by E15 (Figure 2B). Thus, the localization of both putative stem cells and of the Wnt signaling that supports them becomes restricted just before the pre-villus bulges start to emerge. We have previously noted that this transition from zigzags to bulges also correlates with and, indeed, depends upon a progressive restriction of proliferation from the tips of the folded luminal surface E15 (Shyer et al., 2013).

A Signaling Center Correlating with the Timing and Localization of Stem Cells in the Forming Gut

A potential clue for how epithelial proliferation and stem cell identity might be regulated comes from the mouse, where lack of proliferation at the villus tip has previously been correlated with the presence of a signaling center in the distal mesenchyme of the nascent villi, called the “villus cluster” (Karlsson et al., 2000), which expresses PDGFR α , Gli1, Ptc1, Bmp2, and Bmp4 (Karlsson et al., 2000; Walton et al., 2012). In the chick, we find that the same suite of genes is expressed at a high level in the equivalent location at the tip of the highly folded epithelium at E15, although the same genes are expressed at a lower level at earlier time points in a narrow band directly under the entire epithelium (Figure 3A). The time when the villus cluster genes are upregulated is the same stage as when the overlying distal epithelium loses stem cell marker expression and as when proliferation decreases in the distal domain of the epithelium (Shyer et al., 2013).

The chick villus cluster includes cluster-specific expression of Foxf1, a transcription factor implicated in villi formation (Ormes-tad et al., 2006) but not previously observed in the cluster, as well as PDGFR α , Ptc1, and Bmp4 (Figure 3A). We also examined phospho-SMAD staining, as a reporter of Bmp activity, during chick gut morphogenesis. Phospho-SMAD reactivity is identified with a timing that correlates with the onset of high-level Bmp expression in the villus cluster and negatively correlates with the localization of Lgr5 expression (Figure 3B).

It has recently been shown that, in mouse, the villus cluster expression of Bmp4 and the general Shh target Ptc1 are downstream of hedgehog signaling (Walton et al., 2012; Ormestad et al., 2006). Moreover, it has long been known that, at earlier stages in chick gut formation, Sonic hedgehog (Shh) is responsible for inducing expression of Bmp4 in the underlying mesenchyme (Roberts et al., 1995). Accordingly, we find that, in the chick, villus cluster-specific expression of Ptc1 and BMP4, as well as Foxf1, is lost upon inhibition of Hedgehog signaling by cyclopamine and expanded in response to additional Shh protein (Figure 4A). As expected, the decrease or increase of Bmp4 expression, in response to cyclopamine or Shh, respectively, is reflected by a concomitant respective loss of or broadening of phospho-SMAD reactivity (Figure 4B).

A Feedback Loop from the Villus Cluster to the Epithelium Localizes Stem Cells to the Base of the Forming Villi

To test whether signals from the villus cluster, in fact, direct the fate of cells in the neighboring epithelium, we excised a small segment of intestine from an E14 chick embryo, when progenitors are uniformly distributed and before the villus cluster has formed, and manipulated cluster signals in vitro during 36 hr of culture. Control cultures display strong Edu labeling, which is indicative of proliferation exclusively at the base of the fold, just like their E15.5 in vivo counterparts (Figure 4C). However, culturing in the presence of the hedgehog inhibitor cyclopamine or the Bmp inhibitor Noggin results in expansion of proliferation throughout the endoderm, including the villus tips (Figure 4C). Conversely, in explants cultured in the presence Shh or Bmp4, proliferation is absent not just from the tips of the villi, but from the entire endodermal layer. As shown above, Shh activity is responsible for inducing Bmp4 expression in the underlying mesenchyme. To confirm this epistatic relationship in this context, we simultaneously treated cultures with both Shh and Noggin. Application of both Shh and Noggin to gut segments in culture mimics the effects of Noggin alone, maintaining proliferation throughout the endoderm (Figure 4C). Thus, as expected, endodermally derived Shh activity is upstream of mesenchymal Bmp4 expression, and Bmp4 activity represses endodermal proliferation.

Wnt signaling is an important niche signal for maintaining ISCs in the mature intestine. Moreover, mouse mutants with loss of villus cluster signals show an expansion of Wnt expression (Madison et al., 2005; Ormestad et al., 2006), suggesting that the presence of Bmp signaling at the tips of the villi may lead to the observed loss of ISCs in the overlying epithelium by reducing Wnt activity. Blocking Shh or BMP signaling resulted in uniform staining of the Wnt target Sox9 throughout the gut epithelium, whereas control gut tissue only showed Sox9 expression in the

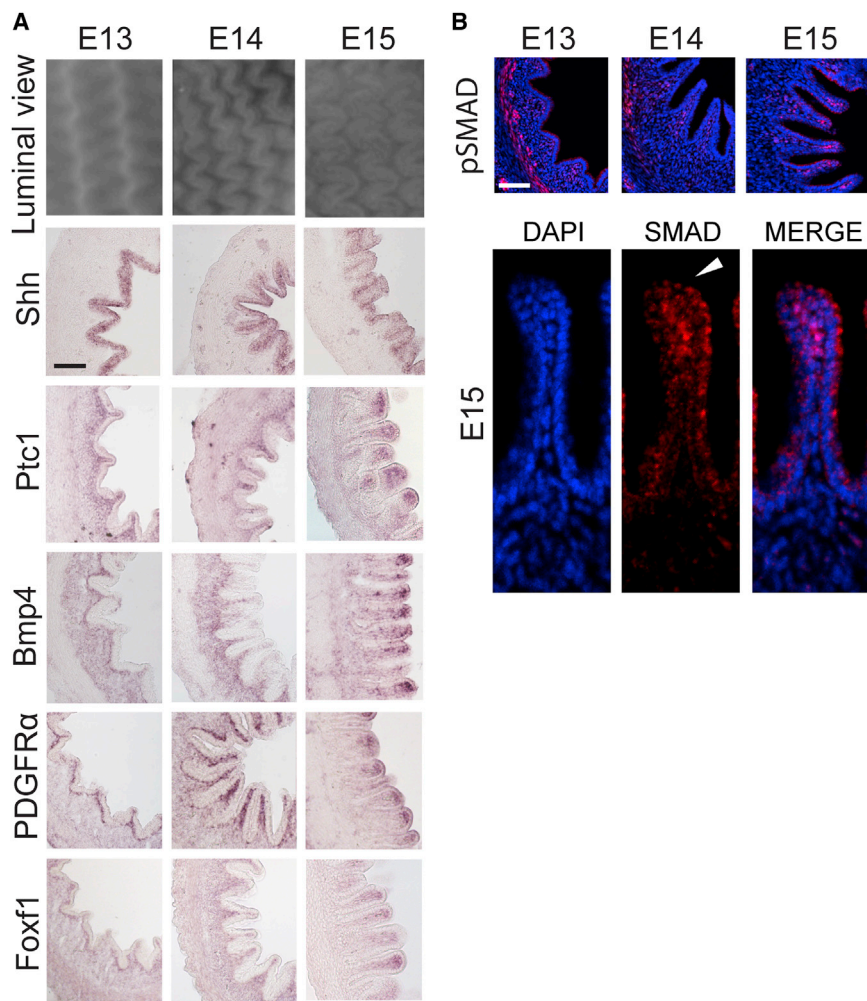


Figure 3. As the Proto-villi Form from E13 to E15, the Villus Cluster Signaling Center Forms in the Mesenchyme at the Distal Tip

(A) Luminal views of the zigzag topography from E13 to E15, and expression of cluster genes goes from uniform under the wide folds of the epithelium at E13 (left) to predominantly localized to the mesenchyme under the forming villi at E15 (right). (B) PhosphoSMAD staining demonstrates high BMP activity in the villus cluster and the adjacent epithelium. Close-up views (below) of a single fold at E15 highlight epithelial staining (arrowhead), which is less intense than staining in the mesenchymal cluster. Scale bars, 50 μ m.

derm at the stages of development under consideration (Figures 3B and 4A), yet the putatively Shh-dependent villus cluster genes are only induced at the distal tips of the villi. A plausible model explaining this localized, elevated response to Shh takes note of the fact that a uniformly secreted protein will be at a higher concentration in locations where the target tissue is surrounded by morphogen-producing tissue (e.g., at the curved tip of the highly folded epithelium) than where it is only adjacent to the source of the morphogen on one side (e.g., at the base of the folds). This is supported by computational modeling, which shows that a highly folded epithelium, or finger-like pocket, indeed results in both an increase in a morphogen concentration gradient and a greater depth of high-level signaling below the endoderm, relative to

lower half of the villi (Figure 4D). Conversely, in explants cultured in the presence of Shh or Bmp4, Sox9 is absent in the endodermal layer (Figure 4D).

To directly verify that this signaling cascade regulates ISC restriction, we assessed the expression of the ISC marker Lgr5 in the presence of repressed Shh activity. As anticipated, when cyclopamine is added, abolishing villus cluster gene expression, the resulting intestine segments maintain expression of Lgr5 throughout the folded epithelium, whereas expression is lost at the tip in control segments (Figures 4E and S2B).

Together, these results support a model in which Shh activity in the gut endoderm induces villus cluster gene expression in the subadjacent mesenchyme at the tips of the villi. This signal center then produces Bmp4, which reciprocally feeds back on the endoderm to block Wnt activity and hence repress ISC identity and cell proliferation at the distal end of the growing villi.

Physical Changes in the Morphology of the Lining of the Gut Create Local Maxima of Signaling Activity to Induce the Villus Cluster

There is, however, an obvious problem with this model: we have shown that Shh is expressed uniformly throughout the gut endo-

a similarly scaled, wider fold (Figure S3 and Extended Experimental Procedures). The slow, stepwise nature of villi formation in chick allows for a detailed investigation of this hypothesis for how the villus cluster arises. During the stages in which the lumen takes on an increasingly compact zigzag topography (E13, E14, and E15) we find that the cross-sectional shape of these structures changes in concert (low peak, narrow peak, and rounded tip, respectively) (Figures 5A and 5B). This would be predicted to lead to increasingly concentrated gradients of endodermally derived signaling at the tip (schematized in Figure 5B).

To directly test this idea, we examined the distribution of Shh with an antibody directed against this protein. Anti-Shh staining intensity was plotted along a line from the tip of the folded epithelium and orthogonal to it (Figure 5D). Prior to E15, anti-Shh reactivity is identified in the epithelium and the mesenchyme just subadjacent to the endoderm. However, at the transition from zigzags to bulges, the mesenchyme in the distal domain of the folded tissue showed significantly elevated Shh protein accumulation. In addition, the shape of the gradient tapers off much more slowly within the highly folded epithelium of the E15 gut than within the broader fold seen at E13. This is consistent with expectations,

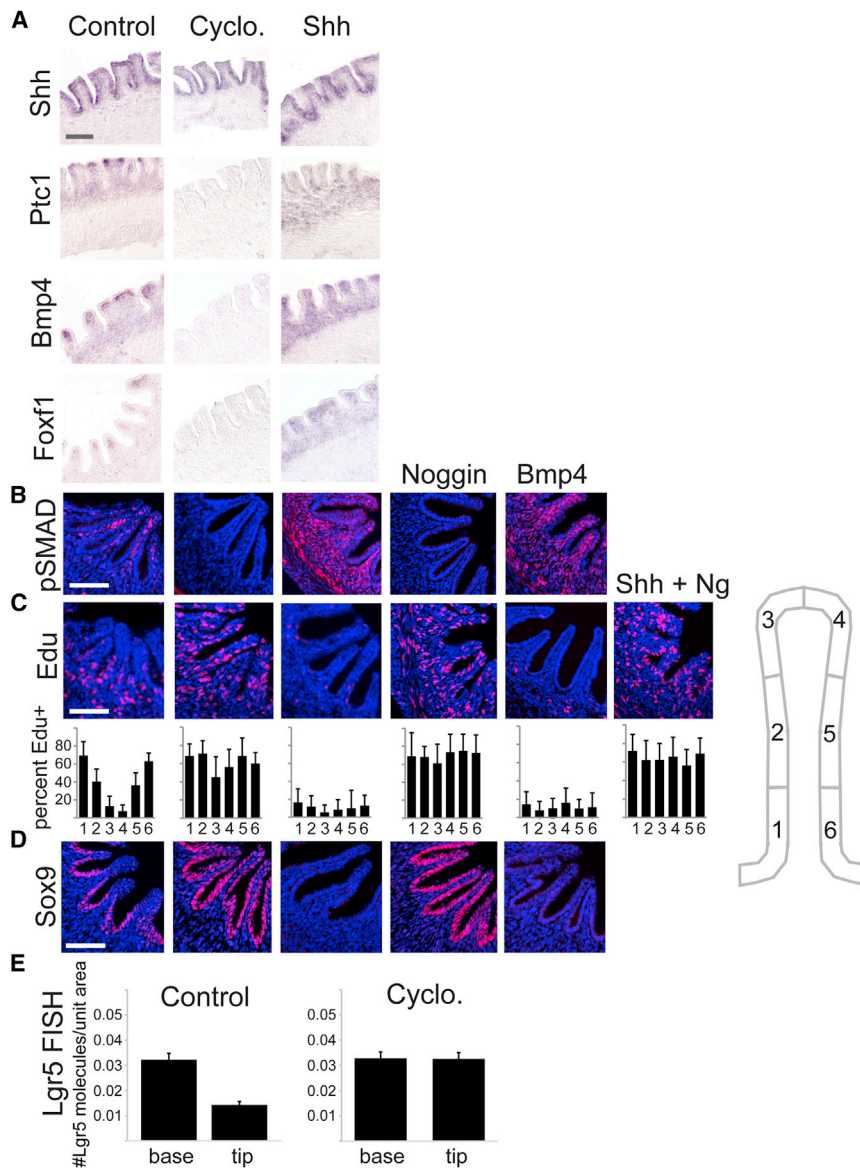


Figure 4. ISC Localization Is Regulated by BMP Signaling from the Underlying Mesenchymal Villus Cluster Signaling Center

(A) In situ hybridizations of E14 chick intestines cultured for 36 hr without (control) or with cyclopamine or recombinant Shh ligand.

(B) PhosphoSMAD staining of cultured samples demonstrates the impact of compounds and recombinant proteins on BMP activity.

(C) Edu labeling of E14 chick intestines cultured for 36 hr with the listed compounds and recombinant proteins. Below: quantification of percent Edu-positive cells across the sub-regions of epithelial folds, and at least three folds on each of three samples were counted.

(D) Sox9 staining of cultured samples demonstrates the effect of compounds and recombinant proteins on Wnt activity.

(E) Quantification of single-molecule FISH for LGR5 performed on sections from at least 3 E14 chick intestines cultured for 36 hr without (control) or with cyclopamine. See also Figure S2. Data are represented as mean \pm 1 SD. Scale bars, 50 μ m.

If the mesenchyme responds to Shh by activating villus cluster genes at a high threshold concentration, this would explain the observed localization of high-level villus cluster gene expression. Indeed, examination of the expression pattern of villus cluster markers such as PDGF α and Bmp4 gives results consistent with this model (Figure 5C). Consistent with epithelial morphogenesis acting upstream of increased Shh signaling and hence villus cluster gene activity, and not vice versa, after treating with cyclopamine to block hedgehog signaling, we observed no alteration in the global structure of the epithelium or in individual epithelial or mesenchymal cell shape, using membrane-bound β -catenin to outline cell contours (Figure S4).

since—in addition to Shh protein diffusing from the tip—the mesenchyme within the narrowly folded E15 epithelium is exposed to Shh secreted from the epithelium lateral to it, augmenting the gradient. At both stages, the highest level of Shh staining is observed within the epithelium itself, which is to be expected as the antibody will detect both extracellular and intracellular protein in the tissue producing the Shh. Importantly, however, the level of Shh produced by the epithelium, averaged for the nine sections assayed at each time point, is equivalent at E13 and E15. To further verify that the architecture of the tissue affects Shh protein accumulation, we compared the concentration of Shh protein 5 microns below the tip of the epithelial fold at E15 versus the concentration present at the same distance below the base of the fold. As expected, the intensity of staining is much higher within the fold, providing a mechanism explaining localized high-level Shh signaling at the epithelial tips.

To test whether the bending of the epithelium into more tightly curved domains, with consequent high levels of localized signaling, is indeed responsible for the upregulation of villus cluster genes in the tips of these structures, we undertook a simple experimental manipulation designed to “open” the normally tightly folded epithelium. Ringlets of embryonic intestine were excised at E14 and placed into culture in vitro. The folds in the epithelium arise due to constraint on the proliferating inner layers by subadjacent differentiated smooth muscle (Shyer et al., 2013). To alter this physical constraint, half of the rings were turned inside out, putting the endoderm and mesenchyme outside of the rings of smooth muscle, allowing the epithelium more length to take on a less folded form (Figure 6A). Following 36 hr of culture, the inside-out ringlets indeed had a broader contour than their right-side-out counterparts. After culture, the ringlets were sectioned and processed for in situ hybridization with

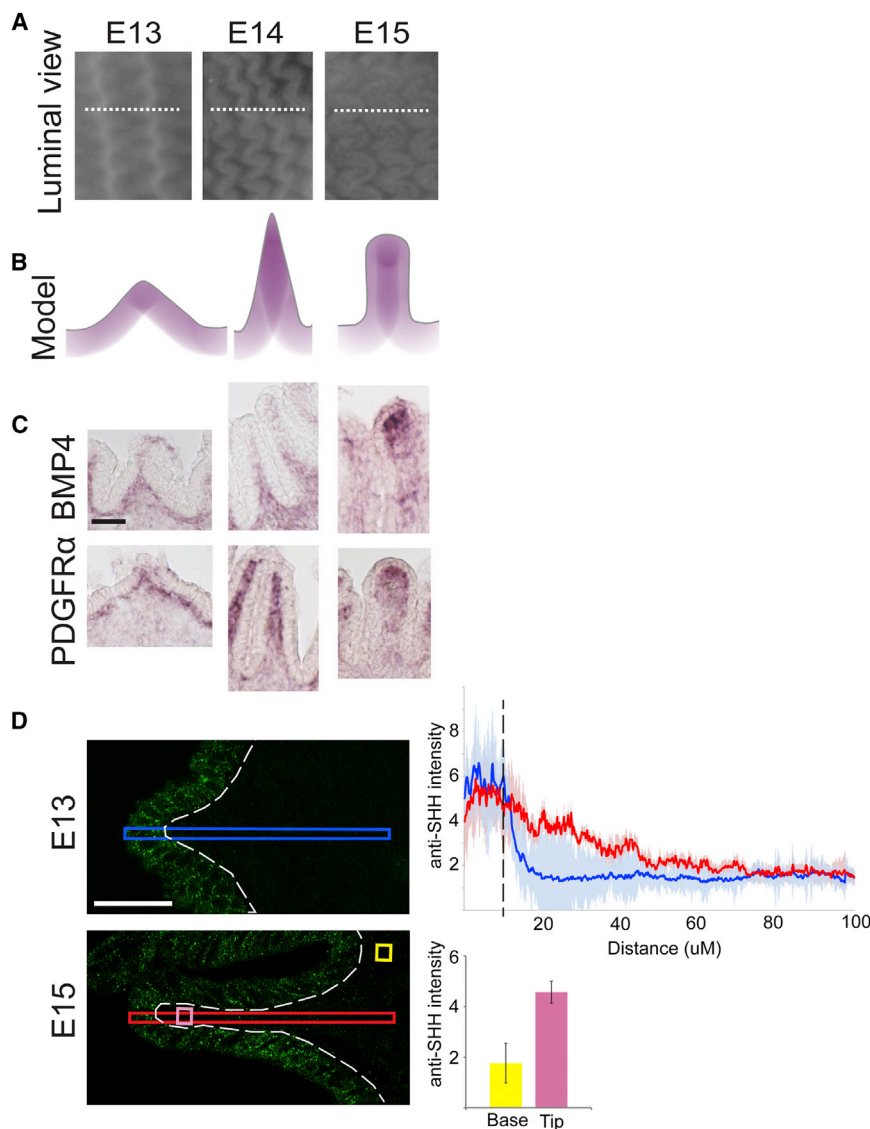


Figure 5. Non-uniform Mesenchymal Signals Are Downstream of Uniform Epithelial Signal

(A) Luminal views of the chick intestine from E13 to E15, as progenitor identity is lost from the tips of the folds (also shown in Figure 3A). Dotted lines represent the plane of section for transverse views in (B)–(D).

(B) Schematic of diffusion of signal from an epithelium of the particular shape at each stage; darker color represents more signal. Note the increasing signal overlap in the underlying mesenchyme as the fold narrows. See also Figure S3.

(C) In situ hybridization for Bmp4 (above) PDGFRα (below) expression from E13 to E15 matches the predicted pattern in (B) (also shown in Figure 3A).

(D) Distribution of Shh protein in folded tips of the chick intestine at E13 and E15 (left). Antibody staining intensity across the 100 μm region boxed on the left was quantified using the Plot Profile function in Fiji (right). Brightness values were normalized to background levels for each image. A comparison of Shh staining intensity in E13 (graphed in blue) versus E15 (graphed in red) shows increased Shh staining in the E15 mesenchyme (dotted line denotes epithelial-mesenchymal border). The staining intensities across the E13 and E15 epithelia are not significantly different ($p < 0.08$). Three different z slices from each of three samples were averaged for each stage. Below, the staining intensity found in a 5 μm by 5 μm region that is 5 μm from the E15 tip epithelium (pink) is significantly brighter than in the same-sized region 5 μm from the E15 base epithelium (yellow) ($p < 0.001$). Measurements from two different z slices from each of three samples were averaged for each E15 region. Data are represented as mean \pm 1 SD. Scale bars, 25 μm.

various villus cluster probes (Ptc1, Bmp4, PDGFRα, and Foxf1). Each of these was strongly expressed at the fold tips of the control ringlets, but all were expressed uniformly at a lower level under the epithelium in the inside-out ringlets (Figure 6B). Moreover, phospho-SMAD staining, indicative of Bmp upregulation in villus clusters, is also greatly diminished in the inside-out ringlets relative to control cultures (Figure 6B). These results suggest that the villus cluster forms in the mesenchyme at the tip of the fold because those cells are almost completely encapsulated by Shh-expressing epithelium, allowing high threshold responses to be activated.

Preventing villus cluster formation by flipping the intestines inside out results in an absence of the localized Bmp signal that we demonstrated is responsible for restricting ISC localization within the gut epithelium. Thus, the inside-out ringlets of guts would be expected to maintain stem cell properties and proliferation throughout their epithelium. Indeed, such manipulations

lead to maintenance of uniform proliferation throughout the epithelium, whereas proliferation is lost in the epithelium surrounding the cluster that forms in control rings (Figure 6B). Similarly, uniform expression of the Wnt target Sox9 and the ISC marker Lgr5 is maintained in the inside-out guts lacking villus cluster gene expression, whereas it is restricted from the folded tips in controls (Figures 6B and S2C).

As a second way of preventing late stages of epithelial morphogenesis, we took advantage of a drug, FK506, that has been shown to block smooth muscle differentiation (Fukuda et al., 1998). As we previously showed (Shyer et al., 2013), differentiation of smooth muscle layers is necessary for generation of the compressive forces that buckle the endoderm into ridges, zigzags, and then villi. We cultured guts in vitro from ridge stage to late zigzag stage, with or without the presence of FK506. Consistent with the results described above, without longitudinal muscle differentiation, and hence without progressing beyond parallel ridges, the entire endoderm remains proliferative, and villus cluster genes are never upregulated. As in vivo, control

cultures display restricted distal proliferation and activation of villus cluster gene expression (Figure S5).

These results indicate that the three-dimensional folding of the epithelium is necessary to locally increase Shh signaling (as seen in *Ptc1* expression) and induce the villus cluster genes. To see if it is also sufficient, we sought to create villus-like structures at a stage when the epithelium is normally not as tightly folded. Slabs of embryonic gut were excised at E10, when the gut is folded into several wide ridges, and placed into culture *in vitro*. Half of the slabs were placed under a fine grid, causing the luminal surface to fold, with continued growth, into many small villus-like bumps, long before endogenous villus formation takes place (Figure 6C). Slabs were cultured for 36 hr and then processed for *in situ* hybridization with various villus cluster probes (*Ptc1*, *Bmp4*, *Foxf1*, and *PDGFR α*). After 36 hr in culture, there is no change in expression of Shh itself, which continues to be expressed uniformly in the epithelium under these conditions (Figure 6D). However, while villus cluster gene expression in control segments is nearly uniform at a low level under the epithelium, samples grown under the grid display elevated expression in the mesenchyme under areas of highest epithelial curvature. PhosphoSMAD staining is observed in the same locations reflecting the change in BMP pathway activity (Figure 6D). Therefore, simply morphing the tissue into the necessary shape can induce villus cluster-like local maxima of Shh responsive genes. Further, whereas proliferation and *Sox9* expression are uniform in the control epithelium, in the samples cultured under the grid, proliferation and *Sox9* expression are lost from the tips of the folds, surrounding the areas where mesenchymal expression of cluster genes is highest (Figure 6D).

Taken together, these results demonstrate that the villus cluster genes are induced at local maxima of Shh activity, resulting from the additive effect of signaling that is compounded through the folding of the overlying epithelium.

Villus Formation in the Mouse

To examine the universality of the mechanism we have described, we returned to the developing mouse gut. As previously described (Sbarbati, 1982; Walton et al., 2012; Shyer et al., 2013), the villi of the embryonic mouse gut form directly within the lumen without going through intermediate ridge and zigzag stages of epithelial folding. A critical question, in terms of the model we derived from the chick, is whether the epithelium buckles prior to expression of the villus cluster genes in mouse. To address this, we serially sectioned E14.5 mouse guts and carefully examined each section. This is the stage when villi first arise in the mouse midgut, forming in a rostral to caudal progression. Thus, at this stage, the caudal-most region of the small intestine exhibits no epithelial projections (Figure 7A). Consistent with our previous studies showing that smooth muscle differentiation is required for villus formation (Shyer et al., 2013), we also see no evidence of the longitudinal smooth muscle in this domain, using smooth muscle actin (SMA) as a marker (Figure 7A). More rostrally, we see the first buckling of the endoderm into small “alcoves,” concomitant with the first appearance of the longitudinal smooth muscle staining (Figure 7B). However, careful examination of serial sections fails to detect any sign of expression of upregulation of the villus cluster gene *PDGFR α*

at this rostrocaudal level (Figure 7B). It is only when one moves still further rostrally that one sees deeper alcoves displaying strong *PDGFR α* expression at their tips (Figure 7C). Thus, epithelial morphogenesis precedes villus cluster gene activation. These descriptive data are at least consistent with the activation of villus cluster gene expression in the mouse being a consequence of higher level Shh signaling in pockets of buckled epithelium.

To directly test whether changing the architecture of the epithelium would affect villus cluster gene expression in the mouse, we returned to the experiment, creating premature pseudo-villi in the mouse gut by forcing growth through a fine grid at E13.5, prior to epithelial buckling. As in the chick, following 24 hr of incubation, the luminal surface folded into many small villus-like bumps extending through the holes in the grid. Whereas control guts did not show any signs of villus cluster gene expression following culture, samples grown under the grid showed strong upregulation of *PDGFR α* at the tip of each pseudo-villus (Figure 7D).

As described above, both proliferation and the stem cell marker *Lgr5* are restricted from the tips of the forming mouse villi once villus cluster gene expression is activated. To see whether, as in chick, this is due to high-level Shh signaling, we cultured developing mouse guts *in vitro* and blocked the Shh pathway with cyclopamine. Cyclopamine treatment was sufficient to expand both proliferation and expression of stem cell markers, *CD44*, *Sox9*, and *Lgr5*, in the tips of the forming villi in the treated guts, whereas control guts cultured in the absence of cyclopamine appeared similar to their *in vivo* counterparts (Figure 7E).

These data support the hypothesis that, as in chick, it is mechanical deformation of the gut epithelium that leads to high concentrations of Shh, hence induction of villus cluster genes in the mesenchyme and consequent restriction of stem cells in the underlying endoderm.

DISCUSSION

Our study has elucidated a series of steps integrating physical morphogenesis of the gut epithelium with restriction of stem cells to the base of the forming villi. Shh expressed by the endoderm is concentrated toward the tips of the buckling epithelial layer because of the repositioning of the source of the signal to surround the distal mesenchyme. This results in the induction of a signaling center, the villus cluster, as a high-threshold response. *Bmp* activity, emanating from the villus cluster, acts to oppose Wnt signaling and thereby leads to the sequestering of Wnt-supported proliferative ISCs to the base of the villi.

Localization of ISCs in Mice

Intriguingly, although the intestinal lining of both birds and eutherian mammals is characterized by the presence of long finger-like villi, this morphology appears to have evolved convergently, as the gut morphology of lower animals, including fish (Walker et al., 2004), amphibians (McAvoy and Dixon, 1978), reptiles (Ferri et al., 1976; Kotzé and Soley, 1995), and even monotremes (Krause, 1975), include various forms of ridges and folds to increase the surface area of the lining of the gut, but not individual villi. The tight packing and long projections of individual villi that

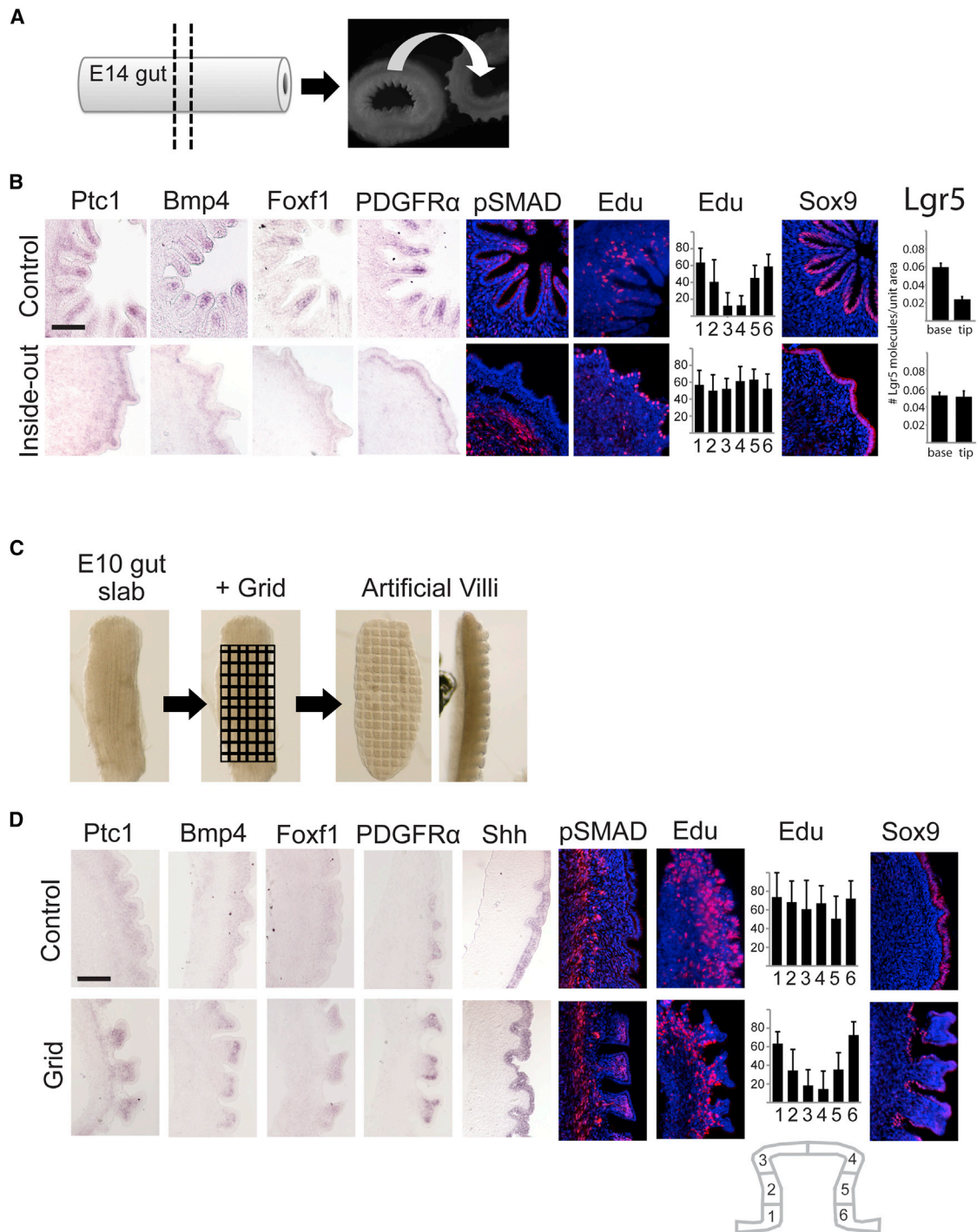


Figure 6. Epithelial Shape Directs Cluster Formation

(A) Experimental schematic: a ring of E14 intestine (left) is cultured for 36 hr either as a control segment or after first being flipped inside out (right).

(B) After 36 hr in culture, the cluster signal arises in the control rings (top), similar to what would be found in an E15 intestine. The rings that were flipped inside out before culture have an epithelial shape similar to E13 intestine and, concomitantly, an in situ pattern and phosphoSMAD staining that matches expression at E13. Proliferation (quantified as in Figure 4), Sox9 expression, and Lgr5 expression are all lost from the tips of folds that form in the control rings. See also Figure S2.

(C) Experimental schematic: a slab of E10 intestine (left) is cultured for 36 hr either as a control segment (where wide ridges will be maintained) or under a fine grid that induces many small villi-like bumps (right).

(legend continued on next page)

represent an optimized solution for increasing surface area (hence allowing maximal absorption of nutrients) may have been selected for independently in the two most highly metabolic lineages, mammals and birds. The stepwise progression of mucosal folds from ridges to zigzags to villi has been well described in the chick (Coulombre and Coulombre, 1958). A similar series of transitions, involving segmentation of pre-villus ridges to form villi, has been described for several mammals, including cattle (Winkler and Wille, 1998) and humans (Hilton, 1902; Lacroix et al., 1984). In striking contrast, the villi of the murine intestine form directly from the floor of a smooth epithelium (Sbarbati, 1982). The process of villus formation in the mouse does, nonetheless, share at least some mechanistic aspects with the chick and other guts where villi form via segmentation. In both chick and mouse embryonic gut, villus formation is prevented by blocking differentiation of the smooth muscle (which, at least in chick, acts as a barrier to expansion of the epithelium, thereby causing mucosal buckling). Moreover, modeling of the physical properties of the embryonic mouse intestine indicates that compressive mechanical forces induced by constrained growth are sufficient to explain the emergence of villi in mice as in chick (Shyer et al., 2013).

Consistent with this, we found that, concomitant with smooth muscle differentiation, the mouse epithelium buckles into small alcoves that could, in principle, lead to local elevated concentrations of Shh protein prior to the onset of villus cluster gene expression. As in the chick, stem cell markers and Wnt-responsive genes are expressed uniformly throughout the gut epithelium prior to this point and are downregulated at the tips of the forming villi as the villus cluster genes are expressed. Also, as in the chick, blocking the Shh pathway, and thus downstream BMP signaling, is sufficient to expand proliferation and the expression of *Lgr5*, suggesting that the presence of Shh signaling normally acts to restrict them from the villus tips. Finally, creating villus-like structures prematurely results in the upregulation of a marker of the villus cluster through geometric constraint. Although the central features involved in gut stem cell localization during villus formation, thus, appear to be the same in mice and chicks, there is some evidence that there may be differences as well. For example, formation of the villus cluster in the mouse appears to involve cell aggregation (Walton et al., 2012), as well as induction of gene expression, a feature we have not observed in the chick. Further work will be required to gain a fuller picture of how villus formation and stem cell location are achieved in mice and to integrate other findings with the results described here.

Bmp Antagonism of Wnt Activity in Restricting Proliferation and Stem Cell Activity

Our data show that the net result of the Shh-Bmp signaling cascade is a restriction of proliferation, as well as a decrease in expression of Wnt-dependent stem cell markers at the tips

of the developing epithelial folds. We did not, in the context of this study, explore how this is achieved. However, a similar Bmp antagonism of Wnt activity has previously been described in the context of the adult intestinal stem cell niche. As we observed embryonically, Bmp ligands are also strongly produced by the inter-villus mesenchyme near the tips of the adult villi with a decreasing gradient toward the crypts (He et al., 2004; Hardwick et al., 2004; Haramis et al., 2004; Batts et al., 2006). Moreover, this Bmp activity in the adult villus acts to suppress Wnt signaling to control the balance of stem cell renewal and differentiation (He et al., 2004). In this context, the Bmp and Wnt pathways are integrated intracellularly at the level of a PTEN/Akt-dependent mechanism (Tian et al., 2005). It seems likely that this same or a similar mechanism is employed downstream of Bmp activity at the earlier stage investigated here.

Mechanically Based Induction of Gene Expression

The physical reshaping of morphogenic gradients represents an intriguing paradigm in the integration of mechanics and developmental signaling. Of course, in addition to this mechanism, many instances have been described wherein forces impact gene expression through mechanosensory signal transduction. In a formal sense, it is certainly possible that mechanosensory signaling also contributes to the activation of target gene expression during gut epithelial morphogenesis. However, we emphasize that ectopic action of Shh is sufficient to induce villus cluster gene expression and to restrict the location of stem cells and proliferation, while blocking Shh activity is sufficient to result in a loss of villus cluster gene expression and expansion of proliferation and stem cell localization. Moreover, addition of cyclopamine has no effect on the contour of the epithelium or the shape of individual epithelial cells (Figure S4). As the epithelium is bent equivalently under conditions with or without cyclopamine, the cells should be seeing equivalent strains and stresses, and hence similar mechanosensory signaling. Yet the cultures with cyclopamine lose villus cluster gene expression, whereas control cultures do not, clearly indicating that there is at least a major part of the process that is independent of mechanosensory transduction.

Initiation of Discrete Signaling Centers

Mesenchymal-epithelial crosstalk is an established principle in developmental biology—for example, the positive feedback loop between the mesenchymal zone of polarizing activity (ZPA) and epithelial apical epidermal ridge (AER) in limb development (Laufer et al., 1994; Niswander et al., 1994) or the reciprocal epithelial-mesenchymal signaling in tooth germ formation (Theis, 2003). A number of mechanisms have been described for establishing the localized signaling centers necessary for such interactions. These include reliance on upstream positional information, such as the posterior pre-pattern of Hox gene expression necessary to establish the mesenchymal ZPA signaling

(D) After 36 hr in culture, the cluster gene expression and phosphoSMAD staining in control segments is nearly uniform under the epithelium. However, samples grown under the grid form villi-like bumps and display non-uniform expression of cluster genes and BMP activity with highest expression in areas of highest curvature. Proliferation and Sox9 expression are uniform in the control epithelium, but in the samples cultured under the grid, proliferation and Sox9 expression are lost from the tips of folds that form particularly in areas where the curvature is highest and where clusters of mesenchymal expression arise. Data are represented as mean \pm 1 SD. Scale bars, 50 μ m.

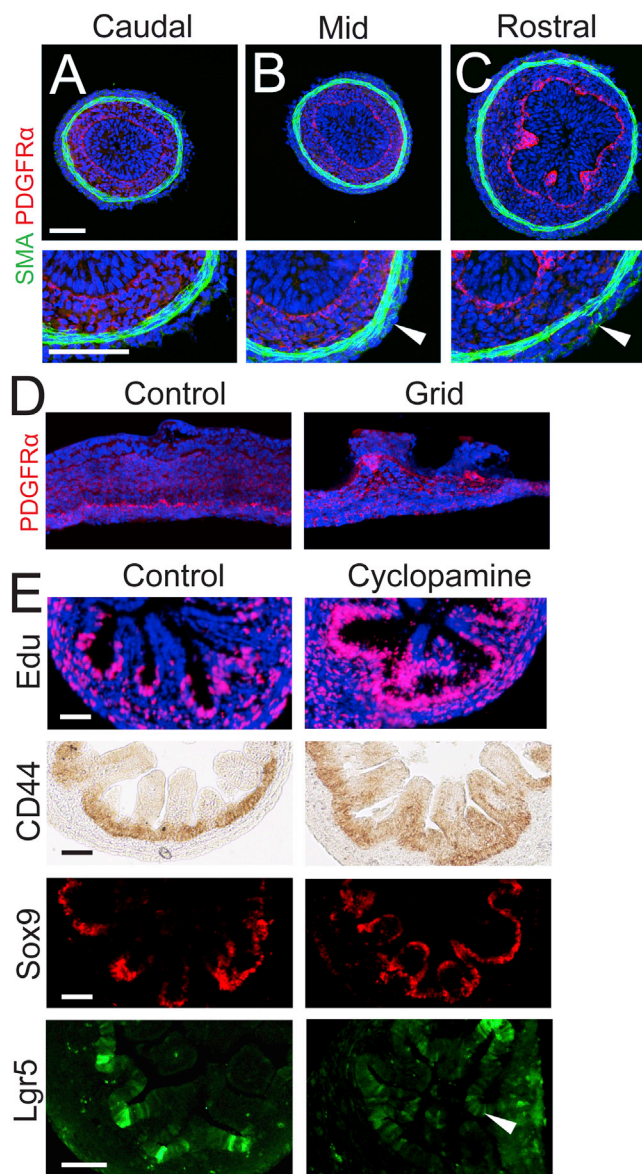


Figure 7. Epithelial-Mesenchymal Signaling in a Deforming Field Drives Localization of Intestinal Stem Cells in Mouse

(A) The caudal-most region of the small intestine exhibits no epithelial projections and no evidence of the outer, longitudinal smooth muscle in this domain, using SMA as a marker.

(B) More rostrally, the first buckling of the endoderm is observed concurrent with the first appearance of the longitudinal smooth muscle staining; however, no cluster expression of PDGFR α at this rostrocaudal level is seen, demonstrating that epithelial morphogenesis precedes villus cluster gene activation. (C) Even more rostrally, where additional longitudinal smooth muscle differentiation has occurred, deeper alcoves display strong villus cluster gene expression at their tips. Close-up views of the developing outer, longitudinal smooth muscle layer (arrowheads) are shown below.

(D) Villus-like structures were generated through constraint with a mesh grid, resulting in the upregulation of the villus cluster marker PDGFR α when compared to control cultures grown without the grid.

(E) Application of cyclopamine to E14.5 mouse guts grown in culture for 30 hr results in maintenance of progenitor identity at the tips of forming villi. Proliferation (Edu), Wnt responsiveness (Sox9), and stem cell markers (CD44 and

center in the limb (Charité et al., 1994; Knezevic et al., 1997), and lateral inhibition such as that seen in setting up the spacing of the enamel knot signal centers in tooth bud development (Salazar-Ciudad, 2012). However, the work here highlights a different mechanism involving the use of a uniformly produced signal, concentrated not by diffusion or feedback loops but by physical deformation of the morphogenic field. Employing the shape changes of the developing tissue to dictate where signals arise artfully links the process of building a structure with the proper placement of its molecularly defined cell types. In the case of the intestine, this mechanism assures that specialized cells, like ISCs, end up in the right location at the base of each villi as these structures take shape. Recently, it has been shown that tissue architecture can similarly concentrate signaling in the context of the developing zebrafish lateral line (Durdu et al., 2014), although, in this instance, the mechanisms that create the luminal pockets where morphogens can accumulate remain unclear and may not be related to upstream physical forces. Together, these studies suggest that local trapping of a broadly secreted signal may be a mechanism that is widely employed in a variety of embryological contexts.

Finally, this study elucidates the embryonic origin of the localized adult intestinal stem cells. Because the origins of most adult stem cell populations are still unknown, our findings compel investigation into potential embryonic origins for other adult stem cells.

EXPERIMENTAL PROCEDURES

Embryos and Dissections

Fertile chicken eggs (White Leghorn eggs) were obtained from commercial sources. Eggs were incubated at 37.5°C. Timed pregnant CD1 mice were obtained from Charles River.

Immunohistochemistry and Edu Staining

Small intestines were collected from embryos at desired stages and fixed in 4% paraformaldehyde in PBS and embedded in OCT, allowing for 14 μ m transverse sections of the gut tube. CD44 immunohistochemistry was performed with rat anti-CD44 (v6) (1:100 Biosciences) and detected using the Anti-Rat HRP-DAB Cell & Tissue Staining Kit (R&D Systems). The following antibodies were used for immunofluorescence staining at the listed concentrations: Sox9 (1:100, R&D Systems), β -catenin (1:100, Sigma), PDGFR α (1:100 in chick, 1:300 in mouse, Santa Cruz), FITC-conjugated smooth muscle actin (1:100, Abcam), phospho-SMAD 1/5 (1:300, Cell Signaling), and Shh (5E1, 1:20). Sections were incubated with primary antibody overnight at 4°C degrees and then incubated with Alexa secondary antibodies used at 1:300 for 2 hr at room temperature. DAPI (molecular probes) was used as a nuclear counter stain. 100 μ M Edu (Invitrogen) was added to guts in culture, and samples were harvested after 4 hr of Edu incubation. Edu was detected in sectioned tissue using the Click-iT Edu system (Invitrogen).

In Situ Hybridization and Single-Molecule FISH

Tissue samples for section in situ hybridization were fixed overnight in 4% PFA. After fixation, the tissue was rinsed in PBS and incubated in 30% sucrose overnight at 4°C before being embedded in OCT. 14- μ m-thick cryosections were collected for DIG-labeled RNA in situ and 10- μ m-thick sections were collected for single-molecule FISH. DIG-labeled in situ were performed as described previously (Brent et al., 2003). Single-molecule FISH experiments

LGR5) are all found along the folded epithelium (arrowhead) when cluster signals are blocked. Control segments show proper restriction to the base of folds. Scale bars, 50 μ m.

were performed according to Raj et al. (2008) and Itzkovitz and van Oudenaarden (2011).

Organ Culture

Chick intestines were dissected from the embryos of the desired stage in cold PBS, connective tissue was removed, and segments of intestines were placed on transwells (Costar 3428) or floating above an agar base in DMEM media supplemented with 1% pen/strep and 10% chick embryonic extract. Chick intestines were cultured for 36 hr (or as indicated in the figure legends) at 37°C with 5% CO₂. Inside-out intestines were obtained by gently coaxing a ring of intestine to invert with forceps. To generate guts with artificial villi, segments of intestine were harvested from E10 embryos, when several ridges are present. These segments were sliced open to create a slab of intestine that was placed lumen side up on a transwell. A small piece of fine mesh was placed gently on top of the slab to induce villi-shaped bumps in culture. Mouse intestines were dissected from embryos and cultured in DMEM media supplemented with 1% pen/strep and 20% FBS in a BTC Engineering rotating incubator with 95% O₂. Recombinant ligands: Shh (4 µg/ml; R&D Systems) and BMP (1 µg/ml R and D Systems), and Inhibitors: cyclopamine (10 µM EMD Biosystems) and Noggin (1 µg/ml R and D Systems) FK506 (10 µM Sigma) were added at the beginning of culture.

SUPPLEMENTAL INFORMATION

Supplemental Information includes Extended Experimental Procedures and five figures and can be found with this article online at <http://dx.doi.org/10.1016/j.cell.2015.03.041>.

ACKNOWLEDGMENTS

We thank Alan Rodrigues and Sandy Klemm for assistance with single-molecule FISH probe design and experiments, Jessica Lehoczy for help with mice, Maxwell Heiman for the use of his microscope, and Jinhyun Choo for help with the simulation. We also thank D. Gumucio and K. Walton for discussions and for sharing data prior to publication. This work was supported by grants from the NIH (HD047360) to C.J.T. and the MacArthur Foundation to L.M.

Received: June 17, 2014

Revised: October 28, 2014

Accepted: February 11, 2015

Published: April 9, 2015

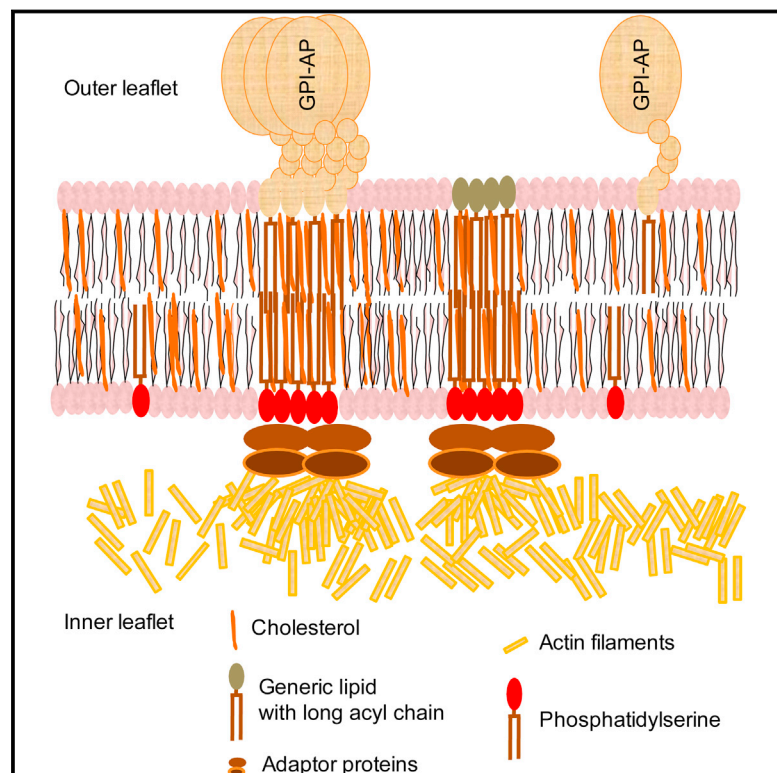
REFERENCES

- Barker, N., van Es, J.H., Kuipers, J., Kujala, P., van den Born, M., Cozijnsen, M., Haegebarth, A., Korving, J., Begthel, H., Peters, P.J., and Clevers, H. (2007). Identification of stem cells in small intestine and colon by marker gene Lgr5. *Nature* 449, 1003–1007.
- Batts, L.E., Polk, D.B., Dubois, R.N., and Kulessa, H. (2006). Bmp signaling is required for intestinal growth and morphogenesis. *Dev. Dyn.* 235, 1563–1570.
- Blache, P., van de Wetering, M., Duluc, I., Domon, C., Berta, P., Freund, J.N., Clevers, H., and Jay, P. (2004). SOX9 is an intestine crypt transcription factor, is regulated by the Wnt pathway, and represses the CDX2 and MUC2 genes. *J. Cell Biol.* 166, 37–47.
- Brent, A.E., Schweitzer, R., and Tabin, C.J. (2003). A somitic compartment of tendon progenitors. *Cell* 113, 235–248.
- Charité, J., de Graaff, W., Shen, S., and Deschamps, J. (1994). Ectopic expression of Hoxb-8 causes duplication of the ZPA in the forelimb and homeotic transformation of axial structures. *Cell* 78, 589–601.
- Coulombre, A.J., and Coulombre, J.L. (1958). Intestinal development. I. Morphogenesis of the villi and musculature. *J. Embryol. Exp. Morphol.* 6, 403–411.
- Crosnier, C., Stamatakis, D., and Lewis, J. (2006). Organizing cell renewal in the intestine: stem cells, signals and combinatorial control. *Nat. Rev. Genet.* 7, 349–359.
- Durdu, S., Iskar, M., Revenu, C., Schieber, N., Kunze, A., Bork, P., Schwab, Y., and Gilmour, D. (2014). Luminal signalling links cell communication to tissue architecture during organogenesis. *Nature* 515, 120–124.
- Ferri, S., Junqueira, L.C.U., Medeiros, L.F., and Medeiros, L.O. (1976). Gross, microscopic and ultrastructural study of the intestinal tube of *Xenodon merremii* Wagler, 1824 (Ophidia). *J. Anat.* 121, 291–301.
- Formeister, E.J., Sionas, A.L., Lorange, D.K., Barkley, C.L., Lee, G.H., and Magness, S.T. (2009). Distinct SOX9 levels differentially mark stem/progenitor populations and enteroendocrine cells of the small intestine epithelium. *Am. J. Physiol. Gastrointest. Liver Physiol.* 296, G1108–G1118.
- Fukuda, K., Tanigawa, Y., Fujii, G., Yasugi, S., and Hirohashi, S. (1998). cFIBP/SMAP: a novel molecule involved in the regulation of smooth muscle differentiation. *Development* 125, 3535–3542.
- Furuyama, K., Kawaguchi, Y., Akiyama, H., Horiguchi, M., Kodama, S., Kuhara, T., Hosokawa, S., Elbahrawy, A., Soeda, T., Koizumi, M., et al. (2011). Continuous cell supply from a Sox9-expressing progenitor zone in adult liver, exocrine pancreas and intestine. *Nat. Genet.* 43, 34–41.
- Haramis, A.P., Begthel, H., van den Born, M., van Es, J., Jonkheer, S., Offerhaus, G.J., and Clevers, H. (2004). De novo crypt formation and juvenile polyposis on BMP inhibition in mouse intestine. *Science* 303, 1684–1686.
- Hardwick, C.J.H., Van Den Brink, G.R., Bleuming, S.A., Ballester, I., Van Den Brande, J.M.H., Keller, J.J., Offerhaus, G.J.A., Van Deventer, S.J.H., and Peppelenbosch, M.P. (2004). Bone morphogenetic protein 2 is expressed by, and acts upon, mature epithelial cells in the colon. *Gastroenterology* 126, 111–121.
- He, X.C., Zhang, J., Tong, W.G., Tawfik, O., Ross, J., Scoville, D.H., Tian, Q., Zeng, X., He, X., Wiedemann, L.M., et al. (2004). BMP signaling inhibits intestinal stem cell self-renewal through suppression of Wnt-beta-catenin signaling. *Nat. Genet.* 36, 1117–1121.
- Hilton, W.A. (1902). The morphology and development of intestinal folds and villi in vertebrates. *Am. J. Anat.* 7, 459–505.
- Itzkovitz, S., and van Oudenaarden, A. (2011). Validating transcripts with probes and imaging technology. *Nat. Methods* 8, S12–S19.
- Itzkovitz, S., Blat, I.C., Jacks, T., Clevers, H., and van Oudenaarden, A. (2012). Optimality in the development of intestinal crypts. *Cell* 148, 608–619.
- Karlsson, L., Lindahl, P., Heath, J.K., and Betsholtz, C. (2000). Abnormal gastrointestinal development in PDGF-A and PDGFR- α deficient mice implicates a novel mesenchymal structure with putative instructive properties in villus morphogenesis. *Development* 127, 3457–3466.
- Kim, T.H., Escudero, S., and Shivdasani, R.A. (2012). Intact function of Lgr5 receptor-expressing intestinal stem cells in the absence of Paneth cells. *Proc. Natl. Acad. Sci. USA* 109, 3932–3937.
- Knezevic, V., De Santo, R., Schughart, K., Huffstadt, U., Chiang, C., Mahon, K.A., and Mackem, S. (1997). Hoxd-12 differentially affects preaxial and post-axial chondrogenic branches in the limb and regulates Sonic hedgehog in a positive feedback loop. *Development* 124, 4523–4536.
- Kotzé, S.H., and Soley, J.T. (1995). Scanning electron microscopic study of intestinal mucosa of the Nile crocodile (*Crocodylus niloticus*). *J. Morphol.* 225, 169–178.
- Krause, W.J. (1975). Intestinal mucosa of the platypus, *Ornithorhynchus anatinus*. *Anat. Rec.* 181, 251–265.
- Lacroix, B., Keding, M., Simon-Assmann, P., and Haffen, K. (1984). Early organogenesis of human small intestine: scanning electron microscopy and brush border enzymology. *Gut* 25, 925–930.
- Laufer, E., Nelson, C.E., Johnson, R.L., Morgan, B.A., and Tabin, C. (1994). Sonic hedgehog and Fgf-4 act through a signaling cascade and feedback loop to integrate growth and patterning of the developing limb bud. *Cell* 79, 993–1003.
- Madison, B.B., Braunstein, K., Kuizon, E., Portman, K., Qiao, X.T., and Gumucio, D.L. (2005). Epithelial hedgehog signals pattern the intestinal crypt-villus axis. *Development* 132, 279–289.

- McAvoy, J.W., and Dixon, K.E. (1978). Cell specialization in the small intestinal epithelium of adult *Xenopus laevis*: structural aspects. *J. Anat.* **125**, 155–169.
- Niswander, L., Jeffrey, S., Martin, G.R., and Tickle, C. (1994). A positive feedback loop coordinates growth and patterning in the vertebrate limb. *Nature* **371**, 609–612.
- Ormestad, M., Astorga, J., Landgren, H., Wang, T., Johansson, B.R., Miura, N., and Carlsson, P. (2006). *Foxf1* and *Foxf2* control murine gut development by limiting mesenchymal Wnt signaling and promoting extracellular matrix production. *Development* **133**, 833–843.
- Raj, A., van den Bogaard, P., Rifkin, S.A., van Oudenaarden, A., and Tyagi, S. (2008). Imaging individual mRNA molecules using multiple singly labeled probes. *Nat. Methods* **50**, 877–879.
- Roberts, D.J., Johnson, R.L., Burke, A.C., Nelson, C.E., Morgan, B.A., and Tabin, C. (1995). Sonic hedgehog is an endodermal signal inducing *Bmp-4* and *Hox* genes during induction and regionalization of the chick hindgut. *Development* **121**, 3163–3174.
- Salazar-Ciudad, I. (2012). Tooth patterning and evolution. *Curr. Opin. Genet. Dev.* **22**, 585–592.
- Sbarbati, R. (1982). Morphogenesis of the intestinal villi of the mouse embryo: chance and spatial necessity. *J. Anat.* **135**, 477–499.
- Shyer, A.E., Tallinen, T., Nerurkar, N.L., Wei, Z., Gil, E.S., Kaplan, D.L., Tabin, C.J., and Mahadevan, L. (2013). Villification: how the gut gets its villi. *Science* **342**, 212–218.
- Spence, J.R., Lauf, R., and Shroyer, N.F. (2011). Vertebrate intestinal endoderm development. *Dev. Dyn.* **240**, 501–520.
- Thesleff, I. (2003). Epithelial-mesenchymal signalling regulating tooth morphogenesis. *J. Cell Sci.* **116**, 1647–1648.
- Tian, Q., He, X.C., Hood, L., and Li, L. (2005). Bridging the BMP and Wnt pathways by PI3 kinase/Akt and 14-3-3zeta. *Cell Cycle* **4**, 215–216.
- Walker, R.L., Buret, A.G., Jackson, C.L., Scott, K.G.-E., Bajwa, R., and Habibi, H.R. (2004). Effects of growth hormone on leucine absorption, intestinal morphology, and ultrastructure of the goldfish intestine. *Can. J. Physiol. Pharmacol.* **82**, 951–959.
- Walton, K.D., Kolterud, A., Czerwinski, M.J., Bell, M.J., Prakash, A., Kushwaha, J., Grosse, A.S., Schnell, S., and Gumucio, D.L. (2012). Hedgehog-responsive mesenchymal clusters direct patterning and emergence of intestinal villi. *Proc. Natl. Acad. Sci. USA* **109**, 15817–15822.
- Winkler, F., and Wille, K.H. (1998). Über die friihfetale Entwicklung der Diinn-darm-Mukosa des Rindes (*Bos pvimigenius taurus*). *Anat. Histol. Embryol.* **27**, 335–343.

Transbilayer Lipid Interactions Mediate Nanoclustering of Lipid-Anchored Proteins

Graphical Abstract



Authors

Riya Raghupathy,
Anupama Ambika Anilkumar, ...,
Madan Rao, Satyajit Mayor

Correspondence

madan@ncbs.res.in (M.R.),
mayor@ncbs.res.in (S.M.)

In Brief

Transbilayer interactions between outer-leaflet long-acyl-chain-containing lipids and inner-leaflet phosphatidylserine are pivotal in generating actin-dependent nanoclusters of membrane lipid-anchored proteins. These interactions may provide an underlying mechanism for the generation of functional lipid domains at the plasma membrane.

Highlights

- Lipids with long saturated acyl chains are required for actin-based nanoclustering
- Inner leaflet phosphatidylserine couples to outer leaflet lipids
- Immobilization of long saturated acyl chain lipids promotes transbilayer coupling
- Actin association can mediate immobilization of phosphatidylserine



Transbilayer Lipid Interactions Mediate Nanoclustering of Lipid-Anchored Proteins

Riya Raghupathy,^{1,3,9} Anupama Ambika Anilkumar,^{1,3,9} Anirban Polley,^{2,8,9} Parvinder Pal Singh,⁶ Mahipal Yadav,⁶ Charles Johnson,⁵ Sharad Suryawanshi,⁵ Varma Saikam,⁶ Sanghapal D. Sawant,⁶ Aniruddha Panda,^{1,7} Zhongwu Guo,⁵ Ram A. Vishwakarma,⁶ Madan Rao,^{1,2,*} and Satyajit Mayor^{1,4,*}

¹National Centre for Biological Sciences (TIFR), Bellary Road, Bangalore 560 065, India

²Raman Research Institute, C.V. Raman Avenue, Bangalore 560 080, India

³Shanmugha Arts, Science, Technology & Research Academy, Thanjavur 613401, India

⁴Institute for Stem Cell Biology and Regenerative Medicine, Bellary Road, Bangalore 560 065, India

⁵Wayne State University, 5101 Cass Avenue, Detroit, MI 48202, USA

⁶Indian Institute of Integrative Medicine (CSIR), Canal Road, Jammu 180001, India

⁷Manipal University, Madhav Nagar, Manipal 576104, Karnataka, India

⁸Tampere University of Technology, Korkeakoulunkatu 10, 33720 Tampere, Finland

⁹Co-first author

*Correspondence: madan@ncbs.res.in (M.R.), mayor@ncbs.res.in (S.M.)

<http://dx.doi.org/10.1016/j.cell.2015.03.048>

SUMMARY

Understanding how functional lipid domains in live cell membranes are generated has posed a challenge. Here, we show that transbilayer interactions are necessary for the generation of cholesterol-dependent nanoclusters of GPI-anchored proteins mediated by membrane-adjacent dynamic actin filaments. We find that long saturated acyl-chains are required for forming GPI-anchor nanoclusters. Simultaneously, at the inner leaflet, long acyl-chain-containing phosphatidylserine (PS) is necessary for transbilayer coupling. All-atom molecular dynamics simulations of asymmetric multicomponent-membrane bilayers in a mixed phase provide evidence that immobilization of long saturated acyl-chain lipids at either leaflet stabilizes cholesterol-dependent transbilayer interactions forming local domains with characteristics similar to a liquid-ordered (*lo*) phase. This is verified by experiments wherein immobilization of long acyl-chain lipids at one leaflet effects transbilayer interactions of corresponding lipids at the opposite leaflet. This suggests a general mechanism for the generation and stabilization of nanoscale cholesterol-dependent and actin-mediated lipid clusters in live cell membranes.

INTRODUCTION

The plasma membrane of living cells is the barrier that segregates the inside of the cell from the outside. It is a fluid bilayer composed primarily of lipids and proteins. It has long been thought of as an equilibrium mixture giving rise to a “fluid mosaic” (Singer and Nicolson, 1972), wherein proteins and lipids form regions of distinct composition driven by thermodynamic

forces. Additionally, liquid ordered (*lo*) -disordered (*ld*) phase segregation of lipids was expected to give rise to membrane “rafts” (Simons and Vaz, 2004). These rafts, in turn, were hypothesized to facilitate a number of cellular functions such as the sorting of specific membrane components for the building of signaling complexes, construction of endocytic pits, and transbilayer communication (Simons and Ikonen, 1997).

Because the cell membrane contains a diverse array of lipids with varying acyl chain length/saturation and significant levels of cholesterol, even if the cell membrane is globally mixed and homogeneous at physiological temperatures, it could exhibit small, transient regions with local *lo*-like character. Indeed, studies using local probes, spin-labeled lipids and electron-spin resonance techniques report deuterium order parameters consistent with the existence of a fraction of membrane lipids exhibiting *lo*-like conformations (Swamy et al., 2006). However, macroscopic domains are rarely seen in live cells. Studies on the phase behavior of giant plasma membrane-derived vesicles from a number of cell types show that large phase segregated domains form only when these membranes are cooled to temperatures well below physiological temperature (Baumgart et al., 2007) or if some of the membrane components are artificially clustered (Kaiser et al., 2009).

The simple equilibrium picture of phase segregation of membrane composition and order runs into several problems. First, the plasma membrane is an asymmetric multicomponent bilayer; our understanding of phase behavior, local composition heterogeneity, and transbilayer coupling in such systems is preliminary (Polley et al., 2012, 2014). Second, the plasma membrane is attached to an actin cortex, whose role in influencing local membrane composition is poorly understood. Finally, the organization and dynamics of a variety of plasma membrane molecules such as membrane proteins (Gowrishankar et al., 2012; Jaqaman et al., 2011), lipid-anchored proteins (Goswami et al., 2008; Prior et al., 2003; Sharma et al., 2004), and glycolipids (Fujita et al., 2007) into nanometer sized clusters cannot be derived from equilibrium-based mechanisms.

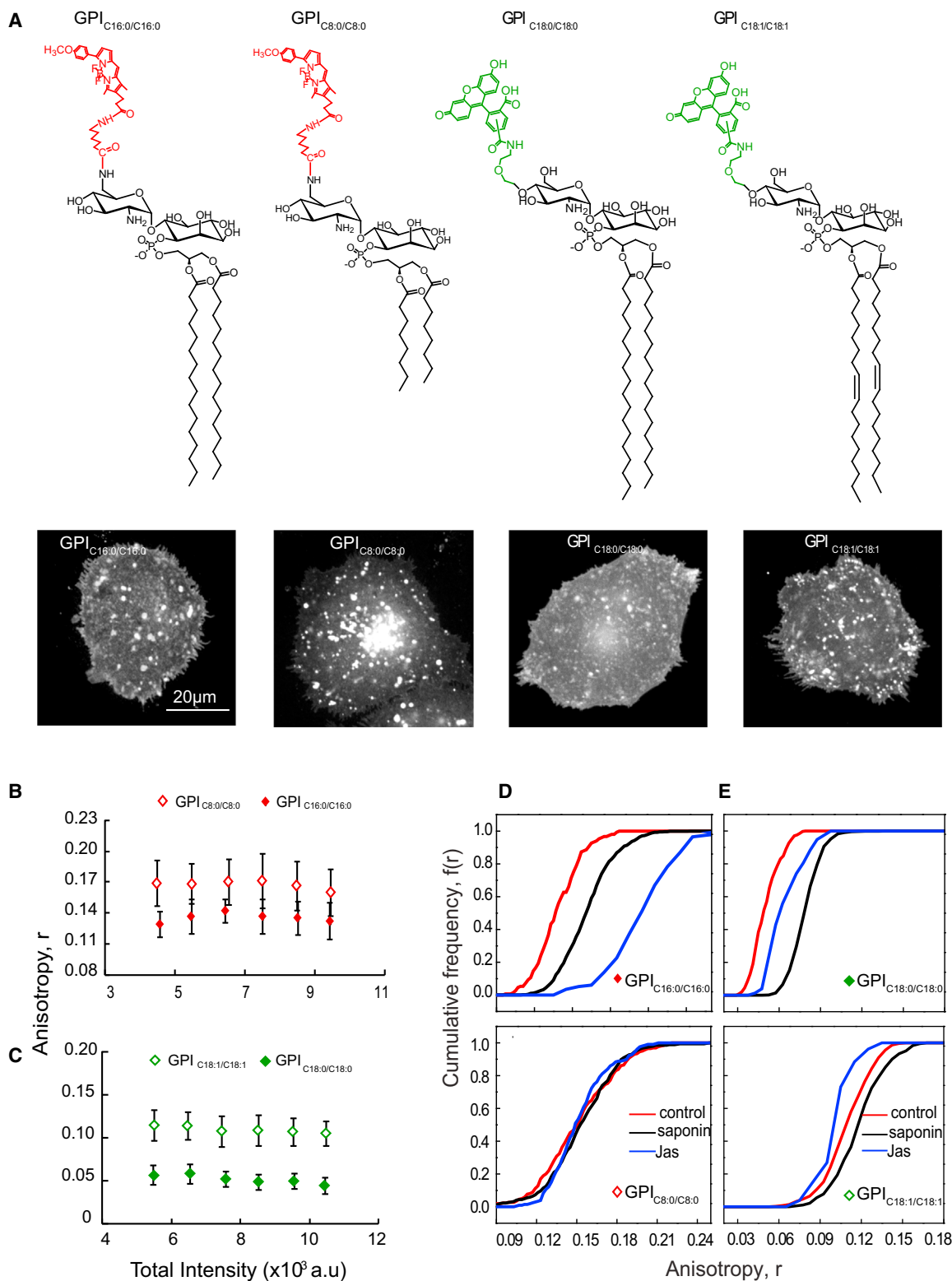


Figure 1. Long-Saturated-Acyl-Chain-Containing GPIs Support Nanoclustering

(A–E) Chemical structures of synthetic minimal GPI analogs (A) outline the variation in the di-acyl glycerolipid chain length (C16:0 and C8:0) and saturation (C18:0 and C18:1) used in this study. GlcNPI carry fluorescent labels BODIPYTM (left) or fluorescein (right). Representative gray scale images of CHO (IA2.2F) cells with exogenously incorporated GPI analogs as indicated are shown below each analog. Fluorescence anisotropy of GPI_{C16:0/C16:0} (red closed diamonds) or

(legend continued on next page)

Studies on glycosylphosphatidylinositol (GPI)-anchored proteins (GPI-APs), a large class of plasma membrane proteins located at the exoplasmic (outer) leaflet (Gowrishankar et al., 2012), in particular have demanded a new framework for understanding the local control of molecular organization at the cell surface. Homo-fluorescence resonance energy transfer (FRET)-based fluorescence anisotropy measurements (Sharma et al., 2004; Varma and Mayor, 1998), near-field scanning microscopy (van Zanten et al., 2009), and photoactivation localization microscopy (Sengupta et al., 2011) show that ~20%–40% of GPI-APs on the membrane are present as nanoclusters, whereas the rest are monomers. Other studies have shown that monomers are in continuous exchange with relatively immobile nanoclusters (Goswami et al., 2008; Sharma et al., 2004). This organization requires both adequate membrane cholesterol and actin dynamics (Goswami et al., 2008).

GPI-AP clusters are formed by the active engagement of dynamic actin adjacent to the membrane cortex and exhibit unusual properties related to their spatial distribution, small size, temperature-independent fragmentation and formation kinetics, and non-Brownian density fluctuations (Goswami et al., 2008; Gowrishankar et al., 2012). These properties have been explained by a theoretical framework (Chaudhuri et al., 2011; Gowrishankar et al., 2012) based on active contractile mechanics (Marchetti et al., 2013) of dynamic polar filaments. This framework also makes predictions that have been experimentally verified (Gowrishankar et al., 2012). In this mechanism, dynamic actin forms transient contractile regions at the cytoplasmic (inner) leaflet that drive the clustering of the outer leaflet GPI-APs, as well as transmembrane proteins that directly associate with actin filaments.

The actin-driven clustering of GPI-APs requires a coupling of the lipid-tethered protein across the bilayer to the dynamic contractile actin configurations at the inner leaflet. Furthermore, understanding the mechanism of formation of these clusters has a functional significance, both in the sorting of GPI-APs (Mayor and Pagano, 2007; Mayor and Riezman, 2004) and in modulating receptor signaling (Coskun et al., 2011). For example, cholesterol-dependent GPI-AP nanoclustering is necessary for promoting integrin function (van Zanten et al., 2009), which appears to take place in focal adhesions that are surrounded by *lo* domains (Gaus et al., 2006).

Here, we show that this transbilayer coupling requires the long acyl chains of outer leaflet GPI anchors in association with cholesterol and inner leaflet lipids that also carry long acyl chains. We identify phosphatidylserine (PS) as the inner leaflet lipid responsible for this coupling. All-atom molecular dynamic (MD) simulations show that local transbilayer coupling occurs even in membranes that are well above their main transition temperature, provided the long-acyl-chain-containing

lipids are immobilized at one leaflet of the bilayer. We show that this immobilization may be mediated by PS binding to actin by constructing a synthetic linker that links PS to actin. Expression of this linker in cells results in coupling of exogenously added lipids with long acyl chains, as well as endogenous GPI-APs, to stable long-lived actin structures located at the inner leaflet.

This supports the idea that dynamic actin filaments at the inner leaflet may have the capacity to immobilize lipids and stabilize local *lo* domains over significant timescales in membranes at physiological temperatures.

RESULTS

Synthetic Fluorescent GPI Analogs with Long Saturated Acyl Chains Mimic GPI-AP Nanoclustering

In mammalian cells, a typical GPI anchor is a complex glycolipid (McConville and Ferguson, 1993), which, in general, possesses long saturated acyl chains either C16:0 or C18:0 (Figure S1A). To test whether the acyl chain length and degree of saturation of the GPI anchor affect nanocluster formation, we generated synthetic GPI analogs (Figure 1A) and studied their nanoclustering ability after their incorporation into the plasma membrane of live cells. The synthesized GPI analogs carry a minimal GPI anchor containing the disaccharide glucosamine-inositol linked to phosphatidic acid (GlcNPI) (instead of the full-length GPI; Figure S1A). Each analog is conjugated to fluorescent probes to the GPI head group (Figure 1A). The incorporated GPI analogs are retained in the outer leaflet of the plasma membrane as indicated by a complete loss of their fluorescence when subjected to phosphatidylinositol-specific phospholipase-C (PI-PLC) cleavage (Figure S1B). Additional confirmation of their correct membrane incorporation comes from the observation that their diffusion properties also resemble endogenous GPI-APs (Figures S1C and S1D).

Monitoring the fluorescence anisotropy of these synthetic fluorescent GPI analogs—differing only in their acyl chain length as a function of their concentration in the live-cell membrane—provides a measure of the extent of clustering of these analogs (Figure S1E). The fluorescence anisotropy of GPI_{C16:0/C16:0} is much lower than GPI_{C8:0/C8:0} (Figures 1B and S2B). It exhibits concentration-independent fluorescence anisotropy over a large concentration range (Figure 1B), similar to endogenous GPI-APs (Sharma et al., 2004). Consistent with the generation of nanoscale clusters, the photobleaching profiles of the GPI_{C16:0/C16:0} also mimicked those of fluorescently tagged folic acid analog (PLB-FR-GPI; Figures S1F and S1G). Furthermore, on depleting membrane cholesterol or on disrupting actin activity (blebs devoid of actin were generated by treatment with jasplakinolide [Goswami et al., 2008]), GPI_{C16:0/C16:0} exhibited an increase in

GPI_{C18:0/C18:0} (green closed diamonds) in comparison to GPI_{C8:0/C8:0} (red open diamonds) or GPI_{C18:1/C18:1} (green open diamonds) determined from images as above were plotted against a wide range of intensity of fluorescent GPI analogs available at the membrane of live cells. Scale bar, 20 μ m (B, C). Cumulative frequency distributions (CFD) derived from data derived from identical intensity ranges of GPI_{C16:0/C16:0} and GPI_{C8:0/C8:0} (D) or GPI_{C18:0/C18:0} and GPI_{C18:1/C18:1} (E) incorporated into cells show the effect of cholesterol depletion by saponin treatment (sap; black line) or on blebs prepared by treatment with jasplakinolide (jas, blue lines) with respect to untreated cells (control, red lines). Each data point in the graphs represents average anisotropy with SD for the corresponding intensity bin obtained from a 10 \times 10 pixel region (20–50 regions per cell) from at least 40 cells from 2 independent experiments. Error bars represent SD. See also Figures S1 and S2.

fluorescence anisotropy (Kolmogorov-Smirnov [KS] test $p < 0.001$) (Figures 1D and S2B) similar to PLB-FR-GPI (Figures S2A, S2C, and S2D), suggesting cholesterol and actin-dependent nanoclustering. By contrast, GPI_{C8:0/C8:0} exhibited a higher fluorescence anisotropy, which did not change upon photobleaching (Figure S1H), cholesterol depletion (Figures 1D and S2B), or actin perturbation, which is consistent with its inability to form nanoclusters in the cell membrane.

Comparable to PLB-FR-GPI, the fluorescence anisotropy of GPI_{C16:0/C16:0} changes upon photobleaching (Figures S1F and S1G), exhibiting a distinct rise in control cells or on the flat membrane (Figures 1D, S2A–S2D, and S1I). Moreover, the fluorescence anisotropy of both PLB-FR-GPI and the GPI_{C16:0/C16:0} analog remain unchanged upon photobleaching the bleb fluorescence (Sharma et al., 2004) (Figure S1I), which is consistent with the lack of clusters on the actin-depleted blebs. By contrast, the fluorescence anisotropy of the GPI_{C8:0/C8:0} on membrane blebs is unaffected by photobleaching (Figures S1H and S1J), confirming its inability to form nanoclusters.

The synthetic GPI analogs allowed us to directly assess the role of (un)saturation in the GPI acyl chains by comparing the clustering abilities of GPI_{C18:0/C18:0} and GPI_{C18:1/C18:1}. Here, we used fluorescein-tagged GPI analogs, and as observed for its BODIPY^{TMR}-labeled counterpart (Figure 1A), the fluorescence anisotropy of GPI_{C18:0/C18:0} is concentration independent (Figure 1C) and rises upon cholesterol depletion and in membrane blebs (KS test $p < 0.001$ in both cases) (Figure 1E), which is consistent with formation of nanoclusters. In contrast, the fluorescence anisotropy of GPI_{C18:1/C18:1} is higher than GPI_{C18:0/C18:0} (Figure 1C) and does not exhibit a significant change (in comparison to GPI_{C18:0/C18:0}) upon cholesterol depletion or on membrane blebs (Figure 1E), indicating reduced ability to be recruited to nanoclusters. These results suggest that GPI anchor clustering requires long-saturated acyl chain lipids to support actin and cholesterol-based nanoclustering.

GPI-Anchored Protein Nanoclustering Is Abrogated in GPI Anchor Remodeling Mutants

During GPI anchor biosynthesis, cells specifically remodel their unsaturated acyl chains present at the *sn*-2 position of the immature GPI-anchor to generate long saturated acyl chain lipids (either 16:0 or 18:0) (McConville and Ferguson, 1993). This process of lipid remodeling is mediated by key enzymes, PGAP2 and PGAP3 (Maeda et al., 2007). Cell lines carrying mutations in both PGAP2 and PGAP3 express cell-surface GPI-APs with un-remodeled GPI anchors containing unsaturated acyl chains at the *sn*-2 position of the glycerophospholipid (Maeda et al., 2007). This enabled us to test the requirement of long saturated acyl chains in endogenous GPI-AP nanoclustering. The extent of clustering of the GPI-APs in mutant and wild-type cells was measured by determining the extent of homo-FRET between GPI-APs at the cell surface by monitoring the fluorescence anisotropy of fluorescently tagged FLAER (A488F) (Brodsky et al., 2000). The fluorescence anisotropy in mutant cells is significantly higher (KS test, $p < 0.001$) than that in wild-type cells (Figure 2A) and is similar to the fluorescence anisotropy of A488F-labeled GPI-APs measured in cells treated with a cholesterol sequestering agent, saponin.

Incorporation of GPI_{C16:0/C16:0} in the plasma membrane of PGAP2/3 mutant cells showed that GPI_{C16:0/C16:0} clusters to the same extent in both the wild-type and mutant cells (KS test, $p < 0.001$) (Figure 2B), confirming that the lack of nanoclustering in these cell lines is due to the presence of unsaturated lipid tail of GPI-APs and not due to any other artifact that may arise as a result of PGAP2/3 perturbation. These experiments indicate that cholesterol and actin-dependent nanoclustering of endogenous GPI-APs also require long saturated acyl chains in their lipid moiety, which is consistent with results obtained with the synthetic GPI analogs.

Inner Leaflet PS Is Required for GPI-AP Nanoclustering

There are two possibilities by which long-acyl-chain-containing GPI-APs can connect to the actin at the inner leaflet; one involving a transmembrane linker and the other via lipidic interactions across the inner leaflet. To distinguish between these possibilities, we looked into the roles of phosphatidylinositol 4,5-bisphosphate (PI(4,5)P₂) and PS, which are obvious candidates for inner leaflet lipids that could couple outer leaflet GPI-APs with actin. Both of these lipids are also known to interact with several actin-binding proteins (Yin and Janmey, 2003). PS, for example, binds specifically to actin-binding proteins such as spectrin, talin, and various others (Makuch et al., 1997; Murguruma et al., 1995), whereas the Pleckstrin homology (PH) domain present in many proteins interact with PIPs and actin (Yin and Janmey, 2003).

To test the role of these lipids in actin-driven nanoclustering, we expressed protein domains capable of binding PS or PI(4,5)P₂, the most abundant plasma membrane PIP_n (Stauffer et al., 1998), to putatively mask the interaction of these lipids with the cytoplasmically disposed actin filaments. We used a fusion construct of GFP with the discoidin-like C2 domain of lactadherin [Lact C2 GFP; Yeung et al., 2008] to mask PS at the inner leaflet and the PH domain of PLC δ fused to the NH₂ terminus of GFP protein [PH-GFP; (Stauffer et al., 1998)] for masking PI(4,5)P₂. Cells expressing Lact C2-GFP exhibited higher fluorescence anisotropy of PLB-FR-GPI, which is consistent with a reduction of the extent of nanoclustering (KS test, $p < 0.001$) (Figures 3A and 3B). This was not due to an alteration in the lipid profile of cells expressing Lact C2-GFP because their lipid composition was unaltered when compared to cells transfected with the GFP alone. Individual lipid classes in transfected cells varied between 93% and 99% of the control values. By contrast, there was no significant effect on the fluorescence anisotropy of PLB-labeled FR-GPI when we expressed PH-GFP (Figures 3A and 3B) nor when PI(4,5)P₂ levels were perturbed using an antibiotic such as neomycin or a Phospholipase C activator such as chlorpromazine (Figure S3), indicating the lack of involvement of PI(4,5)P₂.

Because GPI-AP nanoclusters depend on actin-based mechanisms, masking PS via the Lact C2 domains could reflect a non-specific effect of the inaccessibility of PS to cytosolic factors necessary for actin polymerization. To rule out these effects and show that direct association of PS with actin is sufficient for GPI-AP nanoclustering at the outer leaflet, we expressed the Lact C2 domain fused to the actin-filament binding domain of Ezrin (Lact C2-Ez-YFP; Figures 3C and 3D). Similar to the

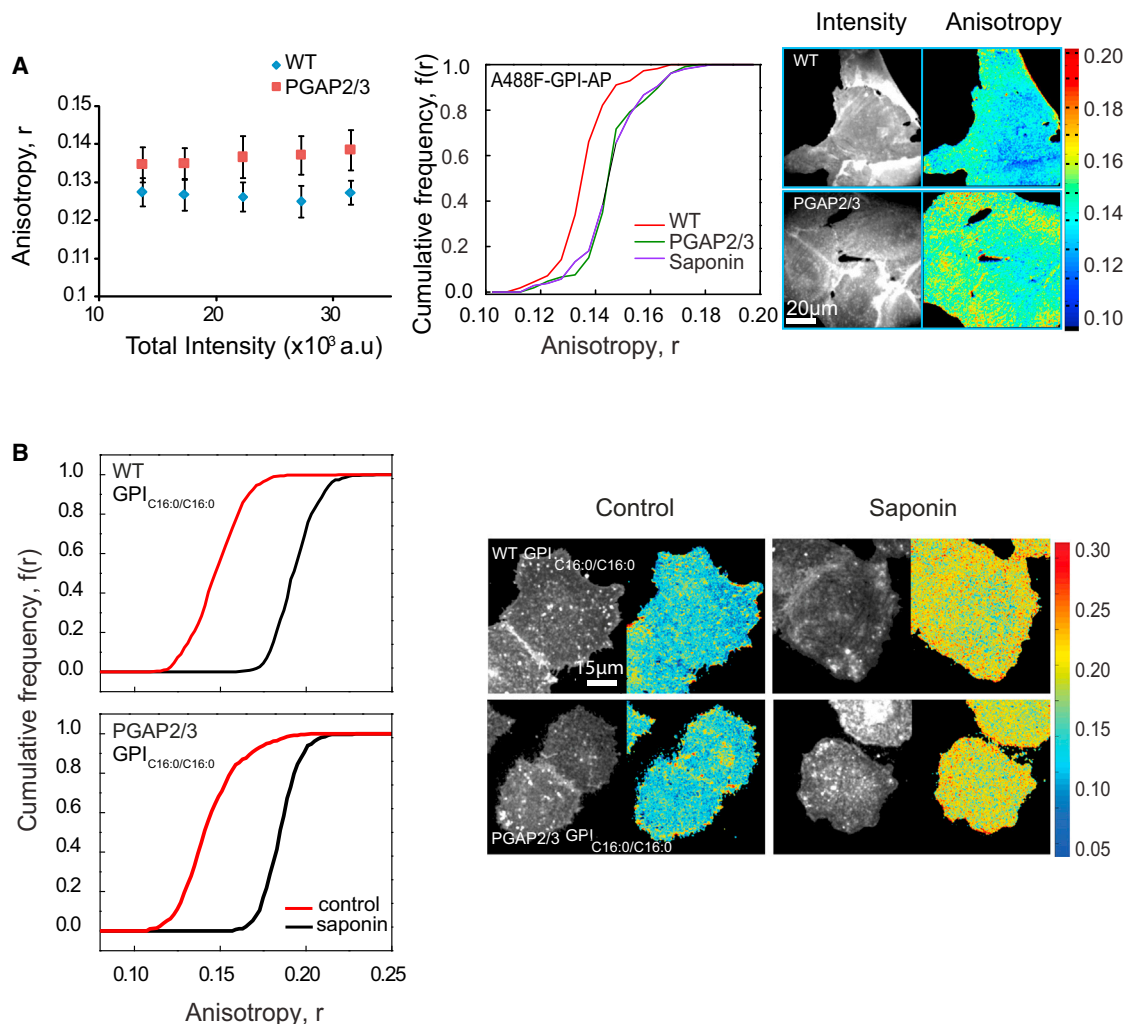


Figure 2. GPI-AP Nanoclustering Is Reduced in GPI Anchor Lipid Remodeling Mutants

(A and B) Fluorescence anisotropy of fluorescently tagged FLAER™ (Alexa-488-FLAER, A488F) in wild-type and PGAP2/3 double-mutant CHO cells (blue diamonds and red squares, respectively) plotted against fluorescence intensity shows an increase in anisotropy in mutant cells (A), corresponding to a loss of homo-FRET between A488F-labeled GPI-APs. Intensity and anisotropy were determined from images collected from cells as shown on the right. CFD plots and images (A) for wild-type (red line), PGAP2/3 double-mutant (green line) and saponin treated (violet line) cells and (B) for GPI_{C16:0/C16:0} in control (red line), and cholesterol-depleted (black line) conditions in WT and PGAP2/3 mutant cells. CFD plots show that A488F-labeled GPI-APs in mutant cells exhibit an increase in anisotropy compared to wild-type cells and exogenously incorporated GPI_{C16:0/C16:0} exhibit significantly depolarized fluorescence anisotropy (control) in both wild-type (top) and mutant cells (bottom) that is sensitive to cholesterol depletion by saponin (black line). Each data point in the graphs and CFDs represents average anisotropy values derived from nearly 40 cells from 3 independent experiments. Error bars represent SD.

Lact C2 construct, this protein is also recruited to the plasma membrane, in contrast to a cytosolic EGFP control that does not have plasma membrane binding capacity (Figures 3C and 3D). More importantly, only the fusion construct that connects PS to actin restores nanoclustering of GPI-APs (Figures 3C and 3D), emphasizing the role of actin and its ability to link up to PS in facilitating nanocluster formation.

GPI-AP Nanoclustering Requires Long-Acyl-Chain-Containing PS

To explore the nature of the acyl chain on the PS that is involved in coupling with GPI-APs at the outer leaflet, we measured GPI-AP

nanoclustering in PS-synthesis-deficient Chinese hamster ovary (CHO) cell lines (PSA3 cells). These cell lines carry a mutation in the PSS1 gene (Nishijima et al., 1986) where the cells are rendered completely dependent on phosphatidylethanolamine (PE) (Figure S4A; Kennedy and Weiss, 1956; Percy et al., 1983). PS levels at the plasma membrane of PSA3 cells grown in absence of ethanolamine (deplete) are drastically reduced compared to cells grown in its presence (replete) (Figures S4B and S4C). To measure the extent of endogenous GPI-AP nanoclustering, we compared the fluorescence anisotropy of the GPI-binding toxin A488F at the surface of PS-depleted and -repleted cells. Nanoclustering of endogenous GPI-AP was disrupted in PS-depleted cells; it is

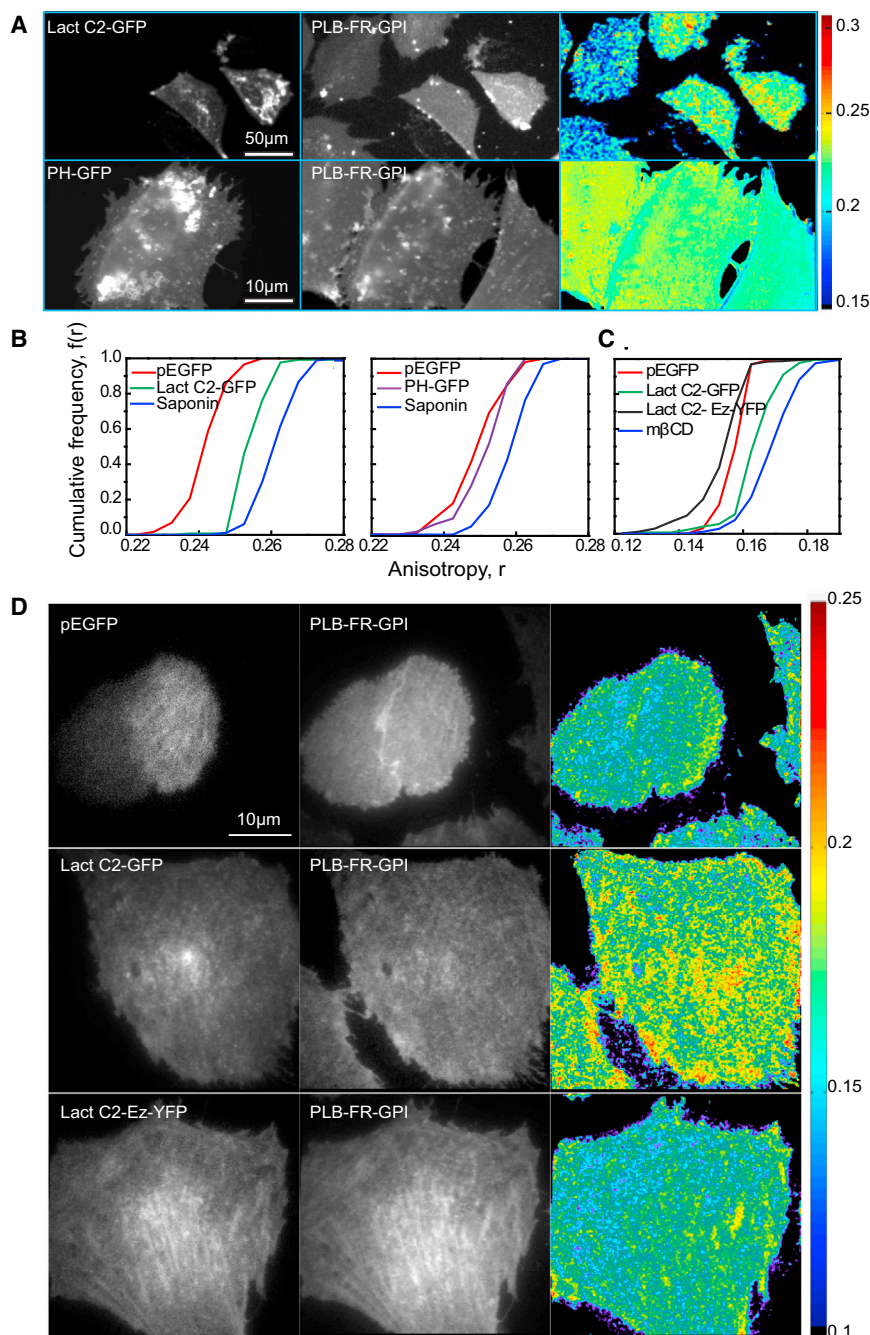


Figure 3. Masking of PS Binding Sites Alters GPI-AP Nanocluster Organization

(A–D) Cropped fluorescence intensity and anisotropy images of FR-GPI-expressing CHO cells (A and D) transfected with EGFP, EGFP tagged to C2 domain of lactadherin (Lact C2 GFP), PH domain of PLC δ (PH GFP), or a fusion construct of Lact C2 and actin binding domain (Lact C2-Ez-YFP) and corresponding CFD plots (B and C) were obtained from wide-field (A and B) and TIRF (C and D) microscopes, respectively. The fluorescence anisotropy of PLB bound to FR-GPI in cells expressing EGFP (red line) is comparable to that obtained in PH-GFP (violet line, middle) or Lact C2-Ez-YFP (black line, right) but is increased in cells expressing Lact C2-GFP (green line, left or right). This is in turn comparable to cells treated with saponin or mβCD (blue line). See also Figure S3.

leaflet by the ability to stain with Annexin V only after ionomycin treatment (Figures S4B and S4C). Our results show that only the long alkyl-chain-containing analog is capable of restoring nanoclustering of GPI-APs (Figures 4A, 4B, and 4E: PS_{C12:0/C12:0}*, PS_{C18:0/C18:0}*, PS_{C18:1/C18:1}*), despite the incorporation of all analogs in the membrane at similar levels (Figure S5C). Here, we used synthetic acyl/alkyl PS analogs that are resistant to phospholipase A₂ (PLA₂) cleavage (Burke and Dennis, 2009) (Figures 4A, 4B, and 4E; PS_{C12:0/C12:0}*, PS_{C18:0/C18:0}*, and PS_{C18:1/C18:1}*). This experimental strategy was adopted because exogenous addition of any di-acyl PS species restored nanoclustering of endogenous GPI-APs (Figure S4F) in the absence of a PLA₂ inhibitor (methyl-arachidonyl-fluorophosphonate; Figures S4F and S4G). By contrast, in the presence of the PLA₂ inhibitor, only the long saturated PS_{C18:0/C18:0} restored GPI-AP nanoclustering, whereas the short and unsaturated lipids, PS_{C12:0/C12:0} and PS_{C18:1/C18:1}, were incapable of restoring GPI-AP nanoclustering (Figures S4F and S4G). This suggested that PLA₂-like enzymes

engage in remodeling the acyl chains of exogenously incorporated PS at the inner leaflet. We also found that the exogenous addition of long-acyl-containing PE or PC to the same levels as the PS species (Figure S5B) in PS-deplete conditions does not rescue the nanoclustering of GPI-AP (Figure S4H).

comparable to that obtained in cells depleted of cholesterol (KS test, $p < 0.001$; Figures 4A and 4B). To confirm that the defect in these cells was not due to any perturbation of the endogenous GPI anchor in the PS-deplete condition, we established that, whereas the PS-replete cells were capable of supporting nanoclustering of exogenously added GPI_{C16:0/C16:0}, PS-deplete cells failed to do so (Figures S4D and S4E).

We next replenished the pool of PS in PS-deplete cells by adding various PS species differing in acyl chain length and saturation, and we have confirmed their incorporation at the inner

engage in remodeling the acyl chains of exogenously incorporated PS at the inner leaflet. We also found that the exogenous addition of long-acyl-containing PE or PC to the same levels as the PS species (Figure S5B) in PS-deplete conditions does not rescue the nanoclustering of GPI-AP (Figure S4H).

In CHO cells, the most abundant PS species is the asymmetric PS_{C18:0/C18:1} (Figure S4I), and hence, we determined nanocluster recovery by adding exogenous asymmetric PS_{C18:0/C18:1} in the presence of PLA₂ inhibitor. The restoration of GPI-AP nanoclustering by the addition of the asymmetric lipid was quantitatively

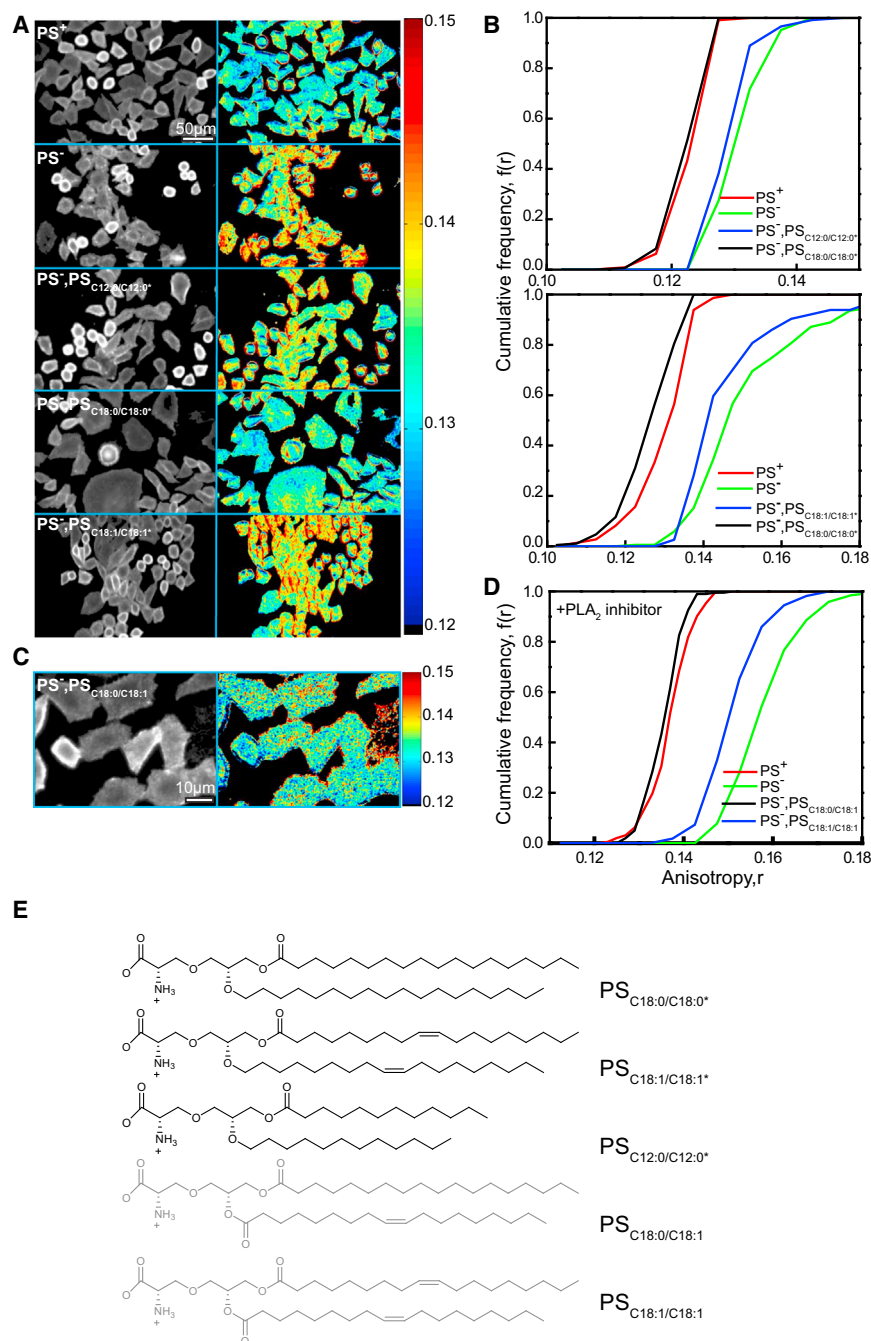


Figure 4. Nanoclustering of GPI-AP at the Cell Surface Requires Long-Acyl-Chain-Containing PS

(A–D) Cropped fluorescence intensity and anisotropy images (A and C) and cumulative frequency distributions (B and D) of A488F-labeled PSA3 mutant CHO cells grown with (PS replete [PS⁺; red line] or without [PS deplete (PS⁻); green line]) ethanolamine and supplemented with PLA₂-insensitive PS analogs of indicated acyl chain lengths and saturation (A and B; blue or black line) or supplemented with PLA₂ inhibitor and PLA₂-sensitive PS analogs of indicated acyl chain saturation (C and D; blue and black lines). (E) Chemical structure depicts the PLA₂-insensitive (black) and -sensitive (gray) PS analogs used in (A)–(D) above, respectively. See also [Figures S4 and S5](#).

molecular dynamic simulations of membrane bilayers comprising a distinct upper (palmitoyloleoyl-phosphatidylcholine [POPC], palmitoyl-sphingomyelin [PSM], and cholesterol [Chol]) and lower leaflet (POPC and Chol) capable of phase segregation into *lo* and *ld* phases ([Polley et al., 2012, 2014](#)). This approach has allowed an exploration of the effect of *lo*-*ld* segregation on either of the two leaflets ([Polley et al., 2012, 2014](#)). Here, we examined the regime where both leaflets of the asymmetric bilayer membrane are macroscopically in the homogenous mixed *ld* phase. We ask under what conditions would trace amounts of GPI on the putative outer (upper) leaflet register with PS in the putative inner (lower) leaflet and what the nature is of this transbilayer coupling. All simulation details, including force fields, tests of approach to thermodynamic equilibrium, and stress profiles at equilibrium are presented in the [Extended Experimental Procedures \(Figure S6B\)](#).

We find that, regardless of chain length/saturation and relative composition, as long as both leaflets of the bilayer are in the *ld* phase (characterized by low values

equivalent to that of the fully saturated long-chain PS_{C18:0/C18:0} ([Figures 4C and 4D](#)). These results strongly suggest that GPI-APs at the outer leaflet couple across the bilayer with PS with the aid of at least one long saturated chain and adequate cholesterol.

Atomistic MD Simulations Provide a General Mechanism for Transbilayer Coupling

To understand the mechanism by which long-chain GPI and PS lipids couple across the fluid bilayer, we developed atomistic

of the deuterium order parameter *S*, a measure of the extent of chain ordering), the distribution of GPI and PS is uniform with no transbilayer registry ([Figures 5A, S6A, and S6C](#)). However, the situation is entirely different if we cluster and immobilize either PS or GPI ([Figures 5A, 5B, and S6A](#)). In this case, we obtain co-segregation and perfect bilayer registry, a situation that represents a constrained equilibrium because of immobilization ([Supplemental Information; Figure S6C](#)). Note that the high transbilayer coupling in the *ld* phase is only obtained at adequate levels of cholesterol in the two leaflets (as shown in [Figure 5C](#)).

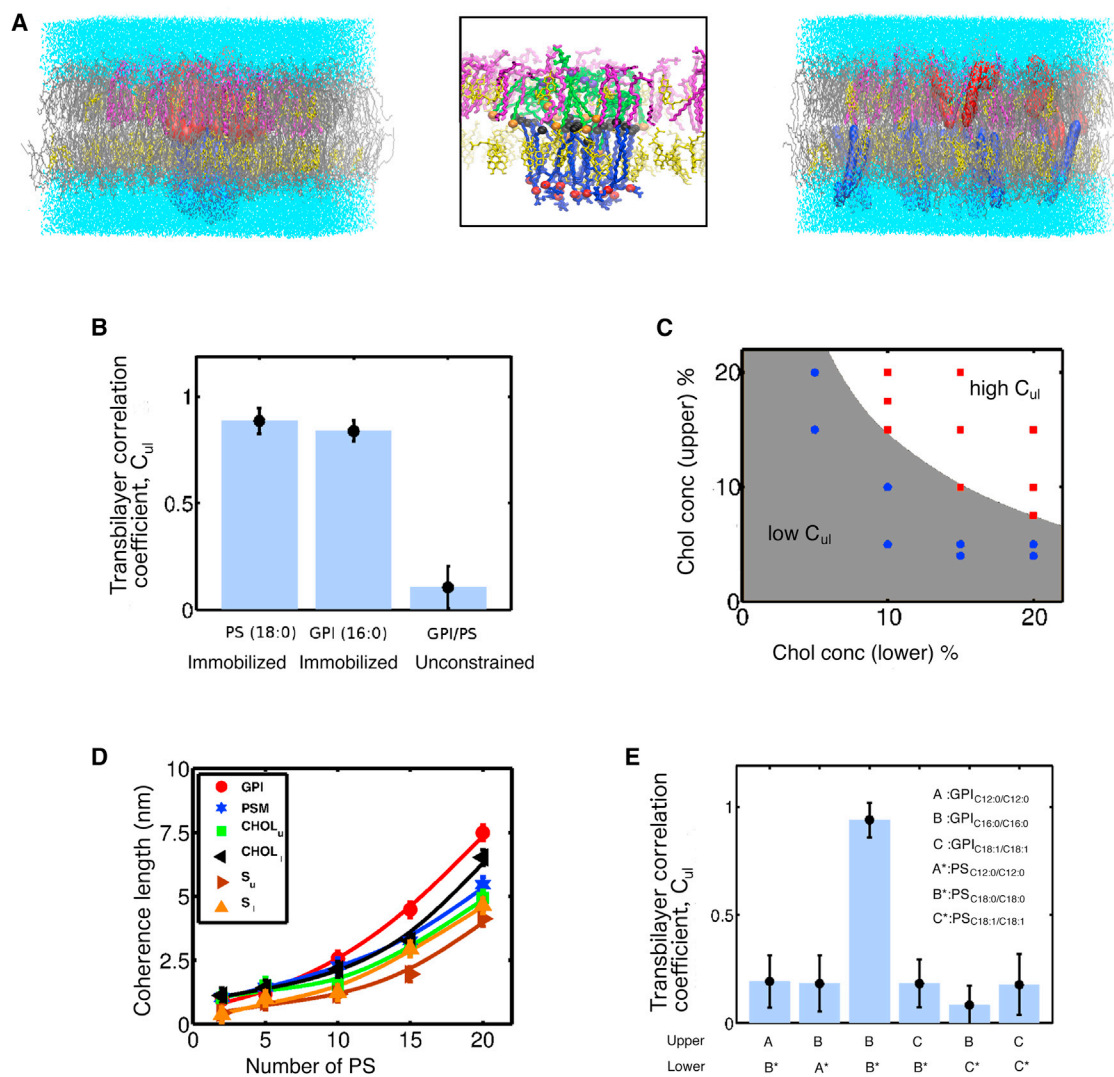


Figure 5. Atomistic MD Simulations Capture Transbilayer Interdigitation of Long Acyl Chain Lipids

(A) Equilibrium configurations of an asymmetric bilayer composed of POPC (gray), PSM (magenta), Chol (yellow), GPI (red or green), and PS (blue) embedded in water (cyan) from MD simulations in the *ld* phase. Upper leaflet comprises 4% PSM, 4% Chol, 10 long saturated GPI_{C16:0/C16:0}, and the rest POPC, whereas lower leaflet has 35% Chol, 25 long saturated PS_{C18:0/C18:0}, and the rest POPC when PS is not constrained (right, Figure S6A) or when PS molecules are immobilized (left and middle) which, when zoomed (middle), shows bilayer registry and interdigitation of GPI and PS. Local region surrounding interdigitating PS and GPI consists of enhanced levels of PSM and Chol, resembling local *lo*-like nanodomain.

(B) Extent of bilayer registry between GPI and PS measured by the transbilayer correlation coefficient C_{ul} (Experimental Procedures), which takes values 1 (0) when bilayer registry is strong (weak). Data shown are for the same bilayer composition as in (A) above. Transbilayer coupling C_{ul} is significant only when either PS or GPI are held in a cluster and immobilized. There is no transbilayer coupling and hence no registry when the GPI and PS are unconstrained.

(C) Levels of cholesterol in upper/lower leaflets that are needed to obtain high transbilayer coupling C_{ul} in the *ld* phase (white [high C_{ul}] or gray [low C_{ul}]). The cholesterol concentrations in the two leaflets are varied as shown (dots), the upper leaflet has 10 PS, and the lower leaflet has 15 PS, with POPC contributing to the rest. PSM concentration at the upper leaflet is same as cholesterol. Red (blue) dots designate high $C_{ul} \approx 1$ (low, $C_{ul} \approx 0$).

(D) Coherence length of membrane component density and deuterium order parameter in the two leaflets at late times when PS is held immobilized, computed from the exponential decay of their profiles. Coherence length increases non-linearly with the number of immobilized PS. Composition in upper leaflet is 92% POPC, 4% PSM, 4% Chol, and 10 GPI and in lower leaflet is 65% POPC, 35% Chol with number of PS varying from 2 to 20.

(E) Transbilayer coupling, C_{ul} between GPI and PS is sensitive to lipid chain length and degree of saturation of acyl chains. Composition of upper leaflet is 33.3% PSM, 33.3% Chol, 10 GPI, and the rest POPC; the composition of the lower leaflet is 10% PS, 10% Chol, and the rest POPC. Chain length and degree of saturation of PS and GPI are varied as indicated. Strong transbilayer coupling and bilayer registry are obtained only when both PS and GPI have long saturated acyl chains.

Error bars represent SD. See also Figure S6.

This co-segregation is accompanied by a steady increase in the local chain stiffness of the membrane components as determined by the local deuterium order parameter S , reflecting local l_o ordering within the co-segregation region (Figure S6C). A similar dynamics toward co-segregation occurs when the PS starts with a uniform distribution and the GPI is kept immobilized (data not shown). We also study the stability of co-clustering when both GPI and PS are initially clustered at the center with PS held immobile (Figure S6D). From the profile of GPI density and order parameter, we can extract a length scale over which the lipids maintain l_o -like order (coherence length) as a function of the number of immobilized PS molecules (Figure 5E). The non-linear increase in the coherence length with the number of immobilized PS also reflects the formation of a local l_o nanodomain.

This transbilayer coupling is surprisingly sensitive to reducing the acyl chain length (or lowering the degree of saturation) of either GPI or PS (Figure S6E), as revealed by the transbilayer correlation coefficient (Figure 5F). This is manifest in the deuterium order parameter profile, which remains small (and close to the l_d value), thus failing to achieve transbilayer coupling that is needed for bilayer registry (Figure S6E). Thus, our atomistic simulations done in the l_d phase of the asymmetric bilayer indicate that it is only in the presence of adequate amounts of cholesterol that the transbilayer coupling of long saturated GPI and PS can be achieved, provided that PS is held immobilized. The lifetime of this co-clustering is therefore set by the lifetime of immobilization of PS. These simulations imply that, in a multicomponent bilayer that is in the mixed l_d phase (not far from the l_o/l_d transition), clustering and immobilization of a few long acyl chain lipids should suffice to effect transbilayer coupling by stabilizing small l_o -like regions that could spontaneously arise due to proximity to an l_o/l_d transition.

Long Saturated Fatty Acyl Chains of Phospholipids Are Sufficient for Their Nanoclustering

To directly test the predictions of the atomistic MD simulations, we incorporated long acyl-chain-containing synthetic PE analog conjugated to Fluorescein (F-DHPE) in CHO cell membranes and determined its nanoscale organization. Similar to endogenous GPI-APs, fluorescence emission anisotropy of F-DHPE is also concentration independent and increases upon cholesterol depletion and photobleaching (data not shown, but see Figure 6E). Furthermore, incorporation of F-DHPE into PS-deplete cells did not result in nanocluster formation, whereas in PS-replete cells, they form cholesterol-sensitive nanoclusters (Figures 6C and 6D). Consistent with the absence of nanoclusters in PS-deplete cells, the fluorescence anisotropy of F-DHPE also does not increase upon photobleaching. By contrast, there is a rise in anisotropy in PS-replete cells, which is consistent with the presence of PS-dependent nanoclusters of F-DHPE (Figure 6E). This verifies the sufficiency of long saturated acyl chains in facilitating cholesterol-sensitive and PS-mediated nanoclusters of lipids in membranes of live cells.

Immobilization Promotes Transbilayer Coupling Mechanism

To test the role of immobilization in effecting transbilayer coupling of specific lipid components in either leaflet as pre-

dicted from our simulations (Figure 5), we determine whether crosslinking outer leaflet GPI-APs into optically resolvable clusters could result in the recruitment of inner leaflet PS molecules to these sites independent of the involvement of the actin machinery. Alternatively, if we are able to immobilize PS at the inner leaflet, long-acyl-chain-containing species at the outer leaflet should be co-localized to these regions. First, we crosslinked the folate receptor (FR-GPI) at the outer leaflet (Mayor and Maxfield, 1995) and examined the co-distribution of the inner leaflet lipid probes in plasma membrane blebs. In cells expressing Lact C2-GFP, which probes inner-leaflet PS, there is a strong correlation between the intensity distribution of Lact C2-GFP and PLB-FR-GPI, whereas a significantly reduced correlation was observed with PH-GFP, the PIP₂ probe (Figures 7A and 7B). Moreover, this correlation reduces upon cholesterol depletion for Lact C2-GFP (KS test, $p < 0.001$) but remains low and unaltered for PH-GFP (Figures 7A and 7B). As a control, we determined whether crosslinking the FR domain linked to transmembrane domain (FR-TM-Ez; Gowrishankar et al., 2012) could recruit Lact C2-GFP. Our results show that there is no significant correlation between crosslinked FR-TM-Ez and Lact C2-GFP (Figures 7A and 7B). These results indicate that PS at the inner leaflet couples strongly with cross-linked GPI-AP patches at the outer leaflet in a cholesterol-sensitive manner. Second, when the actin filament binding Lact C2-Ez-YFP is expressed in CHO cells, it is recruited to the plasma membrane (Figures 3D and 7C), where it is found concentrated on relatively stable actin stress fibers visible at the membrane surface in a TIRF field (Figures 3D and 7C). This provides an experimental handle to visualize actin-immobilized inner leaflet PS. Correspondingly, the fluorescence intensity distribution of an outer leaflet GPI-AP and exogenously added DHPE (B-DHPE; Figure 7C) are correlated with regions that show Lact C2-Ez-YFP enrichment. No enrichment of an exogenously added short chain synthetic lipid analog (GPI_{C8:0/C8:0}) is observed in the region of Lact C2-Ez-YFP enrichment (Figure 7C), confirming that this transbilayer coupling requires long acyl chains. The concentrating effect of PS on the outer leaflet lipid is only observed in the presence of an actin-PS connector because this was absent when the F-actin binding domain of Ezrin or the PS-binding domains are expressed on their own (Figure S7), which is consistent with the role of actin and its PS-binding partners in aiding the formation of nanoclusters. Taken together, the experiments point toward a general mechanism underlying transbilayer coupling where either of the outer or inner leaflet molecules need to be immobilized.

DISCUSSION

Our experimental and simulation results provide evidence that nanoclustering of outer leaflet GPI-APs and indeed any outer leaflet lipid by dynamic cortical actin is effected by the interdigitation and transbilayer coupling of lipids having long, saturated acyl chains, both in the outer and inner leaflets of the PM. This is contingent on properties of the lipid acyl chains, adequate cholesterol levels in the bilayer, and immobilization of the inner leaflet lipid. In contrast to transmembrane-anchored actin binding proteins, which straddle the bilayer, these three features

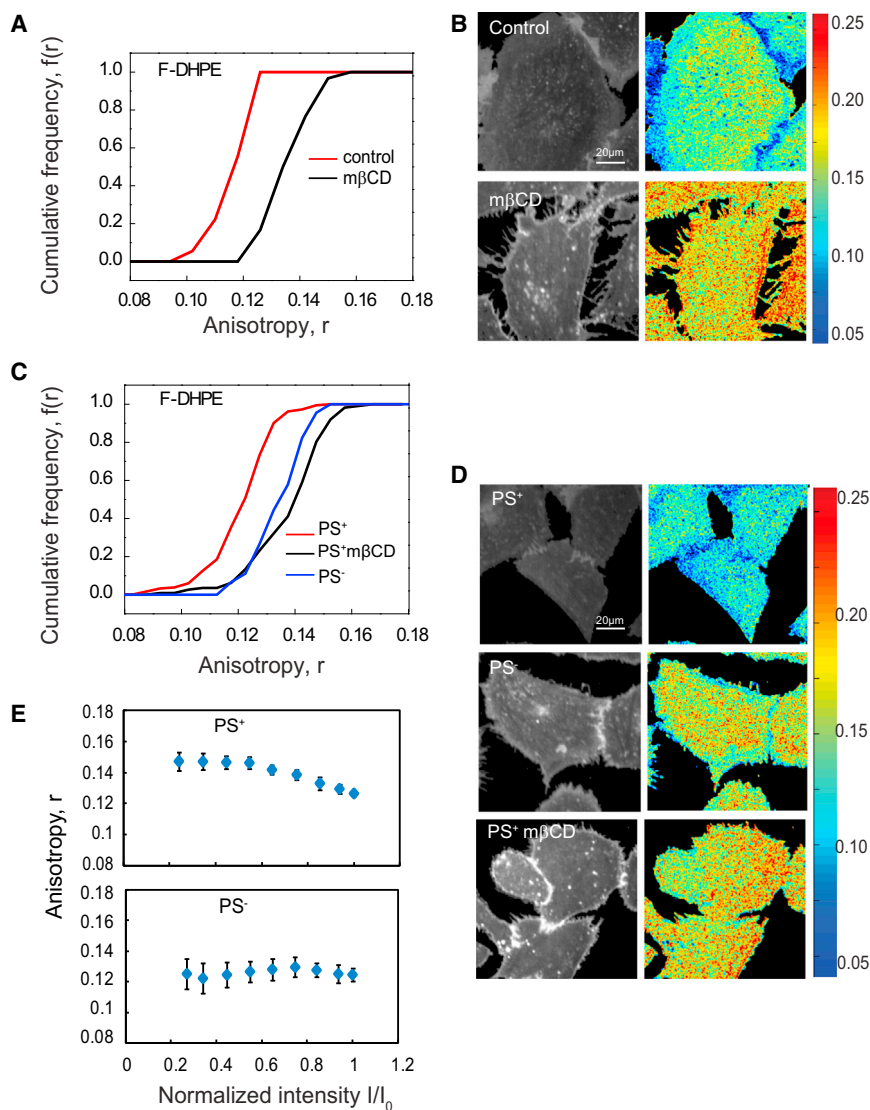


Figure 6. Lipids with Long Saturated Acyl Chains Are Sufficient to Drive Nanocluster Formation

(A–D) Cumulative frequency distribution (A and C) and fluorescence intensity and anisotropy images (B and D) of F-DHPE incorporated in control (IA2.2F) cells (A and B) and PSS1-deficient (PSA3) CHO cells (C and D) show that the fluorescence anisotropy of F-DHPE in control cells and PS replete (control, PS⁺; red line) is depolarized compared to that measured in cholesterol-depleted (black line) or PS-deficient (PS⁻) cells (blue line). Note that fluorescence anisotropy of F-DHPE in PS deplete (PS⁻) cells (blue line) is similar to that measured in saponin-treated cells (black line). Each data point in the graphs represents average anisotropy with SD for the corresponding intensity bin obtained from a 10×10 pixel region (20–50 regions per cell) from at least 40 cells derived from two independent experiments.

(E) Photobleaching profiles of F-DHPE incorporated into PS replete (PS⁺) cells and PS deplete (PS⁻) cells. PS replete (PS⁺) cells and PS deplete (PS⁻) cells were incorporated with exogenously added F-DHPE (E) photobleached and the fluorescence emission anisotropy recorded during the photobleaching process. Note that the profiles of change in fluorescence anisotropy upon change in fluorescence intensity in case of PS replete (PS⁺) cells are characteristic of nanoclustered fluorophores (Sharma et al., 2004), whereas PS deplete (PS⁻) cells exhibit no change, indicating the lack of homo-FRET. The starting intensity for all the samples collected here is similar and normalized to that used in the first frame.

Error bars represent SD. See also Figure S4.

allow for a flexibility and regulation of transbilayer communication of lipids.

The requirement for long acyl or alkyl chains to couple across the bilayer provides a purely lipidic coupling mechanism, obviating the need for any transmembrane protein coupling mechanism. This could also serve as a way to couple many outer leaflet membrane lipids such as Gangliosides and other sphingolipids (Wolf et al., 1998). The results from simulations show that cholesterol can stabilize local *lo*-like order over a length scale that is larger than the size of the immobilized cluster, suggesting that it might also engage in recruiting more components via a positive feedback mechanism leading to a composition gradient of components that favor *lo* domains.

The immobilization of the inner leaflet lipid relates to the mechanism needed for nanoclustering. In the atomistic MD simulations, carried out for a timescale of 200 ns (and reconfirmed by longer 1 μs runs; Supplemental Information), transbilayer coupling requires immobilization of PS lipid; the removal of

anchoring leads to a rapid loss of clustering of the lipids at both leaflets. We had previously shown that GPI-AP nanoclusters are “immobile” for a period of 0.1–1 s (Goswami et al., 2008). This could reflect the time of engagement of dynamic cortical actin filaments at the inner surface of the cell membrane (Gowrishankar et al., 2012). Additionally, immobilization of more than one lipid molecule is necessary to create the transbilayer connection; more molecules need to be immobilized, depending on how far the membrane composition is maintained away from the equilibrium *lo*-*ld* phase transition in order to couple across the bilayer.

Synthetic lipids with long acyl chains couple across the bilayer, forming dynamic actin-based nanoclusters; this mechanism is therefore capable of clustering any endogenous outer leaflet lipid species with long acyl chains if the inner leaflet lipid is sufficiently immobilized. Indeed, coupling of PS to a stable actin template such as a stress fiber via a synthetic PS-actin bridge (Lact C2-Ez-YFP) also served to recruit endogenous GPI-APs and exogenously added long-chain lipids (F-DHPE), but not short-chain lipids. Given that the nanoclusters formed by the contractile actin-based clustering machinery exhibit nanoscale clusters that appear to be co-segregated (Goswami et al., 2008; van

Zanten et al., 2009), this observation suggests that domains that are enriched in nanoclusters created by the transbilayer coupling mechanism will have *lo*-like character. Consistent with this, recent evidence from our group indicates that regions enriched in GPI-APs nanoclusters exhibit “*lo*”-like properties (Suvrajit Saha, A.A.A., and S.M., unpublished data). Together, these principles provide a very general mechanism whereby immobilizing an appropriate inner or outer leaflet lipid with long saturated acyl chains can help stabilize local *lo* domains even in a predominantly homogenous, mixed *ld* membrane.

We show that the co-segregation of GPI and PS is achieved when GPI is clustered and immobilized in the outer leaflet while allowing PS to equilibrate and vice versa. This has implications for the construction of cell-surface signaling platforms or sorting platforms at the inner leaflet by crosslinking long saturated GPI-anchored proteins (Stefanová et al., 1991; Suzuki et al., 2007; Wolf et al., 1998). Here, the clustering of GPI-APs at the outer leaflet appears to build complexes at the inner leaflet to effect specific signaling reactions. Additionally, local lipid organization plays a crucial role in the nanoclustering of cell-surface Ras molecules, thereby regulating signaling mechanisms locally (Ariotti et al., 2014). Inefficient coupling across the membrane can impair several cell-signaling events and can lead to major immune response and neurodegenerative disorders. For instance, deletion of PGAP3 results in enhanced T cell receptor signaling, as evaluated in PGAP3 knockout mice (Murakami et al., 2012), and a mutation in PGAP3 leads to a subtype of hyperphosphatase with intellectual disorders commonly referred to as Mabry syndrome (Howard et al., 2014).

Finally, PS must in turn be connected to endogenous actin-binding proteins. The capacity of the synthetic PS and actin binding fusion protein (LactC2-Ez-YFP) to reconstruct actin-based nanoclustering provides strong support for this idea. Several examples of such proteins exist such as talin (Muguruma et al., 1995), spectrin (An et al., 2004), caldesmon (Makuch et al., 1997), myosin 1A (Mazerik and Tyska, 2012), and vinculin (Ito et al., 1983), and to completely elucidate the mechanism of transbilayer coupling to actin, the identity of this coupling agent(s) needs to be determined.

In conclusion, we show that lipidic interactions mediated by long-chain interdigitation in the presence of cholesterol stabilize a transbilayer connection between outer and inner leaflet lipids when either of the lipid species is immobilized. The deployment of this mechanism in the mixed phase of the bilayer by active clusters of actin filaments, which can engage PS at the inner leaflet, provide a general mechanism to stabilize these *lo* domains locally. The formation of the contractile actin clusters would then determine when and where these domains may be stabilized, bringing the generation of membrane domains in live cells under control of the acto-myosin signaling network.

EXPERIMENTAL PROCEDURES

Detailed experimental conditions are provided in the [Extended Experimental Procedures](#) in the [Supplemental Information](#).

Plasmids, Cell Lines, Antibodies, and Other Reagents

CHO cell lines stably expressing folate receptor (IA2.2; Mayor and Maxfield, 1995) or carrying mutations in PGAP2 and 3 (PGAP2/3; Maeda et al., 2007),

PSA3 (PSA3; Nishijima et al., 1986), C term Ez GFP, and PH-GFP were obtained from several sources as indicated in the [Supplemental Information](#). IA2.2 cells, PSA3 cells, PGAP2/3 double-mutant cells, and FR-TM-Ez cells were maintained in Ham's F12 medium with an appropriate concentration of antibiotics as mentioned in the [Supplemental Information](#).

GPI and PS Analogs

The synthesis of fluorescently tagged GPI analogs and PLA₂-resistant PS analogs is described in detail in the [Extended Experimental Procedures](#).

GPI Analog and Lipid Incorporation

Synthetic GPI analogs were incorporated into cell membranes by the γ -CD method (Koivusalo et al., 2007), whereas PS analogs were incorporated by Lipofectamine method as described (Saha et al., 2015).

Diffusion Measurements

Fluorescence correlation spectroscopy (FCS) and fluorescence recovery after photobleaching (FRAP) measurements to determine proper incorporation were performed as described previously (Gowrishankar et al., 2012).

PI-PLC Treatment

PI-PLC was purified in the laboratory from *Bacillus thuringiensis* as reported (Kobayashi et al., 1996). Cells cooled on ice were incubated with PI-PLC (0.5 U/ml) for 1 hr and then washed with M1 and imaged live.

Anisotropy Measurements

Steady-state homo-FRET-based anisotropy measurements were carried out on a NikonTE2000 epifluorescence microscope equipped with an Andor TuCam dual camera imaging arrangement in the TIRF, spinning-disc confocal, or wide-field mode (Ghosh et al., 2012).

Treatments to Perturb Inner Leaflet Lipids, PIP₂ and PS

To perturb PIP₂, CHO cells were treated with either neomycin (10 μ M) or chlorpromazine (10 μ M) for 15 min at 37°C as described (Arbuzova et al., 2000; Raucher and Sheetz, 2001). For perturbation of PS levels, PSA3 cells were grown under replete (cells grown in the presence of 10 μ M ethanolamine) or deplete (cells grown in dialysed serum for 48 hr) conditions. PS levels were measured by assessing the extent of Annexin V binding as detailed in the [Supplemental Information](#).

Lipid Analysis and Mass Spectrometry Experiments

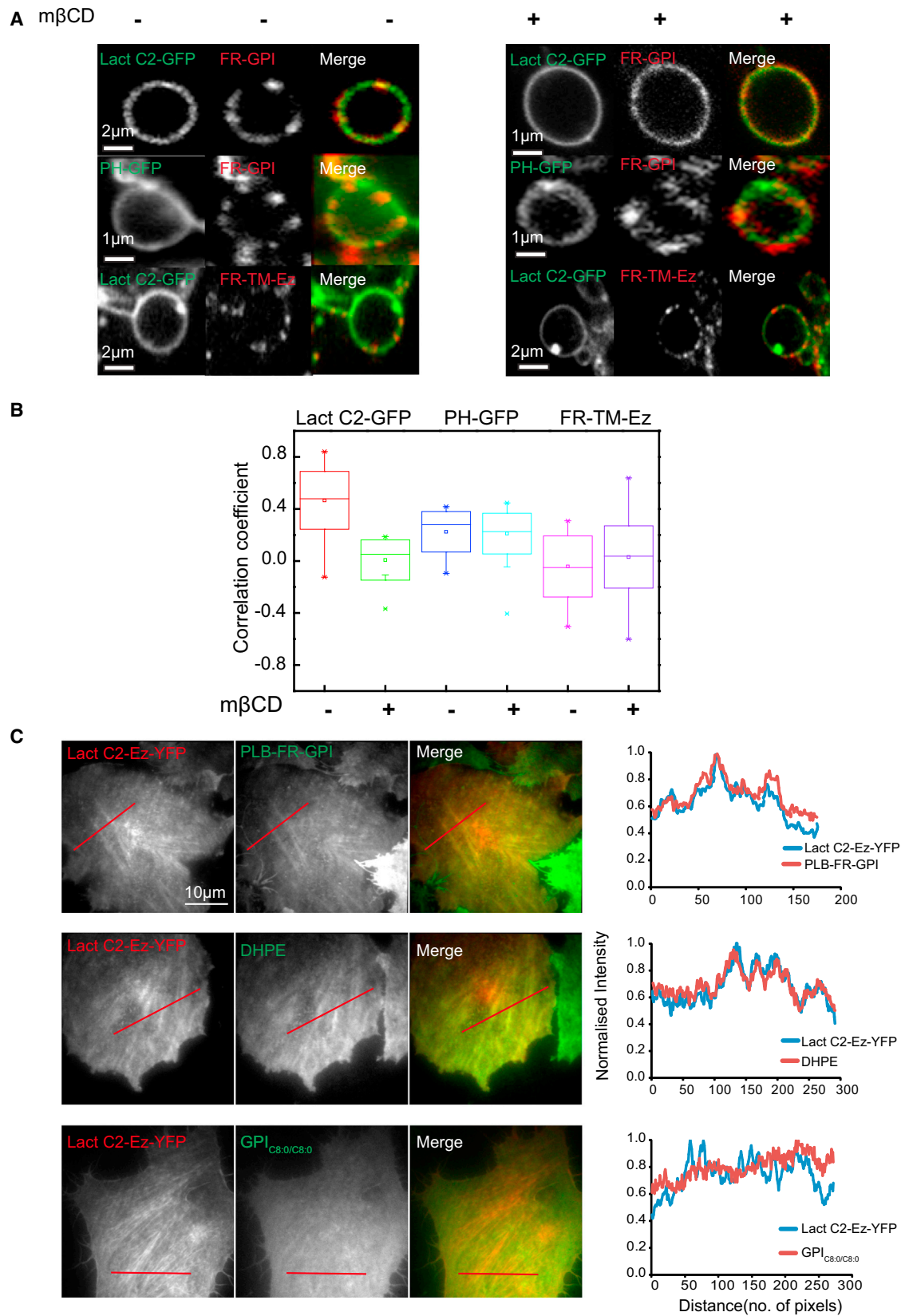
Lipids analysis was carried out on FACS sorted cells expressing specific transgenes (Lact C2-GFP or GFP) or on membrane blebs prepared from cells as detailed previously (Pick et al., 2005). Lipid extraction was done by Bligh and Dyer method (Bligh and Dyer, 1959), and mass spectrometry measurements were carried out on an LTQ Orbitrap XL hybrid mass spectrometer (Thermo Fisher Scientific).

Atomistic MD Simulations

We perform an all-atom MD simulation of the asymmetric, multi-component bilayer with POPC, cholesterol (Chol), and PSM in the upper leaflet and POPC and cholesterol in the lower leaflet at 23°C. GPI-AP and PS are inserted in the upper and lower leaflets, respectively. The relative composition of the bilayer is varied, and the detailed experimental procedures and simulation conditions are provided in the [Supplemental Information](#). The membrane bilayers were equilibrated and deemed to be mechanically stable prior to determining the distribution of various constituents. Immobilization of a molecular species is achieved by setting a high value to its mass without affecting other features of the simulation ([Supplemental Information](#)).

SUPPLEMENTAL INFORMATION

Supplemental Information includes Extended Experimental Procedures and seven figures and can be found with this article online at <http://dx.doi.org/10.1016/j.cell.2015.03.048>.



(legend on next page)

AUTHOR CONTRIBUTIONS

R.R., A.A.A., A.P., S.M., and M.R. designed the study. R.R. standardized the lipid incorporation methods, performed experiments, and analyzed the data involving the GPI analogs; A.A.A. performed experiments and analyzed the data involving the role of phosphatidylserine. A.P. performed the atomistic molecular dynamics simulations. P.P.S., M.Y., and C.J. prepared the GPI analogs, and S.S., V.S., and S.D.S. prepared the PS analogs. The design of the synthetic strategy and supervision was led by R.A.V. and Z.G. A.P. (NCBS) helped in performing the mass spectrometry experiments. R.R., A.A.A., A.P., M.R., and S.M. wrote the paper with input from all the authors.

ACKNOWLEDGMENTS

We thank Suvrajit Saha for help with FCS measurements and MEM analysis; Balaji for Matlab codes to analyze the anisotropy data; Kabir Husain for help with the correlation analysis; Joseph Jose Thottacherry and Darius Koester for FRAP measurement and analysis; Taroh Kinoshita, Tomohiko Taguchi, Tobias Meyer, and Antonio S. Sechi for their generous gifts of various reagents (as indicated in the [Supplemental Information](#)); Max Planck-NCBS lipid centre; Dominik Schwudke and Sudarkodi Sukumar for mass spectrometry; and H. Krishnamurthy and Manoj Mathew at the Central Imaging and Flow Facility (NCBS). R.R. acknowledges Vytas A. Bankaitis for suggestions with lipid incorporation methods. We thank Tampere University of Technology for help with the longer run simulations and all SM lab members for their critical comments on the manuscript. S.M. acknowledges JC Bose Fellowship from DST (Government of India) and a grant from HFSP RGP0027/2012. A.A.A. acknowledges pre-doctoral fellowship from CSIR. M.R. acknowledges a grant from Simons Foundation. Z.G. acknowledges NSF CHE-1053848 and NIH GM090270 for providing financial support.

Received: July 31, 2014

Revised: November 12, 2014

Accepted: March 18, 2015

Published: April 23, 2015

REFERENCES

- An, X., Guo, X., Wu, Y., and Mohandas, N. (2004). Phosphatidylserine binding sites in red cell spectrin. *Blood Cells Mol. Dis.* 32, 430–432.
- Arbuzova, A., Martushova, K., Hangyás-Mihályné, G., Morris, A.J., Ozaki, S., Prestwich, G.D., and McLaughlin, S. (2000). Fluorescently labeled neomycin as a probe of phosphatidylinositol-4, 5-bisphosphate in membranes. *Biochim. Biophys. Acta* 1464, 35–48.
- Ariotti, N., Fernández-Rojo, M.A., Zhou, Y., Hill, M.M., Rodkey, T.L., Inder, K.L., Tanner, L.B., Wenk, M.R., Hancock, J.F., and Parton, R.G. (2014). Caveolae regulate the nanoscale organization of the plasma membrane to remotely control Ras signaling. *J. Cell Biol.* 204, 777–792.
- Baumgart, T., Hammond, A.T., Sengupta, P., Hess, S.T., Holowka, D.A., Baird, B.A., and Webb, W.W. (2007). Large-scale fluid/fluid phase separation of proteins and lipids in giant plasma membrane vesicles. *Proc. Natl. Acad. Sci. USA* 104, 3165–3170.
- Bligh, E.G., and Dyer, W.J. (1959). A rapid method of total lipid extraction and purification. *Can. J. Biochem. Physiol.* 37, 911–917.
- Brodsky, R.A., Mukhina, G.L., Li, S., Nelson, K.L., Chiorazzi, P.L., Buckley, J.T., and Borowitz, M.J. (2000). Improved detection and characterization of paroxysmal nocturnal hemoglobinuria using fluorescent aerolysin. *Am. J. Clin. Pathol.* 114, 459–466.
- Burke, J.E., and Dennis, E.A. (2009). Phospholipase A2 structure/function, mechanism, and signaling. *J. Lipid Res.* 50, S237–S242.
- Chaudhuri, A., Bhattacharya, B., Gowrishankar, K., Mayor, S., and Rao, M. (2011). Spatiotemporal regulation of chemical reactions by active cytoskeletal remodeling. *Proc. Natl. Acad. Sci. USA* 108, 14825–14830.
- Coskun, Ü., Grzybek, M., Drechsel, D., and Simons, K. (2011). Regulation of human EGF receptor by lipids. *Proc. Natl. Acad. Sci. USA* 108, 9044–9048.
- Fujita, A., Cheng, J., Hirakawa, M., Furukawa, K., Kusunoki, S., and Fujimoto, T. (2007). Gangliosides GM1 and GM3 in the living cell membrane form clusters susceptible to cholesterol depletion and chilling. *Mol. Biol. Cell* 18, 2112–2122.
- Gaus, K., Le Lay, S., Balasubramanian, N., and Schwartz, M.A. (2006). Integrin-mediated adhesion regulates membrane order. *J. Cell Biol.* 174, 725–734.
- Ghosh, S., Saha, S., Goswami, D., Bilgrami, S., and Mayor, S. (2012). Dynamic imaging of homo-FRET in live cells by fluorescence anisotropy microscopy. *Methods Enzymol.* 505, 291–327.
- Goswami, D., Gowrishankar, K., Bilgrami, S., Ghosh, S., Raghupathy, R., Chadda, R., Vishwakarma, R., Rao, M., and Mayor, S. (2008). Nanoclusters of GPI-anchored proteins are formed by cortical actin-driven activity. *Cell* 135, 1085–1097.
- Gowrishankar, K., Ghosh, S., Saha, S., C. R., Mayor, S., and Rao, M. (2012). Active remodeling of cortical actin regulates spatiotemporal organization of cell surface molecules. *Cell* 149, 1353–1367.
- Howard, M.F., Murakami, Y., Pagnamenta, A.T., Daumer-Haas, C., Fischer, B., Hecht, J., Keays, D.A., Knight, S.J.L., Kölsch, U., Krüger, U., et al. (2014). Mutations in PGAP3 impair GPI-anchor maturation, causing a subtype of hyperphosphatasia with mental retardation. *Am. J. Hum. Genet.* 94, 278–287.
- Ito, S., Werth, D.K., Richert, N.D., and Pastan, I. (1983). Vinculin phosphorylation by the src kinase. Interaction of vinculin with phospholipid vesicles. *J. Biol. Chem.* 258, 14626–14631.
- Jaqaman, K., Kuwata, H., Touret, N., Collins, R., Trimble, W.S., Danuser, G., and Grinstein, S. (2011). Cytoskeletal control of CD36 diffusion promotes its receptor and signaling function. *Cell* 146, 593–606.
- Kaiser, H.J., Lingwood, D., Levental, I., Sampaio, J.L., Kalvodova, L., Rajendran, L., and Simons, K. (2009). Order of lipid phases in model and plasma membranes. *Proc. Natl. Acad. Sci. USA* 106, 16645–16650.
- Kennedy, E.P., and Weiss, S.B. (1956). The function of cytidine coenzymes in the biosynthesis of phospholipides. *J. Biol. Chem.* 222, 193–214.
- Kobayashi, T., Tamura, H., Taguchi, R., Uda, S., and Ikezawa, H. (1996). High-level expression of *Bacillus thuringiensis* phosphatidylinositol-specific phospholipase C by the *Bacillus brevis* host-vector system. *Jpn. J. Med. Sci. Biol.* 49, 103–112.
- Koivusalo, M., Jansen, M., Somerharju, P., and Ikonen, E. (2007). Endocytic trafficking of sphingomyelin depends on its acyl chain length. *Mol. Biol. Cell* 18, 5113–5123.

Figure 7. Crosslinking of Either FR-GPI at the Outer Leaflet or PS at the Inner Leaflet Demonstrates a Strong Transbilayer Coupling

(A) Cropped images of membrane blebs obtained after jasplakinolide treatment cells expressing Lact C2 GFP or PH GFP (left, green in merge) either with (treated) or without mβCD (control), followed by cross-linking FR-GPI or FR-TM-Ez (middle, as indicated; red in merge) with primary and secondary antibodies to create micron-sized patches of these proteins.

(B) Graph shows the extent of correlation between the intensity fluctuation of crosslinked FR-GPI or FR-TM-Ez and PH GFP or Lact C2 GFP both in the presence (+) and absence (–) of mβCD, determined from images of blebs (pooled from three independent experiments) as shown in (A).

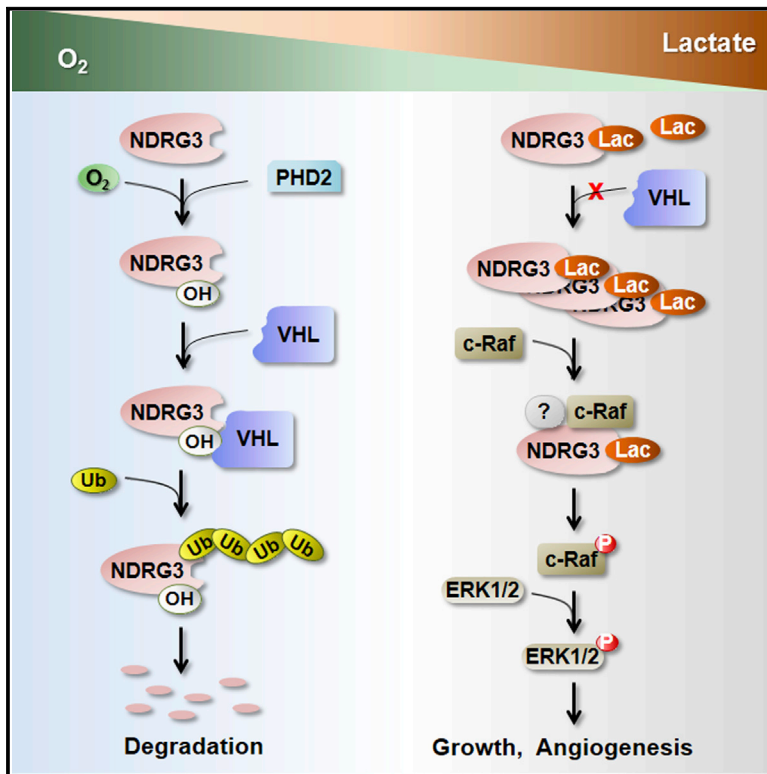
(C) Images and normalized line intensity profiles of Lact C2-Ez-YFP transfected in IA2.2 cells labeled with PLB or DHPE or C8 GPI analog as indicated. This shows a strong colocalization in the distribution of Lact C2-Ez-YFP with FR-GPI and DHPE, but not with C8 GPI analog. Red line in (C) depicts the region of line scan measurement. Scale bar, 10 μm.

The whiskers represent the outliers. See also [Figure S7](#).

- Kumari, S., and Mayor, S. (2008). ARF1 is directly involved in dynamin-independent endocytosis. *Nat. Cell Biol.* **10**, 30–41.
- Maeda, Y., Tashima, Y., Houjou, T., Fujita, M., Yoko-o, T., Jigami, Y., Taguchi, R., and Kinoshita, T. (2007). Fatty acid remodeling of GPI-anchored proteins is required for their raft association. *Mol. Biol. Cell* **18**, 1497–1506.
- Makuch, R., Zasada, A., Mabuchi, K., Krauze, K., Wang, C.L.A.L., and Dabrowska, R. (1997). Phosphatidylserine liposomes can be tethered by caldesmon to actin filaments. *Biophys. J.* **73**, 1607–1616.
- Marchetti, M.C., Joanny, J.F., Ramaswamy, S., Liverpool, T.B., Prost, J., Rao, M., and Simha, R.A. (2013). Hydrodynamics of soft active matter. *Rev. Mod. Phys.* **85**, 1143–1189.
- Mayor, S., and Maxfield, F.R. (1995). Insolubility and redistribution of GPI-anchored proteins at the cell surface after detergent treatment. *Mol. Biol. Cell* **6**, 929–944.
- Mayor, S., and Pagano, R.E. (2007). Pathways of clathrin-independent endocytosis. *Nat. Rev. Mol. Cell Biol.* **8**, 603–612.
- Mayor, S., and Riezman, H. (2004). Sorting GPI-anchored proteins. *Nat. Rev. Mol. Cell Biol.* **5**, 110–120.
- Mazerik, J.N., and Tyska, M.J. (2012). Myosin-1A targets to microvilli using multiple membrane binding motifs in the tail homology 1 (TH1) domain. *J. Biol. Chem.* **287**, 13104–13115.
- McConville, M.J., and Ferguson, M.A. (1993). The structure, biosynthesis and function of glycosylated phosphatidylinositols in the parasitic protozoa and higher eukaryotes. *Biochem. J.* **294**, 305–324.
- Muguruma, M., Nishimuta, S., Tomisaka, Y., Ito, T., and Matsumura, S. (1995). Organization of the functional domains in membrane cytoskeletal protein talin. *J. Biochem.* **117**, 1036–1042.
- Murakami, H., Wang, Y., Hasuwa, H., Maeda, Y., Kinoshita, T., and Murakami, Y. (2012). Enhanced response of T lymphocytes from Pgap3 knockout mouse: Insight into roles of fatty acid remodeling of GPI anchored proteins. *Biochem. Biophys. Res. Commun.* **417**, 1235–1241.
- Nishijima, M., Kuge, O., and Akamatsu, Y. (1986). Phosphatidylserine biosynthesis in cultured Chinese hamster ovary cells. I. Inhibition of de novo phosphatidylserine biosynthesis by exogenous phosphatidylserine and its efficient incorporation. *J. Biol. Chem.* **261**, 5784–5789.
- Percy, A.K., Moore, J.F., Carson, M.A., and Waechter, C.J. (1983). Characterization of brain phosphatidylserine decarboxylase: localization in the mitochondrial inner membrane. *Arch. Biochem. Biophys.* **223**, 484–494.
- Pick, H., Schmid, E.L., Tairi, A., Ilegems, E., Hovius, R., and Vogel, H. (2005). Investigating cellular signaling reactions in single attoliter vesicles. *J. Am. Chem. Soc.* **127**, 2908–2912.
- Polley, A., Vemparala, S., and Rao, M. (2012). Atomistic simulations of a multicomponent asymmetric lipid bilayer. *J. Phys. Chem. B* **116**, 13403–13410.
- Polley, A., Mayor, S., and Rao, M. (2014). Bilayer registry in a multicomponent asymmetric membrane: dependence on lipid composition and chain length. *J. Chem. Phys.* **141**, 064903.
- Prior, I.A., Muncke, C., Parton, R.G., and Hancock, J.F. (2003). Direct visualization of Ras proteins in spatially distinct cell surface microdomains. *J. Cell Biol.* **160**, 165–170.
- Rauchner, D., and Sheetz, M.P. (2001). Phospholipase C activation by anesthetics decreases membrane-cytoskeleton adhesion. *J. Cell Sci.* **114**, 3759–3766.
- Saha, S., Raghupathy, R., and Mayor, S. (2015). Homo-FRET imaging highlights the nanoscale organization of cell surface molecules. *Methods Mol. Biol.* **1251**, 151–173.
- Sengupta, P., Jovanovic-Talman, T., Skoko, D., Renz, M., Veatch, S.L., and Lippincott-Schwartz, J. (2011). Probing protein heterogeneity in the plasma membrane using PALM and pair correlation analysis. *Nat. Methods* **8**, 969–975.
- Sharma, P., Varma, R., Sarasij, R.C., Ira, Gousset, K., Krishnamoorthy, G., Rao, M., and Mayor, S. (2004). Nanoscale organization of multiple GPI-anchored proteins in living cell membranes. *Cell* **116**, 577–589.
- Simons, K., and Ikonen, E. (1997). Functional rafts in cell membranes. *Nature* **387**, 569–572.
- Simons, K., and Vaz, W.L.C. (2004). Model systems, lipid rafts, and cell membranes. *Annu. Rev. Biophys. Biomol. Struct.* **33**, 269–295.
- Singer, S.J., and Nicolson, G.L. (1972). The fluid mosaic model of the structure of cell membranes. *Science* **175**, 720–731.
- Stauffer, T.P., Ahn, S., and Meyer, T. (1998). Receptor-induced transient reduction in plasma membrane PtdIns(4,5)P₂ concentration monitored in living cells. *Curr. Biol.* **8**, 343–346.
- Stefanová, I., Horejší, V., Ansotegui, I.J., Knapp, W., and Stockinger, H. (1991). GPI-anchored cell-surface molecules complexed to protein tyrosine kinases. *Science* **254**, 1016–1019.
- Suzuki, K.G.N., Fujiwara, T.K., Sanematsu, F., Iino, R., Edidin, M., and Kusumi, A. (2007). GPI-anchored receptor clusters transiently recruit Lyn and G α for temporary cluster immobilization and Lyn activation: single-molecule tracking study 1. *J. Cell Biol.* **177**, 717–730.
- Swamy, M.J., Ciani, L., Ge, M., Smith, A.K., Holowka, D., Baird, B., and Freed, J.H. (2006). Coexisting domains in the plasma membranes of live cells characterized by spin-label ESR spectroscopy. *Biophys. J.* **90**, 4452–4465.
- van Zanten, T.S., Cambi, A., Koopman, M., Joosten, B., Figdor, C.G., and Garcia-Parajo, M.F. (2009). Hotspots of GPI-anchored proteins and integrin nanoclusters function as nucleation sites for cell adhesion. *Proc. Natl. Acad. Sci. USA* **106**, 18557–18562.
- Varma, R., and Mayor, S. (1998). GPI-anchored proteins are organized in sub-micron domains at the cell surface. *Nature* **394**, 798–801.
- Wolf, A.A., Jobling, M.G., Wimer-Mackin, S., Ferguson-Maltzman, M., Madara, J.L., Holmes, R.K., Lencer, W.I., Ruston, S., Madara, J.L., and Hirst, T. (1998). Ganglioside structure dictates signal transduction by cholera toxin and association with caveolae-like membrane domains in polarized epithelia. *J. Cell Biol.* **141**, 917–927.
- Yeung, T., Gilbert, G.E., Shi, J., Silvius, J., Kapus, A., and Grinstein, S. (2008). Membrane phosphatidylserine regulates surface charge and protein localization. *Science* **319**, 210–213.
- Yin, H.L., and Janmey, P.A. (2003). Phosphoinositide regulation of the actin cytoskeleton. *Annu. Rev. Physiol.* **65**, 761–789.

A Lactate-Induced Response to Hypoxia

Graphical Abstract



Authors

Dong Chul Lee, Hyun Ahm Sohn, ...,
Kyung Chan Park, Young Il Yeom

Correspondence

kpark@kribb.re.kr (K.C.P.),
yeomyi@kribb.re.kr (Y.I.Y.)

In Brief

Lactate, a common product of anaerobic metabolism, can promote a hypoxic response independent of HIF. It does so by binding as stabilizing the NDRG3 protein that, in turn, triggers signals for cell growth and angiogenesis.

Highlights

- NDRG3 is an oxygen-regulated substrate of PHD2/VHL pathway
- Lactate binds to NDRG3, boosting its levels in hypoxia
- NDRG3 activates Raf-ERK signaling to mediate lactate-triggered hypoxia responses

Accession Numbers

GSE55214



A Lactate-Induced Response to Hypoxia

Dong Chul Lee,¹ Hyun Ahm Sohn,¹ Zee-Yong Park,⁵ Sangho Oh,³ Yun Kyung Kang,⁶ Kyoung-min Lee,⁵ Minho Kang,¹ Ye Jin Jang,¹ Suk-Jin Yang,¹ Young Ki Hong,¹ Hanmi Noh,^{1,7} Jung-Ae Kim,^{1,7} Dong Joon Kim,¹ Kwang-Hee Bae,^{4,7} Dong Min Kim,¹ Sang J. Chung,¹ Hyang Sook Yoo,¹ Dae-Yeul Yu,¹ Kyung Chan Park,^{1,*} and Young Il Yeom^{1,2,7,*}

¹Medical Genomics Research Center

²Ochang Branch Institute

³Korean Bioinformation Center

⁴Research Center for Integrative Cellulomics

Korea Research Institute of Bioscience and Biotechnology (KRIBB), Daejeon 305-806, Korea

⁵Department of Life Science, Gwangju Institute of Science and Technology, Gwangju 500-712, Korea

⁶Department of Pathology, Inje University Seoul Paik Hospital, Seoul 100-032, Korea

⁷Department of Functional Genomics, Korea University of Science and Technology, Daejeon 305-350, Korea

*Correspondence: kpark@kribb.re.kr (K.C.P.), yeomyi@kribb.re.kr (Y.I.Y.)

<http://dx.doi.org/10.1016/j.cell.2015.03.011>

SUMMARY

Organisms must be able to respond to low oxygen in a number of homeostatic and pathological contexts. Regulation of hypoxic responses via the hypoxia-inducible factor (HIF) is well established, but evidence indicates that other, HIF-independent mechanisms are also involved. Here, we report a hypoxic response that depends on the accumulation of lactate, a metabolite whose production increases in hypoxic conditions. We find that the NDRG3 protein is degraded in a PHD2/VHL-dependent manner in normoxia but is protected from destruction by binding to lactate that accumulates under hypoxia. The stabilized NDRG3 protein binds c-Raf to mediate hypoxia-induced activation of Raf-ERK pathway, promoting angiogenesis and cell growth. Inhibiting cellular lactate production abolishes the NDRG3-mediated hypoxia responses. Our study, therefore, elucidates the molecular basis for lactate-induced hypoxia signaling, which can be exploited for the development of therapies targeting hypoxia-induced diseases.

INTRODUCTION

Oxygen homeostasis is essential for metazoan physiology. Under low oxygen conditions, cells resort to hypoxia-induced responses to adapt to and survive harsh environments (Cassavaugh and Lounsbury, 2011). Hypoxia responses are an integral part of normal physiology during embryonic development and postnatal life. They are also pathophysiologic components of many disorders, including cancer, inflammation, and cardiovascular diseases.

Hypoxia inducible factors (HIFs) play central roles in hypoxia responses by controlling the expression of a host of hypoxia-responsive genes functioning in diverse processes, including metabolism, oxygen delivery, pH regulation, angiogenesis, cell proliferation, and survival (Harris, 2002; Cassavaugh and Lounsbury,

2011). In particular, the HIF-mediated upregulation of glycolysis and suppression of the citric acid (TCA) cycle is a crucial adaptive response at the early stage of hypoxia (Cassavaugh and Lounsbury, 2011). The expression and activity of HIFs are tightly regulated by oxygen-dependent hydroxylation of their α subunits (Semenza, 2003).

Growing evidence indicates that hypoxia has many aspects that are not explained by HIF-mediated mechanisms alone. For example, the inhibition of HIF-mediated pathways does not always prevent tumor growth; tumors derived from HIF-1 α -deficient embryonic stem (ES) cells have growth advantages owing to decreased hypoxia-induced apoptosis and increased stress-induced proliferation (Carmeliet et al., 1998). A number of reports suggest that tumor angiogenesis constitutes the major pathway of HIF-independent tumorigenesis. Thus, angiogenesis was preserved when *HIF1A* was knocked-out in ES cells (Höpfl et al., 2002). Several lines of evidence indicate that the pro-angiogenic factor, vascular endothelial growth factor (VEGF), can be induced via both HIF-dependent and HIF-independent pathways (Mizukami et al., 2004). Induction of other pro-angiogenic factors such as IL-8 preserves the angiogenic response in HIF-1 α -deficient colon cancer cells (Mizukami et al., 2005). Moreover, multiple pathways and transcription factors (TFs) other than HIFs are known to respond to hypoxia to induce biological responses in a HIF-independent manner. Among those oxygen-regulatable TFs are NF- κ B, AP-1, and CEBP, which are activated in hypoxia (Cummins and Taylor, 2005). Consequently, several reports demonstrated that some of the genes regulated by hypoxia were not regulated by HIFs, suggesting a role for other oxygen-regulated pathways that are, similar to HIF pathways, controlled by prolyl hydroxylase domain (PHD) enzymes (Elvidge et al., 2006). Also, a number of protein kinases such as PKA, PKC, PI3K, AKT, JNK, PTK2B (Pyk2), SRC, MAPK14 (p38), and ERK1/2 are reported to be activated in hypoxia (Seta et al., 2002). However, despite all of these studies, key elements and mechanisms responsible for oxygen-dependent regulation of the HIF-independent branch of hypoxia responses remain elusive.

In this study, we identified an oxygen-regulated protein, NDRG3 (NDRG family member 3; NM_032013), as a bona fide substrate of the PHD2/VHL system. NDRG3 was highly induced

under oxygen-limited conditions in diverse cell types, although its mRNA expression was independent of HIF levels under hypoxia. Interestingly, NDRG3 required binding by the glycolytic end-product lactate for its hypoxic accumulation, rendering its expression indirectly dependent on HIF expression as HIF-1 α regulates the hypoxic expression of lactate dehydrogenase A (LDHA). We found that NDRG3 plays critical roles in lactate-induced hypoxia signaling by mediating the activation of the Raf-ERK pathway to promote angiogenesis and cell growth during prolonged hypoxia. Thus, *NDRG3* provides a critical genetic element for the oxygen- and lactate-dependent regulation of prolonged hypoxia responses.

RESULTS

Identification of NDRG3 as the Substrate of PHD2

To identify the regulators of hypoxia responses, we searched for PHD2-binding proteins in MCF-7 cells expressing Flag-tagged PHD2 via Flag-mediated immunoprecipitation coupled to mass spectrometry. Among the candidates enriched in the protein bands reproducibly exhibiting differential immunoprecipitation patterns between mock and PHD2-Flag fractions, we chose *NDRG3* for further studies since it belongs to a gene family implicated in cell proliferation, migration, and invasion as well as in differentiation and development (Melotte et al., 2010), which are biological features closely associated with hypoxia (Harris, 2002; Cassavaugh and Lounsbury, 2011) (Figure S1A).

To characterize NDRG3 in detail, we developed an affinity-purified polyclonal antibody specific to NDRG3 among the human *NDRG* family members (Figure S1B). This antibody detected NDRG3 as a 42-KDa band in the PHD2-Flag immunoprecipitation fraction (Figure 1A). We verified the NDRG3-PHD2 interaction by immunoprecipitating endogenous NDRG3 with PHD2-Flag from HeLa cells grown under hypoxia (Figure 1B) and directly by a pull-down assay using recombinant PHD2-His and NDRG3-GST proteins (Figure S1C). Thus, we concluded that NDRG3 is a bona fide PHD2-binding protein.

We then examined possible functional relationships between PHD2 and NDRG3 using a PHD inhibitor, desferrioxamine (DFX). Although the basal-level expression of NDRG3 was negligible, PHD inhibition caused its dose-dependent accumulation in HeLa (Figure 1C) and MCF-7 cells (Figure S1D). These results were reproducible with two other PHD inhibitors, dimethylxaloylglycine (DMOG) and CoCl₂ (Figure S1E), suggesting that the NDRG3 protein expression might be under PHD-mediated posttranslational control. We then examined different PHD family members for their involvement in the regulation of NDRG3 by silencing their expression under normoxia using small interfering RNAs (siRNAs). The analysis results revealed that, as in the case of HIF-1 α , PHD2 is the major regulator of NDRG3 expression among the PHD family members (Figure 1D, left). This was supported by the identification of differential interactions between NDRG3 and PHD2 in a co-immunoprecipitation assay (Figure S1F). Depletion of *VHL*, the targeting element of E3 ubiquitin ligase complex, also caused NDRG3 accumulation under normoxia (Figure 1D, right), suggesting that NDRG3 is likely a target of PHD2/VHL-mediated posttranslational modification. To address this point more thoroughly, we prepared several var-

iants of the NDRG3 protein carrying single amino acid changes in their putative PHD2-docking site, predicted from a docking model between a putative NDRG3 structure and the published PHD2 structure (Chowdhury et al., 2009) (Figure S1G). A co-immunoprecipitation assay showed that the NDRG3 mutants could be ranked according to their PHD2-binding strengths in the following order: V296D > Q97E > R47D \approx N66D, which, interestingly, appeared to be inversely correlated with their protein expression levels in normoxia (Figure 1E). Moreover, NDRG3 variants retaining higher affinity for PHD2 co-immunoprecipitated higher amount of HA-tagged VHL protein (Figure 1E), indicating that the interaction of NDRG3 with PHD2 and VHL is a critical determinant of its protein expression. Next, in an in vivo ubiquitination assay, the amount of ubiquitin immunoprecipitated with NDRG3 was increased by overexpression of NDRG3, while it was decreased by silencing of its expression by different short hairpin RNAs (shRNAs) (Figures 1F and S1H). In addition, proteasome inhibition with MG132 dramatically increased the detected levels of NDRG3 in HeLa cells (Figure S1I). Collectively, these results demonstrate that NDRG3 is a PHD2-interacting protein whose expression is negatively regulated by PHD2/VHL-mediated proteasomal pathways.

Oxygen-Dependent Regulation of NDRG3 Protein Expression

Since PHD2 critically depends on O₂ availability for its activity, we examined whether the NDRG3 protein expression is regulated in an oxygen-dependent manner. NDRG3 accumulated in MCF-7 cells at rates that were inversely correlated with O₂ concentrations (Figures 2A and S2A). Consistent with this, NDRG3 ubiquitination was significantly suppressed in HeLa cells under hypoxia (Figure 2B). The hypoxic induction of NDRG3 was demonstrated in cancer cells of diverse tissue origins as well as in non-transformed cells (Figure S2B), suggesting a universality of the phenomenon. However, in contrast to HIF-1 α protein showing a sort of bell-shaped induction pattern at the early stage of hypoxia, NDRG3 exhibited a sigmoidal expression pattern, starting when HIF-1 α levels began to decline and lasting until later stages of hypoxia (Figure 2C). The hypoxic expression of NDRG3 slowly diminished as cells were reoxygenated (Figure S2C). These results strongly suggest that NDRG3 protein expression is negatively regulated by oxygen.

Next, we investigated the molecular basis of the oxygen-dependent regulation of NDRG3 protein expression. Mass spectrometric analysis revealed that NDRG3 is specifically hydroxylated at proline 294, suggesting that it might be the residue modified by PHD2 (Figure 2D). Site-directed mutagenesis of proline 294 to alanine (P294A) resulted in pronounced accumulation of the variant protein in normoxia (Figure 2E, left). Moreover, a co-immunoprecipitation assay showed that the P294A mutant protein possessed a significantly reduced binding affinity for PHD2 and VHL proteins compared to wild-type (Figure 2E, right), indicating that proline 294 is the critical target site of PHD2-mediated hydroxylation that determines NDRG3 protein stability in normoxia.

Since the expression of HIF-1 α immediately preceded that of NDRG3 (Figure 2C), we investigated the possibility of HIF-1 α transcriptionally regulating *NDRG3* expression during hypoxia.

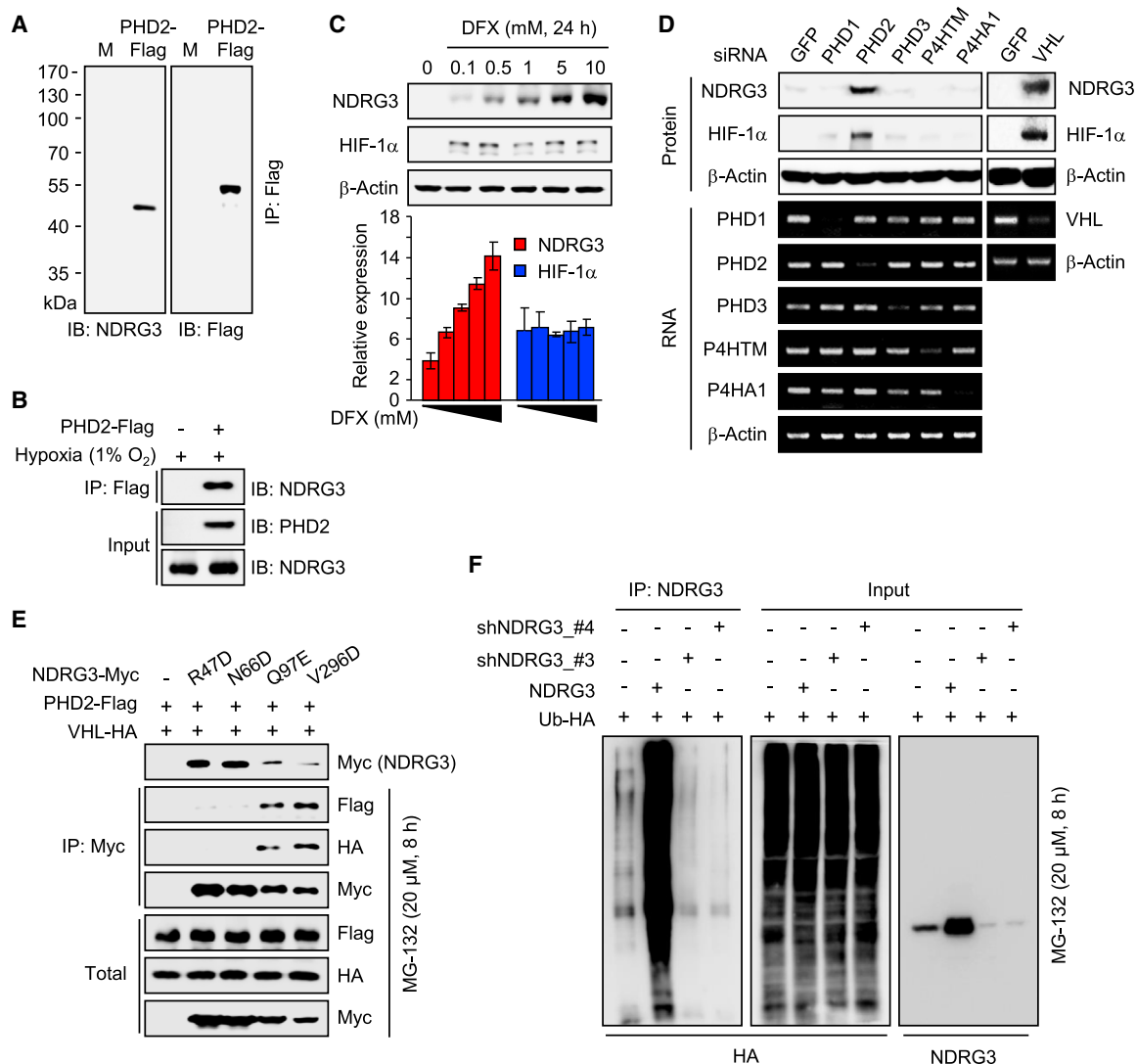


Figure 1. NDRG3 Protein Is Regulated by PHD2/VHL-Mediated Proteasomal Pathway

(A) Identification of NDRG3 as a PHD2-binding protein in MCF-7 cells.

(B) Validation of PHD2-NDRG3 interaction in HeLa cells under hypoxia.

(C) Induction of NDRG3 protein by inhibiting PHDs with desferrioxamine (DFX) in HeLa cells at normoxia. Results are mean \pm SD of three experiments.

(D) Effects of depleting different PHD family members (left) or VHL (right) on NDRG3 protein expression in HeLa cells in normoxia.

(E) Expression pattern of NDRG3 variants mutated in putative PHD2-binding sites and their interaction with PHD2 and VHL in HEK293T cells.

(F) Ubiquitination assay of NDRG3 protein in HeLa cells at normoxia.

See also Figure S1.

RT-PCR analysis showed that *NDRG3* mRNA level remained virtually unchanged during hypoxia, even when HIF proteins reached their peak levels (Figure S2D). This result indicates the HIF independence of *NDRG3* transcription and confirms the posttranslational nature of *NDRG3* expression during hypoxia. Depletion of different subunits of HIF had no effects on *NDRG3* mRNA levels, confirming the HIF independence of its transcription (Figure 2F). It is noteworthy that although *NDRG3* protein expression in hypoxia was clearly detectable in HIF-silenced cells, it was significantly reduced compared to control by HIF-1 β knockdown and, to a much lesser extent, by HIF-1 α knock-

down, suggesting a potential non-transcriptional effect of the HIF pathway on *NDRG3* protein expression. Meanwhile, we could show that HIF played a role as a transcriptional activator for the hypoxic expression of another *NDRG* family member, *NDRG1* (Figure S2E). These results collectively indicate that HIF activity is not required for the transcriptional regulation of *NDRG3* expression during hypoxia.

Role of NDRG3 in the Regulation of Hypoxia Responses

We investigated the potential functions of *NDRG3* in hypoxia by correlating its protein expression profile with the genomic

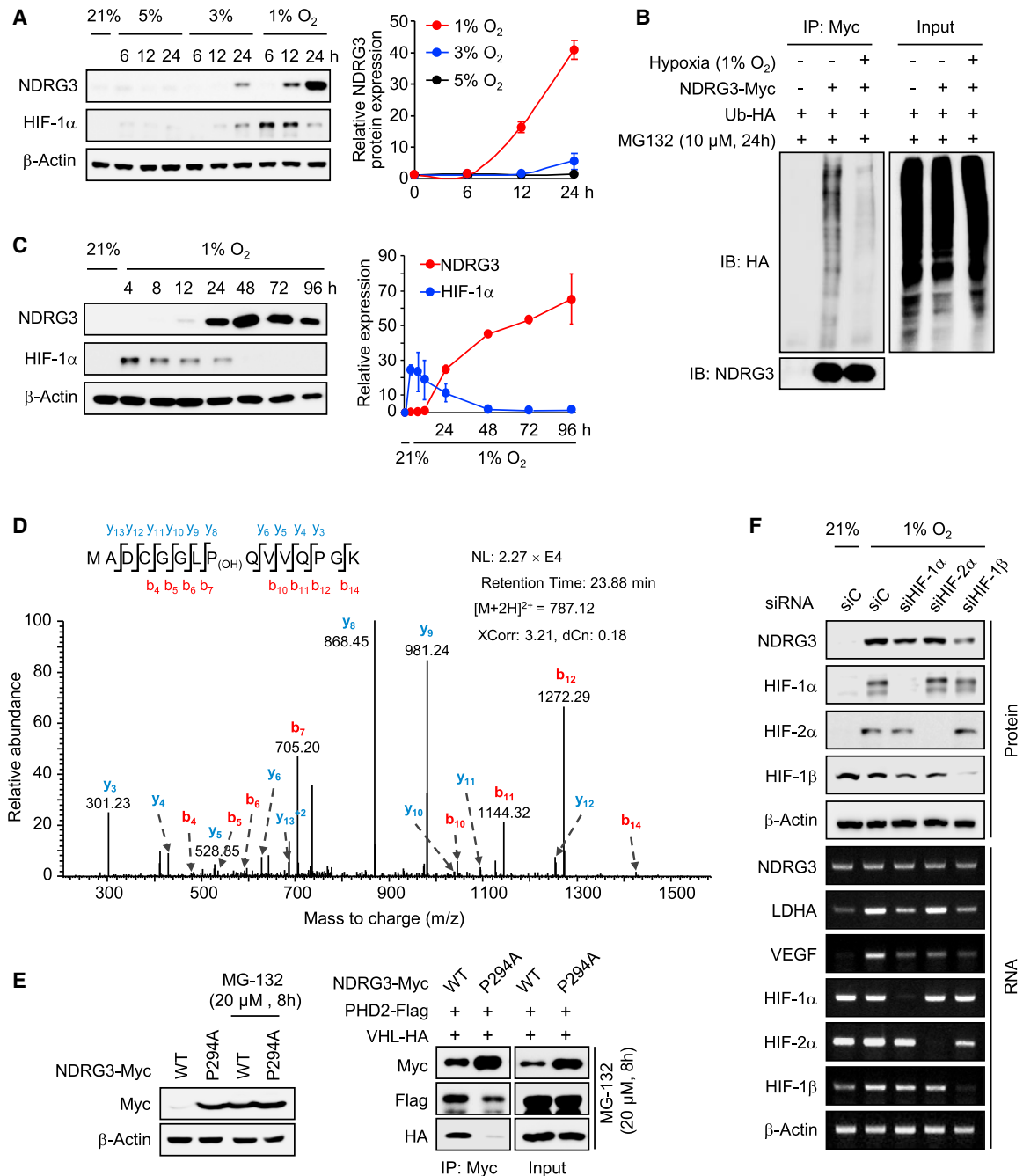


Figure 2. NDRG3 Expression Is Regulated in an Oxygen-Dependent Manner

(A) NDRG3 protein expression at different oxygen concentrations in MCF-7 cells. Quantified values for western blot images are shown on the right. Results are mean ± SD of three experiments.

(B) Oxygen dependency of NDRG3 protein ubiquitination in vivo.

(C) NDRG3 protein expression in MCF-7 cells during prolonged hypoxia. Quantified values for western blot images are shown on the right. Results are mean ± SD of three experiments.

(D) Site of prolyl hydroxylation in NDRG3 identified by micro-LC-MS/MS analysis.

(E) Expression pattern of an NDRG3 variant mutated in putative prolyl hydroxylation site (P294A) (left) and its interaction with PHD2 and VHL proteins (right) in HEK293T cells. WT, wild-type.

(F) Effects of silencing HIF proteins on hypoxic expression of NDRG3 in Huh-1 cells.

See also Figure S2.

activity profile of five gene ontology categories representative of hypoxia responses (Figure S3A). The genomic activity of a gene ontology was estimated via the gene set enrichment analysis, whereby a standardized difference score (Z score) was calculated from transcriptome expression data of Huh-7 cells at a particular time point during hypoxia. The results showed that NDRG3 protein expression was highly correlated with the activity of “angiogenesis,” “anti-apoptosis,” “proliferation (positive),” and “motility” functions but not with “glycolysis” (Figure 3A). On the other hand, depletion of NDRG3 at 24 hr under hypoxia, when cellular NDRG3 protein expression should have otherwise reached a significant level, caused significant changes in the activity of “angiogenesis,” “anti-apoptosis,” “proliferation (positive),” and “motility” categories but not that of “glycolysis” (Figure 3B). In contrast, “glycolysis” was significantly targeted by HIF-1 α depletion at 6 hr under hypoxia, when HIF-1 α protein expression is expected to have reached its peak level (Figure S3B). Consistently, the ectopic expression of a normoxia-stable variant of NDRG3 (N66D in Figure 1E) caused the upregulation (>1.5-fold) of genes having primary functions in angiogenesis > proliferation \approx growth \approx apoptosis \approx migration > glycolysis (Figure S3C).

We then experimentally evaluated the roles of NDRG3 in “angiogenesis,” “anti-apoptosis,” and “proliferation,” the functions often implicated in tumor growth and significantly targeted by NDRG3 depletion (Figure 3B). In tube forming assays using HUVEC cells, NDRG3 depletion caused significant suppression of the angiogenic activity induced by hypoxia in Huh-7 cells (Figure S3D). In parallel, the Matrigel plug assay showed that NDRG3 knockdown inhibited the angiogenic activity of Huh-7 cells in BALB/c-nu mice (Figure 3C). At the molecular level, hypoxia-induced expression of pro-angiogenic markers was abolished by NDRG3 depletion, while it was upregulated in normoxia by NDRG3(N66D) (Figure 3D). Next, examination of the anti-apoptotic activity of NDRG3 via caspase-3/7 and PARP cleavage assays indicated that NDRG3 depletion significantly promotes apoptosis in hypoxia (Figure 3E). Accordingly, the hypoxia-induced expression of anti-apoptotic genes, notably members of the IAP (inhibitor of apoptosis proteins) family, was abolished by NDRG3 depletion in Huh-7 cells (Figure 3F). Moreover, the depletion of NDRG3 using an shRNA targeting its 3'-UTR (Figure S1H, #5) significantly inhibited the growth of Huh-7 cells under mild hypoxia (3% O₂; Figure 3G), but this phenotype was effectively rescued by a recombinant NDRG3(N66D) expression vector lacking the natural 3'-UTR sequences of NDRG3 (Figures 3G and S3E). In addition, NDRG3 knockdown strongly suppressed the tumorous growth of Huh-7 cells in BALB/c-nu mice (Figures 3H and S3F). Interestingly, simultaneous depletion of NDRG3 and either of the HIFs completely abrogated tumor growth, suggesting complementary roles for NDRG3 and HIFs in hypoxic cell growth (Figure 3H). Immunofluorescence microscopy of resected tumors revealed that NDRG3 depletion effectively suppressed the expression of markers of tumor angiogenesis (IL8 and CD31) and cell proliferation (Ki-67), while their levels in HIF-depleted tumors were comparable to those in controls (Figure S3G). In contrast, the ectopic expression of NDRG3(N66D) highly promoted colony formation of Huh-1 cells in soft agar (Figure S4J) as well as their tumorigenic activity in

BALB/c-nu mice (Figures 3I and S3H). These results demonstrate that NDRG3 plays crucial roles in promoting angiogenesis, anti-apoptosis, and cell proliferation during hypoxia.

L-Lactate Triggers the NDRG3-Mediated Hypoxia Responses

Compared to HIF-1 α , which showed an early induction pattern during hypoxia and rapidly disappeared upon reoxygenation of cells, NDRG3 started accumulating relatively later in hypoxia and its levels slowly declined upon reoxygenation (Figures 2C and S2C). The long lag periods observed for the accumulation and degradation of NDRG3 suggested that multiple layers of regulation might be involved in its hypoxic expression. Therefore, we explored biochemical features relevant to “prolonged hypoxia” other than low oxygen levels and found that NDRG3 protein expression is highly correlated with cellular lactate production; NDRG3 protein expression began at \sim 6 hr under hypoxia, closely following the lactate production pattern (Figure 4A). On the other hand, suppression of lactate production with a LDHA inhibitor, sodium oxamate, specifically inhibited the NDRG3 protein accumulation in a dose-dependent manner (Figure 4B). Similarly, inhibition of lactate production via siRNA-mediated depletion of LDHA (Figure 4C) or disruption of glycolysis with 2-deoxyglucose (Figure S4A) suppressed the hypoxic NDRG3 protein expression. Depriving cells of glucose and/or glutamine, the input substrates for glycolysis and glutaminolysis, respectively—two major metabolic pathways leading to intracellular lactate production—also reduced the NDRG3 protein accumulation with a parallel reduction in lactate production but without affecting the transcription of NDRG3 (Figure 4D). However, compared to the significant consequences of glucose deprivation, the glutamine effect seemed relatively minor. In contrast, the facilitation of lactate production (via LDHA overexpression and/or pyruvate overfeeding; Figure S4B) or its intracellular accumulation (by blocking export through MCT4; Figure 4C) augmented the hypoxic accumulation of NDRG3 protein. These results indicate that, unlike HIF proteins, oxygen deprivation per se is not enough to cause the accumulation of NDRG3 protein, but glycolytic production of lactate is additionally required.

We then verified the effects of lactate on NDRG3 protein dynamics more directly by providing exogenous lactate to the cells whose intracellular lactate production had been compromised by genetic or pharmacological means. Lactate exogenously added to Huh-1 cells dose dependently restored the hypoxic NDRG3 protein expression that had been reduced by LDHA silencing, without affecting the level of NDRG3 mRNA or HIF-1 α protein (Figure 4E). Similar results were obtained when lactate production was suppressed by glucose deprivation (Figure S4C) or oxamate treatment (Figure S4D). However, the lactate-mediated restoration of NDRG3 protein expression was abrogated by siRNA targeting MCT1, a monocarboxylate transporter responsible for importing extracellular lactate into the cell, both in normoxic and hypoxic conditions (Figure 4F). We also observed similar effects of MCT1 knockdown in Huh-1 cells subjected to oxamate treatment or glucose deprivation (Figures S4E and S4F). Collectively, these results indicate that NDRG3 requires lactate build-up for its protein accumulation under hypoxia, pointing to the possibility that NDRG3 might function as a

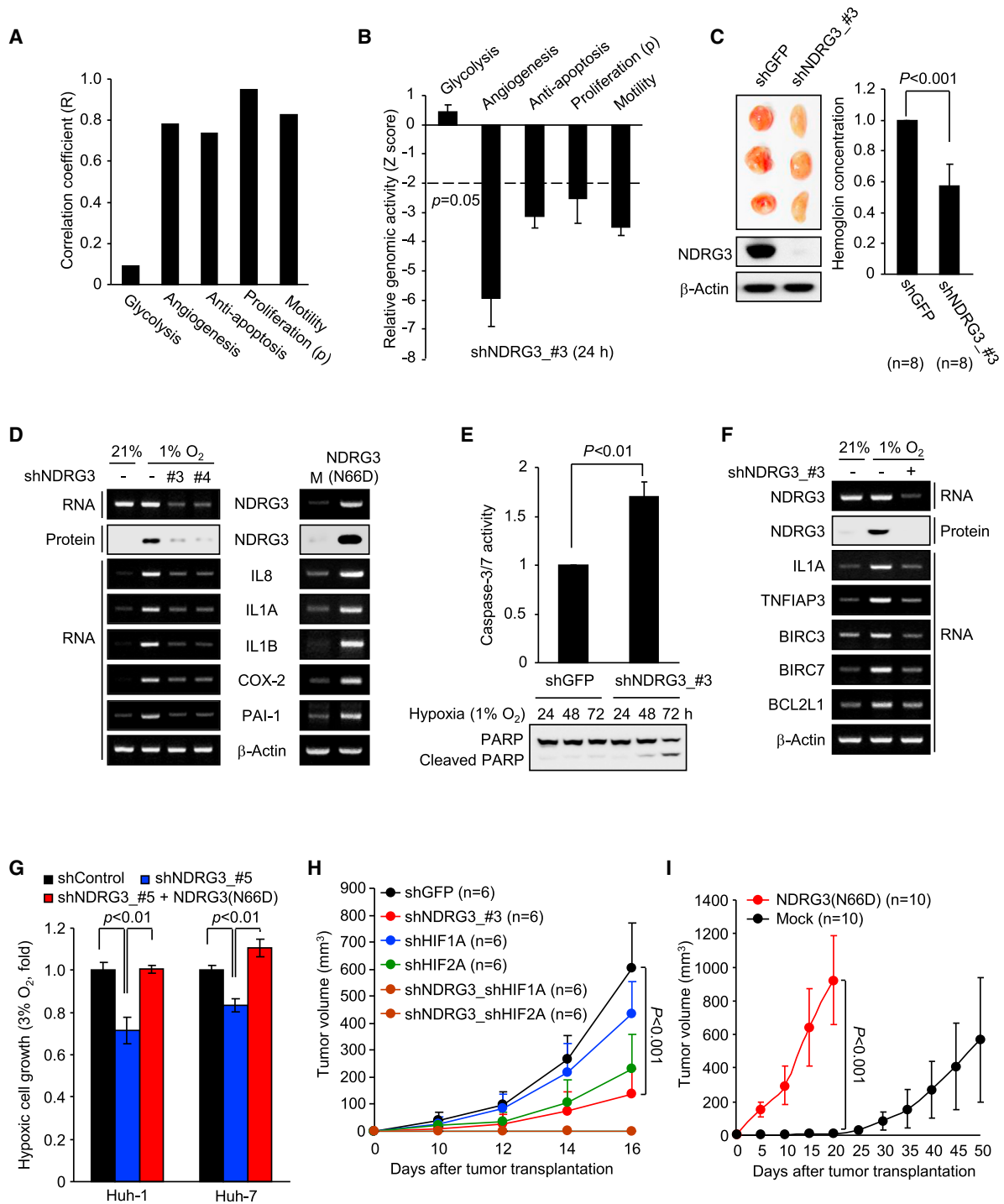


Figure 3. NDRG3 Is a Critical Regulator of Prolonged Hypoxia Responses

(A) Correlation analyses between the NDRG3 protein expression during hypoxia and the activity of five representative hypoxia-responsive gene sets.

(B) Changes in the activity of hypoxia-responsive gene sets upon NDRG3 silencing in Huh-7 cells at 24 hr under hypoxia (1% O₂).

(C) Matrigel plug assay of NDRG3-mediated angiogenic activity. The p value was assessed by Student's t test.

(D) Regulation of pro-angiogenic gene expression by NDRG3. Gene expression in NDRG3-silenced Huh-7 cells under hypoxia (1% oxygen, left) or in NDRG3(N66D)-overexpressing HeLa cells at normoxia (right) was examined by RT-PCR.

(E) Effects of NDRG3 knockdown on hypoxia-induced apoptosis in Huh-7 cells. Results are mean ± SD of three experiments. The p value was assessed by Student's t test.

(F) Regulation of hypoxia-induced anti-apoptotic gene expression by NDRG3.

(legend continued on next page)

hypoxia-inducible lactate sensor, triggering HIF-independent biologic responses in the cell.

We, therefore, examined the functional significance of hypoxic NDRG3 expression in the context of lactate metabolism. Inhibition of lactate production with oxamate caused a dose-dependent suppression of Huh-1 cell growth under mild hypoxia (Figure S4G). However, this effect was effectively rescued by ectopically expressing NDRG3(N66D) (Figure S4G), suggesting that NDRG3 may play a critical role in lactate-induced hypoxic cell growth. Apparently, NDRG3(N66D) exerted no direct effects on lactate production irrespective of oxamate treatment (Figure S4H) nor was its expression affected by oxamate (Figure S4I), indicating that the rescuing effect is truly inherent in NDRG3(N66D) itself. The effect of oxamate on cell growth and its rescue by NDRG3(N66D) were further corroborated by colony forming assays using Huh-1 cells (Figure S4J). We then examined the role of *NDRG3* in the growth of cells whose *LDHA* expression was ablated by RNAi. Depletion of *LDHA* by shRNA suppressed the growth of Huh-1 cells under mild hypoxia (Figure S4K) as well as their tumorous growth in BALB/c-nu mice (Figures 4G and S4L). Again, NDRG3(N66D) effectively compensated for the *LDHA* deficit both in vitro and in vivo. Moreover, in tube forming assays using HUVEC cells, oxamate suppressed the angiogenic activity induced in Huh-1 cells under hypoxia (Figure 4H). However, the ectopic expression of NDRG3(N66D) restored the angiogenic activity in these cells in spite of the oxamate treatment. Thus, lactate appears to be a crucial signal for hypoxic cell growth and angiogenesis, and NDRG3 functions as a key mediator of the lactate-induced hypoxia responses.

Molecular Mechanism of the Lactate Regulation of NDRG3 Protein Expression

We investigated the molecular mechanism for the lactate-induced NDRG3 protein accumulation by examining the effect of lactate on the ubiquitination of NDRG3. In vitro, lactate inhibited NDRG3 ubiquitination, catalyzed by the PHD2/VHL complex immunoprecipitated from HEK293T cells (Figure 5A), indicating that lactate can block the modification of NDRG3 protein by PHD2/VHL. It seems clear that lactate does not affect the HIF-1 α protein expression under hypoxia (Figures 4 and S4). We, therefore, examined the possibility of lactate directly modulating NDRG3 by investigating interactions between the two molecules. An in vitro binding experiment using GST-tagged recombinant NDRG3 protein and [¹⁴C]-labeled L-lactate indicated that NDRG3 physically and directly binds lactate (Figures 5B and S5B). To verify the NDRG3-lactate interaction further, we predicted the putative lactate-binding domain of NDRG3 by a docking simulation (not shown). Site-directed mutagenesis of the predicted lactate-binding domain showed that mutations in some of its amino acid residues can impair the hypoxic accumulation of the mutant proteins (Figure S5A). One of the variants

whose glycine-138 was mutated to tryptophan (N3(G138W) in Figure S5A) hardly accumulated under hypoxia, but accumulated in the presence of MG132, suggesting that it may have lost the lactate-binding capability necessary for escaping PHD2/VHL-mediated proteasomal degradation. Indeed, we observed that recombinant N3(G138W)-GST protein has a severely impaired lactate-binding capability in an in vitro binding assay (Figures 5C and S5B). These results suggest that binding by lactate inhibits proteasomal degradation of NDRG3 by blocking its modification by PHD2/VHL. Moreover, once formed, the NDRG3-lactate complex seems to remain quite resistant to the PHD2/VHL-mediated modification since the hypoxically accumulated NDRG3 protein was maintained for a while after culturing the cells in fresh medium under normoxia (Figure S2C). In contrast, HIF-1 α rapidly disappeared upon reoxygenation, demonstrating the exquisite oxygen dependency of its post-translational regulation.

We further investigated the mechanisms behind the lactate-induced changes in NDRG3 protein dynamics through protein binding analyses in HEK293T cells expressing epitope-tagged NDRG3, PHD2, and VHL. Binding between NDRG3 and PHD2 during early (6 hr) or late (24 hr) hypoxia did not significantly differ from that in normoxia, suggesting that neither low oxygen nor high lactate levels affects the NDRG3-PHD2 interaction (Figure 5D). By contrast, binding between NDRG3 and VHL was significantly reduced at 24 hr under hypoxia, while it was maintained at normoxic levels at 6 hr under hypoxia, indicating that high lactate levels but not low oxygen levels might affect the NDRG3-VHL interaction. We then verified these observations using NDRG3 variants having defects in prolyl hydroxylation by PHD2 (P294A) or lactate binding (G138W). None of the wild-type or variant NDRG3 species showed significant differences in their PHD2-binding capacity between normoxia and hypoxia (24 hr) (Figure 5E). On the other hand, the VHL-binding capacity of wild-type NDRG3 was significantly reduced under hypoxia compared to that in normoxia, while those of P294A and G138W were barely changed by hypoxia. Notably, the interaction of P294A with VHL was negligible whereas the G138W-VHL interaction was strongly maintained, regardless of oxygen level. Consistently, ubiquitination of wild-type NDRG3 was significantly reduced under hypoxia, while P294A and G138W were negligibly and strongly ubiquitinated, respectively, in both normoxia and hypoxia (Figure 5F). Conversely, oxamate treatment specifically augmented the hypoxic interaction of wild-type NDRG3 with VHL as well as its ubiquitination (Figures 5G and S5C). Inhibition of hypoxic lactate production by glucose deprivation also resulted in the augmentation of the NDRG3-VHL interaction (Figure S5D). Addition of exogenous lactate to oxamate-treated cells specifically inhibited the NDRG3-VHL interaction in both normoxia and hypoxia (Figure S5E). Thus, we conclude that the NDRG3-PHD2 interaction is not affected by cellular oxygen or lactate levels, while the NDRG3-VHL

(G) Inhibition of hypoxic cell growth by *NDRG3* knockdown and its rescue by NDRG3(N66D) overexpression. Results are mean \pm SD of three experiments. The p value was assessed by Student's t test.

(H) Effects of the knockdown of *NDRG3* and/or HIF- α on the tumorigenic activity of Huh-7 cells in vivo. The p value was assessed by Student's t test.

(I) Tumorigenic activity of Huh-1 cells overexpressing NDRG3(N66D). The p value was assessed by Student's t test.

See also Figure S3.

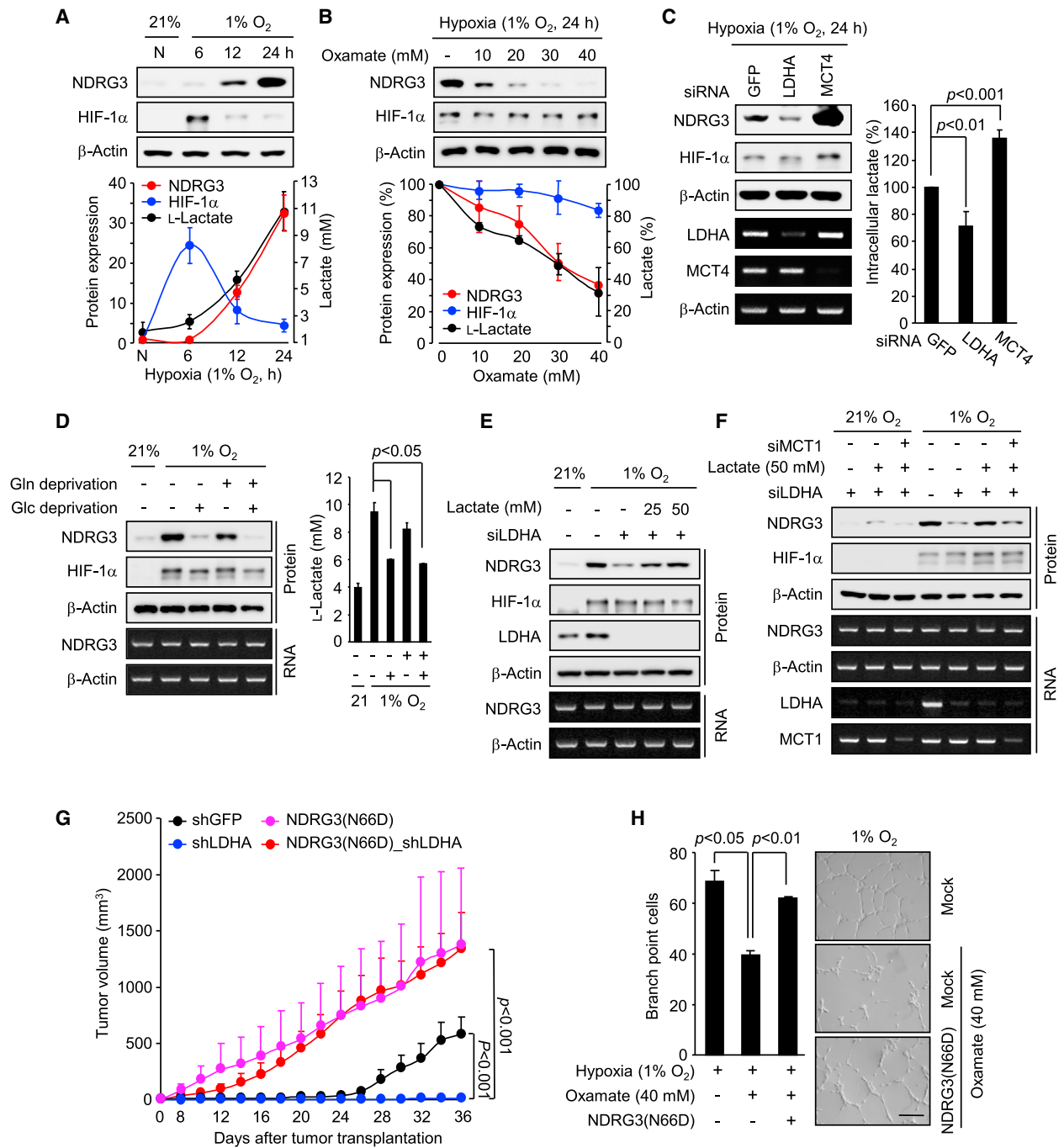


Figure 4. Lactate Signals for the NDRG3-Mediated Hypoxia Responses

(A) Intracellular NDRG3 protein accumulation and gross lactate production by MCF-7 cells during hypoxia. N, normoxia. Results are mean \pm SD of three experiments. The p value was assessed by Student's t test.

(B) Effects of the pharmacological inhibition of lactate dehydrogenase on hypoxic lactate production and NDRG3 protein expression by MCF-7 cells. Results are mean \pm SD of three experiments. The p value was assessed by Student's t test.

(C) Effects of depleting the genes of lactate metabolism on the hypoxic expression of NDRG3 protein and intracellular lactate levels in HeLa cells. Results are mean \pm SD of three experiments. The p value was assessed by Student's t test.

(D) Hypoxic expression of NDRG3 and lactate production in Huh-1 cells deprived of glucose (Glc) or glutamine (Gln). Results are mean \pm SD of three experiments. The p values were assessed by Student's t test.

(E) Effects of exogenous lactate on the hypoxic expression of NDRG3 in LDHA-silenced Huh-1 cells.

(F) Effects of MCT1 depletion on the NDRG3 protein expression induced by exogenous lactate in LDHA-silenced Huh-1 cells.

(legend continued on next page)

interaction is significantly inhibited by lactate but not by low oxygen levels.

In summary, excess lactate built up during hypoxia directly binds to NDRG3 and inhibits its ubiquitination and proteasomal degradation by disrupting the NDRG3-VHL interaction. However, the question remains whether failure of NDRG3 ubiquitination in high lactate conditions is due to the inhibition of PHD2-mediated hydroxylation of NDRG3 that is required for VHL binding and awaits further studies.

Activation of Raf-ERK Signaling by NDRG3 during Hypoxia

To understand the molecular mechanisms of NDRG3's function in hypoxia, we searched for possible NDRG3-regulated kinases via a phosphoarray analysis using PLC/PRF/5 cells stably expressing shRNA for *NDRG3* or *GFP* (Figure S6A). *NDRG3* depletion selectively suppressed hypoxia-induced ERK1/2 phosphorylation (Figures 6A and S6A). We then examined whether the kinases upstream of ERK1/2 could be regulated by NDRG3 and found that hypoxia-induced phosphorylation of c-Raf (at Ser338) and B-RAF1 (at Ser445) is abrogated by *NDRG3* depletion in SK-Hep-1 cells (Figure 6B). These results suggest that NDRG3 might play an essential role in the activation of the RAF-ERK signaling pathway. We, therefore, examined the effect of manipulating NDRG3 expression on c-Raf phosphorylation and found that ectopically expressed c-Raf was significantly phosphorylated in normoxia, with a concomitant phosphorylation of ERK1/2 (Figure 6C). However, depletion of basal-level NDRG3 expression by siRNA abrogated this response. On the other hand, the ectopic expression of NDRG3(N66D) highly induced the phosphorylation of c-Raf and ERK1/2 (Figure 6C). Also, the hypoxia-induced phosphorylation of endogenous c-Raf and ERK1/2, which was suppressed by the 3'-UTR-targeting shRNA of *NDRG3*, could be rescued by the recombinant NDRG3(N66D) expression vector (Figure 6D). Reciprocal in vitro pull-down assays indicated that NDRG3 can physically and directly interact with c-Raf (Figure S6B). Consistently, ectopically expressed c-Raf immunoprecipitated endogenous NDRG3 protein specifically under hypoxia (Figure S6C). Moreover, an NDRG3(N66D)-containing complex immunoprecipitated from HEK293T cells mediated the phosphorylation of recombinant c-Raf in an in vitro kinase assay (Figure 6E). These results indicate that NDRG3 is directly involved in the phosphorylation of c-Raf.

We then examined the biological implications of the NDRG3-mediated c-Raf-ERK1/2 phosphorylation. We observed, from the immunoprecipitation analysis of endogenous proteins, increasing amounts of c-Raf-NDRG3 complexes during the progression of hypoxia, in parallel with a temporal increase in the phosphorylation levels of c-Raf and ERK1/2 (Figure 6F). This result suggests a potential role of NDRG3-mediated c-Raf-ERK1/2 phosphorylation in hypoxia response regulation. Ablation of *LDHA* to inhibit lactate production effectively suppressed

the hypoxia-induced phosphorylation of c-Raf and ERK1/2 as well as NDRG3 protein expression (Figure 6G). Exogenously provided lactate rescued the siLDHA-mediated suppression of c-Raf and ERK1/2 phosphorylation, but this rescue was blocked by silencing *MCT1* expression. In addition, disruption of glycolysis via glucose deprivation effectively suppressed the hypoxic phosphorylation of c-Raf and ERK1/2 as well as NDRG3 expression, which could be rescued by NDRG3(N66D) (Figure 6H). In contrast, glutamine deprivation exhibited negligible effects. These results indicate that hypoxia-induced phosphorylation of c-Raf and ERK1/2 is dependent on lactate production, mainly from glycolysis, and NDRG3 functions as an essential mediator of the lactate-induced activation of Raf-ERK pathway.

Dependence of Lactate-Induced Hypoxic Cell Growth and Angiogenesis on NDRG3-Mediated ERK1/2 Activity

Finally, we examined the biologic relevance of the NDRG3-mediated activation of the Raf-ERK pathway to lactate-triggered hypoxia responses. Exogenously provided lactate significantly compensated for the growth deficit of Huh-1 cells under mild hypoxia, caused by *LDHA* silencing (Figure 7A). However, the lactate-mediated rescue was abrogated by depletion of *NDRG3* or pharmacological blockade of ERK signaling. Similarly, exogenous lactate restored the hypoxia-induced angiogenic capacity of *LDHA*-knockdown Huh-1 cells in tube-forming assays, which was again abolished by *NDRG3* depletion or ERK inhibition (Figure 7B). In parallel, the hypoxic expression of angiogenic marker genes, disrupted by *LDHA* knockdown, was recovered by exogenous lactate but disrupted again by *NDRG3* depletion or ERK inhibition (Figure S7A). We then examined the relevance of NDRG3-mediated Raf-ERK pathway activation to the growth of tumors in vivo. Western blot analysis of the tumors formed by Huh-1 cells engineered for *LDHA* and/or *NDRG3* expression in the in vivo tumorigenesis analysis (Figures 4G and S4L) indicated that phosphorylation of c-Raf and ERK was clearly up-regulated in tumors expressing NDRG3(N66D) compared to mock controls (Figures 7C and S7B). Consistently, we observed a predominant expression of angiogenic marker genes in NDRG3(N66D)-expressing tumors. These results, together with those in Figures 4 and 6, demonstrate that lactate plays essential roles in promoting cell growth and angiogenesis under hypoxia, depending on the NDRG3-mediated activation of the c-Raf-ERK1/2 pathway.

We then examined the clinical relevance of NDRG3 expression and ERK1/2 activity by immunohistochemical analysis of human hepatocellular carcinoma (HCC). NDRG3 was barely expressed in the normal liver, while moderate to strong levels were detectable in HCC tissues in the cytoplasm and the plasma membrane (Figure 7D). Among 103 HCC cases examined using antibodies for NDRG3 and phospho-ERK1/2, 25 cases (24.3%) were positive for NDRG3 protein expression in a manner that was significantly associated with ERK1/2 activation (Figure 7D). In summary, these results indicate that aberrant NDRG3

(G) Dependence of the tumorous growth of Huh-1 cells on *LDHA* and its rescue by *NDRG3*. The p values were assessed by Student's t test. n = 5/group.

(H) Inhibition of hypoxia-induced angiogenesis by oxamate and its rescue by *NDRG3*. Results are mean \pm SD of two experiments. The p values were assessed by Student's t test. Scale bar, 200 μ m.

See also Figure S4.

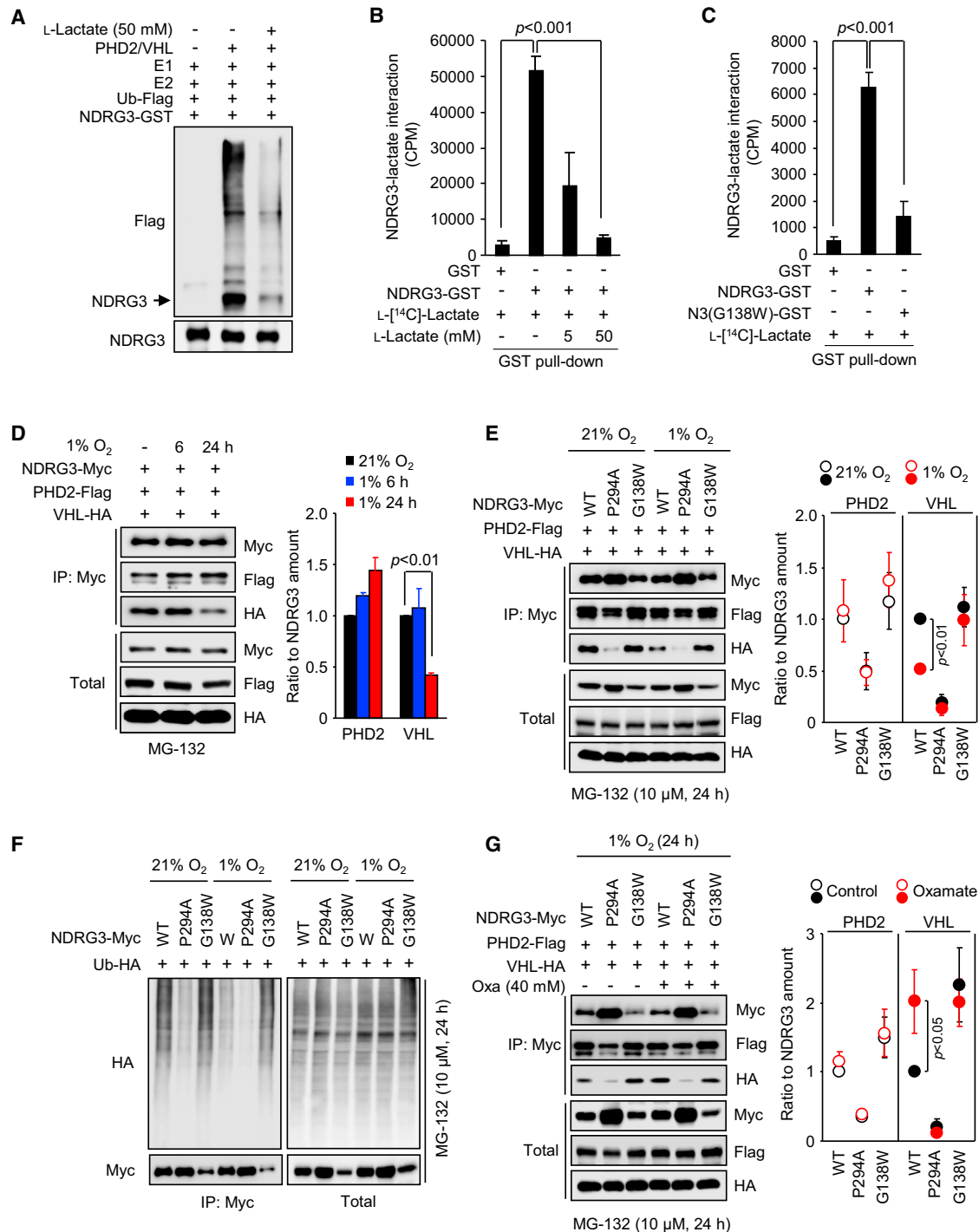


Figure 5. Lactate Binds to NDRG3 and Blocks Its Ubiquitination by VHL

(A) Effects of lactate on in vitro ubiquitination of NDRG3 by recombinant PHD2/VHL complex immunoprecipitated from HEK293T cells expressing PHD2-Flag and VHL-HA.

(B) Molecular interaction between L-lactate and NDRG3 protein in vitro. Results are mean \pm SD of three experiments. The p value was assessed by Student's t test.

(C) Molecular interaction between L-lactate and a variant NDRG3 protein (N3(G138W)) mutated in the putative L-lactate binding site. Results are mean \pm SD of three experiments. The p value was assessed by Student's t test.

(D) Interaction profile of NDRG3 protein with PHD2 or VHL in HEK293T cells during the progression of hypoxia. Quantified values for western blot images are shown on the right. Results are mean \pm SD of two experiments. The p value was assessed by Student's t test.

(legend continued on next page)

expression is closely associated with tumor development in vivo as well as the pathological activation of the ERK pathway.

DISCUSSION

Lactate has been regarded as a dead-end product of glycolysis and glutaminolysis until it recently emerged as an alternative energy source and an inducer of tumor angiogenesis (Doherty and Cleveland, 2013). Knockdown of *LDHA* expression or inhibition of its activity suppressed tumor cell growth in vitro and in vivo (Fantin et al., 2006; Le et al., 2010). However, the key elements and mechanisms of lactate-induced biological responses remained unknown. In this study, we showed the existence of NDRG3-mediated lactate signaling and its roles in hypoxia responses. During hypoxia, low oxygen concentrations and elevated lactate levels highly induced NDRG3 protein expression, leading to the activation of the Raf-ERK pathway to promote angiogenesis and hypoxic cell growth. Thus, NDRG3 acts as a lactate sensor that triggers downstream kinase signaling in a hypoxia-dependent manner, and the NDRG3-Raf-ERK axis provides the genetic basis for the lactate-induced hypoxia responses.

We showed that *NDRG3* expression is genetically independent of HIFs and rather determined at the protein level by lactate. Lactate accumulates at the later phase of hypoxia, promoted by the upregulation of glycolysis and *LDHA* expression during the earlier stages of hypoxia where HIF-1 α plays a critical role as a part of metabolic adaptation (Cassavaugh and Lounsbury, 2011). Therefore, the lactate signaling and subsequent biological responses appear to be functionally coupled to the HIF-1 α -induced metabolic reprogramming, by employing NDRG3 as the critical link. In this regard, it is suggested that portions of the hypoxia responses, especially those occurring at the later phase of hypoxia, that have been so far attributed to HIF-1 α might, in fact, be under the direct control of NDRG3-mediated lactate signaling. The results of gene set enrichment analysis for the functions of NDRG3 and HIF-1 α during hypoxia support this possibility (Figures 3 and S3). Therefore, our study suggests that HIF-1 α and NDRG3 might form an oxygen-dependent regulatory chain for hypoxia responses, which is broadly divided into two chronological phases (Figure 7E); at the early phase, low O₂ levels signal for the accumulation of HIF-1 α , which then regulates the gene expression necessary for early adaptive responses including metabolic reprogramming, while at the later phase, up-regulated lactate production signals for the accumulation of NDRG3, which subsequently activates the Raf-ERK pathway to induce responses necessary for coping with prolonged hypoxia.

The lactate-NDRG3-Raf-ERK axis of hypoxia signaling suggests that hypoxic lactate production might be an integral part of normal physiology, playing active roles in promoting angiogenesis and cell growth under prolonged hypoxia. It stands to reason that the functional coupling between HIF-1 α -induced

metabolic reprogramming and NDRG3-mediated lactate signaling ensures that cells facing prolonged hypoxia achieve the maximal possible growth in a hypoxic environment. This can be achieved by, first, generating biosynthetic building blocks and energy via the HIF-1 α -mediated upregulation of glycolysis, and subsequently, by providing cues for cell growth and angiogenesis via the NDRG3-mediated c-Raf-ERK signaling. Therefore, NDRG3-mediated lactate signaling may provide a self-sufficient mechanism for the cells in local tissues to recover from hypoxia without the need for additional extracellular signals, for example, during development. Moreover, NDRG3-mediated signaling provides an extra layer of biological security for the cells escaping prolonged hypoxia since the NDRG3 protein, once stabilized by lactate binding, remains quite stable even when cells are reoxygenated.

Growing evidence suggests that lactate may play active roles in cancer progression, as it mediates cancer-cell intrinsic effects on metabolism as an oxidative metabolite and non-cancer-cell autonomous effects on several cell types in the tumor microenvironment (Doherty and Cleveland, 2013). Our results indicate that glycolysis is the main source of lactate production that is responsible for the hypoxic induction of NDRG3 protein expression and Raf-ERK activation. Cancer cells frequently exhibit an increased dependence on glycolysis, and therefore, the discovery of the lactate-NDRG3-Raf-ERK axis and its role in angiogenesis and hypoxic cell growth may provide an important explanation for the growth advantage offered by a glycolytic phenotype to cancers. In this regard, lactate might be considered an oncometabolite that drives the progression of solid tumors as an alternative fuel, an agent modulating the tumor microenvironment, and a signaling molecule.

Many characteristics of hypoxia responses are also exploited by diseased cells (Cassavaugh and Lounsbury, 2011). The presence of hypoxia is correlated with poor patient prognosis and poor treatment outcome in cancers (Jubb et al., 2010; Semenza, 2004), and therefore, hypoxia has been an important target for cancer therapy. Although HIF is the prime target in this regard, concerns have been raised that the simple inhibition of HIF may not be enough to prevent the progression of hypoxia-induced diseases, since many studies indicated that compensatory, HIF-independent pathways can be induced when a single factor is inhibited (Mizukami et al., 2005, 2007; Carmeliet et al., 1998; Rapisarda et al., 2009; see Introduction for supporting examples). These observations collectively led to the suggestion that the most successful anti-hypoxia strategy may require a combination of agents inhibiting HIF-independent as well as HIF-dependent pathways (Mizukami et al., 2007; Fong, 2008). Despite the likelihood of functional coupling with HIF-1 α , *NDRG3* seems to have distinct functions in hypoxia response regulation as indicated by gene set enrichment analysis of the transcriptome data for *NDRG3*- and *HIF1A*-depleted cells during

(E) Interaction of different forms of NDRG3 proteins with PHD2 or VHL in HEK293T cells at different oxygen conditions. WT, wild-type. Quantified values for western blot images are shown on the right. Results are mean \pm SD of three experiments. The p value was assessed by Student's t test.

(F) Ubiquitination assay of variant NDRG3 proteins from HEK293T cells grown in normoxia or under hypoxia.

(G) Effects of inhibiting hypoxic lactate production by oxamate on the interaction of different NDRG3 proteins with PHD2 or VHL in HEK293T cells. Quantified values for western blot images are shown on the right. Results are mean \pm SD of three experiments. The p value was assessed by Student's t test.

See also Figure S5.

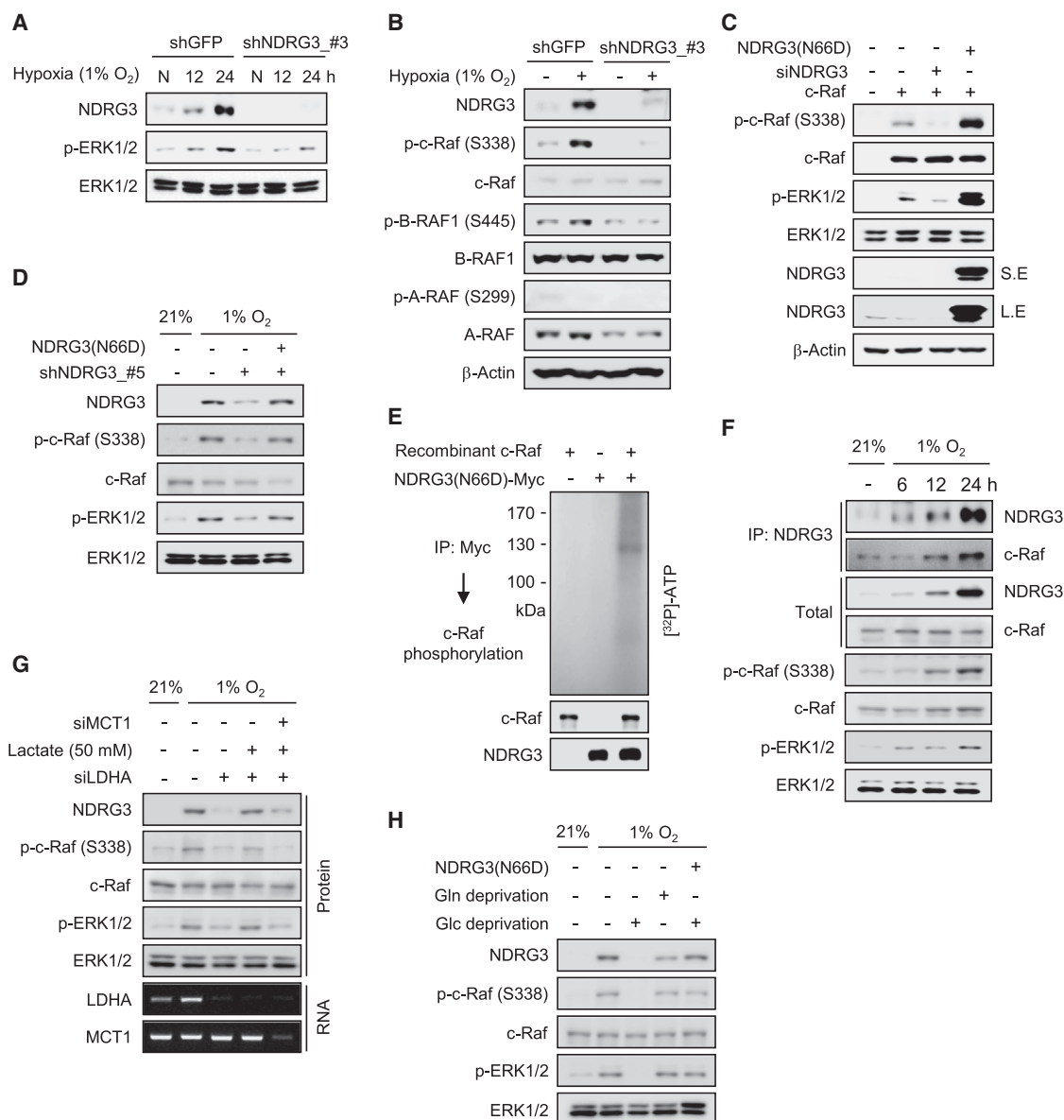


Figure 6. NDRG3 Is Required for Hypoxia-Induced Raf-ERK1/2 Activation

(A) Effects of *NDRG3* knockdown on hypoxia-induced ERK1/2 activation in SK-Hep-1 cells.

(B) Effects of *NDRG3* knockdown on hypoxia-induced RAF activation in SK-Hep-1 cells.

(C) Activation of ERK1/2 and c-Raf by NDRG3 in normoxia in HEK293T cells.

(D) Suppression of the hypoxic phosphorylation of c-Raf and ERK1/2 by *NDRG3* knockdown and its rescue by ectopic expression of NDRG3.

(E) In vitro phosphorylation of recombinant c-Raf protein by the NDRG3-containing complex immunoprecipitated from HEK293T cells.

(F) Interaction profile between endogenous NDRG3 and c-Raf proteins during progression of hypoxia. Phosphorylation profiles of c-Raf and ERK are also shown.

(G) Lactate dependence of the NDRG3-mediated c-Raf-ERK activation during hypoxia in Huh-1 cells.

(H) Suppression of the hypoxic phosphorylation of c-Raf and ERK1/2 by glucose deprivation and its rescue by NDRG3 overexpression.

See also Figure S6.

hypoxia. Therefore, these observations, along with the roles of *NDRG3* in hypoxia responses as shown in this study, suggest that combinatorial targeting of *HIF* and *NDRG3* might prove highly effective in cancer therapy. Abrogation of tumor growth when *NDRG3* was depleted in combination with either HIFs supports the feasibility of this strategy (Figure 3H).

In conclusion, *NDRG3* provides a crucial genetic evidence for the oxygen-dependent regulation of HIF-independent hypoxia signaling. The regulation and functions of *NDRG3* in hypoxia imply that the PHD2/VHL system can control both HIF-dependent and HIF-independent hypoxia responses in an oxygen-dependent manner. Therefore, the lactate-NDRG3-Raf-ERK signaling

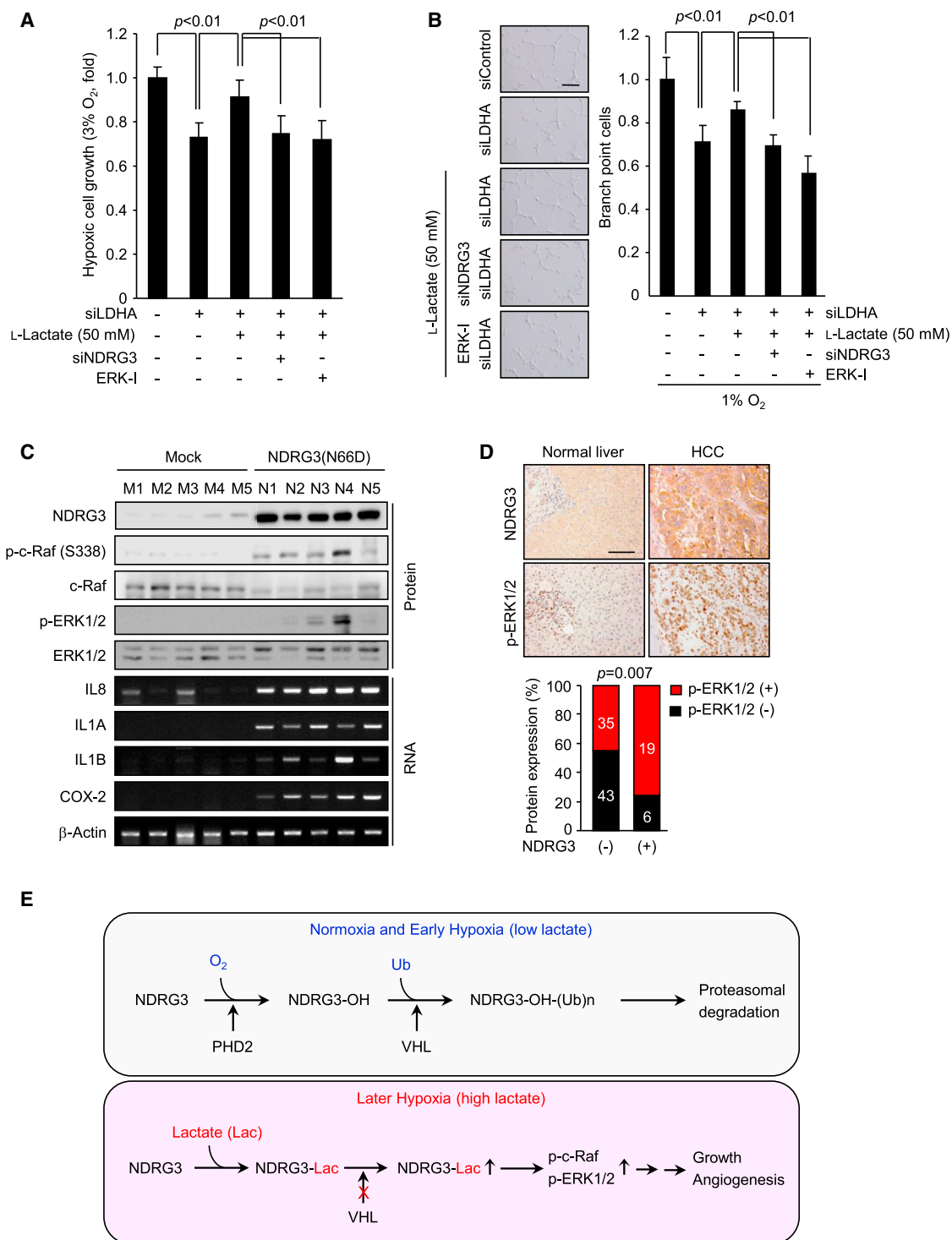


Figure 7. Lactate-Induced Cell Growth and Angiogenesis Depend on NDRG3 Expression and ERK1/2 Activity

(A) Dependence of the hypoxic growth of Huh-1 cells on lactate, NDRG3, and ERK1/2 activity.

(B) Dependence of the hypoxia-induced angiogenic activity of Huh-1 cells on lactate, NDRG3, and ERK1/2 activity.

(C) Upregulation of c-Raf-ERK1/2 phosphorylation and pro-angiogenic gene expression in tumor xenografts formed by Huh-1 cells overexpressing NDRG3.

(D) Immunohistochemical analysis of NDRG3 and phospho-ERK1/2 expression in human liver cancers. Relationship between NDRG3 protein and phospho-ERK1/2 expression was assessed by χ^2 test.

(E) A scheme outlining the regulatory mechanism for prolonged hypoxia responses involving lactate and NDRG3.

See also Figure S7.

pathway may provide an extended mechanistic clue to the understanding of disorders caused by mutations in *VHL* (hemangioblastoma, renal cell carcinoma, pheochromocytoma, etc.) (Maher et al., 2011) or *PHD2* (familial erythrocytosis-3) (Percy et al., 2006) as well as the hypoxia-related physiological and pathophysiological responses (Cassavaugh and Lounsbury, 2011).

EXPERIMENTAL PROCEDURES

Cell Lines

Human cell lines, PLC/PRF/5, SK-HEP-1, MCF-10A, MCF-7, IMR-90, HeLa, SW480, and HEK293T were purchased from American Type Culture Collection. Two human hepatoma cell lines, Huh-1 and Huh-7, were obtained from Japanese Cancer Research Resources Bank. Cells were cultured under standard conditions (see [Extended Experimental Procedures](#)).

Identification of PHD2-Binding Proteins

In order to identify PHD2-binding proteins, we carried out mass spectrometric analysis of the proteins immunoprecipitated from MCF-7 cells cultured under hypoxia for 24 hr in the presence of the proteasome inhibitor, MG132. We avoided the yeast two-hybrid screen as it has known technical limitations for some types of proteins. A detailed method is described in [Extended Experimental Procedures](#) under the subtitle [Micro-LC-MS/MS Analysis and Protein Database Search](#).

RNA Interference

We used commercial pooled siRNA products (SMARTpool, Dharmacon) for transient knockdown of *NDRG3*, *NDRG1*, *HIF-1A*, *EPAS1* (*HIF-2A*), *ARNT* (*HIF-1B*), *VHL*, *LDHA*, *MCT1*, and *MCT4*. Otherwise, siRNAs were synthesized from Samchullypharm (Korea). The sequences of siRNAs are listed in [Table S1](#).

Protein Structure Modeling and Docking Simulation

Prediction of NDRG3 protein structure was achieved using Modeler 9v10 (Eswar et al., 2008). Protein-protein and protein-ligand docking simulations were performed using the HEX6.3 program (Ritchie and Kemp, 2000) and the Auto-dock Vina software (<http://vina.scripps.edu/index.html>), respectively. Detailed methods are described in [Extended Experimental Procedures](#).

L-Lactate Measurement and Binding Assay

L-Lactate production was measured using the EnzyChrom L-Lactate Assay kit (BioAssay Systems). The protocol for the analysis of interaction between recombinant NDRG3-GST protein and L-[¹⁴C]-lactate (PerkinElmer) is described in [Extended Experimental Procedures](#).

Statistical Analysis

Statistical significance of the data was mostly assessed by using the Student's *t* test except for the tissue microarray data for which the χ^2 test was used.

Miscellaneous Methods

Virus-mediated gene expression, immunoprecipitation and western blotting, RT-PCR, site-directed mutagenesis, expression and purification of recombinant proteins, production of anti-NDRG3 antibody, ubiquitination assays, gene expression profiling, cell growth assays, apoptosis assay, in vitro kinase assay, tumorigenesis in a mouse model, in vivo angiogenesis assay, immunofluorescence microscopy, and tissue microarray analysis are described in [Extended Experimental Procedures](#). Contents dealing with human and animal subjects were approved by the Institutional Review Board of Inje University Seoul Paik Hospital (Seoul, Korea) and KRIBB, respectively. Antibodies and primer sequences used for RT-PCR analyses and site-directed mutagenesis are listed in [Tables S2](#), [S3](#), and [S4](#).

ACCESSION NUMBERS

The GEO accession number for the microarray data reported in this paper is GSE55214.

SUPPLEMENTAL INFORMATION

Supplemental Information includes Extended Experimental Procedures, seven figures, and four tables and can be found with this article online at <http://dx.doi.org/10.1016/j.cell.2015.03.011>.

AUTHOR CONTRIBUTIONS

All experiments were conceived by Y.I.Y., D.C.L., K.C.P., and H.S.Y. and mainly carried out by D.C.L. H.A.S. and D.-Y.Y. carried out the animal studies. Y.K.K. performed tissue microarray analysis. S.O. performed protein structure modeling and docking simulation. Z.-Y.P., K.L., and K.-H.B. carried out proteomic analyses. M.K., Y.J.J., and S.-J.Y. performed transcriptomic analyses. Y.K.H. and S.J.C. worked on recombinant proteins. H.N., D.M.K., and D.J.K. performed cell-based assays. Y.I.Y., K.C.P., and D.C.L. wrote the manuscript. Y.I.Y., K.C.P., and J.-A.K. supervised the project.

ACKNOWLEDGMENTS

We thank Chul-Ho Lee (KRIBB) and MoonKyung Kang (Inje University) for the helps with animal studies and viral particles preparation, respectively. This work was supported by the National Research Foundation of Korea (NRF) funded by the Ministry of Science, ICT and Future Planning (NRF-2010-0030020, NRF-2011-0028171, NRF-2013M3A9B5076422, NRF-2006-2006799) and by KRIBB Research Initiative Program.

Received: August 6, 2014

Revised: December 15, 2014

Accepted: February 20, 2015

Published: April 16, 2015

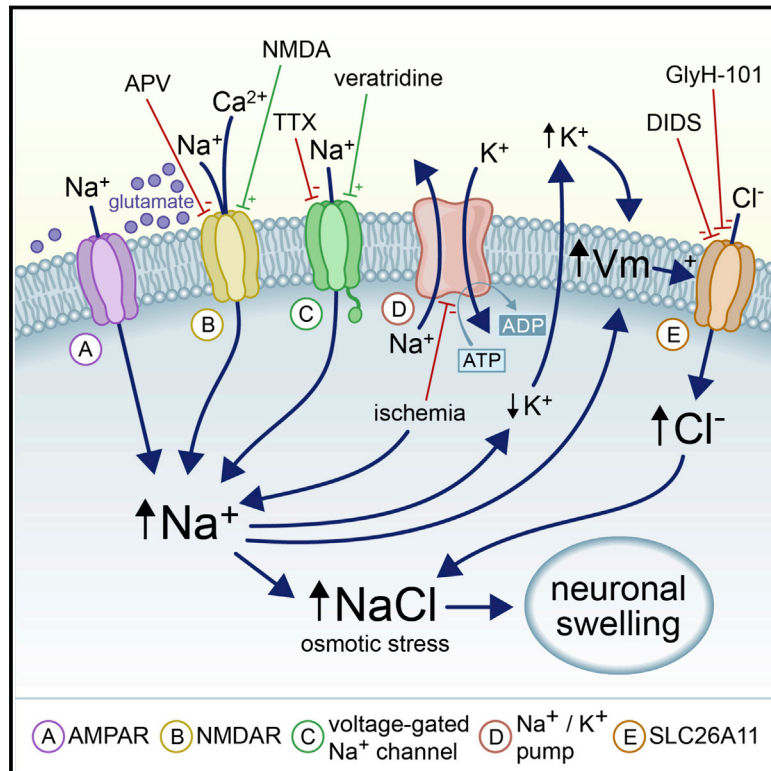
REFERENCES

- Carmeliet, P., Dor, Y., Herbert, J.M., Fukumura, D., Brusselmans, K., Dewerchin, M., Neeman, M., Bono, F., Abramovitch, R., Maxwell, P., et al. (1998). Role of HIF-1 α in hypoxia-mediated apoptosis, cell proliferation and tumour angiogenesis. *Nature* 394, 485–490.
- Cassavaugh, J., and Lounsbury, K.M. (2011). Hypoxia-mediated biological control. *J. Cell. Biochem.* 112, 735–744.
- Chowdhury, R., McDonough, M.A., Mecinović, J., Loenarz, C., Flashman, E., Hewitson, K.S., Domene, C., and Schofield, C.J. (2009). Structural basis for binding of hypoxia-inducible factor to the oxygen-sensing prolyl hydroxylases. *Structure* 17, 981–989.
- Cummins, E.P., and Taylor, C.T. (2005). Hypoxia-responsive transcription factors. *Pflugers Arch.* 450, 363–371.
- Doherty, J.R., and Cleveland, J.L. (2013). Targeting lactate metabolism for cancer therapeutics. *J. Clin. Invest.* 123, 3685–3692.
- Elvidge, G.P., Glenny, L., Appelhoff, R.J., Ratcliffe, P.J., Ragoussis, J., and Gleadle, J.M. (2006). Concordant regulation of gene expression by hypoxia and 2-oxoglutarate-dependent dioxygenase inhibition: the role of HIF-1 α , HIF-2 α , and other pathways. *J. Biol. Chem.* 281, 15215–15226.
- Fantin, V.R., St-Pierre, J., and Leder, P. (2006). Attenuation of LDH-A expression uncovers a link between glycolysis, mitochondrial physiology, and tumor maintenance. *Cancer Cell* 9, 425–434.
- Fong, G.H. (2008). Mechanisms of adaptive angiogenesis to tissue hypoxia. *Angiogenesis* 11, 121–140.
- Harris, A.L. (2002). Hypoxia—a key regulatory factor in tumour growth. *Nat. Rev. Cancer* 2, 38–47.
- Höpfl, G., Wenger, R.H., Ziegler, U., Stallmach, T., Gardelle, O., Achermann, R., Wergin, M., Kaser-Hotz, B., Saunders, H.M., Williams, K.J., et al. (2002). Rescue of hypoxia-inducible factor-1 α -deficient tumor growth by wild-type cells is independent of vascular endothelial growth factor. *Cancer Res.* 62, 2962–2970.
- Jubb, A.M., Buffa, F.M., and Harris, A.L. (2010). Assessment of tumour hypoxia for prediction of response to therapy and cancer prognosis. *J. Cell. Mol. Med.* 14, 18–29.

- Le, A., Cooper, C.R., Gouw, A.M., Dinavahi, R., Maitra, A., Deck, L.M., Royer, R.E., Vander Jagt, D.L., Semenza, G.L., and Dang, C.V. (2010). Inhibition of lactate dehydrogenase A induces oxidative stress and inhibits tumor progression. *Proc. Natl. Acad. Sci. USA* *107*, 2037–2042.
- Maier, E.R., Neumann, H.P., and Richard, S. (2011). von Hippel-Lindau disease: a clinical and scientific review. *Eur. J. Hum. Genet.* *19*, 617–623.
- Melotte, V., Qu, X., Ongenaert, M., van Crielinge, W., de Bruijne, A.P., Baldwin, H.S., and van Engeland, M. (2010). The N-myc downstream regulated gene (NDRG) family: diverse functions, multiple applications. *FASEB J.* *24*, 4153–4166.
- Mizukami, Y., Li, J., Zhang, X., Zimmer, M.A., Iliopoulos, O., and Chung, D.C. (2004). Hypoxia-inducible factor-1-independent regulation of vascular endothelial growth factor by hypoxia in colon cancer. *Cancer Res.* *64*, 1765–1772.
- Mizukami, Y., Jo, W.S., Duerr, E.M., Gala, M., Li, J., Zhang, X., Zimmer, M.A., Iliopoulos, O., Zukerberg, L.R., Kohgo, Y., et al. (2005). Induction of interleukin-8 preserves the angiogenic response in HIF-1 α -deficient colon cancer cells. *Nat. Med.* *11*, 992–997.
- Mizukami, Y., Kohgo, Y., and Chung, D.C. (2007). Hypoxia inducible factor-1 independent pathways in tumor angiogenesis. *Clin. Cancer Res.* *13*, 5670–5674.
- Percy, M.J., Zhao, Q., Flores, A., Harrison, C., Lappin, T.R., Maxwell, P.H., McMullin, M.F., and Lee, F.S. (2006). A family with erythrocytosis establishes a role for prolyl hydroxylase domain protein 2 in oxygen homeostasis. *Proc. Natl. Acad. Sci. USA* *103*, 654–659.
- Rapisarda, A., Shoemaker, R.H., and Melillo, G. (2009). Antiangiogenic agents and HIF-1 inhibitors meet at the crossroads. *Cell Cycle* *8*, 4040–4043.
- Ritchie, D.W., and Kemp, G.J. (2000). Protein docking using spherical polar Fourier correlations. *Proteins* *39*, 178–194.
- Semenza, G.L. (2003). Targeting HIF-1 for cancer therapy. *Nat. Rev. Cancer* *3*, 721–732.
- Semenza, G.L. (2004). Intratumoral hypoxia, radiation resistance, and HIF-1. *Cancer Cell* *5*, 405–406.
- Seta, K.A., Spicer, Z., Yuan, Y., Lu, G., and Millhorn, D.E. (2002). Responding to hypoxia: lessons from a model cell line. *Sci. STKE* *2002*, re11.

The Cellular Mechanisms of Neuronal Swelling Underlying Cytotoxic Edema

Graphical Abstract



Authors

Ravi L. Rungta, Hyun B. Choi, ...,
Terrance P. Snutch, Brian A. MacVicar

Correspondence

bmacvicar@brain.ubc.ca

In Brief

Neuronal swelling, the major cause of death in traumatic and ischemic brain injuries, is initiated when aberrant entry of sodium ions and depolarization activates the voltage-gated chloride channel, SLC26A11. The increase of cytoplasmic sodium and chloride causes an osmotic imbalance that leads to water entry and cytotoxic edema, a mechanism that could be targeted to prevent and treat brain edema.

Highlights

- Neuronal swelling depends on Na^+ and Cl^- influx but is independent of Ca^{2+} influx
- Neuronal swelling after Na^+ and Cl^- influx causes Ca^{2+} -independent neuronal death
- Knockdown of the ion exchanger SLC26A11 attenuates neuronal swelling
- SLC26A11-dependent Cl^- influx occurs via voltage-gated Cl^- channel activity



Rungta et al., 2015, *Cell* 161, 610–621

April 23, 2015 ©2015 Elsevier Inc.

<http://dx.doi.org/10.1016/j.cell.2015.03.029>

The Cellular Mechanisms of Neuronal Swelling Underlying Cytotoxic Edema

Ravi L. Rungta,¹ Hyun B. Choi,¹ John R. Tyson,^{1,2} Aqsa Malik,¹ Lasse Dissing-Olesen,¹ Paulo J.C. Lin,³ Stuart M. Cain,^{1,2} Pieter R. Cullis,³ Terrance P. Snutch,^{1,2} and Brian A. MacVicar^{1,*}

¹Djavad Mowafaghian Centre for Brain Health, University of British Columbia, Vancouver, BC V6T 2B5, Canada

²Michael Smith Laboratories, University of British Columbia, Vancouver, BC V6T 1Z4, Canada

³Department of Biochemistry and Molecular Biology, University of British Columbia, Vancouver, BC V6T 1Z3, Canada

*Correspondence: bmaccvicar@brain.ubc.ca

<http://dx.doi.org/10.1016/j.cell.2015.03.029>

SUMMARY

Cytotoxic brain edema triggered by neuronal swelling is the chief cause of mortality following brain trauma and cerebral infarct. Using fluorescence lifetime imaging to analyze contributions of intracellular ionic changes in brain slices, we find that intense Na^+ entry triggers a secondary increase in intracellular Cl^- that is required for neuronal swelling and death. Pharmacological and siRNA-mediated knockdown screening identified the ion exchanger SLC26A11 unexpectedly acting as a voltage-gated Cl^- channel that is activated upon neuronal depolarization to membrane potentials lower than -20 mV. Blockade of SLC26A11 activity attenuates both neuronal swelling and cell death. Therefore cytotoxic neuronal edema occurs when sufficient Na^+ influx and depolarization is followed by Cl^- entry via SLC26A11. The resultant NaCl accumulation causes subsequent neuronal swelling leading to neuronal death. These findings shed light on unique elements of volume control in excitable cells and lay the ground for the development of specific treatments for brain edema.

INTRODUCTION

Brain edema, the pathological hallmark of excitotoxic injury and traumatic brain injury (Donkin and Vink, 2010; Klatzo, 1987; Marrou et al., 2006; Rosenblum, 2007) was first characterized by Klatzo (1967) as either vasogenic or cytotoxic. Cytotoxic brain edema is caused by water movement into the intracellular compartment of neurons and/or astrocytes leading to brain swelling, while vasogenic edema is due to water entry into the brain from the vasculature (Klatzo, 1967). Excitotoxic swelling of cultured neurons is known to involve influx of both Na^+ and Cl^- , although the influx pathway(s) for Cl^- remain obscure (Choi, 1987; Hasbani et al., 1998; Rothman, 1985). The low resting Cl^- permeability in neurons suggests that a Cl^- channel or exchange mechanism must be activated for Cl^- entry to occur at sufficient levels to increase cell volume and cause cytotoxic edema. In mature pyramidal neurons of the cortex and hip-

pocampus, the equilibrium potential for Cl^- (E_{Cl^-}) is set more hyperpolarized to the resting membrane potential (E_m) by KCC2-mediated active transport of Cl^- out of the cell against its electrochemical concentration gradient (Blaesse et al., 2009). As such, the Cl^- influx required for cytotoxic neuronal edema occurs as a result of either the activation of a Cl^- channel that is not open at rest, or activation of a Cl^- transporter. Putative candidates for Cl^- loading leading to swelling are the volume-regulated anion channel (VRAC), the Na^+ - K^+ - Cl^- cotransporter 1 (NKCC1) and GABA-activated Cl^- channels (Allen et al., 2004; Hasbani et al., 1998; Inoue et al., 2005; Pond et al., 2006). In addition, there are several newly described Cl^- channels and transporters that could also be important contributors to neuronal edema. Our experiments were designed to examine the interrelationship between neuronal volume, intracellular Na^+ concentration ($[\text{Na}^+]_i$) and intracellular Cl^- concentration ($[\text{Cl}^-]_i$) in order to investigate the roles for Cl^- entry pathways that contribute to neuronal swelling leading to cell death.

Neuronal swelling occurs as a result of multiple depolarizing triggers that increase $[\text{Na}^+]_i$, including excessive glutamate receptor activation, intense neuronal spiking, activation of non-selective cation channels, and inhibition of Na^+ / K^+ -ATPase (Liang et al., 2007). We tested the impact of increasing $[\text{Na}^+]_i$ via ligand- or voltage-gated ion channels on neuronal swelling to test the hypothesis that extensive Na^+ influx itself, independent of the route of entry, leads to swelling by triggering Cl^- influx. Two-photon imaging of cell morphology and fluorescence lifetime measurements (FLIM) of $[\text{Na}^+]_i$ and $[\text{Cl}^-]_i$ in hippocampal and cortical neurons in acutely prepared brain slices were combined to specifically examine the relationship between increased $[\text{Na}^+]_i$, subsequent $[\text{Cl}^-]_i$ changes, and neuronal swelling. The cytotoxic nature of this swelling was measured by lactate dehydrogenase (LDH) efflux (e.g., Kajta et al., 2005). Pharmacological blockers of known Cl^- channels and exchangers were further examined in order to determine the relative contribution of different Cl^- loading pathways to neuronal swelling. Finally, a lipid nanoparticle (LNP) strategy to introduce siRNA into neurons in vivo (Rungta et al., 2013) was employed to determine the exact Cl^- pathway critical and required for the majority of neuronal swelling. The results indicate that a significant proportion of neuronal swelling and subsequent cell death requires SLC26A11, a protein that can act as a Cl^- , HCO_3^- , SO_4^{2-} exchanger or a Cl^- channel in expression systems and recently

reported to be highly expressed in cortical and hippocampal neurons (Rahmati et al., 2013). The identification of the principal pathway required for Cl^- entry could potentially lead to novel targets and therapies for treating cytotoxic brain edema.

RESULTS

Increased Intracellular Sodium Triggers Neuronal Swelling

We first investigated whether increasing $[\text{Na}^+]_i$ was itself capable of triggering a cascade leading to an increase in cell volume and second whether this cascade also leads to rapid cell death. Two parallel and independent approaches were taken to increase $[\text{Na}^+]_i$ by either applying veratridine, which removes inactivation of voltage-gated sodium channels (VGSCs) (Strichartz et al., 1987) prolonging Na^+ entry or by applying NMDA to activate NMDA receptors (NMDARs). NMDA activates a non-selective cation conductance leading to entry of Na^+ and also Ca^{2+} . Neuronal Na^+ entry was induced under conditions in which other voltage-gated ion channels and ligand-gated transmitter receptors were blocked by a combination of Cd^{2+} (30 μM), CNQX (20 μM) and picrotoxin (100 μM). Either veratridine or NMDA was rapidly applied by pressure ejection from a pipette positioned directly above the region of the brain slice that was imaged. To ensure the selectivity of either approach veratridine was applied with d-APV (100 μM) to block NMDARs and NMDA was applied with TTX (1 μM) to block VGSCs. Changes in $[\text{Na}^+]_i$ were monitored using the fluorescent Na^+ indicator CoroNa-Green (Meier et al., 2006), which preferentially stains hippocampal and cortical neurons in brain slices (Figure 1A). Astrocytes, which did not show any obvious volume changes under these experimental manipulations, were visualized using Sulforhodamine 101 (SR101) (Nimmerjahn et al., 2004) to provide landmarks to track during swelling of the tissue (red cells in Figures 1A and 1B). The activation of either VGSCs by veratridine or NMDARs by NMDA consistently led to a significant increase in $[\text{Na}^+]_i$ followed, after a delay of seconds, by an increase in neuronal cell volume (Figures 1B–1D, 1J, 1K, 2A, and 2B and Movie S1). We further compared the impact of Ca^{2+} versus Na^+ entry through NMDARs on swelling by repeating experiments in Ca^{2+} or Na^+ free extracellular solutions. The increase in cell volume from NMDAR activation was still observed in extracellular Ca^{2+} free solution (cross sectional area increased to $161.60\% \pm 10.55\%$ of baseline). However, in the presence of low concentration of extracellular Na^+ ($[\text{Na}^+]_{\text{ext}}$) and normal Ca^{2+} , swelling was completely absent and NMDAR activation actually resulted in a decrease in neuronal volume (Figures 1J, 2C, and 2D). Control experiments showed that neuronal $[\text{Na}^+]_i$ increases and swelling induced by veratridine were blocked by the VGSC antagonist, TTX (Figures 1J and 1K; $p < 0.001$, two-tailed Student's t test) and those induced by NMDA were blocked by the NMDAR antagonist, d-APV (Figures 1J and 1K; $p < 0.001$, ANOVA). Our experimental assay was performed at room temperature to facilitate the imaging of AM indicator dyes which are more rapidly extruded from neurons at 37°C (Beierlein et al., 2004) (Figure S1). However, as the function of many transporters and metabolic proteins that govern ion transport are temperature-dependent, we confirmed

that increases in $[\text{Na}^+]_i$ equally cause swelling of neurons at 37°C (Figure S1).

Although an increase in Na^+ preceding swelling was consistently observed, the magnitude and duration of CoroNa fluorescence signals were distorted during cellular swelling due to dye dilution. This is consistent with our observations that swelling was associated with reduced fluorescence intensity of the inert dye, Calcein red-AM (Figure S2). However, without the ability to dissociate changes in $[\text{Na}^+]_i$ from changes in dye concentration, it is not possible to conclude that $[\text{Na}^+]_i$ itself is not also decreasing during swelling. In order to define the true magnitude and time course of the $[\text{Na}^+]_i$ increases, we developed a method to record real-time calibrated measurements of $[\text{Na}^+]_i$ using two-photon FLIM which was independent of changes in dye concentrations. When lifetime measurements of CoroNa were first tested in iso-osmotic salt solutions the time constant of decay (τ) increased with increasing $[\text{Na}^+]$ (Figure 1G). However, as the local environment can affect lifetime measurements of dyes (Berezin and Achilefu, 2010), calibrations of CoroNa lifetimes were obtained within the cytoplasm of neurons by whole-cell voltage-clamping of neurons and dialysis with different $[\text{Na}^+]$ concentrations. CoroNa lifetimes were best fit using a biexponential decay (Figure S3) with a short lifetime (τ_{fast}) predictive of $[\text{Na}^+]_i$ (Figures 1H and 1I). FLIM of CoroNa loaded neurons revealed that $[\text{Na}^+]_i$ increased to approximately 94.46 ± 2.14 mM (calibrated value) throughout veratridine application and gradually recovered after washout (Figures 1E and 1F and Movie S2). These results demonstrate that the decrease in CoroNa fluorescence as the neurons swell is primarily due to dye dilution and not a dilution of $[\text{Na}^+]_i$ itself.

Cl^- Influx Is Required for Na^+ -Induced Neuronal Swelling

Since cytoplasmic impermeant anions make up the bulk of the intracellular anionic milieu, changes in $[\text{Cl}^-]_i$ must be met by an accompanying influx of water, possibly via transporters (Zeuthen, 2010), in an attempt to achieve Gibbs-Donnan equilibrium (Glykys et al., 2014). We therefore examined whether prolonged $[\text{Na}^+]_i$ increases were associated with a secondary influx of Cl^- , and further whether Cl^- entry was ultimately required for neuronal swelling. Using two-photon FLIM of the Cl^- -sensitive dye MQAE (Ferrini et al., 2013; Verkman et al., 1989), we observed that $[\text{Cl}^-]_i$ increased in neurons (indicated by a decrease in the fluorescence lifetime) when Na^+ influx was triggered by veratridine application (Figures 3A and 3B). This Cl^- influx was independent of entry via GABA_ARs as all experiments were performed in the presence of the ligand-gated Cl^- channel antagonist, picrotoxin (100 μM).

Whether neuronal Na^+ and subsequent Cl^- influx was sufficient to increase tissue volume were next investigated by imaging hippocampal/cortical brain slices at low magnification. Application of veratridine triggered dramatic swelling of brain slices that was reduced but still substantial even when a number of Na^+ , Ca^{2+} , and Cl^- entry pathways were reduced by blockade of glutamate-gated AMPARs and NMDARs, voltage-gated Ca^{2+} channels (VGCCs), and GABA activated Cl^- channels with a cocktail of blockers (20 μM CNQX, 100 μM d-APV, 30 μM Cd^{2+} , and 100 μM picrotoxin) (Figures 3C and 3D and Movie

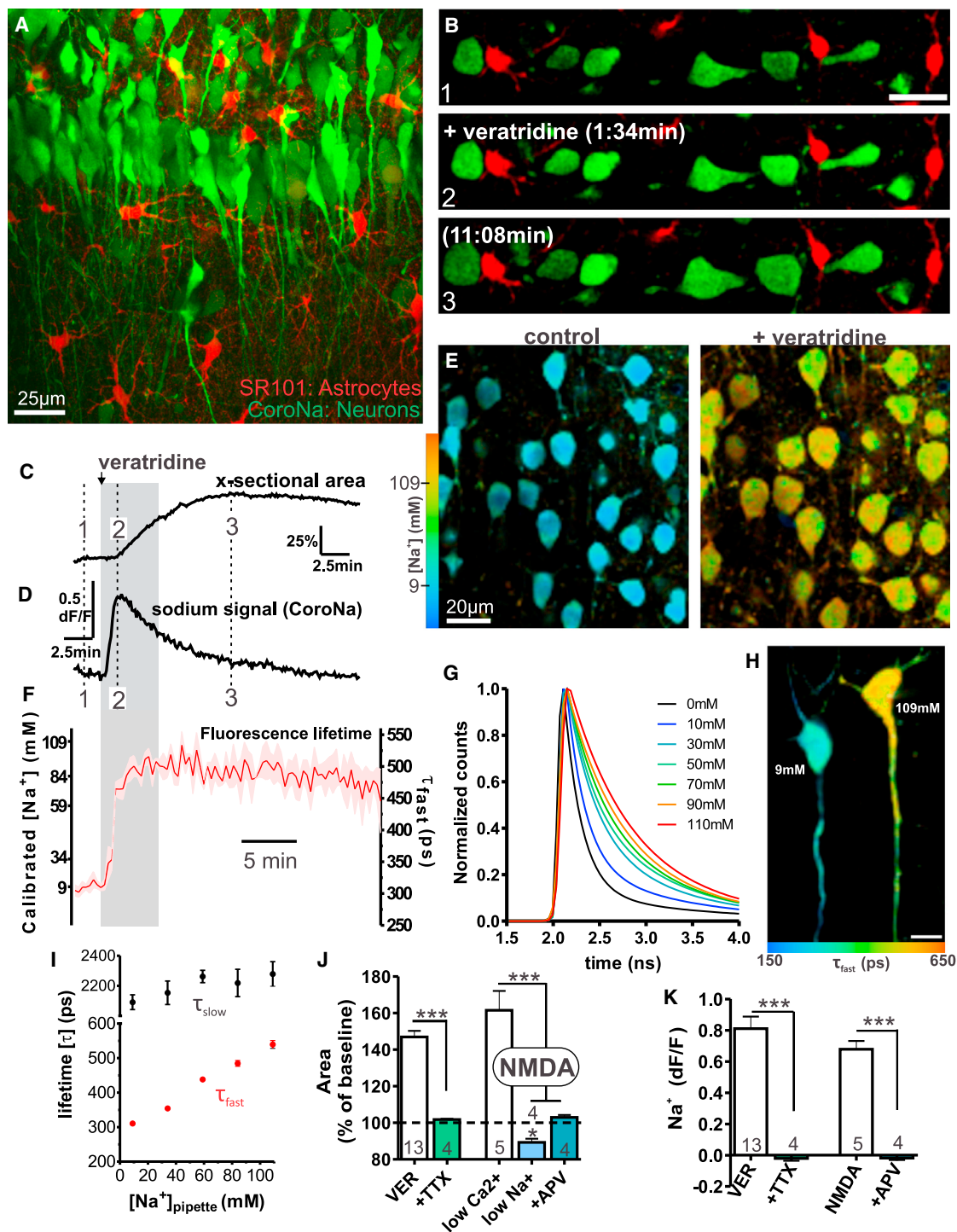


Figure 1. Neuronal Swelling Is Caused by Prolonged Increases in Intracellular Na^+ and Is Independent of Ca^{2+}

(A) CoroNa Green (Na^+ indicator) loaded neurons versus SR101 stained astrocytes (red) in a hippocampal brain slice imaged using two-photon laser scanning microscopy.

(B–D) Cortical neurons treated with veratridine (50 μ M) show increase in $[Na^+]_i$, followed by swelling (increase in cross sectional area). Astrocytes do not swell. (E and F) CoroNa FLIM measurements of $[Na^+]_i$, as neurons swell reveals true time course and magnitude of Na^+ signals that are independent of dye concentration ($n = 4$).

(G–I) Calibration of FLIM measurements of neuronal $[Na^+]_i$ with CoroNa. (G) Decay of CoroNa fluorescence changes in salt solutions with varying $[Na^+]_i$. (H) Dual (simultaneous) whole-cell patch clamping of two neurons dialyzed with high (109 mM) and low (9 mM) $[Na^+]_i$, show distinct separation of lifetimes. (I) Calibration of

(legend continued on next page)

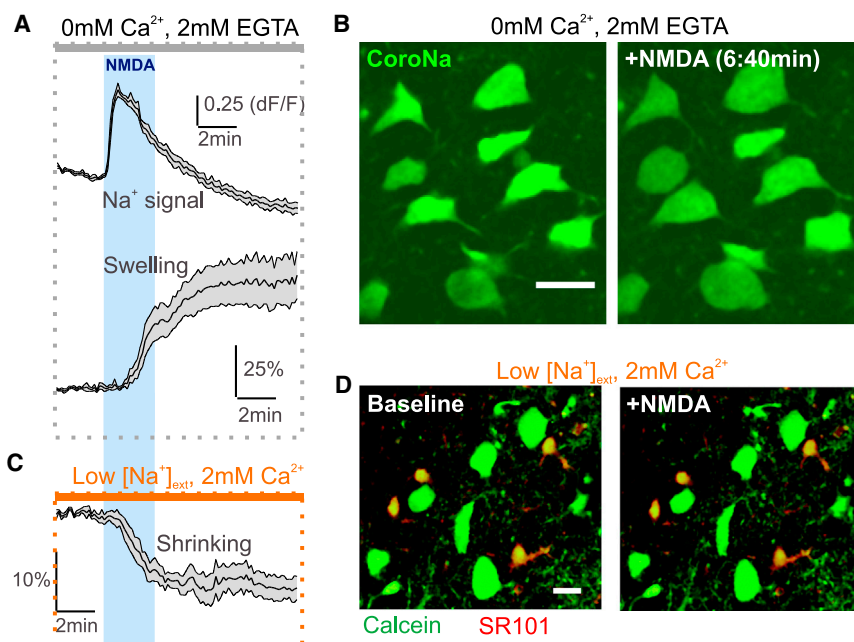


Figure 2. NMDAR Activation Triggers Neuronal Swelling that Requires Na^+ Influx, but That Is Independent of Ca^{2+} Influx

(A and B) Na^+ influx triggers an increase in neuronal volume, measured as the cross sectional area in the absence of extracellular Ca^{2+} (0 mM Ca^{2+} , 2 mM EGTA) ($n = 5$).

(C and D) Iso-osmotic replacement of extracellular Na^+ with NMDG (from 152 mM to 26 mM), to reduce Na^+ entry through NMDARs prevents neurons from swelling and causes them to shrink (86.7% of baseline, $p < 0.05$) ($n = 4$).

Scale bars, 15 μm (B and D). Shaded area above and below mean represent SEM.

S3). In contrast, blocking all Cl^- influx pathways by reducing the concentration of extracellular Cl^- ($[\text{Cl}^-]_{\text{ext}}$) with iso-osmotic replacement of NaCl for Na-gluconate in the extracellular solution dramatically reduced the magnitude of the volume increase of brain slices (Figure 3D; $p < 0.001$, ANOVA). These results suggest that even when fast ionotropic glutamate and GABA activated receptors are blocked, increased neuronal $[\text{Na}^+]_{\text{i}}$ leads to cytotoxic edema of brain tissue that is dependent on Cl^- influx. We next tested whether reducing $[\text{Cl}^-]_{\text{ext}}$ also prevented Na^+ -induced swelling of individual neurons. Indeed, reducing $[\text{Cl}^-]_{\text{ext}}$ reduced the swelling of neurons visualized with CoroNa fluorescence (Figures 3E and 3F and Movie S4; $p < 0.001$, ANOVA), without affecting the $[\text{Na}^+]_{\text{i}}$ signal (Figure 3H; $p > 0.05$, two-tailed Student's *t* test). As it has been previously reported that GABA_AR-mediated Cl^- influx can contribute to both neuronal swelling in cell culture (Hasbani et al., 1998) and to swelling following oxygen glucose deprivation in situ (Allen et al., 2004), the contribution of GABA_AR Cl^- influx to neuronal swelling in our experimental conditions was examined. Consistent with previous reports, pre-application of the GABA_AR antagonist picrotoxin slightly but significantly reduced the magnitude of neuronal swelling (from 161.7% to 146.9%; Figure 3F; $p < 0.05$, ANOVA); however, the majority of the volume increase persisted in

picrotoxin suggesting that the cause of swelling was dominated by Cl^- influx via an as yet unidentified mechanism. NMDA-induced swelling was also blocked by low $[\text{Cl}^-]_{\text{ext}}$ (iso-osmotic replacement of NaCl for Na-isethionate) (Figure 3G; $p < 0.05$, two-tailed Student's *t* test). Together, these data indicate that neuronal swelling requires Cl^- influx

through a mechanism that is triggered by an increase in $[\text{Na}^+]_{\text{i}}$ and that Na^+ entry alone is not sufficient to swell neurons.

Na^+ and Cl^- Dependent Neuronal Swelling Causes Death

Aberrant calcium influx via NMDARs can lead to mitochondrial depolarization and cell death; however, Cl^- removal also reduces ischemia- and glutamate-evoked early neuronal death in cell culture (Choi, 1987; Goldberg and Choi, 1993; Rothman, 1985), suggesting the existence of two independent pathways ultimately leading to cell death. The impact of the $[\text{Na}^+]_{\text{i}}$ -triggered Cl^- entry and neuronal swelling on cell viability was further investigated using LDH release as a measure of cell death (e.g. Kajta et al., 2005). Even in the combined presence of CNQX, picrotoxin, and Cd^{2+} to block fast AMPA/K_A receptors, GABA-activated Cl^- channels, and VGCCs, respectively, application (15 min) of either veratridine (50 μM) or NMDA (100 μM , in artificial cerebrospinal fluid [ACSF] containing 0 mM Ca^{2+} and 2 mM EGTA) caused a rapid and significant increase in LDH release, indicating neurons were dying after 90 min (Figures 3I and 3J; $p < 0.01$, ANOVA). Both the NMDA-induced and veratridine-induced neuronal death, as indicated by LDH release, were abolished by reducing $[\text{Cl}^-]_{\text{ext}}$ throughout the experiment (Figures 3I and 3J; $p < 0.01$, ANOVA). This suggests that Na^+ -induced Cl^-

CoroNa lifetimes measured in soma of neurons dialyzed with different $[\text{Na}^+]_{\text{i}}$ shows that the $[\text{Na}^+]_{\text{i}}$ can be predicted from τ_{fast} . Calibrated values for each $[\text{Na}^+]_{\text{i}}$ were obtained from $n \geq 3$ voltage clamped neurons.

(J and K) Quantified data show neuronal swelling is triggered by sodium influx via independent pathways. NMDAR-mediated swelling was dependent on Na^+ influx and independent of Ca^{2+} . Control confirms Na^+ signal and swelling caused by veratridine and NMDA was via VGSCs and NMDARs respectively, as they were blocked by antagonists, TTX (1 μM) and d-APV (100 μM).

All experiments were done in the presence of 30 μM Cd^{2+} , 20 μM CNQX, 100 μM picrotoxin. Additionally, neurons were pretreated with 100 μM d-APV (NMDAR antagonist) for veratridine experiments and 1 μM TTX (VGSC antagonist) for NMDA experiments to confirm pathways were independent. Scale bars, 20 μm (B) and 15 μm (H). VER, veratridine; x-sectional, cross sectional; VGSC, voltage-gated sodium channel; SR101, sulforhodamine 101. Control values in (J) and (K) are also re-plotted in Figures 3 and 4. Error bars and shaded region above and below the mean represent SEM. See also Figure S1, S2, and S3 and Movie S1, S2, and S3.

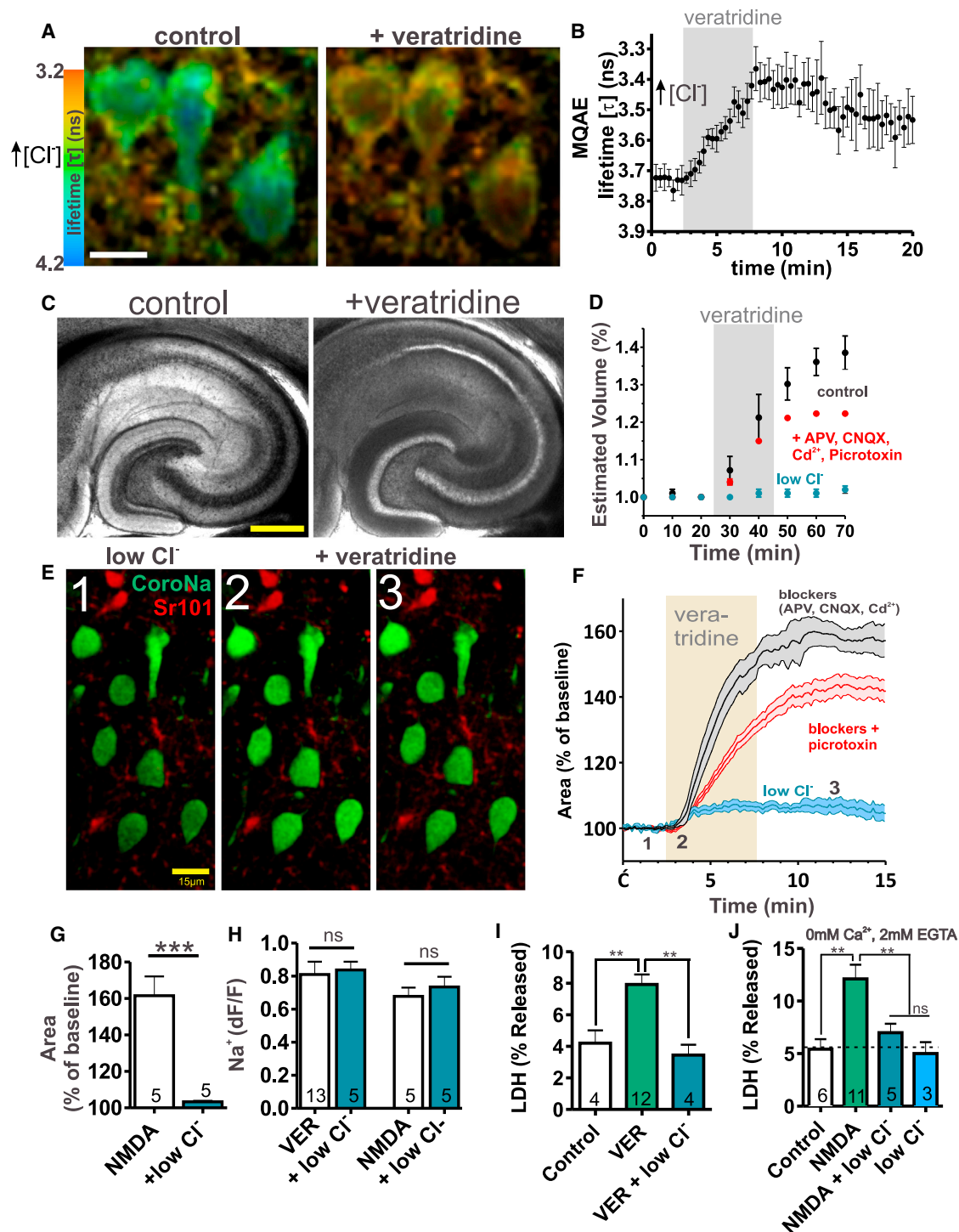


Figure 3. Na^+ Influx Is Correlated with a Secondary Cl^- Influx That Is Required for Neuronal Swelling and Causes Cell Death

(A and B) FLIM of Cl^- -sensitive dye, MQAE, shows that Cl^- influx is correlated with increases in $[\text{Na}^+]_i$ ($n = 5$).

(C and D) Neuronal Na^+ influx triggers an increase in brain tissue volume shown by changes in volume of a hippocampal brain slice. (D) Cocktail of fast glutamate receptor, GABA receptor and VGCC blockers slightly reduce tissue swelling ($p < 0.01$) but significant Cl^- dependent swelling still occurs ($p < 0.01$) indicating that swelling is dominated by other mechanisms.

(E and F) Veratridine triggered neuronal swelling is prevented by reducing extracellular Cl^- (10.5 mM) and is only partially inhibited by blocking GABA_A Rs.

(G) NMDA triggered swelling is blocked by reducing extracellular Cl^- .

(H) Positive control shows veratridine and NMDAR Na^+ signals were unaffected by low Cl^- solution.

(legend continued on next page)

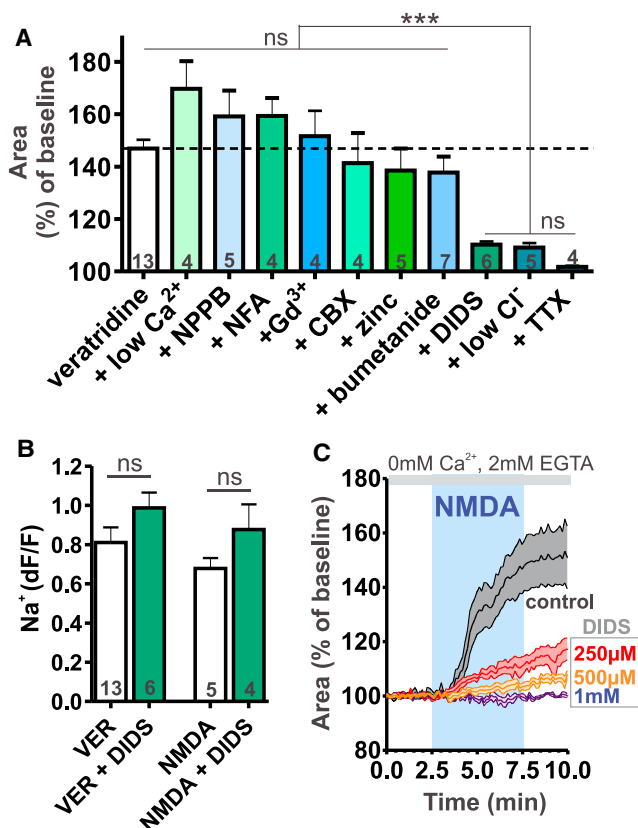


Figure 4. Neuronal Swelling Reflects the Pharmacological Profile of a SLC4 or SLC26 Family Member

(A) Veratridine-induced neuronal swelling was blocked by the $\text{HCO}_3^-/\text{Cl}^-$ exchanger inhibitor, DIDS (250 μM) but not by blockers of several other Cl^- channels or transporters (see Table S1).

(B) Positive control shows veratridine and NMDA-induced Na^+ signal in the presence of DIDS.

(C) NMDA-induced neuronal swelling was blocked by DIDS in a dose dependent manner; control (n = 5), 250 μM (n = 4), 500 μM (n = 5), 1 mM (n = 5). All solutions contained blockers: 30 μM Cd^{2+} , 20 μM CNQX, 100 μM picrotoxin, plus either 100 μM d-APV for veratridine experiments or 1 μM TTX for NMDA experiments. VER, veratridine. Error bars and shaded region above and below the mean represent SEM.

influx and subsequent swelling results in Ca^{2+} -independent cell death.

Pharmacological Analyses of the Predominant Cl^- Influx Pathway Required for Neuronal Swelling and Death

There are several candidates for the transmembrane influx of Cl^- in neurons that can be distinguished based on their sensitivity to

different antagonists (Alvarez-Leefmans and Delpire, 2009; Jentsch et al., 2002; Verkman and Galletta, 2009) (Table S1). We hypothesized that by identifying and blocking the source of Cl^- entry that was triggered by Na^+ entry, both the Na^+ -induced neuronal swelling and corresponding cell death could be prevented. As a first step, pharmacological analyses using the imaging assay of swelling of neurons in brain slices were undertaken in order to screen for the possible involvement of different Cl^- channels and transporters. In separate experiments the following blockers were tested as described in Table S1; NPPB (200 μM) to block the volume-regulated anion channel (VRAC, VSOR), zinc (300 μM) to block CLC-2, Gd^{3+} (100 μM) to block the Maxi-anion channel, niflumic acid (NFA) (200 μM) to block the Ca^{2+} activated Cl^- conductance (CaCC, bestrophin), carbenoxelone (CBX) (100 μM) to block pannexins/connexins, bumetanide (100 μM) to block cation chloride cotransporters (NKCC1 and KCC2), and DIDS (250 μM) to block SLC4 and SLC26 anion exchangers. All antagonists were both bath applied and present in the puffing pipette used to apply either NMDA or veratridine. Of note, of the various Cl^- channel and transporter blockers examined, only DIDS reduced the swelling induced by increased $[\text{Na}^+]_i$ (Figure 4A; $p < 0.05$ compared to all other antagonists, ANOVA). The small volume change in the presence of DIDS was not significantly different from those observed in low Cl^- extracellular solution (Figure 4A; $p > 0.05$, ANOVA). A substantial $[\text{Na}^+]_i$ increase was still observed in DIDS indicating that Na^+ entry was not affected (Figure 4B). This pattern of block by DIDS but no effect of the numerous other blockers suggested that a member of the SLC4 or SLC26 families of anion exchangers was the most likely source of Cl^- entry. Although DIDS also blocks VRAC, which has been implicated in excitotoxic cell death in neuronal cell culture (Inoue and Okada, 2007), under our conditions we observed no protection of either cell volume or cell death in the presence of the potent VRAC blocker, NPPB. DIDS also blocked NMDA-evoked neuronal swelling in a dose-dependent manner (Figure 4C) and was confirmed to block the veratridine-stimulated swelling at 37°C (Figure S1), suggesting a common mechanism.

As it was observed that extracellular Cl^- was required for both neuronal swelling and the subsequent cell death and that DIDS prevented neuronal swelling, we predicted that DIDS would block the Cl^- dependent cell death pathway without affecting the classic Ca^{2+} -dependent death. DIDS was initially tested for its effectiveness in preventing the swelling-induced, Cl^- -dependent cell death as measured by LDH efflux in brain slices exposed to veratridine. Indeed, DIDS prevented cell death from veratridine-induced Na^+ influx and swelling (Figure 5A; $p < 0.005$, ANOVA), whereas the VRAC blocker NPPB had no effect. DIDS was further examined on both the NMDA

(I) Neuronal Na^+ influx via VGSCs causes cell death that is Cl^- -dependent as measured by LDH release.

(J) Neuronal Na^+ influx via NMDARs causes cell death that is Cl^- -dependent and Ca^{2+} -independent. Slices were incubated in low $[\text{Cl}^-]_o$ or control ACSF for the entire experiment starting 20 min. prior to either Veratridine or NMDA (15 min.). LDH was collected from supernatant 1.5 hr following end of Veratridine or NMDA treatment.

Scale bars, 10 μm (A), 1.0 mm (C), 15 μm (E). For experiments in (A, B, E and G–J) solutions contained blockers: 30 μM Cd^{2+} , 20 μM CNQX, 100 μM picrotoxin, plus either 100 μM d-APV for veratridine experiments or 1 μM TTX for NMDA experiments. n values in (F), blockers (n = 5), +picrotoxin (n = 13), low Cl^- (n = 5). VER, veratridine; VGCC, voltage-gated calcium channel; VGSC, voltage-gated sodium channel. Error bars and shaded region above and below the mean represent SEM. See also Movie S3 and Movie S4.

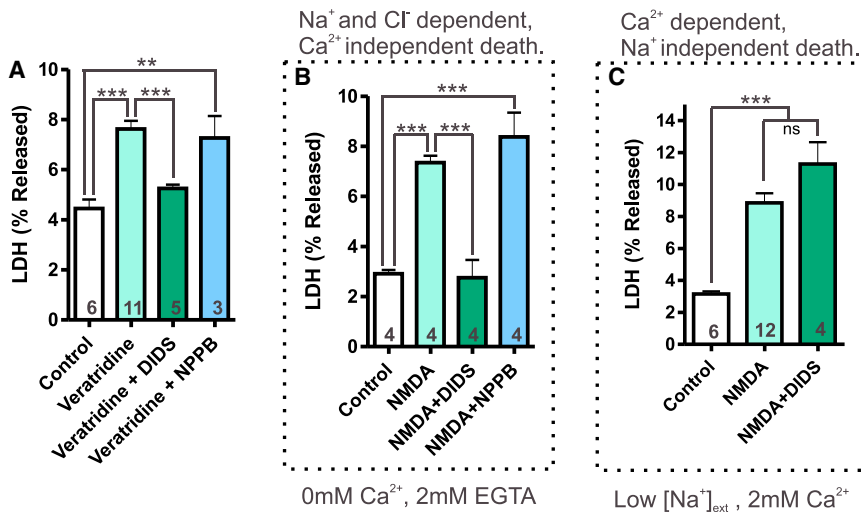


Figure 5. DIDS Blocks Na⁺ and Cl⁻ Dependent, Ca²⁺ Independent Cell Death

(A) LDH release measurements show Na⁺- and Cl⁻-dependent cell death triggered by veratridine was blocked by the HCO₃⁻/Cl⁻ exchanger antagonist, DIDS but not by the VRAC blocker NPPB.

(B) NMDAR Na⁺ influx triggers cell death in the absence of extracellular Ca²⁺ that is blocked by DIDS but not NPPB.

(C) NMDAR Ca²⁺ influx also triggers cell death that is not blocked by DIDS, indicating separate pathways. Error bars above and below the mean represent SEM.

Cl⁻-dependent, Ca²⁺-independent cell death pathway and on the NMDA Ca²⁺-dependent cell death pathway. As predicted, DIDS blocked the cell death caused by NMDA in Ca²⁺ free extracellular solution (Figure 5B; $p < 0.005$, ANOVA). If however, NMDA was applied in the presence of extracellular Ca²⁺ but reduced extracellular Na⁺, cell death still occurred (Figure 5C; $p < 0.005$, ANOVA) but was not blocked by DIDS (Figure 5C; $p > 0.05$, ANOVA). These results suggest that two independent cell death pathways co-exist that can be distinguished based on their ionic basis; one that involves swelling, requires Na⁺ and Cl⁻ influx, is Ca²⁺ independent, and is blocked by DIDS, and one that is triggered by Ca²⁺ influx, but that is not DIDS sensitive.

Identification of SLC26A11 as the Predominant Cl⁻ Influx Pathway Underlying Na⁺ Dependent Cytotoxic Neuronal Swelling

Our data indicate that Na⁺ entry into neurons is linked to a DIDS-sensitive Cl⁻ influx pathway that is required for neuronal swelling and mediates cell death. Several DIDS-sensitive candidates are expressed in CNS neurons of which several act as Cl⁻/HCO₃⁻ exchangers and include the SLC4 family of exchangers (Alvarez-Leefmans and Delpire, 2009; Boron et al., 2009; Romero et al., 2013). The DIDS-sensitive Cl⁻, HCO₃⁻ exchangers that are known to be expressed in the cortex and hippocampus are SLC4A3, SLC4A8, and SLC4A10 (Boron et al., 2009; Romero et al., 2013). In addition, SLC26A11 was recently shown to be highly expressed in CNS cortical neurons (Rahmati et al., 2013). SLC26A11 is a member of the sulfate transporter family that in different expression systems has been reported to act variously as a DIDS-sensitive sulfate transporter, a DIDS-sensitive exchanger for Cl⁻, SO₄²⁻, HCO₃⁻, or H⁺-Cl⁻ or as a Cl⁻ channel (Lee et al., 2012; Rahmati et al., 2013; Vincourt et al., 2003; Xu et al., 2011).

Utilizing qRT-PCR, the expression of SLC4 and SLC26 family members was confirmed in both cortical and hippocampal brain tissue (Figure S4). Based on their combined pharmacological profile and expression profiles, SLC4-A3, -A8, -A10, and

SLC26A11 appeared to be the most promising candidates for the Cl⁻ entry pathway that causes neuronal swelling. We recently reported the development of an efficient LNP-mediated delivery system to introduce siRNAs against specific molecular targets into CNS neurons both in vivo and in vitro (Rungha et al., 2013). Individual siRNAs targeted against the different SLC candidate genes were encapsulated in Dil labeled LNPs and initially tested for their ability to attenuate expression in both primary neuron cultures and a HEK cell expression system (Figure S4). These in vitro-validated siRNA LNPs against the 4 different SLC candidates or a control (luciferase) siRNA were subsequently injected intracranially into the rat somatosensory cortex. After allowing 5-6 days for uptake of LNPs and knockdown of candidate proteins to occur, neurons that had taken up Dil labeled LNPs were examined for Na⁺-induced Cl⁻-dependent swelling in cortical slices. Knockdown of SLC4A-3, -8, or -10 either separately or together had no significant effect on the magnitude of veratridine-induced neuronal swelling compared to the control luciferase siRNA injected animals (Figures 6C and 6G and S5; $p > 0.05$, ANOVA). In striking contrast, knockdown of SLC26A11 with two siRNAs targeted toward different sequences of SLC26A11 mRNA, significantly reduced the magnitude of the swelling in neurons (Figures 6D and 6H and Movie S5; $p < 0.05$, ANOVA was performed comparing results from all siRNA groups (luciferase, A3, A8, A10, A3+A8+A10, A11 No.1 and A11 No.2)). The occurrence of SLC26A11 knockdown was further validated by western blot analysis of SLC26A11 protein in tissue 5 days following injection of SLC26A11 siRNA-LNPs (Figures 6A and 6B). These results indicate that the Cl⁻ influx that is required for neuronal swelling is mediated by a SLC26A11-dependent process.

Studies of the properties of recombinant SLC26A11 have shown that, depending upon the cell type in which it is expressed, this protein can act either as a Cl⁻ channel or a SO₄²⁻ or oxalate transporter that is inhibited by DIDS or the CFTR antagonist GlyH-101 (Alper and Sharma, 2013; Rahmati et al., 2013; Stewart et al., 2011). We therefore investigated whether GlyH-101 has similar actions on preventing neuronal swelling and the associated cell death and whether there exists a neuronal Cl⁻ current that is sensitive to both DIDS and GlyH-101. Similar to the actions of DIDS, GlyH-101 profoundly

inhibited both veratridine-stimulated swelling (Figure 6E; $p < 0.001$, two-tailed Student's t test) and cell death (Figure 6F; $p < 0.001$, ANOVA).

The opening of Na^+ permeable channels causes both $[\text{Na}^+]_i$ accumulation and neuronal depolarization. The large (~ 80 mM) increases in $[\text{Na}^+]_i$ occurred prior to the increases in cell volume (Figure 1) suggesting that there are compensatory mechanisms such as K^+ efflux that are initially sufficient to maintain osmotic equilibrium. Decreased intracellular K^+ and progressive accumulation of extracellular K^+ could also contribute to further depolarization of the membrane. We therefore tested the possibility that SLC26A11 in cortical neurons is required for a DIDS- and GlyH-101-sensitive Cl^- channel that is opened by depolarization. Such outwardly rectifying, non-inactivating DIDS-sensitive conductances have previously been described in neurons (Smith et al., 1995), although their molecular identity remains unknown. Whole-cell voltage clamp recordings were obtained under conditions to reveal voltage-dependent Cl^- currents by blocking other known voltage-gated channels with a cocktail of blockers. We targeted layer 4 neurons in cortical slices (Figure 7A), the same cell types that were also imaged in the swelling studies described above. Depolarization to -20 mV or greater elicited a non-inactivating Cl^- current that was blocked by DIDS and was not present when external $[\text{Cl}^-]$ was reduced (Figures 7C–7E; $p < 0.001$, ANOVA). In addition, dialysis of neurons with GlyH-101 at concentrations that prevented neuronal swelling were found to also inhibit the voltage-dependent Cl^- current and occluded the effect of DIDS (Figures 7D and 7E; $p < 0.001$, ANOVA). Finally, recordings were made from neurons transfected with siRNA against either SLC26A11 or luciferase (control) using LNPs visualized with Dil. We found that knockdown of SLC26A11 attenuated the DIDS and GlyH-101-sensitive Cl^- current (Figures 7C–7E; $p < 0.001$, ANOVA), demonstrating that SLC26A11 protein is a requirement for an outwardly rectifying Cl^- current activated in substantially depolarized neurons.

DISCUSSION

Our results demonstrate that prolonged Na^+ entry via either of two independent pathways (either VGSCs or NMDARs) converge to activate a Cl^- influx pathway via SLC26A11 that is ultimately required for neuronal swelling and subsequent cell death. Unlike $[\text{Na}^+]_i$ whose osmotic influence on the cell can initially be met by a compensating efflux in $[\text{K}^+]_i$, the anionic intracellular milieu of the cell is largely made up of large impermeable anions. As such, increases in $[\text{Cl}^-]_i$ likely maintain electroneutrality by retaining Na^+ and K^+ ions intracellularly, thereby increasing intracellular osmolarity and drawing water into the cell.

In mature pyramidal neurons of the cortex and hippocampus, resting membrane potential (E_m) is set positive compared to the equilibrium potential for Cl^- (E_{Cl^-}) suggesting that Cl^- is not passively distributed across the plasma membrane (Alvarez-Leefmans and Delpire, 2009). Changing membrane potential also has little effect on $[\text{Cl}^-]_i$ indicating that there is little Cl^- membrane permeability at rest (Thompson et al., 1988). As such, in order for $[\text{Cl}^-]_i$ to rapidly increase in neurons either a Cl^- transporter has to be activated or a transmembrane Cl^- channel has to be opened. Membrane depolarization could

also further contribute to Cl^- influx by increasing the driving force for Cl^- entry.

Using an siRNA knockdown approach, we identified the molecular nature of the predominant Cl^- influx pathway that is activated following increases in $[\text{Na}^+]_i$ and causes neuronal cytotoxic edema. Our study demonstrates that SLC26A11 acts as a functional Cl^- influx pathway in neurons. A recent study showed that SLC26A11 protein is expressed in neurons throughout the brain and we would predict that similar mechanisms of swelling and neuronal death likely occur in many other areas such as the cerebellum where expression levels are high (Rahmati et al., 2013). SLC26A11, originally identified as a sulfate transporter has been shown to operate in several modes, including an exchanger for Cl^- SO_4^{2-} , HCO_3^- , or H^+ - Cl^- or as a Cl^- channel, depending upon the tissue type and the expression system (Rahmati et al., 2013; Vincourt et al., 2003; Xu et al., 2011). The mechanism linking Na^+ influx and SLC26A11-mediated Cl^- influx is most simply explained by membrane depolarization activating SLC26A11 in its Cl^- channel mode, thereby leading to a sustained Cl^- influx. Our observation that SLC26A11 is required for Cl^- channel activity (Rahmati et al., 2013) that opens with depolarizations greater than -20 mV suggests that Cl^- would be constantly entering the cell as E_{Cl^-} in mature neurons is initially set close to -70 mV. During sustained depolarization E_{Cl^-} would drift to more depolarized potentials therefore Cl^- influx would continue until equilibrium is met or the membrane repolarizes. Interestingly, depolarization of cortical neurons with high K^+ solution (40 mM) is not sufficient to cause neuronal swelling alone, and only causes swelling when spreading depression occurs, concurrent with depolarizations to approximately 0 mV and substantial extracellular K^+ accumulation (Zhou et al., 2010; Zhou et al., 2013). A similar breakdown of ionic gradients occurs during pathological settings of cytotoxic edema, such as ischemia, when activation of voltage-gated and ligand-gated channels leads to massive increases in $[\text{Na}^+]_i$, followed by increases in extracellular K^+ and almost complete depolarization of the neurons (Dreier, 2011; Somjen, 2001).

Several questions arise as to the specific conditions and times that SLC26A11 may modulate local and global Cl^- concentrations. Aberrant, Cl^- homeostasis is central to several neurological diseases, and it would therefore be interesting to examine whether SLC26A11 expression or localization changes under such conditions. Epileptic seizures are commonly observed in patients following severe traumatic brain injury (TBI) (Annegers et al., 1998; Hung and Chen, 2012; Salazar et al., 1985). Increased $[\text{Cl}^-]_i$ leading to a depolarizing shift in E_{GABA} (Cohen et al., 2002; Miles et al., 2012) has been reported to contribute to the generation of seizure activity. If blocking SLC26A11 reduces the increases in Cl^- that occur during pathologies that are associated with cytotoxic edema, it may be possible to maintain the direction of hyperpolarizing GABA_A currents and reduce the generation of post-traumatic seizures.

In addition to the Cl^- loading that occurs during excitotoxic insults, Cl^- efflux may also be compromised. As KCC2 directional transport is dependent on the K^+ gradient, small changes in extracellular K^+ can have substantial effects on KCC2-mediated Cl^- clearance. Additionally, a recent study demonstrated that glutamate activation of NMDARs leads to phosphorylation and

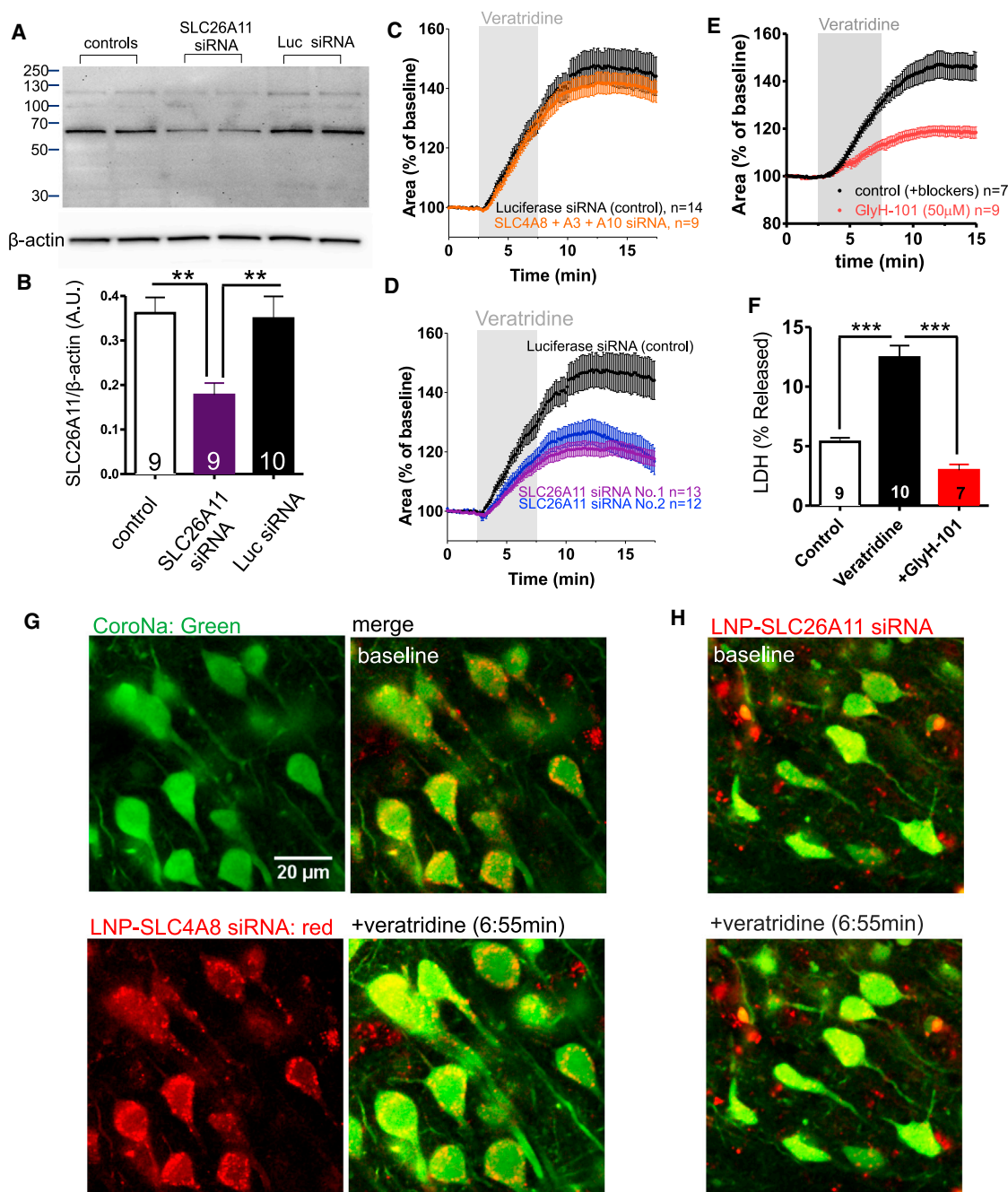


Figure 6. Cl^- Influx via SLC26A11 Causes Cytotoxic Neuronal Edema Following Increased $[\text{Na}^+]_i$

(A and B) Cortical brain tissue tested 5 days following in vivo injection of LNP encapsulated siRNAs shows SLC26A11 No.1 siRNA selectively reduced SLC26A11 protein expression compared to β-actin. Controls show luciferase siRNA had no effect on SLC26A11 expression. Columns in (A) represent samples from different rats.

(C) In vivo knockdown of SLC4A3, A8, A10 with LNP-siRNAs results in no significant difference in the magnitude of neuronal swelling compared to a control (luciferase siRNA) in cortical brain slices imaged 5 days following the injection ($p > 0.05$, ANOVA).

(D) Two different siRNA constructs against SLC26A11 result in a significant reduction in the magnitude of veratridine-induced neuronal swelling compared to luciferase siRNA ($p < 0.05$, ANOVA).

(G and H) Example images of cortical neurons transfected with siRNA using lipid nanoparticle delivery shows SLC26A11 knockdown results in protection from veratridine triggered swelling compared to neurons transfected with SLC4A8 siRNA. Dil staining (red) shows cell uptake of LNP-siRNA.

(E and F) SLC26A11 blocker GlyH-101 significantly reduces the magnitude of neuronal swelling induced by increases in $[\text{Na}^+]_i$, $p < 0.001$, two-tailed Student's *t* test (F) and the resulting cell death measured by LDH released, $p < 0.001$, ANOVA.

(legend continued on next page)

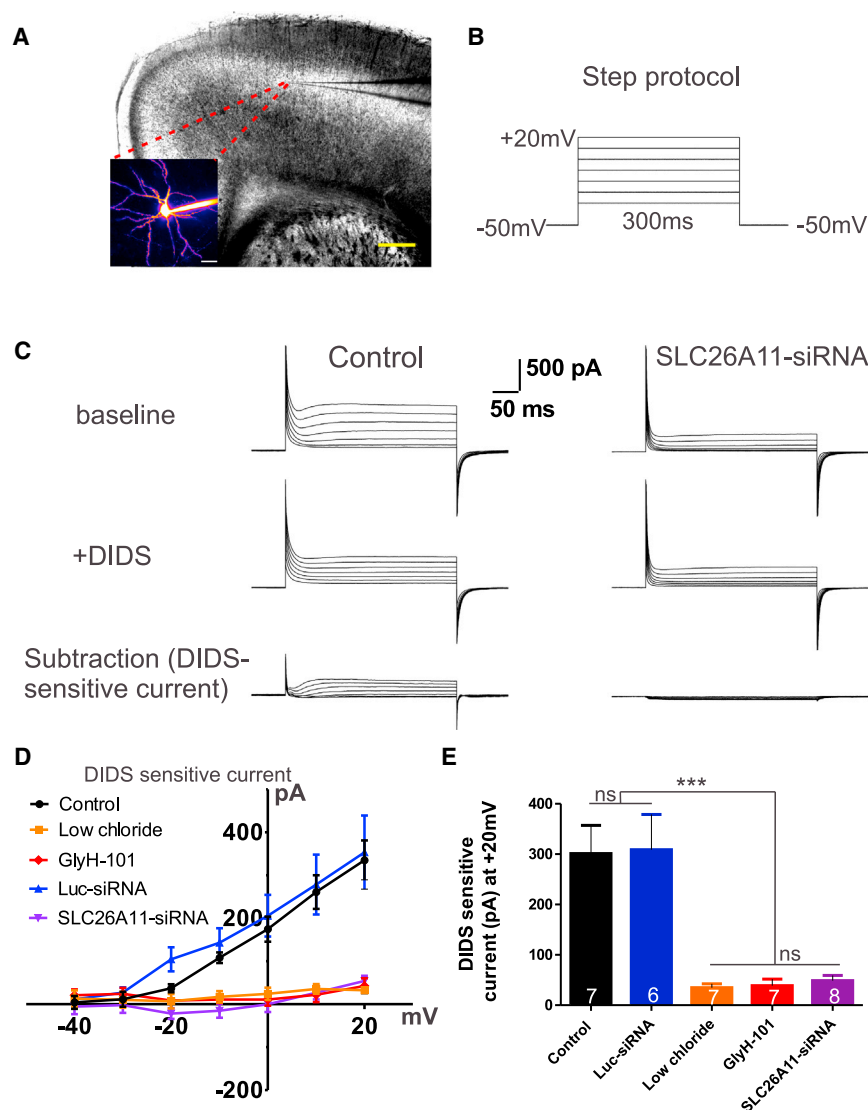


Figure 7. SLC26A11 Gene Product Is Required for Activation of an Outwardly Rectifying Cl^- Channel That Is Activated by Depolarization

(A) Example image of a whole-cell voltage-clamped layer 4 neuron in a coronal brain slice. (B) Voltage clamp protocol used to depolarize neuron in presence of a cocktail to inhibit known voltage-dependent ion channels. (C) Left: Top, Example trace of outward current activated by depolarization. Middle, magnitude of current is reduced in DIDS. Bottom, subtraction showing DIDS-sensitive component. Right: SLC26A11 siRNA transfection attenuates DIDS-sensitive outward current. (D and E) Summarized I/V curves demonstrate that SLC26A11 is required for activation of an outward Cl^- conductance that is activated in depolarized neurons. Low extracellular chloride (10.5 mM), GlyH-101 (50 μM) and SLC26A11 LNP-siRNA all significantly reduce magnitude of DIDS-sensitive current compared to Control and Luc-siRNA transfection. Scale bars in (A): right, 500 μm ; left, 25 μm . Error bars represent SEM.

significantly reduced when overall Cl^- entry is prevented suggests that therapeutic strategies to inhibit SLC26A11 dependent Cl^- entry may have widespread benefit toward treating these different conditions.

EXPERIMENTAL PROCEDURES

Imaging

Live-cell imaging (brain slice) was performed with a two-photon laser-scanning microscope (Zeiss LSM510-Axioskop-2; Zeiss, Oberkochen, Germany) with a 40X-W/1.0 numerical aperture objective lens directly coupled to a Chameleon ultra2 laser (Coherent, Santa Clara, CA). CoroNa, SR101 and Dil were excited at 770 nm, and MQAE was excited at 760 nm. The fluorescence from each fluorophore was split using a dichroic

thereby decreased expression of KCC2, leading to decreased recovery of excitotoxic Cl^- loads (Lee et al., 2011). In this study the authors were unable to identify the source of Cl^- influx, but showed that it was independent of NKCC1. If KCC2-mediated Cl^- efflux is indeed compromised following cytotoxic edema, in addition to blocking the influx of Cl^- perhaps enhancing extrusion of Cl^- (Gagnon et al., 2013) would be additionally beneficial.

The identification of SLC26A11 as a significant Cl^- entry pathway during pathological swelling triggered after Na^+ entry suggests new strategies that could be developed toward reducing brain edema. There are numerous different pathways for Na^+ entry that are activated during conditions such as hypoxia, stroke, and TBI. Our observations that cell death is

mirror at 560 nm, and the signals were each detected with a dedicated photo multiplier tube after passing through an appropriate emission filter (Dil, SR101: 605 nm, 55 nm band pass; CoroNa, MQAE: 525 nm, 50 nm band pass). Transmitted light was simultaneously collected using understage infrared differential interference contrast optics and an additional photo multiplier tube. FLIM methodology is described in detail in the [Extended Experimental Procedures](#).

Data Collection, Analysis, and Statistics

Translational movement was removed using ImageJ software. Fluorescence signals were defined as $\Delta F/F = [(F_1 - B_1) - (F_0 - B_0)] / (F_0 - B_0)$, where F_1 and F_0 are fluorescence at a given time and the control period mean, respectively. B_1 and B_0 are the corresponding background fluorescence signals. Swelling of individual neurons in cortical slices was analyzed as (%) increase in cross sectional area relative to a mean baseline period. The cross sectional area of the neuron was calculated using the fluorescence boundary

Scale bar in (G) matches scale in (H). Luciferase controls are combined and plotted in both (C and D) and in [Figure S5](#). For statistics on magnitude of swelling, ANOVA was performed comparing results from all siRNA groups (luciferase, SLC4A3, -A8, -A10, -A3+A8+A10, SLC26A11 No.1 and No.2). Only SLC26A11 No.1 and No. 2 were significantly different from luciferase (control) siRNA, $p < 0.05$. Error bars represent SEM. See also [Figures S4](#) and [S5](#) and [Movie S5](#).

of the neuron soma stained with CoroNa. To estimate the tissue volume from the two-dimensional images of hippocampal slices a line was drawn to measure the diameter and the volume was estimated based on the equation for volume of sphere: $(4/3)\pi r^2$.

Experimental values are the mean \pm SEM; baseline equals 100%; n is the number of experiments conducted (Imaging data from ≥ 3 individual cells from each experiment were averaged for each n value so that equal weight was given to each experiment and not affected by the number of cells imaged per experiment). Statistical tests were either a two-tailed Student's t test or an ANOVA with a Neumann-Keuls post hoc test for comparison between multiple groups. $p < 0.05$ was accepted as statistically significant (* $p < 0.05$, ** $p < 0.01$, *** $p < 0.001$).

More detailed methodology can be found in the [Extended Experimental Procedures](#).

SUPPLEMENTAL INFORMATION

Supplemental Information includes Extended Experimental Procedures, five figures, two tables, and five movies and can be found with this article online at <http://dx.doi.org/10.1016/j.cell.2015.03.029>.

ACKNOWLEDGMENTS

R.L.R. was supported by a studentship from the Canadian Institutes of Health Research (CIHR), S.L.C. by a fellowship from the BC Epilepsy Society, T.P.S. by an operating grant from the CIHR (#10677) and a Canada Research Chair (CRC) in Biotechnology and Genomics-Neurobiology, P.R.C. by a CIHR Emerging Team Grant: Personalized siRNA-Based Nanomedicines (FRN:111627) and B.A.M. by a CRC in Neuroscience and CIHR operating grants (#8545 and # 115121) and the Fondation Leducq. We thank Dr. Xiling Zhou and Dr. Anne Marie Craig for supplying neuronal cultures and Jeff LeDue for assistance with establishing the FLIM methodology. We thank Kate Campbell for illustrations. The work was also supported by a MIRI grant from Brain Canada, Genome British Columbia, the Michael Smith Foundation for Health Research, and the Koerner Foundation. P.R.C. has greater than 5% ownership of Precision Nanosystems Inc. that makes the systems to formulate the lipid nanoparticles.

Received: December 12, 2014

Revised: February 3, 2015

Accepted: March 12, 2015

Published: April 23, 2015

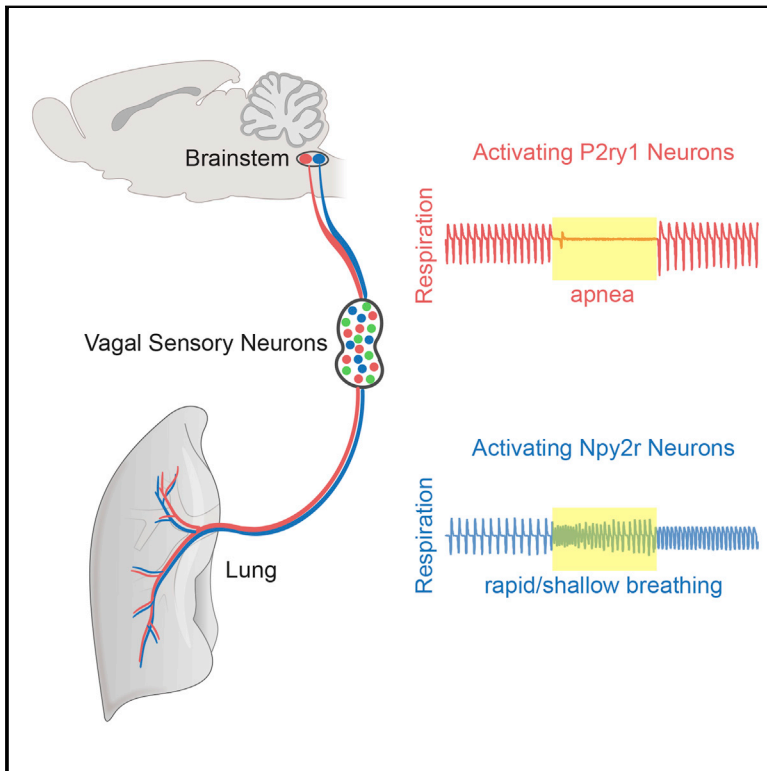
REFERENCES

- Allen, N.J., Rossi, D.J., and Attwell, D. (2004). Sequential release of GABA by exocytosis and reversed uptake leads to neuronal swelling in simulated ischemia of hippocampal slices. *J. Neurosci.* **24**, 3837–3849.
- Alper, S.L., and Sharma, A.K. (2013). The SLC26 gene family of anion transporters and channels. *Mol. Aspects Med.* **34**, 494–515.
- Alvarez-Leefmans, F.J., and Delpire, D. (2009). Physiology and Pathology of Chloride Transporters and Channels in the Nervous System, Vol (London, UK: Elsevier).
- Annegers, J.F., Hauser, W.A., Coan, S.P., and Rocca, W.A. (1998). A population-based study of seizures after traumatic brain injuries. *N. Engl. J. Med.* **338**, 20–24.
- Beierlein, M., Gee, K.R., Martin, V.V., and Regehr, W.G. (2004). Presynaptic calcium measurements at physiological temperatures using a new class of dextran-conjugated indicators. *J. Neurophysiol.* **92**, 591–599.
- Berezin, M.Y., and Achilefu, S. (2010). Fluorescence lifetime measurements and biological imaging. *Chem. Rev.* **110**, 2641–2684.
- Blaesse, P., Airaksinen, M.S., Rivera, C., and Kaila, K. (2009). Cation-chloride cotransporters and neuronal function. *Neuron* **61**, 820–838.
- Boron, W.F., Chen, L., and Parker, M.D. (2009). Modular structure of sodium-coupled bicarbonate transporters. *J. Exp. Biol.* **212**, 1697–1706.
- Choi, D.W. (1987). Ionic dependence of glutamate neurotoxicity. *J. Neurosci.* **7**, 369–379.
- Cohen, I., Navarro, V., Clemenceau, S., Baulac, M., and Miles, R. (2002). On the origin of interictal activity in human temporal lobe epilepsy in vitro. *Science* **298**, 1418–1421.
- Donkin, J.J., and Vink, R. (2010). Mechanisms of cerebral edema in traumatic brain injury: therapeutic developments. *Curr. Opin. Neurol.* **23**, 293–299.
- Dreier, J.P. (2011). The role of spreading depression, spreading depolarization and spreading ischemia in neurological disease. *Nat. Med.* **17**, 439–447.
- Ferrini, F., Trang, T., Mattioli, T.A., Laffray, S., Del'Guidice, T., Lorenzo, L.E., Castonguay, A., Doyon, N., Zhang, W., Godin, A.G., et al. (2013). Morphine hyperalgesia gated through microglia-mediated disruption of neuronal Cl⁻ homeostasis. *Nat. Neurosci.* **16**, 183–192.
- Gagnon, M., Bergeron, M.J., Lavertu, G., Castonguay, A., Tripathy, S., Bonin, R.P., Perez-Sanchez, J., Boudreau, D., Wang, B., Dumas, L., et al. (2013). Chloride extrusion enhancers as novel therapeutics for neurological diseases. *Nat. Med.* **19**, 1524–1528.
- Glykys, J., Dzhalal, V., Egawa, K., Balena, T., Saponjian, Y., Kuchibhotla, K.V., Bacskai, B.J., Kahle, K.T., Zeuthen, T., and Staley, K.J. (2014). Local impermeant anions establish the neuronal chloride concentration. *Science* **343**, 670–675.
- Goldberg, M.P., and Choi, D.W. (1993). Combined oxygen and glucose deprivation in cortical cell culture: calcium-dependent and calcium-independent mechanisms of neuronal injury. *J. Neurosci.* **13**, 3510–3524.
- Hasbani, M.J., Hyrc, K.L., Faddis, B.T., Romano, C., and Goldberg, M.P. (1998). Distinct roles for sodium, chloride, and calcium in excitotoxic dendritic injury and recovery. *Exp. Neurol.* **154**, 241–258.
- Hung, C., and Chen, J.W. (2012). Treatment of post-traumatic epilepsy. *Curr. Treat. Options Neurol.* **14**, 293–306.
- Inoue, H., and Okada, Y. (2007). Roles of volume-sensitive chloride channel in excitotoxic neuronal injury. *J. Neurosci.* **27**, 1445–1455.
- Inoue, H., Mori, S., Morishima, S., and Okada, Y. (2005). Volume-sensitive chloride channels in mouse cortical neurons: characterization and role in volume regulation. *Eur. J. Neurosci.* **21**, 1648–1658.
- Jentsch, T.J., Stein, V., Weinreich, F., and Zdebek, A.A. (2002). Molecular structure and physiological function of chloride channels. *Physiol. Rev.* **82**, 503–568.
- Kajta, M., Trotter, A., Lasorí, W., and Beyer, C. (2005). Effect of NMDA on staurosporine-induced activation of caspase-3 and LDH release in mouse neocortical and hippocampal cells. *Brain Res. Dev. Brain Res.* **160**, 40–52.
- Klatzo, I. (1967). Presidential address. Neuropathological aspects of brain edema. *J. Neuropathol. Exp. Neurol.* **26**, 1–14.
- Klatzo, I. (1987). Pathophysiological aspects of brain edema. *Acta Neuropathol.* **72**, 236–239.
- Lee, H.H., Deeb, T.Z., Walker, J.A., Davies, P.A., and Moss, S.J. (2011). NMDA receptor activity downregulates KCC2 resulting in depolarizing GABA_A receptor-mediated currents. *Nat. Neurosci.* **14**, 736–743.
- Lee, H.J., Yang, W.S., Park, H.W., Choi, H.S., Kim, S.H., Kim, J.Y., and Choi, J.Y. (2012). Expression of anion exchangers in cultured human endolymphatic sac epithelia. *Otolaryngol. & neurotology* **33**, 1664–1671.
- Liang, D., Bhatta, S., Gerzanich, V., and Simard, J.M. (2007). Cytotoxic edema: mechanisms of pathological cell swelling. *Neurosurg. Focus* **22**, E2.
- Marmarou, A., Signoretti, S., Fatouros, P.P., Portella, G., Aygok, G.A., and Bullock, M.R. (2006). Predominance of cellular edema in traumatic brain swelling in patients with severe head injuries. *J. Neurosurg.* **104**, 720–730.
- Meier, S.D., Kovalchuk, Y., and Rose, C.R. (2006). Properties of the new fluorescent Na⁺ indicator CoroNa Green: comparison with SBFI and confocal Na⁺ imaging. *J. Neurosci. Methods* **155**, 251–259.
- Miles, R., Blaesse, P., Huberfeld, G., Wittner, L., and Kaila, K. (2012). Chloride homeostasis and GABA signaling in temporal lobe epilepsy. In *Jasper's Basic Mechanisms of the Epilepsies*, J.L. Noebels, M. Avoli, M.A. Rogawski, R.W.

- Olsen, and A.V. Delgado-Escueta, eds. (National Center for Biotechnology Information).
- Nimmerjahn, A., Kirchhoff, F., Kerr, J.N., and Helmchen, F. (2004). Sulforhodamine 101 as a specific marker of astroglia in the neocortex in vivo. *Nat. Methods* 1, 31–37.
- Pond, B.B., Berglund, K., Kuner, T., Feng, G., Augustine, G.J., and Schwartz-Bloom, R.D. (2006). The chloride transporter Na(+)-K(+)-Cl- cotransporter isoform-1 contributes to intracellular chloride increases after in vitro ischemia. *J. Neurosci.* 26, 1396–1406.
- Rahmati, N., Kunzelmann, K., Xu, J., Barone, S., Sirianant, L., De Zeeuw, C.I., and Soleimani, M. (2013). Slc26a11 is prominently expressed in the brain and functions as a chloride channel: expression in Purkinje cells and stimulation of V H⁺-ATPase. *Pflügers Arch.* 465, 1583–1597.
- Romero, M.F., Chen, A.P., Parker, M.D., and Boron, W.F. (2013). The SLC4 family of bicarbonate (HCO₃⁻) transporters. *Mol. Aspects Med.* 34, 159–182.
- Rosenblum, W.I. (2007). Cytotoxic edema: monitoring its magnitude and contribution to brain swelling. *J. Neuropathol. Exp. Neurol.* 66, 771–778.
- Rothman, S.M. (1985). The neurotoxicity of excitatory amino acids is produced by passive chloride influx. *J. Neurosci.* 5, 1483–1489.
- Rungta, R.L., Choi, H.B., Lin, P.J., Ko, R.W., Ashby, D., Nair, J., Manoharan, M., Cullis, P.R., and Macvicar, B.A. (2013). Lipid Nanoparticle Delivery of siRNA to Silence Neuronal Gene Expression in the Brain. *Mol Ther Nucleic Acids* 2, e136.
- Salazar, A.M., Jabbari, B., Vance, S.C., Grafman, J., Amin, D., and Dillon, J.D. (1985). Epilepsy after penetrating head injury. I. Clinical correlates: a report of the Vietnam Head Injury Study. *Neurology* 35, 1406–1414.
- Smith, R.L., Clayton, G.H., Wilcox, C.L., Escudero, K.W., and Staley, K.J. (1995). Differential expression of an inwardly rectifying chloride conductance in rat brain neurons: a potential mechanism for cell-specific modulation of postsynaptic inhibition. *J. Neurosci.* 15, 4057–4067.
- Somjen, G.G. (2001). Mechanisms of spreading depression and hypoxic spreading depression-like depolarization. *Physiol. Rev.* 81, 1065–1096.
- Stewart, A.K., Shmukler, B.E., Vandrope, D.H., Reimold, F., Heneghan, J.F., Nakakuki, M., Akhavein, A., Ko, S., Ishiguro, H., and Alper, S.L. (2011). SLC26 anion exchangers of guinea pig pancreatic duct: molecular cloning and functional characterization. *Am. J. Physiol. Cell Physiol.* 301, C289–C303.
- Strichartz, G., Rando, T., and Wang, G.K. (1987). An integrated view of the molecular toxinology of sodium channel gating in excitable cells. *Annu. Rev. Neurosci.* 10, 237–267.
- Thompson, S.M., Deisz, R.A., and Prince, D.A. (1988). Relative contributions of passive equilibrium and active transport to the distribution of chloride in mammalian cortical neurons. *J. Neurophysiol.* 60, 105–124.
- Verkman, A.S., and Galletta, L.J. (2009). Chloride channels as drug targets. *Nat. Rev. Drug Discov.* 8, 153–171.
- Verkman, A.S., Sellers, M.C., Chao, A.C., Leung, T., and Ketcham, R. (1989). Synthesis and characterization of improved chloride-sensitive fluorescent indicators for biological applications. *Anal. Biochem.* 178, 355–361.
- Vincourt, J.B., Jullien, D., Amalric, F., and Girard, J.P. (2003). Molecular and functional characterization of SLC26A11, a sodium-independent sulfate transporter from high endothelial venules. *FASEB J.* 17, 890–892.
- Xu, J., Barone, S., Li, H., Holiday, S., Zahedi, K., and Soleimani, M. (2011). Slc26a11, a chloride transporter, localizes with the vacuolar H(+)-ATPase of A-intercalated cells of the kidney. *Kidney Int.* 80, 926–937.
- Zeuthen, T. (2010). Water-transporting proteins. *J. Membr. Biol.* 234, 57–73.
- Zhou, N., Gordon, G.R., Feighan, D., and MacVicar, B.A. (2010). Transient swelling, acidification, and mitochondrial depolarization occurs in neurons but not astrocytes during spreading depression. *Cereb. Cortex* 20, 2614–2624.
- Zhou, N., Rungta, R.L., Malik, A., Han, H., Wu, D.C., and MacVicar, B.A. (2013). Regenerative glutamate release by presynaptic NMDA receptors contributes to spreading depression. *J. Cereb. Blood Flow Metab.* 33, 1582–1594.

Vagal Sensory Neuron Subtypes that Differentially Control Breathing

Graphical Abstract



Authors

Rui B. Chang, David E. Strochlic, ..., Benjamin D. Umans, Stephen D. Liberles

Correspondence

stephen_liberles@hms.harvard.edu

In Brief

Genetic control of vagal sensory neurons revealed two subtypes with distinct lung-to-brain connectivity. Optogenetic activation reveals that one class can acutely silence breathing, while the other can cause rapid, shallow breathing.

Highlights

- Genetic tools deconstruct the vagus nerve into several co-fasciculating labeled lines
- Two vagal sensory neuron types evoke powerful and distinct effects on breathing
- P2ry1 and Npy2r neurons differentially innervate the lung and brainstem
- P2ry1 neurons trap breathing in exhalation and do not impact heart rate



Vagal Sensory Neuron Subtypes that Differentially Control Breathing

Rui B. Chang,^{1,2} David E. Strochlic,^{1,2} Erika K. Williams,¹ Benjamin D. Umans,¹ and Stephen D. Liberles^{1,*}

¹Department of Cell Biology, Harvard Medical School, Boston, MA 02115, USA

²Co-first author

*Correspondence: stephen_liberles@hms.harvard.edu

<http://dx.doi.org/10.1016/j.cell.2015.03.022>

SUMMARY

Breathing is essential for survival and under precise neural control. The vagus nerve is a major conduit between lung and brain required for normal respiration. Here, we identify two populations of mouse vagus nerve afferents (P2ry1, Npy2r), each a few hundred neurons, that exert powerful and opposing effects on breathing. Genetically guided anatomical mapping revealed that these neurons densely innervate the lung and send long-range projections to different brainstem targets. Npy2r neurons are largely slow-conducting C fibers, while P2ry1 neurons are largely fast-conducting A fibers that contact pulmonary endocrine cells (neuroepithelial bodies). Optogenetic stimulation of P2ry1 neurons acutely silences respiration, trapping animals in exhalation, while stimulating Npy2r neurons causes rapid, shallow breathing. Activating P2ry1 neurons did not impact heart rate or gastric pressure, other autonomic functions under vagal control. Thus, the vagus nerve contains intermingled sensory neurons constituting genetically definable labeled lines with different anatomical connections and physiological roles.

INTRODUCTION

Breathing is tightly regulated by the nervous system to ensure appropriate tissue oxygenation. Several classes of central and peripheral sensory neurons acutely regulate the respiratory cycle in response to changes in blood pH and gas composition, as well as external environment (Carr and Udem, 2003; Gonzalez et al., 1994; Guyenet et al., 2010). Among these, sensory neurons of the vagus nerve are the major source of nerve fibers that innervate the lung and airways, and are important for normal breathing. The vagus nerve contains sensory neurons that provide critical information needed to control respiration rate, regulate airway tone and defense, and in some species, evoke cough (Canning et al., 2006; Carr and Udem, 2003; Coleridge and Coleridge, 2011; Tränkner et al., 2014; Widdicombe, 2001). However, the diversity of lung-innervating sensory neurons remains poorly characterized at a molecular level,

with specific neuron types that promote or restrict respiration genetically undefined.

The vagus nerve is the tenth cranial nerve, characterized by a wandering trajectory that provides extensive innervation of the neck, chest, and abdomen (Berthoud and Neuhuber, 2000). The vagus nerve controls not only respiration, but also basic physiological functions of the cardiovascular, immune, and digestive systems. Most vagal neurons (~80%) provide ascending sensory information (Foley and DuBois, 1937), receiving input from thoracic tissues like heart and lung, and abdominal tissues like stomach and intestine. Electrophysiological studies revealed both chemosensory and mechanosensory neurons of the vagus nerve (Berthoud and Neuhuber, 2000; Paintal, 1973). Within the airways, vagal sensory neurons detect irritants, cues associated with inflammation and illness, and mechanical stretch of the lung during cycles of inhalation and exhalation (Carr and Udem, 2003; Paintal, 1973; Widdicombe, 2001). The cell bodies of sensory fibers reside in pairs of ganglia at the base of the skull, including the adjacent nodose and jugular ganglia (the nodose/jugular complex). Afferent vagal axons enter the brain bilaterally through the jugular foramina and primarily target the nucleus of the solitary tract (NTS), a brainstem nucleus that transmits sensory information to deeper brain structures and descending motor nuclei (Berthoud and Neuhuber, 2000; Kubin et al., 2006).

We reasoned that the vagus nerve likely contains a diversity of molecularly distinct neuron types with different anatomical projections and functions. Previous descriptive classifications of vagal sensory neurons were based on neuron response properties like conduction velocity and adaptation rate (Carr and Udem, 2003) and did not enable genetic control for specific analysis. Furthermore, classical procedures to manipulate vagus nerve function—surgical vagotomy and implantation of electrical stimulators—impact many neuron types in both the motor and sensory arms (Groves and Brown, 2005; Schachter and Saper, 1998). These procedures implicate the vagus nerve in many physiological systems and offer therapeutic options for several otherwise intractable diseases (Groves and Brown, 2005; Schachter and Saper, 1998). However, because they lack cell specificity, they are blunt tools for analytical studies and cause unwanted side effects in patients. Gaining genetic access to the diversity of vagal sensory neurons might help disentangle the neural control of autonomic physiology. Here, we used a molecular and genetic approach to reveal the identity of two populations of breathing-control neurons in the vagus nerve.

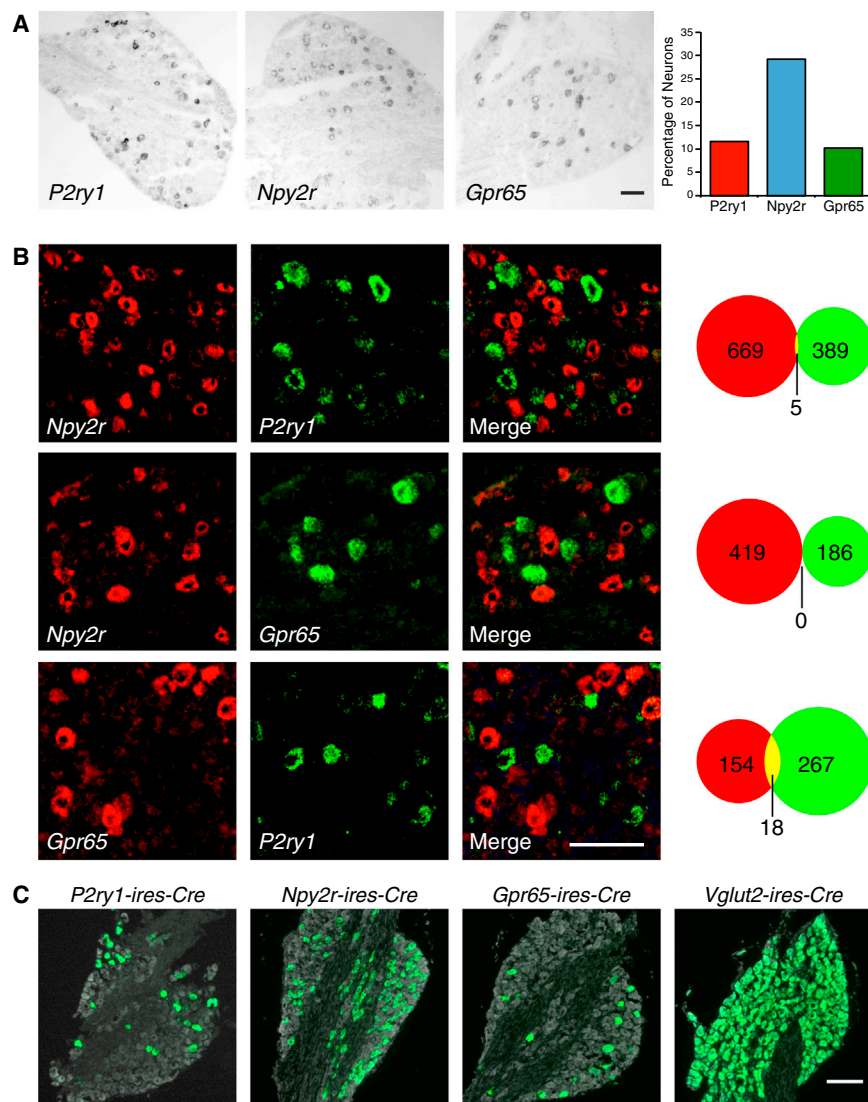


Figure 1. Genetic Control of Sensory Neuron Types in the Vagus Nerve

(A) RNA in situ hybridization experiments in the nodose/jugular complex revealed that *P2ry1*, *Npy2r*, and *Gpr65* are expressed in subsets of vagal sensory neurons.

(B) Two color in situ hybridization experiments for indicated genes revealed largely non-overlapping neuron populations. The numbers of cells expressing one receptor (red or green) or both receptors (yellow) were counted.

(C) The indicated Cre lines were crossed with *lox-L10-GFP* mice, and in offspring, fixed cryosections of the nodose/jugular complex were imaged by fluorescence microscopy. Native GFP fluorescence (green) and a fluorescent Nissl stain (gray) were visualized. Scale bars, 100 μ m. See also Figures S1 and S2.

2001); *Gpr65* is expressed in 10.2% of vagal sensory neurons (126/1,237, ~230 neurons per ganglia complex), *P2ry1* is expressed in 11.6% of vagal sensory neurons (190/1,631, ~280 neurons per ganglia complex), and *Npy2r* is expressed in 29.2% of vagal sensory neurons (445/1,524, ~670 neurons per ganglia complex). Vagal NPY2R was proposed, and debated, to function in nutrient-evoked satiety (Karra and Batterham, 2010), while roles for vagal P2RY1 and GPR65 were not previously reported.

Two color in situ hybridization analysis in the nodose/jugular complex revealed that *Npy2r*, *P2ry1*, and *Gpr65* were predominantly expressed in different vagal sensory neurons (Figure 1B). Most *Npy2r* neurons did not express *P2ry1* (99%, 669/674) or *Gpr65* (100%, 419/

419); most *P2ry1* neurons did not express *Gpr65* (94%, 267/285) or *Npy2r* (99%, 389/394); and most *Gpr65* neurons did not express *P2ry1* (90%, 154/172) or *Npy2r* (100%, 186/186). Thus, three major classes of vagal afferents are distinguishable by genetic markers and together account for ~50%–60% of nodose/jugular sensory neurons.

Genetic Control of Vagus Nerve Sensory Neurons

Cre/LoxP technology enables powerful, genetically guided approaches for connectivity mapping and remote control of neural activity (Rogan and Roth, 2011). We generated *P2ry1-ires-Cre*, *Gpr65-ires-Cre*, and *Npy2r-ires-Cre* knockin mice (Figure S1), in which Cre recombinase is co-transcribed with the receptor gene and independently translated from an internal ribosome entry site (IRES) sequence (Kim et al., 1992). Each Cre knockin line was crossed with reporter mice harboring a Cre-dependent *L10-GFP* allele (*lox-L10-GFP*; similar reporter alleles are herein referred to as *lox-reporter*) (Krashes et al., 2014), and in offspring,

RESULTS

Identifying Cell Surface Receptors of the Sensory Vagus Nerve

Molecularly distinct neuron subtypes have been classified within several sensory systems (Abaira and Ginty, 2013; Basbaum et al., 2009; Dong et al., 2001; Munger et al., 2009; Yarmolinsky et al., 2009). To identify markers for subtypes of vagal afferents, we used a genome-based strategy that previously enabled identification of families of olfactory receptors (Liberles and Buck, 2006; Liberles et al., 2009). Expression levels of ~400 G protein-coupled receptors (GPCRs) were quantified in nodose/jugular complex cDNA by qPCR. Candidate genes were cloned for cRNA riboprobe synthesis and examined for expression in neuronal subsets by in situ hybridization. These experiments revealed three GPCR genes, *P2ry1*, *Npy2r*, and *Gpr65*, to be expressed in subsets of vagus nerve afferents (Figure 1A). Each nodose/jugular complex contains ~2,300 neurons (Fox et al.,

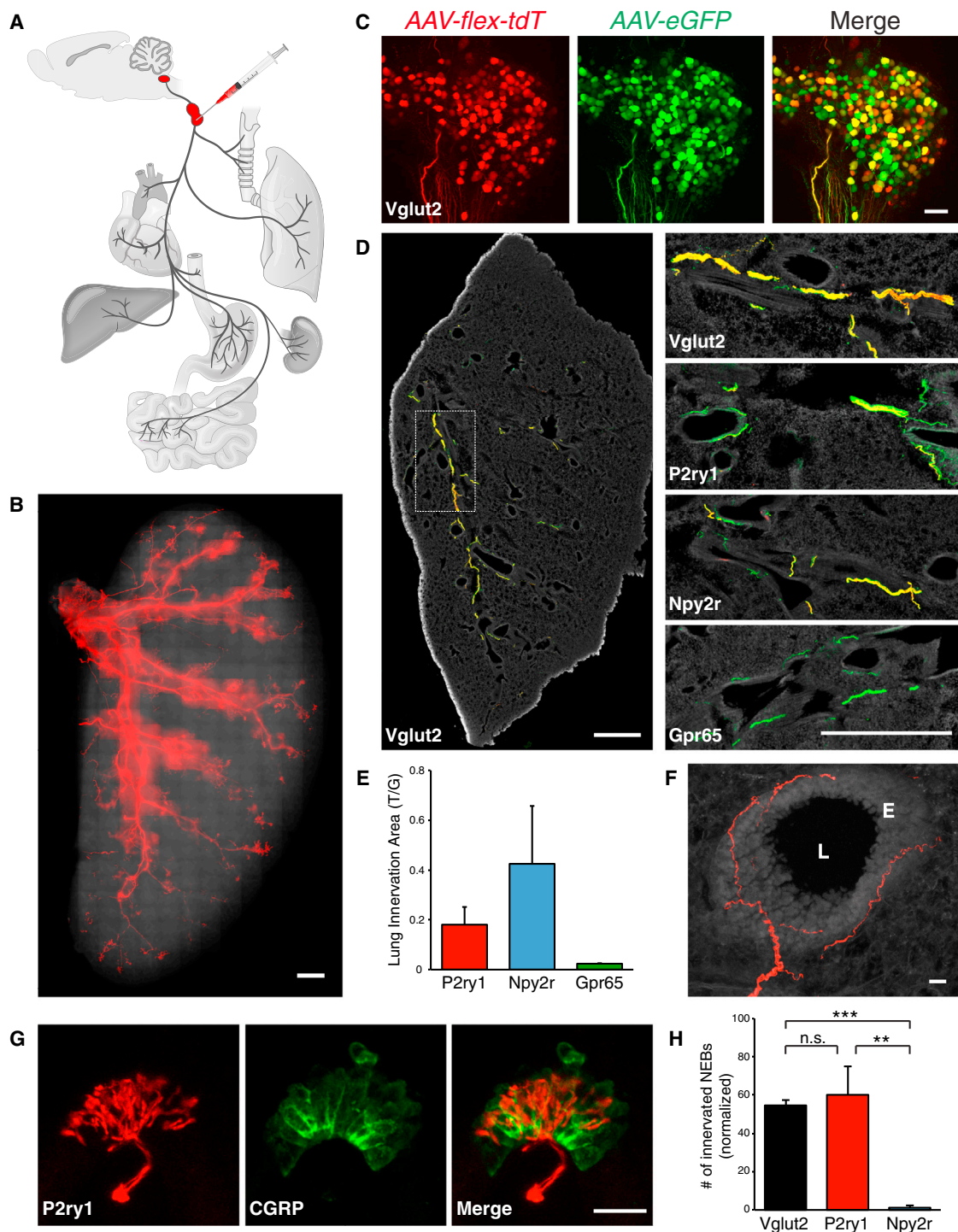


Figure 2. Visualizing Vagal Afferents in the Lung

(A) Cartoon depiction of the neural tracing strategy, which involved infection of a Cre-dependent AAV (AAV-flex-tdTomato) and/or a Cre-independent AAV (AAV-eGFP) in the nodose/jugular complex of *ires-Cre* knockin mice.

(B) Whole-mount analysis of native tdTomato fluorescence in a flattened lung lobe from a *Vglut2-ires-Cre* mouse infected with AAV-flex-tdTomato. Scale bar, 1 mm.

(C) Whole-mount analysis (maximum projection of stacked confocal images) of native tdTomato (tdT) and GFP fluorescence in the nodose/jugular complex of a *Vglut2-ires-Cre* mouse infected with AAV-flex-tdTomato and AAV-eGFP. Scale bar, 100 μ m.

(D) Different *ires-Cre* lines were infected with AAV-flex-tdTomato and AAV-eGFP, and fibers were visualized in fixed lung cryosections by immunohistochemistry for tdTomato (red) and GFP (green). Scale bars, 1 mm.

(legend continued on next page)

subsets of vagal sensory neurons displayed bright, native GFP fluorescence (Figure 1C). Cre recombinase drives reporter expression to appropriate neurons of the nodose/jugular complex, as determined by two color in situ hybridization analysis (Figure S1). In sum, 94% of P2ry1 neurons express reporter in *P2ry1-ires-Cre; lox-Channelrhodopsin2-eYFP* mice, 94% of Npy2r neurons express reporter in *Npy2r-ires-Cre; lox-Channelrhodopsin2-eYFP* mice, and 88% of Gpr65 neurons express reporter in *Gpr65-ires-Cre; lox-tdTomato* mice. In contrast, 3.0% of Npy2r neurons and 2.4% of Gpr65 neurons express reporter in *P2ry1-ires-Cre; lox-Channelrhodopsin2-eYFP* mice. As is commonly observed using Cre/LoxP techniques, we detected some reporter positive, receptor negative neurons (19%–27%), which could be due to imperfect detection of receptor expression by in situ hybridization techniques or transient expression of Cre recombinase during development (Schmidt-Suprian and Rajewsky, 2007).

In addition, we obtained *Vglut2-ires-Cre* and *Chat-ires-Cre* mice (Rossi et al., 2011; Vong et al., 2011), which provided important tools for global control of sensory neurons and motor neurons respectively. Calcium imaging experiments in acute neuron cultures from the nodose/jugular complex of *Vglut2-ires-Cre; lox-tdTomato* mice revealed that 100% (168/168) of KCl-responsive sensory neurons expressed tdTomato. Furthermore, in *Vglut2-ires-Cre; lox-L10-GFP* mice, GFP was expressed in 99.4% (632/636) of sensory neurons, but only rare motor neurons (6/845 dorsal motor nucleus of the vagus or DMV neurons and 28/320 nucleus ambiguus neurons) (Figure S2). We also obtained *Chat-ires-Cre* mice that drive reporter expression in most motor neurons (376/442 DMV neurons and 84/123 nucleus ambiguus neurons), but not in sensory neurons (0/599). In triple transgenic *Vglut2-ires-Cre; lox-tdTomato; Chat-GFP* mice, motor and sensory fibers are differentially visualized and partially segregated within the vagus nerve trunk (Figure S2). Together, this toolbox of Cre lines enables differential genetic access to the vagus nerve motor and sensory arms, as well as three molecularly distinct sensory neuron subpopulations.

Visualizing Lung-to-Brain Sensory Neurons of the Vagus Nerve

We asked whether any of these genetically defined vagal afferents innervated the lung and thus might control breathing. The peripheral projections of Cre-expressing sensory neurons were traced using fluorescent reporters introduced by adeno-associated virus (AAV) infection of the nodose/jugular complex (Figure 2A). Since each *ires-Cre* line drives reporter expression in locations other than the nodose/jugular complex, AAV infections ensured that fluorescent afferents were specifically derived from the sensory vagus nerve. Infection efficiency was assessed by injection of *Vglut2-ires-Cre; lox-L10-GFP* mice with an AAV con-

taining a Cre-dependent *tdTomato* allele (*AAV-flex-tdTomato*). At 4 weeks after infection, tdTomato fluorescence was observed in ~45% of GFP-containing neuronal cell bodies (Figure S3) and was sufficiently bright to detect by whole mount analysis of the nodose/jugular complex and nerve trunk. Cre-expressing cells were similarly infected in *P2ry1-ires-Cre*, *Npy2r-ires-Cre*, and *Gpr65-ires-Cre* mice (Figure S3). Red fluorescence was not observed in uninfected Cre mice or in wild-type mice infected with *AAV-flex-tdTomato* (Figure S3).

Infection of *Vglut2-ires-Cre* mice with *AAV-flex-tdTomato* yielded bright red fibers throughout the lungs and airways that could be readily visualized by whole mount analysis of a flattened lung lobe (Figure 2B). A dual infection strategy was used to quantify airway innervation by vagal afferent populations labeled in different Cre lines (Figures 2C and 2D). The nodose/jugular complex was simultaneously infected with *AAV-flex-tdTomato* and a second AAV containing a Cre-independent GFP allele for normalization (*AAV-eGFP*). Dual immunohistochemistry for GFP and tdTomato was performed on lung cryosections obtained 4 weeks after infection. The areas of tdTomato- and GFP-derived fluorescence were measured in a 17.5-mm² lung region containing several principal airways, and the ratio of tdTomato/GFP (T/G) labeling calculated. Dual virus infection experiments in *Vglut2-ires-Cre* mice yielded GFP- and tdTomato-containing fibers that were highly co-localized throughout the lung and a benchmark T/G fluorescence ratio of 0.79. Related experiments using other Cre lines (Figure 2E) revealed that Npy2r and P2ry1 neurons provided dense innervation of the lung (0.42 T/G and 0.18 T/G respectively, or 54% and 23% of T/G observed in *Vglut2-ires-Cre* mice), while Gpr65 neurons did not (0.02 T/G, 3%). Npy2r and P2ry1 neurons account for the majority of lung-innervating vagal fibers, but not all. Furthermore, Npy2r and P2ry1 neurons do not exclusively innervate the airways, as labeled fibers were also detected in the heart and stomach. It is possible that each neuron type performs a similar sensory function in multiple tissues (such as detecting organ stretch or inflammation), and/or that additional markers are needed to subdivide these neuron classes further.

Within the lung, sensory fibers visualized in *P2ry1-ires-Cre* and *Npy2r-ires-Cre* mice displayed different arborization patterns and terminal morphologies. In both lines, the majority of fibers coursed along the major airways beneath and parallel to the smooth muscle layer (Figure 2F). P2ry1 neurons, but not Npy2r neurons, formed stereotyped candelabra endings at neuroepithelial bodies, clusters of pulmonary secretory cells embedded within the epithelium and revealed by calcitonin gene-related peptide (CGRP) immunoreactivity (Figure 2G) (Brouns et al., 2009). P2ry1 neurons account for most or all vagal innervation of neuroepithelial bodies, based on the frequency of tdTomato-positive fibers in *Vglut2-ires-Cre* and *P2ry1-ires-Cre* mice (Figure 2H). Vagal afferents visualized in

(E) Quantitative analysis of lung innervation in 17.5-mm² lung regions expressed as an area ratio of T/G-derived immunofluorescence (mean ± SEM, see Results and Extended Experimental Procedures for additional detail on T/G calculation).

(F) High resolution image of a representative vagal afferent beneath the epithelial layer, (E), of a major airway (airway lumen, L). Scale bar, 20 μm.

(G) Representative P2ry1 candelabra terminal (tdT fluorescence) at a neuroepithelial body (CGRP immunostaining, green). Scale bar, 20 μm.

(H) The number of neuroepithelial bodies (NEBs) innervated by each neuron type after visualization with *AAV-flex-tdTomato* and normalization with *AAV-eGFP* (n = 3–5, mean ± SEM, **p < 0.01, and ***p < 0.001). See also Figure S3.

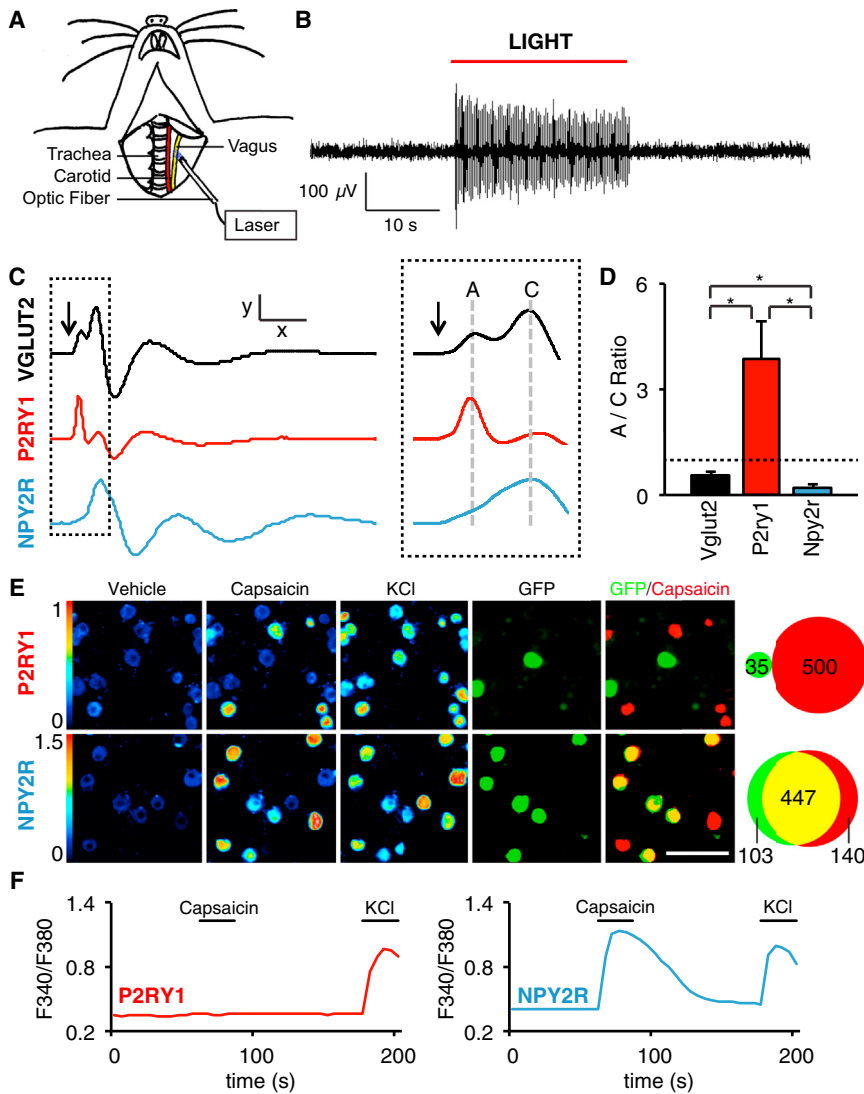


Figure 3. Characterization of Vagal P2ry1 and Npy2r Neurons

(A) Cartoon depiction of optogenetic strategy. The vagus nerve is surgically exposed in anesthetized mice and illuminated to activate ChR2-expressing sensory neurons.

(B) Whole nerve electrophysiological recordings in *Vglut2-ChR2* mice revealed light-induced action potentials.

(C) Compound action potentials following brief optogenetic stimulation (arrow) in *Vglut2-ChR2*, *P2ry1-ChR2*, and *Npy2r-ChR2* mice. A and C fibers were classified based on conduction velocity (Figure S4) $x = 5$ ms, $y = 110$ μ V (Vglut2), 62 μ V (P2ry1), 160 μ V (Npy2r), and dashed inset, $x = 1.45$ ms.

(D) The ratio of A to C fibers was calculated by integrating corresponding peak area in the compound action potential; dashed line: A/C ratio of 1 ($n = 5-8$, mean \pm SEM, and $*p < 0.05$).

(E) Calcium imaging of single neuron responses to capsaisin (2 μ M) and KCl (50 mM) in acute ganglia cultures from *P2ry1-ires-Cre; lox-L10-GFP* and *Npy2r-ires-Cre; lox-L10-GFP* mice. (Left panels, color scale = 340/380 nm Fura-2 excitation ratio and right panels, neurons expressing GFP [green, native fluorescence] and responding to capsaisin [red] are superimposed and counted). Scale bar, 100 μ m.

(F) Representative traces for single neurons imaged in (E). See also Figure S4.

Npy2r-ires-Cre mice did not innervate neuroepithelial bodies, but were instead enriched near alveoli in the lung respiratory zone (Figure S3).

Physiological and Molecular Characterization of Vagal P2ry1 and Npy2r Neurons

Vagal afferents in the lung are a heterogeneous group of fast-conducting myelinated A fibers and slow-conducting unmyelinated C fibers (Carr and Udem, 2003). We used a channelrhodopsin-assisted approach to measure the specific conduction velocities of vagal P2ry1 and Npy2r neurons. We independently crossed wild-type, *Vglut2-ires-Cre*, *P2ry1-ires-Cre*, and *Npy2r-ires-Cre* mice with reporter mice containing a Cre-dependent channelrhodopsin-2 (ChR2) allele (*lox-Channelrhodopsin2-eYFP*, offspring of each cross are subsequently referred to as *driver-ChR2* or, in controls, *lox-ChR2* mice). Optogenetic activation of vagal fibers was achieved in anesthetized animals by focal illumination of the vagus nerve trunk (Figure 3A). Whole nerve recordings revealed robust light-induced action potentials

that were not similarly observed in control animals lacking Cre recombinase (Figure 3B).

Brief optogenetic stimulation (0.8 ms) of all sensory neurons in *Vglut2-ChR2* mice generated a compound action potential resulting from summation of slow-conducting and fast-conducting neurons (Figure 3C). Propagation speed was

calculated by varying the distance between the optic fiber and recording electrodes (Figure S4), and two major peaks were resolved with conduction velocities characteristic of A fibers (10.2 ± 4.0 m/s) and C fibers (0.71 ± 0.04 m/s). Similar experiments in *P2ry1-ChR2* and *Npy2r-ChR2* mice revealed that most P2ry1 neurons were A fibers and most Npy2r neurons were C fibers (Figure 3D).

Sensory afferents in the lung are also heterogeneous with respect to capsaisin sensitivity, with most C fibers being capsaisin-responsive. Acute cultures of nodose/jugular ganglia were prepared from *P2ry1-ires-Cre; lox-L10-GFP* and *Npy2r-ires-Cre; lox-L10-GFP* mice and responses of single, genetically defined neurons were measured by calcium imaging with Fura-2. Capsaisin activated 60.7% (1,087/1,791) of all vagal sensory neurons, 0% (0/35) of P2ry1 neurons, and 81.3% (447/550) of Npy2r neurons (Figures 3E and 3F). Furthermore, two color in situ hybridization analysis revealed that most Npy2r (62%, 193/310) neurons expressed the gene encoding the capsaisin receptor TRPV1, while most P2ry1 neurons (95%, 213/224) did

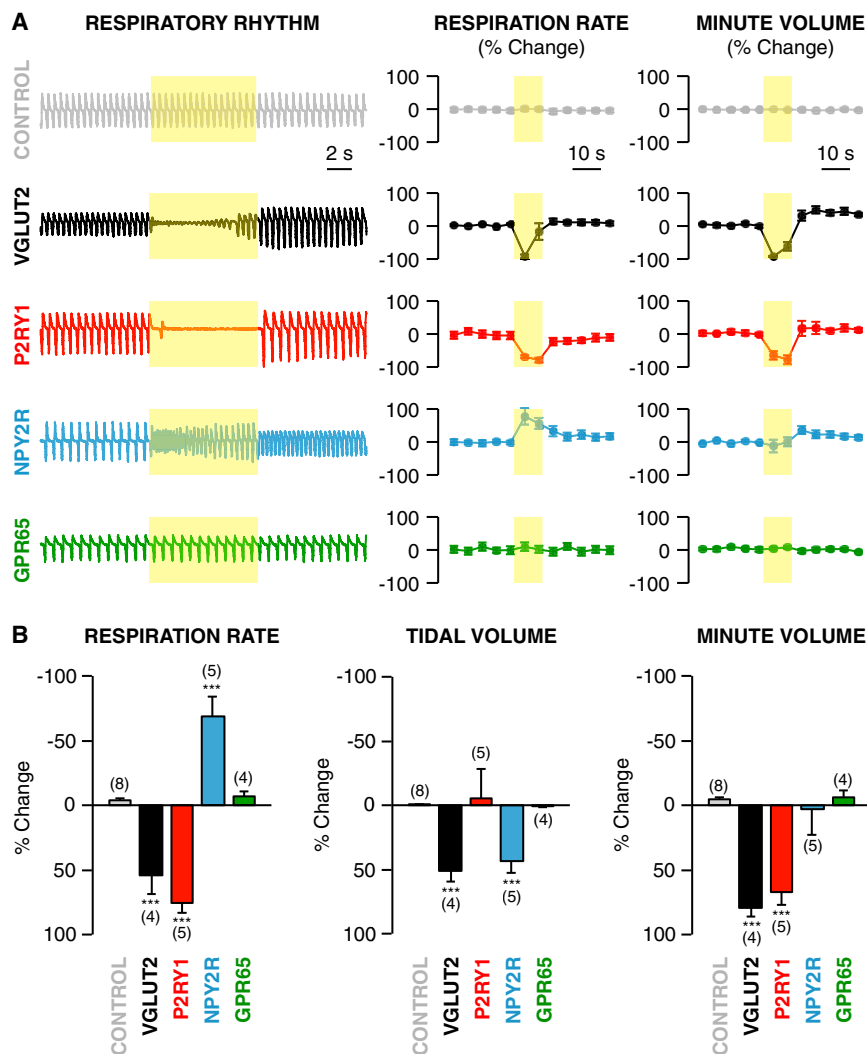


Figure 4. Remote Control of Breathing

(A) Respiratory effects following focal vagus nerve illumination (yellow shading) in *lox-ChR2*, *Vglut2-ChR2*, *P2ry1-ChR2*, *Npy2r-ChR2*, and *Gpr65-ChR2* mice. Respiratory rhythms (representative traces) were measured using a pressure transducer via trachea cannula. Changes in respiration rate and minute volume were calculated over time, with each data point reflecting a 5 s bin.

(B) Light-induced changes in respiration rate, tidal volume, and minute volume were calculated over the 10 s trial ($n = 4-8$ as indicated, mean \pm SEM, and *** $p < 0.001$). See also Figures S5 and S6.

(Figure 4). In each animal tested, illumination caused an abrupt pause in breathing that persisted for an average of 6.2 s, followed by a secondary phase characterized by shallow breathing until the light was turned off. Over the 10 s trial, light-induced activation of vagal sensory neurons caused a 54% decrease in respiration rate, a 52% decrease in tidal volume, and a 79% decrease in minute volume. In contrast, similar changes in respiration were not observed in *Chat-ChR2* or *lox-ChR2* mice (Figures 4 and S5). These findings are consistent with a pronounced role for vagal sensory neurons in breathing regulation via reflex circuitry involving descending spinal motor neurons.

Next, we asked if vagal subpopulations labeled in *P2ry1-ires-Cre*, *Gpr65-ires-Cre*, and *Npy2r-ires-Cre* mice elicited similar effects (Figure 4). Activation of P2ry1 neurons, which represent 11.6% of the vagal sensory neuron repertoire,

not (Figure S4). For comparison, the mechanoreceptor Piezo2 (Coste et al., 2010) was instead co-expressed in many P2ry1 neurons (44%, 170/388), rare Npy2r neurons (4.7%, 14/297), and not in Gpr65 neurons (0%, 0/94) (Figure S4). Taken together, P2ry1 neurons are mostly fast-conducting, capsaicin-insensitive A fibers, while Npy2r neurons are mostly slow-conducting, capsaicin-responsive C fibers.

Optogenetic Control of the Respiratory Cycle

We reasoned that lung-innervating sensory neurons labeled in *P2ry1-ires-Cre* and *Npy2r-ires-Cre* mice might control breathing. Classical techniques to study vagus nerve functions—surgical vagotomy and bulk electrical stimulation—are unable to distinguish the specific contributions of different co-fasciculating fibers. Here, we used optogenetic approaches in freely breathing, anesthetized *lox-ChR2*, *Vglut2-ChR2*, *Chat-ChR2*, *P2ry1-ChR2*, *Gpr65-ChR2*, and *Npy2r-ChR2* mice to query the roles of particular vagal neuron populations in respiratory physiology.

Optogenetic activation of all vagal sensory neurons in *Vglut2-ChR2* mice revealed powerful light-induced changes in respira-

tion (Figure 4). In each animal tested, illumination caused an immediate and striking inhibition of respiration that was of statistically similar acute duration (7.9 s) to that observed in *Vglut2-ChR2* mice. However, the secondary phase involved full breaths that were rarer than those observed during activation of all vagal afferents in *Vglut2-ChR2* mice (Figure S6). Over the 10 s trial, activating P2ry1 neurons caused a 72% decrease in respiration rate, no significant effect on tidal volume (5.5% increase), and a 67% decrease in minute volume. The different respiratory effects observed following light stimulation in *P2ry1-ChR2* and *Vglut2-ChR2* mice suggested contributions from other vagal sensory neurons in breathing control.

Activating Npy2r neurons evoked a different respiratory response characterized by rapid and shallow breathing. In *Npy2r-ChR2* mice, we observed a light-induced 68% increase in respiration rate, a 44% decrease in tidal volume, and a 3% decrease in minute volume. Light-induced respiratory effects in *P2ry1-ires-Cre* and *Npy2r-ires-Cre* mice are seemingly due to stimulation of different sensory neuron populations; contributions from motor fibers are unlikely since bulk activation of motor neurons in *Chat-ires-Cre* mice had no effect on respiration rate,

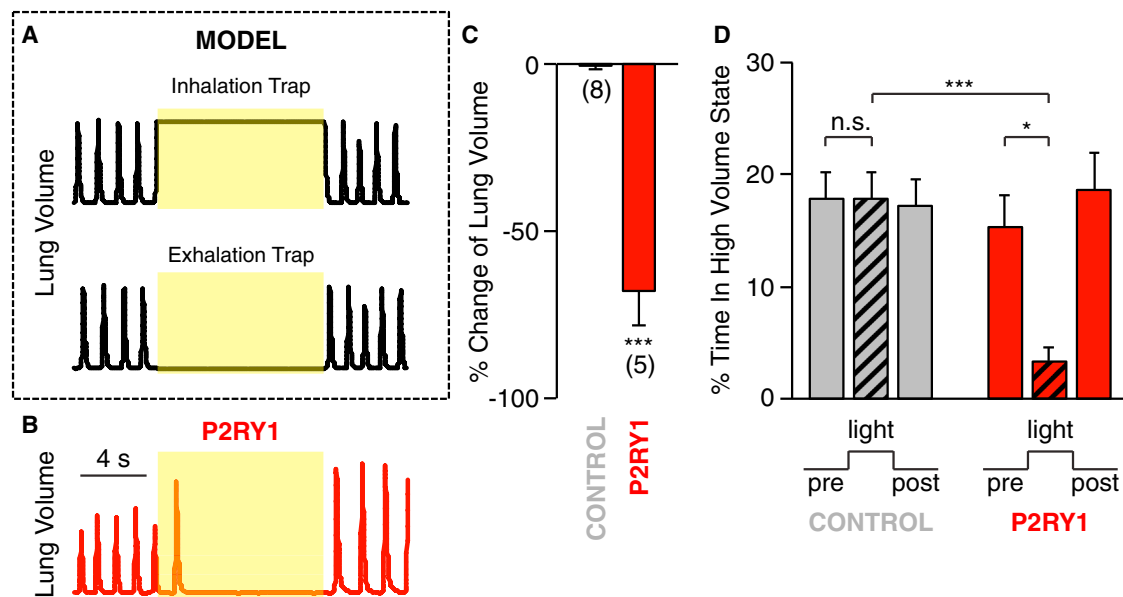


Figure 5. P2ry1 Neurons Trap Respiration in a State of Exhalation

(A) Theoretical models of lung volume changes during light-induced inhalation and exhalation trapping.

(B) Representative data showing changes in lung volume following optogenetic activation of vagal afferents in *P2ry1-ChR2* mice.

(C) Percentage change in total lung volume evoked by light in *P2ry1-ChR2* mice ($n = 5$) and control mice (*lox-ChR2*) ($n = 8$). Total lung volume was calculated by integrating lung volume across 10 s periods before and during light stimulation.

(D) The percentage of time *P2ry1-ChR2* mice and control mice were in a high lung volume state before, during, and after light stimulation. High volume state was defined as greater than mean volume during tidal breathing (mean \pm SEM, * $p < 0.05$, and *** $p < 0.001$).

tidal volume, or minute volume (Figure S5). Likewise, activating Gpr65 neurons had no significant effect on these breathing parameters, and together with their sparse lung innervation, Gpr65 neurons likely mediate other vagus nerve functions. The different respiratory effects of Npy2r, P2ry1, and Gpr65 neurons, or lack thereof, suggest that the vagus nerve contains functionally segregated labeled lines within the context of the respiratory system.

P2ry1 neurons caused an acute pause in respiration that could be due to sustained inhalation (breath holding) or exhalation. These potential mechanisms could be distinguished by measuring light-induced changes in lung volume (Figure 5); animals trapped in inhalation would have increased lung volume, while animals trapped in exhalation would have decreased lung volume. We observed that light-induced activation of P2ry1 neurons decreased lung volume (68% decrease in integrated lung volume over the 10 s trial), consistent with exhalation trapping and decreased time spent with lungs in a high volume state (77% decrease, with high volume state defined as lung volume greater than mean lung volume during tidal breathing). Similar experiments in control animals lacking a Cre driver (*lox-ChR2*) failed to show a significant decrease in lung volume (0.6%) or time in a high volume state (0.4%).

Next, we asked whether P2ry1 and Npy2r neurons control other autonomic functions of the vagus nerve. We used optogenetic approaches to activate vagal sensory neurons in *lox-ChR2*, *Vglut2-ChR2*, *P2ry1-ChR2*, and *Npy2r-ChR2* mice, and measured heart rate by electrocardiogram (ECG) recordings and gastric pressure by a cannulated pressure sensor. Activating

all sensory neurons in *Vglut2-ChR2* mice caused a profound drop in heart rate (–85%) and a decrease in gastric pressure (–11.3%), with both tonic and phasic components affected. Specifically activating P2ry1 neurons, however, had no significant effect on heart rate (–3.8%) or gastric pressure (–2.2%) (Figure 6), while activating vagal Npy2r neurons decreased both heart rate (–41.2%) and gastric pressure (–12.8%) (Figure S5). It is possible that the *Npy2r-ires-Cre* allele drives reporter expression in multiple neuron subtypes with specific functions, or in a single neuron type that impacts multiple organ systems. Results with P2ry1 neurons indicate that vagal control of breathing can be dissociated from effects on heart rate and gastric pressure by acute and selective stimulation of particular sensory neurons.

Regionalization of Sensory Neuron Inputs in the Brainstem

The different respiratory effects evoked by P2ry1 and Npy2r sensory neurons suggest engagement of distinct higher-order neural circuits. The axons of vagal sensory neurons densely innervate the NTS, area postrema, and spinal trigeminal nucleus (Berthoud and Neuhuber, 2000; Kalia and Mesulam, 1980), and topographic organization of vagal inputs in the NTS based on either physiological function or organ innervation has been proposed (Altschuler et al., 1989; Bailey et al., 2006; Katz and Karten, 1983; Kubin et al., 2006), but debated (Andresen et al., 2012). Here, we used genetically encoded neural tracers to ask how inputs from P2ry1 and Npy2r neurons are organized centrally.

We used AAV-directed neural tracing technology to visualize axons of Cre-expressing vagal sensory neurons in the brainstem

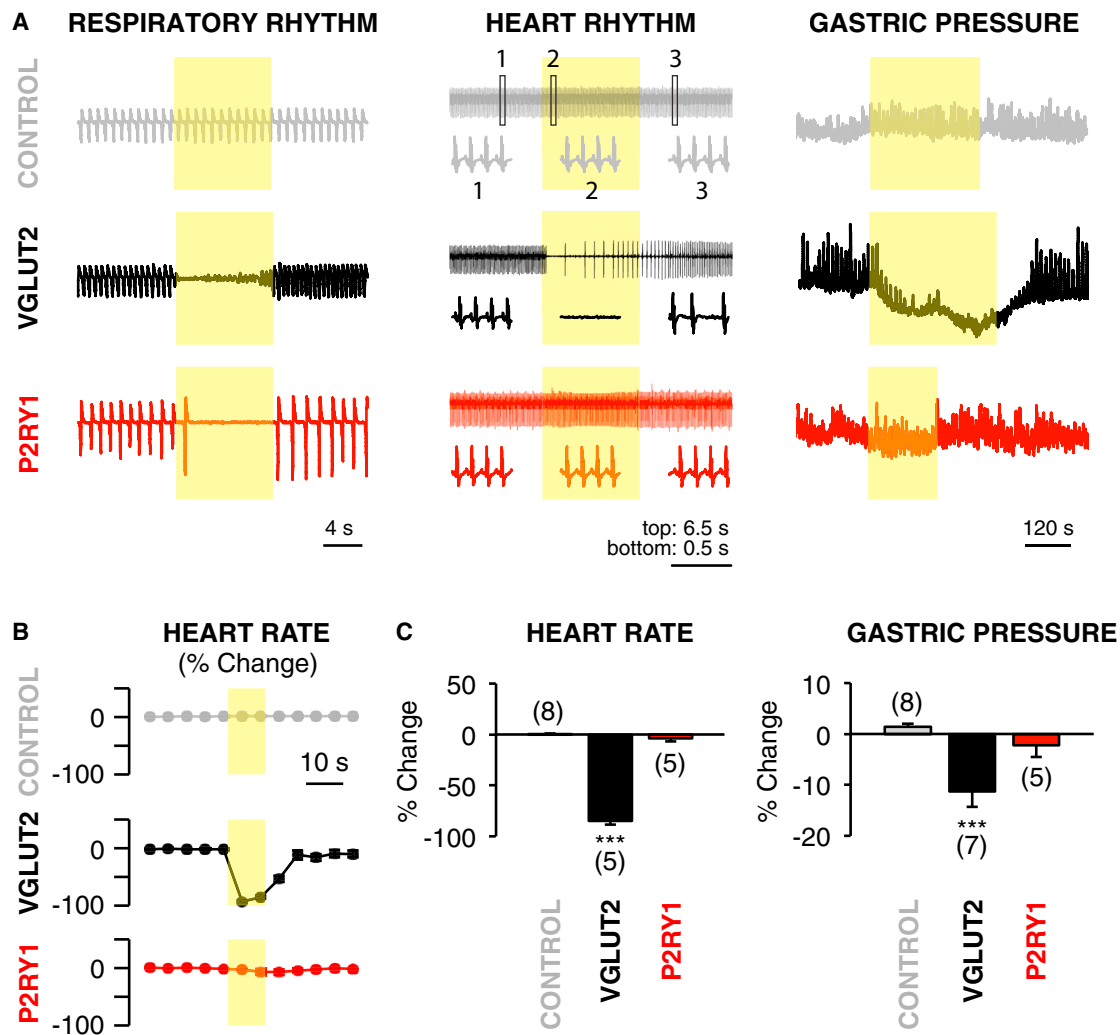


Figure 6. P2ry1 Neurons Acutely Control Breathing, but Not Gastric Pressure or Heart Rate

(A) Measurements (representative traces) of respiratory rhythm, heart rhythm, and gastric pressure following focal illumination (yellow shading) of the vagus nerve in anesthetized *P2ry1-ChR2*, *Vglut2-ChR2*, and control (*lox-ChR2*) mice. Heart rate was measured by ECG, with boxed insets showing rhythms before (1, left), during (2, middle), and after (3, right) light exposure. Intraluminal gastric pressure was measured using a pressure transducer inserted through the pyloric sphincter.

(B) Changes in heart rate (normalized from a 30 s pre-stimulus period) were calculated over time, with each data point reflecting a 5 s bin.

(C) Changes in heart rate and gastric pressure were calculated over the first 10 s or 3 min of light stimulation respectively (mean \pm SEM and *** p < 0.001). See also Figure S5.

(Figures 7 and S7). We infected the nodose/jugular complex with both AAV-*flex-tdTomato* and AAV-eGFP for visualizing Cre-expressing neurons (red) in the context of all types of vagal sensory fibers (green). Dual infection of *Vglut2-ires-Cre* mice yielded red and green fibers penetrating the brain ipsilateral to the injection site and dense arborizations in both the NTS and area postrema. Arborizations occurred bilaterally in the NTS, with enrichment ipsilateral to the infected ganglia. Next, we performed similar experiments in *P2ry1-ires-Cre* mice and observed that the projection field of P2ry1 neurons was spatially confined and did not extend over the entire vagal NTS. Vagal P2ry1 neurons arborized immediately proximal to the ascending fiber tract in the lateral region of the NTS, and these lateral branches were observed throughout

the anterior-posterior axis. Intriguingly, the dorsal respiratory group, which contains second order neurons that control respiration, is located in the lateral NTS (Saether et al., 1987; Speck and Feldman, 1982). Similar experiments in *Npy2r-ires-Cre* mice revealed that Npy2r neurons instead innervated a different NTS region, with fibers predominantly emerging in the medial posterior aspects of the vagal NTS and area postrema, regions known to receive pulmonary C fiber input (Kubin et al., 1991, 2006). We quantified innervation density along the medial-lateral axis of the NTS and in the area postrema by calculating the area of red fibers and normalizing to the area of green fibers. We observed 21-fold higher levels of P2ry1 neuron-derived fluorescence compared with Npy2r neuron-derived fluorescence in laterally arborizing

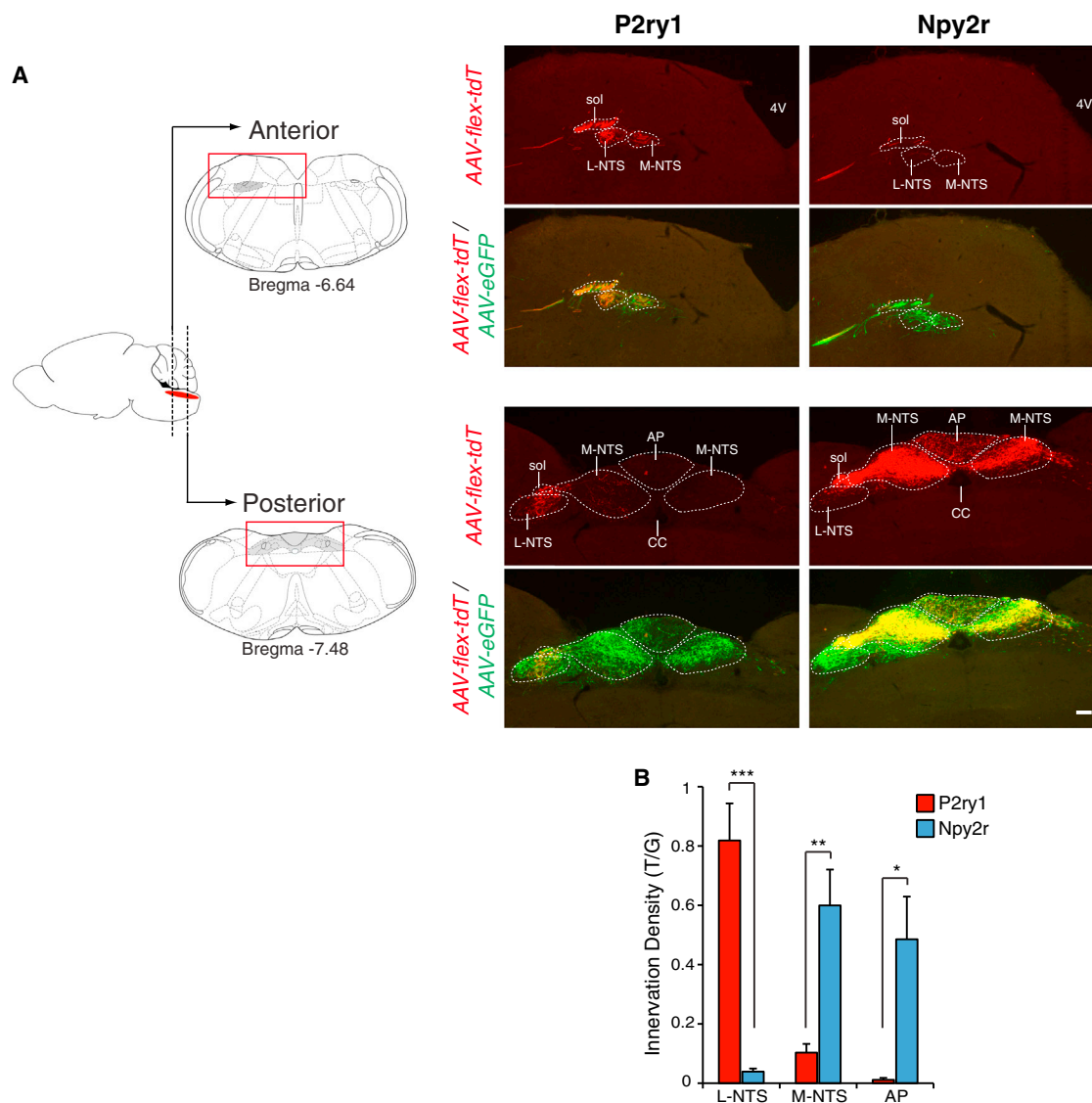


Figure 7. Non-Overlapping Central Projections of Vagal P2ry1 and Npy2r Neurons

(A) The nodose/jugular complex of *P2ry1-ires-Cre* and *Npy2r-ires-Cre* mice was infected with AAV-flex-tdTomato (AAV-flex-tdT) and AAV-eGFP. At 4 weeks after infection, fixed brainstem cryosections were analyzed by two color immunohistochemistry for tdTomato (red) and eGFP (green). Representative images of anterior and posterior brainstem containing the vagal projection field are shown (full rostral-caudal series, Figure S7). Solitary tract, sol; fourth ventricle, 4V; central canal, CC; area postrema, AP; L-NTS includes ventral, lateral, ventrolateral, interstitial, and intermediate NTS subnuclei; and M-NTS includes dorsolateral, dorsomedial, medial, and commissural NTS subnuclei. Scale bar, 100 μ m.

(B) Quantitative analysis of innervation by P2ry1 and Npy2r fibers in L-NTS, M-NTS, and AP, expressed as an area ratio of T/G fluorescence. Fluorescence was summed in every eighth section (25 μ m) from Bregma -6.4 mm to -7.8 mm. ($n = 4$, mean \pm SEM, * $p < 0.05$, ** $p < 0.01$, and *** $p < 0.001$). See also Figure S7.

NTS fibers. In contrast, we observed 6-fold and 43-fold higher levels of Npy2r neuron-derived fluorescence compared with P2ry1 neuron-derived fluorescence in medially arborizing NTS fibers and the area postrema, respectively. Thus, we observed non-overlapping and highly regionalized central projections of P2ry1 and Npy2r neurons that involved innervation of different NTS subnuclei. Together, these findings suggest that P2ry1 and Npy2r neurons engage different higher order neural circuits and are consistent with a brainstem map of vagal inputs that is at least partially linked to physiological function.

DISCUSSION

The vagus nerve provides the major sensory innervation of the lung and mediates basic physiological functions in breathing control and respiratory defense. Understanding the diversity of lung-innervating sensory neurons is an essential step toward disentangling the neural control of respiration.

Lung-innervating sensory neurons have been distinguished by their response kinetics and adaptation rates (Carr and Undem, 2003). Three types of sensory neurons were described based

on these parameters: C-fibers, rapidly adapting stretch receptors (RARs), and slowly adapting stretch receptors (SARs). RARs and SARs both respond to lung inflation, with different adaptation rates, while only RARs respond to lung deflation. RARs have also been proposed, along with C fibers, to detect some irritants and cytokines and perhaps mediate cough responses (Coleridge and Coleridge, 2011). It is possible that there are multiple subclasses of RARs, SARs, and C fibers, and a limitation of this classification scheme is that it does not enable genetic analysis for specific functional manipulation. Here, we initiated an alternative approach to sensory neuron classification in the vagus nerve based on receptor expression.

We identified one vagal sensory neuron type that expresses the purinergic receptor P2RY1, and generated *P2ry1-ires-Cre* mice to enable genetic access for anatomical mapping, physiological characterization, and remote control of neural activity. P2ry1 neurons innervate the lung with characteristic candelabra terminals that account for most or all vagal innervation of neuroepithelial bodies, poorly understood clusters of pulmonary endocrine cells. Ascending axons of P2ry1 neurons cross the jugular foramina and display highly regionalized and stereotyped inputs to the lateral NTS, which contains the dorsal respiratory group, a brainstem nucleus that regulates breathing (Saether et al., 1987; Speck and Feldman, 1982). Channelrhodopsin-assisted conduction velocity measurements showed that P2ry1 neurons are mostly fast-conducting A fibers, consistent with the observation that vagal sensory neurons innervating neuroepithelial bodies are myelinated (Brouns et al., 2009). Furthermore, P2ry1 neurons are capsaicin-insensitive and do not express TRPV1, but instead many express the mechanoreceptor Piezo2. Optogenetic activation of P2ry1 neurons caused an acute and dramatic pause in breathing, trapping animals in a state of exhalation. The Hering-Breuer inflation reflex, first reported in 1868, is a vagally mediated respiratory reflex evoked by pulmonary stretch-detecting SARs that innervate the lateral NTS and cause an inhibition of inspiration (Schelegle and Green, 2001). However, the Hering-Breuer inflation reflex also evokes a mild tachycardia that we did not observe following activation of P2ry1 neurons. Furthermore, pulmonary stretch receptors are thought to reside in the smooth muscle, whereas P2ry1 neurons innervate neuroepithelial bodies. An alternative possibility is that P2ry1 neurons represent a different type of A fiber distinct from RARs and SARs; the recent proposal of an A fiber nociceptor termed HTARs (Yu et al., 2007) supports the possibility of additional A fiber types and highlights the need for better cell classification schemes.

A second class of vagal sensory neuron is defined by expression of NPY2R, and *Npy2r-ires-Cre* mice were likewise generated. Npy2r neurons display enriched innervation of the alveoli-containing respiratory zone of the lung and do not contact neuroepithelial bodies. Npy2r neurons are largely slow-conducting C fibers, express the capsaicin receptor TRPV1, and respond to capsaicin in single neuron imaging experiments involving acute cultures of nodose/jugular ganglia. Centrally, Npy2r neurons target a medial posterior region of the NTS that receives pulmonary C fiber input (Kubin et al., 1991), and this region is distinct from the innervation zone of P2ry1 neurons. Optogenetic activation of Npy2r neurons caused rapid and shallow breathing, a respiratory effect reminiscent of certain pulmonary defense responses (Coleridge

and Coleridge, 2011). Rapid and shallow breathing is a classical response evoked by several C fiber-activating stimuli, including bradykinin, histamine, capsaicin, irritants, and pulmonary congestion (Coleridge and Coleridge, 2011; Coleridge et al., 1983). Based on these findings, lung-innervating Npy2r neurons are likely pulmonary nociceptors.

Powerful and opposing effects on respiratory physiology were evoked by activating only a few hundred P2ry1 or Npy2r neurons in the sensory vagus nerve. Based on evidence presented here, these genetic markers label fundamentally different neuron types within the context of the respiratory system. It is possible that these neuron classes can be further subdivided into even smaller neuron groups with more specific organ targets and functions. Additional studies involving other Cre driver lines and perhaps more complex approaches such as intersectional genetics may help further delineate functionally relevant neuron types (Dymecki and Kim, 2007). P2ry1 and Npy2r sensory neurons innervate the lung as well as other tissues, but their brainstem projections are nevertheless strikingly distinct. It is possible that Cre-expressing afferents from other physiological systems influence respiratory responses. In this scenario, a prime candidate would be fibers from the cardiovascular system. However, in P2ry1 mice, a role for cardiovascular fibers seems unlikely, as activating P2ry1 neurons did not impact heart rate, as would be expected for known cardiac, aortic body, and carotid body reflexes. Furthermore, carotid body chemoreceptors promote rather than inhibit inspiration and gut fibers seem unlikely to impact respiration. Instead, a parsimonious interpretation is that observed effects on breathing are mediated by lung-derived afferents.

Neuron-selective optogenetic experiments revealed that vagal control of breathing could be dissociated from vagal control of heart rate or gastric pressure. These findings indicate that the vagus nerve contains co-fasciculating labeled lines that control specific aspects of autonomic physiology. The existence of dedicated channels in the vagus nerve for particular autonomic functions provides a streamlined flow of information that is similar to coding strategies used in other sensory systems. For example, in the gustatory system, different sensory neurons are devoted to detecting chemicals that evoke sweet, salty, sour, savory, and bitter sensations (Barretto et al., 2015; Hellekant et al., 1998). Likewise the somatosensory system contains a diversity of sensory neuron types, including those that detect gentle touch or pain (Abraira and Ginty, 2013; Basbaum et al., 2009). Here, the selective effects of P2ry1 neuron activation and the differential effects of Npy2r neuron activation indicate that functional segregation of vagal inputs can likewise begin in the periphery and persist in the brainstem, ultimately resulting in specific physiological responses.

Obtaining genetic access to sensory neurons has provided a framework for studying a myriad of perceptions, from our external senses of smell, touch, taste, vision, and hearing to internal senses associated with hunger and satiety. For example, two intermingled classes of hypothalamic neurons exert opposing effects on hunger and identifying neuropeptide markers for these neurons provided a critical basis for studying the neural control of feeding (Elmquist et al., 1999). Here, we gain genetic access to two populations of breathing control-neurons, providing a

molecular and cellular framework for understanding respiration control by the autonomic nervous system.

EXPERIMENTAL PROCEDURES

Animals

All animal procedures complied with institutional animal care and use committee guidelines. *P2ry1-ires-Cre*, *Npy2r-ires-Cre*, and *Gpr65-ires-Cre* were prepared using standard bacterial artificial chromosome (BAC) recombineering approaches (Figure S1), as previously described (Krasheš et al., 2014) (see Extended Experimental Procedures). *Chat-ires-Cre* (006410), *Chat-GFP* (007902), *lox-ChR2* (012569), and *lox-tdTomato* (007914) were purchased (Jackson). *Vglut2-ires-Cre* and *lox-L10-GFP* mice (Krasheš et al., 2014; Vong et al., 2011) were generous gifts from Bradford Lowell (Beth Israel Deaconess Medical Center). All Cre driver lines used are viable and fertile and abnormal phenotypes were not detected.

Receptor Expression Studies

GPCRs were identified in the nodose/jugular complex using techniques established for identifying olfactory receptors (Liberles and Buck, 2006; Liberles et al., 2009). cDNA was prepared from acutely isolated and DNase-treated nodose/jugular RNA and used as a template in qPCR reactions involving primers that recognize ~400 endo-GPCRs (Table S1). In situ hybridization studies were performed on 10 μ m cryosections of nodose/jugular ganglia as previously described (Ferrero et al., 2013; Liberles et al., 2009), except data in Figures S1 and S4C involved digoxigenin probes alternatively visualized with peroxidase conjugated anti-digoxigenin antibody and TSA-Plus-Cy5 (Perkin Elmer). Probes are described in Extended Experimental Procedures.

AAV Infections of the Nodose/Jugular Complex

The left nodose/jugular complex of adult mice was surgically exposed under anesthesia by making an incision along the ventral surface of the neck and blunt dissection. A micropipette containing a 1:1 mixture of AAV-flex-tdTomato (Penn Vector Core, AV-9-ALL864, titer, 1.3×10^{13} genome copies/ml), and AAV-eGFP (Penn Vector Core, AV-9-PV1963, titer: 3.6×10^{13} genome copies/ml), as well as 0.05% Fast Green FCF (Sigma-Aldrich) was inserted into the nodose/jugular complex. Virus solution was injected (140 nl) using a Nanoject II injector (Drummond), and success determined by Fast Green Dye filling of the ganglia. Animals recovered from surgery and were sacrificed 4 weeks later for tissue harvest.

Optogenetic Stimulation of the Vagus Nerve and Physiological Measurements

Animals were deeply anesthetized (isoflurane, 1.5%–2%, Abbott Laboratory), freely breathing, and maintained at normal body temperature. The left nodose/jugular complex was surgically exposed and an optic fiber (200 μ m core, Thorlabs) coupled to a DPSS laser light source (473 nm, 150 mW, Ultralaser) positioned for focal illumination beneath the ganglion and above the pharyngeal and superior laryngeal branches. Light stimulation (5 ms pulses, 75–125 mW/mm² intensity, for respiratory and cardiovascular effects, 50 Hz, 10 s; for gastric pressure measurements, 5 Hz, 3–6 min) was controlled by a shutter system (Uniblitz). Respiration rate was measured using an amplifier-coupled pressure transducer (Biopac) cannulated into the trachea. A breath was scored if lung volume increased to at least 10% of mean tidal volume. Tidal volume was calculated by integrating airflow per breath, and minute volume was calculated by multiplying tidal volume by respirations per minute. Lung volume to determine state of inhalation or exhalation was determined by integrating airflow across time. Heart rhythm was measured by ECG, which was recorded with two needle electrodes placed subcutaneously on the right forepaw and the left hindpaw and amplified with a differential amplifier (A-M systems). To measure intraluminal gastric pressure, stomach contents were emptied by introducing saline through an esophageal cannula and draining through a pyloric cannula. An amplifier-coupled pressure transducer (Biopac) was connected to a fluid-filled catheter and placed into the stomach through the pyloric sphincter. Saline (400 μ L) was introduced through the esophageal cannula, and pressure measurements were acquired (1 kHz sampling, MP150

data acquisition system, Biopac). Data analyzed in 5 s bins (Figures 4C, 6B, S5A, and S5C) were normalized by comparison to values obtained during a 30 s baseline period.

Electrophysiology

For whole nerve electrophysiology, the vagus nerve was cervically transected, and the peripheral transected end was desheathed and placed onto a pair of platinum-iridium electrodes (A-M systems). Optical fibers were positioned distally to illuminate the peripheral trunk, a ground electrode was placed on nearby muscle, and the neck cavity was filled with halocarbon oil. Nerve activities were detected with an audio monitor (Grass), recorded with an alternating current (AC) preamplifier (Grass, at 1 kHz sampling rate unless specifically mentioned), and acquired on a MP150 data acquisition system (Biopac). Compound action potentials in response to a 0.8 ms light stimulus were recorded (50 kHz sampling). Fiber conduction velocity was determined by varying the distance between the optic fiber and recording electrode (travel distance); resulting time lags in peak maxima (Δt) were graphed as a function of travel distance, revealing characteristic A and C fiber types. The ratio of A to C fibers was calculated by integrating corresponding peak area in the compound action potential. Since the A and C peaks were not completely separated in most recordings, the A/C ratio reported is an underrepresentation of fold enrichment.

Data Analysis

Sample sizes are indicated in bar graphs (numbers in parenthesis), and significance was determined by comparisons to the indicated control group using a two-tailed Student's t test.

SUPPLEMENTAL INFORMATION

Supplemental Information includes Extended Experimental Procedures, seven figures, and one table and can be found with this article online at <http://dx.doi.org/10.1016/j.cell.2015.03.022>.

AUTHOR CONTRIBUTIONS

R.B.C., D.E.S., and S.D.L. designed experiments, analyzed data, and wrote the manuscript. R.B.C. generated *P2ry1-ires-Cre* and *Npy2r-ires-Cre* mice and performed optogenetic and physiological experiments; D.E.S. identified GPCR markers and analyzed neuron anatomy; E.K.W. generated *Gpr65-ires-Cre* mice; and B.D.U. analyzed neuron anatomy.

ACKNOWLEDGMENTS

We thank Bradford Lowell for providing *Vglut2-ires-Cre* and *Lox-L10-GFP* mice and for advice on AAV infection, Edward Fox and Jessica Biddinger for technical advice related to nodose/jugular complex injections, Wayne Silver for technical advice on whole nerve electrophysiology, Bernardo Sabatini and Ian Oldenburg for advice on channelrhodopsin studies, Jonathan Tilliss for help with illustrations, and the Nikon Imaging Center at Harvard Medical Center for assistance with microscopy. Genetically modified mice were generated by the Boston Nutrition Obesity Research Center/Boston Area Diabetes Endocrinology Research Center Transgenic Core. We thank Clifford Woolf, Susan Dymecki, and Clifford Saper for valuable comments on the manuscript. Support was from a NSF pre-doctoral fellowship (D.E.S.), an F30 NIH training grant (E.K.W.), and the Harvard-MIT Joint Research Grants Program in Basic Neuroscience (S.D.L.).

Received: September 30, 2014

Revised: January 9, 2015

Accepted: February 20, 2015

Published: April 16, 2015

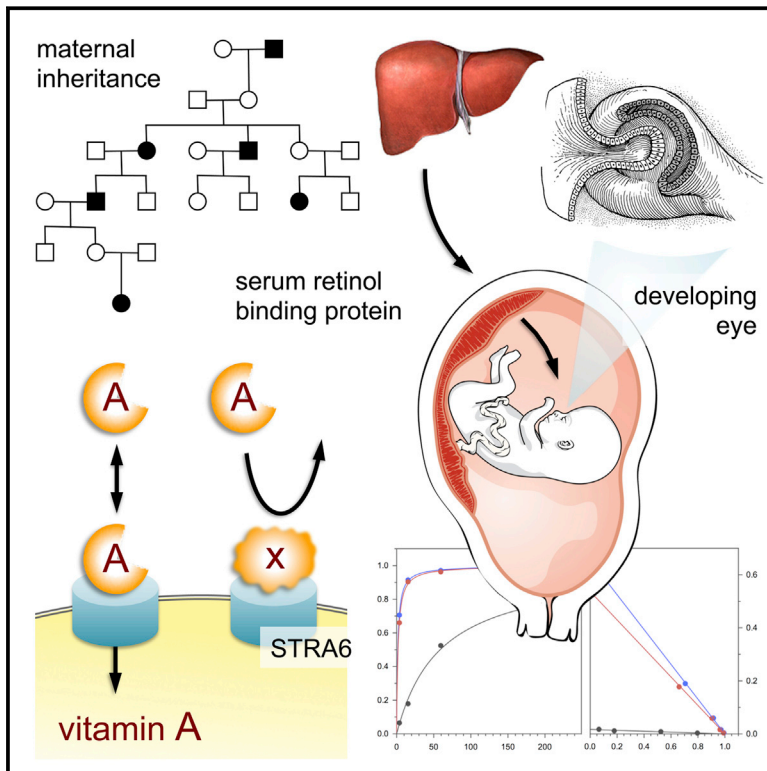
REFERENCES

Abraira, V.E., and Ginty, D.D. (2013). The sensory neurons of touch. *Neuron* 79, 618–639.

- Altschuler, S.M., Bao, X.M., Bieger, D., Hopkins, D.A., and Miselis, R.R. (1989). Viscerotopic representation of the upper alimentary tract in the rat: sensory ganglia and nuclei of the solitary and spinal trigeminal tracts. *J. Comp. Neurol.* 283, 248–268.
- Andresen, M.C., Fawley, J.A., and Hofmann, M.E. (2012). Peptide and lipid modulation of glutamatergic afferent synaptic transmission in the solitary tract nucleus. *Front. Neurosci.* 6, 191.
- Bailey, T.W., Hermes, S.M., Andresen, M.C., and Aicher, S.A. (2006). Cranial visceral afferent pathways through the nucleus of the solitary tract to caudal ventrolateral medulla or paraventricular hypothalamus: target-specific synaptic reliability and convergence patterns. *J. Neurosci.* 26, 11893–11902.
- Barretto, R.P., Gillis-Smith, S., Chandrashekar, J., Yarmolinsky, D.A., Schnitzler, M.J., Ryba, N.J., and Zuker, C.S. (2015). The neural representation of taste quality at the periphery. *Nature* 517, 373–376.
- Basbaum, A.I., Bautista, D.M., Scherrer, G., and Julius, D. (2009). Cellular and molecular mechanisms of pain. *Cell* 139, 267–284.
- Berthoud, H.R., and Neuhuber, W.L. (2000). Functional and chemical anatomy of the afferent vagal system. *Auton. Neurosci.* 85, 1–17.
- Brouns, I., Oztay, F., Pintelon, I., De Proost, I., Lembrechts, R., Timmermans, J.P., and Adriaensen, D. (2009). Neurochemical pattern of the complex innervation of neuroepithelial bodies in mouse lungs. *Histochem. Cell Biol.* 131, 55–74.
- Canning, B.J., Mori, N., and Mazzone, S.B. (2006). Vagal afferent nerves regulating the cough reflex. *Respir. Physiol. Neurobiol.* 152, 223–242.
- Carr, M.J., and Udem, B.J. (2003). Bronchopulmonary afferent nerves. *Respirology* 8, 291–301.
- Coleridge, H.M., and Coleridge, J.C. (2011). Reflexes evoked from tracheo-bronchial tree and lungs. *Compr. Physiol.* 395–429.
- Coleridge, H.M., Coleridge, J.C., and Roberts, A.M. (1983). Rapid shallow breathing evoked by selective stimulation of airway C fibres in dogs. *J. Physiol.* 340, 415–433.
- Coste, B., Mathur, J., Schmidt, M., Earley, T.J., Ranade, S., Petrus, M.J., Dubin, A.E., and Patapoutian, A. (2010). Piezo1 and Piezo2 are essential components of distinct mechanically activated cation channels. *Science* 330, 55–60.
- Dong, X., Han, S., Zylka, M.J., Simon, M.I., and Anderson, D.J. (2001). A diverse family of GPCRs expressed in specific subsets of nociceptive sensory neurons. *Cell* 106, 619–632.
- Dyrmecki, S.M., and Kim, J.C. (2007). Molecular neuroanatomy's "Three Gs": a primer. *Neuron* 54, 17–34.
- Elmqvist, J.K., Elias, C.F., and Saper, C.B. (1999). From lesions to leptin: hypothalamic control of food intake and body weight. *Neuron* 22, 221–232.
- Ferrero, D.M., Moeller, L.M., Osakada, T., Horio, N., Li, Q., Roy, D.S., Cichy, A., Spehr, M., Touhara, K., and Liberles, S.D. (2013). A juvenile mouse pheromone inhibits sexual behaviour through the vomeronasal system. *Nature* 502, 368–371.
- Foley, J.O., and DuBois, F.S. (1937). Quantitative studies of the vagus nerve in the cat. *J. Comp. Neurol.* 67, 49–67.
- Fox, E.A., Phillips, R.J., Baronowsky, E.A., Byerly, M.S., Jones, S., and Powley, T.L. (2001). Neurotrophin-4 deficient mice have a loss of vagal intraganglionic mechanoreceptors from the small intestine and a disruption of short-term satiety. *J. Neurosci.* 21, 8602–8615.
- Gonzalez, C., Almaraz, L., Obeso, A., and Rigual, R. (1994). Carotid body chemoreceptors: from natural stimuli to sensory discharges. *Physiol. Rev.* 74, 829–898.
- Groves, D.A., and Brown, V.J. (2005). Vagal nerve stimulation: a review of its applications and potential mechanisms that mediate its clinical effects. *Neurosci. Biobehav. Rev.* 29, 493–500.
- Guyenet, P.G., Stornetta, R.L., and Bayliss, D.A. (2010). Central respiratory chemoreception. *J. Comp. Neurol.* 518, 3883–3906.
- Helikant, G., Ninomiya, Y., and Danilova, V. (1998). Taste in chimpanzees. III: Labeled-line coding in sweet taste. *Physiol. Behav.* 65, 191–200.
- Kalia, M., and Mesulam, M.M. (1980). Brain stem projections of sensory and motor components of the vagus complex in the cat: II. Laryngeal, tracheobronchial, pulmonary, cardiac, and gastrointestinal branches. *J. Comp. Neurol.* 193, 467–508.
- Karra, E., and Batterham, R.L. (2010). The role of gut hormones in the regulation of body weight and energy homeostasis. *Mol. Cell. Endocrinol.* 316, 120–128.
- Katz, D.M., and Karten, H.J. (1983). Visceral representation within the nucleus of the tractus solitarius in the pigeon, *Columba livia*. *J. Comp. Neurol.* 218, 42–73.
- Kim, D.G., Kang, H.M., Jang, S.K., and Shin, H.S. (1992). Construction of a bifunctional mRNA in the mouse by using the internal ribosomal entry site of the encephalomyocarditis virus. *Mol. Cell. Biol.* 12, 3636–3643.
- Krashes, M.J., Shah, B.P., Madara, J.C., Olson, D.P., Strohlic, D.E., Garfield, A.S., Vong, L., Pei, H., Watabe-Uchida, M., Uchida, N., et al. (2014). An excitatory paraventricular nucleus to AgRP neuron circuit that drives hunger. *Nature* 507, 238–242.
- Kubin, L., Kimura, H., and Davies, R.O. (1991). The medullary projections of afferent bronchopulmonary C fibres in the cat as shown by antidromic mapping. *J. Physiol.* 435, 207–228.
- Kubin, L., Alheid, G.F., Zuperku, E.J., and McCrimmon, D.R. (2006). Central pathways of pulmonary and lower airway vagal afferents. *J. Appl. Physiol.* 101, 618–627.
- Liberles, S.D., and Buck, L.B. (2006). A second class of chemosensory receptors in the olfactory epithelium. *Nature* 442, 645–650.
- Liberles, S.D., Horowitz, L.F., Kuang, D., Contos, J.J., Wilson, K.L., Siltberg-Liberles, J., Liberles, D.A., and Buck, L.B. (2009). Formyl peptide receptors are candidate chemosensory receptors in the vomeronasal organ. *Proc. Natl. Acad. Sci. USA* 106, 9842–9847.
- Munger, S.D., Leinders-Zufall, T., and Zufall, F. (2009). Subsystem organization of the mammalian sense of smell. *Annu. Rev. Physiol.* 71, 115–140.
- Paintal, A.S. (1973). Vagal sensory receptors and their reflex effects. *Physiol. Rev.* 53, 159–227.
- Rogan, S.C., and Roth, B.L. (2011). Remote control of neuronal signaling. *Pharmacol. Rev.* 63, 291–315.
- Rossi, J., Balthasar, N., Olson, D., Scott, M., Berglund, E., Lee, C.E., Choi, M.J., Lauzon, D., Lowell, B.B., and Elmquist, J.K. (2011). Melanocortin-4 receptors expressed by cholinergic neurons regulate energy balance and glucose homeostasis. *Cell Metab.* 13, 195–204.
- Saether, K., Hilaire, G., and Monteau, R. (1987). Dorsal and ventral respiratory groups of neurons in the medulla of the rat. *Brain Res.* 419, 87–96.
- Schachter, S.C., and Saper, C.B. (1998). Vagus nerve stimulation. *Epilepsia* 39, 677–686.
- Schelegle, E.S., and Green, J.F. (2001). An overview of the anatomy and physiology of slowly adapting pulmonary stretch receptors. *Respir. Physiol.* 125, 17–31.
- Schmidt-Suppran, M., and Rajewsky, K. (2007). Vagaries of conditional gene targeting. *Nat. Immunol.* 8, 665–668.
- Speck, D.F., and Feldman, J.L. (1982). The effects of microstimulation and microlesions in the ventral and dorsal respiratory groups in medulla of cat. *J. Neurosci.* 2, 744–757.
- Tränkner, D., Hahne, N., Sugino, K., Hoon, M.A., and Zuker, C. (2014). Population of sensory neurons essential for asthmatic hyperreactivity of inflamed airways. *Proc. Natl. Acad. Sci. USA* 111, 11515–11520.
- Vong, L., Ye, C., Yang, Z., Choi, B., Chua, S., Jr., and Lowell, B.B. (2011). Leptin action on GABAergic neurons prevents obesity and reduces inhibitory tone to POMC neurons. *Neuron* 71, 142–154.
- Widdicombe, J. (2001). Airway receptors. *Respir. Physiol.* 125, 3–15.
- Yarmolinsky, D.A., Zuker, C.S., and Ryba, N.J. (2009). Common sense about taste: from mammals to insects. *Cell* 139, 234–244.
- Yu, J., Lin, S., Zhang, J., Otmishi, P., and Guardiola, J.J. (2007). Airway nociceptors activated by pro-inflammatory cytokines. *Respir. Physiol. Neurobiol.* 156, 116–119.

Biochemical Basis for Dominant Inheritance, Variable Penetrance, and Maternal Effects in *RBP4* Congenital Eye Disease

Graphical Abstract



Authors

Christopher M. Chou, Christine Nelson, ..., Adele Schneider, Tom Glaser

Correspondence

tmglaser@ucdavis.edu

In Brief

Stronger effects of maternal genomes than paternal ones on offspring have been attributed to maternal RNA and imprinting, but here mutations causing congenital eye disease are shown to result from altered biochemistry that becomes combinatorially disruptive for Vitamin A delivery when it occurs both within the fetus and from maternal tissues supplying the placenta. The findings define a new type of physiological maternal inheritance.

Highlights

- RBP4 missense mutations: eye defects with reduced penetrance and maternal inheritance
- Heterozygotes have normal circulating RBP, but reduced vitamin A levels in serum
- Dominant-negative RBPs bind retinol poorly, but occupy STRA6 with very high affinity
- Skewed inheritance due to a functional restriction of placental vitamin A transport



Biochemical Basis for Dominant Inheritance, Variable Penetrance, and Maternal Effects in *RBP4* Congenital Eye Disease

Christopher M. Chou,¹ Christine Nelson,² Susan A. Tarlé,^{1,5} Jonathan T. Pribila,^{2,6} Tanya Bardakjian,³ Sean Woods,⁴ Adele Schneider,³ and Tom Glaser^{1,4,*}

¹Departments of Human Genetics and Internal Medicine, University of Michigan Medical School, Ann Arbor, MI 48109, USA

²Department of Ophthalmology, Kellogg Eye Center, University of Michigan Medical School, Ann Arbor, MI 48109, USA

³Division of Genetics, Einstein Medical Center, Philadelphia, PA 19141, USA

⁴Department of Cell Biology and Human Anatomy, Congenital Eye Disease Study Group, University of California, Davis School of Medicine, Davis, CA 95616, USA

⁵Present address: School of Dentistry, University of Michigan, Ann Arbor, MI 48109, USA

⁶Present address: Department of Pediatric Ophthalmology, Park Nicollet Clinic, St. Louis Park, MN 55416, USA

*Correspondence: tmglaser@ucdavis.edu

<http://dx.doi.org/10.1016/j.cell.2015.03.006>

SUMMARY

Gestational vitamin A (retinol) deficiency poses a risk for ocular birth defects and blindness. We identified missense mutations in *RBP4*, encoding serum retinol binding protein, in three families with eye malformations of differing severity, including bilateral anophthalmia. The mutant phenotypes exhibit dominant inheritance, but incomplete penetrance. Maternal transmission significantly increases the probability of phenotypic expression. RBP normally delivers retinol from hepatic stores to peripheral tissues, including the placenta and fetal eye. The disease mutations greatly reduce retinol binding to RBP, yet paradoxically increase the affinity of RBP for its cell surface receptor, STRA6. By occupying STRA6 non-productively, the dominant-negative proteins disrupt vitamin A delivery from wild-type proteins within the fetus, but also, in the case of maternal transmission, at the placenta. These findings establish a previously uncharacterized mode of maternal inheritance, distinct from imprinting and oocyte-derived mRNA, and define a group of hereditary disorders plausibly modulated by dietary vitamin A.

INTRODUCTION

Congenital eye malformations—including microphthalmia, anophthalmia, and coloboma (MAC) disease—affect two in 10,000 births and are an important cause of childhood blindness (Morrison et al., 2002). The severity depends on timing and the extent that growth and morphogenesis of the developing eye is disrupted (Graw, 2010). Anophthalmia, or total absence of eyes, is the most extreme form. Microphthalmia (small eyes) and coloboma (ventronasal notch-like defects in the iris and/or retina, arising from incomplete closure of the choroid fissure, see Onwochei et al., 2000) are less severe. These can occur as

uni- or bilateral abnormalities, and may coexist in an individual or pedigree. Most cases are isolated, but one-third are associated with systemic birth defects. Few genetic causes have been identified (Williamson and FitzPatrick, 2014). Loss-of-function SOX2 mutations account for 10% of bilateral anophthalmia (Fantes et al., 2003), whereas mutations in *RX*, *CHX10*, *BCOR*, *HCCS*, and *PAX6* transcription factors explain other monogenic cases. Signaling pathways mediated by *BMP4*, *GDF6*, and *SHH* may also be genetically disrupted. Finally, disease risk is affected by environmental factors, such as maternal nutrition (Hornby et al., 2003).

Vitamin A is an essential, fat-soluble nutrient for embryonic development, tissue homeostasis, and physiology. Its most widely recognized function is to supply the visual cycle with 11-*cis*-retinal (vitamin A aldehyde) for generation of the light-sensitive visual pigment rhodopsin (Lamb and Pugh, 2004). Consequently, vitamin A deficiency (VAD) first manifests as night blindness (nyctalopia), a reversible loss of visual adaptation to dark environments (Dowling and Wald, 1958). Vitamin A is also required for epithelial, reproductive, and immune health. At the molecular level, vitamin A is a substrate for synthesis of retinoic acid (RA), a potent signaling molecule needed for vertebrate organogenesis, including eye development (Duester, 2009; Niederreither and Dollé, 2008). Nutritional studies have long associated maternal vitamin A deficiency with eye malformations, as well as urogenital, diaphragmatic, cardiovascular, and pulmonary defects (Hale, 1933; See and Clagett-Dame, 2009; Wilson et al., 1953). Recently, genetic links were established between retinoid signaling defects and MAC disease. Loss-of-function mutations in *STRA6*, encoding the membrane receptor for serum retinol binding protein (RBP), cause autosomal recessive anophthalmia or Matthew-Wood syndrome (OMIM 601186), characterized by structural eye defects, diaphragmatic hernias, cardiac malformations, and pulmonary hypoplasia (Golzio et al., 2007; Pasutto et al., 2007; Casey et al., 2011; Chassaing et al., 2009). Likewise, mutations in *ALDH1A3*, encoding retinaldehyde dehydrogenase, account for a subset of recessive MAC cases (T.G., C.M.C., A.S., T.B., and N.M. Ghiasvand, unpublished data; Fares-Taie et al., 2013; Yahyavi et al., 2013).

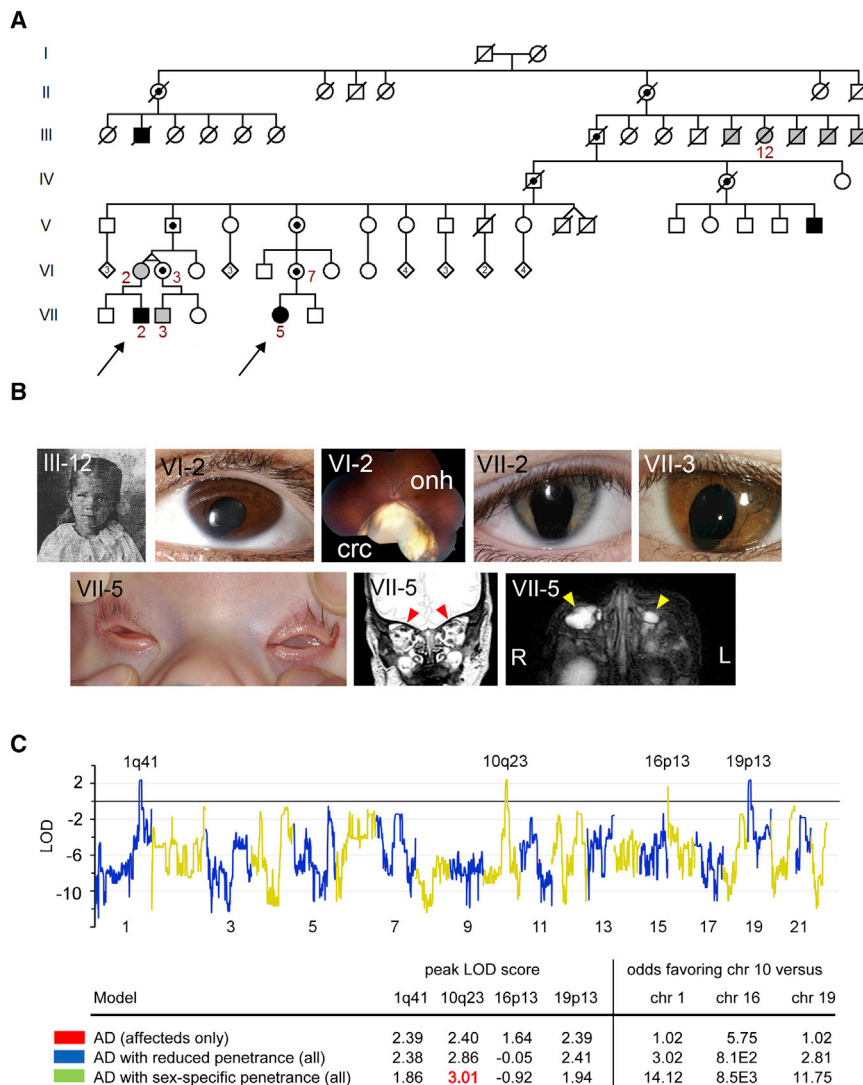


Figure 1. Familial MAC Disease

(A) Family 1 pedigree with two probands (arrows). There are 11 family members with microphthalmia or coloboma (gray symbols) or clinical anophthalmia (black symbols) and 9 obligate carriers (dotted symbols). (B) Anterior eye and fundus photographs of family members with iris or chorioretinal colobomas (VI-2, VII-2, and VII-3), microphthalmia (III-12 and VII-2), or bilateral clinical anophthalmia (VII-5) and orbital MRI views of VII-5. The T2w coronal MRI shows extraocular muscles (red arrowheads), but absent eye globes. The T2wFS axial image shows bilateral hyperintense orbital cysts (yellow arrowheads); optic nerve head, onh; chorioretinal coloboma, crc; left, L; and right, R. See also Table S1. (C) Genetic mapping of MAC disease. (Top) Multipoint LOD plot of autosomes, based on affected individuals and obligate carriers. (Bottom) Expanded linkage analysis favors chromosome 10 localization. See also Figures S1 and S2.

ranging from normal to microphthalmia to complete absence of the eyes (Figure 1B; Table S1). Several individuals have iris and/or chorioretinal colobomas. Transmission is skewed. Nearly all affected individuals (10 of 11) inherited the trait from their mother, such that maternal penetrance is significantly greater than paternal penetrance ($P_{mat} = 0.7$, $P_{pat} = 0.1$; Figure S1B). In the only instance of paternal transmission, one of two monozygous twins (VI-2) was affected.

A New MAC Locus on Chromosome 10q23

We first excluded 23 loci associated with MAC in humans or vertebrate

Here, we show mutations in the serum RBP gene underlie an autosomal dominant form of MAC that is transmitted with incomplete penetrance and a unique maternal parent-of-origin effect (Sturtevant, 1923). We further show that the unliganded mutant RBPs bind STRA6 with much greater affinity than wild-type, and consequently are likely to disrupt delivery of vitamin A to target cells, consistent with a dominant-negative effect. These results shed light on the maternal-fetal nutritional interface, genetic susceptibility to vitamin A deficiency, and the etiology of eye malformations.

RESULTS

Autosomal Dominant MAC Disease with Reduced Penetrance and a Maternal Effect

A seven-generation pedigree (Family 1) was identified through two probands with anophthalmia (Figure 1A). The penetrance of eye disease is incomplete ($P = 0.4$), based on 54 informative meioses (Figure S1A). Carriers have phenotypes

models (Table S2) by comparing haplotypes of the two probands. We then examined available family members and performed genome-wide multipoint linkage analysis (Figures S1C and S1D). We applied a simple autosomal dominant (AD) model, scoring only affecteds and obligate carriers. This analysis suggested three candidate regions: 1q41, 10q23, and 19p13, with peak LOD scores >2 (Figure 1C). To rank these regions, we included at-risk unaffected family members and applied AD models with uniform ($P_{global} = 0.4$) or sex-specific ($P_{mat} = 0.7$, $P_{pat} = 0.1$) penetrance. This indicated a chromosome 10q23 localization with peak LOD score of 3.01 (Figure 1C). The 8.2 megabases (Mb) nonrecombinant interval contains 81 genes (Figure S2). Given the importance of vitamin A in eye development (Warkany and Schraffenberger, 1946) and eye malformations associated with STRA6 and ALDH1A3 mutations (T.G., C.M.C., A.S., T.B., and N.M. Ghasvand, unpublished data); we tested genes in the critical region with roles in vitamin A transport (RBP4) and RA metabolism (CYP26A1 and C1).

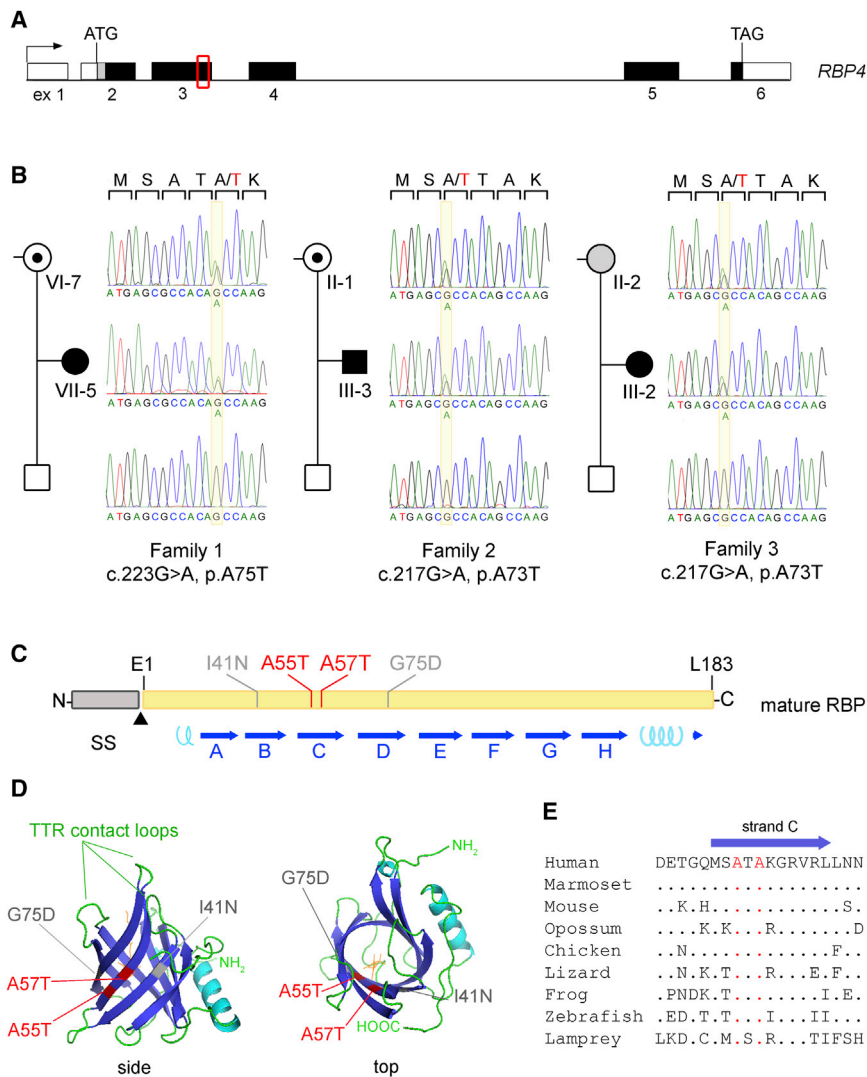


Figure 2. *RBP4* Mutations in Three Independent Families with Congenital Eye Malformations

(A) Map of 9.4 kilobases *RBP4* gene, with signal sequence (gray), mature protein (black) coding regions, and MAC mutations (red box).

(B) Sequence chromatograms showing heterozygous missense mutations, with maternal transmission in each pedigree.

(C) Primary structure of translated RBP with ala-to-thr substitutions (red) in the mature polypeptide (yellow bar) and two alleles associated with recessive nyctalopia (gray). Note that A73T and A75T in the primary translation product correspond to A55T and A57T following cleavage of the signal sequence (gray bar, SS); cyan coils, α -helix; blue arrows A–H; and β strands forming the β -barrel.

(D) Ribbon diagrams showing positions of dominant (red) and recessive (gray) substitutions. There are eight anti-parallel strands (dark blue) that form the ligand pocket. There are three loops (green) at the calyx opening contact TTR. The N terminus is relatively unconstrained. See also Figure S3D.

(E) Alignment showing conservation of alanines 55 and 57 among vertebrates.

cavity (Figures 2D and S3) (Cowan et al., 1990; Zanotti et al., 1993). Both mutations substitute threonine for alanine, in codons 73 and 75 of β strand C (Figure 2C), corresponding to residues 55 and 57 in the mature polypeptide. These alanines face the ligand pocket (Figure 2D), contact carbons C4 and C3 of the retinol β -ionone ring, respectively (Cowan et al., 1990), and are completely conserved among vertebrates (Figure 2E).

Two previously reported *RBP4* mutations, p.I59N and p.G93D, were associ-

ated with recessive night blindness in compound heterozygous sisters (Biesalski et al., 1999). They correspond to I41N and G75D in β strands B and D of the mature protein, after signal peptide cleavage. These residues also interact with side groups of the β -ionone ring, and biochemical data suggest G75D and I41N proteins bind retinol poorly (Folli et al., 2005). Molecular modeling shows that A55T and A57T proteins can accommodate retinol, under increased strain due to steric, hydrophilic, and H-bonding effects of the threonine side chain (Figure S3). To understand the allelic heterogeneity and pathogenic basis of MAC disease, we systematically compared properties of wild-type (WT) and mutant RBPs.

A55T and A57T Proteins Are Stably Secreted

RBP is constitutively expressed by hepatocytes, retained in the ER and secreted into the bloodstream as *holo* RBP (Muto et al., 1972; Soprano and Blaner, 1994), stabilized by three disulfide bonds (Selvaraj et al., 2008). We first evaluated how

Dominant *RBP4* Mutations in Three Unrelated MAC Families

RBP4 encodes serum RBP (Kanai et al., 1968) and contains six exons (Figure 2A). Exon screening revealed a missense mutation (c.223G>A, p.A75T) that cosegregated with the disease trait (Figure 2B) and was not found in >11,330 control chromosomes. We then screened a cohort of 75 unrelated MAC samples and discovered mutations in two cases, a male with bilateral anophthalmia and neurodevelopmental delay (Family 2), and a female with left microphthalmia and coloboma (Family 3). They share a single missense allele (c.217G>A, p.A73T) on distinct haplotypes, indicating recurrence of the mutation, with maternal transmission in both families (Figure S3).

p.A73T and p.A75T Alter the Retinol-Binding Surface

RBP mobilizes all-*trans* retinol from liver stores to target tissues, including the retinal pigment epithelium and placenta (D'Ambrosio et al., 2011). As the archetypal lipocalin (Newcomer and Ong, 2000), RBP folds as a β -barrel with a central hydrophobic ligand

missense mutations affect RBP synthesis and secretion in transfected HeLa cells (Melhus et al., 1992) by western analysis, using an N-terminal hemagglutinin (HA) tag (Figure 3A). The size (21 kilodalton [kDa]) and abundance of A55T and A57T proteins in 48 hr conditioned media (CM) were indistinguishable from WT (Figure 3B). In contrast, G75D and I41N proteins migrated as 42 kDa dimers, or larger multimers (I41N), linked by intermolecular disulfide bonds (Figures 3B and S4). We confirmed this result using glutaraldehyde cross-linked CM, and compared intracellular RBP levels using WT^{KDEL} as an ER retention control (Figure 3C). Intracellular G75D and, to a greater extent, I41N were elevated, suggesting a partial secretion defect, with no evidence of ER stress (Figure S4B). We conclude that A55T and A57T are secreted as stable 21 kDa monomers, whereas G75D and I41N misfold in the ER, aggregate, and exhibit increased cellular retention.

A55T and A57T Complex Normally with Transthyretin

Under normal conditions, *holo* RBP and transthyretin (TTR), a 60 kDa homotetramer (Heller and Horwitz, 1974), are cosecreted in a 1-to-1 molar ratio as a 76 kDa complex (Kanai et al., 1968). The large size of this complex prevents renal filtration, allowing RBP to remain in circulation (Soprano and Blaner, 1994; van Bennekum et al., 2001). In coimmunoprecipitation experiments (Figures 3D and 3E), human TTR interacted strongly with WT, A55T, and A57T proteins, but poorly with G75D or I41N. Similar results were obtained for bovine TTR, present in the media supplement. To quantitatively assess the RBP-TTR interaction, we performed reciprocal surface plasmon resonance (SPR) assays with purified TTR and recombinant RBP^{HA} or his-RBP (Figure 3F). WT *holo* RBP bound TTR with 2- to 3-fold greater affinity than *apo* RBP, giving mean steady state K_d values of 0.9 and 2.2 μ M respectively, similar to previous reports (Folli et al., 2010; Malpeli et al., 1996). The affinity of A55T and A57T mutant RBPs was similar or slightly lower than WT in buffered saline (HBS). However, inclusion of nonionic surfactant (0.005% Tween) significantly reduced *holo* A55T affinity for TTR, presumably by removing retinol ($p < 0.001$, unpaired t test, and $df = 10$, see below).

The in vitro behavior of G75D and I41N proteins is consistent with the absence of immunodetectable serum RBP in p.G93D/p.I59N compound heterozygotes and reduction of RBP in the p.I59N/+ parent, in the setting of normal TTR levels (Biesalski et al., 1999). Conversely, RBP and TTR levels in p.A75T/+ (Family 1, VI-2, VI-3, and VI-7) and p.A73T/+ (Family 3, II-2) carriers were within normal range (Table S3).

WT and A57T Proteins Coexist in p.A75T/+ Carrier Plasma

To assess the ratio of allotypes in vivo, total RBP was purified from obligate carrier VI-2 plasma (Figure S5), digested with trypsin, and analyzed by mass spectrometry (Figure 4). The predicted WT and A57T peptides encompassing amino acid 57 differ by 30 Dalton. Consequently, we identified MALDI-TOF peaks in the 3,100 to 3,220 mass-to-charge ratio (m/z) range corresponding to WT and A57T tryptic peptides, with a 2-to-1 intensity ratio (Figure 4C). These were verified by tandem mass spectrometry (MS²) analysis (data not shown) and parallel MS of RBP^{HA} controls. Since the peptides ionize with equal effi-

ciency (Figure 4D), we conclude that A57T constitutes one-third of circulating RBP in p.A75T/+ heterozygotes.

Because both allotypes were present in carrier plasma, genomic imprinting is unlikely to explain the skewed transmission of the MAC disease (Figure S1B). This conclusion is supported by RT-PCR analysis of F1 mice, which showed comparable levels of allelic *Rbp4* mRNA transcripts in adult and fetal tissues (Figure S4C).

In principle, the unequal ratio of allotypes could be explained by a difference in renal filtration. Under normal circumstances, RBP dissociates from TTR when retinol is delivered to tissues (Malpeli et al., 1996). Most of the resulting *apo* RBP is filtered and metabolized by the kidney, but trace amounts are detected in urine, at 1% of serum levels (Raila et al., 2005) and are assumed to represent the RBP content of the glomerular ultrafiltrate proportionally. To test this hypothesis, we evaluated RBP allotypes in p.A75T/+ carrier urine by MS, but found no evidence for increased urinary elimination of A57T relative to WT (Figure S6).

A55T and A57T Proteins Bind Vitamin A Poorly

We tested retinol-binding properties of mutant RBPs using two assays, double radioisotope labeling and fluorescence enhancement. HeLa cells expressing WT or mutant RBP^{HA} were exposed to ³⁵S-met/cys and ³H-retinol, and the ³H/³⁵S ratio was determined for RBP^{HA} immunopurified from CM (Figures 5A and 5B). We observed a dramatic reduction in retinol binding, as predicted by molecular modeling (Figure S3E). A55T bound negligible ³H-retinol, whereas A57T bound 16% of WT levels. G75D and I41N mutants also bound very little vitamin A, as expected given their misfolded structures. RBP activity is evidently more sensitive to a threonine substitution at position 55 than 57, consistent with X-ray data placing retinol closer to Ala55 (3.6Å) than Ala57 (4Å) (Cowan et al., 1990).

Retinol fluorescence intensity increases 15-fold when it occupies the RBP ligand pocket (Cogan et al., 1976). Accordingly, we added 1 to 5,000 nanomolar (nM) retinol to *apo* RBP^{HA}, purified under native conditions, and measured fluorescence (excitation [ex] 330 nanometer [nm] and emission [em] 460 nm) in PBS (Figure 5C, filled symbols). Surprisingly, A55T and A57T both bound retinol well in this assay, with affinities similar to WT ($K_d \sim 80$ nM). These results are consistent with SPR analysis of *holo* and *apo* forms interacting with TTR in HBS (Figure 3F), but differ sharply from the radioisotope data showing the mutants bind little or no vitamin A (Figure 5B).

WT *holo* RBP is relatively resistant to temperature, pH extremes, and nonpolar solvents (Cogan et al., 1976; Raz et al., 1970), but sensitive to low ionic strength (Peterson, 1971). Our disparate findings may be reconciled if A55T and A57T substitutions destabilize RBP contacts with retinol, particularly under adverse environmental conditions, increasing the probability that ligand is released to the solvent. Whereas the initial fluorescence assay was performed in PBS (Figure 5C, closed symbols), our ³H-retinol binding assay involved sequential washes in PBS containing 1% Triton X-100 and 0.5% deoxycholate (Figure 5A). We therefore systematically tested retinol binding in nonpolar and amphipathic environments (Figure 5D), including a dispersion of phosphatidylcholine (PC) vesicles (Figure 5C, open symbols), to more closely approach in vivo conditions. Within the ER, bloodstream, and

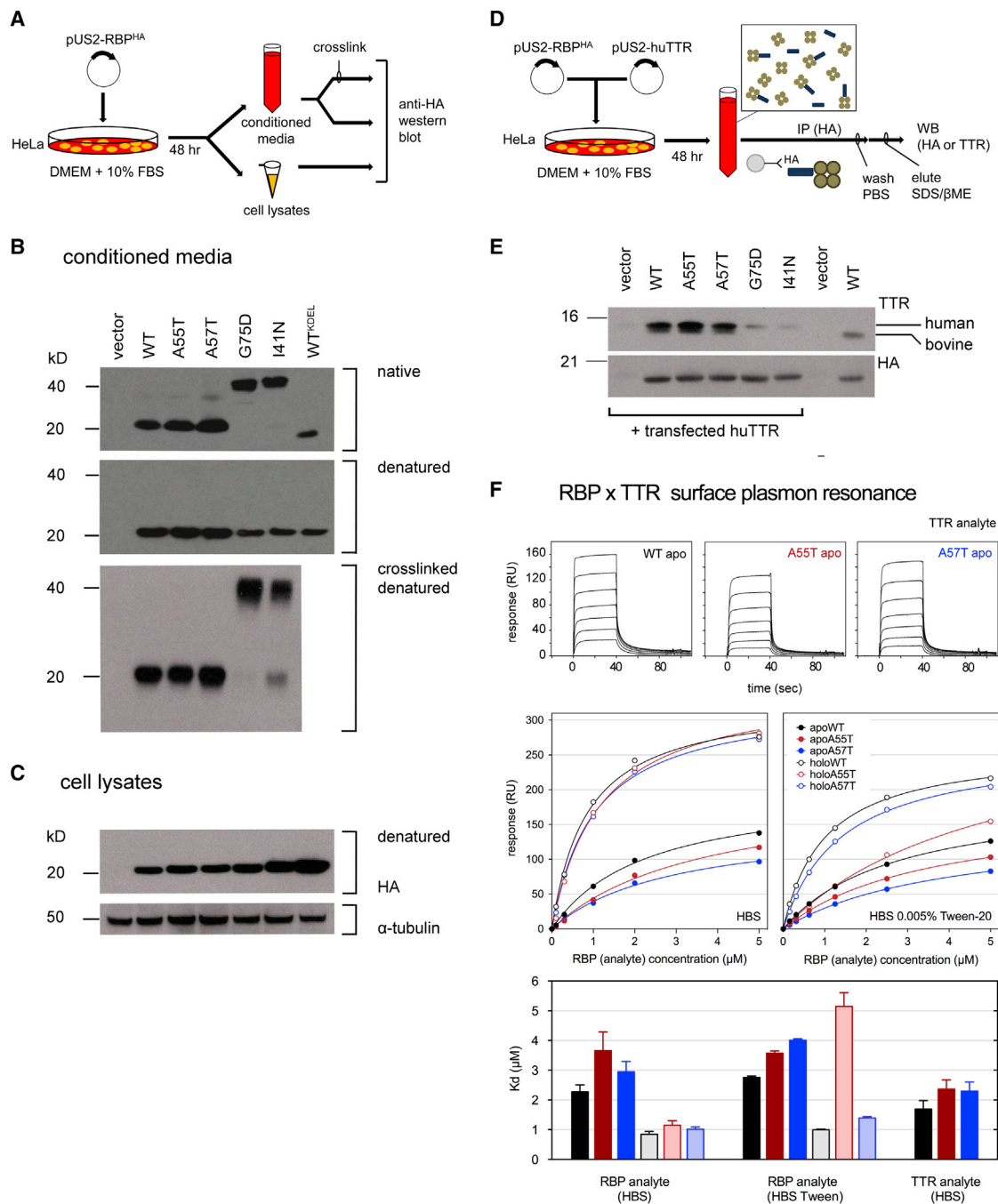


Figure 3. A55T and A57T Proteins Are Secreted as Stable RBP Monomers and Interact with TTR

(A) Test of RBP^{HA} synthesis, secretion, and integrity.

(B) HA western analysis of CM, electrophoresed under native or denaturing conditions, before or after crosslinking.

(C) Western blot of cell lysates, with α -tubulin loading control.

(D) RBP-TTR binding assay in tissue culture. Brown circles, TTR homotetramers and blue bars, RBP monomers.

(E) Western blot of HA immunoprecipitates probed in sequence with TTR and HA antibodies.

(F) SPR analysis of RBP-TTR binding in vitro. (Top) Sensorgrams show a TTR concentration series interacting with apo his-RBPs on a biotin capture chip. (Middle) Steady state isotherms for apo and holo RBP^{HA} binding to TTR. (Bottom) Histogram of K_d values. Error bars give the SEM for nonlinear regression. See also Figure S4.

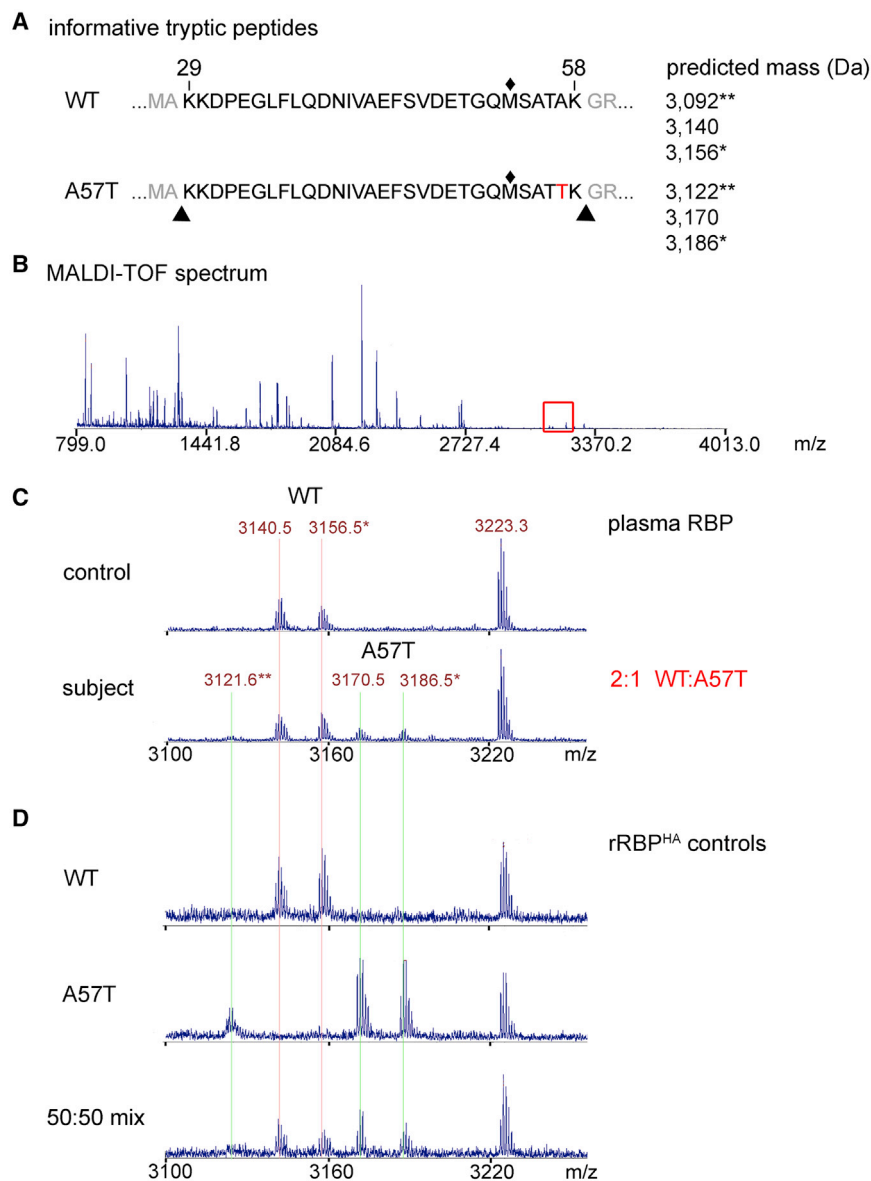


Figure 4. MS of RBP Proteotypes in p.A75T/+ Carrier Plasma

(A) Tryptic peptides encompassing residue 57. Modified peptides (asterisks) arise from alkylation of methionine 53 (◆).

(B) MALDI-TOF spectrum of RBP from control human plasma, indicating the critical *m/z* region (red box). The y axis (ions detected) reflects relative intensity.

(C) Expanded view of control (top) and carrier (bottom) spectra from 3,100 to 3,250 *m/z*. Single-ionization peaks corresponding to WT (red lines) and A57T (green lines) proteins are marked.

(D) MALDI-TOF spectra for recombinant RBP^{HA}. The invariant 3,223.3 *m/z* peak (human keratin, a common contaminant) serves as an internal standard. See also Figures S5 and S6.

vitamin A (Kawaguchi et al., 2007). At target tissues, *holo* RBP binds STRA6 extracellular loop 6 with high affinity (Kawaguchi et al., 2008). Following transfer of vitamin A into cells, *apo* RBP dissociates from the receptor, allowing a new *holo* RBP molecule to dock (Kawaguchi et al., 2007).

To examine binding of A55T and A57T proteins to STRA6, we performed two sets of experiments. We first applied ³⁵S-labeled *apo* WT, *holo* WT, A55T, or A57T RBP in parallel to human embryonic kidney (HEK) 293T cells transfected with STRA6^{myc} or control expression vectors and measured ³⁵S-RBP bound after one hr (Figures 6A–6C). In this assay, *apo* RBP had 3-fold lower steady state binding than *holo* RBP. More dramatically, STRA6+ cells bound 4 to 7 times more mutant *apo* RBP than WT *holo* RBP (*p* < 0.002, unpaired *t* tests, and *df* = 4). These findings, and the mass spectroscopy data (Figure 4), suggest that competition

tissue interstitial space, RBP is continuously exposed to phospholipid membranes and lipoprotein particles (van Meer et al., 2008). Indeed, retinol-binding activity of the mutant proteins was hypersensitive to ethanol, detergents, and phospholipid vesicles, following an A55T > A57T > WT allelic series. Almost no retinol was bound by A55T in 0.1% PC (*K_d* > 30 μM).

Our *in vitro* data predict that RBP4 heterozygotes may have reduced circulating retinol. Indeed, three p.A75T/+ obligate carriers had fasting serum vitamin A levels below the lower normal limit (Table S3), ranging from 50%–60% of the reference mean, and plasma retinol fluorescence was reduced (Figure S5B).

Increased Binding of A55T and A57T Proteins to the STRA6 Receptor

STRA6, or *stimulated by RA 6* (Bouillet et al., 1997), is the transmembrane receptor for RBP that mediates cellular uptake of

may occur between mutant and WT RBP molecules at STRA6 receptors *in vivo*. To explore this possibility, we mixed 8–250-fold excess unlabeled *holo* WT with ³⁵S-labeled RBP^{HA} in parallel assays. In each case, the unlabeled WT competitor displaced much less mutant ³⁵S-RBP than expected if the binding affinities were equivalent.

To characterize the STRA6-RBP interaction more precisely, we determined the binding affinity (*K_d*) and rate constant for the approach to equilibrium of mutant and WT RBPs, using a sensitive ELISA method (Figure S7) to measure RBP^{HA} bound to cells and released into the media. These assays show that the mutant proteins have a 30–40-fold greater affinity for STRA6 than WT (Figure 6D), with *K_d* values of 1.9 nM (A55T) and 1.5 nM (A57T) compared to 59 nM (WT, *p* < 0.001, unpaired *t* tests, and *df* = 6). In principle, two kinetic mechanisms can explain this striking result, which is central to disease

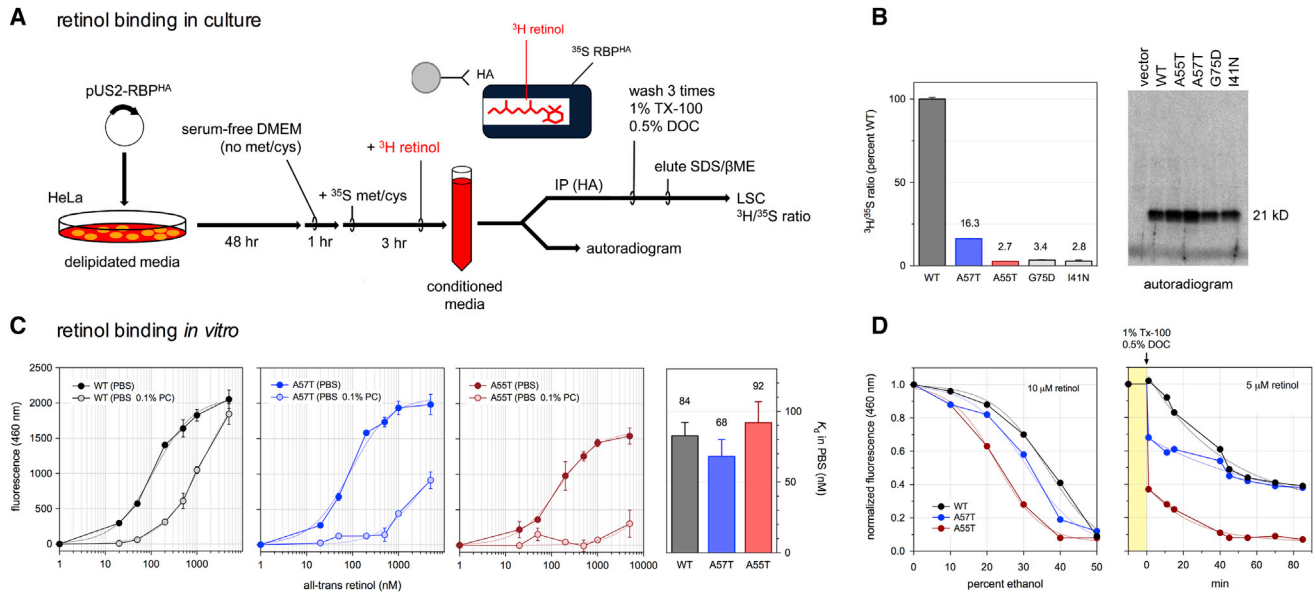


Figure 5. A55T and A57T Proteins Bind Retinol Poorly in a Mixed Aqueous-Lipid Environment

(A) ³H-retinol binding assay.

(B) (Left) ³H-retinol binding data normalized to WT. (Right) Autoradiogram showing secreted ³⁵S-RBP^{HA} in CM.

(C) (Left) *In vitro* retinol binding profiles for WT and mutant RBP^{HA}, measured by fluorescence in PBS \pm 0.1% α -L-PC, with 380 nM protein. (Right) Histogram showing similar K_d values in PBS.

(D) (Left) Normalized retinol binding curves in PBS with 0 to 50% ethanol. (Right) Increased sensitivity of mutant RBPs in an amphipathic environment, measured by loss of retinol fluorescence after exposure to detergent micelles (1% Tx-100, 0.5% DOC) in PBS. Error bars show the SD (fluorescence plots) or SEM (histograms) for three parallel assays.

pathogenesis—either the mutant RBP-STRA6 complex dissociates more slowly or the mutant RBPs bind the receptor more rapidly. To distinguish these possibilities, we measured the release of RBP from STRA6+ and control cells at 25°C and 37°C (Figure 6E) and calculated forward (k_{on}) and reverse (k_{off}) rate constants. As these data show, the major consequence of the mutations is to increase k_{on} by 25–50 fold ($p < 0.001$, unpaired t tests, $df = 42$), with no significant change in k_{off} (Figure 6F; Table S4). The pathogenic RBPs thus bind STRA6 with much higher affinity than WT, yet carry little or no vitamin A.

DISCUSSION

Here, we identify *RBP4* mutations as the cause for autosomal dominant MAC with incomplete penetrance and skewed maternal transmission. These findings demonstrate a new mode of inheritance in mammals, whereby phenotypic expression is governed by maternal genotype. Our conclusions are supported by linkage analysis, the discovery of independent alleles, evolutionary conservation, the established role of vitamin A in eye morphogenesis, and convergent biochemical, functional, modeling and clinical data which prove A55T and A57T proteins have impaired retinol binding, but resist renal filtration and interact strongly with STRA6. Together, these data provide a simple, but elegant mechanism for disease pathogenesis.

A Unified Disease Model

A55T and A57T RBPs act as dominant-negative proteins, most likely by blocking vitamin A delivery at the STRA6 receptor (Fig-

ure 7A). Mutant and WT proteins coexist in plasma (Figure 4) and are therefore both secreted. Following translation, A55T and A57T proteins may transiently bind vitamin A in the hepatocyte ER, but if so, are likely to lose a significant fraction of their retinol content in the amphipathic environments of the ER-Golgi compartment and bloodstream (Figure 5). They are otherwise stable and partner with TTR (Figure 3). At the target cell, mutant RBPs bind STRA6 receptors more avidly than WT (Figure 6), with faster association kinetics, increased affinity, and thus longer net occupancy, creating a molecular restriction point. Consequently, delivery of vitamin A from *holo* RBP should be disrupted.

When the *RBP4* mutation is transmitted by the mother, this *bottleneck effect* is iterated twice, first, at the placenta, involving maternal-derived RBP, and later at the developing eye primordia, involving fetal-derived RBP (Figure 7B). In this setting, retinol delivery to fetal tissues may be dramatically reduced—and penetrance of eye phenotypes increased—compared to paternal transmission of the same mutation, creating a maternal inheritance pattern that resembles genomic imprinting, but does not involve chromatin or DNA modification. This model is supported by data showing that STRA6 is localized in the placenta and fetal eye (Bouillet et al., 1997; Kawaguchi et al., 2007) and that maternal RBP does not cross the placental barrier in mice (Quadro et al., 2004). Furthermore, RBP is expressed in extraembryonic tissues that directly participate in retinol transfer across the maternal-fetal interface, including the visceral yolk sac (Johansson et al., 1997; Sapin et al., 1997; Soprano et al., 1986; Ward et al., 1997). Recently, STRA6 has been shown to mediate

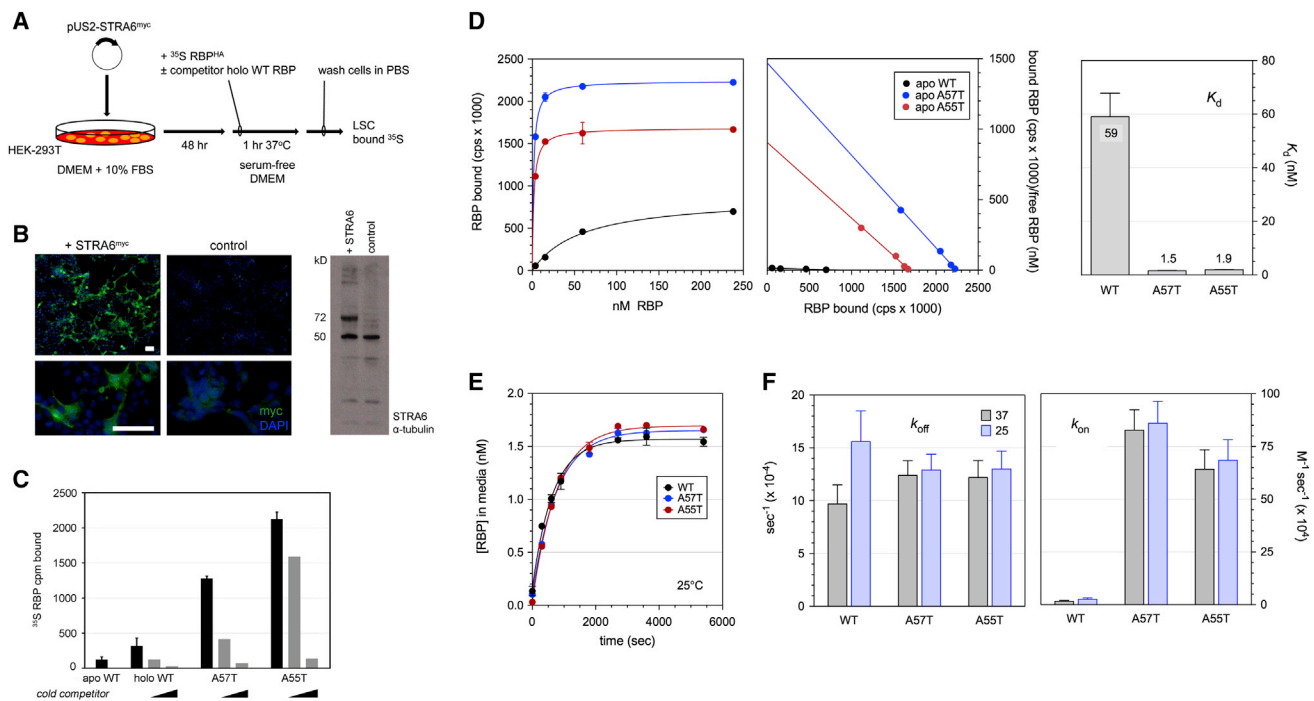


Figure 6. A55T and A57T Proteins Bind the STRA6 Membrane Receptor with Greater Affinity Than WT

(A) STRA6 radioligand binding assay. (B) STRA6^{myc} expression in HEK293T cultures. (Left) Fluorescence micrographs of transfected cells immunostained for myc (green) with nuclear counterstain (blue). Scale bars, 40 μm. (Right) Western blot simultaneously probed with antibodies to human STRA6 (72 kDa) and α-tubulin (50 kDa). (C) Histogram showing binding of 5 pM ³⁵S-labeled WT, A55T, or A57T RBP^{HA} proteins in the absence (black) or presence (gray) of 8- or 250-fold excess unlabeled (cold) competitor. (D) Quantitative equilibrium analysis of RBP-STR A6 interaction by immunoassay. (Left) Binding isotherms and reciprocal plots of apo RBP^{HA} ELISA data. Relative RBP levels are given in counts per second (cps) emitted light, after subtracting nonspecific binding to control cells. (Right) Histogram of K_d values. The mutant RBPs bind to the receptor with 30–40 fold greater affinity than WT. (E) Kinetic analysis of the RBP-STR A6 interaction. Release of bound apo RBP^{HA} to the media over time, from saturated STRA6+ cells at 25°C. (F) Histogram comparing STRA6 association (k_{on}) and dissociation (k_{off}) rate constants calculated from binding data. The A55T and A57T mutations greatly increase the on rate for RBP binding to STRA6. See also Figure S7; Table S4. Error bars show the SEM for three parallel assays or nonlinear regression of triplicate measurements.

retinol efflux from cells as well as influx, loading extracellular apo RBP with cytoplasmic vitamin A (Kawaguchi et al., 2012). This bidirectional mode may be critical during early development, as fetal RBP originating from the visceral yolk sac or liver can, in principle, ferry retinol stepwise between different STRA6+ cells. Because the mutant RBPs are predicted to disrupt STRA6 docking on both sides, this relay mechanism may be highly sensitive to dominant-negative effects. The labyrinthine zone of the murine chorioallantoic placenta, for example, is a major site of maternal-fetal exchange that strongly expresses STRA6, but not RBP (Bouillet et al., 1997; Johansson et al., 1997). Likewise in humans, RBP is expressed by the maternal decidua, but not by villous trophoblasts (Johansson et al., 1999).

When transmitted by the father, the RBP4 mutation can only disrupt vitamin A transfer beyond the placenta. Consequently, the severity of fetal VAD, and the genetic penetrance from males, should be comparatively low. Clinical phenotypes may only be expressed when vitamin A supplied to the placenta is diminished, notably in twin gestation (individual VI-2), where retinol input is divided between two embryos.

Structural Basis for Enhanced STRA6 Binding

RBP is the archetypal lipocalin, an ancient protein family represented in nearly all life forms, including mammals, invertebrates, fungi, and eubacteria (Flower, 1996; Newcomer and Ong, 2000). Its ligand pocket is formed by eight anti-parallel beta strands (A–H) with alternating hydrophilic and hydrophobic amino acids, the latter stabilizing retinol. The orientation of the A–B loop, specifically G34–L35–F36–L37, is the only major structural difference between apo and holo RBP crystals at neutral pH (Zanotti et al., 1993). Threonine substitutions at Ala55 or Ala57, conserved sites deep within the pocket, impair retinol binding and, paradoxically, enhance STRA6 binding. Because these sites are located in the interior of the protein and thus unlikely to contact STRA6, the mutations must increase receptor binding indirectly, by altering RBP conformation. The striking decrease in K_d is driven by a large increase in the association rate constant (k_{on}) with no apparent change in dissociation kinetics (k_{off}). While relatively unusual (Anderson et al., 1998), a small number of protein-receptor affinity mutations are known to specifically affect k_{on} (Lahti et al., 2011; Lengyel et al., 2007). Our findings strongly

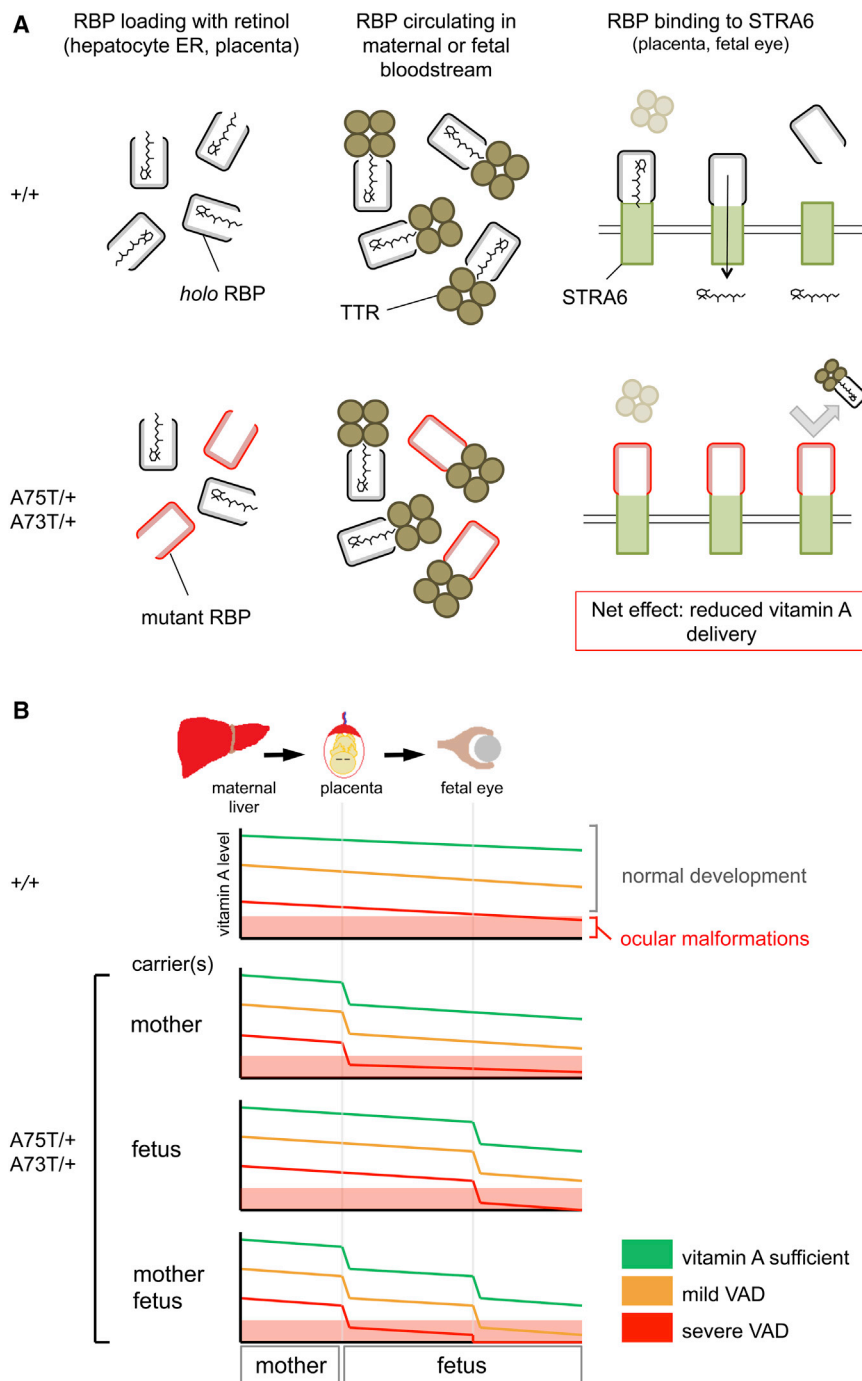


Figure 7. Model for Disease Pathogenesis, Dominant Inheritance, and Maternal Effect on Penetrance

(A) RBP life cycle in WT (top) and heterozygous (bottom) individuals. In mutation carriers, A55T or A57T are cosecreted with WT proteins from the liver and/or extraembryonic tissues (yolk sac). Each RBP circulates in the maternal or fetal bloodstream in a stable complex bound to TTR, but most of the mutant proteins lack retinol. Upon reaching target tissues, the mutant RBPs bind STRA6 receptors with much higher affinity than WT, acting as dominant-negative particles that block vitamin A delivery.

(B) Basis for maternal inheritance. Skewed penetrance arises from functional “bottlenecks” that occur at sequential RBP-STRa6 interaction sites in the placenta and fetal eye. Disruption of vitamin A transfer at both levels, coupled with low maternal dietary retinoids (orange and red lines), predispose the fetus to MAC disease when the trait is maternally transmitted. Vitamin A deficiency, VAD.

ment at the cell surface, favoring retinol release (Bychkova et al., 1998), and may be potentiated by interaction with STRA6. We propose that the A55T and A57T mutations, by altering the shape, polarity, and hydrophilicity of the retinol pocket, lower the activation energy for this transition. Consequently, a significant fraction of the mutant RBP population may exist in a partially melted state under normal physiological conditions. These molecules, which may resemble WT intermediates in the RBP-STRa6 binding reaction, presumably account for the enhanced retinol release observed in the presence of organic solvents, surfactants, or phospholipid vesicles. Indeed, retinol dissociates from the mutant RBPs with biphasic kinetics, in PBS following addition of Tx-100 and deoxycholate (DOC), consistent with the existence of ≥ 2 discrete *holo* conformations (Figure 5D).

Despite their increased forward reaction rates, the mutant *apo* RBPs appear to undock normally from STRA6 (Figure 6E). Likewise, mutant *apo* and *holo*

suggest that RBP-STRa6 docking involves a conformational adaptation of RBP and that this initial step, rather than diffusion, limits the binding reaction, consistent with a selected-fit model (Weigl and von Deuster, 2009). Complementary changes in STRA6 folding may further stabilize the ligand-receptor complex.

The RBP lipocalin undergoes reversible transformation to a molten globule state as pH or solvent polarity is reduced (Calderone et al., 2003; Greene et al., 2006). This cooperative unfolding has been proposed to occur naturally in the local acidic environ-

ment. RBPs bind TTR with an intrinsic affinity similar to WT (Figure 3) and are thus retained in carrier plasma (Figure 4). Indeed, the enhanced binding of mutant RBP to STRA6+ cell surfaces may in part explain the 1:2 ratio of mutant-to-WT protein in carrier plasma, which cannot be accounted for by unequal urinary loss (Figure S6). RBP normally contacts TTR via three external loops (Figure 2D), which form the opening to the retinol pocket, and the C terminus (Newcomer and Ong, 2000). Although the structural details are not known, these same features are likely

to mediate the interaction between RBP and STRA6, allowing retinol to exit (Kawaguchi et al., 2008). For steric reasons, the RBP-TTR complex must dissociate before receptor binding can occur. This step is driven by a 20-fold difference in the steady state affinity of RBP for STRA6 versus TTR. The alanine substitutions affect RBP binding to former, but not the latter. Structural studies of the mutant proteins may shed light on the conformational steps necessary for STRA6 docking and dissociation and vitamin A release.

RBP4 Mutations, Diet, and Vitamin A Physiology

Among organs, the eye is most frequently affected in animal models of vitamin A deficiency (Hale, 1933; See and Clagett-Dame, 2009; Warkany and Schraffenberger, 1946; Wilson et al., 1953). Our findings are consistent with this pattern. Despite a global reduction in vitamin A available to the embryo, phenotypes in Family 1 are limited to the eye. Given the central role of retinoids in light perception, this unique sensitivity is striking and may reflect an evolutionary origin of RA signaling in the visual system (Campo-Paysaa et al., 2008; Drager et al., 2000). Likewise, in humans, total loss of *RBP4* is only associated with night blindness, retinal dystrophy, and chorioretinal coloboma (Biesalski et al., 1999; Cukras et al., 2012).

In addition to retinol, other forms of vitamin A (principally retinyl esters) are delivered to the placenta via chylomicron lipoprotein particles (D'Ambrosio et al., 2011; Wassef and Quadro, 2011). Indeed, 25% of postprandial retinoids, including retinyl esters (RE) and α/β -carotenoids, travel directly to extrahepatic tissues from intestinal enterocytes via this parallel system, with no involvement of RBP (Goodman et al., 1965). However, because chylomicron RE are rapidly cleared (Berr, 1992), RBP accounts for 95%–99% of circulating retinoids in the fasting state (Soprano and Blazer, 1994). Accordingly, the extent and timing of maternal RE consumption during pregnancy, along with other genetic and/or environmental modifiers, may account for the variable penetrance. For women carrying an *RBP4* mutation, careful dietary supplementation with extra vitamin A (RE) in divided doses may be indicated to minimize risk of congenital eye malformations in offspring.

Recent nutritional studies showed that *Rbp4* $-/-$ mouse pups born from *Rbp4* $-/-$ dams are normal when mothers were fed diets replete with RE (Quadro et al., 2005). However, these pups developed microphthalmia or anophthalmia in the absence of dietary retinoids and the severity was determined by maternal vitamin A status. In our study, clinical phenotypes were roughly correlated with the magnitude of biochemical effects (Figure 5). Thus, both affected males in Family 2 (A55T) had neurodevelopmental delay in addition to anophthalmia. The discovery of genes that modify plasma retinoid levels, apart from *RBP4* and *TTR* (Mondul et al., 2011), may shed more light on this disease.

Nutritional Mechanism for Maternal Inheritance of Human Genetic Disease

Maternally skewed inheritance has been reported for other birth defects, including congenital heart disease (Burn et al., 1998; Nora and Nora, 1987), but the molecular basis is unknown. A study of scoliosis identified gestational hypoxia as an environmental factor that disrupts fibroblast growth factor signaling

and somitogenesis, increasing penetrance of Notch pathway defects (Sparrow et al., 2012). Genetic vitamin A deficiency has been previously suggested as a potential factor for eye malformations (Hornby et al., 2003). Dominant-negative *RBP4* alleles provide a further example of gene \times environment effects. Unlike other modes of maternal inheritance, e.g., transmission of ooplasmic mRNA, mitochondrial DNA mutations, or genomic imprinting, these alleles affect fetal and maternal metabolism at a functional level. The sex-specific penetrance has a physiological basis. Our findings highlight the importance of maternal-fetal nutrition and may apply broadly to congenital disease.

EXPERIMENTAL PROCEDURES

Clinical Data

Human studies were approved by the University of Michigan (UM); University of California, Davis; and Einstein Medical Center Institutional Review Boards, and informed consent was obtained from all subjects. Eye exams, fundus photography, and magnetic resonance imaging (MRI) were performed at UM (Table S1). Blood tests for retinol, RBP, and TTR (prealbumin) were performed on carrier samples collected after a 12 hr fast (Table S3). MS of plasma and urine samples and other clinical studies are detailed in the Extended Experimental Procedures.

Genetic Analysis

Family 1 genotypes were determined at 51 simple sequence length polymorphism (SSLP) and 6,070 SNP loci using blood, saliva, or buccal DNA. SNPs were assessed using the HL12 BeadChip platform and BeadStudio software (Illumina). Genetic mapping was performed in three steps. Exclusion tests were performed by comparing probands using SSLP markers flanking 23 candidate loci (Table S2). Multipoint linkage analysis was then performed on a core pedigree consisting of all living affected individuals, obligate carriers, and spouses ($n = 20$) using Merlin v1.1.2 (Abecasis et al., 2002). Finally, linkage analysis was extended to include all collected ($n = 33$; Figures S1C and S1D) and nodal family members. LOD scores from two subpedigrees (Figure S1D) were summed, discarding duplicate phenotypic information (Bellenguez et al., 2009) and applying an AD inheritance model with uniform or sex-specific penetrance, estimated from the pedigree.

To identify *RBP4* coding variants, we screened 75 unrelated MAC probands and 307 controls (National Institute of Neurological Disorders and Stroke panel) by PCR Sanger sequencing (Table S5) and queried the EVS Exome Variant database. Chromosome 10q haplotypes of Families 2 and 3 were compared using the Omni1-Quad SNP platform (Illumina).

RBP Secretion and TTR Interaction Assays

Parallel HeLa cultures were transfected with pUS2-RBP^{HA} vectors expressing WT, mutant (A55T, A57T, G73D, or I41N), or ER retention (WT^{KDEL}) human RBP proteins with an N-terminal HA epitope, or control plasmid (Table S6). After 48 hr, CM and cell lysates were electrophoresed through native or denaturing polyacrylamide gels and compared by HA western analysis. To evaluate RBP multimerization, CM was crosslinked in 0.5% volume per volume (v/v) glutaraldehyde for 30 min, boiled with or without 2 mM 2-mercaptoethanol (β ME), and electrophoresed. To assess RBP-TTR binding in culture, HeLa cells were cotransfected with pUS2-TTR^{myc} and WT or mutant pUS2-RBP^{HA} plasmids. Secreted RBP^{HA} complexes were immunopurified from CM with anti-HA agarose beads (Sigma), washed in PBS, and tested for TTR by western analysis. To fully assess RBP-TTR binding in vitro, reciprocal SPR assays were performed using a Biacore T100 system (GE Healthcare) and biotin capture chip with human plasma TTR (Sigma) and HA- or polyhistidine-tagged RBP purified from HeLa CM. Molecular cloning, cell culture, protein biochemistry, SPR, and data analysis are detailed in the Extended Experimental Procedures.

Retinol Binding Assays

To assess retinol binding to RBP in culture, HeLa cells were transfected with WT or mutant pUS2-RBP^{HA} plasmids in Dulbecco's Modified Eagle media

(DMEM) containing 10% delipidated fetal bovine serum (FBS), metabolically labeled with 6 microcuries per milliliter ($\mu\text{Ci}/\text{ml}$) ^{35}S -methionine and -cysteine in serum-free DMEM for 1 hr, and exposed to 8.25 $\mu\text{Ci}/\text{ml}$ ^3H -retinol (NEN Perkin-Elmer) for an additional 3 hr. Secretion of ^{35}S -labeled RBP in the CM was assessed by gel electrophoresis and autoradiography. Radiolabeled RBP^{HA} was immunopurified from CM using anti-HA agarose beads, washed three times in PBS containing 1% Triton X-100, 0.5% sodium DOC, and eluted in 2% sodium dodecyl sulfate (SDS). The $^3\text{H}/^{35}\text{S}$ isotope ratio was measured by liquid scintillation counting (LSC) and normalized to WT.

For in vitro titration assays, recombinant apo RBP^{HA} was immunopurified from serum-free HeLa CM, eluted with HA peptide (Anaspec), and dialyzed into PBS. Homogeneity was verified by gel electrophoresis. Equal amounts of WT, A55T, or A57T RBP^{HA} proteins were loaded with 0 to 5 μM fresh all-*trans* retinol for 1 hr in PBS. Binding was quantified by retinol fluorescence (ex 330 nm and em 460 nm) enhancement (Cogan et al., 1976) using a microplate reader. To assess binding in nonpolar or amphipathic conditions, parallel assays were performed in PBS with 0 to 50% ethanol; 1% Triton X-100, 0.5% DOC for 0 to 90 min; or 0.1% α -L-PC vesicles dispersed in 5% *n*-butanol.

STRA6-RBP Binding Radioligand Assay

Immunopurified ^{35}S -labeled apo WT, *holo* WT, A55T, or A57T RBP^{HA} (5 picomolar [pM] at 1.2×10^7 counts per minute/picomole specific activity) was added, with or without an 8- or 250-fold excess unlabeled *holo* WT competitor, to paired HEK293T cultures, transfected with pUS2-STRA6^{myc} or pUS2 vector plasmid DNA. After 1 hr at 37°C, the cells were gently washed with prewarmed PBS (Kawaguchi et al., 2007) and the amount of bound ^{35}S was determined by LSC. Receptor-specific binding was calculated by subtracting the vector control. STRA6^{myc} expression was verified by myc immunofluorescence and STRA6 western analysis.

Equilibrium and Kinetic Analysis

STRA6+ or control HEK293T cells were plated on poly-D-lysine (PDL) coated dishes and incubated with CM containing 0–80 $\mu\text{g}/\text{ml}$ A55T, A57T, or WT apo RBP^{HA} and 0.5% BSA for 90 min at 37°C. For K_d analysis, monolayers were washed with ice-cold Hanks balanced salt solution (HBSS) and bound RBP was eluted with 25 mM glycine HBSS pH 3. For kinetic analysis, monolayers were washed with DMEM 0.5% BSA and dissociation was followed at 25°C or 37°C by sampling the media at time points from 0 to 90 min. The concentration of RBP^{HA} was determined by an ELISA (Figure S7). The immunoassay, saturation binding and kinetic methods, and quantitative analysis are detailed in the Extended Experimental Procedures.

SUPPLEMENTAL INFORMATION

Supplemental Information includes Extended Experimental Procedures, seven figures, and six tables and can be found with this article online at <http://dx.doi.org/10.1016/j.cell.2015.03.006>.

AUTHOR CONTRIBUTIONS

C.M.C. performed most experiments and wrote the manuscript. T.G. supervised experiments and wrote the manuscript. S.A.T. assisted with sample genotyping, and S.W. assisted with biochemical assays. J.T.P., C.N., T.B., and A.S. performed clinical studies.

ACKNOWLEDGMENTS

We are grateful for technical support from Bob Lyons and Susan Dagenais (DNA sequencing), Philip Gafken (MS), Peter Hwang and Andrew Hill (SPR), and Paul Kirchoff (molecular modeling). We thank Catherine Downs and Kari Branham for help with genetic counseling; Ed Pugh for quantitative analysis of binding kinetics; Noor Ghiasvand and Hui Sun for valuable discussions; Friedhelm Hildebrandt and Edgar Otto for advice on library construction; Tony Antonellis for sharing control DNAs; James Doss and Sarah Oelrich for clinical data; Ed Pugh, Ala Moshiri, and Zach Farrow for careful reading of the manuscript; and Dellaney Rudolph and Nathan Vale for technical assistance.

We are profoundly grateful to subject families for participating in the study. This research was funded by grants from the NIH (EY19497), Midwest Eye Bank and Transplantation Center, the UM Center for Rare Disease, and the UM Center for Genetics in Health and Medicine. C.M.C. was supported by NIH T32 grants GM07544 and HD07505.

Received: December 5, 2014

Revised: January 30, 2015

Accepted: February 20, 2015

Published: April 23, 2015

REFERENCES

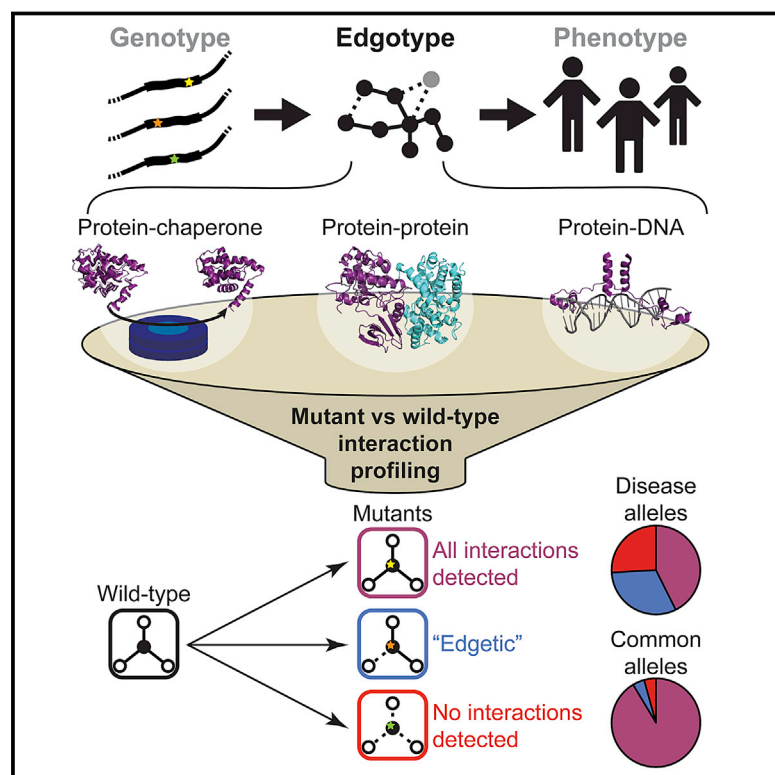
- Abecasis, G.R., Cherny, S.S., Cookson, W.O., and Cardon, L.R. (2002). Merlin—rapid analysis of dense genetic maps using sparse gene flow trees. *Nat. Genet.* 30, 97–101.
- Anderson, J., Burns, H.D., Enriquez-Harris, P., Wilkie, A.O., and Heath, J.K. (1998). Apert syndrome mutations in fibroblast growth factor receptor 2 exhibit increased affinity for FGF ligand. *Hum. Mol. Genet.* 7, 1475–1483.
- Bellenguez, C., Ober, C., and Bourgain, C. (2009). A multiple splitting approach to linkage analysis in large pedigrees identifies a linkage to asthma on chromosome 12. *Genet. Epidemiol.* 33, 207–216.
- Berr, F. (1992). Characterization of chylomicron remnant clearance by retinyl palmitate label in normal humans. *J. Lipid Res.* 33, 915–930.
- Biesalski, H.K., Frank, J., Beck, S.C., Heinrich, F., Illek, B., Reifen, R., Gollnick, H., Seeliger, M.W., Wissinger, B., and Zrenner, E. (1999). Biochemical but not clinical vitamin A deficiency results from mutations in the gene for retinol binding protein. *Am. J. Clin. Nutr.* 69, 931–936.
- Bouillet, P., Sapin, V., Chazaud, C., Messaddeq, N., Décimo, D., Dollé, P., and Chambon, P. (1997). Developmental expression pattern of Stra6, a retinoic acid-responsive gene encoding a new type of membrane protein. *Mech. Dev.* 63, 173–186.
- Burn, J., Brennan, P., Little, J., Holloway, S., Coffey, R., Somerville, J., Dennis, N.R., Allan, L., Arnold, R., Deanfield, J.E., et al. (1998). Recurrence risks in offspring of adults with major heart defects: results from first cohort of British collaborative study. *Lancet* 351, 311–316.
- Bychkova, V.E., Dujsekina, A.E., Fantuzzi, A., Ptitsyn, O.B., and Rossi, G.L. (1998). Release of retinol and denaturation of its plasma carrier, retinol-binding protein. *Fold. Des.* 3, 285–291.
- Calderone, V., Berni, R., and Zanotti, G. (2003). High-resolution structures of retinol-binding protein in complex with retinol: pH-induced protein structural changes in the crystal state. *J. Mol. Biol.* 329, 841–850.
- Campo-Paysaa, F., Marlétaz, F., Laudet, V., and Schubert, M. (2008). Retinoic acid signaling in development: tissue-specific functions and evolutionary origins. *Genesis* 46, 640–656.
- Casey, J., Kawaguchi, R., Morrissey, M., Sun, H., McGettigan, P., Nielsen, J.E., Conroy, J., Regan, R., Kenny, E., Cormican, P., et al. (2011). First implication of STRA6 mutations in isolated anophthalmia, microphthalmia, and coloboma: a new dimension to the STRA6 phenotype. *Hum. Mutat.* 32, 1417–1426.
- Chassaing, N., Golzio, C., Odent, S., Lequeux, L., Vigouroux, A., Martinovic-Bouriel, J., Tiziano, F.D., Masini, L., Piro, F., Maragliano, G., et al. (2009). Phenotypic spectrum of STRA6 mutations: from Matthew-Wood syndrome to non-lethal anophthalmia. *Hum. Mutat.* 30, E673–E681.
- Cogan, U., Kopelman, M., Mokady, S., and Shinitzky, M. (1976). Binding affinities of retinol and related compounds to retinol binding proteins. *Eur. J. Biochem.* 65, 71–78.
- Cowan, S.W., Newcomer, M.E., and Jones, T.A. (1990). Crystallographic refinement of human serum retinol binding protein at 2 Å resolution. *Proteins* 8, 44–61.
- Cukras, C., Gaasterland, T., Lee, P., Gudiseva, H.V., Chavali, V.R., Pullakhandam, R., Maranhao, B., Edsall, L., Soares, S., Reddy, G.B., et al. (2012). Exome analysis identified a novel mutation in the RBP4 gene in a consanguineous pedigree with retinal dystrophy and developmental abnormalities. *PLoS ONE* 7, e50205.

- D'Ambrosio, D.N., Clugston, R.D., and Blaner, W.S. (2011). Vitamin A metabolism: an update. *Nutrients* 3, 63–103.
- Dowling, J.E., and Wald, G. (1958). Vitamin A deficiency and night blindness. *Proc. Natl. Acad. Sci. USA* 44, 648–661.
- Drager, U.C., Wagner, E., Andreadis, A., and McCaffery, P. (2000). The role and evolutionary development of retinoic-acid signalling in the eye. In *Vitamin A and Retinoids: An Update of Biological Aspects and Clinical Applications*, M.A. Livrea, ed. (Basel: Birkhauser Verlag), pp. 73–82.
- Duester, G. (2009). Keeping an eye on retinoic acid signaling during eye development. *Chem. Biol. Interact.* 178, 178–181.
- Fantes, J., Ragge, N.K., Lynch, S.A., McGill, N.I., Collin, J.R., Howard-Peebles, P.N., Hayward, C., Vivian, A.J., Williamson, K., van Heyningen, V., and FitzPatrick, D.R. (2003). Mutations in *SOX2* cause anophthalmia. *Nat. Genet.* 33, 461–463.
- Fares-Taie, L., Gerber, S., Chassaing, N., Clayton-Smith, J., Hanein, S., Silva, E., Serey, M., Serre, V., Gérard, X., Baumann, C., et al. (2013). *ALDH1A3* mutations cause recessive anophthalmia and microphthalmia. *Am. J. Hum. Genet.* 92, 265–270.
- Flower, D.R. (1996). The lipocalin protein family: structure and function. *Biochem. J.* 318, 1–14.
- Folli, C., Viglione, S., Busconi, M., and Berni, R. (2005). Biochemical basis for retinol deficiency induced by the I41N and G75D mutations in human plasma retinol-binding protein. *Biochem. Biophys. Res. Commun.* 336, 1017–1022.
- Folli, C., Favilla, R., and Berni, R. (2010). The interaction between retinol-binding protein and transthyretin analyzed by fluorescence anisotropy. *Methods Mol. Biol.* 652, 189–207.
- Golzio, C., Martinovic-Bouriel, J., Thomas, S., Mougou-Zrelli, S., Grattagliano-Bessieres, B., Bonniere, M., Delahaye, S., Munnich, A., Encha-Razavi, F., Lyonnet, S., et al. (2007). Matthew-Wood syndrome is caused by truncating mutations in the retinol-binding protein receptor gene *STRA6*. *Am. J. Hum. Genet.* 80, 1179–1187.
- Goodman, D.W., Huang, H.S., and Shiratori, T. (1965). Tissue distribution and metabolism of newly absorbed vitamin A in the rat. *J. Lipid Res.* 6, 390–396.
- Graw, J. (2010). Eye development. *Curr. Top. Dev. Biol.* 90, 343–386.
- Greene, L.H., Wijesinha-Bettoni, R., and Redfield, C. (2006). Characterization of the molten globule of human serum retinol-binding protein using NMR spectroscopy. *Biochemistry* 45, 9475–9484.
- Hale, F. (1933). Pigs born without eyeballs. *J. Hered.* 24, 105–106.
- Heller, J., and Horwitz, J. (1974). The binding stoichiometry of human plasma retinol-binding protein to prealbumin. *J. Biol. Chem.* 249, 5933–5938.
- Hornby, S.J., Ward, S.J., and Gilbert, C.E. (2003). Eye birth defects in humans may be caused by a recessively-inherited genetic predisposition to the effects of maternal vitamin A deficiency during pregnancy. *Med. Sci. Monit.* 9, HY23–HY26.
- Johansson, S., Gustafson, A.L., Donovan, M., Romert, A., Eriksson, U., and Dencker, L. (1997). Retinoid binding proteins in mouse yolk sac and chorio-allantoic placenta. *Anat. Embryol. (Berl.)* 195, 483–490.
- Johansson, S., Gustafson, A.L., Donovan, M., Eriksson, U., and Dencker, L. (1999). Retinoid binding proteins-expression patterns in the human placenta. *Placenta* 20, 459–465.
- Kanai, M., Raz, A., and Goodman, D.S. (1968). Retinol-binding protein: the transport protein for vitamin A in human plasma. *J. Clin. Invest.* 47, 2025–2044.
- Kawaguchi, R., Yu, J., Honda, J., Hu, J., Whitelegge, J., Ping, P., Wiita, P., Bok, D., and Sun, H. (2007). A membrane receptor for retinol binding protein mediates cellular uptake of vitamin A. *Science* 315, 820–825.
- Kawaguchi, R., Yu, J., Wiita, P., Honda, J., and Sun, H. (2008). An essential ligand-binding domain in the membrane receptor for retinol-binding protein revealed by large-scale mutagenesis and a human polymorphism. *J. Biol. Chem.* 283, 15160–15168.
- Kawaguchi, R., Zhong, M., Kassai, M., Ter-Stepanian, M., and Sun, H. (2012). *STRA6*-catalyzed vitamin A influx, efflux, and exchange. *J. Membr. Biol.* 245, 731–745.
- Lahti, J.L., Lui, B.H., Beck, S.E., Lee, S.S., Ly, D.P., Longaker, M.T., Yang, G.P., and Cochran, J.R. (2011). Engineered epidermal growth factor mutants with faster binding on-rates correlate with enhanced receptor activation. *FEBS Lett.* 585, 1135–1139.
- Lamb, T.D., and Pugh, E.N., Jr. (2004). Dark adaptation and the retinoid cycle of vision. *Prog. Retin. Eye Res.* 23, 307–380.
- Lengyel, C.S., Willis, L.J., Mann, P., Baker, D., Kortemme, T., Strong, R.K., and McFarland, B.J. (2007). Mutations designed to destabilize the receptor-bound conformation increase MICA-NKG2D association rate and affinity. *J. Biol. Chem.* 282, 30658–30666.
- Malpeli, G., Folli, C., and Berni, R. (1996). Retinoid binding to retinol-binding protein and the interference with the interaction with transthyretin. *Biochim. Biophys. Acta* 1294, 48–54.
- Melhus, H., Laurent, B., Rask, L., and Peterson, P.A. (1992). Ligand-dependent secretion of rat retinol-binding protein expressed in HeLa cells. *J. Biol. Chem.* 267, 12036–12041.
- Mondul, A.M., Yu, K., Wheeler, W., Zhang, H., Weinstein, S.J., Major, J.M., Cornelis, M.C., Männistö, S., Hazra, A., Hsing, A.W., et al. (2011). Genome-wide association study of circulating retinol levels. *Hum. Mol. Genet.* 20, 4724–4731.
- Morrison, D., FitzPatrick, D., Hanson, I., Williamson, K., van Heyningen, V., Fleck, B., Jones, I., Chalmers, J., and Campbell, H. (2002). National study of microphthalmia, anophthalmia, and coloboma (MAC) in Scotland: investigation of genetic aetiology. *J. Med. Genet.* 39, 16–22.
- Muto, Y., Smith, J.E., Milch, P.O., and Goodman, D.S. (1972). Regulation of retinol-binding protein metabolism by vitamin A status in the rat. *J. Biol. Chem.* 247, 2542–2550.
- Newcomer, M.E., and Ong, D.E. (2000). Plasma retinol binding protein: structure and function of the prototypic lipocalin. *Biochim. Biophys. Acta* 1482, 57–64.
- Niederreither, K., and Dollé, P. (2008). Retinoic acid in development: towards an integrated view. *Nat. Rev. Genet.* 9, 541–553.
- Nora, J.J., and Nora, A.H. (1987). Maternal transmission of congenital heart diseases: new recurrence risk figures and the questions of cytoplasmic inheritance and vulnerability to teratogens. *Am. J. Cardiol.* 59, 459–463.
- Onwochei, B.C., Simon, J.W., Bateman, J.B., Couture, K.C., and Mir, E. (2000). Ocular colobomata. *Surv. Ophthalmol.* 45, 175–194.
- Pasutto, F., Sticht, H., Hammersen, G., Gillesen-Kaesbach, G., Fitzpatrick, D.R., Nürnberg, G., Brasch, F., Schirmer-Zimmermann, H., Tolmie, J.L., Chitayat, D., et al. (2007). Mutations in *STRA6* cause a broad spectrum of malformations including anophthalmia, congenital heart defects, diaphragmatic hernia, alveolar capillary dysplasia, lung hypoplasia, and mental retardation. *Am. J. Hum. Genet.* 80, 550–560.
- Peterson, P.A. (1971). Studies on the interaction between prealbumin, retinol-binding protein, and vitamin A. *J. Biol. Chem.* 246, 44–49.
- Quadro, L., Hamberger, L., Gottesman, M.E., Colantuoni, V., Ramakrishnan, R., and Blaner, W.S. (2004). Transplacental delivery of retinoid: the role of retinol-binding protein and lipoprotein retinyl ester. *Am. J. Physiol. Endocrinol. Metab.* 286, E844–E851.
- Quadro, L., Hamberger, L., Gottesman, M.E., Wang, F., Colantuoni, V., Blaner, W.S., and Mendelsohn, C.L. (2005). Pathways of vitamin A delivery to the embryo: insights from a new tunable model of embryonic vitamin A deficiency. *Endocrinology* 146, 4479–4490.
- Raila, J., Willnow, T.E., and Schweigert, F.J. (2005). Megalin-mediated reuptake of retinol in the kidneys of mice is essential for vitamin A homeostasis. *J. Nutr.* 135, 2512–2516.
- Raz, A., Shiratori, T., and Goodman, D.S. (1970). Studies on the protein-protein and protein-ligand interactions involved in retinol transport in plasma. *J. Biol. Chem.* 245, 1903–1912.
- Sapin, V., Ward, S.J., Bronner, S., Chambon, P., and Dollé, P. (1997). Differential expression of transcripts encoding retinoid binding proteins and retinoic acid receptors during placentation of the mouse. *Dev. Dyn.* 208, 199–210.

- See, A.W., and Clagett-Dame, M. (2009). The temporal requirement for vitamin A in the developing eye: mechanism of action in optic fissure closure and new roles for the vitamin in regulating cell proliferation and adhesion in the embryonic retina. *Dev. Biol.* 325, 94–105.
- Selvaraj, S.R., Bhatia, V., and Tatu, U. (2008). Oxidative folding and assembly with transthyretin are sequential events in the biogenesis of retinol binding protein in the endoplasmic reticulum. *Mol. Biol. Cell* 19, 5579–5592.
- Soprano, D.R., and Blaner, W.S. (1994). Plasma retinol-binding protein. In *The Retinoids: Biology, Chemistry, and Medicine*, M.B. Sporn, A.B. Roberts, and D.S. Goodman, eds. (New York: Raven Press), pp. 257–282.
- Soprano, D.R., Soprano, K.J., and Goodman, D.S. (1986). Retinol-binding protein and transthyretin mRNA levels in visceral yolk sac and liver during fetal development in the rat. *Proc. Natl. Acad. Sci. USA* 83, 7330–7334.
- Sparrow, D.B., Chapman, G., Smith, A.J., Mattar, M.Z., Major, J.A., O'Reilly, V.C., Saga, Y., Zackai, E.H., Dormans, J.P., Alman, B.A., et al. (2012). A mechanism for gene-environment interaction in the etiology of congenital scoliosis. *Cell* 149, 295–306.
- Sturtevant, A.H. (1923). Inheritance of direction of coiling in *Limnaea*. *Science* 58, 269–270.
- van Bennekum, A.M., Wei, S., Gamble, M.V., Vogel, S., Piantedosi, R., Gottesman, M., Episkopou, V., and Blaner, W.S. (2001). Biochemical basis for depressed serum retinol levels in transthyretin-deficient mice. *J. Biol. Chem.* 276, 1107–1113.
- van Meer, G., Voelker, D.R., and Feigenson, G.W. (2008). Membrane lipids: where they are and how they behave. *Nat. Rev. Mol. Cell Biol.* 9, 112–124.
- Ward, S.J., Chambon, P., Ong, D.E., and Båvik, C. (1997). A retinol-binding protein receptor-mediated mechanism for uptake of vitamin A to postimplantation rat embryos. *Biol. Reprod.* 57, 751–755.
- Warkany, J., and Schraffenberger, E. (1946). Congenital malformations induced in rats by maternal vitamin A deficiency; defects of the eye. *Arch. Ophthalmol.* 35, 150–169.
- Wassef, L., and Quadro, L. (2011). Uptake of dietary retinoids at the maternal-fetal barrier: in vivo evidence for the role of lipoprotein lipase and alternative pathways. *J. Biol. Chem.* 286, 32198–32207.
- Weikl, T.R., and von Deuster, C. (2009). Selected-fit versus induced-fit protein binding: kinetic differences and mutational analysis. *Proteins* 75, 104–110.
- Williamson, K.A., and FitzPatrick, D.R. (2014). The genetic architecture of microphthalmia, anophthalmia and coloboma. *Eur. J. Med. Genet.* 57, 369–380.
- Wilson, J.G., Roth, C.B., and Warkany, J. (1953). An analysis of the syndrome of malformations induced by maternal vitamin A deficiency. Effects of restoration of vitamin A at various times during gestation. *Am. J. Anat.* 92, 189–217.
- Yahyavi, M., Abouzeid, H., Gawdat, G., de Preux, A.S., Xiao, T., Bardakjian, T., Schneider, A., Choi, A., Jorgenson, E., Baier, H., et al. (2013). ALDH1A3 loss of function causes bilateral anophthalmia/microphthalmia and hypoplasia of the optic nerve and optic chiasm. *Hum. Mol. Genet.* 22, 3250–3258.
- Zanotti, G., Ottonello, S., Berni, R., and Monaco, H.L. (1993). Crystal structure of the trigonal form of human plasma retinol-binding protein at 2.5 Å resolution. *J. Mol. Biol.* 230, 613–624.

Widespread Macromolecular Interaction Perturbations in Human Genetic Disorders

Graphical Abstract



Authors

Nidhi Sahni, Song Yi, ..., Susan Lindquist, Marc Vidal

Correspondence

lindquist@wi.mit.edu (S.L.),
marc_vidal@dfci.harvard.edu (M.V.)

In Brief

A large-scale characterization of disease mutations reveals surprisingly widespread, yet specific perturbations in macromolecular interactions. Different mutations in the same gene lead to different interaction profiles, often resulting in distinct disease phenotypes.

Highlights

- Most missense disease mutations appear not to impair protein folding or stability
- Interaction profiling helps distinguish disease mutations from non-disease variants
- Distinct interaction perturbations underlie distinct disease phenotypes
- Integrative interaction networks enhance genotype-to-phenotype understanding



Widespread Macromolecular Interaction Perturbations in Human Genetic Disorders

Nidhi Sahni,^{1,2,3,21} Song Yi,^{1,2,3,21} Mikko Taipale,^{4,21} Juan I. Fuxman Bass,^{5,21} Jasmin Coulombe-Huntington,^{6,21} Fan Yang,^{1,2,7,8,9} Jian Peng,¹⁰ Jochen Weile,^{1,2,7,8,9} Georgios I. Karras,⁴ Yang Wang,^{1,2,3} István A. Kovács,^{1,2,11} Atanas Kamburov,^{2,3} Irina Krykbaeva,⁴ Mandy H. Lam,⁸ George Tucker,¹⁰ Vikram Khurana,⁴ Amitabh Sharma,^{1,2,11} Yang-Yu Liu,^{2,11} Nozomu Yachie,^{1,2,7,8,9} Quan Zhong,^{2,3} Yun Shen,^{1,2,3} Alexandre Palagi,^{2,3} Adriana San-Miguel,^{2,3} Changyu Fan,^{1,2,3} Dawit Balcha,^{1,2,3} Amelie Dricot,^{1,2,3} Daniel M. Jordan,^{12,13} Jennifer M. Walsh,^{2,3} Akash A. Shah,^{2,3} Xinping Yang,^{2,3} Ani K. Stoyanova,^{2,3} Alex Leighton,¹⁰ Michael A. Calderwood,^{1,2,3} Yves Jacob,^{2,3,14} Michael E. Cusick,^{1,2,3} Kourosh Salehi-Ashtiani,^{2,3} Luke J. Whitesell,^{4,15} Shamil Sunyaev,^{12,16} Bonnie Berger,^{10,17} Albert-László Barabási,^{1,2,11,18} Benoit Charlotteaux,^{1,2,3} David E. Hill,^{1,2,3} Tong Hao,^{1,2,3} Frederick P. Roth,^{1,2,7,8,9,19,22} Yu Xia,^{2,6,22} Albertha J.M. Walhout,^{2,5,22} Susan Lindquist,^{4,15,20,22,*} and Marc Vidal^{1,2,3,22,*}

¹Genomic Analysis of Network Perturbations Center of Excellence in Genomic Science (CEGS), Dana-Farber Cancer Institute, Boston, MA 02215, USA

²Center for Cancer Systems Biology (CCSB) and Department of Cancer Biology, Dana-Farber Cancer Institute, Boston, MA 02215, USA

³Department of Genetics, Harvard Medical School, Boston, MA 02115, USA

⁴Whitehead Institute for Biomedical Research, Cambridge, MA 02142, USA

⁵Program in Systems Biology, Program in Molecular Medicine, University of Massachusetts Medical School, Worcester, MA 01605, USA

⁶Department of Bioengineering, Faculty of Engineering, McGill University, Montreal, QC H3A 0C3, Canada

⁷Departments of Molecular Genetics and Computer Science, University of Toronto, Toronto, ON M5S 3E1, Canada

⁸Donnelly Centre, University of Toronto, Toronto, ON M5S 3E1, Canada

⁹Lunenfeld-Tanenbaum Research Institute, Mt. Sinai Hospital, Toronto, ON M5G 1X5, Canada

¹⁰Computer Science and Artificial Intelligence Laboratory, Massachusetts Institute of Technology, Cambridge, MA 02139, USA

¹¹Center for Complex Network Research (CCNR) and Departments of Physics, Biology and Computer Science, Northeastern University, Boston, MA 02115, USA

¹²Division of Genetics, Department of Medicine, Brigham and Women's Hospital, Harvard Medical School, Boston, MA 02115, USA

¹³Program in Biophysics, Harvard University, Cambridge, MA 02139, USA

¹⁴Département de Virologie, Unité de Génétique Moléculaire des Virus ARN (GMVR), Institut Pasteur, UMR3569, Centre National de la Recherche Scientifique, and Université Paris Diderot, Paris, France

¹⁵Department of Biology and Howard Hughes Medical Institute, Massachusetts Institute of Technology, Cambridge, MA 02139, USA

¹⁶The Broad Institute of MIT and Harvard, Cambridge, MA 02142, USA

¹⁷Department of Mathematics and Electrical Engineering and Computer Science, Massachusetts Institute of Technology, Cambridge, MA 02139, USA

¹⁸Department of Medicine, Brigham and Women's Hospital, Harvard Medical School, Boston, MA 02115, USA

¹⁹Canadian Institute for Advanced Research, Toronto, ON M5G 1Z8, Canada

²⁰Howard Hughes Medical Institute, Cambridge, MA 02139, USA

²¹Co-first author

²²Co-senior author

*Correspondence: lindquist@wi.mit.edu (S.L.), marc_vidal@dfci.harvard.edu (M.V.)

<http://dx.doi.org/10.1016/j.cell.2015.04.013>

SUMMARY

How disease-associated mutations impair protein activities in the context of biological networks remains mostly undetermined. Although a few renowned alleles are well characterized, functional information is missing for over 100,000 disease-associated variants. Here we functionally profile several thousand missense mutations across a spectrum of Mendelian disorders using various interaction assays. The majority of disease-associated alleles exhibit wild-type chaperone binding profiles, suggesting they preserve protein folding or stability. While common variants from healthy individuals rarely affect interactions, two-thirds of disease-associated alleles perturb protein-protein interactions, with half corresponding to

“edgetic” alleles affecting only a subset of interactions while leaving most other interactions unperturbed. With transcription factors, many alleles that leave protein-protein interactions intact affect DNA binding. Different mutations in the same gene leading to different interaction profiles often result in distinct disease phenotypes. Thus disease-associated alleles that perturb distinct protein activities rather than grossly affecting folding and stability are relatively widespread.

INTRODUCTION

Over a hundred thousand genetic variants have been identified across a large number of Mendelian disorders (Amberger et al., 2011), complex traits (Hindorf et al., 2009), and cancer types

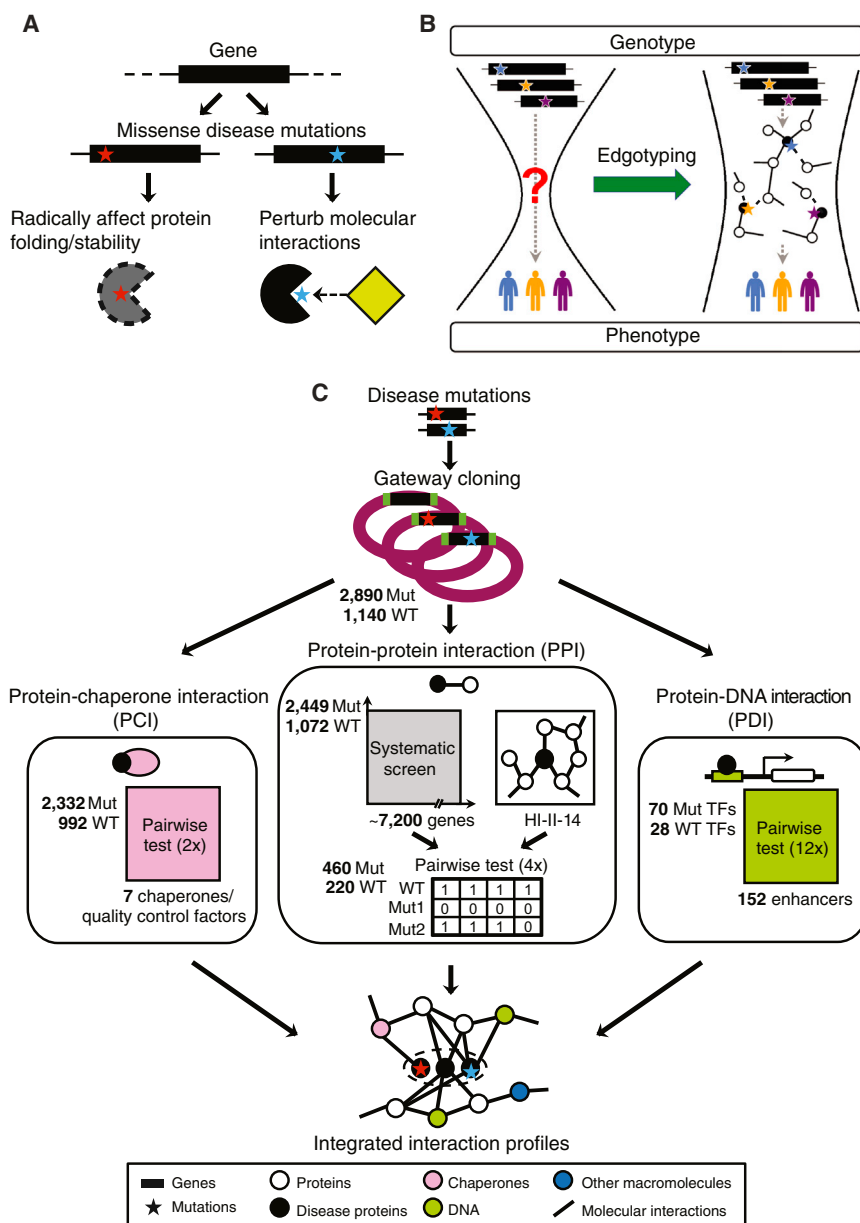


Figure 1. Systematic Characterization of Human Disease Missense Mutations

(A) Two possible effects of missense disease mutations: protein folding/stability changes and molecular interaction perturbations.

(B) Understanding mutational effects by edgotyping links genotype to phenotype. Solid and dashed lines represent retained and perturbed interactions, respectively.

(C) Experimental pipeline for characterizing alterations of molecular interactions, including protein-chaperone (PCI), protein-protein (PPI) and protein-DNA (PDI) interactions. WT: Wild-type, Mut: mutation. TF: transcription factor. "1," detected PPI; "0," not detected PPI. Dashed oval: variants in the same gene. See also Figure S1.

distinguishable diseases (Zhong et al., 2009). In addition, since genes and gene products do not function in isolation but interact with each other in the context of interactome networks (Vidal et al., 2011), it is likely that many diseases result from perturbations of such complex networks (Goh et al., 2007).

Missense mutations are among the most common sequence alterations in Mendelian disorders, accounting for more than half of all reported mutations in the Human Gene Mutation Database (HGMD) (Stenson et al., 2014). In principle, missense mutations may have no functional consequences, disrupt the three-dimensional structure of the corresponding protein, or exert specific effects on particular molecular or biochemical interactions, while leaving all other functional properties unperturbed. We previously reported that a considerable portion of Mendelian disease mutations could indeed be predicted computationally to cause interaction-specific, or "edgetic," perturbations (Zhong et al., 2009). However, only a small number of genes and associated mutations were experimentally tested in that study, and the extent to which disease mutations globally lead to interaction perturbations remains to be determined.

Here we describe a multi-pronged approach to systematically decipher molecular interaction perturbations associated with missense mutations. Since chaperones and associated quality control factors (QCFs) can salvage unstable proteins by assisting with folding, and an increase in protein-chaperone interactions (PCIs) has been observed for a number of disease mutants (Whitesell and Lindquist, 2005), our systematic approach begins with characterizing PCIs for large numbers of disease-associated alleles, followed by systematic measurements of PPI and

(Chin et al., 2011). However, many fundamental questions regarding genotype-phenotype relationships remain unresolved (Vidal et al., 2011). One critical challenge is to distinguish causal disease mutations from non-pathogenic polymorphisms. Even when causal mutations are identified, the functional consequence of such mutations is often elusive (Sahni et al., 2013).

Genotypic information alone rarely elucidates the mechanistic insights pertaining to disease pathogenesis. Although genotype-phenotype relationships can be modeled under the assumption that most disease-associated mutations lead to complete loss of protein function, e.g., through radical changes such as protein misfolding and instability (Subramanian and Kumar, 2006) (Figure 1A), the reality is often more complex, as in the case of mutations affecting the same gene but giving rise to clinically

PDI profile changes caused by mutations, a strategy referred to as “edgotyping” (Figure 1B).

We provide evidence for widespread interaction perturbations across a broad spectrum of human Mendelian disorders. Our results suggest that interaction profiling helps distinguish disease-causing mutations from common variants. Furthermore, the integration of different types of molecular interactions expands our ability to understand complex genotype-phenotype relationships.

RESULTS

Human Mutation ORFeome Version 1.1

To globally characterize disease-associated alleles, we selected mutations associated with a wide range of disorders, including cancer susceptibility and heart, respiratory, and neurological diseases. We retrieved from HGMD (Stenson et al., 2014) a list of ~16,400 mutations affecting over 1,200 genes for which we have a wild-type (WT) open-reading frame (ORF) clone in our human “ORFeome” collection (Yang et al., 2011) and selected up to four mutations per gene (Figure 1C; Tables S1A and S1B; Extended Experimental Procedures). Using properties related to RNA abundance, GO annotation, and protein domains (Extended Experimental Procedures), we verified there is no significant bias between our selected genes and the rest of the human genome or all genes represented in HGMD (Figures S1B–S1G).

Altogether, we cloned and sequence-verified 2,890 human mutant ORFs (hmORFs), each harboring a single nucleotide change that results in an amino acid change relative to the corresponding WT ORF of 1,140 genes. To our knowledge, this human mutation ORFeome version 1.1 resource (hmORFeome1.1; Figure S1A) is the most extensive human mutation collection reported to date.

Disease Mutations and Protein Folding and Stability

Using enhanced binding to a chaperone as an indicator of protein instability or misfolding, we examined how disease mutations impact protein folding and disposition. We determined the extent to which hmORF-encoded proteins and their WT counterparts interact with QCFs using a quantitative high-throughput LUMIER assay (Taipale et al., 2012; Taipale et al., 2014) (Figure 1C and Table S2A). We selected the following QCFs based on their broad specificity (Taipale et al., 2014): (1) the cytoplasmic chaperones HSP90 and HSC70, (2) their co-chaperones BAG2 and CHIP/STUB1, (3) the proteasomal regulatory subunit PSMD2 (formerly known as RPN1), and (4) the ER chaperones GRP78/BIP and GRP94 (Extended Experimental Procedures). We did not survey mitochondrial chaperones since only ~7% of disease-associated gene products are predicted to localize solely in mitochondria (Huntley et al., 2015).

Increased interaction between a QCF and mutant or WT protein, as measured by the LUMIER assay, indicates a mutation-induced perturbation in conformational stability, often associated with compromised or complete loss of function (Taipale et al., 2012). The interaction profiles of most mutant proteins correlated with their WT counterparts. However, compared to a background control set, we observed a significant enrichment

of mutant alleles showing increased interaction with QCFs (Figures 2A–2H and S2A) but little or no enrichment for decreased interaction (Figures 2A and S2B; Extended Experimental Procedures). The interaction profiles of mutant proteins with the different cytoplasmic QCFs were highly correlated, distinct from those with ER factors (Figure 2I). These results highlight the coordination and specificity of cellular quality control pathways. Altogether ~28% of the tested alleles exhibited increased binding to at least one of the seven QCFs tested. Although this fraction is likely a conservatively low estimate due to limited assay sensitivity, the strong correlation between chaperone interaction profiles (Figure 2I) suggests that the estimate would not increase substantially by assaying more chaperones. We validated several mutant-specific interactions with endogenous chaperones by co-immunoprecipitation followed by western blot, corroborating the results obtained with the LUMIER assay (Figure 2J).

We next estimated protein abundance using semiquantitative ELISA, which provides a proxy for steady-state protein stability. Although the expression levels of mutant alleles correlated with their WT counterparts (Figure S2C), mutant proteins exhibiting enhanced interactions with cytoplasmic, but not ER, chaperones were detected at lower steady-state levels than their WT counterparts ($p < 1.0 \times 10^{-4}$; Figure 3A). This is possibly a result of retention in the ER of mutant proteins that would normally be secreted and therefore not be detected by an assay that captures intracellular proteins. Interestingly, recessive alleles exhibited lower protein abundance levels and increased binding with QCFs compared with proteins encoded by dominant alleles (Figures S2D and S2E). This is consistent with the hypothesis that recessive mutations are more likely to result in loss-of-function phenotypes than dominant mutations (Lesage and Brice, 2009).

To gain insight into the structural properties of mutant proteins that exhibit increased binding to QCFs, we assessed the impact of different disease mutations on predicted protein structures. The disease alleles associated with increased binding to QCFs corresponded significantly more often to mutations of residues buried in the core of the protein (Figure 3B and Table S1C), and less often to mutations in intrinsically disordered regions (Figure 3C) when compared to mutant proteins with no change in binding. Next, we estimated the relative “deleteriousness” associated with distinct genetic mutations using PolyPhen-2 algorithm (Adzhubei et al., 2010). Deleterious mutations predicted by PolyPhen were significantly enriched in alleles that exhibited increased binding to QCFs (Figure S2F).

Previous studies suggested that increased chaperone binding reflects a change in protein stability (Falsone et al., 2004; Taipale et al., 2012). To provide further evidence for this, we assessed protein stability in cellular lysates by measuring solubility in a cellular thermal shift assay (CeTSA). We found that the majority (5 of 6) of mutant proteins with increased chaperone binding also exhibited decreased stability as measured by CeTSA (Figures S3A–S3D). In addition, computational predictions by the FoldX program (Schymkowitz et al., 2005) suggest that mutant proteins with increased binding to QCFs are likely to be significantly less stable than their WT counterpart (Figure 3D and Table S2B). Taken together, experimental and computational analyses

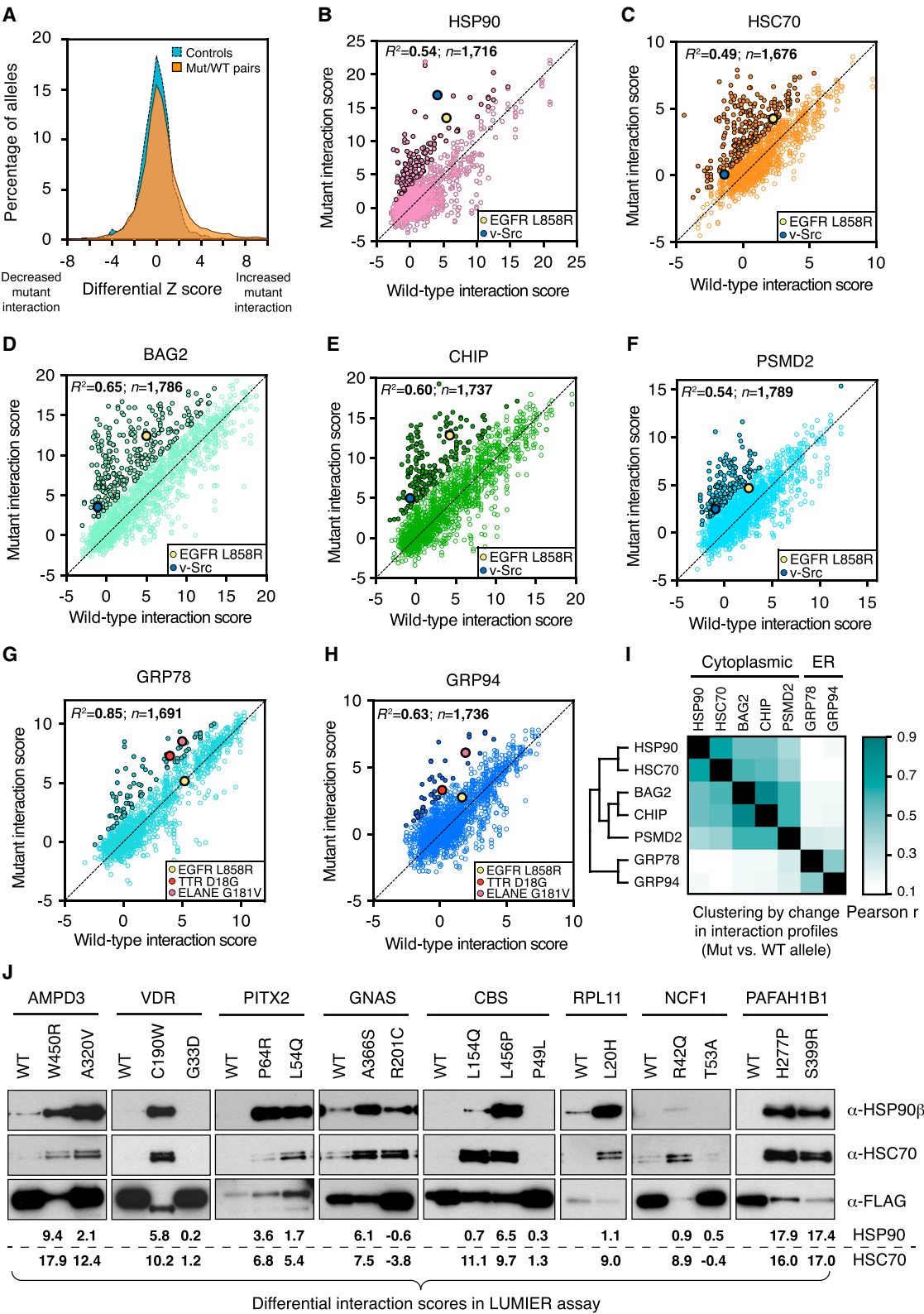


Figure 2. Most Disease Missense Mutations Do Not Impair Protein Folding or Stability
(A) Differential Z score distributions in LUMIER assay. Normalized differential Z scores are calculated as the difference in chaperone binding between all mutant/WT pairs expressed at detectable levels ($n = 12,131$). Non-expressed pairs serve as controls ($n = 1,567$).
(legend continued on next page)

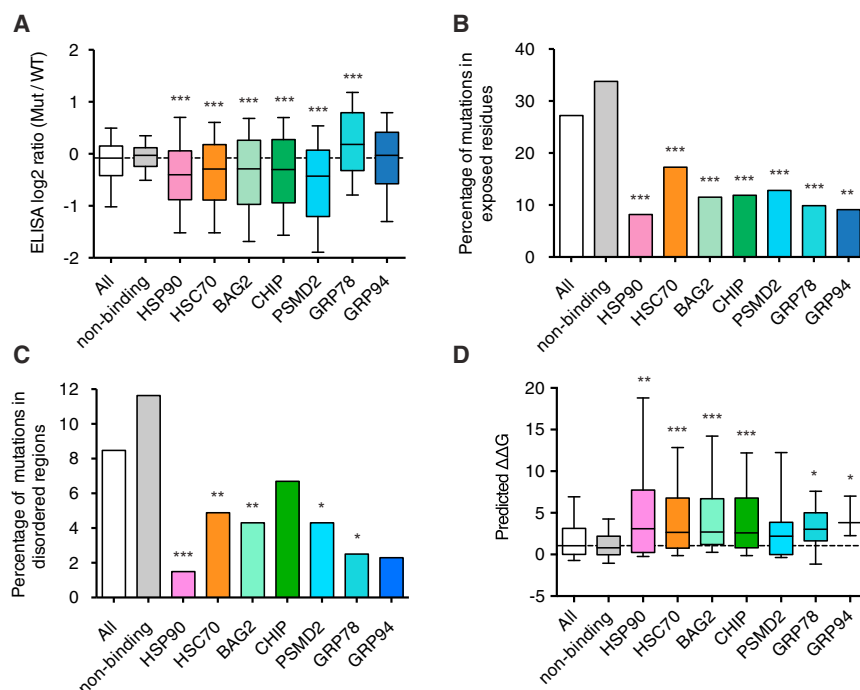


Figure 3. Mutant Proteins with Enhanced Binding to QCFs Are Likely to Be Unstable

(A) Protein expression levels measured by ELISA. x axis shows all tested mutants (All), mutants with no change (non-binding) or an increase in binding to QCFs. (B) Solvent accessibility of mutant proteins. (C) Disorder analysis of mutant proteins. (D) Stability predictions by FoldX. ΔΔG, free energy change. Dashed line (A and D) represents the median of all mutants. p values (A) and (D) by one-sided Wilcoxon rank sum test; (B) and (C) by Chi-square test. For n values, see Table S7B. *p < 0.05; **p < 0.01; ***p < 0.001. See also Figures S2 and S3.

suggest that mutant proteins with enhanced binding to QCFs have a destabilized protein structure.

Our quantitative survey of allele-specific interactions estimates that the majority of missense disease mutations do not dramatically impact protein structure or folding (Tables S1D and S2). Therefore, they may exert their deleterious effects through other mechanisms such as perturbation of molecular interactions.

Disease Mutations and PPI Perturbations

In principle, the effects of missense disease mutations on molecular interactions (Zhong et al., 2009), or “edgotype” (Sahni et al., 2013), could range from no apparent detectable change in interactions (“quasi-WT”), to specific loss of some interaction(s) (“edgetic”), to an apparent complete loss of interactions (“quasi-null”) (Figure 4A). To systematically characterize PPI perturbations associated with disease mutations and identify potential gain of interactions, we used the yeast two-hybrid (Y2H) interaction assay followed by a stringent validation assay. After autoactivator removal, we screened 2,449 mutant proteins and their 1,072 corresponding WT proteins for interactions with proteins encoded by the ~7,200 ORFs in the human ORFeome v1.1 (Rual et al., 2004). Mutant and WT proteins were then tested pair-wise against all partners found both in these Y2H screens

and in our human interactome map HI-II-14 (Rolland et al., 2014) (Figure 1C). Altogether, we obtained interaction profiles for 460 mutant proteins and their 220 WT counterparts and found 521 perturbed interactions out of 1,316 PPIs (Table S3A).

To validate these results, we used the orthogonal in vivo *Gaussia princeps* luciferase protein complementation assay (GPCA) performed in human 293T cells (Cassonnet et al., 2011) (Table S3B). Unperturbed interactions were recovered at a rate statistically indistinguishable from that of a well-documented positive reference set (PRS), similar to the interactions of the WT alleles (Braun et al., 2009; Venkatesan et al., 2009). Perturbed interactions were recovered at a rate as low as a negative control “random reference set” (RRS) (Figures 4B and S4A), demonstrating the high quality of the identified perturbations induced by disease mutations.

To analyze global and topological characteristics of gene products with edgetic, quasi-null, or quasi-WT mutations, we used the human interactome map HI-II-14 (Rolland et al., 2014). According to the studied network properties (betweenness, k-core centrality, degree, closeness), the nodes (genes) examined in our edgotyping study appear unbiased, in that their topological properties are statistically indistinguishable from other genes in the network (Figures S4B–S4F). Interestingly, we found that the genes carrying edgetic mutations tend to be more central than either non-edgetic genes or the rest of the network (Table S4).

Out of a total of 197 mutations, corresponding to 89 WT proteins with two or more interaction partners, our interaction profiling identified 26% as quasi-null alleles, 31% edgetic and 43% quasi-WT (Figure 4C and Table S3C). We also analyzed

(B–H) Interaction scatter plots for 2,332 disease alleles. Alleles were assayed for interaction with QCFs HSP90 (B), HSC70 (C), BAG2 (D), CHIP (E), PMSD2 (F), GRP78 (G), and GRP94 (H). EGFR L858R and v-Src can interact with HSP90 (Shimamura et al., 2005; Taipale et al., 2012), and TTR D18G and ELANE G181V can interact with GRP78 (Köllner et al., 2006; Sörgjerd et al., 2006); hence used as controls. Filled circles with black border represent significantly increased chaperone binding. Correlations by Pearson coefficient of determination, R^2 .

(I) Clustering analysis based on chaperone interaction profile similarity.

(J) Validation by co-immunoprecipitation (co-IP). LUMIER scores are shown below the blots.

See also Figure S2.

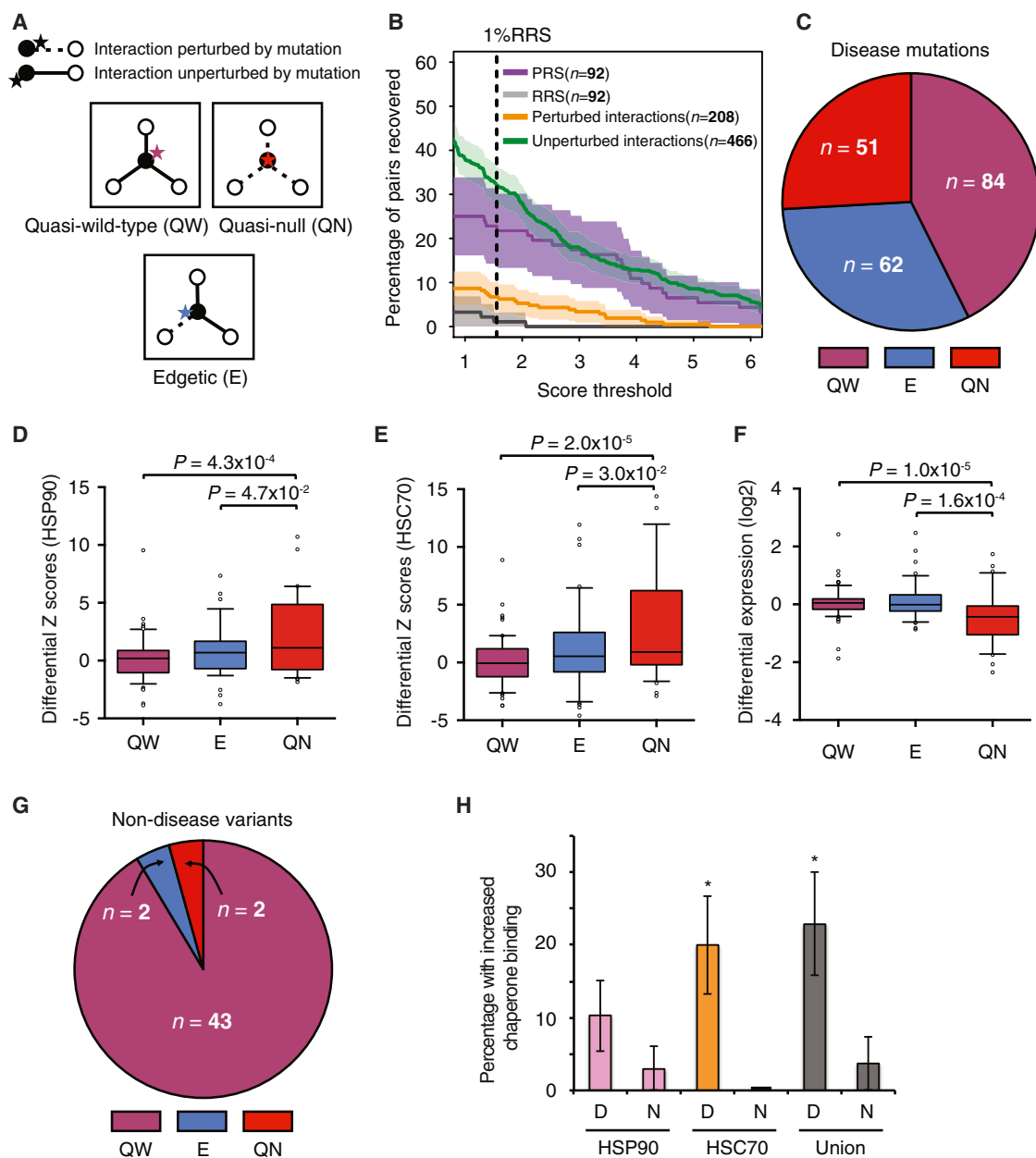


Figure 4. Interaction Perturbation Profiles Distinguish Disease Mutations from Non-Disease Variants

(A) Three classes of PPI profiles (edgotypes) for mutations.

(B) Percentage of protein pairs recovered in GPCA at increasing score thresholds. Shading indicates SE of the proportion.

(C) Distribution of different edgotypes for disease mutations.

(D and E) Differential LUMIER interaction scores among different edgotypes, for binding to HSP90 (D) and HSC70 (E). p values by one-sided unpaired t test.

(F) Differential expression among different edgotypes (ELISA log2 ratio of mutant over WT). QW: $n = 75$, E: $n = 49$, QN: $n = 42$. p values by one-sided Wilcoxon rank sum test.

(G) Distribution of different edgotypes for non-disease variants.

(H) Increased binding to HSP90, HSC70, or either (Union) for non-disease (N) or disease (D) variant proteins. p values by one-sided Fisher's exact test. Error bars indicate SE of the proportion. * $p < 0.05$.

See also Figures S4 and S5.

disease mutations annotated by ClinVar (Landrum et al., 2014) and found the distribution of quasi-null, edgetic, and quasi-WT alleles was statistically indistinguishable from that of HGMD (Figure S4G). We only identified two mutations that conferred PPI gains, suggesting that gain of interactions may be a rare event in human disease.

Protein Folding and Expression Levels of Edgetic Mutations

Differences between edgotypes classes could be due to protein folding and/or relative expression levels. Quasi-null proteins associated significantly more with cytoplasmic, but not ER, chaperones, whereas edgetic and quasi-WT proteins did not significantly change their chaperone association (Figures 4D–4E, and S5A–S5E). Quasi-null proteins appeared to be poorly expressed, while edgetic and quasi-WT proteins were expressed at levels similar to those of their WT controls (Figure 4F). We validated several mutant-chaperone interactions and expression profiles by co-immunoprecipitation with endogenous chaperones, followed by western blot (Figure S5F). All tested quasi-null proteins exhibited more binding to HSP90 and HSC70, although they were expressed at lower levels than their WT controls. However, the edgetic TAT-P220S protein and the quasi-WT NCF2-R395W protein did not show any detectable chaperone association. Among mutant proteins with no change in chaperone binding, edgetic (28%) and quasi-WT (57%) proteins comprised the majority, while quasi-null proteins comprised a significantly lower percentage (15%) (Figure S5G). Altogether, these results suggest that quasi-null proteins are more often unstable/misfolded and diminished in their steady-state expression levels. In contrast, edgetic and quasi-WT proteins likely exhibit normal folding and expression levels, further supporting the idea that they may cause disease through interaction perturbations or other mechanisms rather than simple loss of protein function.

Disease-Causing Mutations Versus Common Variants

Genome-wide association studies have identified hundreds of loci linked to particular disorders. However, these loci often contain several genes and multiple variants, making it challenging to distinguish causal mutations from non-pathogenic variants. We observed previously that among binary interactions found by WT proteins, disease-causing alleles were more likely to perturb interactions than non-disease variants (Rolland et al., 2014). We further investigated both disease-causing alleles from HGMD and common variants identified in healthy individuals from diverse geographical sites (1000 Genomes Project Consortium, 2012) (Table S1A) with respect to the edgetic character and chaperone binding of their protein products. Interaction profiling showed that only a small fraction of non-disease alleles lost interactions (8%, Figure 4G), a 7-fold reduction relative to disease mutations (57%; $p = 1.7 \times 10^{-9}$; Figure 4C). In addition, non-disease alleles on average did not alter chaperone association (Table S2A), a characteristic distinct from disease mutations annotated by HGMD (Figure 4H) or ClinVar (Figure S5H). Together, interaction perturbations can help distinguish disease-associated alleles from non-disease alleles.

To assess the predictive power of edgotyping to identify disease-causing mutations, we determined its precision and sensitivity in classifying an allele as causal based on interaction perturbation profiles. As a “gold standard” for causal alleles, we used a set of mutations annotated in HGMD as disease-causing (“DM” in Table S1A). As a negative control, we used a set of alleles most likely not associated with disease. We observed that 96% (105 of 109) of the alleles found to perturb interactions (E or QN)

were disease-causing (Figure S6A). Conversely, 61% (105 of 172) of disease-causing mutations annotated by HGMD were interaction-perturbing (Figure S6B). Together, our prediction achieved a precision (96%) and sensitivity (61%) significantly higher than random expectation. It is possible that current incompleteness of interaction network maps might limit the power of edgotyping to properly classify disease-causing mutations. To evaluate this possibility, we performed a down-sampling analysis and found negligible effect on mutation classification over a broad range of network sizes (Figure S6C).

Edgetic Mutations and Interaction Interfaces

To explore edgotypes from a structural point-of-view, we assessed the possible impact of distinct classes of mutations on protein function using PolyPhen-2 analysis (Adzhubei et al., 2010). Interaction-perturbing mutations are significantly more often predicted to be deleterious than non-interaction-perturbing mutations (Figure 5A). We next investigated whether mutations from the different classes might differ in evolutionary conservation, based on the presumption that conservation of amino acid residues is a property that generally reflects functionality (1000 Genomes Project Consortium, 2012; Subramanian and Kumar, 2006; Sunyaev, 2012). The residues affected by interaction-perturbing mutations are significantly more conserved across species compared to non-interaction-perturbing mutations (Figure S6D). However, PolyPhen and conservation analysis could not distinguish between edgetic and quasi-null mutations within the interaction-perturbing group.

Given that structural domains often mediate protein interactions, different classes of mutation might vary in their locations relative to protein domains. Interaction-perturbing mutations are indeed significantly enriched within structural domains compared to non-interaction-perturbing alleles (Figure 5B and Table S1C). In addition to structural domains, intrinsically disordered regions and linear motifs could also play a role in mediating PPIs. However, we found interaction-perturbing disease alleles to be depleted in intrinsically disordered regions (Figure S6E), and occurring in linear motifs as frequently as non-perturbing alleles (Figure S6F). These results suggest that mutations perturbing PPIs are preferentially located within structural domains. Nevertheless, none of the above properties could reliably predict whether a mutation would give rise to an edgetic or quasi-null PPI effect.

We next investigated whether edgetic and quasi-null mutations differ in their physical location within three-dimensional protein structures (Zhong et al., 2009). Edgetic mutations are significantly more enriched in structurally exposed residues compared to quasi-null mutations (Figure 5C). Consistently, edgetic mutations do not tend to cause a change in hydrophobicity, a destabilizing feature that generally disrupts protein function (Balasubramanian et al., 2005), while quasi-null mutations often lead to a decrease in hydrophobicity (Figure S6G).

We also investigated whether or not edgetic mutations are more frequently located at an interface that supports interaction with a partner protein. Starting from all available structures of co-crystal complexes in the Protein Data Bank (PDB) involving a disease gene product, we determined the relative location of each mutated residue within these structures (Extended Experimental

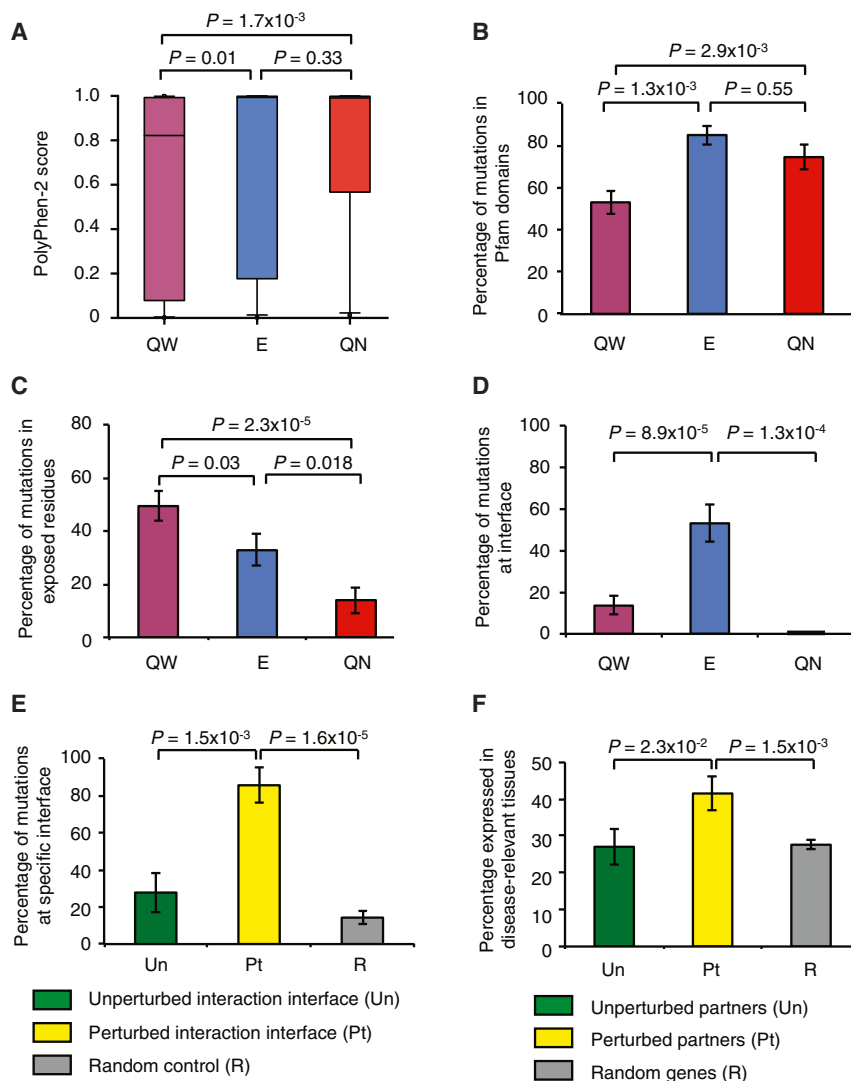


Figure 5. Edgetic Mutations Perturb Interaction Interfaces with Protein Partners Expressed in Disease-Relevant Tissue

(A) PolyPhen-2 scores for mutations in different edgotype classes. p values by one-sided Wilcoxon rank sum test. (B) Percentage of mutations within Pfam domains. p values by one-sided position-shuffling test. (C) Percentage of mutations in exposed residues. QW: n = 83; E: n = 61; QN: n = 50. (D) Percentage of mutations at PPI interfaces. QW: n = 59; E: n = 32; QN: n = 16. (E) Percentage of interfacial mutations for perturbed (n = 14) and unperturbed (n = 18) interactions, compared to random mutations. (F) Percentage of perturbed (n = 118) and unperturbed (n = 85) interactors expressed in disease relevant tissues. Thirty random genes from RNA-Seq dataset are assessed for each disease gene. p values from (C) to (F) by one-sided Fisher's exact test. Error bars (B) to (F), SE of the proportion. See also Figure S5.

ease-relevant tissues compared with unperturbed interactors or random genes (Figures 5F and S6H; Table S5B). These results indicate that disease mutations most often perturb interactions that are functionally relevant in the particular tissue(s) affected by a specific disease.

Distinct Interaction Perturbations May Underlie Diverse Disease Phenotypes

Our edgotyping model suggests that different mutations in the same gene may result in different, pleiotropic phenotypic outcomes through perturbation of distinct interactions (Figure 6A). To test this, we compared mutation edgotype

Procedures and Table S5A). In contrast to quasi-null mutations, edgetic mutations are significantly enriched at interaction interfaces identified from the corresponding co-crystal structures (Figure 5D). Notably, edgetic mutations also exhibit a significant tendency to reside at interaction interfaces with the perturbed partners, as compared to unperturbed partners or random controls (Figure 5E). These results suggest that edgetic mutations are preferentially located at PPI interfaces, perturbing the corresponding interaction.

Edgetic Mutations Perturb Interactions with Protein Partners Expressed in Disease-Relevant Tissues

We hypothesized that protein interaction partners perturbed by edgetic mutations are likely to function together within the tissue known to be affected by the relevant disease. To test this, we compared gene expression patterns for perturbed and unperturbed partners in disease-relevant tissues using RNA-seq data from the Illumina Human Body Map 2.0 project. Perturbed interactors exhibit a striking tendency to be expressed in dis-

classes and the resulting disease phenotypes. Among pleiotropic genes associated with two or more diseases, mutant alleles associated with different disease manifestations were more likely to exhibit different edgotype classes of perturbed PPI profiles (Table S5C).

This is exemplified by mutations in *TPM3*, which encodes slow muscle alpha-tropomyosin. Three *TPM3* edgetic mutations L100M, R168G, and R245G are associated with fiber-type disproportion myopathy through an unknown mechanism (Adzhubei et al., 2010; Clarke et al., 2008) (Figure 6B). These edgetic mutations perturb five of the ten interaction partners of the WT gene product. The majority of perturbed partners are expressed in muscle, the tissue most relevant to this disease (Figure 6C). One of the disrupted interactions is the interaction between *TPM3* and troponin, which was shown to be vital for the transduction of calcium-induced signals required for muscle contraction (Gunning et al., 1990). Two other perturbed interactors, HSF2, involved in myotube regeneration (McArdle et al., 2006), and CCHCR1, required for cytoskeleton organization (Tervaniemi

et al., 2012), could also be of disease relevance. In contrast to these edgetic mutations, the quasi-WT mutation M9R causes a different disease, nemaline myopathy. M9R might affect actin binding, thus leading to the formation of abnormal nemaline rods (Laing et al., 1995).

The possible disease relevance of our approach was further illustrated by edgetic mutations in the gene *EFHC1*, mutations in which can cause epilepsy. One perturbed partner, ZBED1, plays a role in a major cell proliferation pathway affected by *EFHC1* knockouts (Yamashita et al., 2007), while another perturbed interactor, TCF4, is required for neuronal differentiation (Flora et al., 2007) (Figure 6D).

We next reasoned that mutations perturbing a greater number of interactions would be likely to have a larger impact on protein function, and hence result in more severe phenotypic effects. We used the age of disease onset as a proxy for severity and determined whether an increase in the fraction of interactions lost correlated with an increase in severity for each pair of mutations causing the same disease (as annotated by HGMD) (Figure 6E and Table S5D). We found that mutations perturbing more PPIs were associated with an earlier age of disease onset significantly more often than random expectation (Figure 6E). Although computational predictions based on PolyPhen-2 were able to distinguish between interaction-perturbing versus non-perturbing alleles (Figure 5A), they did not perform as well as our approach in predicting disease severity (Figure S6I). This limitation is consistent with the inability of PolyPhen-2 to distinguish between edgetic and quasi-null mutations (Figure 5A).

Protein-DNA Interactions

We hypothesized that mutations for which no PPI perturbation has yet been detected likely cause changes in other types of molecular interactions. As a proof-of-concept, we examined the effect of disease mutations on protein-DNA interactions (PDIs) between human transcription factors (TFs) (Reece-Hoyes et al., 2011a) and developmental enhancers (Fuxman Bass et al., 2015). Our hmORFeome1.1 mutant library contains 70 TF ORFs altogether harboring 173 mutations (Table S6A). A primary screen using enhanced yeast-one hybrid (eY1H) assays (Reece-Hoyes et al., 2011b) identified PDIs between 152 enhancers (Visel et al., 2007) and 28 WT TFs (Figure 1C and Extended Experimental Procedures). We then performed pairwise assays to compare the PDIs of mutant TFs and their WT counterparts in eY1H assays (Table S6B).

Using systematic PDI profiling, we determined edgotype classes for 58 mutations in 22 TFs that bound at least two enhancers. We identified 38% of the mutations as quasi-null, 43% as edgetic (loss or gain of interaction), and 19% as quasi-WT (Figure 7A). More than 80% of TF missense disease mutations tested either abrogated DNA binding or caused partial change of PDIs. Interestingly, almost half of the mutations are edgetic, challenging the assumption that TF mutations that affect DNA binding do so in a similar fashion across their targets. Among these, a significant fraction of mutations exhibit gain of PDIs, likely because these mutations cause a reduction in DNA-binding specificity and allow greater promiscuity in target recognition.

Given that TFs interact with their DNA targets through DNA-binding domains (DBDs), we assessed whether disease muta-

tions perturbing PDIs are enriched within DBDs. Mutations within versus outside DBDs exhibited strikingly different PDI perturbation patterns ($p = 1.1 \times 10^{-3}$; Figure 7B and Table S6C). Among quasi-null mutations, the proportion of mutations within DBDs was ~10-fold higher than outside DBD regions. These results confirm that most PDI perturbing mutations reside within the DBDs of proteins, further supporting the quality and validity of our PDI perturbation data.

Mutations within the same TF that cause different PDI changes would affect the expression of different targets, resulting in different diseases. We examined disease-causing TF mutations in pleiotropic genes associated with two or more diseases. Mutations with different PDI edgotype classes were likely to be associated with different clinical manifestations (Figure 7C), consistent with our results for PPI perturbations (Figure 6A).

Of the disease mutations for which both PPI and PDI data were available, about half did not perturb any PPIs (Figure 7D). Interestingly, for ~80% of these we did identify PDI perturbations. For instance, mutations in the TGF- β -induced transcription factor *TGIF1* cause holoprosencephaly (Gripp et al., 2000). While the two mutant variants S28C and P63R are still able to bind their protein partners CTBP1 and CTBP2 (quasi-WT for PPI), both mutations completely abrogated the ability of TGIF1 to bind any of the tested DNA targets (quasi-null for PDI) (Figure S7A). Clearly, integrating different types of molecular interactions will enhance our ability to understand specific mechanisms that underlie many genetic disorders.

To gain further insights into alternative molecular interaction perturbations, we computationally examined the effect of disease mutations on protein-chemical interactions (Reva et al., 2011). We found that the frequency with which disease mutations are at protein-chemical interfaces is significantly higher than that of non-disease variants (Figure S7B). In addition, disease mutations that perturb PPIs have no discernable tendency to locate at protein-chemical interfaces (Figure S7C), suggesting that protein-protein and protein-chemical interfaces do not tend to overlap. Interestingly, ~13% of PPI non-perturbing mutations are located at protein-chemical interfaces, supporting the conclusion that these mutations could cause disease through perturbation of alternative types of molecular interactions.

We combined computational predictions and interaction profiling to optimize our performance in disease mutation stratification. Although computational methods such as PolyPhen-2 could predict interaction-perturbing alleles as deleterious (Figure 5A), they fail to explain many disease-causing mutations, and misclassify them as “benign” (Figure S7D). Among these misclassified mutations, ~50% could be explained by molecular interaction perturbations (PCI, PPI, or PDI). For instance, the S140F mutation in *PKP2* encoding the adhesion protein plakophilin leads to arrhythmogenic right ventricular dysplasia (Gerull et al., 2004). While PolyPhen-2 predicts S140F as benign, the S140F mutant exhibited increased binding to the chaperones HSC70 and BAG2, and lost all the PPIs of the WT protein (Table S7A). All together, existing computational methods alone fail to precisely predict disease causality. Examining different types of molecular interaction perturbations is critical for a full comprehension of disease-causing mutations in human.

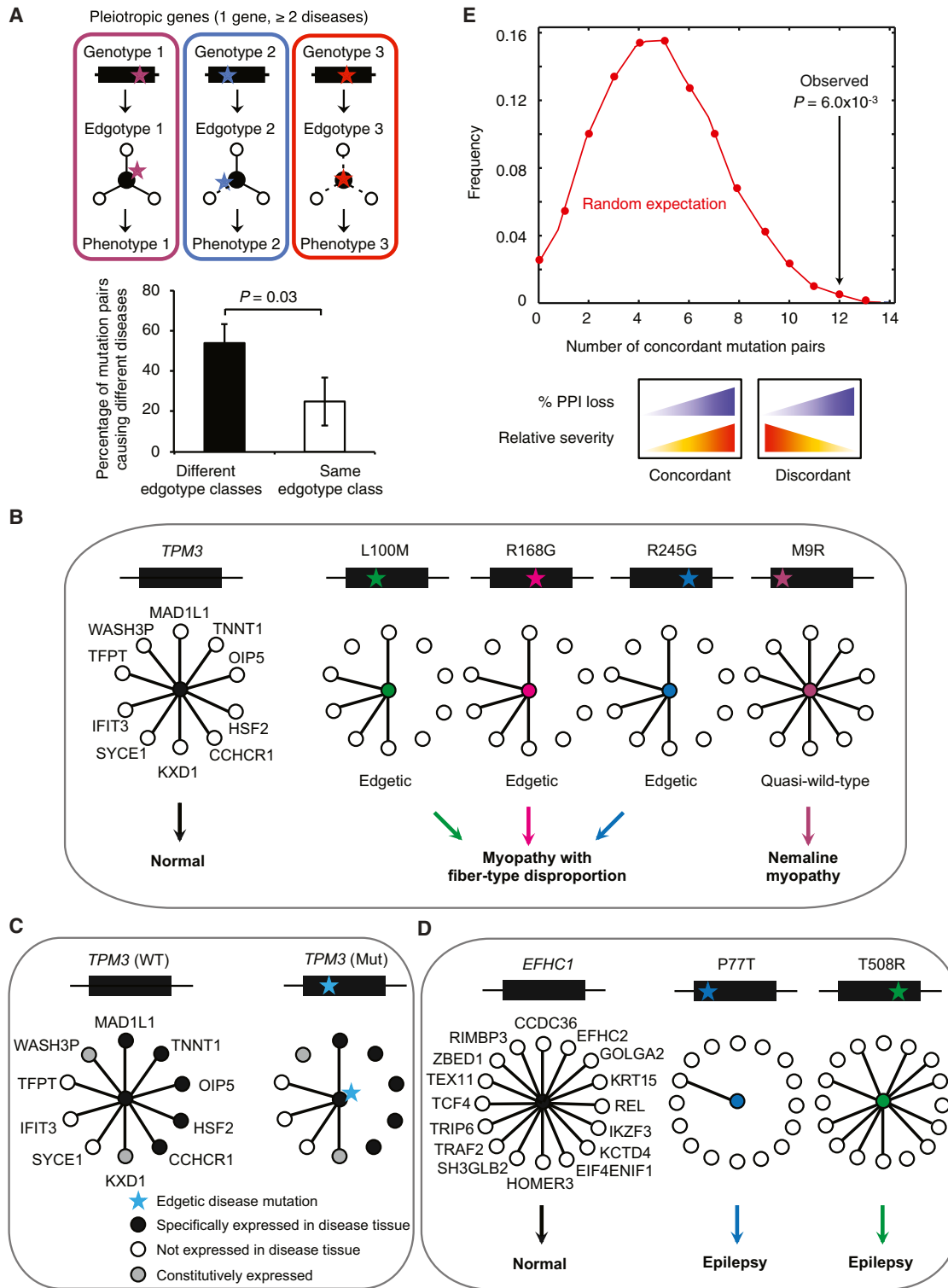


Figure 6. Heterogeneous Genetic Mutations Give Rise to Diverse Disease Outcomes through Distinct Interaction Perturbations

(A) Schematic of pleiotropic disease outcomes resulting from distinct interaction patterns (edgotypes) caused by distinct mutations. Percentage of mutation pairs causing different diseases out of all pairs with different or the same edgotypes classes is shown. $n = 52$. Error bars, SE of the proportion. p values by one-sided Fisher's exact test.

(B) Example of edgotyping four disease mutations in the pleiotropic gene *TPM3*.

(legend continued on next page)

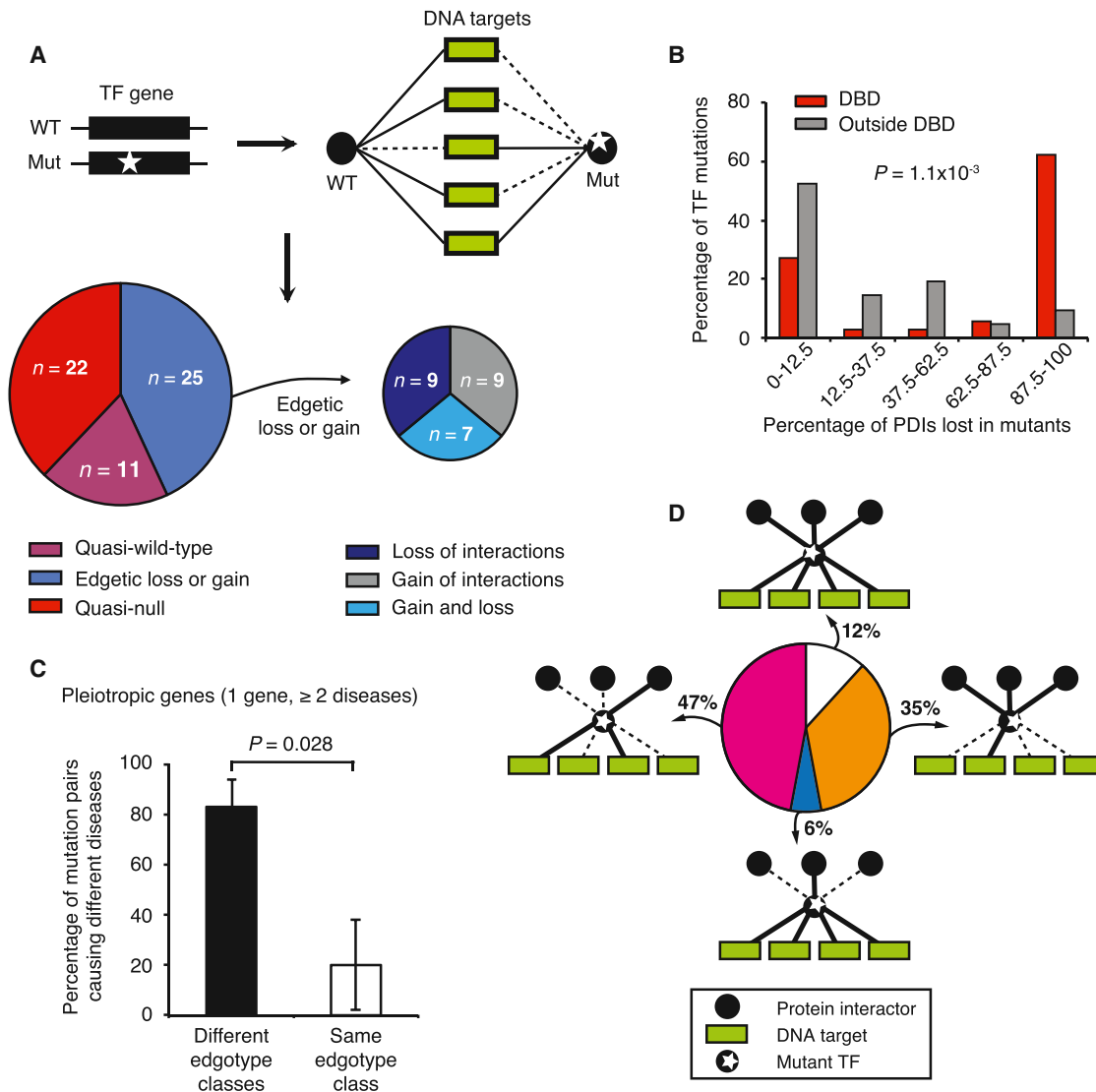


Figure 7. Integration of Protein-Protein and Protein-DNA Interaction Perturbations

(A) PDI edgotype distribution for disease mutations in 22 TFs that bind to more than one enhancer.

(B) Histogram showing percentage of mutations within and outside DBDs as a function of the percentage of PDI loss. Numbers on x axis indicate bin range. p values by one-sided Wilcoxon rank sum test.

(C) Percentage of TF mutation pairs that cause different diseases out of all pairs with different or the same PDI edgotype classes ($n = 17$). Error bars, SE of the proportion. p values by one-sided Fisher's exact test.

(D) PPI-PDI integration enables mutation characterization at higher resolution. Percentage of mutations is shown for: PPI and PDI unperturbed; PPI unperturbed and PDI perturbed; PPI perturbed and PDI unperturbed; and PPI and PDI perturbed in the integrated network.

See also Figure S7.

DISCUSSION

In this systematic characterization of mutations across various human Mendelian disorders, we have found surprisingly wide-

spread disease-specific perturbations of macromolecular interactions. Approximately 60% of disease-associated missense mutations perturb PPIs, among which half result in complete loss of interactions, generally caused by protein misfolding and

(C) Most perturbed partners of TPM3 are expressed in the disease-relevant tissue.

(D) Edgetic mutations in *EFHC1* perturb epilepsy-related protein partners.

(E) Correlation between the fraction of PPI perturbation and age of onset for mutation pairs causing the same disease. p values by comparing the observed value to 100,000 random controls ($n = 13$; Extended Experimental Procedures).

See also Figure S6.

impaired expression, and the other half lead to edgetic perturbations. Importantly, different mutations in the same gene frequently result in different interaction perturbation profiles. This strongly suggests that the “edgotype” of a mutation represents a fundamental link between genotype and phenotype.

Our systematic edgotyping strategy provides a practical approach to classifying candidate disease alleles emerging from genome-wide association studies and from sporadic and somatic mutation sequencing approaches. Edgotyping achieves a high precision in identifying candidate disease-causing mutations based on the interaction perturbations relative to WT alleles (Figure S6A). However, the overall sensitivity of an edgotyping approach is compromised due to the false negative rate inherent to the assays used. We expect that a significant fraction of variants currently viewed as non-interaction-perturbing (quasi-WT) will eventually be proven to be edgetic and possibly cause disease. This circumstance likely arises from the incomplete nature of current human interactome network maps (Rolland et al., 2014). Nevertheless, because edgetic mutations cannot become quasi-WT or quasi-null even as interactome maps improve, our estimate of edgetic mutations already provides a reliable minimum lower bound for their frequency.

An alternative possibility is that quasi-WT mutations affect disease phenotypes through perturbation of different types of molecular interactions. Biological signaling is regulated at multiple levels, and various types of molecular interactions are involved (Sahni et al., 2013) as we have shown for PPI and PDI networks. In addition, protein-RNA (Lee et al., 2006) and protein-metabolite (Carpten et al., 2007) interactions have also been shown to be involved in disease. Perturbations of these alternative interaction networks will undoubtedly result in distinct disease consequences. One can envision that integration of additional types of interaction perturbation information with computational predictions will be necessary for a complete understanding of the cellular networks governing a particular disease state (Figure S7D). As a major benefit, perturbed interactions spotlight specific targets and pathways that are altered in a patient-specific context. This type of information could provide a much-needed guide in efforts to developing better diagnostic tools and more personalized medical treatments.

EXPERIMENTAL PROCEDURES

Using ORFs in the human ORFeome v8.1 collection as template, we PCR amplified the two DNA fragments flanking the mutations, followed by a fusion PCR to stitch the fragments together. The resulting fusion ORFs harboring the mutations were Gateway cloned into the Donor vector pDONR223 to derive Entry clones (Rual et al., 2004), which were subsequently verified by next-generation sequencing (Yang et al., 2011).

Interaction with chaperones and other QCFs was performed using a quantitative LUMIER assay (Taipale et al., 2012; Taipale et al., 2014). All wild-type and mutant allele clones were transferred via Gateway recombination into a mammalian expression vector containing a C-terminal 3xFLAG-V5 tag. Stable HEK293T cell lines expressing luciferase-QCF fusion proteins were generated by lentiviral infection, and plasmids carrying wild-type and disease mutation alleles were transfected into the stable HEK293T lines (Taipale et al., 2012). Following capture of FLAG-tagged proteins, luminescence was measured to determine QCF-target interaction. Following luminescence measurement, FLAG-tagged mutant and wild-type proteins were detected as described (Taipale et al., 2012).

We performed a binary protein-protein interaction screen for all mutant and wild-type alleles as baits against ~7,200 human prey proteins (Rual et al., 2004). The identified interactions were combined with the known pairs cataloged by the human binary interaction dataset HI-II-14 (Rolland et al., 2014). All first-pass pairs from the primary Y2H screens were subjected to pairwise testing in which all interactors of any allele of a gene were then tested against all alleles of that gene. The resulting verified protein-protein interaction profiles of disease mutants were compared with their wild-type counterparts. We validated perturbed and unperturbed interactions from mutation-mediated interaction perturbation data (“edgotyping” data) using an orthogonal in vivo *Gaussia princeps* luciferase protein complementation assay (GPCA). Human HEK293T cells were co-transfected with each construct expressing complementary fragments of the *Gaussia* luciferase fused in frame with the tested protein pairs and luciferase activity was measured as described (Cassonnet et al., 2011).

An enhanced yeast one-hybrid (eY1H) assay was used to detect binary protein-DNA interactions (PDIs) between a DNA bait and a protein prey (Reece-Hoyes et al., 2011a; Reece-Hoyes et al., 2011b). DNA baits corresponding to human enhancers were retrieved from the Vista Enhancer Browser (<http://enhancer.lbl.gov>) (Visel et al., 2007). Protein preys were a set of TFs for which mutant clones are available in our human mutation ORFeome version 1.1. We performed pairwise eY1H assays of an arrayed collection of TF preys comprising all the wild-type TFs and their mutant clones against 152 available enhancer baits.

Disease-causing mutations were annotated by HGMD, and the deleteriousness of amino acid substitutions was predicted by PolyPhen-2 program (Adzhubei et al., 2010). For structural features, distinct mutations were compared with respect to protein domains from the Pfam database, and interaction interfaces on co-crystal structures from PDB. Tissue-specific gene expression was analyzed with normalized RNA-seq data from Human Body Map 2.0 (GSE30611). Network properties analyzed included betweenness centrality, k-core centrality, degree, and closeness centrality (de Nooy et al., 2005).

Full details are provided in the [Extended Experimental Procedures](#).

SUPPLEMENTAL INFORMATION

Supplemental Information includes Extended Experimental Procedures, seven figures, and seven tables and can be found with this article online at <http://dx.doi.org/10.1016/j.cell.2015.04.013>.

AUTHOR CONTRIBUTIONS

M.V., S.L., L.J.W., D.E.H., and K.S.-A. conceived the project. N.S., S.Y., M.T., and J.I.F.B. designed and performed experiments, with help from G.I.K., I.K., M.H.L., Q.Z., A.P., D.B., A.D., J.M.W., A.A.S., X.Y., A.K.S., and Y.J. J.C.-H., F.Y., J.P., J.W., Y.W., I.A.K., and T.H. performed computational analyses with contributions from N.S., S.Y., M.T., J.I.F.B., A.K., G.T., V.K., A.S., Y.-Y.L., Y.S., A.S.-M., C.F., D.M.J., A.L., and B.C. V.K., Y.J., N.Y., M.E.C., M.A.C., S.S., B.B., L.J.W., B.C., and D.E.H. provided constructive feedback. M.A.C., S.S., B.B., D.E.H., A.-L.B., T.H., F.P.R., Y.X., A.J.M.W., S.L., and M.V. supervised research and provided critical advice on the study. N.S., S.Y., M.T., J.I.F.B., J.C.-H., M.A.C., B.C., D.E.H., F.P.R., Y.X., A.J.M.W., S.L., and M.V. wrote the manuscript, with contributions from other co-authors.

ACKNOWLEDGMENTS

We thank the members of the DFCI Center for Cancer Systems Biology (CCSB) for valuable discussions and acknowledge A.A. Chen, M. Koeva, and E. Guney for helpful suggestions. This work was supported by NHGRI (P50HG004233 to M.V., F.P.R. and A.-L.B.; RC4HG006066 to M.V., T.H., D.E.H., K.S.-A., L.J.W., and S.L.; and R01HG001715 to M.V., D.E.H., and F.P.R.), NIGMS (GM082971 to A.J.M.W.), NSF (CCF-1219007 to Y.X.), NSERC (RGPIN-2014-03892 to Y.X.), and the Krembil Foundation, a Canada Excellence Research Chair, an Ontario Research Fund–Research Excellence Award awarded to F.P.R. J.I.F.B. is supported by a Pew Latin American Fellowship. A.K. is supported by an EMBO Long-Term Fellowship. S.L. is an investigator

of the Howard Hughes Medical Institute. M.V. is a Chercheur Qualifié Honoraire from the Fonds de la Recherche Scientifique (FRS-FNRS, Wallonia-Brussels Federation).

Received: December 15, 2014

Revised: March 5, 2015

Accepted: April 6, 2015

Published: April 23, 2015

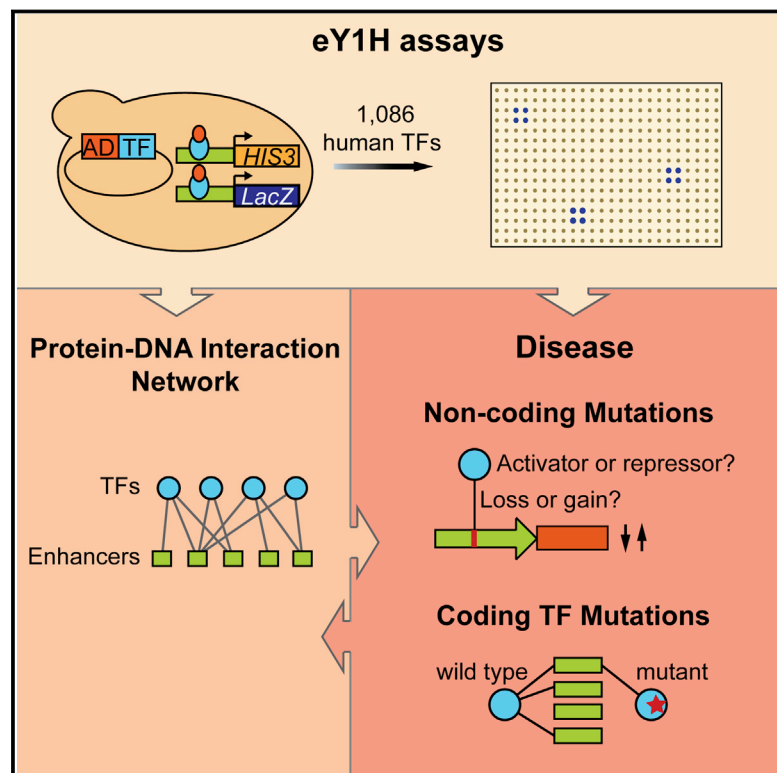
REFERENCES

- 1000 Genomes Project Consortium, Abecasis, G.R., Auton, A., Brooks, L.D., DePristo, M.A., Durbin, R.M., Handsaker, R.E., Kang, H.M., Marth, G.T., and McVean, G.A. (2012). An integrated map of genetic variation from 1,092 human genomes. *Nature* 491, 56–65.
- Adzhubei, I.A., Schmidt, S., Peshkin, L., Ramensky, V.E., Gerasimova, A., Bork, P., Kondrashov, A.S., and Sunyaev, S.R. (2010). A method and server for predicting damaging missense mutations. *Nat. Methods* 7, 248–249.
- Amberger, J., Bocchini, C., and Hamosh, A. (2011). A new face and new challenges for Online Mendelian Inheritance in Man (OMIM). *Hum. Mutat.* 32, 564–567.
- Balasubramanian, S., Xia, Y., Freinkman, E., and Gerstein, M. (2005). Sequence variation in G-protein-coupled receptors: analysis of single nucleotide polymorphisms. *Nucleic Acids Res.* 33, 1710–1721.
- Braun, P., Tasan, M., Dreze, M., Barrios-Rodiles, M., Lemmens, I., Yu, H., Sahalie, J.M., Murray, R.R., Roncari, L., de Smet, A.-S., et al. (2009). An experimentally derived confidence score for binary protein-protein interactions. *Nat. Methods* 6, 91–97.
- Carpten, J.D., Faber, A.L., Horn, C., Donoho, G.P., Briggs, S.L., Robbins, C.M., Hostetter, G., Boguslawski, S., Moses, T.Y., Savage, S., et al. (2007). A transforming mutation in the pleckstrin homology domain of AKT1 in cancer. *Nature* 448, 439–444.
- Cassonnet, P., Rolloy, C., Neveu, G., Vidalain, P.O., Chantier, T., Pellet, J., Jones, L., Muller, M., Demeret, C., Gaud, G., et al. (2011). Benchmarking a luciferase complementation assay for detecting protein complexes. *Nat. Methods* 8, 990–992.
- Chin, L., Hahn, W.C., Getz, G., and Meyerson, M. (2011). Making sense of cancer genomic data. *Genes Dev.* 25, 534–555.
- Clarke, N.F., Kolski, H., Dye, D.E., Lim, E., Smith, R.L., Patel, R., Fahey, M.C., Bellance, R., Romero, N.B., Johnson, E.S., et al. (2008). Mutations in TPM3 are a common cause of congenital fiber type disproportion. *Ann. Neurol.* 63, 329–337.
- de Nooy, W., Mrvar, A., and Batagelj, V. (2005). *Exploratory Social Network Analysis with Pajek* (Cambridge University Press).
- Falsone, S.F., Leptihn, S., Osterauer, A., Haslbeck, M., and Buchner, J. (2004). Oncogenic mutations reduce the stability of SRC kinase. *J. Mol. Biol.* 344, 281–291.
- Flora, A., Garcia, J.J., Thaller, C., and Zoghbi, H.Y. (2007). The E-protein Tcf4 interacts with Math1 to regulate differentiation of a specific subset of neuronal progenitors. *Proc. Natl. Acad. Sci. USA* 104, 15382–15387.
- Fuxman Bass, J.I., Sahni, N., Shrestha, S., Garcia-Gonzalez, A., Mori, A., Bhat, N., Yi, S., Hill, D.E., Vidal, M., and Walhout, A.J.M. (2015). Human Gene-Centered Transcription Factor Networks for Enhancers and Disease Variants. *Cell* 161, this issue, 661–673.
- Gerull, B., Heuser, A., Wichter, T., Paul, M., Basson, C.T., McDermott, D.A., Lerman, B.B., Markowitz, S.M., Ellinor, P.T., MacRae, C.A., et al. (2004). Mutations in the desmosomal protein plakophilin-2 are common in arrhythmic right ventricular cardiomyopathy. *Nat. Genet.* 36, 1162–1164.
- Goh, K.I., Cusick, M.E., Valle, D., Childs, B., Vidal, M., and Barabási, A.L. (2007). The human disease network. *Proc. Natl. Acad. Sci. USA* 104, 8685–8690.
- Gripp, K.W., Wotton, D., Edwards, M.C., Roessler, E., Ades, L., Meinecke, P., Richieri-Costa, A., Zackai, E.H., Massagué, J., Muenke, M., and Elledge, S.J. (2000). Mutations in TGIF cause holoprosencephaly and link NODAL signalling to human neural axis determination. *Nat. Genet.* 25, 205–208.
- Guerois, R., Nielsen, J.E., and Serrano, L. (2002). Predicting changes in the stability of proteins and protein complexes: a study of more than 1000 mutations. *J. Mol. Biol.* 320, 369–387.
- Gunning, P., Gordon, M., Wade, R., Gahlmann, R., Lin, C.S., and Hardeman, E. (1990). Differential control of tropomyosin mRNA levels during myogenesis suggests the existence of an isoform competition-autoregulatory compensation control mechanism. *Dev. Biol.* 138, 443–453.
- Hindorff, L.A., Sethupathy, P., Junkins, H.A., Ramos, E.M., Mehta, J.P., Collins, F.S., and Manolio, T.A. (2009). Potential etiologic and functional implications of genome-wide association loci for human diseases and traits. *Proc. Natl. Acad. Sci. USA* 106, 9362–9367.
- Huntley, R.P., Sawford, T., Mutowo-Muilenet, P., Shypitsyna, A., Bonilla, C., Martin, M.J., and O'Donovan, C. (2015). The GOA database: gene Ontology annotation updates for 2015. *Nucleic Acids Res.* 43, D1057–D1063.
- Köllner, I., Sodeik, B., Schreek, S., Heyn, H., von Neuhoof, N., Germeshausen, M., Zeidler, C., Krüger, M., Schlegelberger, B., Welte, K., and Beger, C. (2006). Mutations in neutrophil elastase causing congenital neutropenia lead to cytoplasmic protein accumulation and induction of the unfolded protein response. *Blood* 108, 493–500.
- Laing, N.G., Wilton, S.D., Akkari, P.A., Dorosz, S., Boundy, K., Kneebone, C., Blumbergs, P., White, S., Watkins, H., Love, D.R., et al. (1995). A mutation in the alpha tropomyosin gene TPM3 associated with autosomal dominant nemaline myopathy. *Nat. Genet.* 9, 75–79.
- Landrum, M.J., Lee, J.M., Riley, G.R., Jang, W., Rubinstein, W.S., Church, D.M., and Maglott, D.R. (2014). ClinVar: public archive of relationships among sequence variation and human phenotype. *Nucleic Acids Res.* 42, D980–D985.
- Lee, Y., Hur, I., Park, S.Y., Kim, Y.K., Suh, M.R., and Kim, V.N. (2006). The role of PACT in the RNA silencing pathway. *EMBO J.* 25, 522–532.
- Lesage, S., and Brice, A. (2009). Parkinson's disease: from monogenic forms to genetic susceptibility factors. *Hum. Mol. Genet.* 18 (R1), R48–R59.
- McArdle, A., Broome, C.S., Kayani, A.C., Tully, M.D., Close, G.L., Vasilaki, A., and Jackson, M.J. (2006). HSF expression in skeletal muscle during myogenesis: implications for failed regeneration in old mice. *Exp. Gerontol.* 41, 497–500.
- Reece-Hoyes, J.S., Barutcu, A.R., McCord, R.P., Jeong, J.S., Jiang, L., MacWilliams, A., Yang, X., Salehi-Ashtiani, K., Hill, D.E., Blackshaw, S., et al. (2011a). Yeast one-hybrid assays for gene-centered human gene regulatory network mapping. *Nat. Methods* 8, 1050–1052.
- Reece-Hoyes, J.S., Diallo, A., Lajoie, B., Kent, A., Shrestha, S., Kadreppa, S., Pesyna, C., Dekker, J., Myers, C.L., and Walhout, A.J. (2011b). Enhanced yeast one-hybrid assays for high-throughput gene-centered regulatory network mapping. *Nat. Methods* 8, 1059–1064.
- Reva, B., Antipin, Y., and Sander, C. (2011). Predicting the functional impact of protein mutations: application to cancer genomics. *Nucleic Acids Res.* 39, e118.
- Rolland, T., Tasan, M., Charlotiaux, B., Pevzner, S.J., Zhong, Q., Sahni, N., Yi, S., Lemmens, I., Fontanillo, C., Mosca, R., et al. (2014). A proteome-scale map of the human interactome network. *Cell* 159, 1212–1226.
- Rual, J.F., Hirozane-Kishikawa, T., Hao, T., Bertin, N., Li, S., Dricot, A., Li, N., Rosenberg, J., Lamesch, P., Vidalain, P.O., et al. (2004). Human ORFeome version 1.1: a platform for reverse proteomics. *Genome Res.* 14 (10B), 2128–2135.
- Sahni, N., Yi, S., Zhong, Q., Jaikhan, N., Charlotiaux, B., Cusick, M.E., and Vidal, M. (2013). Edgotype: a fundamental link between genotype and phenotype. *Curr. Opin. Genet. Dev.* 23, 649–657.
- Schymkowitz, J., Borg, J., Stricher, F., Nys, R., Rousseau, F., and Serrano, L. (2005). The FoldX web server: an online force field. *Nucleic Acids Res.* 33, W382–W388.
- Shimamura, T., Lowell, A.M., Engelman, J.A., and Shapiro, G.I. (2005). Epidermal growth factor receptors harboring kinase domain mutations

- associate with the heat shock protein 90 chaperone and are destabilized following exposure to geldanamycins. *Cancer Res.* 65, 6401–6408.
- Sörgjerd, K., Ghafouri, B., Jonsson, B.H., Kelly, J.W., Blond, S.Y., and Hammarström, P. (2006). Retention of misfolded mutant transthyretin by the chaperone BiP/GRP78 mitigates amyloidogenesis. *J. Mol. Biol.* 356, 469–482.
- Stenson, P.D., Mort, M., Ball, E.V., Shaw, K., Phillips, A., and Cooper, D.N. (2014). The Human Gene Mutation Database: building a comprehensive mutation repository for clinical and molecular genetics, diagnostic testing and personalized genomic medicine. *Hum. Genet.* 133, 1–9.
- Subramanian, S., and Kumar, S. (2006). Evolutionary anatomies of positions and types of disease-associated and neutral amino acid mutations in the human genome. *BMC Genomics* 7, 306.
- Sunyaev, S.R. (2012). Inferring causality and functional significance of human coding DNA variants. *Hum. Mol. Genet.* 21 (R1), R10–R17.
- Taipale, M., Krykbaeva, I., Koeva, M., Kayatekin, C., Westover, K.D., Karras, G.I., and Lindquist, S. (2012). Quantitative analysis of HSP90-client interactions reveals principles of substrate recognition. *Cell* 150, 987–1001.
- Taipale, M., Tucker, G., Peng, J., Krykbaeva, I., Lin, Z.Y., Larsen, B., Choi, H., Berger, B., Gingras, A.C., and Lindquist, S. (2014). A quantitative chaperone interaction network reveals the architecture of cellular protein homeostasis pathways. *Cell* 158, 434–448.
- Tervaniemi, M.H., Siitonen, H.A., Söderhäll, C., Minhas, G., Vuola, J., Tiala, I., Sormunen, R., Samuelsson, L., Suomela, S., Kere, J., and Elomaa, O. (2012). Centrosomal localization of the psoriasis candidate gene product, CCHCR1, supports a role in cytoskeletal organization. *PLoS ONE* 7, e49920.
- Venkatesan, K., Rual, J.F., Vazquez, A., Stelzl, U., Lemmens, I., Hirozane-Kishikawa, T., Hao, T., Zenkner, M., Xin, X., Goh, K.I., et al. (2009). An empirical framework for binary interactome mapping. *Nat. Methods* 6, 83–90.
- Vidal, M., Cusick, M.E., and Barabási, A.L. (2011). Interactome networks and human disease. *Cell* 144, 986–998.
- Visel, A., Minovitsky, S., Dubchak, I., and Pennacchio, L.A. (2007). VISTA Enhancer Browser—a database of tissue-specific human enhancers. *Nucleic Acids Res.* 35, D88–D92.
- Whitesell, L., and Lindquist, S.L. (2005). HSP90 and the chaperoning of cancer. *Nat. Rev. Cancer* 5, 761–772.
- Yamashita, D., Sano, Y., Adachi, Y., Okamoto, Y., Osada, H., Takahashi, T., Yamaguchi, T., Osumi, T., and Hirose, F. (2007). hDREF regulates cell proliferation and expression of ribosomal protein genes. *Mol. Cell. Biol.* 27, 2003–2013.
- Yang, X., Boehm, J.S., Yang, X., Salehi-Ashtiani, K., Hao, T., Shen, Y., Lubonja, R., Thomas, S.R., Alkan, O., Bhimdi, T., et al. (2011). A public genome-scale lentiviral expression library of human ORFs. *Nat. Methods* 8, 659–661.
- Zhong, Q., Simonis, N., Li, Q.R., Charloteaux, B., Heuze, F., Klitgord, N., Tam, S., Yu, H., Venkatesan, K., Mou, D., et al. (2009). Edgetic perturbation models of human inherited disorders. *Mol. Syst. Biol.* 5, 321.

Human Gene-Centered Transcription Factor Networks for Enhancers and Disease Variants

Graphical Abstract



Authors

Juan I. Fuxman Bass, Nidhi Sahni, ...,
Marc Vidal, Albertha J.M. Walhout

Correspondence

marian.walhout@umassmed.edu

In Brief

A yeast one-hybrid approach assays what transcription factors bind to which human noncoding sequences and how binding patterns are influenced by mutations, including those associated with disease.

Highlights

- Different models for TF enhancer sharing: redundancy and opposing functions
- eY1H assays can interrogate differential TF binding to non-coding disease variants
- Concordant TF binding and expression changes conferred by non-coding variants
- eY1H assays provide a powerful addition to the TF network mapping toolkit



Human Gene-Centered Transcription Factor Networks for Enhancers and Disease Variants

Juan I. Fuxman Bass,¹ Nidhi Sahni,^{2,3} Shaleen Shrestha,¹ Aurian Garcia-Gonzalez,¹ Akihiro Mori,¹ Numana Bhat,¹ Song Yi,^{2,3} David E. Hill,^{2,3} Marc Vidal,^{2,3} and Albertha J.M. Walhout^{1,2,*}

¹Program in Systems Biology and Program in Molecular Medicine, University of Massachusetts Medical School, Worcester, MA 01605, USA

²Department of Cancer Biology, Center for Cancer Systems Biology (CCSB), Dana-Farber Cancer Institute, Boston, MA 02215, USA

³Department of Genetics, Harvard Medical School, Boston, MA 02115, USA

*Correspondence: marian.walhout@umassmed.edu

<http://dx.doi.org/10.1016/j.cell.2015.03.003>

SUMMARY

Gene regulatory networks (GRNs) comprising interactions between transcription factors (TFs) and regulatory loci control development and physiology. Numerous disease-associated mutations have been identified, the vast majority residing in non-coding regions of the genome. As current GRN mapping methods test one TF at a time and require the use of cells harboring the mutation(s) of interest, they are not suitable to identify TFs that bind to wild-type and mutant loci. Here, we use gene-centered yeast one-hybrid (eY1H) assays to interrogate binding of 1,086 human TFs to 246 enhancers, as well as to 109 non-coding disease mutations. We detect both loss and gain of TF interactions with mutant loci that are concordant with target gene expression changes. This work establishes eY1H assays as a powerful addition to the toolkit of mapping human GRNs and for the high-throughput characterization of genomic variants that are rapidly being identified by genome-wide association studies.

INTRODUCTION

Gene regulatory networks (GRNs) comprising physical and functional interactions between transcription factors (TFs) and regulatory elements play a critical role in development and physiology (Davidson et al., 2002; Walhout, 2006). Consequently, inappropriate gene regulation underlies a variety of human diseases. A broad variety of disease-associated mutations have been uncovered, including mutations in TF-encoding genes as well as mutations in non-coding sequences such as enhancers and promoters. Importantly, ~90% of disease-associated variants identified by genome-wide association studies (GWAS) reside in the non-coding part of the genome (Hindorf et al., 2009; Maurano et al., 2012), and a main challenge is to determine the interactions with TFs that may be perturbed as a consequence of such mutations.

TF-DNA interactions can be mapped with either “TF-centered” (protein-to-DNA) or “gene-centered” (DNA-to-protein) methods (Figure 1A) (Arda and Walhout, 2009; Deplancke

et al., 2006). Chromatin immunoprecipitation (ChIP) is the most widely used TF-centered method to identify the DNA regions with which a TF interacts in vivo. The last decade has seen an explosion of ChIP data. While progress has been impressive, several challenges remain. First, even for large consortia such as ENCODE, ChIP data have been generated for only ~150 of the ~1,500 human TFs (Gerstein et al., 2012). This is because ChIP critically depends on suitable anti-TF antibodies, which are only available for a minority of human TFs. Second, each TF has been assayed only in a limited number of cell lines and conditions. Third, ChIP may work better for some TFs than for others. For instance, TFs with restricted expression patterns and/or expressed at low levels may be less amenable to ChIP compared to highly and broadly expressed TFs. Fourth, ChIP is not optimal for characterizing disease-associated mutations in large-scale, high-throughput settings, because it requires disease cells or tissues that harbor the relevant mutation, which may be difficult to obtain. Finally, ChIP cannot be used to identify TFs with altered binding to mutant regulatory regions *ab initio* because the method is TF-centered and as a result one needs to first identify candidate TFs and then test these one at a time.

Enhanced yeast one-hybrid (eY1H) assays provide a gene-centered method for the detection and identification of TF-DNA interactions (Reece-Hoyes et al., 2011b, 2013; Arda et al., 2010; Brady et al., 2011; Fuxman Bass et al., 2014; Martinez et al., 2008). Briefly, eY1H assays measure TF-DNA interactions in the milieu of the yeast nucleus. DNA regions to be assayed (DNA baits) are fused upstream of two reporter genes, *LacZ* and *HIS3*, and integrated into the yeast genome, enabling their incorporation into chromatin. TFs (preys) are introduced into the DNA bait strains by mating using a robotic platform and are tested in quadruplicate, providing an inherent interaction retest (Figure 1B).

Here, we test our human eY1H platform (Reece-Hoyes et al., 2011a) to identify TFs interacting with human enhancers and to determine protein-DNA interaction changes caused by mutant TFs as well as non-coding disease-associated mutations. We find that eY1H assays more effectively retrieve TFs with limited expression patterns or levels when compared to ChIP. We provide examples of functional models of target sharing by TFs, including redundancy, which may provide robustness and opposing function (activation versus repression), which can ascertain proper timing of enhancer activity during development. Finally, we demonstrate that eY1H assays can be effectively

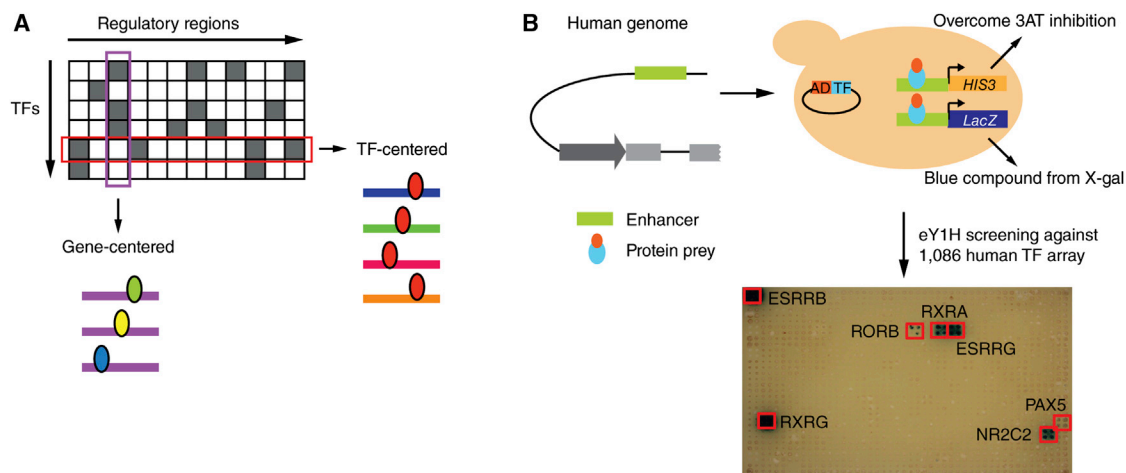


Figure 1. Gene-Centered Yeast One-Hybrid Assays

(A) Gene-centered versus TF-centered approaches for mapping protein-DNA interactions. Rectangles, regulatory regions; ellipses, TFs. (B) Cartoon of eY1H assays. A DNA sequence of interest is cloned upstream of two reporter genes (*HIS3* and *LacZ*) and integrated into the yeast genome (i.e., each DNA bait is tested in duplicate by activation of each reporter in the same yeast nucleus). The resulting yeast DNA bait strain is mated to a collection of yeast strains harboring TFs fused to the Gal4 activation domain (AD). Positive interactions are determined by the ability of the diploid yeast to grow in the absence of histidine and overcome the addition of 3AT a competitive inhibitor of the *HIS3* enzyme and turn blue in the presence of X-gal. Each TF is tested in quadruplicate. Red boxes show positive interactions.

used to identify changes in TF binding conferred by disease-associated coding or non-coding mutations.

RESULTS

A Gene-Centered Human TF-Enhancer Interaction Network

We first focused on a set of human developmental enhancers that were previously tested for embryonic activity in mouse transgenic assays at day E11.5 (Table S1) (Visel et al., 2007). We expanded the human eY1H platform to 1,086 full-length human TFs (76% of all 1,434) and examined interactions for 360 enhancers. Thus, in total we tested 390,960 putative TF-DNA interactions. To ensure the technical quality of the data, we only considered interactions in which both eY1H reporters and at least two of the four colonies of a TF quadrant tested positively. For the majority of cases, all four colonies scored positively. Limitations and advantages of eY1H data are discussed extensively below. The resulting TF-enhancer interaction network contains 2,230 interactions between 246 enhancers and 283 TFs (Figure 2A; Table S2).

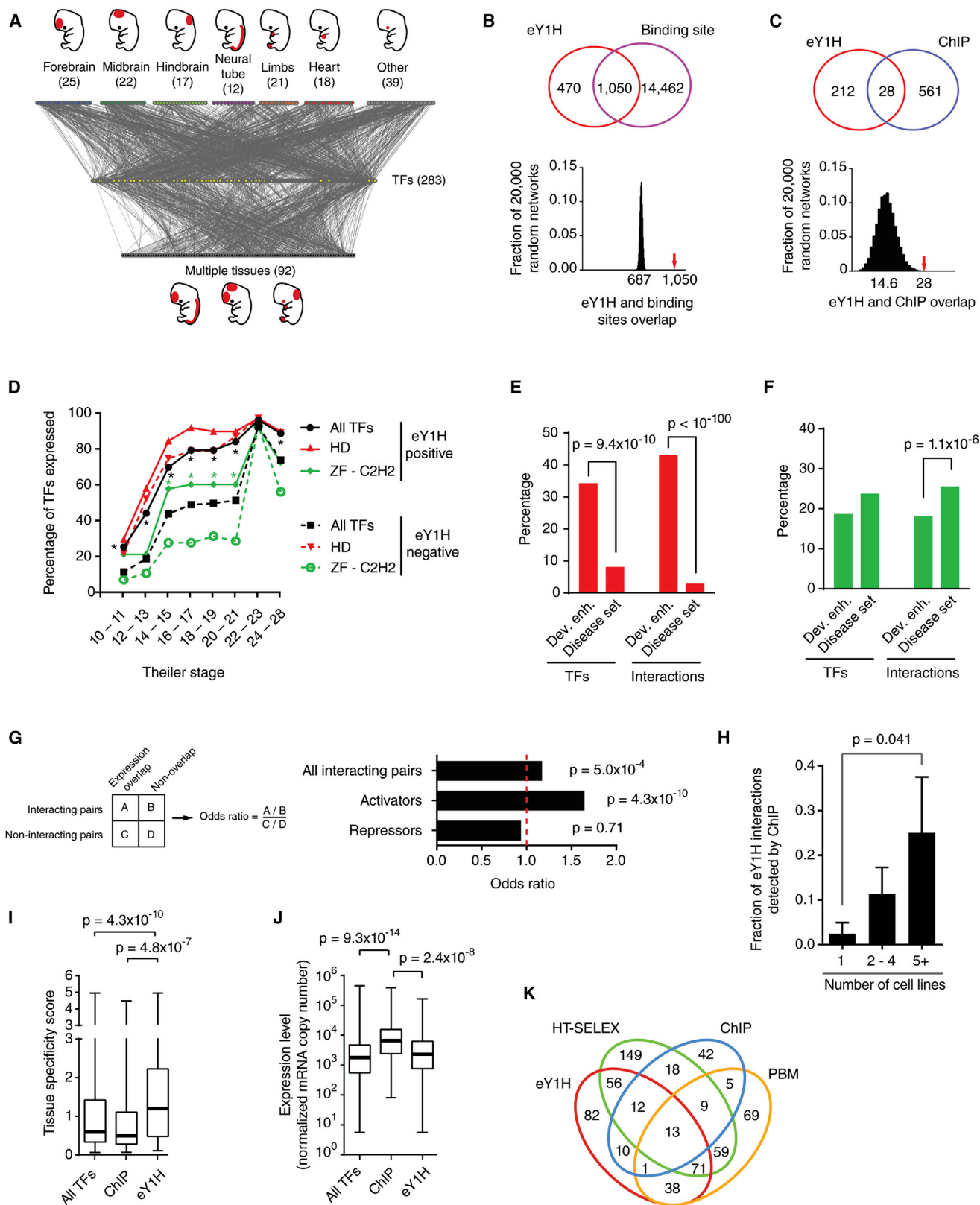
We ascertained the quality of the network using several different metrics. First, we observed a statistically significant overlap between eY1H interactions and the presence of TF binding sites, which indicates that most interactions are likely direct (Figure 2B, $p < 0.0001$). Second, we found a statistically significant overlap between eY1H and ENCODE ChIP interactions (Gerstein et al., 2012) (Figure 2C, $p < 0.0001$). Third, TFs that interact with developmental enhancers are enriched for those expressed early in development, which is consistent with the timing of enhancer activity (Figure 2D). Finally, the network is enriched for homeodomain TFs, well-known regulators of developmental gene expression (Chi, 2005) (Figure S1). This enrichment

is specific for the developmental enhancers because we did not observe it with the eY1H data set related to disease mutations that is discussed below (Figures 2E and S1). The network is depleted for interactions involving ZF-C2H2 TFs (Figures 2F and S1), and consistently, these TFs are overall expressed at later stages in development. Importantly, however, ZF-C2H2 TFs that do interact with the developmental enhancers are expressed at earlier stages than those that do not (Figure 2D).

To further assess the quality of the network, we reasoned that if a TF truly binds an enhancer in vivo, the TF would be expressed at the same time and place where the enhancer is active. Indeed, we found a modest but significant overlap between enhancer activity and spatiotemporal TF expression (Figure 2G). We wondered if the enrichment was relatively modest because the TFs identified in eY1H assays are a collection of transcriptional activators and repressors. We observed a more striking enrichment for known transcriptional activators, while repressors are not enriched (Figure 2G; Table S3). Altogether, these findings provide general support for the quality of the human TF-enhancer interaction network.

eY1H Assays Provide a Powerful Addition to the GRN Mapping Toolkit

Several of our findings demonstrate that eY1H assays are complementary to other TF-DNA interaction mapping methods. For instance, we found that the fraction of eY1H interactions also detected by ChIP is larger for TFs that have been assayed by ChIP in multiple cell lines (Figure 2H). This underscores that ChIP in a given tissue/cell line only uncovers a subset of interactions in which the relevant TF engages, while eY1H assays interrogate the available repertoire of TFs for a given enhancer in a single experiment. Further, TFs that interact with developmental enhancers in eY1H assays exhibit more tissue-specific expression



(legend on next page)

compared to all TFs tested or to TFs assayed by ChIP (Figure 2I). In addition, TFs assayed by ChIP are expressed at higher levels than those detected in eY1H assays (Figure 2J). These observations indicate that each method has particular strengths of detecting certain types of TFs. Indeed, we detected interactions for 82 TFs that had not been detected by any other high-throughput method (Figure 2K) (Badis et al., 2009; Jolma et al., 2013).

The TF-Enhancer Network Reveals Functional Relationships between TFs

In eY1H assays, DNA baits often interact with multiple members of the same TF family (Reece-Hoyes et al., 2013). This is likely because such TFs have similar DNA binding domains and recognize similar DNA sequences (Badis et al., 2009; Grove et al., 2009; Weirauch et al., 2014). To visualize enhancer sharing by TFs, we calculated the target profile similarity for each pair of TFs: i.e., the number of overlapping enhancer targets relative to the number of targets that interact with either TF (Fuxman Bass et al., 2013). We delineated a TF association network in which TFs with target profile similarity ≥ 0.2 are connected (Figures 3A and S2). As expected, TFs generally cluster by family. Further, there is a significant correlation between DNA binding domain identity, DNA motif similarity, and target profile similarity (Figures 3B, 3C, and S3). However, similar to our observations in *C. elegans*, there are many examples of TF pairs with high DNA binding motif similarity but low target profile similarity (Figure 3C) (Reece-Hoyes et al., 2013).

The sharing of enhancers by paralogous TFs begs the question of whether only one of these actually interacts with that DNA fragment in vivo, or if there could be a biological explanation for enhancer sharing between TFs. Conceptually, there are several possibilities. First, two TFs may share enhancers in the same tissue at the same time to provide redundancy that can lead to robustness of enhancer function when one TF is genet-

cally or environmentally perturbed (Macneil and Walhout, 2011). Second, TFs may bind the same enhancer, but in different tissues, or at different developmental times. Finally, TFs that share enhancers could have opposing regulatory effects where one activates and the other represses transcription, for instance at different developmental stages.

There are several examples of redundancy between TF paralogs. For instance, three ETS TFs share targets in human T cells and function redundantly (Hollenhorst et al., 2007). If redundancy is prevalent in human GRNs, one would expect that TFs that share targets would also tend to be co-expressed. Indeed, TFs that bind to highly overlapping sets of enhancers are generally more co-expressed than TFs that bind different enhancers (Figure 3D). An example is a group of six redundant Abdominal-B (Abd-B) HOX TFs (Maconochie et al., 1996) that bind a highly overlapping set of enhancers in eY1H assays (Figure 3A, blue box). These TFs are also highly co-expressed and neither of them is essential for viability, although overall 60% of TFs in the network confer lethality when knocked out in mouse. Importantly, TF pairs with both high target profile similarity and high co-expression similarity are overall enriched for pairs in which both TFs are non-essential (Figure 3E). Altogether, these results suggest a potentially widespread redundancy between TFs.

TFs that share a large proportion of targets could have opposing functions if one is an activator and the other is a repressor. For instance, the activator LHX4 and two repressors, LHX6 and HESX1, share a large proportion of enhancers (Figure 3F). HESX1 and LHX6 can both repress activation by LHX4 in transient transfection assays (Figures 3G and 3H). LHX4 is expressed after HESX1 in the developing pituitary and before LHX6 in the developing CNS (Figure 3F), suggesting that HESX1 may prevent precocious activation by LHX4 in the developing pituitary, while LHX6 repression prevents prolonged activation by LHX4 in the developing CNS. Thus, the network can identify TF

Figure 2. A Human Gene-Centered TF-Enhancer Interaction Network

(A) The TF-enhancer interaction network comprises 2,230 interactions between 246 human developmental enhancers and 283 TFs. Enhancers that are active in a single tissue at day E11.5 (top nodes) or multiple tissues (bottom nodes) are connected to the TFs (middle yellow nodes) with which they interact.

(B and C) eY1H interactions significantly overlap with the occurrence of known TF binding sites (B) and ChIP peaks (C). The Venn diagrams (top) illustrate the number of overlapping interactions. The eY1H network was randomized 20,000 times by edge switching (Martinez et al., 2008) and the overlap in each randomized network was calculated (bottom panel). The numbers under the histogram peaks indicate the average overlap in the randomized networks. The red arrows indicate the observed overlap in the real network.

(D) Timing of expression during mouse development for homeodomain (HD) and ZF-C2H2 families. The fraction of TFs whose expression was detected at a particular Theiler Stage during development is shown. * $p < 0.01$ versus eY1H-negative TFs by Fisher's exact test.

(E and F) Percentage of TFs or interactions involving homeodomains (E) or ZF-C2H2 TFs (F) for two data sets. Statistical significance determined by proportion comparison test.

(G) Overlap between enhancer activity and TF expression pattern. The fraction of TF-enhancer pairs that overlap in expression was compared between interacting and non-interacting pairs. The same analysis was performed for known activators and repressors. Statistical significance was determined using Fisher's exact test.

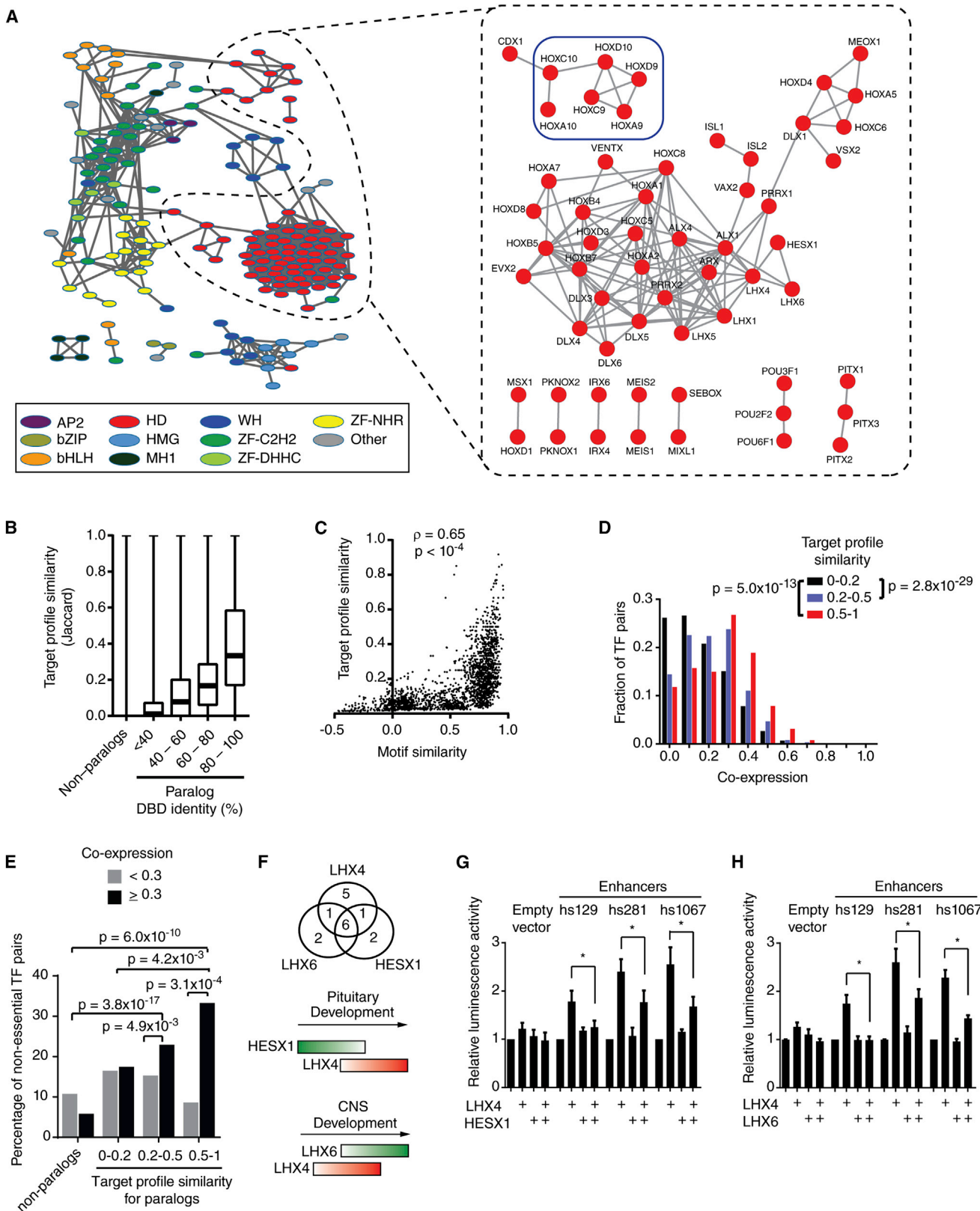
(H) The fraction of eY1H interactions that were also detected by ChIP were partitioned based on the number of cell lines in which a particular TF was tested by ChIP. $p = 0.041$ by Mann-Whitney's U test. Error bars represent SEM.

(I) Tissue specificity score for TFs detected by eY1H ($n = 266$), ChIP ($n = 96$) or all TFs present in the eY1H array ($n = 896$), based on their expression levels across 34 tissues (Ravasi et al., 2010). This score quantifies the departure of the observed TF expression pattern from the null distribution of uniform expression across all tissues, using relative entropy. Each box spans from the first to the third quartile, the horizontal lines inside the boxes indicate the median value and the whiskers indicate minimum and maximum values. Statistical significance determined by Mann-Whitney's U tests.

(J) The maximum expression level across 34 tissues were obtained from Ravasi et al. (2010) for each TF detected by eY1H ($n = 266$), ChIP ($n = 96$), or all TFs present in the eY1H array ($n = 896$) are plotted. Each box spans from the first to the third quartile, the horizontal lines inside the boxes indicate the median value and the whiskers indicate minimum and maximum values. Statistical significance determined by Mann-Whitney's U tests.

(K) Venn diagram depicting the overlap between TFs detected by eY1H and those detected by high-throughput SELEX (HT-SELEX), ChIP-seq, and protein binding microarrays (PMBs).

See also Figure S1 and Tables S1, S2, and S3.



(legend on next page)

pairs that bind to similar targets but that may have opposing functions in target gene regulation. This may be crucial to tightly control the expression of particular programs during development. Altogether, these data indicate that multiple TFs from the same family found to interact with overlapping sets of enhancers in eY1H assays may be relevant *in vivo* and can provide different gene regulatory functionality.

Human Disease and TF Network Connectivity

Mutations in TF coding sequences can cause a variety of diseases that could impact GRNs in different ways. Some mutations may abrogate DNA binding completely while others affect binding to only a subset of targets. We hypothesized that mutations in TFs that bind a large set of targets are more likely to affect an important biological function. It has been shown previously that TFs that bind to many promoters in *C. elegans* are more frequently essential for viability than TFs that only bind a few promoters (Deplancke et al., 2006). Similarly, protein-protein interaction hubs are more frequently essential (Goh et al., 2007). Interestingly, a combined protein-protein and protein-DNA interaction degree was more strongly associated with phenotypic output for human TFs than either degree alone. Essential and disease-associated TFs have a higher combined degree than non-essential TFs (Figures 4A and 4B). In addition, there is a significant correlation between combined TF degree and the density of somatic mutations in cancer (Figure 4C). This is specific to somatic mutations as no correlation was observed between TF degree and the density of protein altering variants in healthy individuals from the 1000 Genomes Project (Abecasis et al., 2010) (Figure 4D). In sum, mutations in highly connected TFs more frequently affect phenotypic outcomes leading to disease.

Disease-Associated TF Coding Mutations

Both coding (in TFs) and non-coding (in regulatory DNA elements) mutations can cause human disease, likely by changing

target gene expression in *trans* or *cis*, respectively. Such disease-associated mutations can potentially affect GRNs by: (1) complete loss of all TF-DNA interactions, (2) loss of a subset of interactions, (3) gain of interactions, or (4) a combination of interaction loss and gain. However, because no suitable methods were available to discriminate between these possibilities it remains unclear, in the vast majority of cases, which TF-DNA interactions are lost or gained as a result of specific mutations.

We hypothesized that eY1H assays would be highly suitable to interrogate differential TF binding caused by disease-associated mutations because: (1) mutations can readily be introduced in DNA baits or TF preys by molecular cloning, circumventing the need for patient samples harboring mutant TFs or mutant regulatory sequences; (2) eY1H assays enable direct, unbiased comparisons between wild-type and mutant TFs, and (3) eY1H assays test all available TFs in parallel in one experiment, enabling the direct determination of differential TF binding to mutant regulatory DNA sequences.

To determine the impact of TF coding mutations on enhancer binding, we first focused on four mutant LHX4 TFs that confer pituitary hormone deficiency (Pfaeffle et al., 2008; Tajima et al., 2007) (Figure 5A). The P389T mutation is located outside the DNA binding domain and this mutant retains most (18 of 19) protein-DNA interactions (Table S4). However, two mutations in the homeodomain (L190R and A210P) result in complete loss of interactions, which is consistent with previous *in vitro* experiments (Pfaeffle et al., 2008) (Figures 5A and 5B; Table S4). Interestingly, we detected partial loss and gain of weak interactions caused by the R84C mutation, which is located in the LIM domain and is known to modulate DNA binding (Pfaeffle et al., 2008). These results were further confirmed with luciferase assays in which we found changes in the transcriptional activation capacity that correlate with changes in DNA binding (Figure 5C).

We also evaluated two missense mutations in the homeodomain of HESX1: the R160C mutation leads to septo-optic

Figure 3. TF Redundancy and Opposing Functions

(A) TF association network. Each node represents a TF and edges connect TFs with a target profile similarity ≥ 0.2 (left, all TF families) or ≥ 0.45 (right, homeodomains). TFs with degree ≥ 3 in the eY1H network are shown. Node color indicates TF families. The blue square highlights a set of HOX Abd-B TFs discussed in the main text. AP2, activating protein 2; bZIP, Basic Leucine Zipper Domain; bHLH, basic helix-loop-helix; HD, homeodomain; HMG, High-Mobility Group; MH1, Mad homology 1; WH, Winged Helix; ZF-C2H2, Zinc Finger C2H2; ZF-DHHC, Zinc Finger DHHC; ZF-NHR, Nuclear Hormone Receptor.

(B) Target profile similarity between TFs according to DNA binding domain identity. For each pair of TF paralogs with different DNA binding domain amino acid identity their target profile similarity was determined. Each box spans from the first to the third quartile, the horizontal lines inside the boxes indicate median value and the whiskers indicate minimum and maximum values. All pairwise comparisons between groups are significant ($p < 0.01$) by Dunn's multiple comparison test.

(C) Correlation between motif similarity and target profile similarity. For each TF pair, target profile similarity was plotted against their DNA motif similarity determined as the Pearson correlation coefficient of the Z scores obtained for all possible 8-mers in protein binding microarrays.

(D) Histogram of spatiotemporal co-expression for TF pairs according to their target profile similarity. Statistical significance determined by Mann-Whitney's U tests.

(E) Redundancy between TFs. Each pair of TF paralogs was binned according to their target profile similarity and according to their spatiotemporal co-expression. The percentage of TF-pairs for which both TF knockouts are viable was determined. Statistical significance was determined using the proportion comparison test.

(F) Top: overlap between enhancers bound by LHX4, LHX6 and HESX1. Bottom: cartoon of developmental expression. Red, transcriptional activator; green, transcriptional repressor.

(G) HESX1 represses LHX4-induced enhancer activity. HEK293T cells were co-transfected with enhancer constructs cloned upstream of a Firefly luciferase reporter vector and the indicated TF expression vectors. After 48 hr, cells were harvested and luciferase assays were performed. Relative luminescence activity is plotted as fold change compared to cells co-transfected with control vector expressing GFP. Experiments were performed three times in three to six replicates. Average relative luminescence activity \pm SEM is plotted. * $p < 0.05$ by Student's t test.

(H) LHX6 represses LHX4-induced enhancer activity. Experiments were performed three times in three to six replicates. Average relative luminescence activity \pm SEM is plotted. * $p < 0.05$ by Student's t test.

See also Figures S2 and S3.

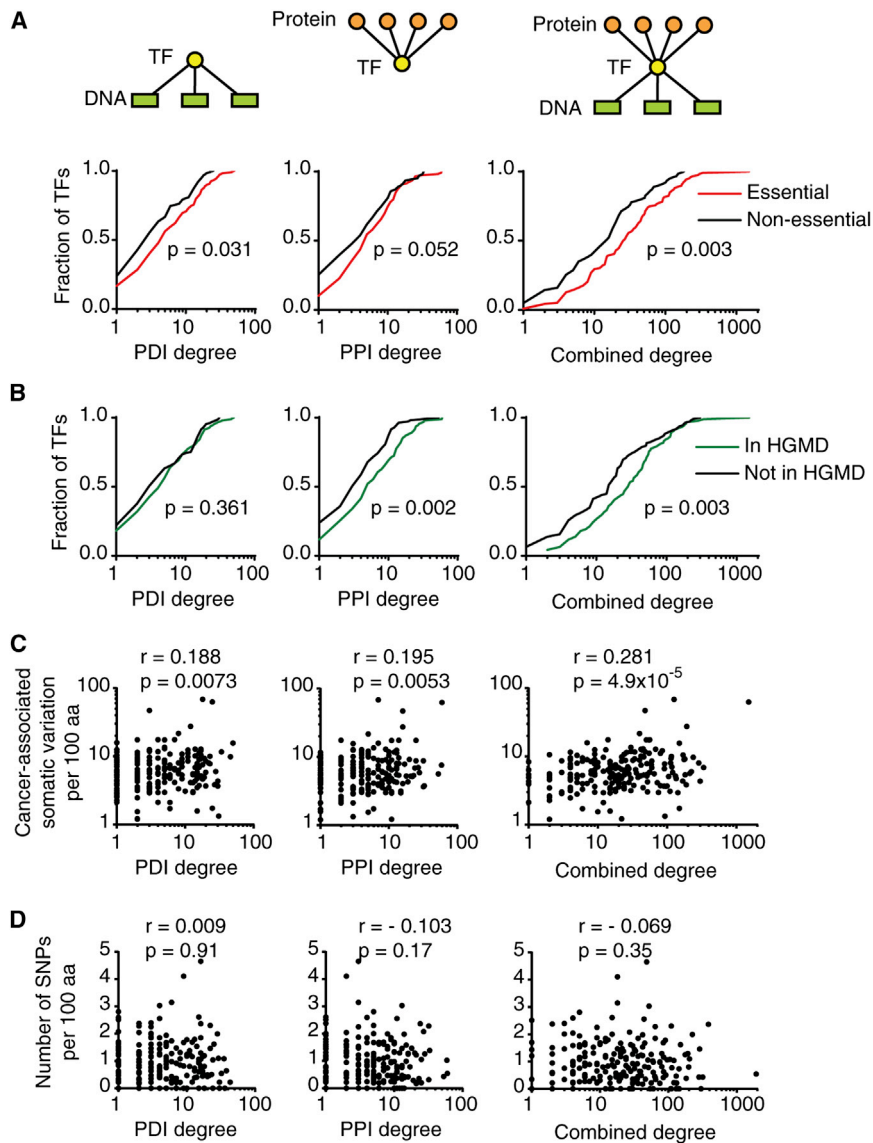


Figure 4. Relationship between TF Connectivity and Human Disease

(A) Cumulative distribution of TF protein-DNA interaction (PDI), protein-protein interaction (PPI), and combined degrees for essential and non-essential TFs. Combined TF degree is defined as the product of PPI and PDI degrees and represents the number of paths connecting the protein interactors of a TF with its DNA targets. Statistical significance determined by Mann-Whitney's U tests.

(B) Cumulative distribution of TF degrees for TFs reported as disease-associated genes in the Human Gene Mutation Database (HGMD) and genes not reported in HGMD. Statistical significance determined by Mann-Whitney's U tests.

(C) Correlation between TF degree and the number of protein-altering SNPs and short indel variants per 100 amino acids in cancer samples obtained from the Catalogue of Somatic mutations in Cancer (COSMIC). Statistical significance was determined using Pearson correlation coefficient.

(D) Correlation between TF degree and the number of protein-altering SNPs and short indel variants per 100 amino acids in the 1000 genomes project. Statistical significance was determined using Pearson correlation coefficient.

dysplasia (Dattani et al., 1998), whereas the N125S variant is a natural polymorphism in the Afro-Caribbean population (Brickman et al., 2001) that is not associated with disease. Interestingly, the R160C mutation completely abolishes all interactions, while the N125S variant has a wild-type target profile (Figures 5D and 5E; Table S4). Wild-type and the N125S variant of HESX1 repressed reporter gene expression in transient transfection assays while the R160C mutant did not, further confirming our findings (Figure 5F). Altogether, these data show that eY1H assays can be effectively used to determine the consequences of TF-coding mutations on DNA target binding.

Non-Coding Mutations Associated with Human Disease

To determine the effect of non-coding mutations on TF binding, we selected 227 disease-associated mutations, affecting the expression of 137 genes. We identified interacting TFs for both wild-type and mutant clones of each regulatory element with

eY1H assays and detected differential TF binding for 109 mutations (75 genes) associated with a variety of diseases (Figures 6A and 6B; Table S5). Literature searches indicate that 66 of these mutations result in an increase while 39 confer a decrease in expression of the associated target gene (for four mutations the effect on gene expression is not known; Table S5). The majority of mutations resulted in interaction loss (64 of 109, or 59%). Remarkably, however, 32 mutations resulted in gain of interactions (29%) and 13 caused both interaction loss and gain (12%) (Figure 6C). Thus, gain of TF interactions may be a pervasive disease-causing mechanism. Overall, these mutations affect interactions with 111 TFs from all major families (Table S5). Strikingly, TFs involved in differential interactions are more frequently essential for viability and/or annotated as disease-associated in HGMD compared to TFs that are not involved in differential interactions (Figure 6D).

To validate the differential eY1H interactions, we first compared them to published differential interactions. Out of 227 mutations tested, 54 had reported differential interactions that were experimentally supported by reporter assays, in vitro binding assays and/or by ChIP. For 34 of these the reported TF was either absent from our collection (19 mutations) or was never detected in eY1H assays (15 mutations). We detected the reported differential interaction for four of the remaining 20 mutations and differential interaction with a close TF paralog for three additional mutations (Table S6). Importantly,

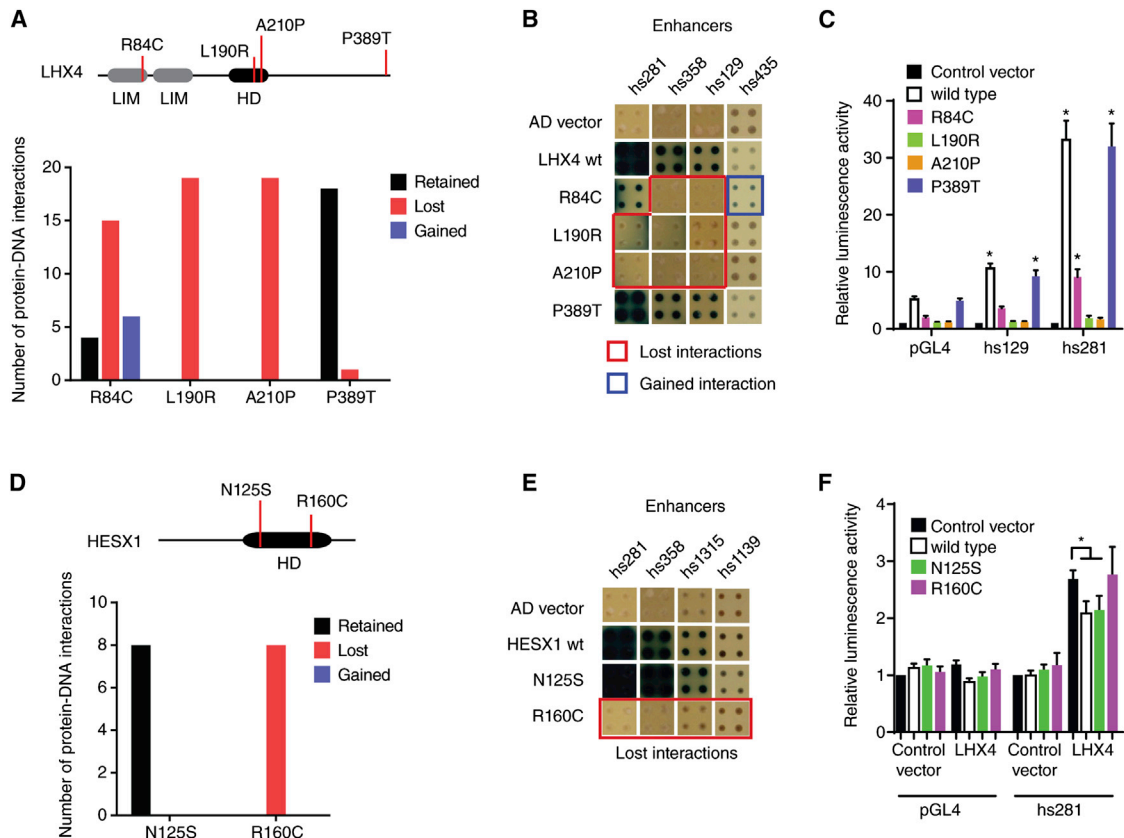


Figure 5. Disease-Associated Coding Mutations in TFs

(A) Four missense mutations in LHX4 were tested for loss or gain of protein-DNA interactions in eY1H assays against 152 enhancers. The top panel depicts a cartoon of LHX4, including the location of the mutations and the homeodomain (HD) and LIM domains. The bottom panel shows the number of interactions retained (black bar), lost (red bar) or gained (blue bar) for each mutant compared to wild-type interactions.

(B) Examples of interactions lost and gained for LHX4 missense mutations. Each TF-enhancer combination was tested in quadruplicate three times. One random quadruplicate test is shown corresponding to four enhancers. Red squares, interaction lost with TF mutant; blue square, gained interaction with TF mutant; AD vector, empty prey vector.

(C) Transcriptional activation mediated by wild-type and mutant LHX4 alleles. HEK293T cells were co-transfected with enhancer constructs cloned upstream of a Firefly luciferase reporter vector and the indicated TF expression vectors. Relative luminescence activity is plotted as fold change compared to cells co-transfected with empty expression vector. Experiments were performed four times with three replicates each. Average relative luminescence activity \pm SEM is plotted. * $p < 0.05$ versus empty expression vector by Student's *t* test.

(D) Two missense mutations in HESX1 were tested for changes in protein-DNA interactions as in (A).

(E) Examples of interactions lost for HESX1 missense mutations.

(F) Repression of LHX4-induced enhancer activity by wild-type and mutant HESX1 alleles. HEK293T cells were co-transfected with enhancer constructs cloned upstream of a Firefly luciferase reporter vector and the indicated TF expression vectors. Relative luminescence activity is plotted as fold change compared to cells co-transfected with control vector expressing GFP. Experiments were performed six times with three replicates each. Average relative luminescence activity \pm SEM is plotted. * $p < 0.05$ by Student's *t* test.

See also Table S4.

the TFs detected by eY1H assays were not tested in the latter three studies, even though they have similar DNA binding specificity and are expressed in the relevant disease tissue (Table S5). Hence, it could be that either or both TF(s) contribute to the disease in vivo.

Next, we devised a “supporting evidence score” (see Extended Experimental Procedures) for each interaction involving a mutant regulatory element, in which we weighted the interactions according to: (1) co-expression of the differentially interacting TF and the target gene in disease-relevant tissues, (2) if the differentially bound TF is associated with a similar

disease or mouse phenotype as the target gene mutation, and (3) if the target gene expression change caused by the mutation (increase or decrease) was concordant with gain/loss of a protein-DNA interaction with an activator/repressor (Figure 6E). It is of course important to note that the data used in this integration are not yet complete and have their own confidence issues. Out of the 294 differential interactions (with 109 non-coding mutants), 98 have a medium/high to high level of confidence (Table S5). Importantly, the differential interactions involving TFs expressed in disease-relevant tissues and/or associated with a similar disease are generally consistent with changes in target

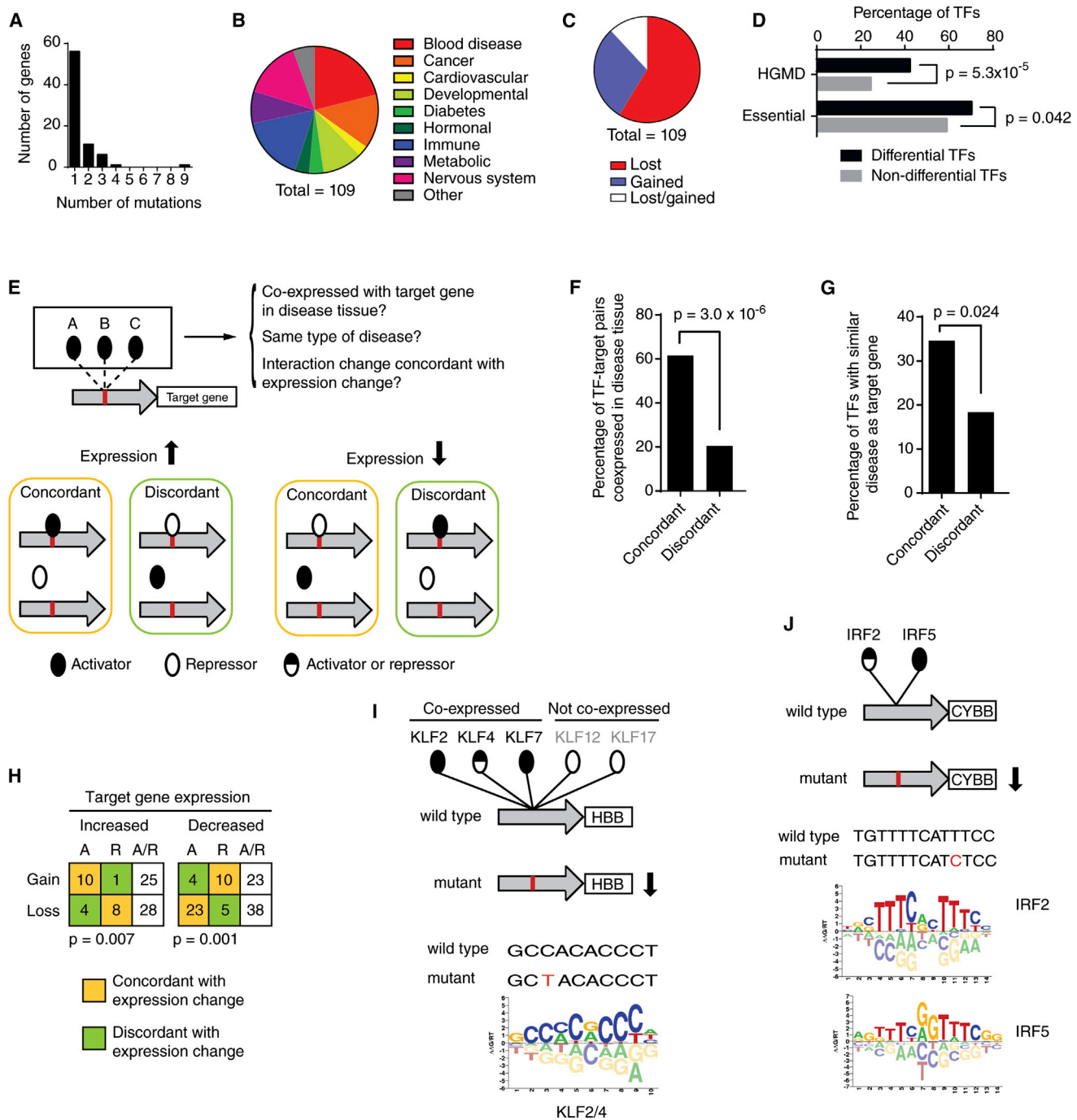


Figure 6. Disease-Associated Non-Coding Mutations

(A) Number of mutations per gene for which differential TF interactions were detected by eY1H assays.
 (B) Distribution of diseases associated with tested non-coding mutations.
 (C) Distribution of mutations that result in loss of interactions, gain of interactions, or both.
 (D) Fraction of essential (per MGI) or disease-associated TFs (per HGMD) differentially interacting with non-coding mutations (differential TFs) and the remaining TFs in the eY1H human TF collection (non-differential TFs). Statistical significance determined by proportion comparison test.
 (E) Cartoon depicting data integration used to obtain a supporting evidence score for differential eY1H interactions (see [Extended Experimental Procedures](#)).
 (F and G) Percentage of differential TF-target gene pairs in which the TF is co-expressed with the target gene in the disease tissue (F) or is associated with a similar disease or mouse phenotype (G) for interaction changes concordant or discordant with target gene expression changes. Statistical significance determined by proportion comparison test.

(legend continued on next page)

gene expression: an increase in expression is concordant with gain of interaction with an activator or loss of an interaction with a repressor, while a decrease in expression correlates with gain of interaction with a repressor or loss of interaction with an activator (Figures 6F–6H). All differential interactions, gene expression changes, as well as expression and disease information are provided in Table S5.

Several mutations cause differential interactions with multiple TFs, often from the same family. Two examples illustrate how such interactions can be evaluated for in vivo relevance. The first example involves a C to T mutation in the beta globin gene promoter that results in reduced gene expression leading to thalassemia. This mutation results in loss of interactions with five paralogous TFs: KLF2, KLF4, KLF7, KLF12, and KLF17, that bind similar DNA sequences (Figure 6I). Two of these paralogs, KLF2 and KLF4, are more likely involved than the other three TFs, because they are expressed in erythroid cells and have been shown to activate beta globin gene expression (Alhashem et al., 2011; Gardiner et al., 2007). The second example involves a T to C mutation in the CYBB promoter that causes a reduction in expression leading to chronic granulomatous disease. eY1H assays identified loss of binding for IRF2 and IRF5, both of which are expressed in disease-relevant cells. Again, the mutation occurs in the binding site of these TFs (Figure 6J). IRF2 has been shown to activate the CYBB promoter (Luo and Skalnik, 1996) and, therefore, it is likely that loss of this interaction is most relevant to the disease. However, IRF5 cannot be entirely excluded because these two TFs may share targets in vivo as discussed above for the developmental enhancers.

Dominant Mutations in the Sonic Hedgehog ZRS Enhancer

We identified differential interactions for nine dominant mutations in the ZRS enhancer of SHH that result in ectopic gene expression along the anterior margin of the limb bud, causing digit malformations and polydactyly (Sharpe et al., 1999) (Figure 7A; Table S5). Interestingly, we found both loss and gain of interactions with these mutations, involving many TFs that are expressed in the developing limb. Data integration showed that gain of interactions involving limb-expressed TFs mostly involves activators, while loss of interactions occurred more frequently with transcriptional repressors ($p = 0.018$, Figure 7B), both of which are concordant with the increased gene expression elicited by these dominant mutations. Thus, similar diseases can result from gain or loss of TF interactions caused by different mutations within an enhancer.

We characterized the 105C → G mutation in more detail. This mutation results in gain of interactions with three AP2 TFs, two of which are expressed in the limb and could be responsible for the gain of SHH expression (Figures 7A and 7C). Indeed, this mutation creates a consensus AP2 binding site (Badis et al., 2009)

(Figure 7D). TFAP2B is a transcriptional activator and activates the mutant, but not wild-type enhancer in luciferase assays (Figure 7E). Together, these results show that TFAP2B can bind and activate 105C → G enhancer mutant, suggesting that aberrant binding of TFAP2B may result in the ectopic expression of SHH, thereby causing digit malformations.

DISCUSSION

This study presents a gene-centered human TF-enhancer interaction network delineated by eY1H assays. The technical quality of this network is ensured by the inherent retest of interactions with two reporter genes and the testing of TFs in quadruplicate, as well as due to the high demonstrated rate of reproducibility between independent experiments (~90%) (Reece-Hoyes et al., 2011b, 2013). The biological quality of this network is also high, as indicated by several metrics, including significant overlap with TF binding sites, ChIP interactions, TF expression and enhancer activity, enrichment for homeodomains, and reporter assays. The relatively modest overlap with ChIP data reflects the notion that ChIP may retrieve indirect TF interactions, as well as a lack of sensitivity of ChIP data that were only obtained in one or two cell types. Like any other method, however, eY1H assays may also yield false positive and negative interactions with both enhancers and disease-causing mutant elements. False positive interactions may be retrieved when multiple members of the same TF family with highly similar consensus binding sites are found to bind to the same enhancer(s) and only a subset of these actually bind the enhancer in vivo. Importantly, however, we illustrate several mechanisms by which enhancer sharing can be biologically meaningful in attaining redundancy or in the precise timing of enhancer activity, for instance during development. The careful integration of eY1H interactions with high-resolution spatiotemporal expression and other types of data over time will provide protein-DNA interaction data of increasing validity and resolution.

The rate of false negatives in eY1H assays is likely to be considerable (Walhout, 2011). For instance, TFs that exclusively interact with DNA as heterodimers or after post-translational modification by another human protein will not be detected. In addition, eY1H assays cannot as of yet detect cooperative interactions with multiple TFs. Therefore, the retrieval of several known differential interactions with non-coding disease-causing mutations in a single experiment is highly encouraging.

A particularly powerful feature of the eY1H approach is that it uniquely enables the comparison of wild-type and mutant TFs or regulatory elements, in a single experiment and in a high-throughput manner. Our findings show that both coding mutations in TF-encoding genes and non-coding mutations in regulatory sequences can result in rewiring of GRNs. While

(H) Number of interactions lost or gained involving activators (A), repressors (R) or bifunctional TFs (A/R, activators and repressors) for mutations that cause increased or decreased target gene expression. Only interactions in which the TF is co-expressed with the target gene in disease-relevant tissue, or associated with a similar disease or phenotype are shown. Statistical significance was determined using Fisher's exact test.

(I and J) Examples of differential eY1H interactions with the HBB promoter (I) and the promoter of the CYBB gene (J). Disease-associated mutations are indicated in red. Reported TF binding site logos are shown (Weirauch et al., 2014).

See also Tables S5 and S6.

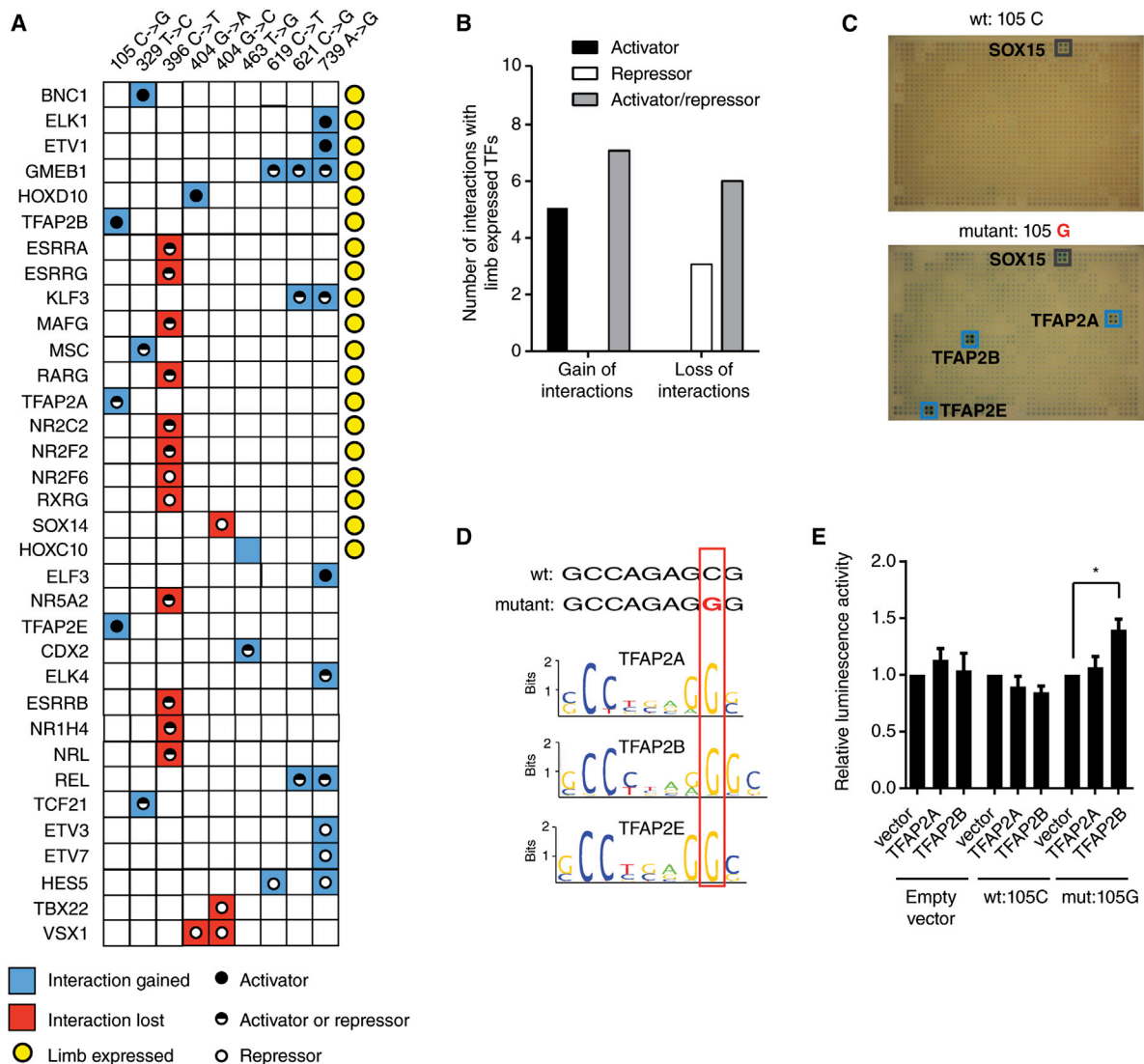


Figure 7. Mutations in the Limb SHH Enhancer

(A) Summary of interactions lost (red) or gained (blue) for different mutations in the ZRS enhancer of sonic hedgehog. Yellow circles, TFs expressed in limb during development; black dots, activators; white dots, repressors; black/white dots, TF that can be both activators or repressors.

(B) Number of interaction changes occurring with limb-expressed activators, repressors or bifunctional TFs (activators/repressors) for interactions gained or lost in ZRS enhancer mutations. $p = 0.018$ by Fisher's exact test.

(C) Gain of interactions detected by eY1H assays in the 105C → G mutant in the ZRS enhancer of sonic hedgehog. Blue boxes indicate differential positive interactions.

(D) DNA binding motifs for TFAP2A, TFAP2B, and TFAP2E discriminate wild-type and mutant enhancer sequences.

(E) HEK293T cells were co-transfected with enhancer fragments containing wild-type (105C) or mutant (105G) sequences cloned upstream of a Firefly luciferase reporter vector and the indicated TF expression vectors. Relative luminescence activity is plotted as fold change compared to cells co-transfected with control vector expressing GFP. Experiments were performed four times in three to six replicates. Average relative luminescence activity \pm SEM is plotted. * $p < 0.05$ by Student's t test.

See also Table S5.

coding mutations cause mostly loss of protein-protein interactions (Sahni et al., 2015, in this issue of *Cell*), protein-DNA interaction changes caused by either coding or non-coding mutations involve both gain and loss of interactions, sometimes with the same mutation (Sahni et al., 2015). We provide a guide for interpreting eY1H data with non-coding disease-causing mutations. Specifically, we would prioritize differential interactions

involving TFs that are co-expressed with the target gene, in the disease-relevant tissue. Further, we emphasize that concordant interactions, for instance increased gene expression and gain of interaction with an activator or loss with a repressor, are more likely relevant in vivo than other interactions. Obtaining additional, high-resolution gene expression and TF function data will be critical for the continued integration not only of eY1H

data, but also of interaction data inferred by DNase I hypersensitivity assays or predicted based on TF binding sites.

Most variants identified by GWAS reside in non-coding regions of the genome (Hindorf et al., 2009; Maurano et al., 2012). We propose that eY1H assays will provide a facile method with which differential TF interactions involving these variants can be analyzed. Overall this work provides an initial blueprint to study enhancer networks, as well as to determine how network connectivity is affected in disease.

EXPERIMENTAL PROCEDURES

eY1H Assays

Enhanced yeast one-hybrid (eY1H) assays were performed as described (Reece-Hoyes et al., 2011b). This method detects protein-DNA interactions and involves two components: a “DNA-bait” (e.g., a gene promoter or enhancer) and a “TF-prey.” We generated DNA-bait strains for 360 human developmental enhancers selected from the Vista Enhancer Browser (<http://enhancer.lbl.gov>; Table S1). Enhancers (0.4–2.4 kb) were amplified by PCR (Table S7) from human genomic DNA (Clontech) and were then Gateway-cloned (Reece-Hoyes et al., 2011b). Entry clones were sequenced using PacBio (Yale Center for Genomic Analysis; Table S8). The DNA-baits were cloned upstream of two Y1H reporter genes (*LacZ* and *HIS3*) and both DNA-bait::reporter constructs were integrated into the yeast genome to generate chromatinized “DNA-bait strains.” Yeast strains that express different TFs fused to the activation domain (AD) of yeast Gal4 were mated into the DNA bait strain. If a TF binds the regulatory region, the AD moiety activates reporter gene expression. *LacZ* activation was detected via the conversion of colorless X-gal into a blue compound, while *HIS3* expression allows the yeast to grow on media lacking histidine and to overcome the addition of 3-amino-triazole (3AT), a competitive inhibitor of the *HIS3* enzyme (Deplancke et al., 2004; Reece-Hoyes and Walhout, 2012). We updated the previously published arrayed collection of 988 human TFs (Reece-Hoyes et al., 2011a) by adding 146 TFs and removing 48 for which the clone turned out to be incorrect, was truncated or did not encode the DNA binding domain. The resulting collection contains one variant of 1,086 full-length TFs (76% of all 1,434 human TFs, Table S9).

eY1H assays were performed using a Singer robot that manipulates yeast strains in a 1,536-colony format. Images of readout plates lacking histidine and containing 3AT and X-gal were processed using the Mybrid web-tool to automatically detect positive interactions (Reece-Hoyes et al., 2013). Each interaction was tested in quadruplicate and only those that were positive at least twice were considered genuine (Reece-Hoyes et al., 2011b). However, the vast majority of interactions detected (~90%) were supported by all four colonies as previously published (Reece-Hoyes et al., 2011b). Interactions detected by Mybrid were then manually curated. False positives detected by Mybrid on plates with uneven background were removed. We included false negative interactions missed by Mybrid, for instance because they occur next to very strong positives or occur with baits that exhibit high background reporter gene expression. Positive colonies were sequenced to determine prey identity. Fourteen quads in the array were removed from the interaction list as they did not match the expected TF (see Extended Experimental Procedures). A total of 2,230 high-quality protein-DNA interactions between 246 enhancers and 283 TFs were included in the final data set (Table S2).

Target Profile Similarity

Target profile similarity between TFs was calculated using the Jaccard index as the number of enhancer targets shared between two TFs A and B divided by the number of enhancers that interact with either A or B (Fuxman Bass et al., 2013). Target profile similarities range from 0 to 1, with 0 indicating no target overlap and 1 indicating complete target overlap.

Mutated Regulatory Regions

Mutant DNA baits were generated by introducing mutations in the primers in the PCR step prior to generating entry clones (Table S10). Yeast DNA-bait strains were sequenced to verify the mutation and ensure the absence of addi-

tional mutations. eY1H screens were performed for two or three independent yeast strains per construct. Interactions that occurred with at least two out of three or two out of two of the strains were considered positive while interactions not occurring in any of the strains were considered negative (Table S5).

SUPPLEMENTAL INFORMATION

Supplemental Information includes Extended Experimental Procedures, three figures, and ten tables and can be found with this article online at <http://dx.doi.org/10.1016/j.cell.2015.03.003>.

AUTHOR CONTRIBUTIONS

J.I.F.B. and A.J.M.W. conceived the project. J.I.F.B., S.S., N.B., and A.G.-G. performed eY1H experiments. J.I.F.B. performed the data analysis with assistance of A.M. J.I.F.B. and S.S. performed the luciferase assays. J.I.F.B., N.S., and S.Y. performed the experiments and data analysis for Figure 5. N.S. and S.Y. were supervised by D.H. and M.V. J.I.F.B. and A.J.M.W. wrote the paper with contributions of the other authors.

ACKNOWLEDGMENTS

We thank members of the A.J.M.W. laboratory, R. McCord, N. Kaplan, and J. Dekker for discussions and critical reading of the manuscript. We thank J. Gibcus for the pGL4 plasmid and expression vectors and advice on the luciferase assays. We thank N. Beittel and B. Parmentier for technical assistance. This work was supported by US NIH grants GM082971 to A.J.M.W., HG004233 to M.V., and HG006066 to M.V. and D.E.H. J.I.F.B. was partially supported by a postdoctoral fellowship from the Pew Latin American Fellows Program.

Received: September 16, 2014

Revised: November 26, 2014

Accepted: January 30, 2015

Published: April 23, 2015

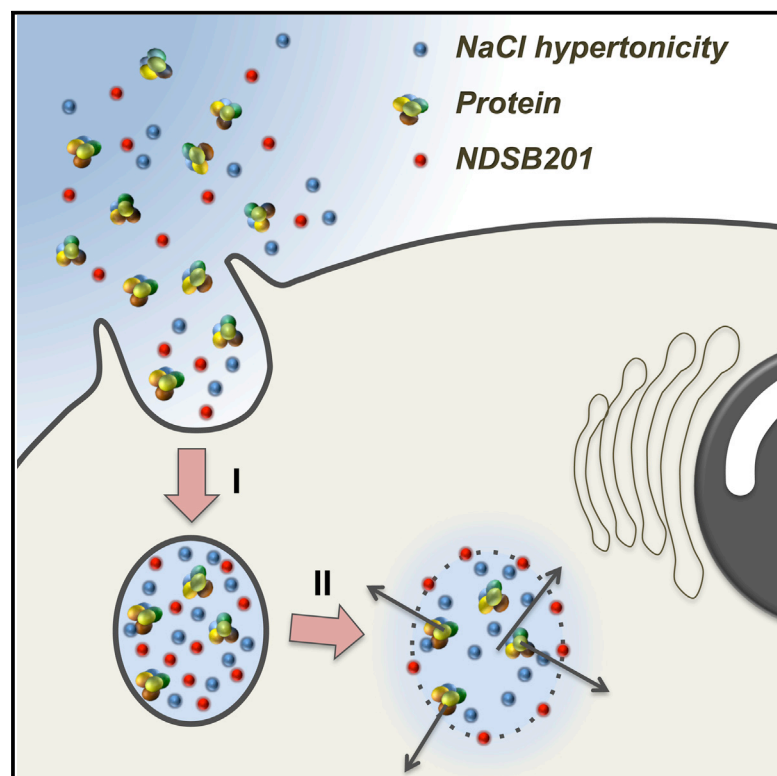
REFERENCES

- Abecasis, G.R., Altshuler, D., Auton, A., Brooks, L.D., Durbin, R.M., Gibbs, R.A., Hurles, M.E., and McVean, G.A.; 1000 Genomes Project Consortium (2010). A map of human genome variation from population-scale sequencing. *Nature* 467, 1061–1073.
- Alhashem, Y.N., Vinjamur, D.S., Basu, M., Klingmüller, U., Gaensler, K.M., and Lloyd, J.A. (2011). Transcription factors KLF1 and KLF2 positively regulate embryonic and fetal beta-globin genes through direct promoter binding. *J. Biol. Chem.* 286, 24819–24827.
- Arda, H.E., and Walhout, A.J.M. (2009). Gene-centered regulatory networks. *Brief. Funct. Genomics* 9, 4–12.
- Arda, H.E., Taubert, S., Conine, C., Tsuda, B., Van Gilst, M.R., Sequerra, R., Doucette-Stam, L., Yamamoto, K.R., and Walhout, A.J.M. (2010). Functional modularity of nuclear hormone receptors in a *Caenorhabditis elegans* metabolic gene regulatory network. *Mol. Syst. Biol.* 6, 367.
- Badis, G., Berger, M.F., Philippakis, A.A., Talukder, S., Gehrke, A.R., Jaeger, S.A., Chan, E.T., Metzler, G., Vedenko, A., Chen, X., et al. (2009). Diversity and complexity in DNA recognition by transcription factors. *Science* 324, 1720–1723.
- Brady, S.M., Zhang, L., Megraw, M., Martinez, N.J., Jiang, E., Yi, C.S., Liu, W., Zeng, A., Taylor-Teeples, M., Kim, D., et al. (2011). A stele-enriched gene regulatory network in the *Arabidopsis* root. *Mol. Syst. Biol.* 7, 459.
- Brickman, J.M., Clements, M., Tyrell, R., McNay, D., Woods, K., Warner, J., Stewart, A., Beddington, R.S., and Dattani, M. (2001). Molecular effects of novel mutations in *Hesx1/HESX1* associated with human pituitary disorders. *Development* 128, 5189–5199.
- Chi, Y.I. (2005). Homeodomain revisited: a lesson from disease-causing mutations. *Hum. Genet.* 116, 433–444.

- Dattani, M.T., Martinez-Barbera, J.P., Thomas, P.Q., Brickman, J.M., Gupta, R., Mårtensson, I.L., Toresson, H., Fox, M., Wales, J.K., Hindmarsh, P.C., et al. (1998). Mutations in the homeobox gene *HESX1/Hesx1* associated with septo-optic dysplasia in human and mouse. *Nat. Genet.* 19, 125–133.
- Davidson, E.H., Rast, J.P., Oliveri, P., Ransick, A., Caestani, C., Yuh, C.-H., Minokawa, T., Amore, G., Hinman, V., Arenas-Mena, C., et al. (2002). A genomic regulatory network for development. *Science* 295, 1669–1678.
- Deplancke, B., Dupuy, D., Vidal, M., and Walhout, A.J.M. (2004). A gateway-compatible yeast one-hybrid system. *Genome Res.* 14 (10B), 2093–2101.
- Deplancke, B., Mukhopadhyay, A., Ao, W., Elewa, A.M., Grove, C.A., Martinez, N.J., Sequerra, R., Doucette-Stamm, L., Reece-Hoyes, J.S., Hope, I.A., et al. (2006). A gene-centered *C. elegans* protein-DNA interaction network. *Cell* 125, 1193–1205.
- Fuxman Bass, J.I., Diallo, A., Nelson, J., Soto, J.M., Myers, C.L., and Walhout, A.J. (2013). Using networks to measure similarity between genes: association index selection. *Nat. Methods* 10, 1169–1176.
- Fuxman Bass, J.I., Tamburino, A.M., Mori, A., Beittel, N., Weirauch, M.T., Reece-Hoyes, J.S., and Walhout, A.J. (2014). Transcription factor binding to *Caenorhabditis elegans* first introns reveals lack of redundancy with gene promoters. *Nucleic Acids Res.* 42, 153–162.
- Gardiner, M.R., Gongora, M.M., Grimmond, S.M., and Perkins, A.C. (2007). A global role for zebrafish *klf4* in embryonic erythropoiesis. *Mech. Dev.* 124, 762–774.
- Gerstein, M.B., Kundaje, A., Hariharan, M., Landt, S.G., Yan, K.K., Cheng, C., Mu, X.J., Khurana, E., Rozowsky, J., Alexander, R., et al. (2012). Architecture of the human regulatory network derived from ENCODE data. *Nature* 489, 91–100.
- Goh, K.I., Cusick, M.E., Valle, D., Childs, B., Vidal, M., and Barabási, A.L. (2007). The human disease network. *Proc. Natl. Acad. Sci. USA* 104, 8685–8690.
- Grove, C.A., De Masi, F., Barrasa, M.I., Newburger, D.E., Alkema, M.J., Bulyk, M.L., and Walhout, A.J. (2009). A multiparameter network reveals extensive divergence between *C. elegans* bHLH transcription factors. *Cell* 138, 314–327.
- Hindorf, L.A., Sethupathy, P., Junkins, H.A., Ramos, E.M., Mehta, J.P., Collins, F.S., and Manolio, T.A. (2009). Potential etiologic and functional implications of genome-wide association loci for human diseases and traits. *Proc. Natl. Acad. Sci. USA* 106, 9362–9367.
- Hollenhorst, P.C., Shah, A.A., Hopkins, C., and Graves, B.J. (2007). Genome-wide analyses reveal properties of redundant and specific promoter occupancy within the *ETS* gene family. *Genes Dev.* 21, 1882–1894.
- Jolma, A., Yan, J., Whittington, T., Toivonen, J., Nitta, K.R., Rastas, P., Morgunova, E., Enge, M., Taipale, M., Wei, G., et al. (2013). DNA-binding specificities of human transcription factors. *Cell* 152, 327–339.
- Larkin, M.A., Blackshields, G., Brown, N.P., Chenna, R., McGettigan, P.A., McWilliam, H., Valentin, F., Wallace, I.M., Wilm, A., Lopez, R., et al. (2007). Clustal W and Clustal X version 2.0. *Bioinformatics* 23, 2947–2948.
- Luo, W., and Skolnik, D.G. (1996). Interferon regulatory factor-2 directs transcription from the gp91phox promoter. *J. Biol. Chem.* 271, 23445–23451.
- Macneil, L.T., and Walhout, A.J.M. (2011). Gene regulatory networks and the role of robustness and stochasticity in the control of gene expression. *Genome Res.* 21, 645–657.
- Maconochie, M., Nonchev, S., Morrison, A., and Krumlauf, R. (1996). Paralogous Hox genes: function and regulation. *Annu. Rev. Genet.* 30, 529–556.
- Martinez, N.J., Ow, M.C., Barrasa, M.I., Hammell, M., Sequerra, R., Doucette-Stamm, L., Roth, F.P., Ambros, V.R., and Walhout, A.J.M. (2008). A *C. elegans* genome-scale microRNA network contains composite feedback motifs with high flux capacity. *Genes Dev.* 22, 2535–2549.
- Maurano, M.T., Humbert, R., Rynes, E., Thurman, R.E., Haugen, E., Wang, H., Reynolds, A.P., Sandstrom, R., Qu, H., Brody, J., et al. (2012). Systematic localization of common disease-associated variation in regulatory DNA. *Science* 337, 1190–1195.
- Pfaeffle, R.W., Hunter, C.S., Savage, J.J., Duran-Prado, M., Mullen, R.D., Neeb, Z.P., Eiholzer, U., Hesse, V., Haddad, N.G., Stobbe, H.M., et al. (2008). Three novel missense mutations within the *LHX4* gene are associated with variable pituitary hormone deficiencies. *J. Clin. Endocrinol. Metab.* 93, 1062–1071.
- Reece-Hoyes, J.S., and Walhout, A.J. (2012). Gene-centered yeast one-hybrid assays. *Methods Mol. Biol.* 812, 189–208.
- Reece-Hoyes, J.S., Barutcu, A.R., McCord, R.P., Jeong, J.S., Jiang, L., MacWilliams, A., Yang, X., Salehi-Ashtiani, K., Hill, D.E., Blackshaw, S., et al. (2011a). Yeast one-hybrid assays for gene-centered human gene regulatory network mapping. *Nat. Methods* 8, 1050–1052.
- Reece-Hoyes, J.S., Diallo, A., Lajoie, B., Kent, A., Shrestha, S., Kadreppa, S., Pesyna, C., Dekker, J., Myers, C.L., and Walhout, A.J.M. (2011b). Enhanced yeast one-hybrid assays for high-throughput gene-centered regulatory network mapping. *Nat. Methods* 8, 1059–1064.
- Reece-Hoyes, J.S., Pons, C., Diallo, A., Mori, A., Shrestha, S., Kadreppa, S., Nelson, J., Diprima, S., Dricot, A., Lajoie, B.R., et al. (2013). Extensive rewiring and complex evolutionary dynamics in a *C. elegans* multiparameter transcription factor network. *Mol. Cell* 51, 116–127.
- Sahni, N., Yi, S., Taipale, M., Fuxman Bass, J.I., Coulombe-Huntington, J., Yang, F., Peng, J., Weile, J., Karras, G.I., Wang, Y., et al. (2015). Widespread macromolecular interaction perturbations in human genetic disorders. *Cell* 161, this issue, 647–660.
- Sharpe, J., Lettice, L., Hecksher-Sorensen, J., Fox, M., Hill, R., and Krumlauf, R. (1999). Identification of sonic hedgehog as a candidate gene responsible for the polydactylous mouse mutant *Sasquatch*. *Curr. Biol.* 9, 97–100.
- Tajima, T., Hattori, T., Nakajima, T., Okuhara, K., Tsubaki, J., and Fujieda, K. (2007). A novel missense mutation (P366T) of the *LHX4* gene causes severe combined pituitary hormone deficiency with pituitary hypoplasia, ectopic posterior lobe and a poorly developed sella turcica. *Endocr. J.* 54, 637–641.
- UniProt Consortium (2015). UniProt: a hub for protein information. *Nucleic Acids Res.* 43, D204–D212.
- Visel, A., Minovitsky, S., Dubchak, I., and Pennacchio, L.A. (2007). VISTA Enhancer Browser—a database of tissue-specific human enhancers. *Nucleic Acids Res.* 35, D88–D92.
- Walhout, A.J.M. (2006). Unraveling transcription regulatory networks by protein-DNA and protein-protein interaction mapping. *Genome Res.* 16, 1445–1454.
- Walhout, A.J.M. (2011). What does biologically meaningful mean? A perspective on gene regulatory network validation. *Genome Biol.* 12, 109.
- Weirauch, M.T., Yang, A., Albu, M., Cote, A.G., Montenegro-Montero, A., Drewe, P., Najafabadi, H.S., Lambert, S.A., Mann, I., Cook, K., et al. (2014). Determination and inference of eukaryotic transcription factor sequence specificity. *Cell* 158, 1431–1443.

Efficient Intracellular Delivery of Native Proteins

Graphical Abstract



Authors

Diego S. D'Astolfo, Romina J. Pagliero, ..., Holger Rehmann, Niels Geijsen

Correspondence

n.geijsen@hubrecht.eu

In Brief

A small-molecule-based method called iTOP serves as an efficient method for the transduction of native proteins and other macromolecules into primary cells.

Highlights

- iTOP enables the intracellular delivery of macromolecules
- iTOP allows the highly efficient transduction of native proteins
- This protein transduction is independent of a transduction peptide sequence
- iTOP mediates efficient manipulation of a wide variety of primary cell types



Efficient Intracellular Delivery of Native Proteins

Diego S. D'Astolfo,^{1,2} Romina J. Pagliero,² Anita Pras,¹ Wouter R. Karthaus,^{1,2} Hans Clevers,^{1,2} Vikram Prasad,³ Robert Jan Lebbink,² Holger Rehmann,² and Niels Geijsen^{1,2,4,*}

¹KNAW-Hubrecht Institute, Uppsalalaan 8, 3584 CT Utrecht, the Netherlands

²University Medical Center Utrecht, Heidelberglaan 100, 3584 CX Utrecht, the Netherlands

³Department of Molecular Genetics, Biochemistry, and Microbiology, University of Cincinnati College of Medicine, Cincinnati, OH 45267, USA

⁴Department of Clinical Sciences of Companion Animals, Faculty of Veterinary Medicine, Utrecht University, Yalelaan 108, 3584 CM Utrecht, the Netherlands

*Correspondence: n.geijsen@hubrecht.eu

<http://dx.doi.org/10.1016/j.cell.2015.03.028>

SUMMARY

Modulation of protein function is used to intervene in cellular processes but is often done indirectly by means of introducing DNA or mRNA encoding the effector protein. Thus far, direct intracellular delivery of proteins has remained challenging. We developed a method termed iTOP, for induced transduction by osmocytosis and propanebetaine, in which a combination of NaCl hypertonicity-induced macropinocytosis and a transduction compound (propanebetaine) induces the highly efficient transduction of proteins into a wide variety of primary cells. We demonstrate that iTOP is a useful tool in systems in which transient cell manipulation drives permanent cellular changes. As an example, we demonstrate that iTOP can mediate the delivery of recombinant Cas9 protein and short guide RNA, driving efficient gene targeting in a non-integrative manner.

INTRODUCTION

Modulation of protein function is a powerful means of intervention in disease. Protein manipulation is usually achieved indirectly, at the DNA or RNA level, either by “knockdown” or mutation of the encoding gene or by ectopic overexpression of wild-type or mutant genes. Transient, non-integrative modulation of cell function by direct intracellular delivery of proteins has appealing application, both in research and the clinic. However, the currently available toolset for the intracellular transduction of proteins is limited.

In 1982, Okada and Rechsteiner reported that brief hypertonic shock followed by a hypotonic treatment can induce the intracellular uptake of proteins into cells (Okada and Rechsteiner, 1982). Unfortunately, this technique proved limited to immortalized cell lines and yielded poor protein transduction efficiencies and poor cell survival in primary cells. The discovery of cell-penetrating peptides (CPPs) sparked renewed interest in protein-mediated cell manipulation. Independent discoveries from Green and Frankel demonstrated that the HIV TAT protein can

transduce itself across the cell membrane (Schwarze et al., 2000). Nagahara and colleagues subsequently demonstrated that TAT-peptide-mediated protein transduction also worked when the TAT peptide was cloned as an in-frame fusion to a recombinant protein of interest, providing a tractable method for the transduction of recombinant proteins (Schwarze et al., 2000). CPP-mediated protein transduction appears to work with all cell types, but the dependence of physical fusion of the CPP with the cargo protein can disrupt protein function or alter the subcellular localization of the fusion protein (Lundberg and Johansson, 2001). Thus, the success of CPP-driven protein transduction is variable and dependent on the nature and physical properties of the protein cargo.

Here, we describe a method for the efficient delivery of native proteins and other macromolecules, such as small RNAs, into primary cells. We discovered that a combination of small molecules drives the highly efficient intracellular delivery of native proteins, independent of any transduction peptide. We termed this process “iTOP” for induced transduction by osmocytosis and propanebetaine. iTOP is an active uptake mechanism in which an NaCl-mediated hyperosmolality, in combination with a transduction compound (a propanebetaine), triggers macropinocytotic uptake and intracellular release of extracellularly applied macromolecules. We demonstrate that iTOP allows the highly efficient delivery of recombinant cytoplasmic and nuclear proteins into a wide variety of primary cell types. Finally, we demonstrate that iTOP of recombinant Cas9 protein and in-vitro-transcribed short guide RNA provides a highly efficient and non-integrative means of gene editing.

RESULTS

Transduction of Native Protein Independent of a Cell-Penetrating Peptide

Protein transduction provides an attractive means to transiently manipulate cell behavior without risk of permanent changes to the cell's genome. We set up a system for protein transduction into cells by generating recombinant Oct4-VP16 protein with an N-terminal histidine tag (H6) and a C-terminal poly-arginine CPP (R11-CPP), to drive self-transduction of the protein across the cell membrane (Zhou et al., 2006) (Figure 1A). To validate the system, we also generated recombinant Oct4-VP16 protein

without the R11-CPP or without both the R11-CPP and histidine purification tags (Figure 1A, top). We used a firefly luciferase reporter plasmid containing six tandem Oct4 binding sites (Tomilin et al., 2000) to measure intracellular activity of transduced Oct4 protein (Figure 1A, bottom). Luciferase activity was measured 12 hr after adding the recombinant Oct4 protein. Transduced H6-Oct4-VP16-R11 protein activated the Oct4-luciferase reporter in a dose-dependent manner (Figure 1B). Surprisingly, addition of the H6-Oct4-VP16 protein (without R11-CPP) or Oct4-VP16 protein (without R11-CPP and H6 tag) elicited the same response (Figure 1B). This finding was highly unexpected, yet the dose-dependent activation of the Oct4 reporter suggested that Oct4 protein was incorporated into the cells independent of the CPP sequence.

We hypothesized that one or more components of the buffer in which we purified the recombinant protein were responsible for the CPP-independent protein transduction. To test this, we examined the effect of omitting individual components of the buffer on Oct4 transduction. As shown in Figure 1C, Oct4-luciferase reporter activation was abrogated when either NaCl or non-detergent SulfoBetaine-201 (NDSB-201) was omitted from the buffer, indicating that a combination of NaCl and NDSB-201 is required for the introduction of Oct4 protein into cells. Because omission of either compound could potentially affect Oct4 protein solubility, it is important to note that the absence of NaCl or NDSB-201 did not result in Oct4 protein precipitation from the solution (data not shown). To exclude the possibility that luciferase reporter activation occurred through an Oct4-protein-independent manner, we also analyzed the effect of the Oct4 protein on a luciferase reporter without Oct4 binding sites. As shown in Figure S1A, the Oct4 protein did not activate the luciferase reporter without Oct4 binding sites, demonstrating that the observed effect was indeed dependent on binding of the transduced Oct4 protein to the target sites. Oct4 specificity was further confirmed using a tandem Oct4-Sox2 reporter (Boyer et al., 2005) and recombinant Oct4 protein synergized with Sox2, again demonstrating its functional specificity (Figure S1B).

Effect of Osmolality, NDSB-201, Time, and Protein Concentration

To further examine the protein transduction parameters, we set up a more direct detection system to quantify transduced protein. We detected intracellular beta-lactamase, a small highly soluble protein (Figures S1C and S1D), using CCF2/AM, a non-fluorescent lipophilic substrate that can readily cross the cell membrane (Figure 1D, see Experimental Procedures). Once in the cytosol, CCF2/AM is cleaved by cytosolic esterases, which activate its fluorescence and leave the now negatively charged form, CCF2, trapped inside the cell. Upon excitation at 409 nm, CCF2 emits (green) light at 520 nm. Cleavage of CCF2 by intracellular beta-lactamase results in a shift in the emission wavelength to blue (447 nm). Thus, the ratio of blue versus green signal accurately quantifies intracellular beta-lactamase.

Using this assay, we explored the effect of time and/or NaCl, NDSB-201, and protein concentration on protein transduction of murine embryonic fibroblasts (MEFs). We discovered that optimal transduction time was directly proportional to the

level of NaCl-induced hyperosmolality, with higher osmolalities resulting in faster protein transduction. Figure 1E integrates the effect of transduction time and different media osmolalities on beta-lactamase protein transduction. As control, beta-lactamase was transduced in isotonic media with addition of NDSB-201 (open squares). At 800 mOsmol/kg, transduction occurred rapidly (orange line) with optimal transduction time at 1.5 hr. In contrast, at 500 mOsmol/kg, transduction proceeded slowly, reaching optimal levels after 12 hr (red line). Intermediate osmolalities resulted in corresponding optimal transduction times as indicated (red and green lines). Extension of protein transduction time beyond the optimal timeframe was detrimental to the cells, resulting in lower transduction efficiency and cell death (Figure 1E, dashed lines).

We next tested whether other hypertonicity-inducing molecules could mediate protein transduction as well. As shown in Figure 1F, NaCl, RbCl, KCl, and LiCl all induced protein transduction at varying levels (Figure 1F). In addition, Na-gluconate supported protein transduction, indicating that the Cl⁻ anion in the added NaCl is dispensable for this process. In contrast, sucrose-, lactulose-, sorbitol-, and mannitol-induced hypertonicity did not support beta-lactamase protein transduction (Figure 1F). The above data demonstrate that protein transduction is critically dependent on hypertonicity induced by alkali metal cation-containing salts, especially Na⁺ and Rb⁺.

Next, we explored the effect of the NDSB-201 concentration on the beta-lactamase transduction. As shown in Figure 1G, beta-lactamase transduction was NDSB-201 dependent and most efficient at an NDSB-201 concentration of 10–25 mM NDSB-201. At high concentrations, NDSB-201 displays some toxicity, resulting in a decrease in protein transduction (Figure S1E).

Finally, we measured CCF2 cleavage as a function of beta-lactamase concentration. As shown, transduction of increasing concentrations of beta-lactamase protein for 3 hr in the presence of 25 mM NDSB-201 and NaCl-adjusted media (osmolality of 700 mOsmol/kg) resulted in increased intracellular beta-lactamase activity (Figure 1H, bars). Beta-lactamase transduction was not observed in the isotonic controls in the presence of 25 mM NDSB-201 (Figure 1H, open circles).

Altogether, this demonstrates that recombinant beta-lactamase protein is incorporated into the cell and released into the cytoplasm and is dependent on hypertonicity induced by Na⁺- or Rb⁺-containing salts, NDSB-201 concentration, transduction time, and extracellular protein concentration. We termed this process “iTOP” (induced transduction by osmocytosis and propanebetaine). Accurate determination of the amount of protein transduced into the cytosol is extremely challenging and is dependent on cell type, protein solubility, half-life, and the concentration at which it can be applied to the cells. Indeed, Figure 1H demonstrates a direct relationship between the extracellular concentration of beta-lactamase protein and the amount transduced into a cell. To provide a reference for the amount of transduced protein, we compared iTOP protein transduction to CCP-dependent protein delivery or the protein transduction method reported by Okada and colleagues. As shown, iTOP delivery is at least four times more efficient in transducing protein into primary fibroblasts than these previously reported methods (Figure S1F).

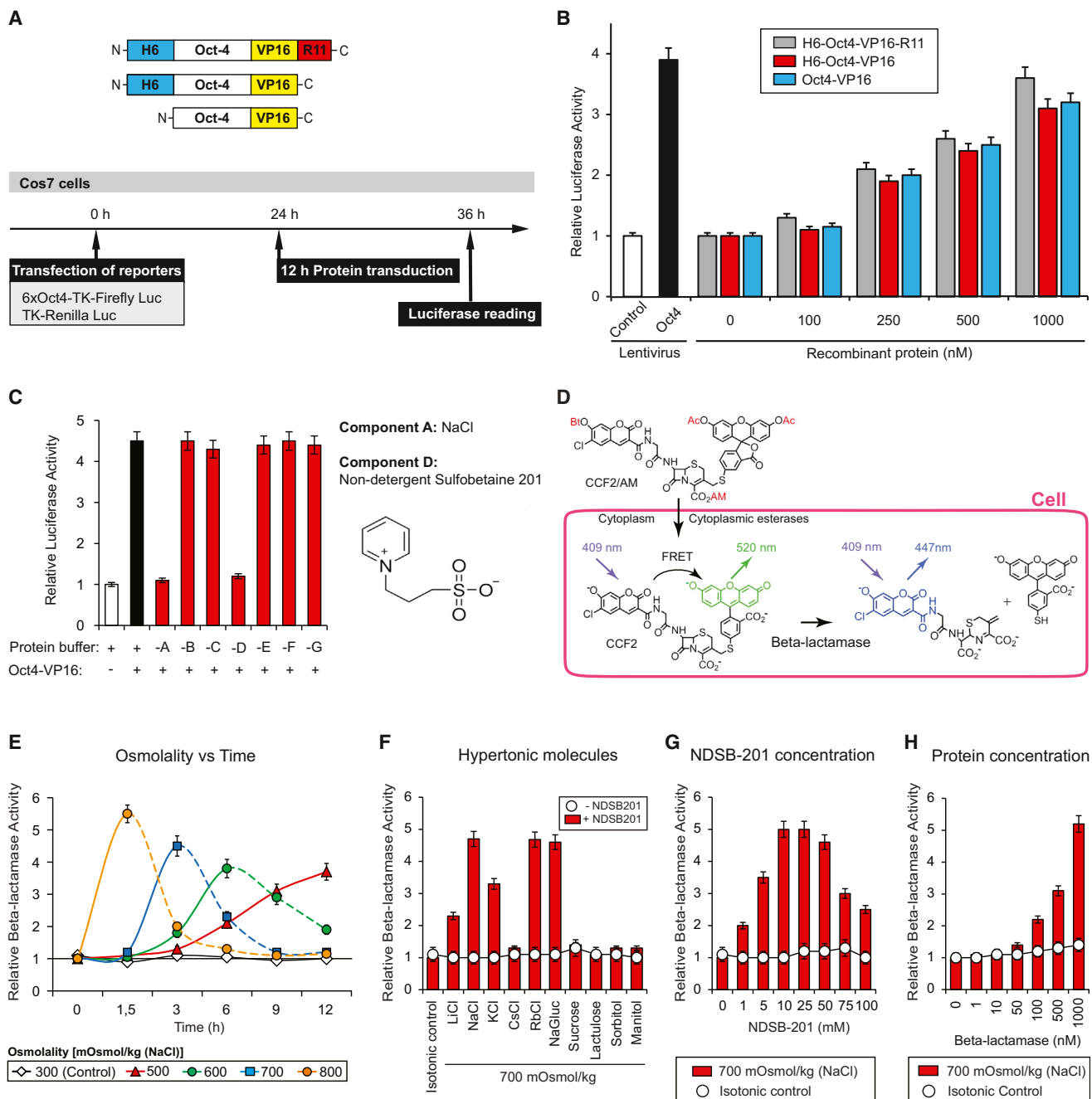


Figure 1. A Combination of NaCl Hypertonicity and NDSB-201 Induces Transduction of Native Proteins

(A) Top: schematic representation of the Oct4 recombinant proteins used in this study. Bottom: timeline of Oct4 protein transduction assay.

(B) Cos-7 cells were transfected with 6xOct4-TK-Firefly-Luc reporter and, 12 hr later, were transduced with increasing amount of Oct4 proteins as indicated. Firefly luciferase activity was normalized by co-transfection of Renilla luciferase construct. Controls were cells transduced with an empty or an Oct4-expressing lentivirus (white and black bars, respectively). Mean \pm SD; n = 3.

(C) Cos-7 cells were transfected with 6xOct4-TK-Firefly-Luc reporter and incubated with Oct4-VP16 protein (Oct4 protein in elution buffer, 1:10 diluted in culture media, black bar) or without protein (white bar). Red bars represent cells transduced with Oct4-VP16 protein in the absence of one of the elution buffer components: A: NaCl (1 M), B: NaH_2PO_4 (50 mM), C: Tris-HCl (50 mM), D: NDSB-201 (250 mM), E: 2-mercaptoethanol (100 μM), F: MgCl_2 (125 μM), and ZnCl_2 (125 μM). Firefly luciferase activity was normalized with co-transfected Renilla luciferase. Mean \pm SD; n = 3.

(D) Schematic representation of the beta-lactamase reporter assay. The cell-permeable CCF2/AM compound is trapped in the cytoplasm by intracellular esterases, which convert it to the non-membrane-permeable, fluorescent CCF2. Excitation of CCF2 at 409 nm results in an emission signal at 520 nm (green signal). CCF2 cleavage by intracellular beta-lactamase abrogates intramolecular FRET, resulting in a shift in the emission wavelength to 447 nm (blue signal).

(legend continued on next page)

Protective Osmolytes Rescue Hypertonicity-Induced Cell-Cycle Inhibition

Although the combination of NaCl-induced hyperosmolality and NDSB-201 promoted efficient protein transduction, it also affected cell proliferation. Hyperosmotic stress is well known to induce cell-cycle arrest, followed by apoptosis in mammalian cells (Kültz et al., 1998). We observed by BrdU incorporation that protein transduction for 3 hr at 700 mOsmol/kg or for 12 hr at 500 mOsmol/kg reduces MEF proliferation by more than 60% compared to untreated cells, independent of the presence of beta-lactamase (Figure 2A). Apoptosis, measured by caspases 3/7 activity assay, was not detected in transduced cells (data not shown).

Osmoprotectants (or protective osmolytes) help cells cope with osmotic stress by accumulating in the cytosol, thereby balancing the osmotic difference between the intra- and extracellular environment. We tested whether the addition of osmoprotectants to media would prevent cell-cycle arrest during protein transduction. MEFs were treated with transduction media alone or supplemented with different osmoprotectants, and BrdU incorporation was measured as indicated in Figure 2B. In the absence of osmoprotectants, incubation of MEFs with transduction media reduced the cell proliferation rate to 34% compared to non-transduced controls (Figure 2B, red bar). The addition of osmoprotectants during transduction ameliorated this cell-cycle arrest to various degrees as shown in Figure 2B (green bars). The combination of glycerol and glycine was found most effective and almost completely prevented the hypertonicity-induced cell-cycle arrest, while still allowing protein transduction (Figure 2C). Unless otherwise indicated, we therefore included glycerol and glycine in subsequent protein transduction experiments.

To explore whether other cell types could similarly be transduced with minimal effect on cell proliferation, we transduced murine embryonic stem cells (mESCs) with beta-lactamase. mESCs appeared more sensitive to the hypertonic conditions. mESC transduction for 3 hr at 700 mOsmol/kg reduced cell proliferation even with added osmoprotectants glycine and glycerol (Figure 2D). We therefore examined whether lowering NaCl-mediated hypertonicity and extending transduction time (as shown in Figure 1E) would allow transduction of more sensitive cell types. Indeed, transduction of mESCs for 12 hr at 500 mOsmol/kg resulted in effective beta-lactamase transduction and minimal effect on cell proliferation (Figure 2D). In fact, it was possible to perform two subsequent rounds of beta-lactamase transduction with BrdU incorporation values of 75% compared to untreated cells (Figure 2E). Thus, a combination of NaCl-mediated hypertonicity, NDSB-201, glycine, and gly-

cerol allows the transduction of native proteins with minimal effect on cell proliferation.

Efficient Protein Transduction in Multiple Primary Cell Types

To determine iTOP efficiency and the range of cell types that could be transduced using this method, we transduced Cre recombinase protein in mESC and other primary cells. We used mESCs containing a single copy of a Cre-activatable GFP-fluorescent reporter integrated in the Rosa26 locus (Srinivas et al., 2001). As outlined in Figure 3A, Cre-mediated removal of a loxP-flanked stop cassette activates a GFP reporter, allowing assessment of the percentage of successfully transduced cells in a population. mESCs were transduced with Cre protein at 500 mOsmol/kg for 12 hr. Increasing concentrations of recombinant Cre-protein resulted in increased percentage of GFP-positive (GFP+) cells (Figure 3B). One round of transduction with 10 μ M of Cre protein activated the GFP reporter in 51% of the mESCs and increased to 79% after a second round of transduction (Figure 3B). To confirm that protein transduction did not affect mESC function, we tested the ability of transduced mESCs to form chimeras upon injection into recipient blastocyst embryos. Figure 3C shows an image of one of the chimeric mice, demonstrating that Cre protein transduction does not affect mESC pluripotency. Chimeric mice were able to generate offspring, demonstrating that Cre-transduced mESCs contributed to the germline (Figure 3D).

We next explored Cre recombinase protein transduction in multiple murine primary cell types isolated from mice carrying one copy of a loxP-mRFP-loxP-mGFP reporter. Single Cre protein transduction for 12 hr at 500 mOsmol/kg efficiently activated the GFP reporter in multiple cell types, including neuronal and gut stem cells, dendritic cells, embryonic fibroblasts, glia cells, and neurons (Figure 3E). The above experiments demonstrate a highly efficient protein transduction method that is applicable to many primary cell types.

We also explored whether human embryonic stem cells (hESCs) could be transduced using this method. We used H1 hESCs stably transduced with a lentiviral Cre-activatable reporter containing an active red fluorescence protein (RFP) gene flanked with LoxP sites, followed by a stop sequence and a (inactive) GFP reporter gene (Figure 3F). Cre-mediated deletion of the loxP-flanked RFP-stop segment activates the GFP reporter. The H1 reporter hESC line was transduced with Cre protein for 12 hr at 500 mOsmol/kg. As shown in Figure 3G, we obtained 64% and 78% of GFP-positive cells after one and two rounds of Cre protein transduction, respectively.

(E) MEFs were transduced with 1 μ M of beta-lactamase protein, 25 mM NDSB-201 at different NaCl-adjusted osmolalities (indicated by the color lines) and for varying amounts of time as indicated. Isotonic media (open rhombs) containing NDSB-201 and beta-lactamase protein, but without additional NaCl, were used as a negative control. Relative beta-lactamase activity calculated per well is plotted as a function of transduction time. Dotted lines indicate the presence of cell death due to prolonged transduction conditions. Mean \pm SD, $n = 4$.

(F) Analysis of the transduction activity of different hypertonicity inducers. MEFs were transduced for 3 hr with 1 μ M beta-lactamase protein at an osmolality of 700 mOsmol/kg induced by different compounds as indicated (red bars, transduction with NDSB-201; open circles, control transduction in the absence of NDSB-201). Relative beta-lactamase protein uptake in isotonic transduction media (bar #1) was set at 1. Mean \pm SD; $n = 3$.

(G) Beta-lactamase reporter assay on MEFs transduced for 3 hr with 1 μ M of beta-lactamase protein with different concentrations of NDSB-201 with an osmolality of 700 mOsmol/kg induced by NaCl (red bars). The controls were cells treated as before but with isotonic media (white circles). Mean \pm SD; $n = 3$.

(H) Beta-lactamase reporter assay on MEFs transduced as in (G) with different concentrations of beta-lactamase protein (red bars). The controls were cells treated as before in isotonic media (white circles). Mean \pm SD; $n = 3$.

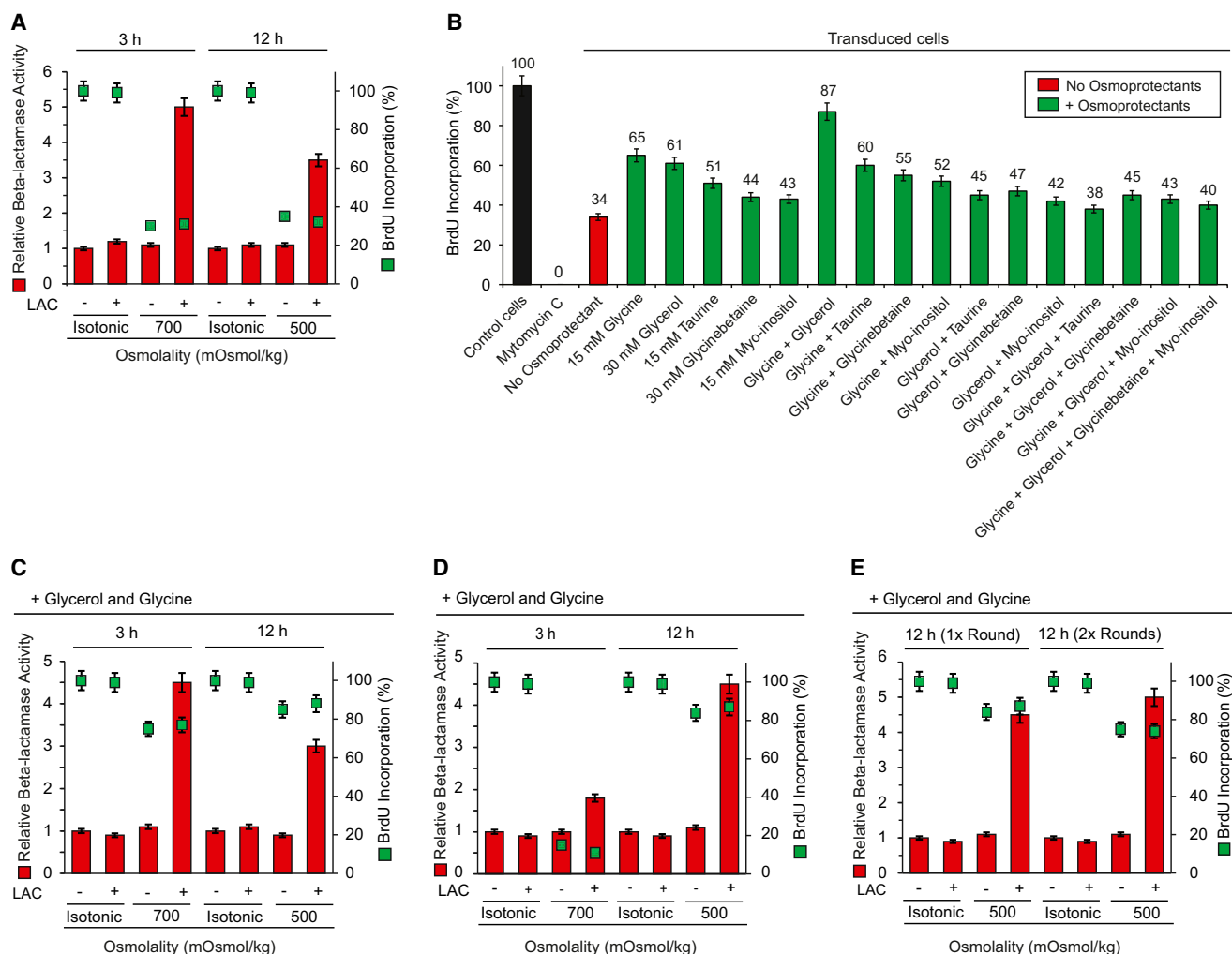


Figure 2. Addition of Osmoprotectants to the Transduction Media Ameliorates Hypertonicity-Induced Cell-Cycle Inhibition

(A) Beta-lactamase assay (red bars) coupled with BrdU incorporation assay (green squares). MEFs were transduced with 25 mM NDSB-201 at different osmolalities and time points with or without beta-lactamase as indicated. Beta-lactamase activity was measured relative to cells incubated in isotonic media, which were set at 1. Cell proliferation was measured by BrdU incorporation as described in the methods. BrdU incorporation of untreated cells was set at 100% (not shown). Mean \pm SD; n = 3.

(B) MEFs were incubated with transduction media, containing 1 μ M of beta-lactamase protein, 50 mM of NDSB-201, and an osmolality induced by NaCl of 500 mOsmol/kg (red bar) or with transduction media supplemented with different osmoprotectants as indicated (green bars). The BrdU incorporation values of untreated cells (left black bar) were set at 100%. BrdU incorporation values of mitomycin-C-treated cells used as control for cell-cycle arrest were set at 0%. Mean \pm SD; n = 3.

(C) Beta-lactamase transduction (red bars) and BrdU incorporation (green squares) in MEFs. Cells were transduced with 25 mM NDSB-201 at different osmolalities and time points with or without Beta-lactamase as indicated with addition of 30 mM of glycerol and 15 mM of glycine as osmoprotectants. Beta-lactamase activity was measured relative to cells incubated in isotonic media, which were set at 1. The BrdU incorporation values of untreated cells and mytomycin-C-treated cells were set at 100% and 0%, respectively (not shown). Mean \pm SD; n = 3.

(D) Beta-lactamase transduction (red bars) and BrdU incorporation (green squares) in mESCs as in (C). Mean \pm SD; n = 3.

(E) Beta-lactamase transduction (red bars) and BrdU incorporation (green squares) in mESCs after one or two rounds of protein transduction. mESCs were transduced once or twice as indicated with a 12 hr interval between transductions. The relative beta-lactamase activity was measured in relation to cells incubated in isotonic media, which were set at 1. The BrdU incorporation values of untreated cells and mytomycin C treated cells were set at 100% and 0%, respectively (not shown). Mean \pm SD; n = 3.

Essential Structural Features of the Transduction Compound

As shown, the small-molecule NDSB-201 is essential for the introduction of native protein into cells. NDSB-201 is part of a

group of zwitterionic compounds used to reduce protein aggregation and facilitate protein refolding (Vuillard et al., 1995). Six different NDSB molecules are commercially available (Figure 4A). To determine the essential chemical properties of NDSB-201,

we analyzed the transduction activity of these NDSBs and their effect on cell survival. As described before, MEFs were transduced with beta-lactamase protein for 3 hr with NaCl-adjusted osmolality of 700 mOsmol/kg. Beta-lactamase protein transduction of NDSB-201 (reference molecule #01) was set as 100%. As shown in Figure 4A, all NDSB molecules were capable of transducing beta-lactamase protein but with varying efficiencies and impact on cell proliferation. Whereas molecules #02 and #03 performed similar or better than our reference compound, molecules #04 and #06 lowered beta-lactamase transduction levels and reduced cell proliferation rate; molecule #05 performed poorly and arrested cell cycle, even in the presence of osmoprotectants.

It is well known that the sulfonate group is a potential cause of small-molecule toxicity. Thus, we replaced the sulfonate group in molecules #01 and #03 with a carboxyl group (generating molecules #09 and #10, Figure 4B) and tested the effect on transduction and cell proliferation. As shown in Figure 4B, replacement of the sulfonate group did not affect protein transduction efficiency but further improved cell proliferation, reaching values of 95% of BrdU incorporation compared to non-transduced controls.

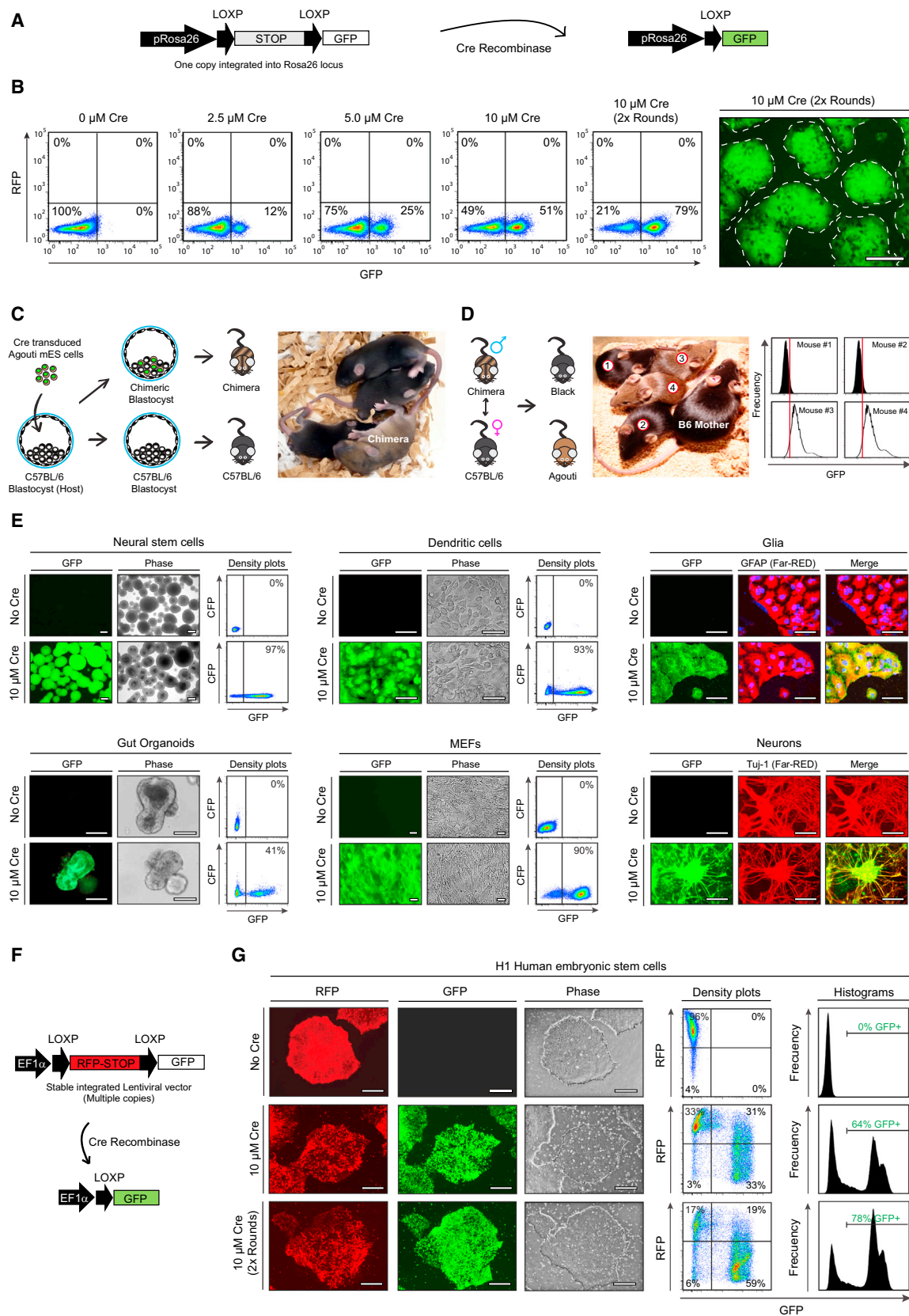
Further reducing the complexity of compound #09 yielded compound #11, in which the permanently positively charged quaternary amine group of compound #09 was replaced by a primary amine. The resulting molecule is gamma-amino-butyric acid (GABA), which exists as a zwitterion at neutral pH and thus contains a similar positive and negative charge at the molecule's termini. As shown in Figure 4B, GABA yielded excellent protein transduction efficiency and minimal effect on cell proliferation, with BrdU incorporation rate of 95% compared to untransduced controls. The finding that GABA, a well-known neurotransmitter, can mediate protein transduction was unexpected and suggested the involvement of GABA signaling in this process. However, protein transduction was not affected by neither the addition of well-known GABA agonists (Figure S2A) nor specific inhibitors of GABA receptor signaling (Figure S2B). Moreover, the concentration at which GABA is effective in protein transduction (25 mM) is similar to the concentration of NDSB-201 and is about 10,000-fold higher than its EC_{50} as a neurotransmitter ($\pm 2.5 \mu\text{M}$; Mortensen et al., 2010). Therefore, it seemed likely that the physicochemical properties of GABA, rather than its role as a signaling molecule, were responsible for its protein-transducing activity. As mentioned above, the non-detergent sulfobetaine (NDSB) compounds were developed for their ability to enhance protein solubility (Vuillard et al., 1995). We therefore tested whether GABA could similarly prevent protein aggregation. A particularly insoluble protein is Cas9, an RNA-guided nuclease that can be used for specific gene editing, which we will describe in more detail below. Production and purification of recombinant Cas9 protein proved particularly challenging and required a higher concentration of NDSB-201 to prevent the protein aggregation and precipitation. To test whether GABA was similarly able to promote protein solubility, we made a dilution series of either NDSB-201 or GABA and added recombinant Cas9 protein at a final concentration of 10 μM . NDSB-201 efficiently prevented protein precipitation at a concentration of 200 mM. As shown, GABA could substitute

NDSB-201 and prevent protein aggregation at similar concentrations (Figure 4C).

At neutral pH, NDSBs and its analogs (Figure 4) are zwitterionic compounds that have a negatively charged hydrophilic group, a short 3-carbon hydrophobic chain and a positively charged amine terminus with various possible substituents. The hydrophobic middle domain is too short to form micelles, and thus, NDSBs are not considered detergents (Vuillard et al., 1995). To identify the minimal essential structure necessary for transduction, we tested the beta-lactamase protein transduction activity of several analogs of NDSB and/or GABA (Figure 4D). We analyzed the importance of the charged amine and sulfonate/carboxyl termini of the molecules by removing these groups from the structure. The analogs lacking the amine (#07 and #12, Figure 4D) or the sulfonate/carboxyl groups (#08 and #13, Figure 4D) yielded very poor protein transduction levels and reduced cell proliferation, although cell survival and beta-lactamase protein solubility were not affected (data not shown). These data demonstrate that the presence of the amine and sulfonate/carboxyl groups at the transduction compound termini is essential for protein transduction. Finally, we evaluated the optimal distance between the amine and sulfonate/carboxyl groups by varying the length of the carbon chain in molecules #10 and #11 (Figure 4E). As shown in Figure 4E, a deleterious effect on protein transduction was observed when the carbon chain was shorter or longer than three carbons. Above data demonstrate that the minimal structure necessary to allow efficient protein transduction is a zwitterionic molecule, which, at neutral pH, consists of a positively charged amino group and a negatively charged sulfonyl or carboxyl group separated by a three-carbon chain. To assure that the reduced transduction efficiencies observed by some of the compounds were not the result of poor protein solubility, we analyzed beta-lactamase protein precipitation in the presence of different betaine compounds. With the exception of the control sample, in which protein precipitation was induced by adding ethanol, the different transduction compounds mentioned above did not induce beta-lactamase protein precipitation (Figure S2C).

Dissecting the Mechanism of Protein Transduction

Because proteins are too large to diffuse through the plasma membrane, we suspected that protein transduction involved an active transport mechanism. Extracellular particles can enter via several distinct endocytic pathways: dynamin-dependent endocytosis, which is further subdivided in clathrin- and caveolae-mediated endocytosis, and dynamin-independent endocytosis, which includes macropinocytosis, the uptake of large (0.5–5 μm) vesicles containing gulps of extracellular fluid. We used specific inhibitors of these endocytic pathways to determine the mechanism of protein uptake. MEFs were incubated with inhibitors of dynamin-, clathrin-, or caveolin-mediated endocytosis or macropinocytosis for 1 hr prior to transduction with beta-lactamase protein. As shown in Figure 5A, inhibition of dynamin-, clathrin-, or caveolin-mediated endocytosis did not affect beta-lactamase uptake. In contrast, the macropinocytosis inhibitors 5-(N-Ethyl-N-isopropyl)amiloride (EIPA) and 5-(N,N-Dimethyl)amiloride (DMA) resulted in a profound reduction in beta-lactamase transduction. Macropinocytosis requires



(legend on next page)

active rearrangements of the actin cytoskeleton, which is mediated by the small GTPases Rac1 and CDC42 through activation of the downstream effector kinase Pak1. As expected, cytochalasin D or latrunculin A, which potently block actin polymerization, inhibited beta-lactamase transduction (Figure 5A). In addition, specific inhibitors of RAC1, CDC42, and Pak1 alone or in combination efficiently block beta-lactamase transduction in MEFs (Figures S3A and S3B). Altogether, these results indicate that protein transduction is mediated through macropinocytosis.

Macropinocytosis is regulated by a family of Na^+/H^+ antiporters, which are targeted by the EIPA and DMA inhibitors described above. These NHE antiporters are rapidly activated in response to a wide variety of extracellular stimuli, including hypertonicity induced by Na^+ -containing salts. Nhe1 (Slc9A1) is a ubiquitously expressed member of this family and therefore is a likely candidate to be involved in the protein transduction process. To determine the role of Nhe1 in protein transduction, we analyzed beta-lactamase protein transduction in Nhe1 mutant MEFs. Heterozygous or homozygous deletion of Nhe1 resulted in a profound reduction in intracellular beta-lactamase activity, demonstrating that Nhe1 plays an important role in protein transduction (Figure 5B). The residual protein transduction activity observed in the absence of Nhe1 function is likely a redundant effect of other members of the Nhe antiporter family.

Several growth factor activators of tyrosine kinase signaling were shown to stimulate macropinocytosis. Therefore, we examined whether the addition of growth factors could enhance intracellular delivery of beta-lactamase protein. As shown in Figure 5C, EGF, bFGF, PDGF, IGF, and insulin all enhanced beta-lactamase transduction, and combinations demonstrated an additive effect.

The above data demonstrate that iTOP protein transduction occurs through macropinocytosis uptake of extracellularly

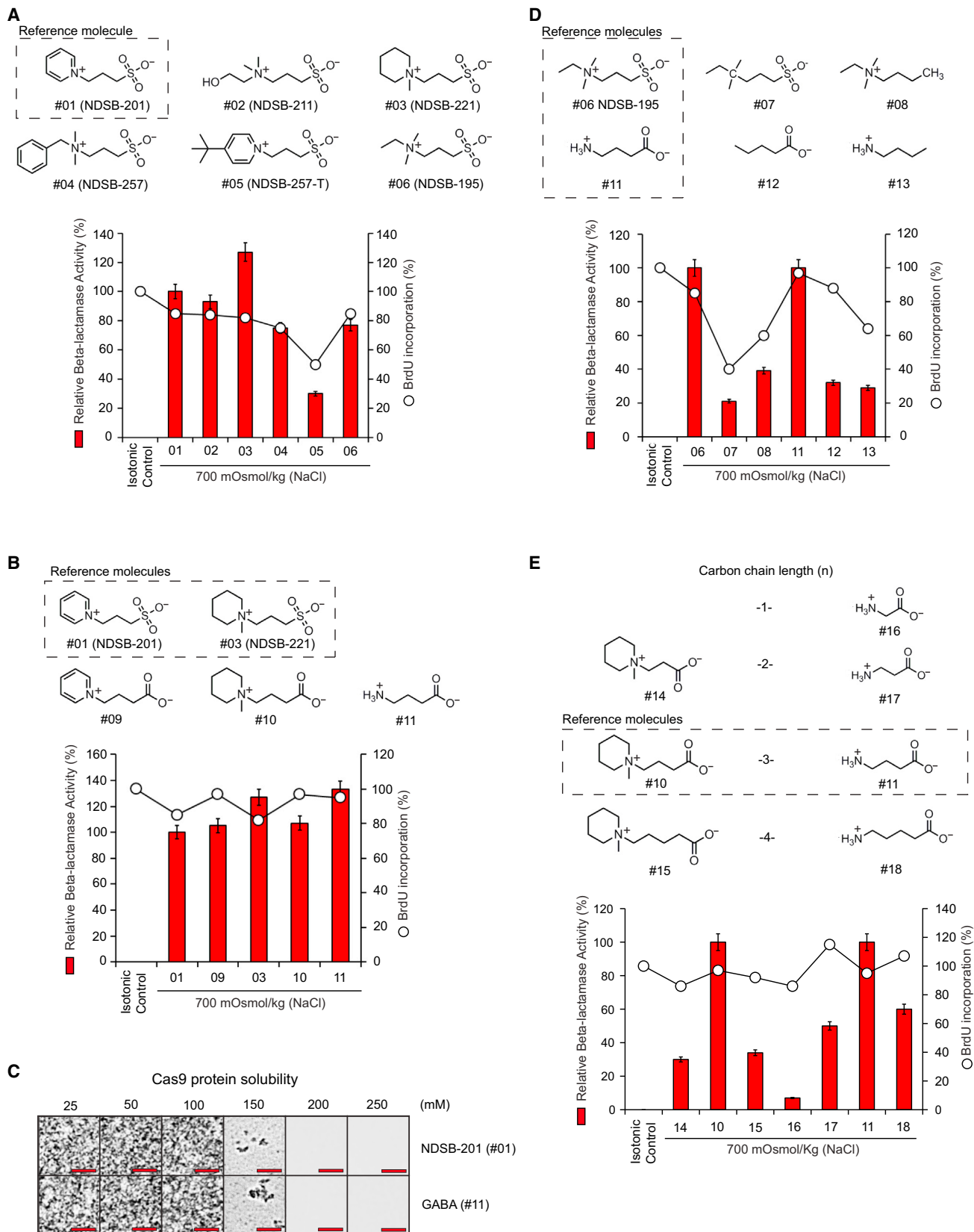
applied protein, which is subsequently released from the internalized macropinosomes. To quantify the differential roles of NaCl hypertonicity and the transduction compound in protein uptake and intracellular release, we set up two imaging-based assays.

Macropinocytosis can be quantified by measuring the uptake of fluorescently labeled high-molecular-weight dextran (Figure 5D; Commisso et al., 2014). To determine whether dextran carbohydrate uptake and protein uptake followed the same path, MEFs were co-transduced with red fluorescent dextran (TMR-dextran) and far-red fluorescent BSA protein (BSA-Alexa647) for 1 hr at 700 mOsmol/kg. As shown in Figure 5D, all dextran-positive macropinosomes contained BSA and vice-versa, demonstrating that the uptake of TMR-dextran and proteins proceed via the same mechanism (Figure 5D). Moreover, the simultaneous uptake of Dextran and BSA was blocked by the macropinocytosis inhibitor EIPA (Figure 5D). Together, these data demonstrate that the recently described TMR-dextran assay for the quantification of macropinocytosis (Commisso et al., 2014) can be utilized to accurately monitor the macropinocytotic uptake step in the iTOP process.

To quantify the release of internalized macropinosomes, we used a galectin3-fluorescent reporter system that has been described earlier to monitor vesicle leakage induced by drugs or pathogens (Paz et al., 2010; Ray et al., 2010). Galectin-3 is a small soluble cytosolic protein that can bind betagalactoside sugar-containing carbohydrates. These are normally present only on the exterior of the plasma membrane and the interior of intracellular endocytic vesicles. Rupture of internalized vesicles results in galectin-3 relocalization and accumulation at the internal vesicle membrane. Fusion of galectin-3 to a monomeric green fluorescent protein (mAG-GAL3) allows visualization of galectin-3 relocalization and has been used as a tool to monitor vesicle rupture during pathogen infection (Paz et al., 2010; Ray

Figure 3. Efficient Cre Protein Transduction in Multiple Primary Stem and Differentiated Cells

- (A) Schematic representation of the Cre reporter in mESCs. A single copy of a loxP-Stop-loxP-GFP reporter was inserted in the Rosa26 locus. Excision of the Stop cassette by Cre-recombinase protein induces GFP expression.
- (B) Left: FACS analysis of a dose response curve of mESCs transduced with Cre at different concentrations as indicated (panels 1–4) or after two rounds of Cre transduction (panel 5). Right: fluorescence microscopy image of mESCs treated with two rounds of Cre transductions as described above. Dashed lines indicate the border of each colony. Scale bar, 50 μm .
- (C) Left: schematic representation of the mouse chimera assay. mESCs were injected into host blastocyst embryos, and mESC contribution to resulting chimeras is assessed by coat color. Cre-protein transduced GFP-positive mESCs derived from agouti (F1BL6/129Sv) mice (brown hair color) were injected into C57BL/6 host blastocyst (black hair color). Brown hair in the resultant pups indicates chimera contribution of the injected ESCs. Right: image of litter with chimera.
- (D) Left: schematic representation of the germline transmission assay. Chimera in C was mated with a C57BL/6 female. Agouti coat color of resultant pups demonstrates the ESC origin of the germ cells. Center: image of litter with two agouti pups demonstrating germline transmission of the injected ESCs. Right: FACS analysis of GFP expression in blood cells of the pups depicted in the central panel. The agouti pups (#3 and #4) display GFP expression, whereas the black pups (#1 and #2) are negative.
- (E) Left and middle: Cre protein transduction of multiple cells types derived from loxP-mRFP-loxP-mGFP reporter mice. Representative fluorescence and phase contrast images of Cre transduced cells. The control was cells incubated with transduction media without Cre protein. Scale bar, 50 μm . Percentage of GFP-positive cells was determined by flow cytometry. Right top: fluorescence microscopy images of Cre transduced glia cells. As control, cells were incubated with transduction media without Cre protein. Left: GFP expression. Middle: expression of GFAP, a glia-specific marker. Right: merge. Scale bar, 50 μm . Right bottom: fluorescence microscopy images of Cre transduced neural cells derived from loxP-stop-loxP-GFP mESCs. As control, cells were incubated with transduction media without Cre protein. Left: GFP expression. Middle: expression of TuJ1, a neural cell-specific marker. Right: merge. Scale bar, 50 μm .
- (F) Schematic representation of the Cre recombinase reporter. A lentiviral EF1a-loxP-RFP-loxP-GFP/ires-PuroR construct was stably introduced into hESCs. Cre excises the loxP-flanked RFP-STOP cassette and switches fluorescence from red (RFP) to green (GFP).
- (G) Left: fluorescence and phase contrast images of Cre-transduced human ESCs. hESCs were transduced once or twice with Cre protein as indicated. Control was cells incubated with transduction media without Cre protein. Left row, RFP expression; middle row, GFP expression; right row, phase contrast. Scale bar, 50 μm . Right: flow cytometry analysis of Cre-transduced human ESCs. The density plots show the percentage of cells expressing RFP (upper left area) or GFP (lower right area). Double-positive cells (upper right area) result from multiple integrations of the lentiviral reporter. Total percentage GFP expressing cells is shown in the histogram plots.



(legend on next page)

et al., 2010). Upon mAG-GAL3 binding to carbohydrates in the interior of ruptured vesicles, a multimer complex is formed with intense green fluorescence (Figure 5E). Transduction of MEFs expressing mAG-GAL3 protein for 1–3 hr at 700 mOsm/kg resulted in the appearance of bright green vesicles, demonstrating leakage of the internalized macropinosome membrane under iTOP conditions. mAG-GAL3 vesicles were not formed when cells were pre-incubated with macropinocytosis inhibitor EIPA or under isotonic conditions (Figure 5E). These results demonstrate that iTOP conditions promote protein uptake from the extracellular space via macropinocytosis and induce macropinosome vesicle leakage to release proteins into the cytosol.

Using the above assays to quantify uptake and release, we measured beta-lactamase protein transduction, macropinocytosis, and vesicle leakage (Figure 5F). As expected, protein transduction measured by beta-lactamase assay was only observed in cells treated with hypertonic media in the presence of either NDSB-201 or GABA transduction compounds (Figure 5F, blue bars). Control compounds with a shorter carbon chain, glycine, and glycine-betaine, did not mediate beta-lactamase transduction even though macropinocytosis was induced in all hypertonic conditions (Figure 5F, red bars), indicating that NaCl hypertonic media alone are sufficient to efficiently induce macropinocytosis. Transduction compound alone, in the absence of NaCl-mediated hypertonicity, did not induce macropinocytosis (data not shown). The combined data on beta-lactamase transduction and macropinocytosis suggested that the transduction compounds were responsible for the release of protein from the internalized macropinosomes. Indeed, the mAG-GAL3 reporter assay demonstrated that intracellular macropinosome leakage only occurred in the presence of NDSB-201 or GABA (Figure 5F, green bars). When macropinosome leakage occurred, the vesicle contents were completely released into the

cytoplasm (data not shown). Images of the mAG-GAL3 assay on the various compounds used in Figure 5F are shown in Figure S3C. The macropinocytosis inhibitor EIPA efficiently blocked both beta-lactamase protein transduction, macropinocytosis, and the appearance of mAG-GAL3-positive vesicles. Together, these data indicate that NaCl hypertonicity induces macropinocytosis-mediated uptake of protein from the extracellular space, whereas NDSB-201 or GABA molecules promote intracellular macropinosome leakage, allowing the release of the vesicle content into the cytosol.

Protein-Mediated Gene Editing

The high efficiency of iTOP has appealing application in systems in which transient cell manipulation can elicit a binary cellular effect or response. The recently discovered CRISPR-Cas9 system consists of the *Streptococcus Pyogenes* Cas9 nuclease protein, which is guided to specific genomic loci by a small guide RNA (sgRNA) (Chapientier and Doudna, 2013). The Cas9 nuclease creates a double-strand break at the target locus, which, when repaired through non-homologous end joining (NHEJ), frequently results in gene disruption by the resulting frame shift mutation. Due to its elegant simplicity, the CRISPR-Cas9 system has quickly become a popular tool for gene editing. However, application of this system by means of DNA or RNA transfection is inefficient in primary cells and typically requires marker selection of transfected cells. We explored whether iTOP of recombinant Cas9 protein and its guide RNA can offer an alternative, more efficient means of applying this gene-editing system.

As shown above, Cas9 protein requires high concentrations of both salt (500 mM NaCl) and the transduction compound (250 mM) to remain soluble (Figures 4C and S4A). We noticed that, under this condition, the NSDB-201 transduction compound was toxic to the cells, but GABA was well tolerated (Figures S4B and S4C). At this tonicity (1,250 mOsm/Kg),

Figure 4. Structure-Activity Analysis of Protein Transduction Compounds

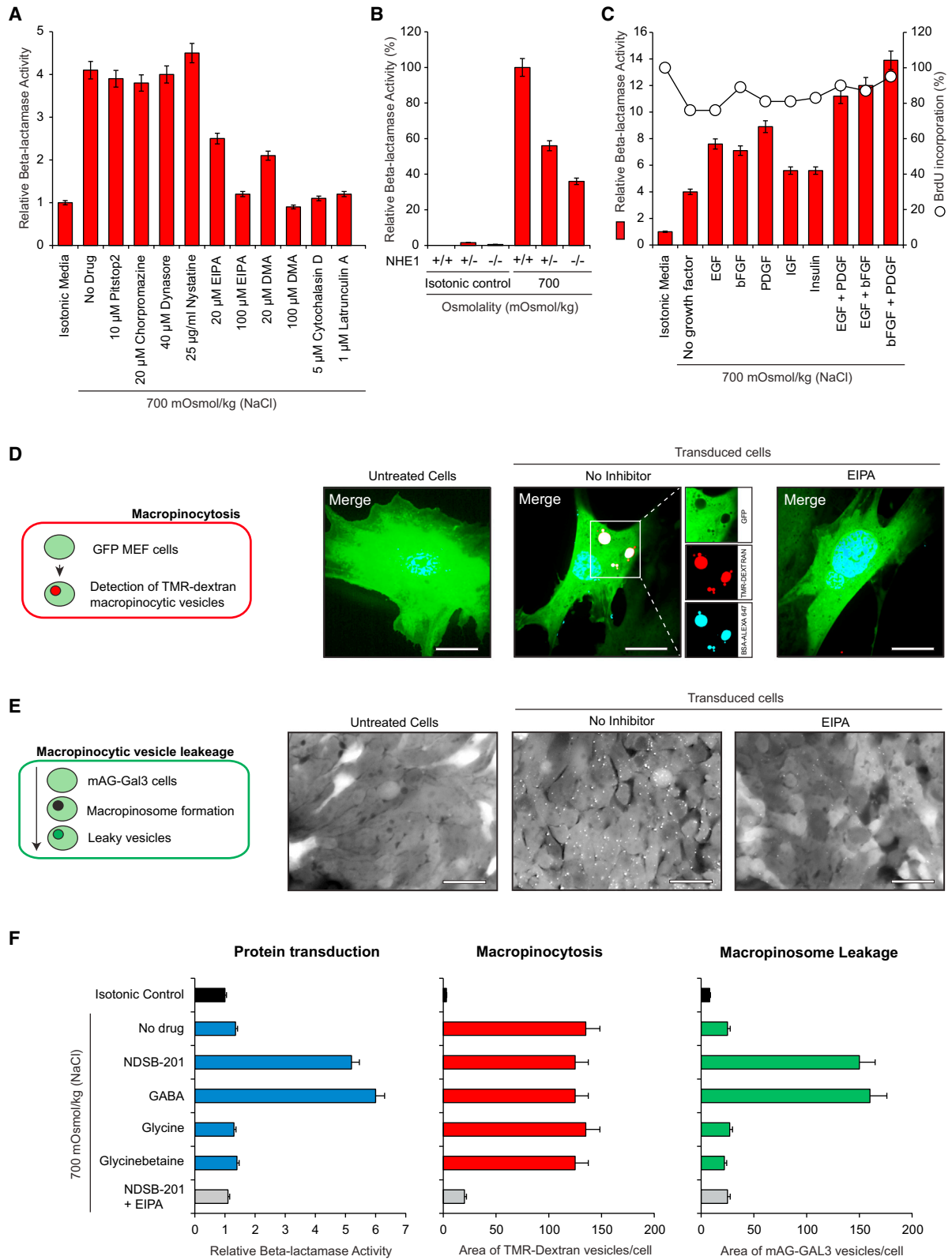
(A) Top: chemical structures of tested non-detergent sulfobetaines. Compound numbers are indicated below the structure. Bottom: beta-lactamase and BrdU incorporation assays using the different transduction compounds as indicated. MEFs were transduced for 3 hr with transduction media containing a NaCl-adjusted osmolality of 700 mOsm/kg, 1 μ M Beta-lactamase protein, 30 mM of Glycerol, 15 mM of Glycine, and 25 mM of the indicated transduction compounds. Beta-lactamase incorporation values of cells treated with transduction media with the reference compound (NDSB-201, #01) were set as 100%, and values of cells treated with isotonic transduction media were set as 0%, as described in the Experimental Procedures. Open circles indicate relative BrdU incorporation by the transduced cells. BrdU incorporation of untransduced cells was set at 100%, and BrdU incorporation of mitomycin-C-treated cells was set at 0%. Mean \pm SD; n = 3.

(B) Top: chemical structures transduction compound analogs. First row: tested analogs with sulfonic group. Second row: analogs with carboxy group. Compound numbers are indicated below the structure. Bottom: beta-lactamase and BrdU incorporation assays using the different transduction compounds as indicated. MEFs were transduced as described in (A). Beta-lactamase activity and BrdU incorporation values were analyzed as in (A). Mean \pm SD; n = 3.

(C) Images demonstrating the effect of increasing concentrations of the transduction compounds NSDB-201 or GABA on Cas9 protein solubility. From left to right, increasing transduction compound concentration (mM). Rows are different transduction compounds. Scale bar, 50 μ m.

(D) Top: chemical structures of transduction compounds analogs. Compounds in left columns contain amine and sulfonate or carboxy group. Central column shows analogs without amine group. Right column shows analogs without sulfonate or carboxy group. Compound numbers are indicated below the structure. Bottom: beta-lactamase and BrdU incorporation assays using the different transduction compounds as indicated. MEFs were transduced with beta-lactamase protein and beta-lactamase activity and BrdU incorporation were analyzed as in (A). Beta-lactamase activity of the reference compounds (NDSB195, #06 and GABA, #11) was set at 100%. Values derived from compounds #07 and #08 were referred to compound #6. Values derived from compounds #12 and #13 were referred to compound #11. Beta-lactamase activity of cells treated with isotonic transduction media was set as 0%. BrdU incorporation is shown as open circles as in (A). Mean \pm SD; n = 3.

(E) Analysis of the role of the carbon-chain length. Structures are examples of two transduction compounds (reference molecules #10 and #11) with carbon-chain length variations of these. Bottom: beta-lactamase and BrdU incorporation assays using the different transduction compounds as indicated. MEFs were transduced with beta-lactamase protein, and beta-lactamase activity and BrdU incorporation were analyzed as in (A). Beta-lactamase incorporation of the reference compounds (#10 and #11) was set at 100%. Beta-lactamase activity of cells treated with isotonic transduction media was set as 0%. Values derived of compound #14 and #15 were referred to compound #10. Values derived of compound #16, #17, and #18 were referred to compound #11. BrdU incorporation is shown as open circles as in (A). Mean \pm SD; n = 3. For more details of the transduction compounds and their analogs, see Table S2.



(legend on next page)

transduction occurs within 60–90 min and is extremely efficient, as shown by the transduction of recombinant Cre protein (Figures S4D–S4F). Previous reports have demonstrated that hypertonic stress can cause DNA breaks in inactive regions of the genome (Redon and Bonner, 2011). However, our iTOP transduction conditions include osmoprotectants, which should prevent DNA damage from occurring. We performed a TUNEL (terminal deoxynucleotyl transferase dUTP nick end labeling) assay to determine the effect of our iTOP hypertonic conditions in the presence or absence of osmoprotectants. As expected, the osmoprotectants in the iTOP transduction buffer effectively prevented hypertonicity-induced DNA damage (Figure S4G). In addition to the recombinant Cas9 protein, CRISPR/Cas9 gene editing requires intracellular delivery of sgRNAs. To determine whether iTOP transduction allows the intracellular delivery of RNA molecules as well, we analyzed the effect of siRNA transduction in knocking down target GAPDH. As shown in Figure S4H, iTOP transduction of siRNA resulted in efficient and specific knockdown of target GAPDH, demonstrating that, in addition to protein, iTOP transduction can be used for the delivery of small RNAs as well.

To explore whether recombinant Cas9 protein and guide RNA could be co-transduced into cells under iTOP conditions (iTOP-CRISPR/Cas9), we produced recombinant Cas9 protein and generated sgRNAs by in vitro transcription from DNA templates (Figure 6A). A reporter in which the presence of an AAVS1 target sequence produces an out-of-frame non-fluorescent dTomato gene was used to monitor the introduction of recombinant Cas9-sgRNA (Figure 6B). CRISPR-Cas9 targeting

of the AAVS1 sequence results in a frame shift and activates dTomato fluorescence. KBM7 cells stably expressing the reporter were transduced with Cas9 protein together with the corresponding AAVS1 sgRNA. After one round of Cas9-sgRNA transduction, 30% of reporter KBM7 cells reestablished dTomato protein expression (Figure 6C). Upon a second round of Cas9-sgRNA transduction, 56% of the cells became dTomato positive. Targeting was specific to the AAVS1 sequence because off-target sgRNAs with two nucleotide substitutions did not activate the dTomato reporter (Figure 6C). Similar experiments were performed in H1 human embryonic stem cells with an observed efficiency of 10% and 26% of dTomato-positive cells after one and two rounds of transduction, respectively (Figure 6D). The above results demonstrate that iTOP of recombinant Cas9 protein and sgRNA allows efficient and specific gene modification in reporter cells.

To determine the efficiency of the iTOP-CRISPR/Cas9 system, we targeted an endogenous gene. We chose to target *DPH7* (WDR85), a gene that was identified as an essential host factor for Diphtheria toxin lethality (Carette et al., 2009). Biallelic deletion of *DPH7* renders human cells resistant to Diphtheria toxin-induced cell death, providing a simple and effective means of identifying knockout cells and measuring the efficiency of biallelic gene knockout upon iTOP-CRISPR/Cas9. We used a near-diploid clone of the KBM7 cells to disrupt the *DPH7* gene (Figure S5A). KBM7 cells were transduced twice with Cas9 protein, plus one of six different sgRNAs as are indicated in Figure 7A. Seven days after protein transduction, cells were treated with diphtheria toxin for 48 hr, after which the number of viable

Figure 5. Protein Transduction Is Mediated by Macropinocytosis

(A) MEFs were preincubated for 1 hr and transduced for 3 hr in the presence of small-molecule inhibitors of dynamin-mediated endocytosis (Dynasore), Clathrin-mediated endocytosis (Pitstop2 and chlorpromazine), Caveolin-mediated endocytosis (Nystatin), macropinocytosis (EIPA, Ethylisopropylamiloride and DMA, Dimethylamiloride), or actin polymerization (Cytochalasin D and Latrunculin A) as indicated. MEFs were transduced for 3 hr with 1 μ M beta-lactamase protein at a NaCl-adjusted osmolality of 700 mOsmol/kg in transduction media containing 25 mM of NDSB-201, 30 mM of Glycerol, and 15 mM of Glycine supplemented with small-molecule inhibitors as indicated. Relative beta-lactamase protein uptake in isotonic transduction media (left bar) was set at 1. Mean \pm SD; n = 3.

(B) Role of Nhe1 in protein transduction. MEFs derived from wild-type, Nhe1 heterozygous ($+/+$), and Nhe1 knockout ($-/-$) embryos were transduced for 3 hr with 1 μ M beta-lactamase as in (A). Beta-lactamase transduction values of wild-type cells (bar #4) were set at 100%, and beta-lactamase transduction of wild-type cells in isotonic media (bar #1) was set at 0%. Mean \pm SD; n = 3.

(C) The effect of growth factors on beta-lactamase transduction. MEFs were transduced for 3 hr with 1 μ M beta-lactamase protein at a NaCl-adjusted osmolality of 700 mOsmol/kg as in (A) in the presence of 20 ng/ml of epidermal growth factor (EGF), 20 ng/ml of basic fibroblast growth factor (FGF), 20 ng/ml of platelet-derived growth factor (PDGF), 20 ng/ml of insulin growth factor (IGF), 2.5 μ g/ml of insulin, and combinations of growth factors as indicated. Beta-lactamase values of cells in transduction media without growth factor (bar #2) were set at 100%, and beta-lactamase values of cells in isotonic transduction media (bar #1) were set at 0%. Open circles indicate relative BrdU incorporation by the transduced cells. BrdU incorporation of untransduced cells was set at 100%, and BrdU incorporation of mitomycin-C-treated cells was set at 0%. Mean \pm SD; n = 3.

(D) Left: schematic representation of the macropinocytosis quantification. Right: to assess whether the transduction buffer would permit the simultaneous incorporation of proteins and non-protein molecules, we analyzed macropinocytosis-mediated uptake of TMR dextran (red) and fluorescently labeled BSA protein (cyan) by GFP-expressing MEFs. Merge of red and cyan gives white by additive color mixture. Transduced cells were incubated at 700 mOsmol/kg with 25 mM NDSB-201. The macropinocytosis inhibitor, EIPA (ethylisopropylamiloride), inhibits uptake of TMR dextran and BSA protein. Nuclei were stained with Hoechst 33342 (blue). Scale bar, 50 μ m.

(E) Left: schematic representation of the mAG-GAL3 reporter assay. Upon initiation of transduction, extracellularly applied protein is taken up into macropinosomes (black vesicles). Intracellular disruption of the macropinosome membrane releases the macropinosome content into the cytoplasm and allows entry of cytosolic mAG-GAL3 protein, resulting in a bright fluorescent signal (bright green vesicles). Right: mAG-GAL3 cells were incubated with transduction media at 700 mOsmol/kg supplemented with 25 mM NDSB-201 with or without the macropinocytosis inhibitor EIPA as indicated. Untreated cells were included as negative control. Note that, under transducing conditions (middle), mAG-GAL3 accumulates in the compromised macropinosomes. Scale bar, 200 μ m.

(F) Measurement of protein transduction activity, macropinocytosis, and macropinosome vesicle leakage of NDSB-201 and examples of derivative compounds. Cells were incubated with transduction buffer at 700 mOsmol/kg with different transduction compounds or left untreated, as indicated. Left: relative beta-lactamase protein incorporation in MEFs. Beta-lactamase transduction of cells in isotonic transduction media (black bar) was set at 1. Middle: macropinocytosis levels were measured by TMR dextran incorporation in cells treated as described above, and total area of dextran positive vesicles per cell was determined. Right: macropinosome leakage was determined by measuring total area of mAG-Gal3-positive vesicles per cell. Mean \pm SD; n = 3.

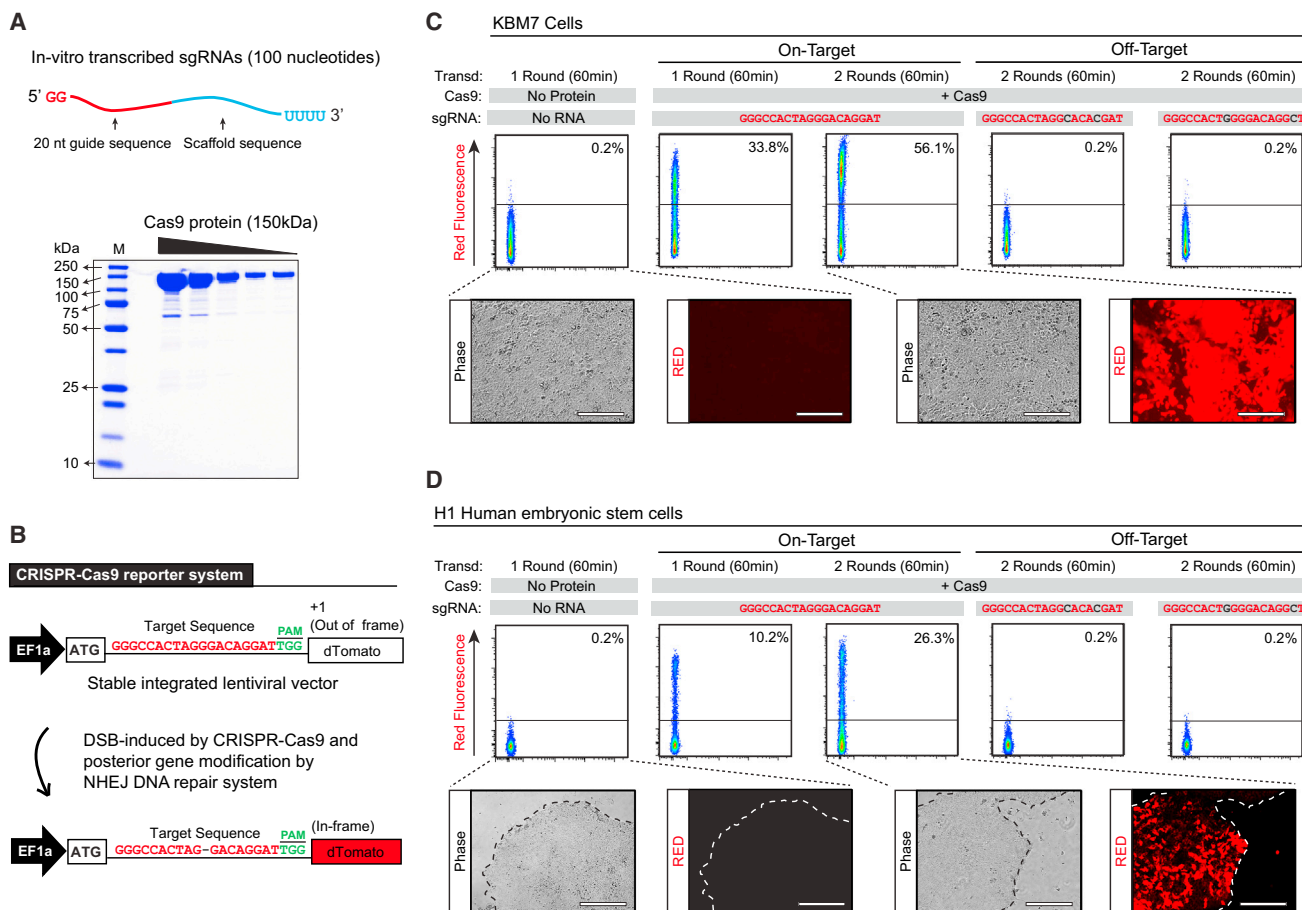


Figure 6. Gene Editing Using Simultaneous Transduction of Recombinant Cas9 Protein and sgRNA

(A) Top: schematic representation of the in-vitro-transcribed sgRNAs containing 20 nucleotides of guide sequence and 80 nucleotides of scaffold sequence. Bottom: protein gel of recombinant purified *Streptococcus pyogenes* Cas9 protein.

(B) Schematic representation of the CRISPR-Cas9 reporter system. Cells were transduced with a lentiviral vector containing the CRISPR-Cas9 target sequence followed by an out-of-frame sequence of dTomato gene. CRISPR-Cas9 induced DNA double-strand break in the target sequence, followed by NHEJ repair that induces DNA deletions and/or insertions. Those DNA modifications may restore the dTomato reading frame, producing red cellular fluorescence. DNA sequences in red and green represent the "target sequence," where red and green text represents the "sgRNA binding" sequence and the "protospacer-adjacent motif, PAM" sequence, respectively.

(C) CRISPR-Cas9 reporter KBM7 cells were transduced with Cas9 protein and target sgRNA. Negative control was cells transduced without Cas9 and sgRNA. Specificity controls were performed by transducing cells with Cas9 protein and off-target sgRNAs. The percentage of dTomato-positive cells was determined by flow cytometry analysis. Bottom shows phase contrast and fluorescent images for indicated conditions. Scale bar, 250 μ m.

(D) CRISPR-Cas9 reporter H1 human embryonic stem cells were transduced with Cas9 protein and on-target sgRNA. Negative control was cells transduced without Cas9 and sgRNA. Specificity controls were performed by transducing cells with Cas9 protein and off-target sgRNAs. The percentage of dTomato-positive cells was determined by flow cytometry analysis. Bottom shows phase contrast and fluorescent images for indicated conditions. Dotted lines delineate the border of the hES colony. White scale line represents 50 μ m.

cells was determined. Samples transduced with Cas9 protein and *DPH7* sgRNAs yielded high levels of cell survival, whereas no viable cells were detected in diphtheria-toxin-treated wild-type KBM7 cells or in cells transduced with Cas9 protein with a control sgRNA (Figure 7A). DNA sequence analysis on the pool of diphtheria-toxin-resistant cells demonstrated *DPH7* gene disruption at the sgRNA target site in all resistant cells (Figures 7B and S5B), confirming that diphtheria toxin resistance was the result of Cas9-sgRNA targeting. Similar results were obtained when H1 human ESCs were targeted with recombinant Cas9 protein coupled to *DPH7* sgRNAs (Figure 7C).

To determine the frequency of biallelic *DPH7* gene disruption, we transduced KBM7 and H1 cells with Cas9 protein and the corresponding *DPH7* sgRNA as described above. Upon transduction, single cells were sorted into 384-well plates (Figure 7D). After a week, emerging clones were treated with diphtheria toxin, and resistant clones were counted to quantify the percentage of knockout clones. Four out of six sgRNAs yielded around 70% resistant clones, which is a remarkable efficiency considering that diphtheria resistance requires biallelic deletion of *DPH7* gene (Figure 7D). Indeed, sequence analysis revealed biallelic mutations at the sgRNA target sites in all clones analyzed

(Figure 7E, top). Similar results and knockout efficiency were obtained upon transduction of human ESCs (Figure 7E, bottom). Above results demonstrate the particular strength of the iTOP-CRISPR/Cas9 system in enabling high-efficiency gene editing in primary (stem) cells (Figure S5C). *DPH7* knockout clones of hESCs retained expression of essential hESC markers, as well as the ability to generate derivatives of all three germ layers in vitro, demonstrating that iTOP-CRISPR/Cas9 gene knockout did not affect stem cell pluripotency (Figure S6).

Conclusions

Despite vast improvement in technologies for the delivery of DNA or RNA into cells, the manipulation of primary cells often remains difficult, with low percentages of targeted cells, poor control over insert copy number, and/or unstable gene expression levels. The ability to efficiently transduce native proteins into primary cells offers new opportunities for direct cell manipulation without the need for DNA or RNA intermediates. Proteins allow cell manipulation in a non-integrative manner and are particularly suited in binary systems in which a single, transient cell manipulation results in a permanent change in cell function, identity, or (epi)genetic state.

The iTOP system described here is highly efficient and flexibly adaptable. Variation in NaCl hypertonicity, type and concentration of transduction compound, and variation in transduction time can be fine-tuned to the needs of the user, the specific target cell type, and the biochemical characteristics of the transduced protein. Because the amount of transduced protein is directly related to the extracellular protein concentration, the system allows narrow dosage of the effective intracellular protein levels.

The CRISPR/Cas9 gene editing has revolutionized our ability to modulate the genome and development of a safe and efficient means to apply this technology in primary cells allowing the use of CRISPR/Cas9 in the modulation of genetic defects. Recent reports demonstrate that delivery of recombinant Cas9 protein using CPPs, electroporation, or cationic lipids results in effective gene editing of immortalized cell lines, but primary cells remain a challenge (Kim et al., 2014; Ramakrishna et al., 2014; Zuris et al., 2014). We demonstrate that the iTOP system allows highly efficient gene modification upon transduction of recombinant Cas9 protein and in-vitro-transcribed sgRNA (iTOP-CRISPR/Cas9). The transient nature of iTOP-CRISPR/Cas9 assures that the transduced gene-editing system does not remain inside the cell, leaving only the editing event as a permanent result of the cell manipulation. The high efficiency to knockout genes using protein iTOP has appealing application in research and perhaps will allow new therapeutic avenues for the treatment of genetic disease. In addition to gene editing, protein iTOP may have application in other areas, for example in the modulation of intracellular signaling pathways, in cell differentiation/dedifferentiation, or as adjuvants in dendritic cell immunization.

EXPERIMENTAL PROCEDURES

Cell Lines

COS7 cells—ATCC, H1 human ESCs—WiCell, and KBM7 cells were a gift from Dr. Brummelkamp, NKI Amsterdam. Mouse embryonic neural stem (NSC) cells

were derived from E13.5 mice embryos as described by Louis and Reynolds (2005). Mouse gut organoids were derived from adult mice as reported by Sato et al. (2009).

Cell Proliferation Assay

Cell proliferation was determined using the Cell Proliferation ELISA kit, BrdU (Roche, 11669915001) following manufacturer's instructions. For more details, see Supplemental Information.

Transduction Buffer

5× Transduction Buffer

500 mM NaCl, 25 mM NaH₂PO₄, 250 mM NDSB-201, 150 mM glycerol, 75 mM glycine, 1.25 mM MgCl₂, 1 mM 2-mercaptoethanol at pH 8.0. For more details, see Supplemental Information.

CRISPR/Cas9 Transduction Media

Opti-MEM media (Life Technologies) supplemented with 542 mM NaCl, 333 mM GABA, 1.67× N2, 1.67× B27, 1.67× non-essential amino acids, 3.3 mM Glutamine, 167 ng/ml bFGF2, and 84 ng/ml EGF. For more details on media preparation and catalog numbers, see Supplemental Information.

Recombinant Protein Production

His-tagged recombinant proteins were produced in *E. Coli* and purified using Ni-agarose affinity chromatography. Detailed methods and procedures are described in the Extended Experimental Procedures, as well as Tables S1 and S5.

Protein Transduction

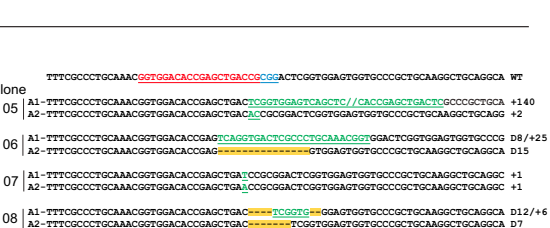
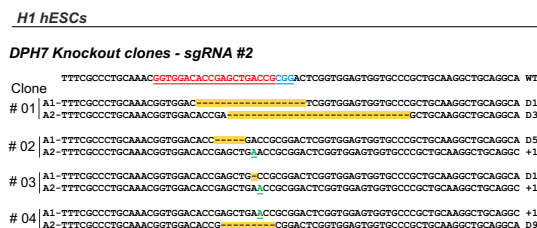
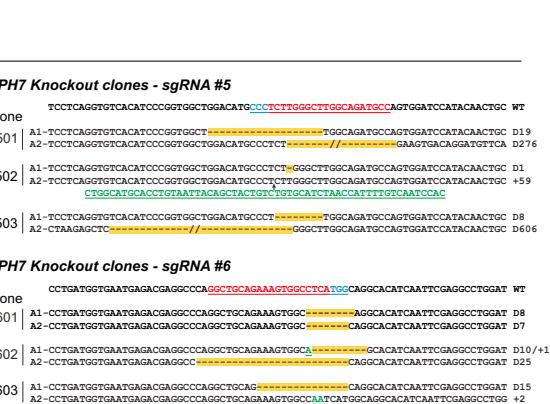
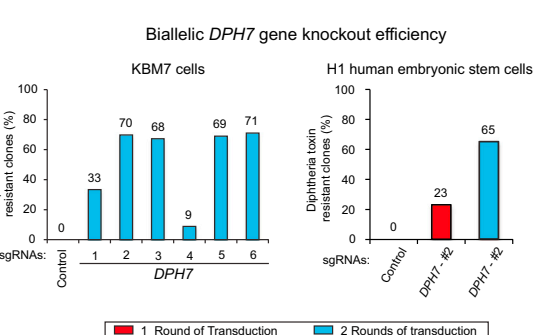
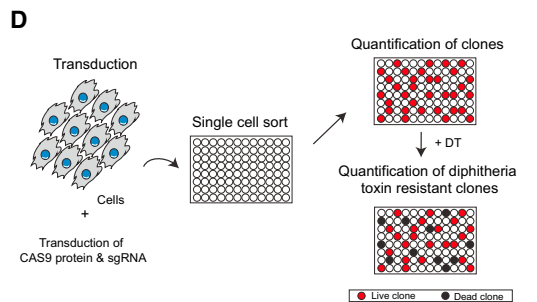
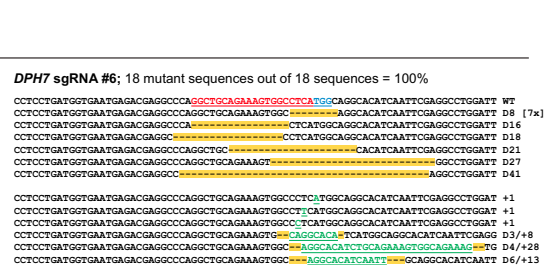
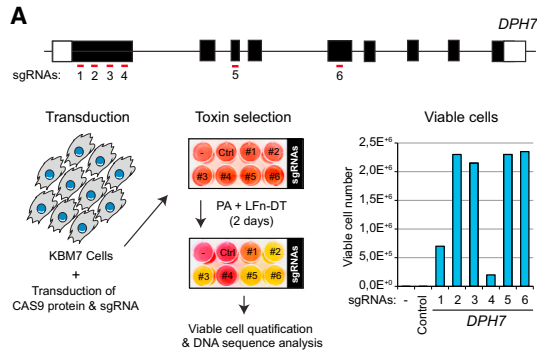
We have established two transduction protocols that work best for most cell types and proteins to be transduced, typically yielding transduction efficiencies of 60%–90%. In the first protocol, transduction is performed for 12 hr at an osmolality of 500 mOsmol/kg (protocol 12/500). In brief, a day before protein transduction, cells were plated in the appropriate culture media without antibiotics. Next day, 5× transduction buffer with the protein of interest was mixed with cell culture media to obtain 1× transduction media at a tonicity of 500 mOsmol/kg and added to the cells. Cells were incubated for 12 hr, after which transduction media were removed and exchanged for regular culture media. In the second protocol, protein transduction is performed for 3 hr at an osmolality of 700 mOsmol/kg (protocol 3/700). Cells were plated as above. The next day, 1× transduction media with the protein of interest were added as above, and final osmolality was adjusted to 700 mOsmol/kg using NaCl. Cells were incubated for 3 hr, after which transduction media were removed and exchanged for regular culture media.

Beta-Lactamase Transduction and Quantification of Beta-Lactamase Incorporation

Beta-lactamase transduction in MEFs and mES cells was performed using the 3/700 and 12/500 protocol, respectively. After protein transduction, beta-lactamase activity was measured using the CCF2-AM loading kit (Life Technologies, K1032) following the manufacturer's instructions. Relative beta-lactamase activity was calculated using the following formula: relative beta-lactamase activity (%) = $(X - B) / (A - B) \times 100$, where X represents the beta-lactamase value of the sample; A is the beta-lactamase value of a reference sample, and B is the beta-lactamase value of cells transduced in isotonic media. For more details see Supplemental Information.

CRISPR-Cas9 Transduction

KBM7 cells were transduced with Cas9 protein and sgRNA with transduction media at 1,250 mOsmol/kg during 60 min in a 96-well format. In brief, 120,000 KBM7 cells were seeded per well using KBM7 media (IMDM supplemented with 10% FBS, non-essential amino acids, glutamax, 2-mercaptoethanol). The next day, 3 hr before transduction, cells were incubated 250 ng/ml of the interferon inhibitor B18R (eBiosciences). Then, cell culture media was removed and complete transduction mixture (10 μl of Cas9 in 5× transduction buffer, 30 μl of CRISPR/Cas9 transduction media, and 10 μl of sgRNA solution) was added to cells. sgRNA and DNA plasmid sequences are shown in Data S1, Data S2, and Data S3. Cells were incubated during 60 min at 37°C, and the transduction



(legend on next page)

media was carefully replaced by standard culture media supplemented with 250 ng/ml of B18R. Cells were incubated for 48 hr and analyzed by flow cytometry. Knockout of endogenous *DPH7* gene was determined by adding LFn-DT (Carette et al., 2009) and DNA sequencing of the surviving cells. Two rounds of Cas9/sgRNA transduction were performed as above with a recovery time between transductions of 5–7 days. See Tables S3 and S4 for primer sequences for genomic DNA amplification and surveyor assay.

H1 human ESCs were transduced as above with slight modifications. Cells were passaged by mechanical dissociation into small clumps following mTeSR1 manufacturer's instructions and seeded on a matrigel-coated plate. Cells were transduced 2–3 days after seeding when they reached a confluency of 80%–90%. Two rounds of Cas9/sgRNA transduction were performed the same as above with a recovery time between transductions of 5–7 days. Cells were not passaged between two transductions.

SUPPLEMENTAL INFORMATION

Supplemental Information includes Extended Experimental Procedures, six figures, five tables, and three data files and can be found with this article online at <http://dx.doi.org/10.1016/j.cell.2015.03.028>.

AUTHOR CONTRIBUTIONS

D.S.D. conceived the project, designed and performed all experiments, interpreted the results, and wrote the manuscript. R.J.P. helped to set up and execute imaging-based quantification of macropinocytosis and vesicle release, and A.P. performed imaging experiments, aided with data analysis. W.R.K. and H.C. helped with the culture and transduction of gut organoids, and V.P. generated the Nhe1 knockout cells. R.J.L. helped with the setup of the CRISPR/Cas system. H.R. helped with recombinant protein synthesis, and N.G. conceived and directed the project, designed experiments, interpreted the results, and wrote the manuscript.

ACKNOWLEDGMENTS

The authors thank Sarah Opitz for critically reading the manuscript; Nune Schelling for technical support; Stefan van der Elst of the Hubrecht Institute FACS facility for help with cell sorting; Anko de Graaf of the Hubrecht Institute imaging facility; David Egan of the Cell Screening facility at the UMCU; Gustavo Mostoslavsky for providing lentiviral vectors; Saravanan Manikam and Antoinette Killian for help with NDSB analysis; Thijn Brummelkamp for providing the KBM7 cells; Liquan Luo and Paul Krimpenfort for providing mTmG reporter mice; and Bart van Steen and Jack den Hartog for help with compound synthesis. This work was funded in part by The Netherlands Organization for Scientific Research (NWO, project 91796323 and 91610138, and American Heart Association 11BGIA7720005). D.S.D. and

N.G. are co-inventors on a patent application describing the transduction technology PCT/IB2014/064127 and co-founders of NTrans technologies.

Received: October 28, 2014

Revised: December 19, 2014

Accepted: March 12, 2015

Published: April 23, 2015

REFERENCES

- Boyer, L.A., Lee, T.I., Cole, M.F., Johnstone, S.E., Levine, S.S., Zucker, J.P., Guenther, M.G., Kumar, R.M., Murray, H.L., Jenner, R.G., et al. (2005). Core transcriptional regulatory circuitry in human embryonic stem cells. *Cell* 122, 947–956.
- Carette, J.E., Guimaraes, C.P., Varadarajan, M., Park, A.S., Wuethrich, I., Godarova, A., Kotecki, M., Cochran, B.H., Spooner, E., Ploegh, H.L., and Brummelkamp, T.R. (2009). Haploid genetic screens in human cells identify host factors used by pathogens. *Science* 326, 1231–1235.
- Charpentier, E., and Doudna, J.A. (2013). Biotechnology: Rewriting a genome. *Nature* 495, 50–51.
- Commisso, C., Flinn, R.J., and Bar-Sagi, D. (2014). Determining the macropinocytic index of cells through a quantitative image-based assay. *Nat. Protoc.* 9, 182–192.
- Kim, S., Kim, D., Cho, S.W., Kim, J., and Kim, J.S. (2014). Highly efficient RNA-guided genome editing in human cells via delivery of purified Cas9 ribonucleoproteins. *Genome Res.* 24, 1012–1019.
- Kültz, D., Madhany, S., and Burg, M.B. (1998). Hyperosmolality causes growth arrest of murine kidney cells. Induction of GADD45 and GADD153 by osmosensing via stress-activated protein kinase 2. *J. Biol. Chem.* 273, 13645–13651.
- Louis, S.A., and Reynolds, B.A. (2005). Generation and differentiation of neurospheres from murine embryonic day 14 central nervous system tissue. *Methods Mol. Biol.* 290, 265–280.
- Lundberg, M., and Johansson, M. (2001). Is VP22 nuclear homing an artifact? *Nat. Biotechnol.* 19, 713–714.
- Mortensen, M., Ebert, B., Wafford, K., and Smart, T.G. (2010). Distinct activities of GABA agonists at synaptic- and extrasynaptic-type GABAA receptors. *J. Physiol.* 588, 1251–1268.
- Okada, C.Y., and Rechsteiner, M. (1982). Introduction of macromolecules into cultured mammalian cells by osmotic lysis of pinocytotic vesicles. *Cell* 29, 33–41.
- Paz, I., Sachse, M., Dupont, N., Mounier, J., Cederfur, C., Enninga, J., Leffler, H., Poirier, F., Prevost, M.C., Lafont, F., and Sansonetti, P. (2010). Galectin-3, a marker for vacuole lysis by invasive pathogens. *Cell. Microbiol.* 12, 530–544.

Figure 7. Endogenous Gene Disruption Induced by CRISPR-Cas9 Transduction

(A) Top: schematic depiction of the *DPH7* gene and target sites of six different sgRNAs used in the experiments. Bottom: schematic depiction of the Cas9-sgRNA transduction and diphtheria toxin selection procedure. KBM7 cells were transduced twice with Cas9 and *DPH7* sgRNAs with a 7 day interval between transductions. Controls were untreated cells and cells transduced with Cas9 together an AAVS1 sgRNA (CrtI). 7 days after the second transduction, cells were treated with LFn-DTA. Bar graph shows the number of viable cells after 2 days of diphtheria toxin selection.

(B) Analysis of target-site mutations in the endogenous *DPH7* gene in diphtheria-toxin-resistant KBM7 cells after transduction of recombinant Cas9 protein and in-vitro-transcribed sgRNA. The wild-type (WT) sequence is shown at the top. Start codon is indicated with underlined ATG. Deletions are indicated by dashes and yellow background and insertions with underlined green text. The sizes of the insertions (+) or deletions (D) are indicated to the right of each mutated site. Numbers in brackets show the amount of sequences obtained. In the wild-type sequences are indicated the sgRNA binding site and PAM sequence in underlined red and blue text, respectively. The primers used to amplify the different *DPH7* genomic regions are listed in Table S3.

(C) Analysis of target-site mutations at endogenous *DPH7* gene in diphtheria toxin-resistant H1 hESCs after transduction of recombinant Cas9 protein and in-vitro-transcribed *DPH7* sgRNAs. Annotation as in (B).

(D) Schematic representation of the experimental design used for the quantification of biallelic *DPH7* gene knockout by Cas9-sgRNA transduction. KBM7 or hESCs were transduced once or twice (as indicated) with Cas9 together with *DPH7* sgRNAs. Control was cells transduced with Cas9 and an AAVS1 sgRNA. After 3 days, single cells were sorted into 384-well plates using a flow cytometer. 7 days later, the number of expanding clones was counted, and cells were treated with diphtheria toxin. After 2 days of diphtheria toxin treatment, surviving clones were counted. *DPH7* knockout efficiency was calculated as the percentage of total single-cell clones that were diphtheria toxin resistant of total clones obtained.

(E) Biallelic DNA sequence analysis of diphtheria toxin-resistant clones in KBM7 cells and H1 hESCs. Annotation as in (B). A1, allele 1; A2, Allele2. The sizes of the insertions (+) or deletions (D) are indicated to the right of each mutated site.

- Ramakrishna, S., Kwaku Dad, A.B., Beloor, J., Gopalappa, R., Lee, S.K., and Kim, H. (2014). Gene disruption by cell-penetrating peptide-mediated delivery of Cas9 protein and guide RNA. *Genome Res.* 24, 1020–1027.
- Ray, K., Bobard, A., Danckaert, A., Paz-Haftel, I., Clair, C., Ehsani, S., Tang, C., Sansonetti, P., Tran, G.V., and Enninga, J. (2010). Tracking the dynamic interplay between bacterial and host factors during pathogen-induced vacuole rupture in real time. *Cell. Microbiol.* 12, 545–556.
- Redon, C.E., and Bonner, W.M. (2011). High salt and DNA double-strand breaks. *Proc. Natl. Acad. Sci. USA* 108, 20281–20282.
- Sato, T., Vries, R.G., Snippert, H.J., van de Wetering, M., Barker, N., Stange, D.E., van Es, J.H., Abo, A., Kujala, P., Peters, P.J., and Clevers, H. (2009). Single Lgr5 stem cells build crypt-villus structures in vitro without a mesenchymal niche. *Nature* 459, 262–265.
- Schwarze, S.R., Hruska, K.A., and Dowdy, S.F. (2000). Protein transduction: unrestricted delivery into all cells? *Trends Cell Biol.* 10, 290–295.
- Srinivas, S., Watanabe, T., Lin, C.S., William, C.M., Tanabe, Y., Jessell, T.M., and Costantini, F. (2001). Cre reporter strains produced by targeted insertion of EYFP and ECFP into the ROSA26 locus. *BMC Dev. Biol.* 1, 4.
- Tomilin, A., Reményi, A., Lins, K., Bak, H., Leidel, S., Vriend, G., Wilmanns, M., and Schöler, H.R. (2000). Synergism with the coactivator OBF-1 (OCA-B, BOB-1) is mediated by a specific POU dimer configuration. *Cell* 103, 853–864.
- Vuillard, L., Braun-Breton, C., and Rabilloud, T. (1995). Non-detergent sulphobetaines: a new class of mild solubilization agents for protein purification. *Biochem. J.* 305, 337–343.
- Zhou, J., Fan, J., and Hsieh, J.T. (2006). Inhibition of mitogen-elicited signal transduction and growth in prostate cancer with a small peptide derived from the functional domain of DOC-2/DAB2 delivered by a unique vehicle. *Cancer Res.* 66, 8954–8958.
- Zuris, J.A., Thompson, D.B., Shu, Y., Guiling, J.P., Bessen, J.L., Hu, J.H., Maeder, M.L., Joung, J.K., Chen, Z.-Y., and Liu, D.R. (2014). Cationic lipid-mediated delivery of proteins enables efficient protein-based genome editing in vitro and in vivo. *Nat. Biotech.* 33, 73–80.

Injury-Induced HDAC5 Nuclear Export Is Essential for Axon Regeneration

Yongcheol Cho, Roman Sloutsky, Kristen M. Naegle, and Valeria Cavalli*

*Correspondence: cavalli@pcg.wustl.edu

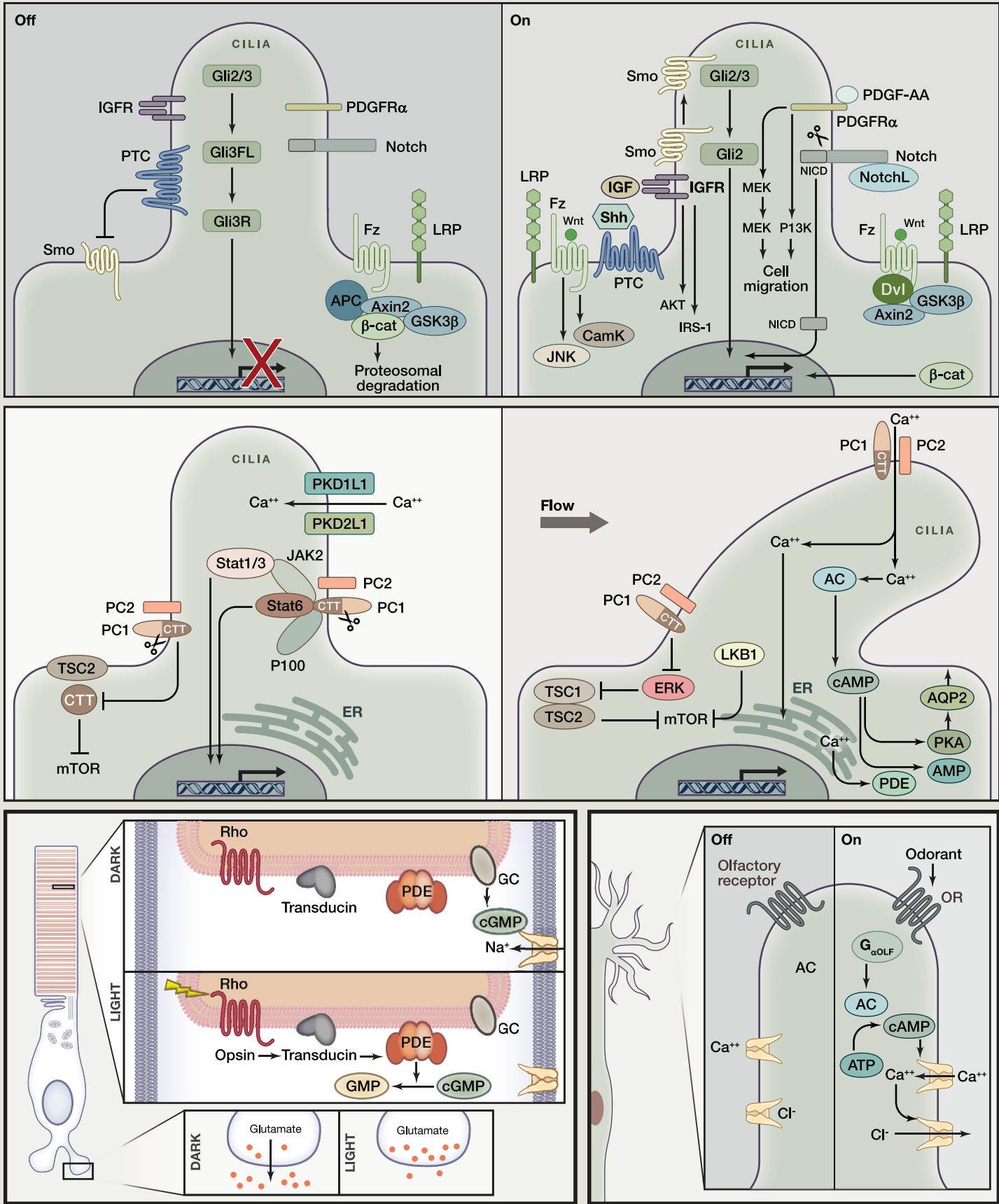
<http://dx.doi.org/10.1016/j.cell.2015.04.019>

(Cell 155, 894–908; November 7, 2013)

After the publication of this article, we noticed an error in the text describing the generation of cytosolic-trapped HDAC5 (GFP-HDAC5cyto) in both the Results and Extended Experimental Procedures sections. The original text mistakenly referred to mutation of serine residues 259 and 498 to aspartic acid, generating a mostly cytoplasmic HDAC5 (GFP-HDAC5cyto) mutant. This sentence omitted that, in addition, serine residue 280 was mutated to alanine. Indeed, the sequential mutagenesis process of the three point mutations was first serine 280 to alanine, second serine 259 to aspartic acid, and third serine 498 to aspartic acid. Hence, the accurate description is that mutation of serine residues 259 and 498 to aspartic acid and serine residue 280 to alanine generated mostly cytoplasmic HDAC5 (GFP-HDAC5cyto) mutant. This error in the description of the HDAC5cyto construct, which was used in Figures 5E and S2A, does not affect the interpretation of the data, the results in the paper, or the overall conclusion of the study. We apologize for any confusion that this error may have caused.

SnapShot: Sensing and Signaling by Cilia

Kurt Zimmerman and Bradley K. Yoder
Department of Cell, Developmental, and Integrative Biology, University of Alabama at Birmingham, Birmingham, AL 35294, USA



SnapShot: Sensing and Signaling by Cilia

Cell

Kurt Zimmerman and Bradley K. Yoder

Department of Cell, Developmental, and Integrative Biology, University of Alabama at Birmingham, Birmingham, AL 35294, USA

Primary cilia are cellular appendages that coordinate diverse sensory and signaling activities. They are important for proper mammalian development, adult tissue homeostasis, and vision and odorant detection, and their dysfunction contributes to disease pathology and developmental defects.

Signaling

The most extensively defined cilia-associated signaling pathway is hedgehog (Hh). Hh ligands bind to the receptor patched (Ptc) located in the cilium. Ptc then exits the cilium, relieving inhibition of Smoothened (Smo). Smo accumulates in the cilium and promotes activation and nuclear translocation of the Gli2 transcription factor and prevents formation of the Gli3 repressor. Many of the developmental defects observed in cilia mutants such as polydactyly and neural tube mis-patterning are caused by dysfunctional Hh signaling. Hh signaling also regulates autophagy by acting on autophagy-related proteins at the cilium base.

In the absence of canonical Wnt, β -catenin is targeted for destruction by the GSK3 β /Axin2/APC complex. Upon binding of Wnt to the Frizzled (Fz) receptor, Dishevelled (Dvl) is recruited to Fz, resulting in the destruction of the β -catenin degradation complex. Stabilized β -catenin translocates to the nucleus activating Wnt target genes. The noncanonical Wnt pathway is independent of β -catenin and functions through calmodulin kinase (CamK) and JNK to cause cytoskeletal rearrangements that regulate cell morphology and orientation in a planar field, referred to as planar cell polarity (PCP). Cilia mutant mice have PCP defects in the inner ear, and knockdown of ciliary proteins in zebrafish results in PCP phenotypes, including defective convergent extension movements and tail malformations. Furthermore, the ciliary localized protein, Inversin, binds to and blocks Dvl-mediated activation of the canonical Wnt pathway and functions as a switch between canonical and non-canonical Wnt pathways.

Platelet-derived growth factor receptor α (PDGFR α) accumulates in the cilium upon growth arrest. Following PDGF-AA binding, PDGFR α activates the Mek1/2-Erk1/2 pathway or the PI3K/AKT pathway, promoting directional cell migration. Cells lacking cilia exhibit non-directed migration.

Upon binding of the Notch ligand to its receptors, the Notch intracellular domain (NICD) is cleaved and translocates to the nucleus, where it associates with the DNA-binding protein RBP-j. Notch receptors and processing enzymes co-localize in cilia of skin epidermal cells. Activation of the Notch pathway induces skin barrier formation that fails to occur in the absence of cilia.

Both PKD patients and mouse models of ciliary dysfunction exhibit increased mTOR activity. mTOR activity is regulated through PC1 function, either directly upstream through MEK/ERK or via a TSC-dependent pathway. Bending of the cilium decreases mTOR activity in an LKB1-dependent manner.

The hormone leptin signals through its receptor (ObRb) to regulate Jak/Stat activity and food intake. Bardet-Biedl syndrome (BBS) patients and mice exhibit obesity. BBS1 can bind ObRb and may mediate its localization near the base of cilia; however, ObRb has yet to be observed in the cilia. Mice lacking cilia in the leptin-responsive POMC hypothalamic neurons also develop obesity; however, leptin signaling is normal in these mice. Thus, the connection between leptin and cilia remains controversial.

The insulin growth factor 1 (IGF-1) receptor is localized to the primary cilium in 3T3-L1 preadipocytes and has increased sensitivity to insulin stimulation compared to non-ciliary IGF-1 receptors. AKT and IRS-1 are recruited to the basal body during cilium formation and are phosphorylated by the receptor kinase located in the cilium. Loss of IFT88 or Kif3a, which disrupts ciliogenesis, prevents IGF-1-receptor-mediated adipocyte differentiation.

Mechanosensation

In epithelial cells, bending the cilium by fluid flow increases cytoplasmic calcium through polycystin 1 (PC1) and polycystin 2 (PC2), which form a channel complex. Mutations in PC1 or PC2 impair calcium signaling and result in polycystic kidney disease (PKD). The polycystin-related proteins PKD1L1 and PKD2L1 also act as ciliary localized calcium channels.

Cilia function as a mechanosensor on the embryonic node, an important structure formed during gastrulation that specifies left-right body axis. Motile cilia on the node generate fluid movement that is sensed by neighboring non-motile cilia. Deflection of the non-motile cilia induces a left-sided calcium signal that is dependent on PC2, thereby explaining the left-right axis defects in PC2 mutant mice.

Cilia mechanosensation is also important for STAT signaling. STAT6 binds to the C-terminal tail (CTT) of PC1. PC1 CTT is proteolytically cleaved in the absence of flow, allowing STAT6 and the CTT to enter the nucleus and interact with the co-activator P100. Mutations preventing CTT cleavage cause PKD. PC1 also regulates STAT1 and STAT3, although it may not be dependent on mechanosensation.

Vision and Smell

Light activation of the G-protein-coupled receptor (GPCR) rhodopsin (Rho), located in the outer segment of rods (highly modified form of cilia), initiates the visual transduction pathway through the G protein transducin. Transducin induces phosphodiesterase, causing cGMP to be converted to GMP. The drop in cGMP leads to closure of sodium channels and hyperpolarization of the rod inhibiting glutamate release. In the olfactory system, each olfactory neuron expresses a single type of olfactory receptor (OR) located in the cilium. ORs are GPCRs that bind a specific odorant and activate adenylyl cyclase (AC) through the G protein associated with the OR. The AC-mediated increase in cAMP opens cyclic nucleotide-gated ion channels in the cilia membrane, resulting in an influx of sodium and calcium and efflux of chloride, depolarizing the neuron.

Multiple other GPCRs localize to cilia, including somatostatin receptor 3 (Sstr3), melanin-concentrating hormone receptor 1 (Mchr1), serotonin subtype 6 receptor (5-HT₆), dopamine receptor 1, and G-protein-coupled receptor 161 (Gpr161), but the role of cilia in their regulation is not currently known.

ACKNOWLEDGMENTS

We would like to gratefully acknowledge funding provided for K.Z. (2K12GM088010-06) and B.Y. (DK065655).

REFERENCES

- Ezratty, E.J., Stokes, N., Chai, S., Shah, A.S., Williams, S.E., and Fuchs, E. (2011). *Cell* 145, 1129–1141.
- Goetz, S.C., and Anderson, K.V. (2010). *Nat. Rev. Genet.* 11, 331–344.
- Ibragimov-Beskrovnaya, O., and Natoli, T.A. (2011). *Trends Mol. Med.* 17, 625–633.
- Kleene, S.J. (2008). *Chem. Senses* 33, 839–859.
- Praetorius, H.A. (2015). *Am. J. Physiol. Cell Physiol.* 308, C198–C208.
- Takao, D., Nemoto, T., Abe, T., Kiyonari, H., Kajiura-Kobayashi, H., Shiratori, H., and Nonaka, S. (2013). *Dev. Biol.* 376, 23–30.
- Weimbs, T., Olsan, E.E., and Talbot, J.J. (2013). *JAK-STAT* 2, e23650.
- Yildiz, O., and Khanna, H. (2012). *Vision Res.* 75, 112–116.
- Zhu, D., Shi, S., Wang, H., and Liao, K. (2009). *J. Cell Sci.* 122, 2760–2768.